A numerical and reliability-based investigation into the technical feasibility of a Dutch radioactive waste repository in Boom Clay

Radioactive substances and ionizing radiation are used in medicine, industry, agriculture, research, education and electricity production. This generates radioactive waste. In the Netherlands, this waste is collected, treated and stored by COVRA (Centrale Organisatie Voor Radioactief Afval). After interim storage for a period of at least 100 years radioactive waste is intended for disposal. There is a world-wide scientific and technical consensus that geological disposal represents the safest long-term option for radioactive waste.

Geological disposal is emplacement of radioactive waste in deep underground formations. The goal of geological disposal is long-term isolation of radioactive waste from our living environment in order to avoid exposure of future generations to ionising radiation from the waste. OPERA (OnderzoeksProgramma Eindberging Radioactief Afval) is the Dutch research programme on geological disposal of radioactive waste.

Within OPERA, researchers of different organisations in different areas of expertise will cooperate on the initial, conditional Safety Cases for the host rocks Boom Clay and Zechstein rock salt. As the radioactive waste disposal process in the Netherlands is at an early, conceptual phase and the previous research programme has ended more than a decade ago, in OPERA a first preliminary or initial safety case will be developed to structure the research necessary for the eventual development of a repository in the Netherlands. The safety case is conditional since only the long-term safety of a generic repository will be assessed. OPERA is financed by the Dutch Ministry of Economic Affairs and the public limited liability company Electriciteits-Produktiemaatschappij Zuid-Nederland (EPZ) and coordinated by COVRA. Further details on OPERA and its outcomes can be accessed at www.covra.nl.

This report concerns a study conducted in the framework of OPERA. The conclusions and viewpoints presented in the report are those of the author(s). COVRA may draw modified conclusions, based on additional literature sources and expert opinions. A .pdf version of this document can be downloaded from www.covra.nl.

TUDelft Delft University of Technology

A numerical and reliability-based investigation into the technical feasibility of a Dutch radioactive waste repository in Boom Clay

January 2015

Patrick Arnold[1], Philip J. Vardon[1], Michael A. Hicks[1]
Jan Fokkens[2] and Peter A. Fokker[3]

[1] Delft University of Technology (TUD), Geo-Engineering Section, Delft
[2] Nuclear Research and consultancy Group (NRG), Petten
[3] Nederlandse Organisatie voor Toegepast Natuurwetenschappelijk Onderzoek (TNO), Utrecht

Executive summary

The *Onderzoeks Programma Eindberging Radioactief Afval* (OPERA) is the third national research programme for the geological disposal of radioactive waste in the Netherlands, operating during the period 2011 to 2016. This document is the final report of Work Package 3.1, where the principal technical feasibility of the current OPERA reference design of a radioactive waste disposal facility, in Boom Clay at a depth of about 500m was investigated, during the period 12-2012 till 12-2014.

The literature review revealed a significant uncertainty in the in situ Boom Clay property values at larger depths. This can be attributed to both the scarcity of high quality data as well as the variability of the geological, geochemical and geomechanical host rock properties between potential disposal sites. One of the main objectives of this work was to develop a *Reliability Based Design* (RBD) framework which, based on probability theory and the current knowledge, accounts for the uncertainties in the Boom Clay property values in a quantitative manner and thus allows for a more rigorous assessment of the geomechanical feasibility of the repository system, than by means of a deterministic design approach.

The feasibility of the current OPERA repository reference design has been assessed for individual tunnel galleries at realistic disposal depths with respect to the geomechanical Boom Clay behaviour, due to the excavation, the pre-operational and early post-closure phases. An analytical elasto-plastic strain-softening model has been developed for the preliminary assessment of the main features of the host rock response, but also to provide a computationally cheap tool to test the RBD framework. A more advanced constitutive soil model, the *Hardening Soil* (HS) model, was selected to model the Boom Clay response numerically in two and three dimensions by utilising the PLAXIS *Finite Element* (FE) software package. These geomechanical models have been modularised and implemented in the RBD model framework, which was developed in this work, based on the *Open source initiative to Treat Uncertainties, Risks'N Statistics* (OpenTURNS) scientific library. Using the simulation-based *Monte Carlo Method* (MCM), as well as the approximate *First-* and *Second Order Reliability Method* (FORM/SORM), the probability of failure, as well as the sensitivity of the performance with respect to the degree of uncertainty in the Boom Clay parameters, can be computed.

The scarcity of data (quality, quantity and specification) limited a statistical interpretation of the Boom Clay parameters. Lumping aleatory and epistemic uncertainties, the results show significant uncertainty in the soil strength. The importance of data selection, depth trends and parameter cross-correlation has been emphasised.

A number of geomechanical material models have been assessed against laboratory data, and the models produced and selected include the majority of the observed material features.

The developed analytical model includes strain-softening and elasto-plastic behaviour, while the selected numerical model (HS model) includes hardening behaviour during plastic yielding.

Deterministic investigations into the extent of the plastic zone around the tunnel galleries, as well as the radial pressure on the concrete liner, showed that both are strongly dependent on the strength, as well as the stiffness, of the Boom Clay. The analytical model was found to be most sensitive to a variation in the friction angle and Young's modulus, whereas the deterministic response computed from the numerical model was most sensitive to variations in the cohesion, friction angle, oedometer modulus and secant modulus.

The reliability based assessment showed that, given the input statistics, the current OPERA tunnel gallery design (diameter, liner thickness, spacing) can be deemed fully reliable; that is, no analysis reached the set ultimate limit state criterion (for stability of the tunnels). The performance functions computed via the MCM for different cases show that, besides the mean and variance, the cross-correlation between parameters can have a significant influence. Given the level of reliability, there is, therefore, scope to reduce the tunnel spacing, and consequently reduce the overall tunnel lengths, although further research would be required to ensure that other safety functions are not unduly affected.

FORM and SORM were found to approximate well the system performance and simultaneously decreasing the computational effort. Reliability based sensitivity indices describing the importance of each random variable with respect to the probability of failure were computed. The results show that, besides a variation in the mean estimate, the variance and covariance describing the parameter uncertainty may influence significantly these importance factors.

A set of initial post-closure thermal analyses was undertaken. Due to substantially fewer available data on the Boom Clay thermal material parameters, a deterministic sensitivity analysis was undertaken. Due to the long term interim storage plan in the Netherlands, the peak temperatures were significantly below those likely to cause concerns for safety. This again offers scope to reduce the tunnel spacing.

The current OPERA repository design has been shown to be principally feasible with respect to the geomechanical stability of individual tunnel galleries and thermal performance. A reduction in gallery spacing and/or concrete liner thickness may be considered in further designs. To ensure an optimum design, it is suggested to reduce the uncertainty in the Boom Clay properties, e.g. by performing tests on intact Boom Clay samples, in particular from the proposed repository depth, and to extend the RBD framework to account for the three-dimensional behaviour of a system of parallel and intersecting tunnel galleries by utilising coupled numerical modelling. Furthermore, aspects that have not been included in this work, such as plugs and seals, have not yet been assessed.

Contents

List of Figures

List of Tables

Notation

This list contains definitions of acronyms and symbols including there dimensions and main units used in this dissertation. All symbols are defined within the text. The units are: length [L], mass [M], time [T] and thermodynamic temperature [Θ].

Symbol	Definition	Unit
Acronyms		
ATLAS	Admissible Thermal Loading for Argillaceous Storage	
BENCHPAR	BENCHmark Tests and Guidance on Coupled Processes for Performance Assessment of Nuclear Waste Repositories	
CAR	tertiary Clay As potential host Rock	
CC	Cam-Clay	
CCM	Convergence-Confinement Method	
CDF	Cumulative Distribution Function	
CEC	Cation Exchange Capacity	
CLIPEX	CLay Instrumentation Programme for the EXtension of an underground research laboratory	
Cobyla	Constrained optimization by linear approximation	
COGEMA	Compagnie Générale des Matières Nucléaires	
CORA	Commission on Disposal of Radioactive Waste	
COVRA	Centrale Organisatie Voor Radioactief Afval	
CPT	Cone Penetration Test	
CS	Critical State	
CSD-C	Colis Standard de Déchets - Compactés	
CSD-V	Colis Standard de Déchets - Vitrified	
CSL	Critical State Line	
CT	Computer Tomography	
CU	Consolidated Undrained	
DP	Drucker-Prager	
DZ	Damaged Zone	
EBS	Engineered Barrier System	
ECN	Energieonderzoek Centrum Nederland (Netherlands Energy Research Foundation)	
EP	Elasto-Plastic	
EURATOM	European Atomic Energy Community	
FE	Finite Element	
FEA	Finite Element Analysis	
FORM	First Order Reliability Method	
FOSM	First Order Second Moment method	
GRC	Ground Response Curve	

HB	Hoek-Brown
HLW	High Level Waste
HS	Hardening Soil
HSR	Support Characteristic Curve
ICK	Interdepartementale Commissie voor de Kernenergie
ICL	Intrinsic Compression Line
LDP	Longitudinal Deformation Profile
LEPPMC	Linear Elastic-Perfectly Plastic Mohr Coulomb
LILW	Low- and Intermediate-Level Waste
MBS	Multi-Barrier System
MC	Mohr Coulomb
MCC	Modified Cam-Clay
MCM	Monte Carlo Method
MLW	Medium Level Waste
NATM	New Austrian Tunnelling Method
NC	Normally Consolidated
NCL	Normal Compression Line
NRG	Nuclear Research and consultancy Group (NL)
OC	Over-Consolidated
OCR	OverConsolidation Ratio
OED	Oedometer
OpenTURNS	Open source initiative to Treat Uncertainties, Risks'N Statistics
OPERA	Onderzoeks Programma Eindberging Radioactief Afval
OPLA	OPberging te LAnd
PA	Performance Assessment
PEM	Point Estimate Method
PMF	Probability Mass Function
PMT	Pressuremeter Test
POP	Pre-Overburden Pressure
PRACLAY	Preliminary demonstration test for clay disposal of highly radio-active waste
R&D	Research and Development
RBD	Reliability Based Design
RP	Residual Plastic
SBPTM	Selfboring Pressuremeter Test
SCC	Support Characteristic Curve
SCL	Sedimentation Compression Line
SELFRAC	Fractures and Self-healing within the Excavation Disturbed Zone in Clays
SEM	Scanning Electron Microscopy
SM	Shield Machine
SNF	Spent Nuclear Fuel
SORM	Second Order Reliability Method
SPT	Standard Penetration Test
SQP	Sequential Quadratic Programming
SSC	Soft Soil Creep
TBM	Tunnel Boring Machine

TENORM	Technically Enhanced Naturally Occurring Radioactive Materials	
THMC	Thermo-Hydro-Mechanical and Chemical	
TIMODAZ	Thermal Impact on the Damage Zone around a Radioactive Waste Disposal in Clay Host	
TNO	Nederlandse Organisatie voor Toegepast Natuurwetenschappelijk Onderzoek (NL)	
TOC	Total Organic Carbon	
TRACTOR	Transport of RAdionuclides disposed of in Clay of Tertiary ORigin	
TRUCK	TeRUgneembaar opbergConcept in Klei	
TUD	Delft University of Technology (NL)	
UCT	Uniaxial Compression Test	
URL	Unloading-Reloading Line	
VROM	Ministerie van Volkshuisvesting, Ruimtelijke Ordening en Milieubeheer (Ministry of Housing, Spatial Planning and the Environment - the Netherlands)	
VST	Vane Shear Test	
WP	Work Package	
YSR	Yield Stress Ratio	

Greek letters

α	Angle between the normal bedding plane and the major principle stress	$[\text{L L}^{-1}]$
α	Biot's coefficient	$[^{(2)}]$
α	Cap parameter of the HS model	$[1]$
α	Importance factor	$[1]$
α_c	Isotropic thermal dilation coefficient	$[\text{L}^3 \text{L}^{-3} \text{K}^{-1}]$
α_i	Coefficient	$[1]$
β	Reliability index	$[1]$
$\bar{\varepsilon}_{\theta\theta}$	Tangential strain at EP interface	$[\text{L L}^{-1}]$
$\bar{\varepsilon}_{rr}$	Radial strain at EP interface	$[\text{L L}^{-1}]$
$\dot{\varepsilon}^{pc}$	Rate of plastic cap strains	$[\text{L L}^{-1}]$
$\dot{\varepsilon}_v^p$	Rate of plastic volumetric strain	$[\text{L L}^{-1}]$
$\tilde{\varepsilon}^p$	Cumulative plastic strain	$[\text{L L}^{-1}]$
ε	Residuals	$[1]$
ε	Strain	$[\text{L L}^{-1}]$
ε_a	Axial strain	$[\text{L L}^{-1}]$
ε_a^e	Elastic axial strain	$[\text{L L}^{-1}]$
ε_a^p	Plastic axial strain	$[\text{L L}^{-1}]$
ε_l	Lateral strain	$[\text{L L}^{-1}]$
ε_v	Volumetric strain	$[\text{L L}^{-1}]$
ε_v^p	Plastic volumetric strain	$[\text{L L}^{-1}]$
ε_v^{pc}	Plastic volumetric cap strain	$[\text{L L}^{-1}]$
$\varepsilon_{\theta\theta}$	Tangential strain	$[\text{L L}^{-1}]$

ε_{rr}	Radial strain	[L L^{-1}]
ε_{zz}	Axial strain	[L L^{-1}]
$\dot{\gamma}^p$	Rate of plastic shear strain	[L L^{-1}]
γ	Shear strain	[L L^{-1}]
γ	Soil unit weight	[M L^{-3}]
γ^p	Strain hardening parameter of the HS model	[L L^{-1}]
γ_d	Dry unit weight	[M L^{-3}]
γ_{ij}	Shear strain $(i \neq j)$	[L L^{-1}]
γ_w	Unit weight of water	[M L^{-3}]
$\dot{\gamma}_s^p$	Plastic deviatoric strain rate	[L L^{-1} T^{-1}]
κ	URL slope	[L^2 M T^{-2}]
κ^*	Modified swelling index	[(2)]
λ	Lame's constant	[M L^{-1} T^{-2}]
λ	NCL slope	[L^2 M T^{-2}]
λ	Thermal conductivity	[M L T^{-3} Θ^{-1}]
λ^*	Modified compression index	[(2)]
λ^p	Plastic scalar multiplier	[1]
λ^{rp}	Residual plastic scalar multiplier	[1]
λ_h	Horizontal thermal conductivity	[M L T^{-3} Ω^{-1}]
λ_i	Fitting parameter for Equation 8.1	[T^{-1}]
λ_v	Vertical thermal conductivity	[M L T^{-3} Ω^{-1}]
Λ	Undrained thermal pressurisation coefficient	[M L T^{-2} Ω^{-1}]
μ	Mean	[(1)]
μ^*	Modified creep index	[(2)]
ν	Degrees of freedom	[1]
ν	Poisson's ratio	[L^2 L^{-2}]
ν	Un-/reloading Poisson's ratio	[L^2 L^{-2}]
ν_0	Initial Poisson's ratio	[L^2 L^{-2}]
ν_l	Poisson's ratio of concrete liner	[L^2 L^{-2}]
ν_{ur}	Unloading-reloading Poisson's ratio	[L^2 L^{-2}]
Ω	Heat content	[M L^2 T^{-2}]
$\Phi(\cdot)$	CDF in standard normal space	[1]
ρ	Bulk density	[M L^{-3}]
ρ	Normalised radial polar coordinate	[L L^{-1}]
ρ	Product-moment (Pearson) Correlation coefficient	[1]
ρ_d	Dry density	[M L^{-3}]
ρ_s	Solid (grain) density	[M L^{-3}]
ρ_w	Normalised radius beyond which the pore water pressure is not influenced by the cavity	[L L^{-1}]
ρ_w	Water density	[M L^{-3}]
$\bar{\sigma}_{\theta\theta}$	Total tangential (hoop) stress at EP interface	[M L T^{-2}]
$\bar{\sigma}_{rr}$	Total radial stress at EP interface	[M L T^{-2}]
$\hat{\sigma}_{\theta\theta}$	Total tangential (hoop) stress at RP interface	[M L T^{-2}]
$\hat{\sigma}_{rr}$	Total radial stress at RP interface	[M L T^{-2}]

σ	Standard deviation	[1]
σ	Total stress	[M L T^{-2}]
σ'	Effective stress	[M L T^{-2}]
σ'_1	Major principal effective stress	[M L T^{-2}]
σ'_3	Minor principal effective stress	[M L T^{-2}]
σ'_a	Effective axial stress (UCT)	[M L T^{-2}]
σ'_c	Effective vertical pre-consolidation pressure	[M L T^{-2}]
σ'_f	Effective failure stress	[M L T^{-2}]
σ'_r	Effective residual stress	[M L T^{-2}]
σ'_y	Effective yield stress	[M L T^{-2}]
σ'_{123}	Effective principle stress	[M L T^{-2}]
$\sigma'_{\theta\theta}$	Effective tangential (hoop) stress	[M L T^{-2}]
σ'_{rr}	Effective radial stress	[M L T^{-2}]
$\sigma'_{v,0}$	In situ vertical effective stress	[M L T^{-2}]
$\sigma'_{v,c}$	Vertical effective preconsolidation stress	[M L T^{-2}]
$\sigma'_{y,0}$	Effective in situ yield stress	[M L T^{-2}]
σ'_{zz}	Effective axial stress	[M L T^{-2}]
σ^2	Variance	[1]
σ^l_θ	Tangential (hoop) stress of the liner	[M L T^{-2}]
σ^l_r	Radial stress of the liner	[M L T^{-2}]
σ^{hs}_{ten}	Tensile strength (HS model)	[M L T^{-2}]
σ_0	Total in situ (far-field) stress	[M L T^{-2}]
$\sigma_{\theta\theta}$	Total tangential (hoop) stress	[M L T^{-2}]
σ_{cc}	Uniaxial compressive strength of concrete	[M L T^{-2}]
$\sigma_{h,0}$	Total in situ total horizontal stress	[M L T^{-2}]
σ_{ij}	Total stress tensor	[M L T^{-2}]
σ'_{ij}	Effective stress tensor	[M L T^{-2}]
σ_{rr}	Total radial stress	[M L T^{-2}]
$\sigma_{v,0}$	Total in situ total vertical stress	[M L T^{-2}]
σ_{zz}	Total axial stress	[M L T^{-2}]
τ'_{ij}	Effective shear stress $(i \neq j)$	[M L T^{-2}]
θ	Angle of y-axis rotation	[L L^{-1}]
θ	Diffraction angle	[L L^{-1}]
φ'	Effective friction angle	[L L^{-1}]
φ_f	Post-rupture friction angle	[L L^{-1}]
φ_p	Peak friction angle	[L L^{-1}]
φ_r	Residual friction angle	[L L^{-1}]
φ_{cu}	Consolidated undrained friction angle	[L L^{-1}]
φ_{cv}	Critical state friction angle	[L L^{-1}]
φ_f	Friction angle at failure	[L L^{-1}]
φ_m	Mobilised friction angle	[L L^{-1}]
χ	Hardening/softening parameter	[L L^{-1}]
$\tan\xi$	Material constant defining DP yield function	[L L^{-1}]

ψ	Dilation angle	[L L^{-1}]
ψ_m	Mobilised dilatancy angle	[L L^{-1}]
ψ_f	Dilatancy angle at failure	[L L^{-1}]

Latin letters

A	Activity ($A = I_p$/clay fraction $< 2\mu$[%]; Skempton (1984))	[M^2 M^{-2}]
A	Cross-section area	[L^2]
a	Scalar relating plastic strain to yield stress	[1]
A_e	Excavation area	[L^2]
A_i	Fitting parameter for Equation 8.1	[L^2 T^{-3}]
B	Hardening/softening material parameter	[1]
b	Coupling coefficient	[$^{(2)}$]
b	Material constant	[L^3 L^{-3}]
b_c	Cavity spacing	[m]
c	Specific heat capacity	[M^2 T^{-2} K^{-1}]
c'	Effective cohesion	[M L T^{-2}]
c_r'	Residual effective cohesion	[M L T^{-2}]
c_{inc}^{hs}	Increase in cohesion per unit depth (HS model)	[M L T^{-2} L^{-1}]
c_0	Initial effective cohesion	[M L T^{-2}]
C_c	Compression index	[M^{-1} L^{-1} T^2]
C_c^*	Intrinsic compression index	[M^{-1} L^{-1} T^2]
c_i	Integration constant $(c_i \in \mathbb{R})$	[1]
C_p	Specific heat capacity	[M L^2 T^{-3}]
c_p	Peak cohesion	[M L T^{-2}]
c_r	Convergence	[L^3 L^{-3}]
C_s	Swelling index	[M^{-1} L^{-1} T^2]
c_u	Undrained cohesion	[M L T^{-2}]
c_{cu}	Consolidated undrained cohesion	[M L T^{-2}]
CC	Carbonate content	[L^3 L^{-3}]
COV	Covariance	[1]
e_{1000}^*	Void ratio on ICL for $\sigma_v' = 1\,000$kPa	[L^{-3} L^3]
e_{100}^*	Void ratio on ICL for $\sigma_v' = 100$kPa	[L^{-3} L^3]
e_0	In situ void ratio	[L^{-3} L^3]
$\mathbf{D}$	Stiffness matrix	[M L T^{-2}]
d	Diameter of gallery	[L]
d	Global depth coordinate	[L]
d_l	Concrete liner thickness	[L]
d_{oc}	Overcut thickness	[L]
d_{sc}	Outer diameter of OPERA Supercontainer	[L]
dec	Initial equivalent plastic strain (Salehnia et al., 2013)	[L L^{-1}]
E	Young's modulus	[M L T^{-2}]
E_l	Young's modulus of concrete liner	[M L T^{-2}]
E_s	Compressibility modulus	[M L T^{-2}]
E_t	Tangential modulus	[M L T^{-2}]

E_{50}	Secant modulus	[M L T^{-2}]
E_{50}^{ref}	Reference secant modulus	[M L T^{-2}]
E_D	Dilatometer modulus	[M L T^{-2}]
E_i	Initial secant modulus	[M L T^{-2}]
E_{oed}	Oedometer modulus	[M L T^{-2}]
E_{oed}^{ref}	Reference Oedometer modulus	[M L T^{-2}]
E_{PMT}	Pressuremeter modulus	[M L T^{-2}]
E_{ur}	Elastic unloading-reloading modulus	[M L T^{-2}]
E_{ur}^{ref}	Reference unloading-reloading modulus	[M L T^{-2}]
f	Yield function	[(2)]
$F(\cdot)$	CDF in physical space	[1]
$f(\cdot)$	PDF in physical normal/non-normal space	[1]
f^c	Cap yield function	[1]
f^s	Shear yield function	[1]
$F_{1,2}$	Coefficients	[1]
g	Plastic potential	[(2)]
G	Elastic shear modulus	[M L T^{-2}]
G	Performance function	[(1)]
G	Shear modulus	[M L T^{-2}]
G_s	Specific gravity	[M L^3 M^{-1} L^{-3}]
G_{50}^{ref}	Reference shear modulus in primary loading	[M L T^{-2}]
$\mathbf{I}$	Identity matrix	[1]
I	Indicator function	[1]
I	Moment of intertia	[L^4]
I_L	Plasticity index $(w - w_p)/(w_l - w_p)$	[M M^{-1}]
I_P	Plasticity index $(w_l - w_P)$	[M M^{-1}]
I_v	Void ratio index (Burland, 1990)	[L^3 L^{-3}]
$\mathbf{K}$	Compliance matrix	[M^{-1} L^{-1} T^2]
K	Bulk modulus	[M L T^{-2}]
k	Material constant	[L^6 L^{-6}]
k	Scalar to set effective mean stress	[1]
k'	Material constant defining DP yield function	[M L^2 T^{-2} L^{-1}]
K_0	Coefficient of earth pressure at rest	[(2)]
K_0^{NC}	Coefficient of earth pressure at rest for NC conditions	[1]
k_ν	Statistical parameter	[1]
K_c	Elasto-plastic iso. compression bulk modulus	[M L T^{-2}]
K_s	Bulk modulus of the solid matrix	[M L T^{-2}]
k_s	Intrinsic saturated permeability	[L T^{-1}]
K_s^{ref}	Reference unloading-reloading bulk modulus	[M L T^{-2}]
K_w	Bulk modulus water	[M L T^{-2}]
$K_{sat,h}$	Horizontal saturated hydraulic conductivity	[L T^{-1}]
$K_{sat,v}$	Vertical saturated hydraulic conductivity	[L T^{-1}]
K_{sat}	Saturated hydraulic conductivity	[L T^{-1}]

$\mathbf{L}$	Lower triangular matrix	[1]
L	Load	[(1)]
l	Length of gallery	[L]
l_e	Unsupported excavation length	[L]
l_l	Length of liner segment	[L]
l_{sc}	Outer length of OPERA Supercontainer	[L]
M	Slope of the CSL	[(2)]
m	Rate of stress dependency	[1]
m	Sample mean	[(1)]
$M_{l,max}$	Maximum bending moment in liner	[M L^2 T^{-2} L^{-1}]
M_{tHM}	Mass of heavy metal per supercontainer	[M]
MBV	Methylene blue value	[M M^{-1}]
$\vec{n}$	Normal bedding plane	[L L^{-1}]
N	Number of samples	[1]
n	Porosity	[L^3 L^{-3}]
N_f	Number of failed Monte Carlo realisations	[1]
N_r	Number of total Monte Carlo realisations	[1]
$N_{l,max}$	Maximum axial (tangential) force in liner	[M L T^{-2} L^{-1}]
OCR	OverConsolidation Ratio	[(2)]
$\hat{P}_f$	Approximate failure probability	[1]
p'	Mean effective stress	[M L T^{-2}]
p'_c	Isotropic pre-consolidation stress	[M L T^{-2}]
p_c^{eq}	Equilibrium cavity pressure	[M L T^{-2}]
p_c^{eq}	Equivalent isotropic pre-consolidation stress (HS model)	[M L T^{-2}]
p_l^{max}	Maximum compressive liner support (collapse) load	[M L T^{-2}]
p^{ref}	Reference stress	[M L T^{-2}]
p_c	Isotropic pre-consolidation stress	[M L T^{-2}]
p_c	Total cavity pressure	[M L T^{-2}]
P_f	Probability of failure	[1]
p_L	PMT limit stress	[M L T^{-2}]
$p_{c,cirt}$	Critical total cavity pressure	[M L T^{-2}]
POP	Pre-Overburden Pressure	[M L T^{-2}]
$\mathbf{Q}$	Heat flux	[M L^2 T^{-3}]
$\tilde{q}$	Stress measure of the HS model	[M L T^{-2}]
q	Deviatoric stress	[M L T^{-2}]
q_a	Assymptotic shear strength	[M L T^{-2}]
q_c	CPT tip resistances	[M L T^{-2}]
q_c	Deviatoric pre-consolidation stress	[M L T^{-2}]
q_f	Ultimate deviator stress	[M L T^{-2}]
q_p	Peak deviatoric stress	[M L T^{-2}]
Q_T	Heat source term	[M L^2 T^{-3}]
q_T	CPT corrected tip resistance	[M L T^{-2}]
$Q_{l,max}$	Maximum shear liner force in liner	[M L T^{-2} L^{-1}]
Q_m	Heat flux per metre of the disposal gallery	[M L T^{-3}]

Q_{tHM}	Heat flux per tonne of heavy metal	[$L^2 T^{-3}$]
$\mathbf{R}$	Cross-correlation matrix	[1]
R	Resistance	[(1)]
r_c	Cavity excavation radius	[L]
r_e	Excavation radius	[L]
R_f	Reliability	[1]
R_f	Failure ratio	[(2)]
r_i	Inner tunnel (target) radius	[L]
r_w	Radius beyond which the pore water pressure is not influenced by the cavity	[L]
r_{HZ}	Radial extent of the shear hardening zone (HS model)	[L]
$r_{p,lim}$	Limiting plastic radius	[m]
r_{PZ}	Radial extent of the plastic failure zone (HS model)	[L]
r_p	Plastic (yield) radius	[L]
r_{rp}	Residual plastic radius	[L]
S	Degree of saturation	[$L^6 L^{-6}$]
s	Sample standard deviation	[(1)]
s	Spacing between galleries	[L]
s_u	VST undrained shear strength	[$M L T^{-2}$]
T	Temperature	[Θ]
t	Unit time	[T]
t_ν	Student's t-value	[1]
$\bar{u}_w$	Pore-water pressure at EP interface	[$M L T^{-2}$]
$\hat{u}_w$	Pore-water pressure at RP interface	[$M L T^{-2}$]
U	Random variable in standard normal space	[1]
u^*	Design point	[1]
u_c^0	Initial cavity deformation during excavation	[L]
u_c^δ	Closing of the residual overcut after liner installation	[L]
u_θ	Tangential displacement	[L]
u_a	Pore-water pressure	[$M L T^{-2}$]
u_l	Radial liner deformation	[L]
u_r	Radial displacement	[L]
u_r^l	Radial displacement of the liner	[L]
u_w	Pore-water pressure	[$M L T^{-2}$]
u_z	Axial displacement	[L]
u_c	Total soil deformation at the cavity interface	[L]
$u_{w,0}$	In situ (far-field) pore water pressure	[$M L T^{-2}$]
$u_{w,c}$	Pore-water pressure at cavity	[$M L T^{-2}$]
V	Coefficient of variation	[1]
v	Specific volume	[$L^3 M^{-1}$]
v_e	Excavation velocity	[$L T^{-1}$]
w	Gravimetric water content	[$M M^{-1}$]
w_L	Liquid limit	[$M M^{-1}$]
w_P	Plastic limit	[$M M^{-1}$]

$\mathbf{X}$	Vector holding random soil variables X_i	[(1)]
$\mathbf{X}_l$	Vector holding liner variables	[(1)]
X	Random variable in physical space	[(1)]
x	Discrete observation of X	[(1)]
x	Non-dimensional radius (r/r_p)	[L L^{-1}]
x_{rp}	Non-dimensional residual plastic radius (r_{rp}/r_p)	[L]
y_{ex}	Longitudinal position of the excavation front	[L]
YSR	Yield Stress Ratio	[(2)]
Z	Safety margin	[(1)]

Operators

$\mathcal{D}_f$	Failure domain
$\ln\mathcal{N}$	Log-normal distribution
$\mathcal{N}$	Normal distribution

Sub- and Superscripts

$'$	Effective
$*$	Intrinsic property (e.g. of reconstituted material)
$//$	Parallel to bedding plane
$\perp$	Perpendicular to bedding plane
0	In situ (far-field)
a	Axial
c	Cavity
CU	Consolidated undrained
e	Elastic
f	Failure
h	Horizontal
HZ	Hardening zone
k	Characteristic
l	Lateral
l	Liner
l	Longitudinal
lim	Limit
max	Maximum
p	Peak
p	Plastic
p	Primary (gallery)
PZ	Plastic zone
r	Radial
r	Residual
ref	Reference
rp	Residual plastic
s	Secondary (gallery)
s	Solid phase
θ	Tangential

t	Disposal (Tertiary gallery)
u	Ultimate
v	Vertical
v	Volumetric
w	Water phase
z	Axial

[1] Individually defined

[2] $M\,L\,T^{-2}M^{-1}\,L^{-1}\,T^{2}$

1. Introduction

This report is an investigation into the principle feasibility of a reference design of a deep geological repository for radioactive waste in the Netherlands. This work has been undertaken as part of the *Onderzoeks Programma Eindberging Radioactief Afval* (OPERA) research programme in *Work Package* (WP) 3.1. The work focuses on numerical and reliability-based methods and has been undertaken by the *Delft University of Technology* (TUD), *Nuclear Research and consultancy Group* (NRG) and *Nederlandse Organisatie voor Toegepast Natuurwetenschappelijk Onderzoek* (TNO) during the period from 12-2012 till 12-2014.

1.1. Background

Research on the storage and disposal of radioactive waste in the Netherland started in 1971. In 1979 the *Interdepartementale Commissie voor de Kernenergie* (ICK), as part of the *Ministerie van Volkshuisvesting, Ruimtelijke Ordening en Milieubeheer* (VROM), recommended deep geological disposal, possibly in the rock salt formations in the north eastern part of the Netherlands (ICK, 1979), as shown in Figure 1.1(a).

Following a public debate on energy policy starting in 1979, the *Centrale Organisatie Voor Radioactief Afval* (COVRA) was founded subsequent to on a report on the position of the Dutch government delivered to parliament in 1984 (VROM, 1984). In the same year, the Dutch government formed the scientific steering committee *OPberging te LAnd* (OPLA), which launched the first research programme to investigate the possibility of disposing of radioactive waste in salt rock. The research focused mainly on the analysis of the galleries proposed to contain high level radioactive waste and investigated the requirements for possible retrieval. Broek et al. (1993) concluded in the final OPLA report that disposal in salt was feasible, including the possibility of future retrievability, but that more investigations on the technical provision as well as safety consequences were required.

In a position paper, the Dutch Government (1993) outlined its policy regarding the disposal of highly toxic and radioactive waste. With a target of minimising waste it was decided that non-avoidable waste was to be reprocessed. For the residual waste, based on the outcome of the OPLA programme, as well as on the national and international requirements of sustainable development, disposal in a deep geological repository was chosen to be the preferred approach, under the premise that every step of the process is reversible, so that any waste could be retrieved, if and when deemed necessary. In order to oversee and coordinate all research related to radioactive waste disposal, the *Commission on Disposal of Radioactive Waste* (CORA) research programme was initiated.
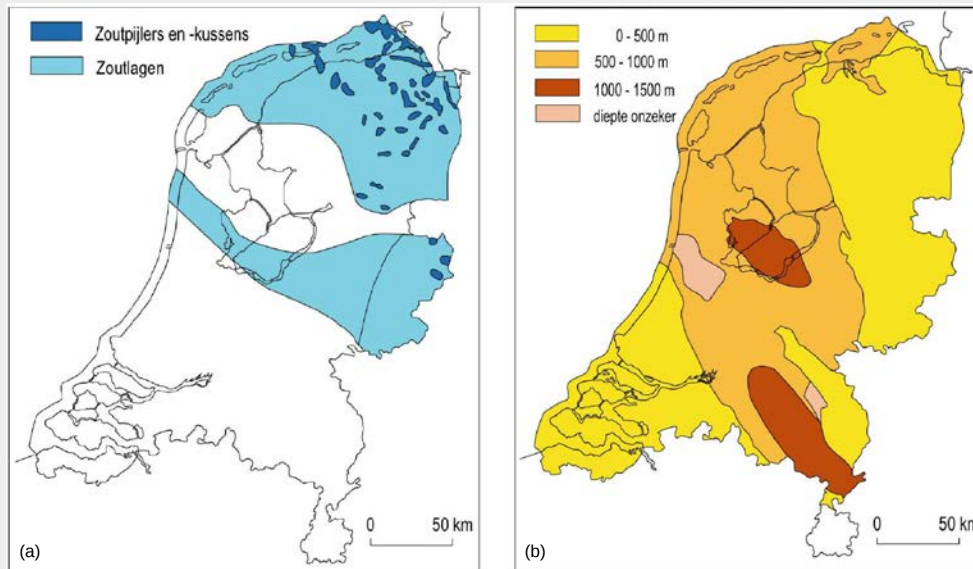
Figure 1.1.: Potential host rock for the disposal of radioactive waste in the Netherlands: rock salt deposits (a) and formations of Boom Clay (b) (CORA, 2001b).

The CORA programme started in 1995, comprised 21 projects, cost around €3.5 million, with 20 research institutions (both national and international) participating and concluded in 2001. The research focused on the technical feasibility of a retrievable deep underground repository in salt rock, as well as on the suitability of Boom Clay as a host rock (Figure 1.1(b)) and of long-term storage above ground; for each of these options the evaluation of retrievability, as well as safety, was key. The main conclusions from this project were that:

- the retrieval of radioactive waste from repositories in salt and clay was technically feasible, with the disposal concept envisaging the construction of short, horizontal disposal cells each containing one *High Level Waste (HLW)* canister;

- the safety criteria could be met even in a situation of neglect, with the maximum radiation dose that an individual could incur remaining far below 10 μSv/year;

- structural adjustments to the repository design were required to maintain accessibility. This applies particularly to a repository in clay, which needs additional support to prevent borehole convergence and eventual collapse of the disposal drifts; and

- the costs would be higher than those for a non-retrievable repository, mainly due to maintenance of accessibility of the disposal drifts (CORA, 2001a,b).

Based on the outcomes of the CORA project and previous investigations, in 2002 the Dutch Ministry of Housing, Spatial Planning and the Environment submitted a statement to parliament (VROM, 2002), which to date, with reference to VROM (1984) and the Dutch

Government (1993), is setting the current Dutch policy on radioactive waste. Two key features of this policy (relevant for this report) are:

- ○ to store all radioactive waste for a period of at least 100 years by COVRA; and

- ○ to eventually dispose of all radioactive waste retrievably in a deep geological facility (CORA, 2001b).

Ongoing research was deemed to be required to resolve outstanding issues, to preserve expertise and knowledge, as well as to prepare for site selection in the case of any change in the current time table (Kgd. of the Netherlands, 2011). Hence, in September 2009 the third Research Programme for the Geological Disposal of Radioactive Waste, the *Onderzoeks Programma Eindberging Radioactief Afval* (OPERA[1]), was launched, for operation during 2011-2016. As the existing national safety and feasibility studies for the disposal of radioactive waste were between 10 to 20 years old, the OPERA research programme aimed to evaluate existing national and international safety and feasibility studies, to modify individual concepts, frameworks and analyses and to adopt this information when designing a generic waste repository in the Netherlands.

A short list of key milestones in the research and development of a radioactive waste management strategy in the Netherlands can be found in NEA (2007, 2008) and Kgd. of the Netherlands (2011).

1.2. The OPERA research programme

The main focus of the OPERA national research programme lies in the disposal concept in Boom Clay, which is outlined by Verhoef et al. (2011). OPERA consists of seven main work packages, of which the interfaces are are outlined in Figure 1.2. This research is part of WP 3.1 concerning the feasibility of the OPERA reference design (see Section 1.3). The individual research tasks have been described in the OPERA Research plan (Verhoef and Schröder, 2011). A guideline for the execution is presented in the Meerjarenplan (Verhoef, 2011). More information can be found on the OPERA website[2].

1.3. Work Package 3.1

WP 3.1 investigates the principal technical feasibility of the OPERA reference design of a radioactive waste disposal facility in Boom Clay at depth of about 500m. The objectives, methodology, and scope and limitations are outlined briefly below.

---

[1]OPERA website: http://www.covra.nl/disposal/opera-disposal
[2]OPERA website: http://www.covra.nl/downloads/opera-info
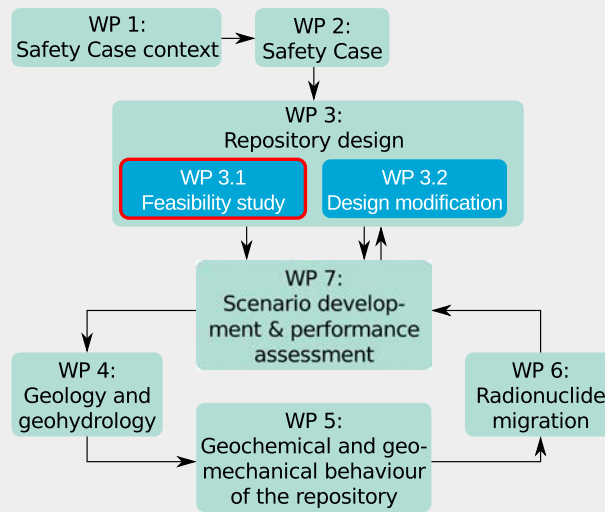
Figure 1.2.: Work Packages of the OPERA research project (after Verhoef and Schröder, 2011)

1.3.1. Objectives

The objectives of this report are:

○ to provide a comprehensive state of the art literature review on the deep geological disposal of radioactive waste, with the focus on the geomechanical description of the Boom Clay in terms of soil property values, in situ conditions, Thermo-Hydro-Mechanical (THM) material behaviour and tunnel construction;

○ to assess the uncertainties in the Boom Clay property values based on the current knowledge;

○ to develop an analytical model to describe the basic behaviour of the Boom Clay due to the excavation of a single tunnel gallery;

○ to perform two- and three-dimensional numerical analyses on the Boom Clay response due to tunnel excavation utilising an advanced constitutive soil model;

○ to implement a *Reliability Based Design* (RBD) framework, to asses the performance of the repository as well as the sensitivity of the response with respect to the parameter uncertainty in a quantitative, verifiable and traceable manner;

○ to assess the response of the Boom Clay due to thermal loading; and

○ to provide a judgement on whether, and under which conditions, the current OPERA disposal concept is feasible and which design modifications may enhance the performance and safety.

1.3.2. Methodology

The assessment strategy for this feasibility study is outlined in Figure 1.3 and consists of three parts. For every part of the repository, the response of all system functions needs to be assessed

Design process	Assessment strategy	Quantify uncertainty
Life-cycle phases	Consitutive formulation	Random variables
Response functions	Deterministic analysis	Performance functions
Limit states	RBD framework	Sensitiviy analysis
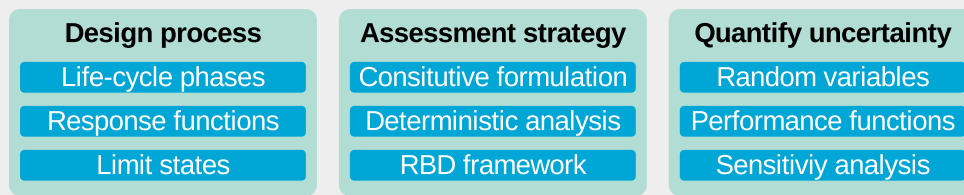
Figure 1.3.: Assessment strategy for feasibility study.

with respect to given limit states, during all considered life-cycle phases. For this research, one system response is the deformation of the Boom Clay due to the excavation of a tunnel gallery, which is assessed with respect to a limiting extent of the zone in which the soil plastifies. The employed assessment strategy consists of a model describing the constitutive response of the Boom Clay, an analytical or numerical tool to perform single deterministic analyses of the problem, and a RBD framework. In order to quantify the impact of uncertainties on the system, a set of random variables is described by means of statistical measures, which, when introduced in the RBD framework, will result in a quantified judgement of the performance of a part, or multiple parts, of the system being assessed and of the sensitivity of the performance with respect to given criteria. For instance, accounting for the uncertainty in the Boom Clay properties, the probability of the extent of the plastic zone exceeding a set limit state criterion, i.e. failing to perform, can be computed and the importance of each random variable on the outcome can be quantified.

Figure 1.4 outlines the components of the implemented RBD framework in a flow chart. This study focuses on the uncertainty in the Boom Clay property values, or model constitutive parameters, which are treated as random variables. Given a set of boundary conditions, a set of random variables is sampled and passed onto the mechanical model, where a single deterministic analysis, e.g. of the tunnel excavation process, is performed. In the probabilistic model the response, e.g. the extent of the plastic zone, is then post-processed. This single model cycle is called a realisation and repeated multiple times. For each realisation the algorithm samples a new set of soil property values from the set of input statistics, the computed responses can be evaluated in terms of exceedance probabilities with respect to a given limit state.
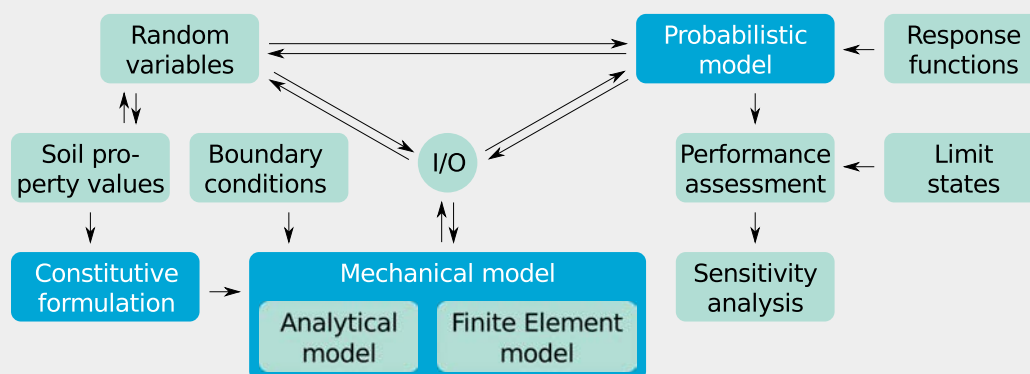
Figure 1.4.: Components of the RBD design framework.
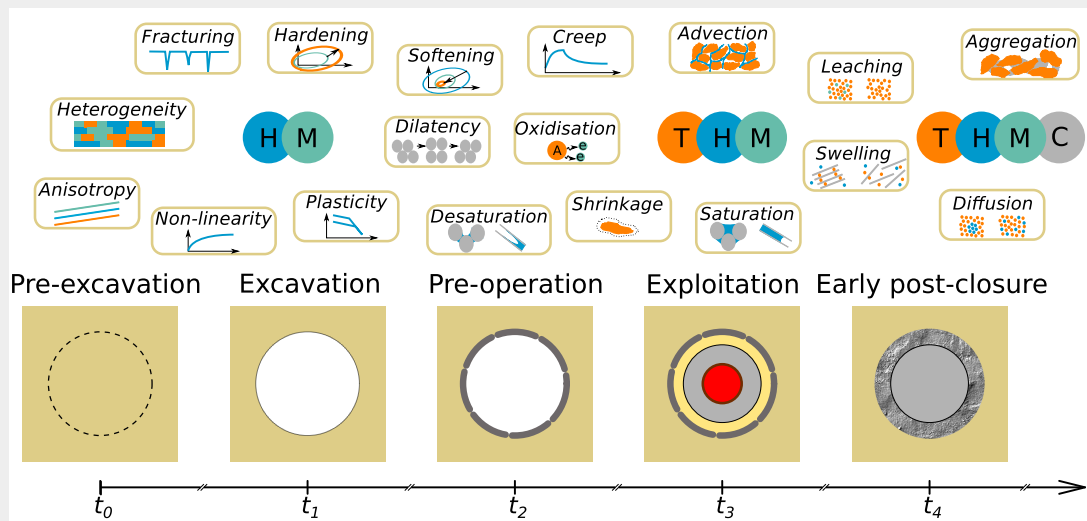
Figure 1.5.: Schematic outline of life-time phases of a radioactive waste repository and processes influencing the repository performance.

1.3.3. Scope of this research

The life-time of a radioactive waste repository may be categorised into five phases, which are schematically outlined in Figure 1.5. The research fits within this concept in the following areas:

- Excavation
  - Evaluation of the OPERA disposal concept for construction: safe distance between disposal galleries and safe concrete thickness
    - Development of an analytical model Chapter 4
    - Selection of a constitutive model Chapter 5
    - Undrained analysis in Chapter 6
    - Accounting for uncertainties via probabilistic assessment in Chapter 7
  - Building the OPERA disposal concept with tunnelling boring machine
    - Overcut, staged excavation Chapter 6.
- Pre-operation (whole disposal concept is built; disposal galleries are not backfilled)
  - Development of an analytical model Chapter 4
  - Selection of a constitutive model Chapter 5
  - Drained analysis in Chapter 6
  - Accounting for uncertainties via probabilistic assessment in Chapter 7
- Exploitation (emplacement of waste and backfilling of disposal gallery after completion of emplacement)

   ○ Drained analysis in Chapter 6
   ○ Further analyses not performed because safe distance between galleries and con-
     crete thickness are expected not to be more limiting in this phase than Excavation
     and Pre-operation due to backfill
 ○ Early post-closure
   ○ Thermal phase in Chapter 8

The scope of this research is as follows:

 ○ the work was limited to Boom Clay as the host rock for a deep repository;
 ○ the assessment of the constitutive behaviour was based on the current knowledge and
   available material data from the literature;
 ○ the analytical and numerical assessment was limited to the excavation, pre-operational
   and early post-closure phases;
 ○ the analyses were limited to available experimental data;
 ○ no THM coupling has been accounted for;
 ○ no material degradation of the concrete liner has been considered; and
 ○ quantification of uncertainties was limited to the variation in soil property values.

1.4. Outline of the report

This report is divided into nine chapters and contains one appendix.
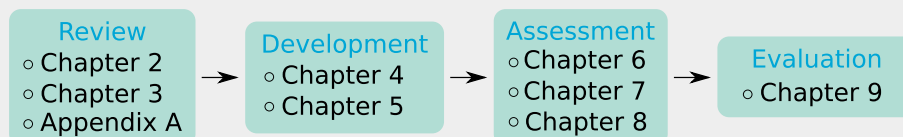
Figure 1.6.: Outline of the report.

Chapter 2 provides a selective literature review on various aspects of radioactive waste
management and deep geological disposal, aiming to provide a background for the development
of a technically feasible Dutch radioactive waste repository in Boom Clay. In Chapter 3 the
data collected in the literature on the Boom Clay material properties and boundary conditions
are assessed and, as far as possible, interpreted statistically.

In Chapter 4 an analytical formulation accounting for elasto-plastic strain-softening Boom
Clay behaviour has been developed, to assess the host rock response due to the excavation
of a deep tunnel. The performance of different advanced constitutive models is assessed in
Chapter 5 to select the most suitable model for the numerical modelling of the excavation of
the OPERA repository galleries.

In Chapter 6 the excavation of a tunnel in a deep Boom Clay formation is assessed numeric-
ally in two and three dimensions, utilising the PLAXIS *Finite Element* (FE) software package.

In Chapter 7 the analytical and numerical assessment mechanical models are implemented within a Reliability Based Design framework, to account for the uncertainties in the material properties in a systematic, quantitative and verifiable manner. An initial thermal assessment of the OPERA reference design is presented in Chapter 8.

A summary, discussion and conclusion on the finding of this report is presented in Chapter 9, including some recommendations on the further work.

Appendix A provides a database of Boom Clay property values and state variables collected from the literature.

2. Selective literature review

2.1. Introduction

This chapter provides a selective literature review on the development of a technically feasible Dutch radioactive waste repository in Boom Clay. The review is limited to only the salient information relevant to undertake this reserach.

In Section 2.2 the *Research and Development* (R&D) into deep geological radioactive waste disposal facilities is reviewed. Two main research programmes have been conducted on the design and feasibility of a Dutch radioactive waste repository, namely OPLA and CORA. A detailed summary of five CORA projects related to disposal in clay is provided in Section 2.2.1. In Section 2.2.2 relevant research work undertaken as part of the OPERA project is briefly reviewed. A summary of salient international R&D activities on deep geological repositories is presented in Section 2.2.3.

Section 2.3 provides an overview of the Dutch OPERA reference design for the disposal of *Low- and Intermediate-Level Waste* (LILW) and HLW/ *Spent Nuclear Fuel* (SNF) in Boom Clay. Section 2.3.1 describes briefly the life-time phases of a radioactive waste repository. Subsequently, in Section 2.3.2 the proposed OPERA deep geological disposal concept in clay is outlined in detail, on which the feasibility study conducted in this report is based.

A review on the in situ conditions and soil property values of the Boom Clay formation is presented in Section 2.4. Beyond the results of the CORA projects, test data on Boom Clay collected from the literature will be presented and discussed. The Boom Clay lithology, mineralogy, organic matter and pore-water chemistry are presented in Section 2.4.1. Relevant in situ conditions are discussed in Section 2.4.2. Section 2.4.3 summarises the in situ soil property values relevant for this study; that is, influencing the mechanical, hydraulic and thermal responses.

Section 2.5 provides a selective overview of primarily physical processes potentially governing the response of the OPERA repository system in the time frame between the construction of the repository and the end of the thermal (early closure) phase.

Section 2.6 summarises this Chapter.

2.2. R&D into deep geological radioactive waste disposal facilities

2.2.1. Summary of CORA projects related to disposal in clay

In the 1995-2001 framework, the *Commission Disposal Radioactive Waste* (CORA) initiated a second research programme investigating the feasibility of a retrievable deep underground

repository in salt or clay host rock. Twenty research institutions participated in the programme which comprised 21 projects. The associated reports, i.e. CORA 01-21, can be downloaded from the COVRA website (http://www.covra.nl/downloads/opera).

As the current OPERA disposal concept in clay is based particularly on the outcomes of the *tertiary Clay As potential host Rock* (CAR) I+II, *TeRUgneembaar opbergConcept in Klei* (TRUCK) I+II and *Transport of RAdionuclides disposed of in Clay of Tertiary ORigin* (TRACTOR) studies, Section 2.2.1 will discuss the performed research in more detail.

2.2.1.1. CAR I - Mapping of tertiary clay formations

Based on RGD (1984), the CAR I study (Bremmer et al., 1996) provides a sound basis on the regional extent, depth and thickness of the seven tertiary clay formations, of which the lithological names and ages are summarised in Table 2.1.

The report is divided between shallow formations (<500m depth) and deep formations (>500m depth), as well as thick formations with a vertical extent of >100m.

The Boom Clay, as part of the Rupel formation, is a marine unit deposited in the early and middle Oligocene, mainly in the shallow sea in the southern parts of the Netherlands and in northern parts of Belgium. However, the Boom Clay is present in most of the Netherlands. Figures 2.1 and 2.2 show detailed maps of the depth and thickness of the Boom Clay strata. The Boom Clay can be found at an intermediate depth of about 500m in Rotterdam and at 400-800m in the provinces of South Holland and Utrecht, and at a larger depth 1250m in the Zuid-IJsselmeer and Veluwe-bekken and 1700m in the south west of Boxel in Tilburg. Its maximum thickness varies from 100-150m in the Peelgebied (North Brabant and Limburg), 150m in the Noordoostpolder (Flevoland), 250m in the area of Arnhem, and 275m near Schiermonnikoog and Ameland (to the west of Frisland).

The Boom Clay was found to consist of a sandy part in the top 10-25m of the stratum. With increasing depth the clay becomes more silty, then more clayey and silty at the bottom. Silty clay zones have been reported in stratifications of 0.1-0.15m and 2.0-3.0m. The Boom Clay formations are reported to be homogeneous; however, calcareous zones with septarian nodules and plates of varying diameters (0.1-1.5m) and thickness (0.1-0.3m) as well as sandy units (lenses) can be found locally. In shallow depths of the Boom Clay, cracks/ruptures have been reported.

Table 2.1.: Lithological names and ages of clay formations analysed in CAR I (after Bremmer et al., 1996).

Formation	Geological age
Oosterhout-eenheid (Oosterhout-formation)	Plioceen (1.5-5 million years)
Breda-eenheid (Breda-formation)	Mioceen (5-23 million years)
Klei van Veldhoven (Veldhoven clay)	Late Oligocene (23-30 million years)
Klei van Boom[1] (Boom Clay)	Oligocene (30-35 million years)
Klei van Asse (Asse clay)	Late Eocene (35-42 million years)
Klei van Ieper (Ieper clay)	Early Eocene (50-57 million years)
Klei van Landen (Landen clay)	Late Paleocene (57-61 million years)

[1] Part of the *Formatie van Rupel* (Rupel formation)
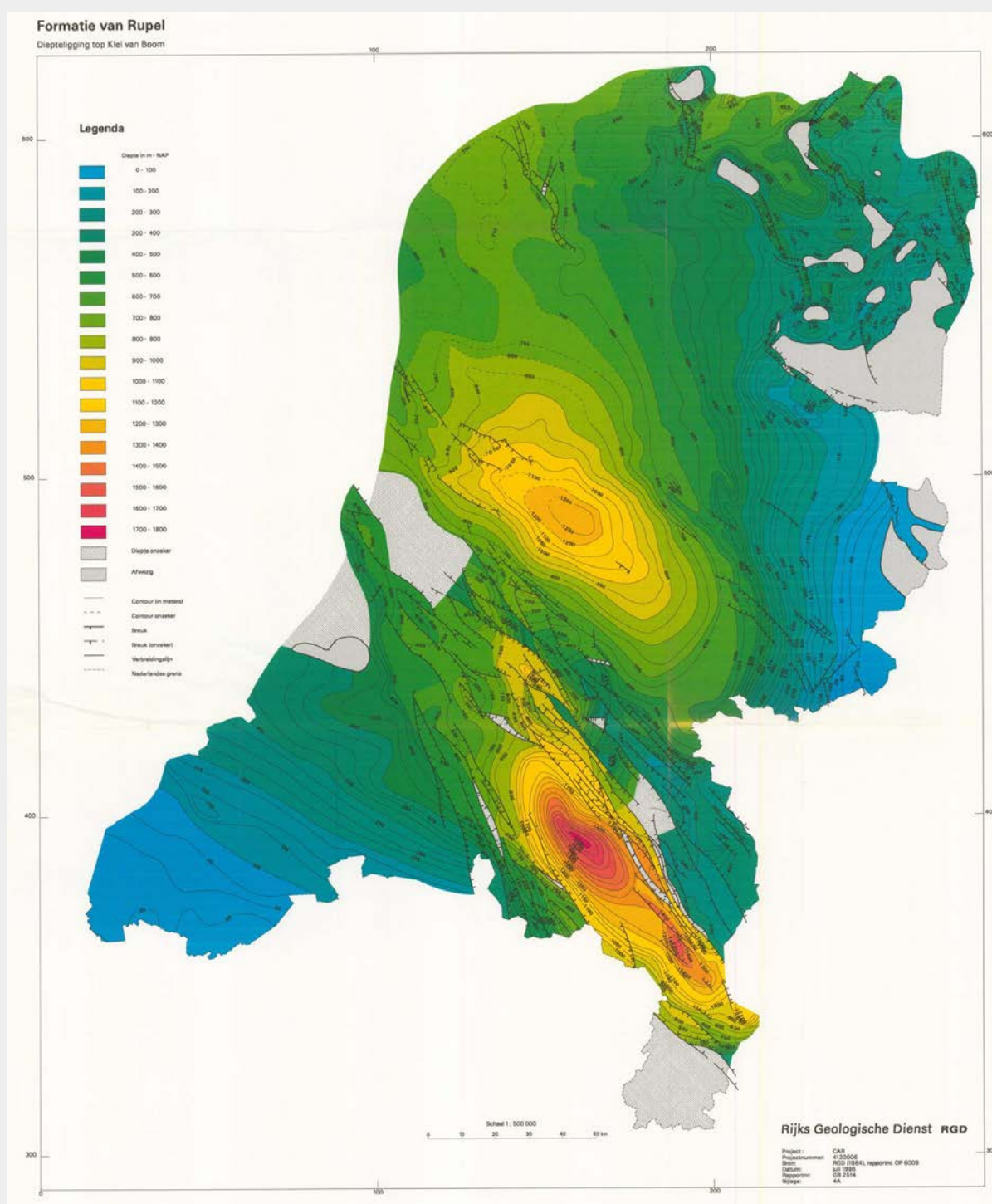
Figure 2.1.: Depth of the top of the Boom Clay strata in the Netherlands (Bremmer et al., 1996).
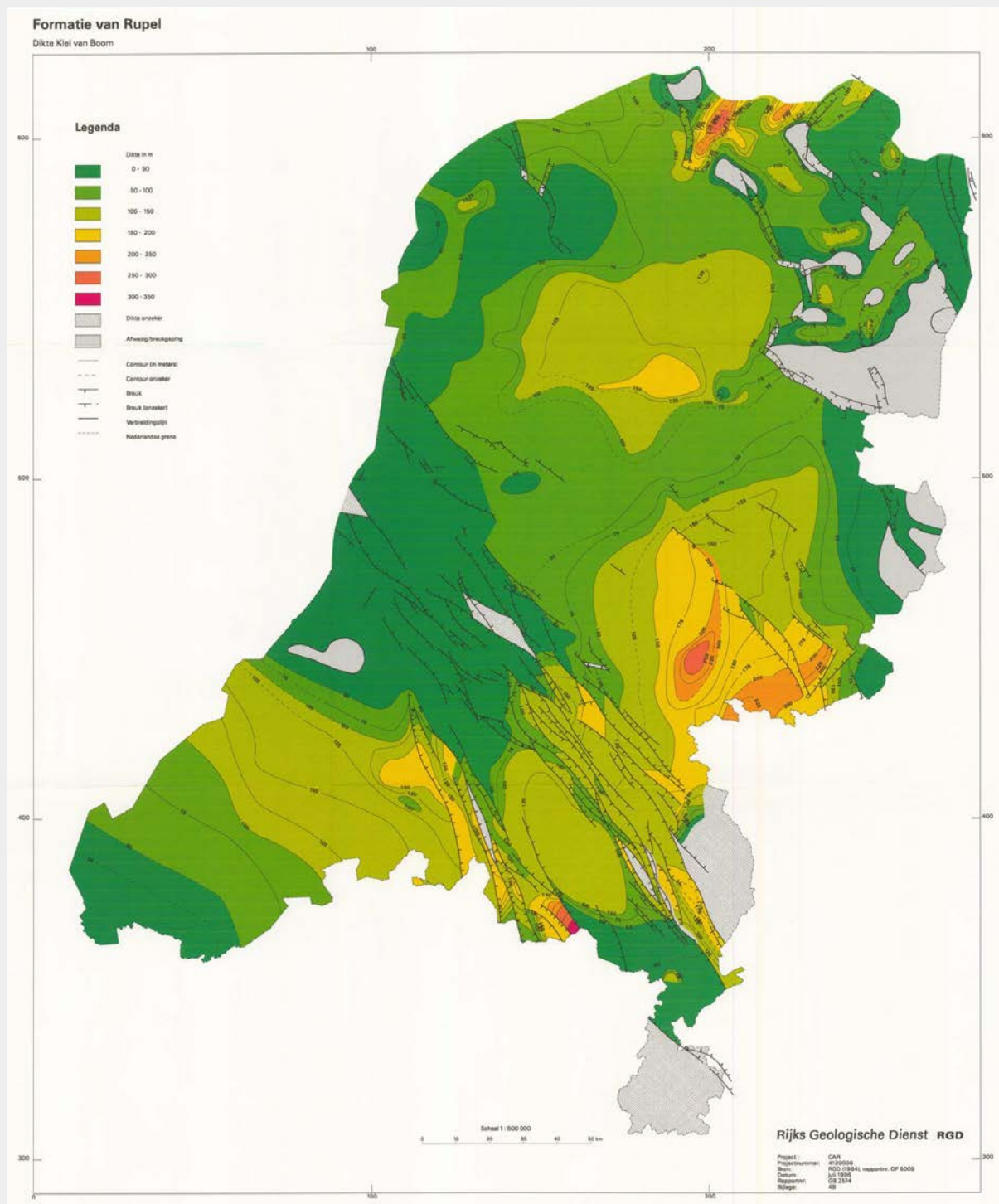
Figure 2.2.: Layer thickness of Boom Clay in the Netherlands (Bremmer et al., 1996).

The CAR I report summarised some soil property values of Boom Clay for a depth of 0-260m, mainly based on samples from the vicinity of Mol, Belgium (Table 2.2). A detailed evaluation of the lithology, mineralogy and hydro-mechanical features as well as thermal property values, follows in Section 2.4.

2.2.1.2. CAR II - Characterisation of tertiary clay formations

The CAR II study (Rijkers et al., 1998) is a follow up of the CAR I study, investigating the geomechanical, geochemical and hydrogeological soil property values of the seven tertiary clay formations. Existing data relevant for the CORA programme have been collected, analysed and inventarised with respect to their spatial variation at the basin scale, using geophysical logs as well as borehole data from the Westerscheldetunnel (Westerschelde Oever Verbinding, Netherlands) and the SCK·CEN hades URL at Mol (Belgium) for the Boom Clay formation.

By assessing borehole data from the Oosterschelde-Ameland geologic cross section of clay formations cutting the Voorne Trog (Voorne trench), the Kijkduin Hoog (Kijkduin high), the Midden-Nederlandse breukzone (Dutch central fault zone), and the Noordzee Bekken (North sea basin), the Boom Clay was found to be interspersed with thin silty and sandy layers, with the clay becomming increasingly sandy and silty approaching the top and bottom of the formation (Rijkers et al., 1998). The clay further was reported to be rich in pyrite, containing little glauconite and calciumcarbonate is concentrated in septarian layers.

Table 2.2.: Soil property values of Boom Clay from a depth of 0-260m (Bremmer et al., 1996).

Definition	Symbol	Unit	Value
Clay fraction $< 2\mu$m		[%]	49-62
Gravimetric water content	w	[%]	23-32
Liquid Limit	w_L	[%]	60-81
Plastic limit	w_P	[%]	26-30
Plasticity index	I_P	[%]	35-63
Activity	A	[$-$]	0.65-1.06
Solid (grain) density	ρ_s	[kg m^{-3}]	1.937-2.049
Dry density	ρ_d	[kg m^{-3}]	1.488-1.682
Undrained cohesion	c_u	[MPa]	0.08-0.760
Consolidated undrained cohesion	c_{cu}	[MPa]	0.1-0.25
Consolidated undrained friction angle	φ_u	[°]	17-25
Saturated permeability	k_s	[m s^{-1}]	10^{-9}-10^{-11}
Thermal conductivity	λ	[W m^{-1} K^{-1}]	0.30 (100°C)
			0.44 (200°C)
Specific heat capacity	c	[J kg^{-1} K^{-1}]	0.26 (25°C)
			0.41 (275°C)

In order to avoid confusion with the Belgium Boom Clay, a new stratigraphic nomenclature was suggested (Adrichem van Boogaert and Kouwe, 1993–1997). The Rupel formation was divided into three layers, i.e. with two sand layers, namely the Steensel Laagpakket and the Vessem Laagpakket, enclosing the Rupel Clay (Boom Clay) at the top and bottom respectively.

Based on the analogue gamma-ray (GR), sonic (DT), neutron (CNL), resistivity (LLS-LLD) and density (FDC) geophysical data-logs from offshore boreholes in the Oosterschelde-Ameland profile, some basic geomechanical parameters have been derived. The bulk density ρ (FDC), the gravimetric water content w (CNL), the porosity n (CNL) as well as the Young's modulus E (DT). The logs were interpreted based on a clay compaction trend from the sonic velocity of the DT logs (Rider, 2002), a method which was defined as particularly useful for homogeneous clay layers. As this is an indirect measurement technique, no confidence interval was provided, however the significance level for the geomechanical parameters was given as 10%.

Evaluation of the borehole data showed an increasing trend of compaction with depth, with the results agreeing well with data from Mol and at the Westerschelde. The variability of soil shear strength property values (c' and φ') was found to be large with no obvious depth trend being evident. As suggestion made in the CAR II report on a possible extrapolation of data to a depth of 500-800m was based on the assumption that the soil strength and stiffness will increase with increasing in situ stress. A large variation in clay mineralogical and geochemical property values was observed. In particular, there was a large variation in the content of organic matter and activity, potentially influencing the stability and swelling pressures within the ground, as well as the presence of sand layers, carbonate sediments and sulfides affecting the porosity and geochemical reactions. Due to its marl sedimentation regime, i.e. the heterogeneity of the Rupel clay in the north of the Netherlands, the prediction of the in situ permeability was found to be difficult (unpredictable).

The CAR II report suggests that, given the preconditions of a burial depth of 500-800m in a layer with a minimum thickness of 150m, on the Dutch mainland the Rupel clay, the Asse clay and the Ieper clay seem suitable for future research on nuclear waste disposal, as the other four clay formations investigated have been classified as unsuitable mostly due to their strong inherent heterogeneity and/or shallow burying depth.

2.2.1.3. TRUCK I - TeRUgneembaar opbergConcept in Klei I

The TRUCK I project (Steen and Vervoort, 1998) resulted in the first design of a generic repository for all Dutch radioactive waste, to be situated at a depth of 500m in a Boom Clay layer of 100m thickness. The layout of the facility consisted of three zones located next to each other in a rectangular pattern in a single level. Two primary access galleries connected each zone with each other and led to the access shafts. Each zone has been dimensioned for the disposal of the heat generating HLW, the *Medium Level Waste* (MLW) and the non heat generating HLW respectively; that is, based on same waste quantities being applied in the OPLA study (Broek et al., 1993). The waste canisters were proposed to be placed in disposal galleries mined horizontally from secondary access galleries laid out in a regular grid. For the

heat generating HLW a centre distance spacing of $s_s = s_d = 50$m (Figure 2.3) was proposed. For the TRUCK I design the effective length (minus 0.5m concrete plug) of the tertiary disposal galleries was set to $l_t = 12.2$m, with an inner and outer diameter of $d_t = 2.2/3.4$m. For the primary and secondary galleries, $d_p = d_s = 3.5/4.6$m defined the inner and outer diameters respectively.

An implicitly coupled elastic perfectly-plastic *Mohr Coulomb* (MC) type soil model, implemented within the Finite Difference code FLAC, was utilised to analyse the hydro-mechanical short- and long-term behaviour of the tunnel galleries within an axisymmetric set-up. The consequences of the thermal load induced by the HLW canisters on the soil response, and thus repository design, have been analysed using analytical formulations within the Boundary element code MAP3D for steady state conditions. As no data were available from a depth of 500m, the set of deterministic soil property values was selected based on the CAR II report (Rijkers et al., 1998), other literature sources and laboratory results of the SCK·CEN URL at Mol (223m). The governing strength parameters considered were the effective cohesion $c' = 0.3$MPa and effective friction angle $\varphi' = 18°$. They were deemed to be a conservative estimate given the premise that stiffness and strength increase with depth and that the thermal conductivity was the same or larger than at 223m depth.

Given an elastic zone of about 36m between two adjacent galleries, the spacing of 50m was deemed to be sufficiently stable for the short term excavation. For the long term, assuming a situation with a permeable lining, the plastic zone was found to increase slightly but remain stable. For a possible situation in which the lining was impermeable, an increase in the liner
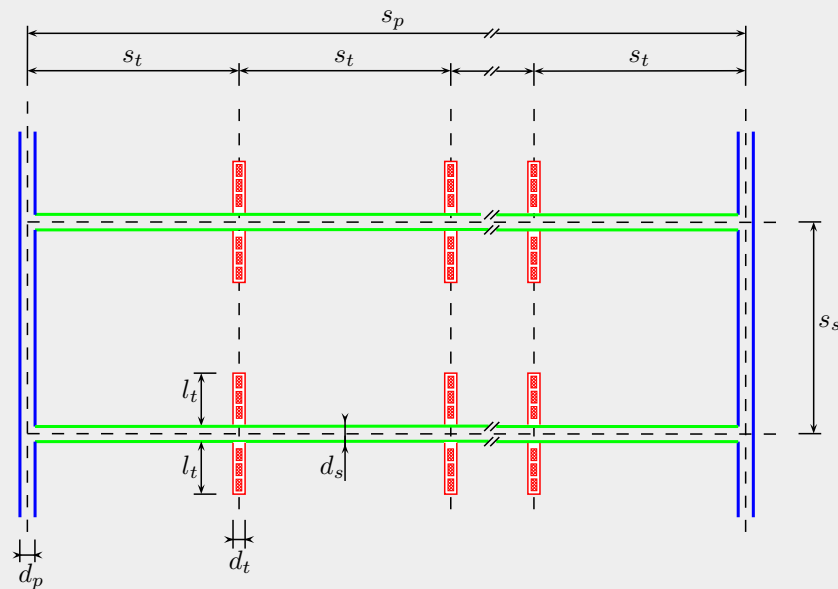
Figure 2.3.: Basic square pattern TRUCK repository design scheme consisting of primary galleries, secondary galleries and tertiary disposal galleries (after Steen and Vervoort, 1998).

thickness in order to sustain the high total radial stresses was found to be of significant influence on the feasibility.

A mechanical sensitivity analysis was performed for six discrete random variables, i.e. effective cohesion c', effective friction angle φ', excess pore-water pressure Δu_w, tunnel excavation diameter, repository depth and gallery spacing. The analysis showed that the design is most sensitive to the effective friction angle φ' of the Boom Clay, with the influence of the effective cohesion c' being rather small. The decrease in friction angle, in the analysis from $\varphi' = 18°$ to $\varphi' = 16°$, led to a significant increase in the plastic zone and convergence of the tunnel wall. However within the tested range the elastic zone between two galleries remained larger than 30m.

An increase in temperature of $\Delta T_{max} = 4°C$ at the top clay layer (50m above the container), set as a desired acceptance criteria based on the Belgian reference repository concept ($\Delta T_{max} = 6°C$ referenced in ONDRAF/NIRAS, 2001a,b), was not satisfied based on the analytical steady state thermal analyses for a spatial distribution of $s_s \times s_d = 50 \times 50$m between the galleries. As a larger spacing of $s_s \times s_d = 100 \times 100$m requires the construction of a larger tunnel system (increasing the construction time, ventilation, transport, etc.) and a mixed disposal of non heat generating and heat generating waste removes the benefits of segregation, longer storage above ground was deemed to have the least consequences and was thus suggested as a solution to meet the $4°C$ criteria.

The construction and conceptual aspects have only been studied for the zone in which the heat generating HLW is to be disposed. For the whole repository, the TRUCK I study also provides a time schedule for the excavation (shafts, primary and secondary access tunnels, tertiary disposal galleries), the waste emplacement and the refilling of the disposal galleries in successive steps. A total of 2 950 working days, corresponding to 13 years, was estimated to be required to excavate the entire mining complex with a total excavation volume of 1 358 400m^3.

Steen and Vervoort (1998) concluded that the proposed design for a mined repository in Boom Clay is feasible.

2.2.1.4. TRUCK II - TeRUgneembaar opbergConcept in Klei II

The TRUCK II study (Barnichon et al., 2000) was an extension of the TRUCK I study. Based on more realistic soil property values for a relevant depth of 500m and more realistic transient thermal loading conditions, the main aim of this feasibility study was the optimisation of the repository in terms of layout, timing and costs.

An elasto plastic Mohr Coulomb soil model and the *Modified Cam-Clay* (MCC) soil model were utilised for describing the mechanical constitutive behaviour of the Boom Clay. A review of the evolution laws to extrapolate some of the required time-independent mechanical soil property values available for depths between 0m and 225m to the desired depth of 500m resulted in a significant variance, which was deemed unrepresentative and potentially leading to doubtful results.

Core samples at different depths obtained from four boreholes in Belgium, drilled in the

1996-1998 time frame by ONDRAF/NIRAS, as well as from one borehole in the Netherlands, have been used to assess directly the change in mechanical soil property values with increasing depth (Table 2.3). A follow up test programme was performed as part of the TRACTOR study within the CORA research programme (see later Section 2.2.1.5). The location of the four Belgium boreholes is indicated in Figure 2.4. Using the same coring technique, the test samples were selected using a medical *Computer Tomography* (CT) scanner to ensure the least disturbed samples.

The particle size distribution curves show that the specimens from Doel 2B, Zoersel and Mol 1 (224.5m) were slightly coarser that the samples from Mol 1 (229.2m), Weelde 1 and Blija (Figure 2.5). The mineralogical analysis over the whole spectrum indicated the presence of large amounts of quartz and feldspar. Following sedimentation, the diffraction showed three distinct peaks at $\theta = 6°$ (Smectite-Montmorillonite), $\theta = 8.5°$ (Illite) and $\theta = 12°$ (Kaolinite). There was no significant difference between the clay samples consisting of between 30% and 50% of Smectite.

The densities, that is, dry density $\rho_d = 1.540 - 1.666 \mathrm{kg\,m^{-3}}$, bulk density $\rho = 1.956 - 2.054 \mathrm{kg\,m^{-3}}$ and solid density $\rho_s = 2.658 - 2.741 \mathrm{kg\,m^{-3}}$, were found to increase linearly

Table 2.3.: Core samples used in TRUCK II study (after Barnichon et al., 2000).

Location	Doel 2B (B)	Zoersel (B)	Mol 1 (B)		Weelde 1 (B)		Blija (NL)	
Core number	63c	38c	76c	80c	87c	86c	—	—
Depth [m]	69.5	120.6	224.5	229.2	313.3	313.5	454.7	478.0
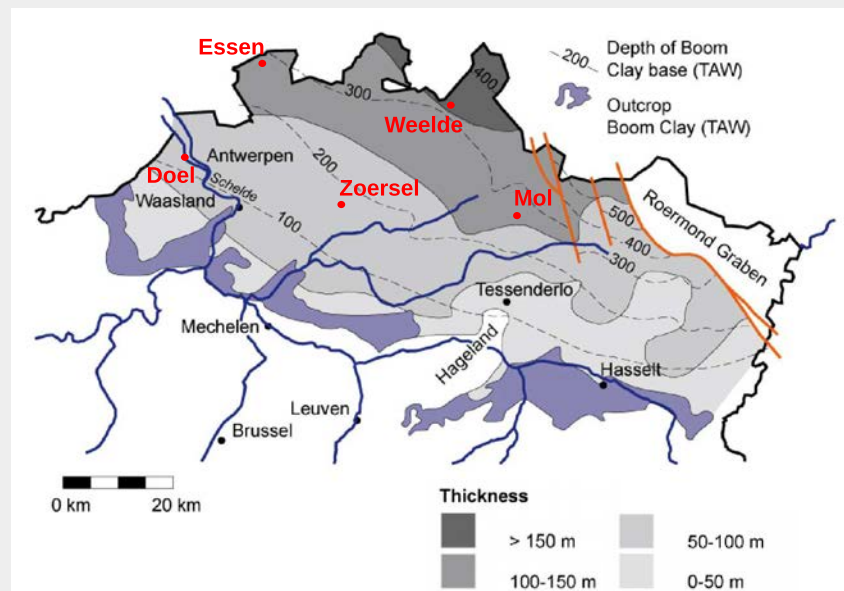
Figure 2.4.: Depth of the base, and thickness, of the Boom Clay Formation in Belgium with location of core-drilled boreholes (modified from ONDRAF/NIRAS, 2001b).
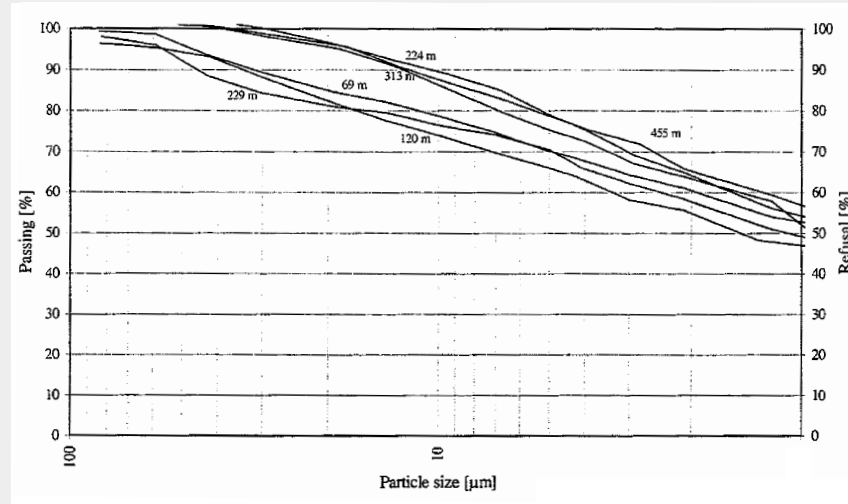
Figure 2.5.: Particle size distribution curves for specimens from Doel 2B (69m), Zoersel (120m), Mol 1 (224m & 229m), Weelde 1 (313m) and Blija (455m) (Barnichon et al., 2000).

with depth. The soil porosity decreased from $n = 0.4203$ to $n = 0.3923$. Except for the Doel 2B specimens, the initial and saturated water content decreased with depth ($w_{ini} = 27.30 - 23.31\%$ and $w_s = 27.70 - 23.52\%$). The increase in soil stiffness G and undrained shear strength (undrained cohesion c_u) with depth was accompanied by a significant increase in variance with depth.

With the exception of one data set from the Weelde site, the effective cohesion c' showed a regular increase with depth (Figure 2.6). The stability analysis performed within the TRUCK I study was based on the assumption that the hydro-mechanical soil property values become more favourable for stability (excavation) and serviceability (barrier function) with increasing depth. The results in Figure 2.6 show that the effective cohesion of $c' = 0.3$MPa, which was deemed in the TRUCK I study to be a conservative assumption for the depth of 500m, agrees well with the effective cohesion of $c' = 0.396$MPa obtained from the core sample of the Mol 1 borehole.

However, Figure 2.6 shows that the effective friction angle φ' seems to decreases slightly with depth. This reduction in φ' contradicts other results indicating an increase in consolidation with depth, a phenomenon which could not be explained by soil mechanical, geological or geomorphological processes based on the data given in the TRUCK II study. It is worth mentioning that Barnichon et al. (2000) specifically pointed out the good quality of the *Consolidated Undrained* (CU) triaxial test data based on the homogeneous samples selected using the CT scanner. Furthermore, the effective friction angle of $\varphi' = 18°$ applied in the TRUCK I study was significantly overestimated. Although a maximum friction angle of $\varphi'_{max} = 17.94°$ was obtained for the Doel 2B core at 69.5m depth, the friction angle φ ranges from $8.81°$ to $11.01°$ for any depth in excess of 100m.
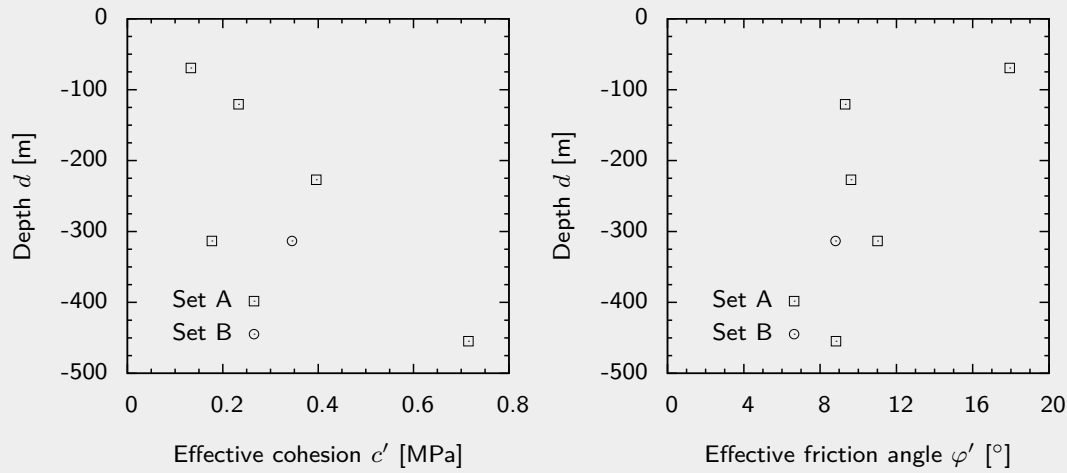
Figure 2.6.: Effective cohesion c' and effective friction angle φ' at different depths d obtained from CU triaxial tests on samples retrieved from cores of five boreholes within the TRUCK II research programme (after Barnichon et al., 2000).

In order to mainly study the drop in effective cohesion c' at about 313m, a second CU test Set B was performed on samples from the Weelde core (Figure 2.6). Whereas the cohesion increased approaching the mean trend, the friction angle further decreased.

Although prior CT scans were performed to ensure the homogeneity of samples being tested, the high variance may be mainly attributed to the aleatory uncertainty (see Section 3.2).

With respect to the MCC parameters $(p_c, \kappa, \lambda, M)$ the results presented were very sparse. For instance, the pre-consolidation pressure p_c was found to decrease linearly with depth and for some samples tested in the triaxial cell the volume decreased significantly whilst unloading. Barnichon et al. (2000) concluded that the lack of data paired with its scatter and inconsistency "… makes it very difficult and almost meaningless to interpret the obtained results in the critical state framework.".

The underlying assumption which distinguishes the TRUCK II from the TRUCK I design is the diameter and length of the tertiary disposal galleries. With $d_t = 0.75$m the disposal cell diameter is much smaller than the $d_t = 2.2/3.4$m inner/outer diameter of the TRUCK I design (see Figure 2.3). This reduction was chosen to reduce the size of the plastic zone, as well as to reduce the heat produced per canister to satisfy the prescribed $\Delta T_{max} = 4°$C upper bound for the top of the Boom Clay layer 50m above the canister center. In order to further increase the stability and safety, as well to emplace the canisters from the secondary galleries, the effective length of the disposal galleries was reduced to $l_t = 4.5m$, compared to the $l_t = 12.2m$ used in the TRUCK I design. As all operations associated with the tertiary disposal gallery (excavation, emplacement, sealing) have to be performed from the secondary gallery and require larger equipment, the inner diameter was increased to $d_p = d_s = 6$m.

The transient thermal analysis was performed using a one dimensional analytical solution (Giraud, 1993) as well as a three dimensional finite difference program FLAC 3D v2.0. The heat decay of the canisters was accounted for by applying the analytical relationship (Giraud, 1993; Heijdra et al., 1995) as a heat source over the canister area. The response of the variation in temperate ΔT computed via the 3D numerical and 1D analytical solutions was close to identical for the far field (50m) and in satisfactory accordance for the intermediate field (10m). The $4°C$ criterion 50m above the repository was satisfied by providing a minimum repository area per COGEMA (Compagnie Générale des Matières Nucléaires) canister of 271m^2, 179m^2 and 141m^2, for a period of 50year, 75year and 100year cooling time before disposal respectively. The proposed TRUCK II design with a 30×30m grid spacing between the tertiary disposal galleries, as well as the secondary galleries, would result in a repository area per COGEMA canister of 450m^2 and thus satisfy the thermal criterion.

A preliminary one-dimensional axisymetric analysis of the short term response (ideally undrained) of the saturated Boom Clay using the convergence-confinement method (Labiouse and Giraud, 1998) showed the extent of the plastic damage zone (Table 2.4). The extent of the plastic zone decreased employing the data from the URL at Mol. For the most optimistic combination (c), the extent of the plastic zone reduced by nearly a factor two. Given the low confidence in the consistency of the TRUCK II data discussed earlier, these results are only of qualitative importance.

In the subsequent three-dimensional finite difference analysis, the effective friction angle φ' was again chosen to be the most relevant parameter, although no sensitivity measure was given supporting this assumption. As for the TRUCK I study, the stability criterion was simply said to be satisfied if at least half the distance between two galleries remains elastic. Employing the lower and upper bound set of soil property values (Table 2.4) the extent of the plastic zone results in an unsatisfactory performance for case (a) and is just satisfactory for case (b) (Table 2.5). For cases (c) and (d), both with $\varphi' = 18°$, the stability criterion was satisfied.

Within the TRUCK II concept, one HLW waste COGEMA canister is disposed per disposal gallery. Two canister concepts have been proposed and some general conceptual aspects on the possible retrieval procedure for the canister for both concepts are discussed briefly by Barnichon et al. (2000).

Table 2.4.: Extent of plastic damage zone for secondary gallery for three sets of soil property values in the TRUCK II configuration based on one-dimensional axisymetric analytical solution (after Barnichon et al., 2000).

Data set	E' [MPa]	c' [kPa]	φ' [°]	r_p [m]
(a) TRUCK II set	1000	800	9	13.11
(b) URL MOL set	300	300	18	9.82
(c) updated TRUCK II	1000	800	18	7.06

Table 2.5.: Extent of plastic damage zone computed in horizontal and vertical directions, $r_{p,h}$ and $r_{p,v}$, for secondary gallery with a spacing s_s, for two sets of soil friction angles φ' utilizing three-dimensional numerical simulations (after Barnichon et al., 2000).

Case	s_s [m]	φ' [°]	$r_{p,h}$ [m]	$r_{p,v}$ [m]
(a)	30	9	∞	10.0
(b)	50	9	16.8	10.0
(c)	30	18	8.5	6.5
(d)	40	18	8.0	6.5

2.2.1.5. TRACTOR - Transport of RAdionuclides disposed of in Clay of Tertiary ORigin

The TRACTOR study (Wildenborg et al., 2000) assessed the influence of a potential ice sheet loading during a glacial period on the transport of radionuclides through the clay barrier. This work incorporated numerical simulations as well as experimental investigations on the hydro-mechanical soil property values. As the numerical simulations performed in the TRACTOR study are only of minor relevance for this feasibility study, they are not described here. However, the results of the additional experimental test program performed on the hydro-mechanical behaviour of the Boom Clay to complement the TRUCK II results is of significant relevance for this feasibility study and is thus discussed in detail.

Within the TRACTOR test program 4 CU triaxial tests and 6 oedometer (OED) consolidation tests have been performed on clay specimens sampled from the Weelde 1 and Blija site (Table 2.6). This set-up complements the two CU tests performed on specimens from a depth of 313.22-313.55m (Weelde 1) and 453.50-453-80m (Blija) within the TRUCK II study (see Table 2.3). Wildenborg et al. (2000) reported that the Weelde samples had the tendency to swell when they were extruded directly after retrieval in the laboratory. One sample is reported to have exploded upon extrusion, with evidence of a gas bubble being visible in the sample. The samples at 561.50-561-85m depth at Blija are from the Asse member. While these samples are not from the Boom Clay, they provide additional information on depths larger than 500m. The mineralogical analysis showed that the Smectite content of 50% in the clay specimens from the Asse member (lower Blija samples) is higher than for the Boom Clay (30-50% of Smectite). As for the TRUCK II set, X-ray tomography scans were used to identify the most homogeneous samples for the tests.

The sample characteristics follow the trend of the TRUCK II results, that is, with the soil density increasing with depth ($\rho_d = 1.576 - 1.666$kg m^{-3} and $\rho_s = 1.712 - 2.760$kg m^{-3}) and the gravimetric water content $w = 0.261 - 0.230$ and soil porosity $n = 0.4211 - 0.3923$ decreasing with depth. The Atterberg limits, i.e. the liquid limit $w_L = 0.7520 - 1.0510$, plastic limit $w_P = 0.2850 - 0.3250$ and plasticity index $I_P = 0.4670 - 0.7270$ increase with depth.

The TRACTOR triaxial results broadly agree with the TRUCK II results, however including the three TRACTOR tests, the variance of c' and φ' at the Weelde site (314m) increases

Table 2.6.: Core samples used in TRACTOR study (after Wildenborg et al., 2000).

Location	Weelde 1 (B)	Blija (NL)	
Depth [m]	313.22-315.10	453.50-453-80	561.50-561-85*
Tests	2×CU;4×OED	1×OED	1×CU;1×OED

* Clay specimens from the Asse member

and thus remains significant (Figure 2.7). Different consolidation pressures have been used, ranging from $\sigma_c = 3.1$MPa to $\sigma_c = 9.39$MPa, to simulate the present in situ state and that of a potential ice sheet loading. However, no correlation between σ_c and c' as well as φ' was evident.

As for the TRUCK II study the elastic shear modulus $G = E/\left[2(1+\nu)\right]$, where ν is the Poisson's ratio, was found to increase with depth (Figure 2.8). In the oedometer tests a compression index of around $C_c = 0.35 - 0.4$ for pressures above 10MPa was observed. The swelling index for the Weelde specimens was found to be about $C_s = 0.07 - 0.12$. The compression index λ, i.e. the slope of the *Normal Compression Line* (NCL, e.g. Wood (1990, 2004)), and swelling index κ, i.e. the slope of the *Unloading-Reloading Line* (URL), derived from the oedometer tests range from $\kappa = 0.06 - 0.07$ and $\lambda = 0.14 - 0.24$. It must be noted that Wildenborg et al. (2000) points out that the samples were disturbed due to the long time after extrusion. An *OverConsolidation Ratio* $OCR = \sigma'_{v,c}/\sigma'_{v,0}$, where $\sigma'_{v,c}$ is the vertical effective preconsolidation stress and $\sigma'_{v,0}$ is in situ vertical effective stress, of $OCR = 1.9 - 2.2$ for the Weelde specimens, and $OCR = 1.9 - 2.2$ for the Blija specimens was reported. Wildenborg et al. (2000) states that there was no conclusive evidence for ice age loading in the northern part of the Netherlands and that overconsolidation was to a large degree caused by ageing effects including creep and diagenesis.

2.2.2. Research undertaken as part of the OPERA project

This section briefly reviews relevant research work undertaken as part of the OPERA project and which has been finalised within the time frame of this project.

A desk study was carried out to update the geological and geohydrological characteristics of Boom Clay (Vandenberghe et al., 2014). Differences of up to 250 m in the depth to the top over the CORA study (Section 2.2.1) were noted in two regions, mainly caused by better information now being available. Qualitative trends in the depth and thickness reported in CORA were supported.

It was identified that in both vertical and lateral directions grain-size trends are apparent, and calculated permeabilities are therefore also heterogeneous. It was reported that there are only a limited number of measured data for both permeability and porosity, and those that exist were restricted to shallow depths. Therefore an approach utilising empirical formulations was undertaken and utilised to calculate vertical permeabilities.
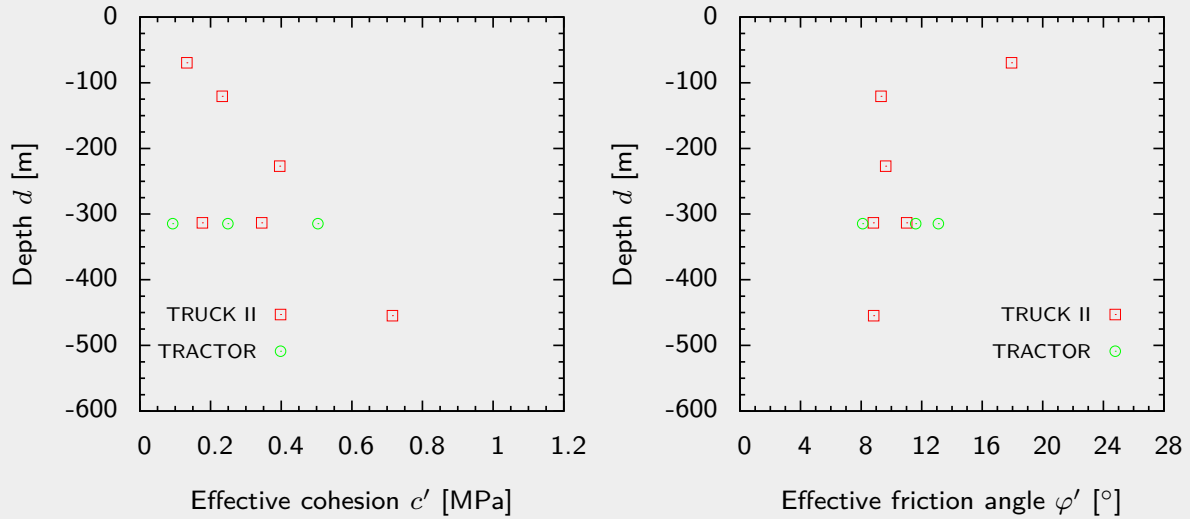
Figure 2.7.: Effective cohesion c' and effective friction angle φ' at different depths d, obtained from CU triaxial tests on Boom Clay samples retrieved from the Weelde 1 and Blija boreholes within the TRACTOR study complimenting the TRUCK II results (after Wildenborg et al., 2000).
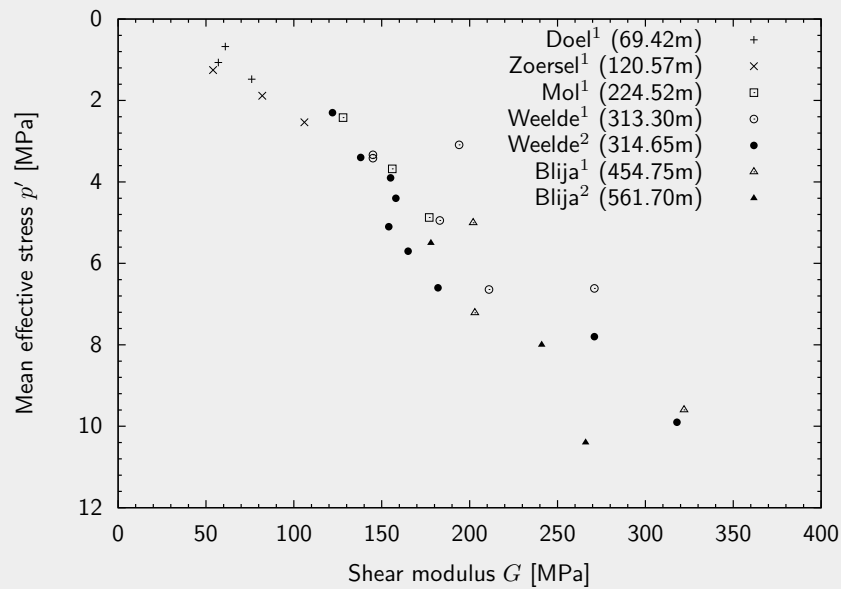
Figure 2.8.: Elastic shear modulus G vs. mean effective stress p' based on TRUCK II[1] and TRACTOR[2] CU triaxial results, computed assuming $\nu = 0.5$ and thus $G = 3E$ (after Barnichon et al., 2000; Wildenborg et al., 2000).

2.2.3. Salient international R&D activities on deep geological repositories

2.2.3.1. High-Activity Disposal Experimental Site Underground Research Facility (HADES)

The Hades URF is located in the north of Belgium in the vicinity of the town of Mol (Figure 2.4). The excavation of the first access shaft started in 1980 and the facility has since been extended several times (Figure 2.9(a)). The Hades URF is located at a depth of about 223m in the tertiary Boom Clay formation present between 190m and 290m depth (Figure 2.9(b)). The HADES URF is a generic URL studying the marine fine grained sediment as a potential host rock formation for HLW commissioned by ONDRAF/NIRAS.

The Boom Clay in Mol is underlain by the Lower Rupelian (sand and clay layers), the Asse Clay and the Lede-Brussel (sand), and is overlain by sandy layers of the Quaternary, Neogene and late Paleogene ages (Wemaere et al., 2008, Figure 2.9(b)). The experiences gained during excavation, as well as in situ experiments and long-term tests at the HADES URF, are well summarised and reviewed in Bastiaens et al. (2003, 2007), Bernier et al. (2007a,b,c) and Yu et al. (2013b). As will be discussed later in Section 3.5 in more detail, amongst other differences, the higher water content and lower bonding/cementation in the plastic Boom Clay results in time-dependant deformation and conductivity behaviours which can be significantly different to the ones observed for the indurated Callovo-Oxfordian and Opalinus argillite (e.g. Delage et al., 2007; Tsang et al., 2005; Volckaert et al., 2004; Wileveau and Bernier, 2008).

SELFRAC

The *European Atomic Energy Community* (Euratom) FP5 *Fractures and Self-healing within the Excavation Disturbed Zone in Clays* (SELFRAC) project (Bernier et al., 2007b) aimed to investigated the characteristics and evolution of the EDZ with time and its associated impact on the performance of deep geological repositories for radioactive waste. In the 1998 to 2002 time frame over 90 tests were performed, including four in-situ tests in the plastic Boom Clay (HADES URF) and indurated Opalinus clay (Mont Terri rock laboratory), to understand and quantify the fracturing and sealing/healing processes (Bernier et al., 2007b). During the construction of the Connecting Gallery at the HADES URF (see next item) a consistent fracturing pattern was recognised due to stress redistribution (see Figure 2.10). A set-up of parallel piezometers and seismic and acoustic measurement techniques have been used to evaluate the evolution of the EDZ at the HADES URF (see Bastiaens et al., 2007; Bernier et al., 2007b, and http://www.euridice.be/eng/ex_selfrac.shtm). Whereas the observed sealing effect of fractures in Boom Clay was very quick, only weak or partial healing was observed. Sealing in the Opalinus clay was observed to be significantly slower (Bastiaens et al., 2007; Bernier et al., 2007b).
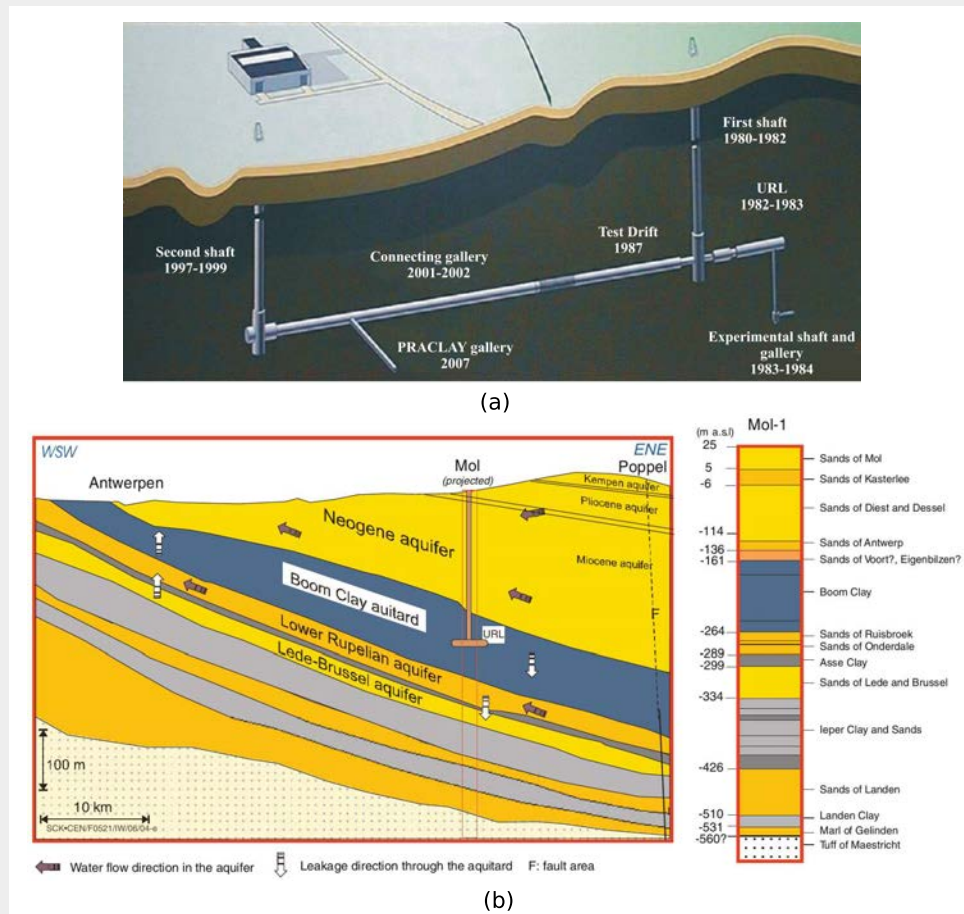
Figure 2.9.: (a) Hydrological cross-section and profile (Wemaere et al., 2008). (b) Outline of the Hades URF (http://www.sckcen.be/en/Our-Research/Research-facilities/HADES-Underground-laboratory).

Extension of the HADES URF in Mol

The construction of the Connecting Gallery, extending the HADES URF in Mol (see Figure 2.9(a)), was for facilitating the experimental basis for the SELFRAC as well as later described CLIPEX and PRACLAY measurement campaigns for characterise the extent and evolution of the EDZ/EdZ (see Bastiaens et al., 2003; Mertens et al., 2004, and http://www.euridice.be/eng/ex_connGal.shtm). With this excavation being the first of its kind in poorly-indurated clay at a depth of 223m, Bastiaens et al. (2003) describes in detail the experiences gained during the excavation and construction process using conventional tunnelling techniques (Figure 2.11(a)). Figure 2.11(b) shows the fracture patterns observed due to the stress relief associated with the excavation of the tunnel with 4.82m diameter, based on measurements obtained in an interval velocity and cross-hole seismic campaign as well as from two horizontal cored borings which are described by Bastiaens et al. (2003) and Mertens et al. (2004).

CLIPEX

The *CLay Instrumentation Programme for the EXtension of an underground research laboratory* (CLIPEX) project was performed within the frame of the extension of the HADES URF (see Bernier et al., 2007a, or http://www.euridice.be/eng/ex_clipex.shtm). The CLIPEX project aimed to asses the hydro-mechanical response due to the mechanised excavation. The measurement campaign consisting of pressuremeter, dilatometer and hydro-fracturing tests to investigate the in situ stresses, permeabilities, deformability and strength of the Boom Clay is summarised in Bernier et al. (2007a).

2.2.3.2. TIMODAZ

The *Thermal Impact on the Damage Zone around a Radioactive Waste Disposal in Clay Host* (TIMODAZ) project was one of the most significant research projects in recent years, studying the combined effect of the excavation and the thermal impact on the host rocks in the near field of the radioactive waste repository (http://www.timodaz.eu). Research within TIMODAZ was conducted in the 2006-2010 time frame as part of the Sixth Framework Programme FP6, by a consortium composed of 15 participating organisations representing 8 countries in total. It considered three types of clay, that is, the Boom Clay, the Opalinus clay and the Callovo-Oxfordian argilitte (Li, 2013a; Li, 2006).

The aim of the TIMODAZ project was to assess the impact of the *Thermo-Hydro-Mechanical and Chemical* (THMC) modifications of the clay properties, especially those of an irreversible nature, in the mechanically or thermal induced *Damaged Zone* (DZ), on the safety functions of the disposal system.
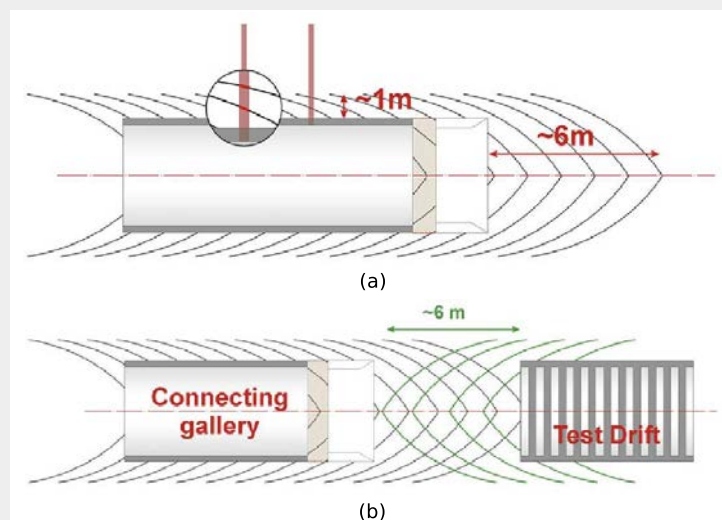
Figure 2.10.: (a) Vertical cross-section of the observed fracture pattern around the Connecting Gallery; the fractures originate about 6m ahead of the excavation face and their radial extent is about 1m. (b) Reactivated fractures induced by the construction of the test drift constructed in 1987. (Bastiaens et al., 2007)

(a)

(b)
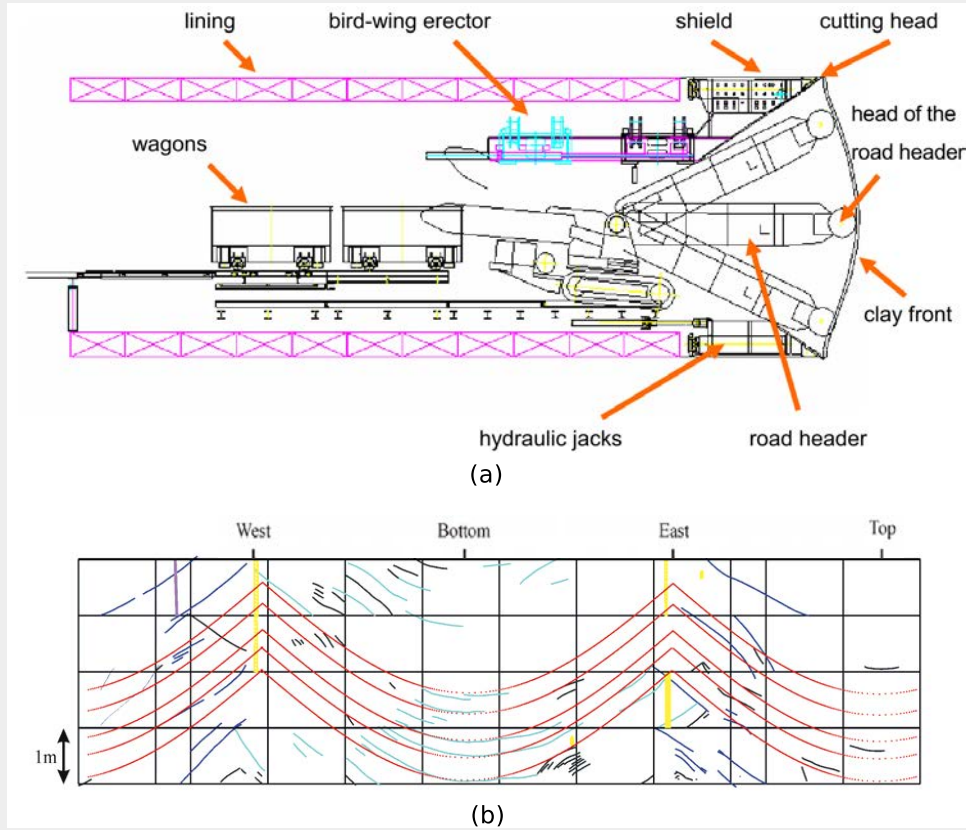
Figure 2.11.: (a) Cross-section showing the tunnelling machine in the Connecting Gallery. (b) Theoretical traces on the excavated profile (represented as an unfolded cylinder) of a (slightly simplified) fracture pattern and part of the fracture map, with one band corresponding to 1 meter. (Bastiaens et al., 2003)

Figure 2.12.: Location of the instrumentation in the CLIPEX programme, with σ, u and δ specifying locations of total pressure, pore-water pressure and displacement measurements respectively (Bernier et al., 2007a)

All experimental and modelling activities performed to answer these questions as part of the TIMODAZ project are summarised in Li et al. (2010b).

For the OPERA feasibility study three experimental campaigns are of interest.

(i) The gallery for the *preliminary demonstration test for clay disposal of highly radioactive waste* (PRACLAY), with a diameter of 2.5m and length of 45m, was excavated perpendicular to the Connecting Gallery in the HADES URF in 2007 (see Figure 2.9(b)). The PRACLAY Gallery comprised three large in situ tests (see Figure 2.13(a)), that is; (a) the Gallery and Crossing Test to investigate and demonstrate the feasibility of constructing a potential disposal gallery utilising industrial methods focusing on the crossing between the galleries; (b) the Seal Test, which examines the feasibility of a hydraulic seal; and (c) the long term Heater Test, assessing the response of the Boom Clay due to the thermal impact; these are described in detail in Li and Bernier (2005), Charlier et al. (2010b) and Li et al. (2010a). The PRACLAY test is fully installed, the swelling pressures of the bentonite seal (Figure 2.13(b)) are evolving slowly in a heterogeneous pattern and the heater test is to be switched on soon (Li, 2012).

(ii) The third phase of the *Admissible Thermal Loading for Argillaceous Storage* (ATLAS III) small-scale in situ heating test was performed in the HADES URF as part of TIMODAZ. The ATLAS III test set-up consisted of a heater element installed in a heater borehole, surrounded by multiple observation boreholes equipped with temperature sensors as well as flatjacks and piezometer filters to measure the total pressure and pore-water pressure repressively (Chen et al., 2011). Given the results obtained in previous small-scale heating tests performed at Mol, that is, CACTUS 1+2, CERBERUS and ATLAS I+II (Bernier and Neerdael, 1996; De Bruyn and Labat, 2002; François et al., 2009; Picard et al., 1994), ATLAS III aimed to investigate the spatial and temporal variation in temperature, pore-water pressure and total stress to a higher accuracy and larger extent using improved data acquisition systems (Chalindar et al., 2010). Confirming the results of previous in situ tests, the ATLAS III results show a mechanical and thermal

Figure 2.13.: (a) Layout of the PRACLAY In-Situ Experiment which is constituted of the Gallery and Crossing Test, the Seal Test and the Heater Test (Van Marcke and Bastiaens, 2010a); (b) Structure of PRACLAY Seal (Charlier et al., 2010b).

anisotropy of the Boom Clay, which is discussed in more detail in Chalindar et al. (2010) and Chen et al. (2011). At a later stage the results of the small-scale ATLAS and field scale PRACLAY heating tests will be correlated.

(iii) Hollow cylinder tests have been performed as part of the TIMODAZ project on Boom Clay samples, in order to study the development and evolution of the fracturing of the damage zone due to gallery excavation as well as subsequent thermal loading (Charlier et al., 2010a). Numerical simulations have been performed in order to predict the THM response in the experiments and to interpret the results in terms of constitutive behavioural features. The tests have been performed at the Laboratory for Mechanics of Rock of EPFL (`http://lmr.epfl.ch`) in Lausanne, Switzerland, and evaluated recently by François et al. (2013) and Labiouse et al. (2013) confirming the observation at the HADES URF in Mol of the development of an anisotropic excavation damaged zone around horizontally driven galleries in the Boom Clay. Four features are suspected to govern this response, that is, the strong mechanical irreversibility, the softening behaviour in the vicinity of the gallery, the strain localisation and the in situ anisotropy. Hollow cylinder tests have been performed as well on the Opalinus clay (Dedecker and Billaux, 2010).

The results of TIMODAZ integrated in a *Performance Assessment* (PA), show that the effect of the heat emitted from radioactive waste packages in a geological repository, on the barrier function of the clay host rock in the damage zone, is not detrimental, to the safety function of a repository system being expected to be maintained after the heating-cooling cycle (e.g. Li et al., 2012b; Yu et al., 2010, 2014).

2.3. Deep geological disposal of radioactive waste in Boom Clay

2.3.1. Phases of a radioactive waste repository

The life-time of a radioactive waste repository may be categorised into five phases, which are schematically outlined in Figure 1.5. *Phase 0* describes the in situ situation prior to excavation. *Phase 1* describes the staged excavation process of the repository. This *"open phase"*, starting at time t_1 with the physical excavation, ends with the installation of the concrete liner support structure at t_2. *Phase 2* is the pre-operational phase for the parts of the repository which are ready for the waste emplacement. *Phase 3* describes the staged emplacement of the radioactive waste. *Phase 4* is the post-closure which starts at time t_4 with the sealing of individual compartments of the repository.

The radioactive waste disposal process in the Netherlands is at an early, conceptual phases with the operational phase not expected to start before 2130 (Verhoef et al., 2011). Figure 2.14 outlines the anticipated phases of the Dutch deep geological repository for radioactive waste (Verhoef et al., 2011).

Figure 1.5 schematically outlines some of the main THMC coupled physical processes governing the response and safety functions within the multi-barrier system of the repository, that is, within each individual compartment as well as at the boundary between them in the near and far fields. The individual processes, their coupling as well as their impact at the different stages, will be assessed in Section 2.5. The compartments of the OPERA deep geological disposal concept in clay will be described in the following section.

2.3.2. The proposed OPERA deep geological disposal concept in clay

The current OPERA deep geological disposal concept in clay has been developed by COVRA and NRG (Verhoef et al., 2011). The HLW disposal concept is based on the Belgian *Super-container*, based on a contained environment concept (e.g. Craeye, 2010; Kursten and Druyts, 2008) orienting itself on the guidelines for building a Safety Case for a hypothetical underground repository in clay (Baekelandt et al., 1996) and on the TRUCK I design (Steen and Vervoort, 1998).

The OPERA reference design (Verhoef et al., 2011) is schematically outlined in Figure 2.15. As for the TRUCK-I and TRUCK-II designs, the OPERA repository consists of one single level with the waste being segregated in specific zones. For consistency, in this feasibility study the zones will be subdivided into: *Zone A* - LILW & *Technically Enhanced Naturally Occurring Radioactive Material* (TENORM); *Zone B* - non heat producing HLW; and, *Zone C* - heat producing HLW and SNF. For scenarios where LILW and HLW are disposed in one deep geological facility, the concept of co-location is commonly employed for the design, a.g. in France (ANDRA, 2005a,b,c,d) and in the United Kingdom (NDA, 2010a,b; Watson et al., 2009).

Two vertical access shafts and/or an (optional) inclined ramp will lead from the surface facilities to the repository level. As for the TRUCK-I and TRUCK-II concepts, the tunnel galleries are subdivided into one main (primary) gallery, secondary galleries and disposal galleries (Figure 2.15). The main dimensions have been tabulated in Table 2.7.
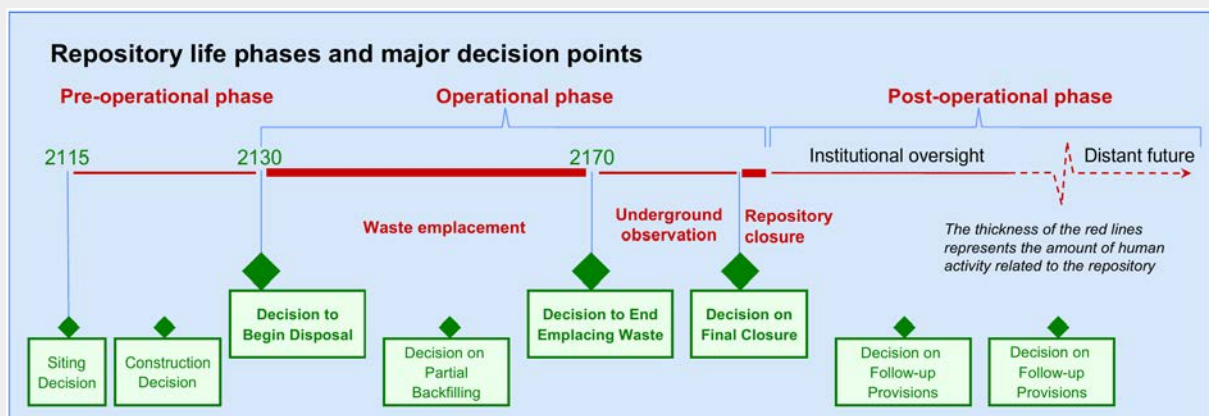
Figure 2.14.: Phases of Dutch repository for radioactive waste (Verhoef et al., 2011).

Cross Section: A-A'

Cross Section: B-B'

Cross Section: C-C'

Top View: Disposal facility

	LILW		Pilot facility
	Non heat producing HLW		Workshop
	SNF		Main Gallery
	Vitrified HLW		Secondary Galleries
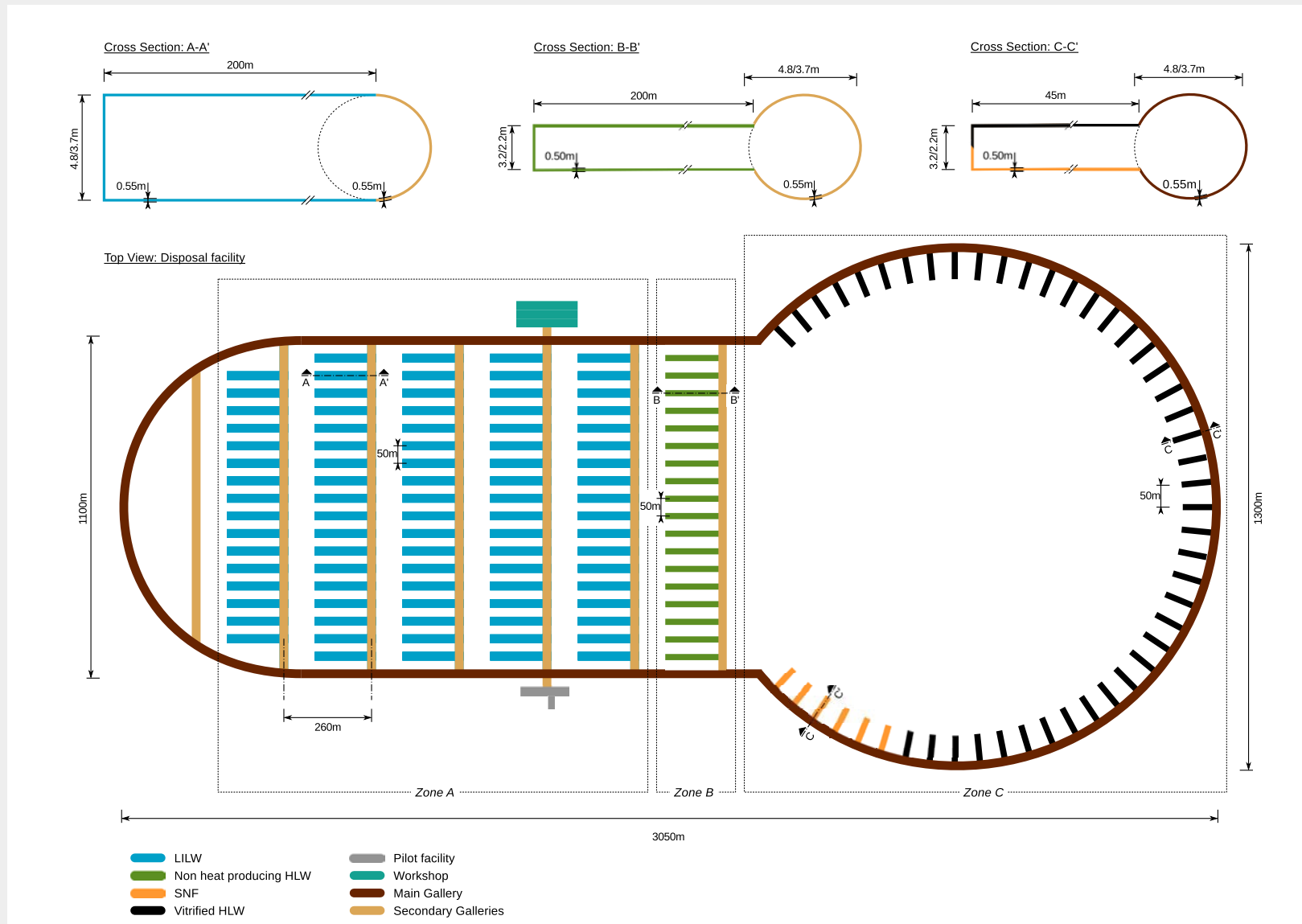
Figure 2.15.: Schematic outline of the OPERA deep geological underground disposal facility in Boom Clay (after Verhoef et al., 2011).

Table 2.7.: Dimensions of the shafts, galleries and tunnels (Verhoef et al., 2011).

Part	Number	Length [m]	Diameter[1] [m]	Concrete liner thickness [m]	Gallery spacing [m]
Shaft	2	500	6.2/5.0	0.60	1110
Main Gallery	1	7200	4.8/3.7	0.55	N.A.
Secondary Galleries	6	1100	4.8/3.7	0.55	260
Disposal Galleries					
↪Heat-generating HLW	47	45	3.2/2.2	0.50	50
↪Spent fuel	6	45	3.2/2.2	0.50	50
↪Non-heat-generating HLW	21	200	3.2/2.2	0.50	50
↪LILW and (TE)NORM	103	200	4.8/3.7	0.55	50

[1] Excavated diameter/Inner diameter of the gallery concrete support structure.

The main gallery, connecting the shafts with all disposal zones in the repository, is excavated in a single loop and will serve all transportation and access purposes. The secondary access galleries are of same dimension. In Zones A and B, dead end disposal drifts with an envisaged length of $l_d = 200$m are excavated perpendicular to the secondary galleries. The inner (liner) and outer (excavation) diameters of the disposal galleries are $d_d = 3.7$m and $d_d = 4.8$m for Zone A, and $d_d = 2.2$m and $d_d = 3.2$m for Zone B, the latter of which is nearly identical to the TRUCK-I concept ($d_d = 2.2/3.4$m). The disposal galleries in Zone C are excavated directly from the primary gallery, with a length of $l_d = 45$m and an inner/outer diameter of $d_d = 2.2/3.2$m. The location of the disposal drifts, on the inside of the curved part of Zone C, was chosen to have the possibility of extending the heat generating HLW or SNF section to the outside of the curved part in a modular fashion if more waste is to be disposed.

Further underground installations include a pilot facility and a workshop for maintenance. The pilot facility is envisaged to consist of a short disposal drift comparable to the layout foreseen for the emplacement of the HLW and contain one single OPERA Container with vitrified HLW (Verhoef et al., 2011).

The deep geological repository concept consists of an *Engineered Barrier System* (EBS) and multiple natural barriers, in order to satisfy all containment and long-term isolation requirements for the disposal of radioactive waste. Figure 2.16 outlines the OPERA *Multi-Barrier System* (MBS) which has six compartments:

○ The near-field

    ↪ Durable waste forms (waste matrix).

    ↪ Waste package (canister, overpack, buffer).

    ↪ Further EBS components (buffer materials, backfill, seals, plugs).

○ The far-field
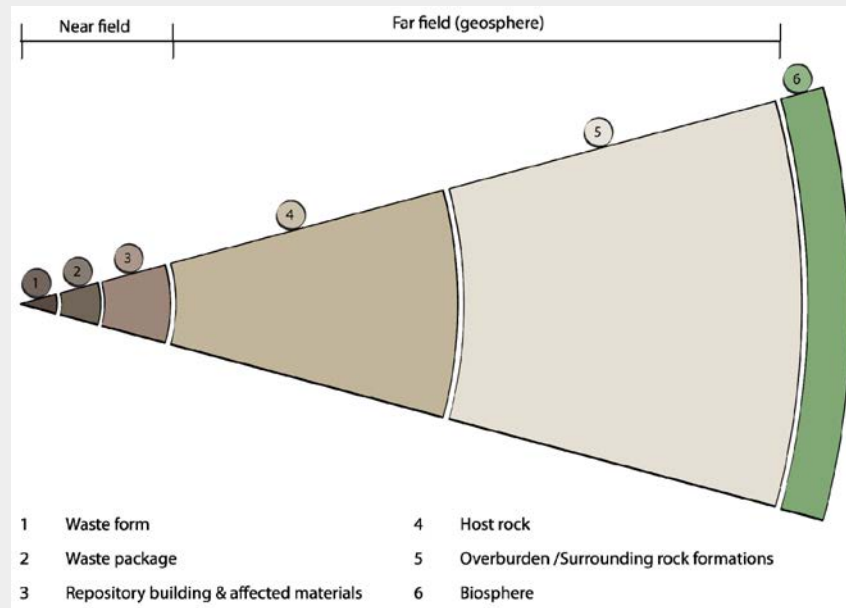
Figure 2.16.: Compartments of design of the OPERA repository concept (Verhoef et al., 2011).

> ↪ Host rock (a.g. plastic clay, shale, crystalline rock, sedimentary rock).

> ↪ Underlying and overlying geological formations.

○ The biosphere

> ↪ Living organisms and physical near surface media.

The provisional OPERA Supercontainer, in which the waste is to be packed, has an outer diameter of $d_{sc} = 1.6 - 1.8$m and an outer length of $l_{sc} = 2.5$m, which are smaller dimensions than its Belgian counterpart. Figure 2.17 schematically outlines the OPERA EBS.

Each Supercontainer can hold three types of waste canister, that is, either:

○ one *Colis Standard de Déchets - Vitrified* (CSD-V[3]) canister for heat generating vitrified HLW (OPERA-A),

○ two spent fuel *Energieonderzoek Centrum Nederland* (ECN) baskets (OPERA-B), or

○ one *Colis Standard de Déchets - Compactés* (CSD-C[4]) canister for non heat generating HLW (OPERA-C).

The dimensions of the canisters can be found in Verhoef et al. (2011). Subsequent to the fabrication of the concrete buffer inside the stainless steel envelope, the carbon steel overpack containing the canisters is emplaced, the remaining annular gaps filled under thermal load

---

[3] CSD-V containers designed by the French company COGEMA as well as glass matrix, presently AREVA.
[4] CSD-C containers designed by the French company COGEMA.

and the concrete lid is fitted (Craeye, 2010). A 30mm carbon steel overpack and a 700mm concrete buffer surrounded by a stainless steel envelope enclose the Supercontainer.

For tunnels in Boom Clay, a permanent support structure needs to be installed in order provide stability and minimise the convergence of the excavated galleries. In the Meuse/Haute-Marne (France), excavated in Callovo-Oxfordian clay, concrete support was used to support the access shafts, but for the 445m deep drifts a concrete lining was not necessary (Delay et al., 2008). For a later repository a steel welded mesh, with rock bolts and about 20-30cm shotcrete is planned to be used (ANDRA, 2005b). In the Mont Terri Rock laboratory (Switzerland), situated in Opalinus clay, the lining consists of a 15-20cm thick shotcrete layer reinforced with steel or plastic fibres (Bossart and Thury, 2007). Experiences with the HADES URF (e.g Bastiaens et al., 2003; Bernier et al., 2007c) as well as from the TRUCK projects (Sections 2.2.1.3 and 2.2.1.4) show that, for the plastic Boom Clay, a much stiffer support structure is required. For the OPERA design this support is thought to be provided by pre-fabricated concrete segments emplaced during the mechanical excavation of the tunnels.

In the OPERA concept, the backfill (or buffer) material which fills the void between the Supercontainer and concrete lining (Figure 2.17) primarily serves to hold the Supercontainer in place, and to eventually adsorb deformations induced by the host rock, to contain radionuclides, to transport the potential heat from the Supercontainer and to create a favourable geochemical environment to limit corrosion and leaching.

The near field host rock will be perturbed by the mechanical excavation and/or by the thermal loading. The area affected by the excavation induced stress relief in the host rock is generally referred to as the *Excavation Damaged Zone* (EDZ) or *Excavation disturbed Zone* (EdZ), which may be generally defined based on the suggestions by Davies and Bernier (2005) and Tsang and Bernier (2005) as:

> *"The Excavation Disturbed Zone (EdZ) is a zone with hydromechanical and geochemical modifications, without major changes in flow and transport properties."*

> *"The Excavation Damaged Zone (EDZ) is a zone with hydromechanical and geochemical modifications inducing significant changes in flow and transport properties. These changes can, for example, include one or more orders of magnitude increase in flow permeability."*

Note that the host rock in close vicinity to the repository that is influenced by potential perturbations (a.g. Edz/EDZ) is part of the near field and grouped in the OPERA concept under "affected material" in compartment three.

2.4. In Situ conditions of Boom Clay

The in situ conditions and soil property values of the Dutch Boom Clay formation, serving as the potential host rock, will significantly influence the coupled THMC response of the intact and perturbed MBS compartments. In order to interpret the THMC processes taking place

Gallery for heat generating HLW & SNF

Cross Section: B-B'

Longitudinal Section: A-A'

Legend:
- Waste canister
- Steel overpack (30mm)
- Concrete buffer with stainless steel envelope
- Backfill
- Plug
- Gallery floor
- Concrete lining
- Boom Clay
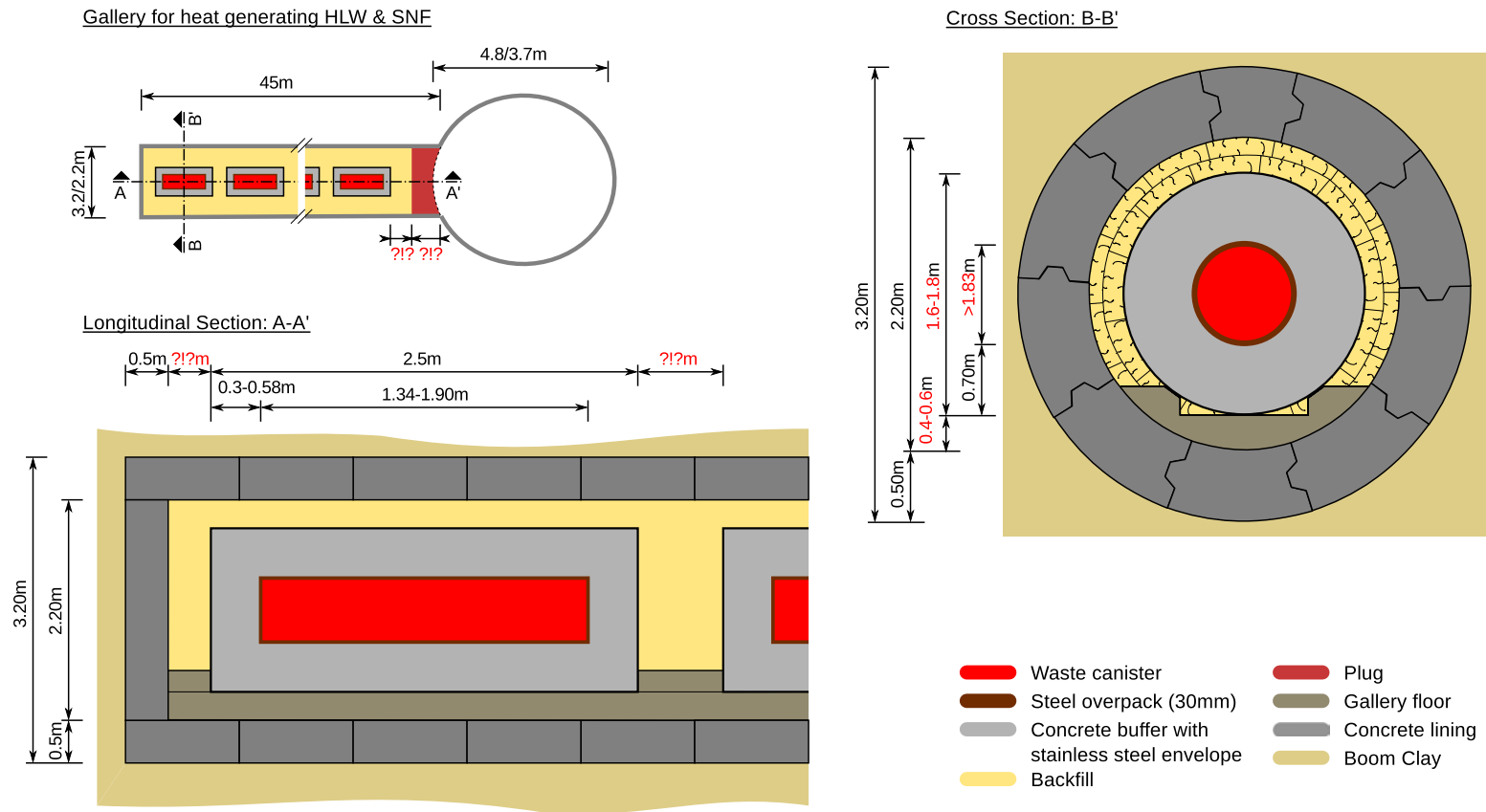
Figure 2.17.: Schematic outline of the Supercontainer concept for HLW and SNF disposal in tertiary Boom Clay galleries (after Verhoef et al., 2011).

Table 2.8.: Lithostratigraphy of the Rupel Group (taken from Delécaut, 2004, after Vandenberghe, 2003).

Group	Formation	Member	Lithology
Rupel	Eigenbilzen		Fine clayey glauconite-rich bioturbated sands
	Boom	Putte	Dark, blackish-brown organic-rich clays
		Terhagen	Blueish grey to grey, partially carbonate-rich clay
		Belsele-Waas	Grey silty clay
	Bilzen	Kerniel	Fine- to medium-grained whitish-yellowish to brownish quartz sand
		Kleine-Spouwen	Greenish to yellowish grey clay containing carbonate concretions and Nucula compta
		Berg	Yellow to white homogeneous quartz sands

during the repository phases discussed in the subsequent sections 2.5.1 to 2.5.4, some of them will be addressed briefly in this section. Focusing on the Boom Clay host rock, individual property values and states obtained from the literature including additional information, e.g. on data quality, test procedure used, etc., are currently implemented in a database which will serve as the necessary basis for the envisaged probabilistic assessment of the generic OPERA repository.

2.4.1. Lithology, mineralogy, organic matter and pore-water chemistry

This subsection is a complement to the CAR-I and CAR-II project discussed in Sections 2.2.1.1 and 2.2.1.2, primarily based on investigations on the Belgium Boom Clay performed by SCK·CEN.

The Boom Clay Formation is a marine Oligocene shelf deposit from the Lower Oligocene Rupelian stage and builds with the Bilzen and Eigenbilzen Formations the Rupel Group (Table 2.8). The Boom Clay has three members, that is, Putte Member (Upper dark clay), the Terhagen Member (carbonate-rich blue clay), and the lower Belsele-Waas Member (gray silty clay). Detailed information on the stratigraphy and lithology of the tertiary sequences can be found in, amongst others, Vandenberghe (1978, 2003), Wouters and Vandenberghe (1994), Weerts et al. (2000) and Vandenberghe et al. (1998, 2004).

Since the 1970s, the Boom Clay mineralogy at different depths and locations has been assessed both on a more qualitative or quantitative level (e.g. Decleer et al., 1983; Laenen, 1997; Vandenberghe, 1978; Wouters et al., 1999). Decleer et al. (1983) provide the variance and covariance of the mineralogical components. More recently, the mineralogical composition of the Belgian Boom Clay was quantified for samples from boreholes Mol-1, Doel-2b and Zoersel-1 (De Craen et al., 2000), from the HADES borehole 2003/9 (De Craen, 2005), from Essen-1 borehole (Honty and De Craen, 2009) and from the borehole Mol-1 and a limited number of outcrop samples (Zeelmaekers, 2011).

As part of the preparation of the Belgian Safety and Feasibility Case 1 (SFC1), a detailed characterisation of the mineralogical composition of the Boom Clay, primarily in the Campine

area, was performed by Honty and De Craen (2012). Re-evaluating existing data in combination with the recent results obtained by Zeelmaekers (2011) using a new and improved methodology, resulted in an extensive description of the Boom Clay mineralogy both on the local scale at Mol as well as over the regional scale, that is, providing parameter ranges and, where available, point variance and covariance measures.

From a mineralogical point of view the Boom Clay is a homogeneous sediment in both the vertical and horizontal directions, with variations present at the regional scale (Honty and De Craen, 2012). Figure 2.18 illustrates the local scale characteristic layered structure of Boom Clay for two vertical Boom Clay cross-sections. The regularly alternating silty clay and heavy clay layers in the Boom Clay, with a thickness of up to one tenth of a centimetre, reflect previous sea level fluctuations showing strong variations in grain-size, content of non-clay materials and organic matter (e.g. Decleer et al., 1983; Honty and De Craen, 2012; Van Keer and De Craen, 2001).

Table 2.9 provides an overview of the main mineralogical components collected in the literature. From the ternary diagram (Figure 2.19) it is apparent that, based on the grain size distribution, most samples are clayey silts (Yu et al., 2011). However, this does not imply that the mineralogical ranges are biased by the predominance of silt-rich layers, but only that for example silty beds contain relatively more quartz (the dominant non-clay mineral) and less clay minerals (Honty and De Craen, 2012). Smectite and kaolinite are the dominant clay minerals, the former significantly influencing the the swelling potential (e.g. Yilmaz, 2009). Investigating five cores from the Essen-1 borehole, Deng et al. (2011a) found that the smectite content from one sample of the Terhagen member was significantly higher (≈ 0.5) compared to other samples in the close vicinity taken from cores in the Putte and Terhagen members (0.1-0.3) or to samples for the Mol Boom Clay.

Samples taken from calcareous-rich horizons show a significant increase in siderite and calcite content. However, the calcite content in the Opalinus clay (0.06-0.22) and the Callovo-Oxfordian mudstone (0.23-0.42) is significantly higher (e.g. Gens et al., 2007). Also regional variations can be observed; the mineralogical composition varies with location but is comparable at the Mol site and in the outcrops (Honty and De Craen, 2012). From its deposition about 30Ma ago, the Boom Clay underwent little diagenesis with the mineralogical composition not being changed significantly. Honty and De Craen (2012) conclude that *"no significant mineralogical changes are expected as a result of a changing geochemical environment (changes in the pore water composition), or due to neo-tectonic vertical movements (subsidence/burial or uplift and associated temperature changes)"*.

In the organic rich horizons the concentration of *Total Organic Carbon* (TOC) ranges between 1% and 8% (see Table 2.9). About 99.9% of this TOC is immobile, and 0.1% (about 115±15 mg C l^{-1}) is dissolved in the pore water and mobile (e.g. Bruggeman and De Craen, 2011; De Craen et al., 2004; Van Geet, 2004).

The pore water is found to be mildly alkaline with an in situ pH value of about 8.2-8.5 (Table 2.9). The pore-water chemistry of both the Mol-1 and Essen-1 boreholes was assessed in more detail by De Craen et al. (2004, 2006). Decreasing of the pH value to lower than 7.5 was observed by De Craen et al. (2004) on samples after two months storage at room
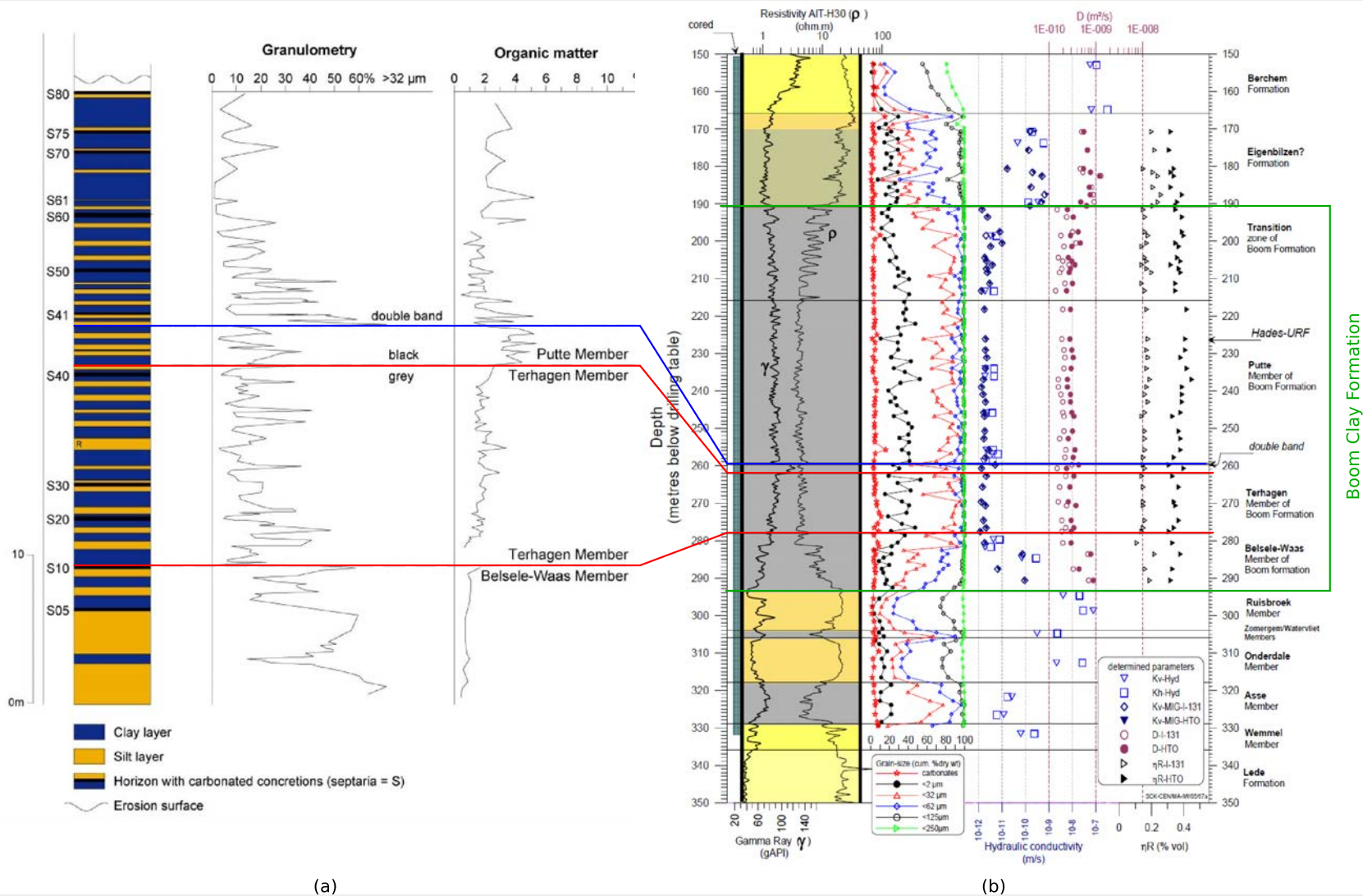
Figure 2.18.: (a) Lithostratigraphic profile of the Boom Clay and lithological variation (after ONDRAF/NIRAS, 2001b); (b) Vertical profiles of resistivity, Gamma Ray, cumulative grain sizes, hydraulic conductivity, dispersion coefficient and water content in the Boom Clay and overlaying/underlying layers for the Mol-1 borehole (after Aertsens et al., 2005).

Table 2.9.: Cumulative ranges of the mineralogical composition, organic matter and pore-water chemistry of the Boom Clay obtained from literature.

Definition	Range [% 100^{-1}]		Source
Clay minerals	0.23	0.71	1,2,9,10,11,12
Kaolinite	0.01	0.36	1,2,7,10,12,14
Smectite	0.068	0.561	1,2,4,7,14
Illite/muscovite	0.01	0.37	1,2,7,12,14
Veermiculite/chlorite	0.01	0.04	10,12
Non-clay materials	0.335	0.77	10,12
Quartz	0.2	0.66	1,3,7,10,12,14
K-feldspar	0	0.11	3,10,12,14
Na-plagioclase	0	0.063	10,12,14
Albite	0	0.063	3,7
Orthoclase	0	0.018	7
Carbonates	0.0024	0.05	10,13
Pyrite	0	0.096	3,7,10,12,14
Calcite	0	0.042	3,7,9,12,14
Siderite	0	0.209	3,14
Chlorite	0	0.04	7,14
Dolomite	0	0.04	14
Apatite	0	0.01	14
Organic matter	0.0064	0.08	1,10,12
pH-value	8.2	8.5	5,6,10
Salinity [mg l^{-1}]	1287	7249	3,6,8
Alkalinit [meq l^{-1}]	7.2	15.0	6,8
TOC [mg C l^{-1}]	23	150	3,6,8

Sources: [1]Decleer et al. (1983), [2]Barnichon et al. (2000), [3]De Craen et al. (2000), [4]Wildenborg et al. (2000), [5]ONDRAF/NIRAS, 2001b, [6]De Craen et al., 2004, [7]De Craen (2005), [8]De Craen et al. (2006), [9]Gens et al. (2007), [10]Li et al. (2007), [11]Bock et al. (2010), [12]Zeelmaekers et al. (2010), [13]Deng et al. (2011a), [14]Honty and De Craen (2012)

temperature, due to potential bacterial activity. Furthermore, an increase of the pH value up to 9.3 was observed by sample stirring during the measurement, i.e. complete degassing of CO_2, or by leaching the samples in distilled water.

The pore-water of the Boom Clay becomes more saline with increasing depth and towards the north of Belgium, i.e. when coming in closer contact with aquifers with waters of marine origin (De Craen et al., 2000, 2004, 2006). The average dissolved TOC seems to decrease with increasing salinity.

The *Cation Exchange Capacity* (CEC) is a measure of the adsorption of cations on clays and was found to vary between 12-27 meq/100g, i.e. indicating a variation in the smectite content (Honty, 2010; Honty and De Craen, 2012).
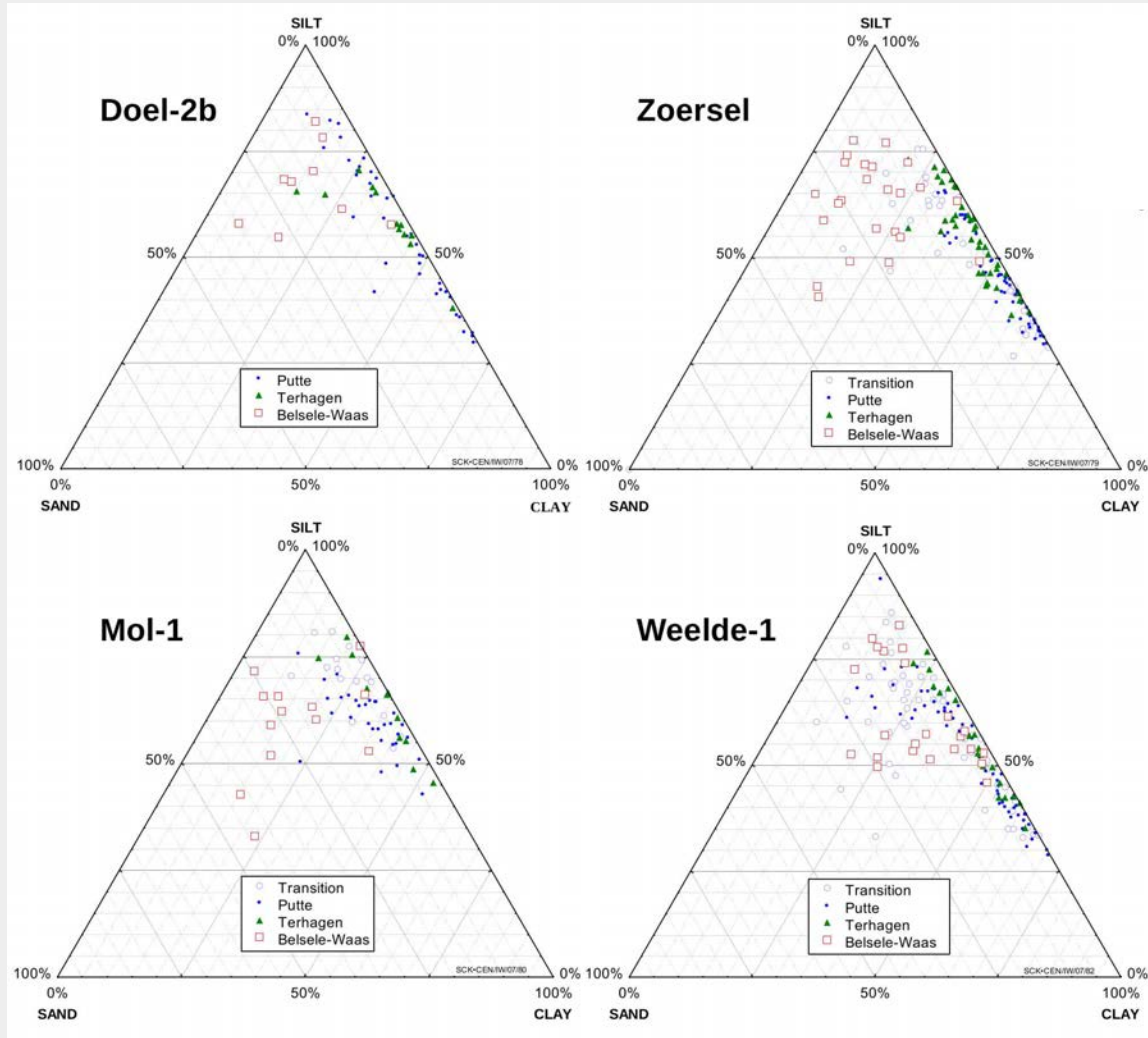
Figure 2.19.: Shepard's diagrams of the Boom Clay grain-sizes in Doel-2b, Zoersel, Mol-1 and Weelde-1 boreholes (clay: $< 2\mu$m, silt: $\geq 2\mu$m and $< 62.5\mu$m, sand: $\geq 62.5\mu$m) (Yu et al., 2011).

2.4.2. In-situ conditions

At the HADES URF (223m depth) the total vertical stress and pore water pressure are approximately hydrostatic, i.e. $\sigma_v = 4.5 - 4.6$MPa and $u_w = 2.2 - 2.25$MPa (e.g. Bastiaens et al., 2006; Bernier et al., 2007c). However, the definition of an earth pressure at rest value, $K_0 = \sigma_h/\sigma_v$, is more complex with open questions remaining (Li et al., 2007). The K_0 value obtained via in situ pressuremeter, dilatometer, self-boring pressuremeter (SBP), hydrofracturing tests, borehole breakout analysis and back-analysis of linear cavity pressures suggested values in the range of $0.3 - 0.9$ (Bernier et al., 2007c). Laboratory results by Horseman et al. (1987, 1993) show a range of $K_0 = 0.5 - 0.8$, whereas $K_0 = 0.84$ was back-calculated by Baldi et al. (1991b).

2.4.3. In situ soil property values

The specification of the in situ soil property values of the intact and undisturbed Boom Clay is vital for assessing the feasibility and safety, e.g. the susceptibility to potential perturbations. This subsection is a complement to the discussion on the results of the CORA projects TRUCK I+II (Sections 2.2.1.3 and 2.2.1.4) and TRACTOR (Section 2.2.1.5), assessing primarily the stiffness, strength and permeability of Boom Clay.

Numerous laboratory and in situ tests on natural Boom Clay samples have been performed in recent years. However, a significant amount of research was performed on reconstituted Boom Clay, which may be used as a backfill material (Section 2.5.3). The advantage of using reconstituted Boom Clay is that the samples can be easily adjusted to obtain a desired constitution and consolidation history. However, significant differences in the hydraulic and mechanical behaviour of reconstituted and natural Boom Clay results from this process.

Table 2.10 summarises the ranges of some soil property values potentially governing the THM response of the Boom Clay host rock. For each variable, multiple sets of data with as much information as possible on the directly and indirectly obtained values have been implemented within a currently developed local database. Furthermore, the following literature references provide a general summary on some soil property values for argillaceous rocks, that is, as well for the indurated Opalinus clay and the Callovo-Oxfordian mudstone, e.g. Volckaert et al. (2004), Boisson (2005), Gens et al. (2007), Li et al. (2007), François et al. (2009), Delage et al. (2010) and FORGE (2010).

2.4.3.1. Configuration of phases and classification

The plastic Boom Clay (Table 2.10) has a relatively low density and thus a higher porosity than the Opalinus clay ($\rho = 2220-2330 \text{kg m}^{-3}$; $n = 0.135-0.179$) and the Callovo-Oxfordian mudstone ($\rho = 2210 - 2330 \text{kg m}^{-3}$; $n < 0.13$) (e.g. Gens et al., 2007). The Boom Clay is a stiff clay, with a plasticity index of about $I_p = 0.3123 - 0.727$ and a specific gravity of $G_s = 2.64 - 2.71$.

The porosity of the Boom Clay ranges from about 0.204 to 0.46 (Table 2.10). Recently, Desbois et al. (2009, 2010) and Hemes et al. (2011, 2012, 2013) characterised the porosity of the Boom Clay at nano- to micrometer scale, using BIB/FIB (Broad Ion Beam/Focussed Ion Beam) SEM methods. The measurements were found to agree well with mercury porosimetry data, but were mostly much lower than the water content porosity (Desbois et al., 2010). Furthermore, two different porosity regimes have been identified, that is the *intra-* and *inter-phase porosity*, for which the boundary in Boom Clay was found to be at a pore-size of $\approx 500 \text{nm}$ (Hemes et al., 2012). The results further show that the larger pores at *inter-aggregate* level are predominantly found at the interface between different mineral phases and are strongly dependent on the grain size distribution (Hemes et al., 2011, 2012). Previous investigations employing mercury injection porosimetry (e.g. Della Vecchia et al., 2010; Romero and Vaunat, 2000; Romero et al., 1999, 2011) showed similar results, indicating that, for defining the water retention properties, reaching the *intra-aggregate* level the water content is no longer affected by mechanical effects.

Table 2.10.: Some Boom Clay property value ranges governing the thermo-hydro-mechanical behaviour. Status May 2013

Definition	Symb.	Unit	Range	Source
Dry density	ρ_d	[kg m^{-3}]	1540 - 1780	*
Bulk density (sat.)	ρ	[kg m^{-3}]	1900 - 2100	*
Solid (grain) density	ρ_s	[kg m^{-3}]	2650 - 2760	*
Specific gravity	G_s	[$-$]	2.64 - 2.71	*
Porosity	n	[$-$]	0.204 - 0.460	*
Void ratio	e	[$-$]	0.665 - 0.785	*
Gravimetric water content	w	[$-$]	0.095 - 0.400	*
Liquid Limit	w_L	[$-$]	0.309 - 1.051	*
Plastic limit	w_P	[$-$]	0.210 - 0.330	*
Plasticity index	I_P	[$-$]	0.312 - 0.727	*
Effective Young's modulus	E	[MPa]	150 - 500	*
Effective Poisson's ratio	ν	[$-$]	0.125 - 0.45	*
Compression index	C_c	[$-$]	0.180 - 0.405	*
Swelling index	C_s	[$-$]	0.022 - 0.680	*
Effective cohesion	c'	[MPa]	0.01 - 1.818	*
CU cohesion	c_{cu}	[MPa]	0.125 - 1.823	*
Effective friction angle	φ'	[°]	2.1 - 25.0	*
CU friction angle	φ_{cu}	[°]	2.0 - 15.21	*
Dilation angle	ψ	[°]	0 - 11	*
UCS	q_u	[MPa]	2 - 2.8	*
NCL slope	λ	[$-$]	0.0685 - 0.24	*
URL slope	κ	[$-$]	0.0128 - 0.07	*
CSL slope	M	[$-$]	0.3236 - 0.87	*
Saturated hydraulic conductivity	K_{sat}	[m s^{-1}]	1.00E-12 - 9.30E-12	*
Vertical saturated hydr. cond.	$K_{sat,v}$	[m s^{-1}]	1.00E-12 - 5.43E-10	*
Horizontal saturated hydr. cond.	$K_{sat,h}$	[m s^{-1}]	2.00E-12 - 6.22E-10	*
K-anisotropy	$\frac{K_{sat,h}}{K_{sat,v}}$	[$-$]	1.04 - 10.98	*
Thermal conductivity	λ	[W m^{-1} K^{-1}]	1.35 - 1.7	*
Vertical thermal conductivity	λ_v	[W m^{-1} K^{-1}]	1.06 - 1.31	*
Horizontal thermal conductivity	λ_h	[W m^{-1} K^{-1}]	1.55 - 1.7	*
Degree of anisotropy	λ_h/λ_v	[$-$]	1.260 - 1.462	*
Iso. thermal dilation coefficient	α_c	[K^{-1}]	1.00E-05 - 5.00E-05	*
Undr. thermal pressurisation coeff.	Λ	[MPa K^{-1}]	0.060 - 0.189	*

* For sources to ranges of the individual parameters please see Tables A.2 and A.3.

CSL...Critical State Line; CU...Consolidation Undrained; NCL...Normal Compression Line; UCS...Unconfined Compression Strength; URL...Unloading-Reloading Line
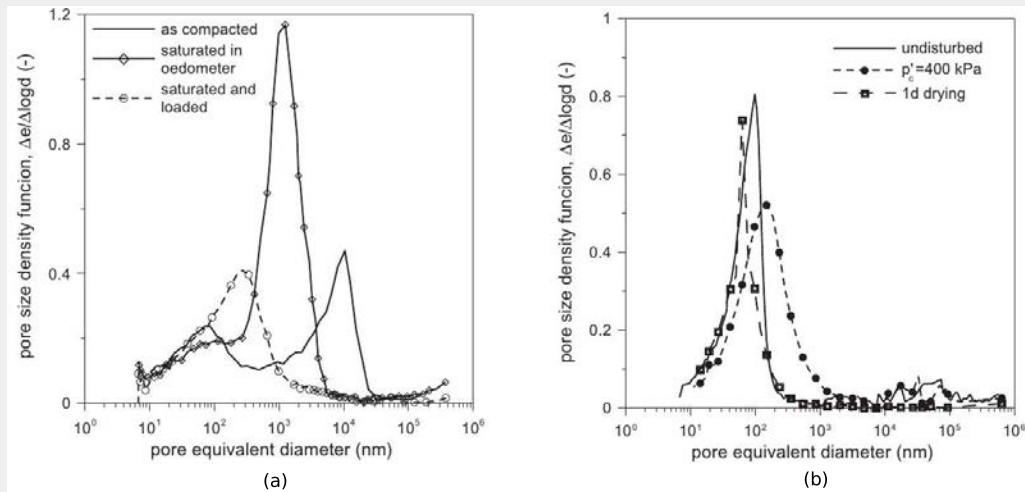
Figure 2.20.: Pore size distribution of; (a) a compacted Boom Clay (initial state of the as-compacted sample, after saturation, and after loading), and (b) a natural Boom Clay (undisturbed sample, sample after unloading in saturated conditions, sample after one dimensional drying) (Della Vecchia et al., 2010).

For reconstituted Boom Clay a distinct bi-modal porosity distribution can be observed, whereas for natural Boom Clay the porosity distribution is uni-modal (Figure 2.20). Uppresian clay results by Lima et al. (2012b) show that, in the natural state, the porosity distribution is also bi-modal.

The water retention properties of Boom Clay have been further investigated by Bernier et al. (1997), Romero (1999), Romero et al. (1999, 2011), Romero and Vaunat (2000), Delage et al. (2007), Le et al. (2008), Romero and Jommi (2008), Lima (2011), Lima et al. (2012a,b) and Lima et al. (2013).

2.4.3.2. Mechanical properties

Several studies on the hydro-mechanical behaviour of natural Boom Clay have been conducted, e.g. Horseman et al. (1987, 1993), Baldi et al. (1991a,b), Bernier et al. (1997), Barnichon and Volckaert (2003), Dehandschutter et al. (2004, 2005), Mendoza (2004), Piriyakul (2006), Cui et al. (2009), Sultan et al. (2010), Deng et al. (2011a,b, 2012), Lima (2011), Monfared et al. (2012), Yu et al. (2012), Bésuelle et al. (2013), Chen et al. (in press, 2015) and Labiouse et al. (2013).

Volume change behaviour

Both the Opalinus and Callovo-Oxfordian argillite behave as a rock, with Young's moduli about 10 times higher than for Boom Clay (e.g. Delage et al., 2010). The Boom Clay is characterised by a highly non-linear and anisotropic stress-strain response.

Figure 2.21(a) confirms the findings of the TRUCK and TRACTOR projects in that the
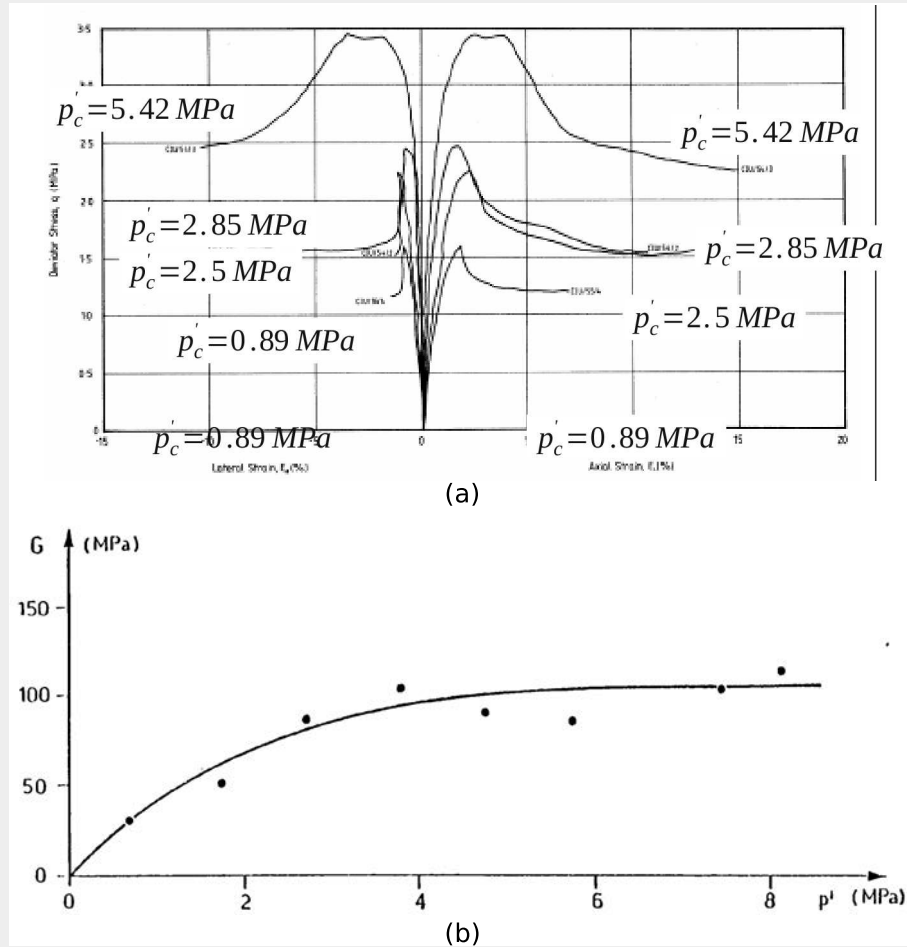
Figure 2.21.: (a) Stress-strain curves for specimens isotropically consolidated at various pressures $p'_c = 0.89 - 5.42$MPa (Deng et al., 2011a, after Horseman et al., 1987). (b) Variation in shear modulus G with effective pressure p' (Baldi et al., 1987).

stiffness, i.e. the Young's modulus, increases with the deposition depth (stress level) and eventually decreases with accumulating irreversible deformation (Li et al., 2007). Based on undrained shear tests, the elastic shear modulus G back-calculated by Baldi et al. (1987) was found to vary substantially with depth (Figure 2.21(b)). See Figure 2.8 for comparison.

Table 2.10 indicates a significant variation in the Young's modulus. Despite potential aleatory uncertainties given the different test locations, epistemic uncertainties such as induced by applying different strain rates (e.g. Burland, 1989; Clayton, 2011; Clayton and Heymann, 2001; Piriyakul, 2006; Simpson, 2010), may influence the sample variance (see later Section 3.2).

In order to assess the transferability of Boom Clay soil property values, Deng et al. (2011a) compared laboratory test results of samples taken from the Essen-1 borehole (Essen, Belgium) with test data taken from the Mol site. At the Essen site two cores of the Putte member; i.e.

Ess75 at depth 219m, and Ess83 at depth 227m; and three cores of the the Terhagen member; i.e. Ess96, Ess104 and Ess112 at depths of 240m, 248m and 256m; were sampled. In order to compare the volumetric response for the different initial (in situ) void ratios e_0 of the Essen and Mol Boom Clay, Deng et al. (2011a) employed the void ratio index I_v (Burland, 1990)

$$I_v = \frac{(e - e^*_{100})}{(e^*_{100} - e^*_{1000})} = \frac{(e - e^*_{100})}{(C^*_c)} \tag{2.1}$$

where e^*_{100} and e^*_{1000} are the void ratios of reconstituted samples at 100 and 1000kPa stress, respectively, and C^*_c is the intrinsic compression index. The values of e^*_{100} and $(e^*_{100} - e^*_{1000})$ back-calculated for the samples from the Essen site at Ess83, Ess96 and Ess104 compared well with the Boom Clay from Mol, but differed significantly for the samples taken at the depth of Ess75 and Ess112, a difference which was well reflected in the difference in mineralogical composition and particle size distribution (Deng et al., 2011a).

Figures 2.22(a) and (b) show the Oedometer results in $I_v - \sigma'_v$ space. It can be seen that for stresses below the pre-consolidation σ'_c the void ratio index depends on the loading path, whereas for $\sigma'_v > \sigma'_c$ the results lie on a straight compression line between the *Intrinsic Compression Line* (ICL), defining the unique (intrinsic) compression response of reconstituted clay normalised by using, void ratio index I_v (Burland, 1990), and the *Sedimentation Compression Line* (SCL), defining a unique curve relating the in situ void ratio e_0 to the effective overburden pressure σ'_v for a normally consolidated argillaceous sediment (Skempton, 1969). The results of Deng et al. (2011a) agree well with tests performed by Horseman et al. (1987).
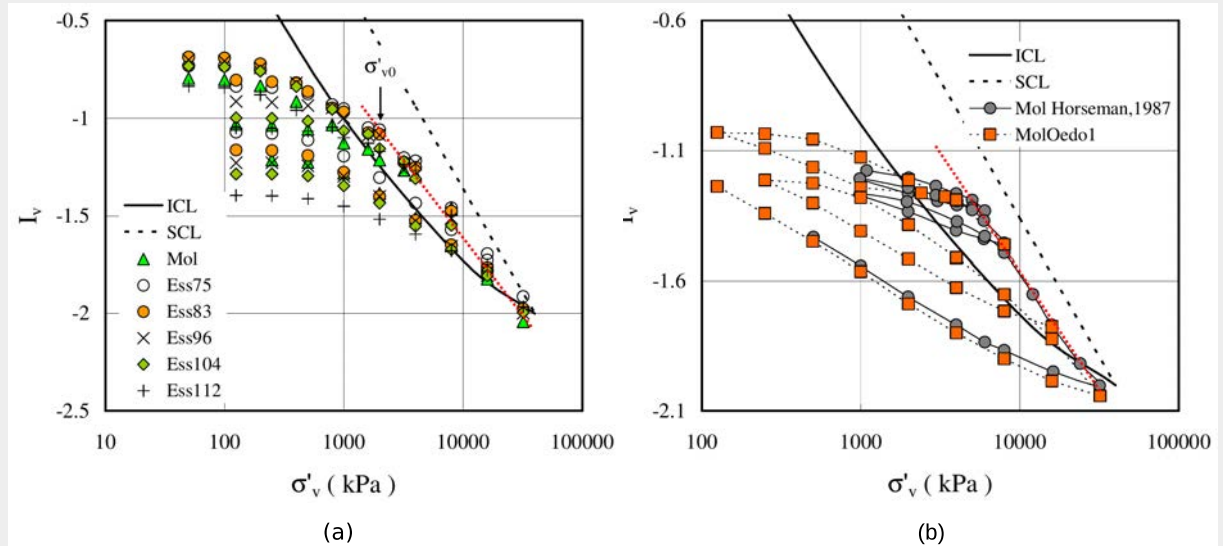
Figure 2.22.: (a) $I_v - \sigma'_v$ curves for all Essen cores, and (b) $I_v - \sigma'_v$ curves for Boom Clay at Mol (Deng et al., 2011a).

Structure and mechanical anisotropy

The ICL, as defined by Burland (1990), suggests that the intrinsic soil is insensitive to any initial and test condition, i.e. any structure. The *fabric*, i.e. the orientation and distribution of soil particles, and the *bonding*, i.e. the frictional and/or non-frictional forces, defining the soil structure (e.g. Lambe and Whitman, 1969, pp71ff) influence significantly the compression and strength behaviour of stiff natural clays (e.g. Burland, 1990; Chandler, 2000, 2010; Clayton and Heymann, 2001; Coop et al., 1995; Cotecchia and Chandler, 1997, 2000; Simpson, 2010). In the TIMODAZ workshop Gens (2012) pointed out that anisotropy is a key feature of the hydromechanical behaviour, which is closely related to microfabric and discontinuities as a result of soil deposition and subsequent diagenesis (see also Gens, 2011). The Boom Clay is an uncemented fine-grained compacted mud and, with the local dislocation and rearrangement of contact particles under the action of pore-water and/or external forces at the mirco-scale, this leads to swelling and softening at the macro-scale (Yu et al., 2012).

Using SEM images, Dehandschutter et al. (2004, 2005) assessed the microstructure of Boom Clay. They found that the clay particles in the samples show a well developed preferred (anisotropic) alignment parallel to the bedding surface (Figure 2.23(a)). No flocculation was observed. An open structure with a high porosity and distinct larger pores was observed, which results from the irregularity of the clay particles and the presence of silt particles (Figure 2.23(b)), around which the clay particles tend to be wrapped (Figure 2.23(c)). Dehandschutter et al. (2005) concluded that this configuration indicates a compaction corresponding to a clay which is slightly overconsolidated. A similar investigation by Hicher et al. (2000) studied the influence of natural and induced anisotropy of the arrangement of the particles on the mechanical response of different clays. Results of high-capacity triaxial tests on undisturbed Boom Clay on specimens from trimmed blocks sampled at the HADES URL at Mol, by Sultan et al. (2010), showed a rotation of the yield surface about the K_0 line in $p' - q$ space for samples taken in their initial state, indicating fabric anisotropy. Furthermore, the position of the yield surface and flow properties were dependent on the recent stress-strain history. The swelling of Boom Clay due to stress relief on the other hand does not seem to be affected by the anisotropy (Sultan et al., 2010).
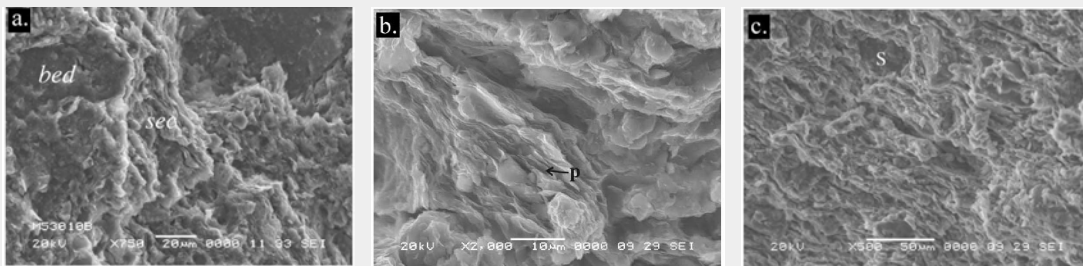
Figure 2.23.: SEM images of undisturbed Boom Clay structure. (a) View on the bedding plane (bed) and on a section perpendicular (sec). (b) View on section perpendicular to the bedding, with interstitial pores (p). (c) View perpendicular to the bedding, showing clay particles wrapped around silt grain (s). (Dehandschutter et al., 2005)

Using measurements of shear wave velocity derived via multi-directional bender elements, Piriyakul (2006) investigated the influence of inherent, as well as stress and strain induced, anisotropy on the elastic response of Boom Clay. Using a triaxial apparatus the undisturbed Boom Clay samples, which has been cored at the research site at Sint-Katelijne-Waver (Belgium) from a shallow depth (5-8m), were tested by applying small strain rates down to $10^{-3}\%$. Employing a dimensionless elastic stiffness coefficient, Piriyakul (2006) found that the inherent anisotropy resulting from the soil structure and fabric results in a significantly higher stiffness in the vertical than in the horizontal direction. No difference was observed in the coefficients for virgin loading and unloading-reloading. A similar response was observed for stress-induced anisotropy with the reconstituted Boom Clay, which responded as a normally consolidated material at initial loading conditions. For strain induced anisotropy, that is, on the young reconstituted Boom Clay without ageing effects, cross-anisotropy (e.g. $G_{hh} = G_{hv}$) was observed, which was not the case for the inherent and stress induced anisotropy. However, Piriyakul and Haegeman (2009) state that a possible reason for $G_{hh} \neq G_{hv}$ in the latter case might be the inclination of the Boom Clay formation with respect to the coring direction and/or the fissuring of the undisturbed sample. Based on this work the void ratio function of Boom Clay has been derived (Piriyakul and Haegeman, 2007). Recent studies show a similar anisotropy of the elastic stiffness parameters in London Clay (Gasparre et al., 2007) and Shanghai Clay (Li et al., 2012a).

Baldi et al. (1987) performed a number of isotropic loading tests on natural Boom Clay from Mol. Figure 2.24 shows two average monotonic loading curves, that is, one for the axial strain ε_a and one for the volumetric strain ε_v. Calculating the lateral strain as $\varepsilon_l = (\varepsilon_v - \varepsilon_a)/2$, it can be seen that the ratio $\varepsilon_l/\varepsilon_a^{-1}$ varies between 3.4 and 1.0, indicating a decrease in anisotropy with increase in overburden pressure. Similarly, Della Vecchia et al. (2010) state that an isotropic response would be expected at stress levels above 10MPa.

Yield and pre-consolidation

Figure 2.25 illustrates schematically a rotation in the yield surface due to soil structure, which is more or less centred around the K_0 line in clays with an anisotropic structure (Leroueil and Vaughan, 1990). Three types of yield may occur, that is, *compressive yield* due to an increase in the mean and/or deviatoric stress away from the peak shear strength, *shear yield* occurring just before shear failure, or *swelling yield* due to the inability of the soil to retain the stored strain energy and potentially resulting in an irreversible degradation of soil structure (Leroueil and Vaughan, 1990).

Figures 2.26(a) and (b) summarise the stress paths of two series of triaxial shear tests performed by Sultan et al. (2010). The first series was performed on Boom Clay samples isotropically consolidated to mean effective stresses levels lower than the measured preconsolidation pressure (Figure 2.26(a)). The second series involved a consolidation under $p'_c = 9$MPa and an unloading to five different mean effective stresses corresponding to *Over Consolidation Ratio's* (OCRs) of 10, 9, 1.8, 1.25 and 3 (Figure 2.26(b)).

Figures 2.26(c) and 2.26(d) show the difference in the yield curves obtained for the two test series. Whereas the yield curve for the "initial state" is rotated about the K_0 line, the
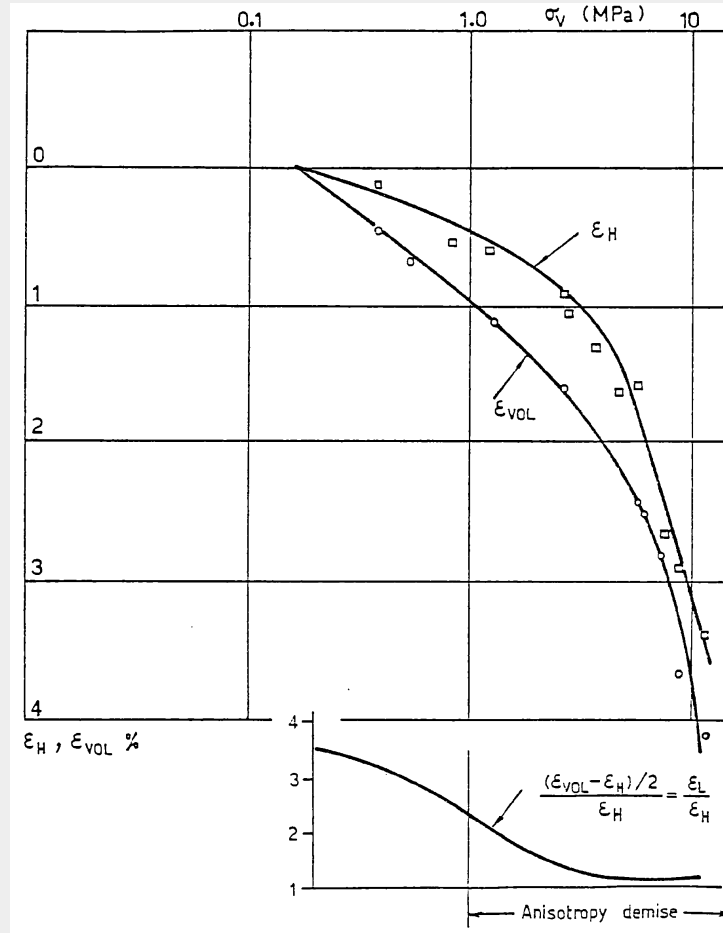
Figure 2.24.: Isotropic consolidation test results with ε_a, ε_l and $\varepsilon_{vol} = \varepsilon_v$ being the axial, lateral and volumetric strains respectively (Baldi et al., 1987).

yield curve resulting from the series of triaxial tests performed on the overconsolidated samples is orientated about the isotropic axis, that is, erasing the initial structural anisotropy. This is congruent with the observations by Baldi et al. (1987), discussed earlier with respect to Figure 2.24. Furthermore, Figures 2.26(c) and 2.26(d) also suggest a change in the shape of the yield surface.

Prior to consolidation, the samples tested by Sultan et al. (2010) were saturated under a confining pressure of 1.08 MPa and a back pressure of 1 MPa. They noted that, during the saturation, a volumetric swelling of about 1.5% was observed with potential consequences on the initial fabric anisotropy. Very recently, results by Bésuelle et al. (2013) showed that Boom Clay samples confined under very low mean effective stresses ($p' = 0.4$MPa), with respect to a p'_c of about 5MPa, lead to a volumetric strain of about $\epsilon_v = -10\%$ after 800 hours with the swelling still continuing at a constant rate. Similar trends were observed for higher confining pressures, with the swelling rate decreasing. Performing low and high pressure oedometer
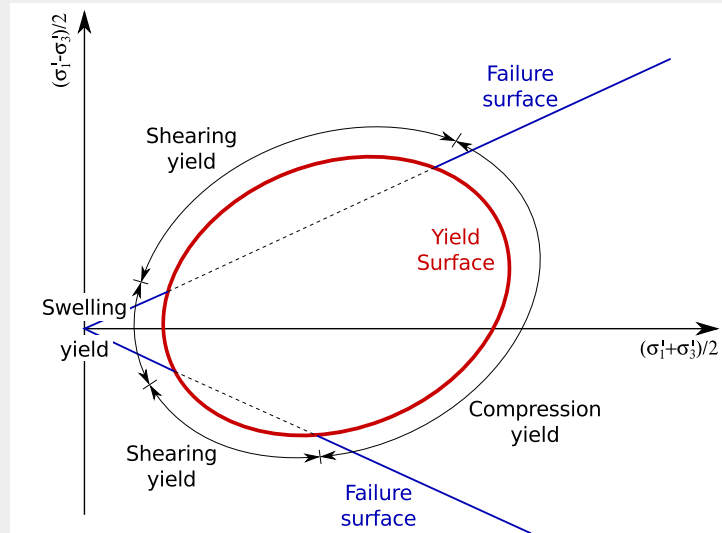
Figure 2.25.: Schematic definition of different types of yielding (after Leroueil and Vaughan, 1990).

tests on Boom Clay samples from the Mol and Essen sites, Deng et al. (2012) found that the secondary compression index and the compressibility index are strongly linearly positively correlated and that the relationship between the secondary compression index and the swelling index follows a less correlated bi-linear negative trend.

The compression curves of the Oedometer tests on undisturbed Boom Clay, presented by Deng et al. (2011a), show that the yield stress $\sigma'_{v,y}$ is lower than the pre-consolidation stress $\sigma'_{v,c}$. Similar observations for natural Boom Clay have been reported by Horseman et al. (1987), Coop et al. (1995) and Chandler (2000, 2010). To account for the fact that increased resistance to compression can develop due to ageing as part of the micro-fabric independent of any creep induced volume reduction, Burland (1990) introduced the *Yield Stress Ratio* $(YSR = \sigma'_{v,y}/\sigma'_{v,0})$. The YSR is different to the *OverConsolidation Ratio* $(OCR = \sigma'_{v,c}/\sigma'_{v,0})$, a term which should be used for describing a known stress history, e.g. by geological means (Burland, 1990, p335).

> *"Clays which retain a post-sedimentation structure at gross yield have a yield stress ratio which exceeds the overconsolidation ratio. In general, it is the yield stress ratio, rather than the geological overconsolidation ratio, which controls compression and strength behaviour. ... As burial depths increase, pressure and temperature effects become greater, making diagenesis more likely, so that deeper and stiffer (although still geologically normally consolidated) clays may be expected to have a yield stress ratio greater than the OCR."* (Cotecchia and Chandler, 2000, p433)

Given that the compression curves lie between the ICL and SCL and cross the ICL far beyond the $\sigma'_{v,c}$, as well as that the effective overburden pressure $\sigma'_{v,0}$ is significantly higher
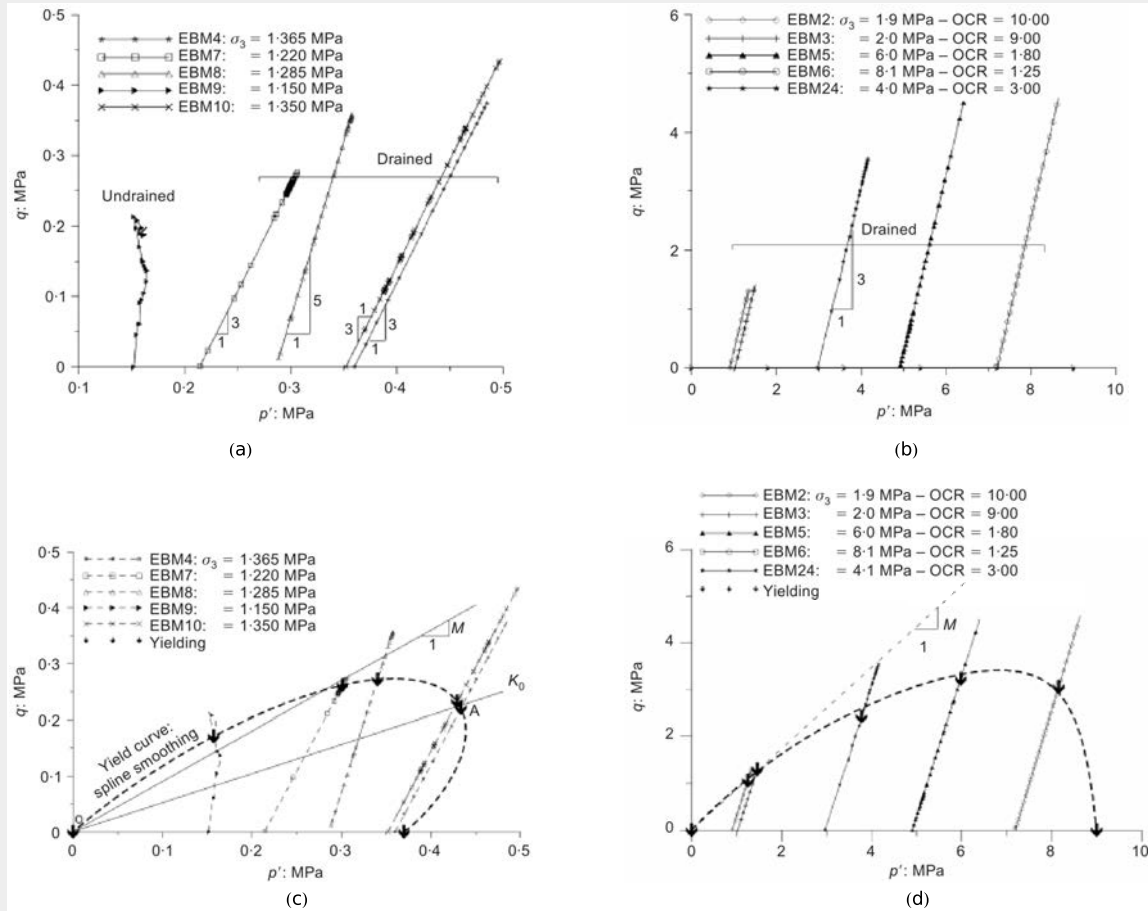
Figure 2.26.: Effective stress paths for series of triaxial tests on Boom Clay samples; (a) at initial state - effective stress paths, and (b) previously isotropically consolidated to 9 MPa. Yield curve obtained by a spline smoothing of the data for samples; (c) at initial state - effective stress paths, and (d) previously isotropically consolidated to 9 MPa. (Sultan et al., 2010)

than the swelling pressure (Figure 2.22), it may be concluded that the Boom Clay is only lightly overconsolidated. Based on geological interpretation, Horseman et al. (1987) determined an OCR of about 1.2. Back-analysing tests on Boom Clay, Chandler (2000) computed an OCR of 1.16 and 1.18 for samples taken from depths of 247m and 223m respectively at the HADES URL in Mol. The associated YSR were computed as 1.7 and 2.0, respectively. Hence, for stiff and structured clays, such as Boom Clay, estimating the OCR with $\sigma'_{v,y}$ obtained for instance via Oedometer tests would result in an underestimate of the real values (Burland, 1990; Chandler, 2000, 2010; Deng et al., 2011a). The spatial variation in OCR, e.g. between the Mol and Essen sites, cannot be directly linked to geological precesses (Li, 2013b) and thus may be attributed to the soil structure.
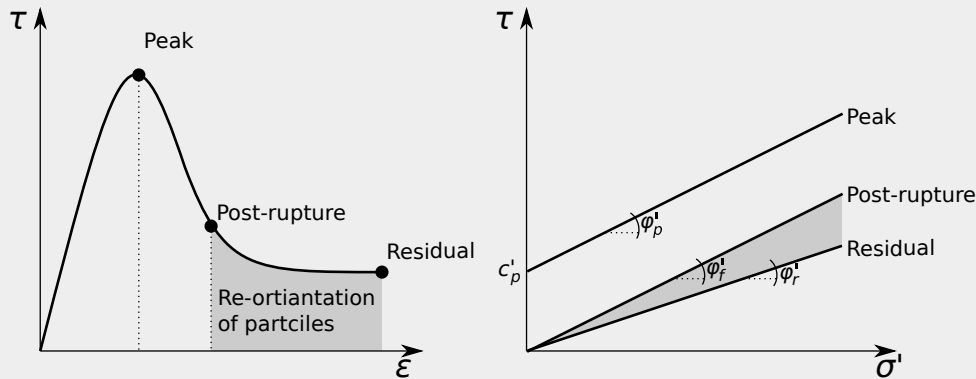
Figure 2.27.: Conceptual scheme for the drained strength of argillaceous hard soils & weak rocks, where c_p is the peak cohesion, φ_p is the peak friction angle, φ_f is the post-rupture friction angle an φ_r is the residual friction angle (after Simpson et al., 1979, and Gens, 2011, 2012).

Shearing

The change in the micro-structure of undisturbed Boom Clay samples subjected to undrained shearing has been assessed by Yu et al. (2012) using *Scanning Electron Microscopy* (SEM). The Boom Clay was found to become denser with a larger directional rearrangement (anisotropy) of the clay particles around fissures. The volumetric strain curves of the undrained shear test show that an initial compaction, accompanied by the development and propagation of small micro-fractures, was followed by an increase in radial strains due to the development and dilatancy of macro-fractures. Similar results on fractured Boom Clay (Dehandschutter et al., 2004, 2005) and other clay (e.g. Djéran-Maigre et al., 1998; Hicher et al., 2000) have been reported.

Overconsolidated stiff clays, such as Boom Clay, subjected to shearing generally show a contracting-dilating response (Atkinson, 2007; Baldi et al., 1991b; Baudet and Stallebrass, 2004; Bésuelle et al., 2013; Burland, 1990; Chandler, 2000; Deng et al., 2011a; Sultan et al., 2010; Yu et al., 2012). Figure 2.27(a) schematically describes the potential stress-strain path of a drained shear test. Figure 2.27(b) shows the associated failure envelopes of a set of shear tests. The bounds of the effective and undrained shear strengths tabulated in Table 2.10 define ranges in which soil parameters obtained at different shear stages have been lumped together.

Figure 2.28(a) shows the results at failure of intact Boom Clay from Mol merged from different sources, that is, Horseman et al. (1987), Baldi et al. (1991b), van Impe (1993), Coll (2005) and Sultan (1997), and from samples retrieved from the Essen site (Cui and Tang, 2013). Whereas the slope of failure envelope is similar, 0.46 for the Mol and 0.47 for the Essen samples, that is, despite the different depths, the increase in cohesion was attributed to the higher carbonate content at the Mol site.

In Figure 2.28(b), the literature values of the Boom Clay samples for the Mol site (grey symbols) coincide with other literature values plotted in the blue symbols in Figure 2.28(b). Once again, the fact that the failure envelope of the intact Mol Boom Clay is above that of

the the Essen Boom Clay (and of the reconstituted Mol Boom Clay), is attributed to the much higher carbonate content at the Mol site resulting in a much higher shear strength due to the cementation (Deng et al., 2011a). For the reconstituted Boom Clay from Mol, the linear CSL with $M = 0.71$ corresponds to $\varphi' = 18.5°$ (Bouazza et al., 1996).

Figure 2.28(b) shows that the failure envelope may not be interpreted as linear for the intact Boom Clay in Mol, that is, especially for the lower stress region. Coll (2005) compiled sets of triaxial compression and extension tests (Figure 2.29), the former showing a significant non-linearity in the peak compressive failure envelope. Deng et al. (2011a) state that the friction angle of $\varphi' = 18.0°$ given by Coll (2005) (see Table A.2) appears to be too large, as it based on the consideration of a single linear failure envelope. However, more data are required in order to further evaluate the non-linear trend in the failure envelope of Boom Clay (Deng et al., 2011a). Tests on other overconsolidated stiff clays, e.g. Burland et al. (1996), Georgiannou and Burland (2001), Gasparre et al. (2007), Hight et al. (2007) and Nishimura et al. (2007), showed that both the intact peak and post-rupture strength may follow a curved failure envelope.

The soil strength of Boom Clay is smaller than that of the Opalinus clay and Callovo-Oxfordian mudstone (Gens et al., 2007; Volckaert et al., 2004, e.g.). For indurated argillites similar results with respect to peak and residual strength have been reported, e.g. Zhang and Rothfuchs (2004), Zhang et al. (2007a,b) and Bossart (2012).

Figure 2.30 compiles all data on the effective cohesion c' and effective friction angle φ', from the TRUCK II and TRACTOR studies as well as data collected from literature. The literature values comprise directly measured and averaged values and, as such, are associated with different uncertainties. It can be seen that the variation in the cohesion data observed
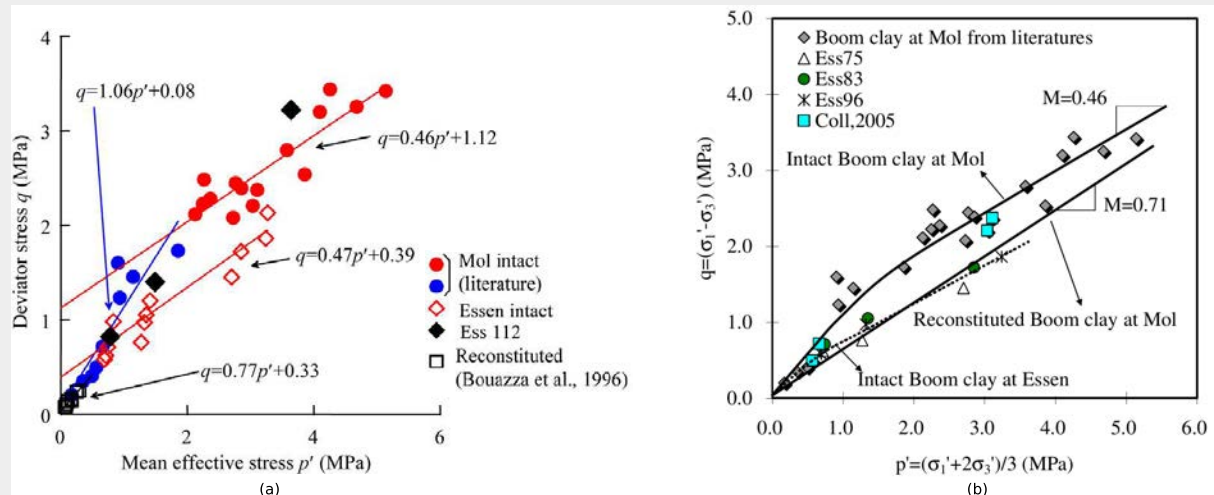
Figure 2.28.: (a) Summary of some failure envelopes for Boom Clay (Cui and Tang, 2013). (b) Failure envelopes in p'-q plane for intact Boom Clay at Mol (results from Coll, 2005), reconstituted Boom Clay at Mol (results from Bouazza et al., 1996), and intact Boom Clay at Essen (Deng et al., 2011a).

in TRUCK II and TRACTOR is confirmed, whereas a larger variation in soil friction angle becomes apparent. The values will be discussed in more detail in Chapter 3.
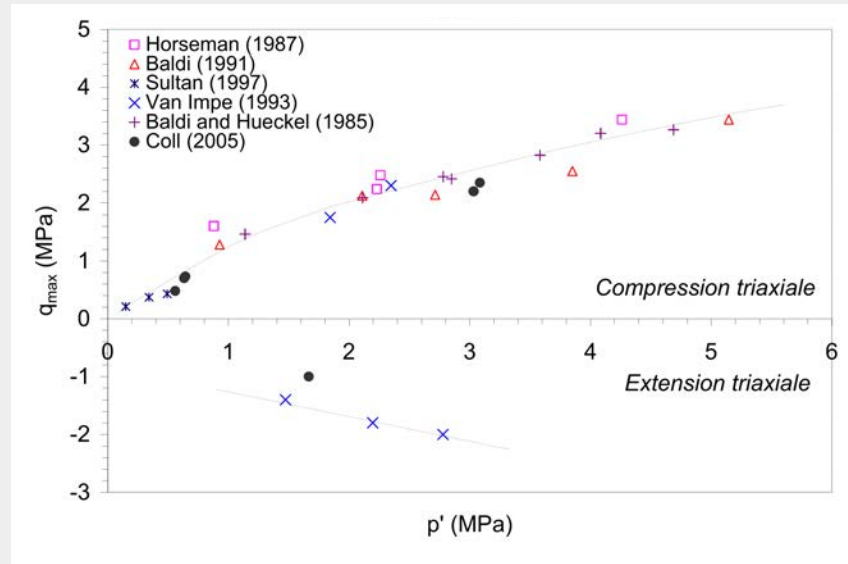
Figure 2.29.: Non-linear and linear failure envelopes obtained for triaxial shear tests performed under compressive and extensive loading, shown in effective mean stress, p', versus peak deviatoric stress, q, space (Coll, 2005).
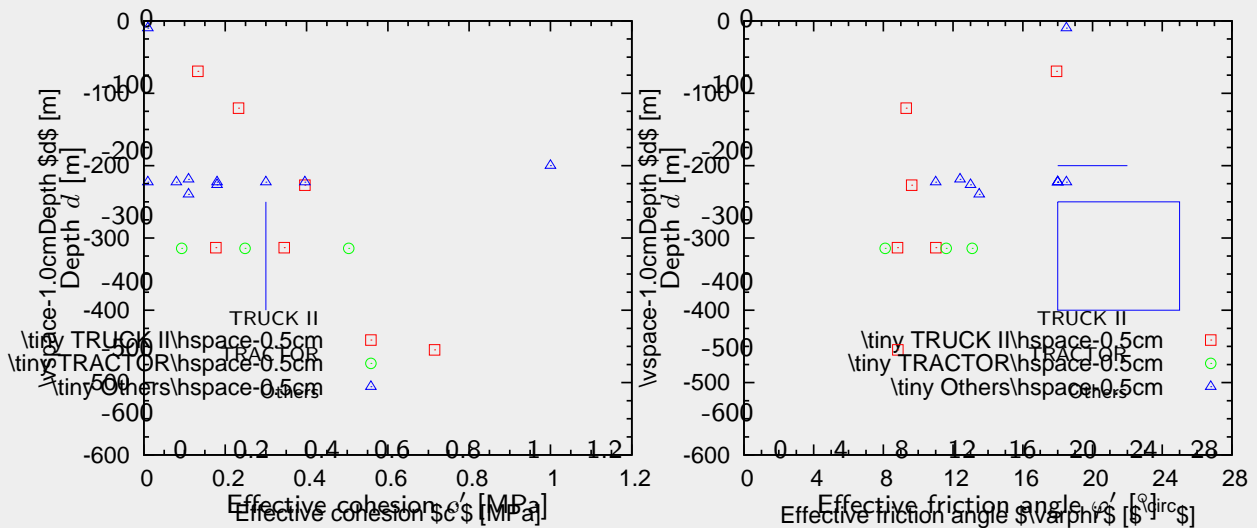
Figure 2.30.: Effective cohesion c' and effective friction angle φ' of Boom Clay samples at different depths d: TRUCK II, TRACTOR and some other data collected in the literature (measured and averaged values).

2.4.3.3. Hydraulic properties

In the last three decades a significant number of studies investigating the hydraulic and transport properties of Boom Clay in the laboratory and/or in situ has been conducted, e.g. Horseman et al. (1987), Beaufays et al. (1994), Volckaert et al. (1995), De Cannière et al. (1996), Ortiz et al. (1996, 1997), Bernier et al. (1997, 2007b), Romero et al. (1999, 2011), Delage et al. (2000, 2007), Barnichon and Volckaert (2003), Aertsens et al. (2004, 2005, 2008b, 2013a,b), Maes et al. (2004), Coll (2005), Labat et al. (2008), Le et al. (2008), Wemaere et al. (2008), Marivoet et al. (2009), Delage (2010), Deng et al. (2011b), Gedeon et al. (2011), Lima et al. (2012a,b), Lima et al. (2013) and Yu et al. (2011, 2013b).

Saturated hydraulic conductivity

The saturated hydraulic conductivities K_{sat} of intact Opalinus clay and Callovo-Oxfordian mudstone are smaller than that of Boom Clay (e.g. Boisson, 2005; Gens et al., 2007; Mazurek et al., 2011; Volckaert et al., 2004). All values and ranges collected from the literature, along with the associated test and boundary conditions, have been implemented within the database (see Appendix A). The large variance in the overall ranges summarised in Table 2.10 ($1.00E - 012 \leq K_{sat} \leq 9.30E - 012 \, \mathrm{m \, s^{-1}}$, $1.00E - 012 \leq K_{sat,v} \leq 5.43E - 010 \, \mathrm{m \, s^{-1}}$, $2.00E - 012 \leq K_{sat,h} \leq 6.22E - 010 \, \mathrm{m \, s^{-1}}$) mainly results from the differences in the Boom Clay composition at the testing/sampling site.

Figure 2.18(b) shows the profile of vertical and horizontal saturated hydraulic conductivities, i.e. $K_{sat,v}$ and $K_{sat,h}$ respectively, for the Mol site in Belgium. A more detailed profile of the Mol-1 borehole is presented in Figure 2.31. This profile is the result of a very recent study by Yu et al. (2011, 2013b), critically reviewing all laboratory and in-situ measurements of saturated hydraulic conductivity conducted by SCK·CEN in the Boom Clay formation at the Mol site, as well as at the boreholes in Zoersel, Doel-2b, Weelde-1 and Essen-1 (see Figure 2.4) over the last 30 years.

The interpretation of the hydraulic conductivity obtained in situ via single-point piezometers averages out both components (isotropy flow hypothesis) and thus $K_{sat,v} < K_{sat} < K_{sat,h}$. The decrease in clay content in the Boeretang Member and the increase in sand content in the Belsele-Waas Member (as well as in the double band) lead to an increase in hydraulic conductivity (Figure 2.31).

In sedimentary deposits the hydraulic conductivity is generally anisotropic (Gens, 2011). From both Mol profiles presented in Figures 2.18(b) and 2.31, it is evident that Boom Clay exhibits a hydraulic anisotropy. The range of the degree of anisotropy reported in the literature varies $\langle K_{sat,h}/K_{sat,v} \rangle = [1.04, 10.98]$ (Table 2.10), although an average degree of anisotropy of about 2.0-2.5 is generally reported (e.g. Aertsens et al., 2005; De Cannière et al., 1996; Labat et al., 2008; Wemaere et al., 2008; Yu et al., 2011, 2013b).
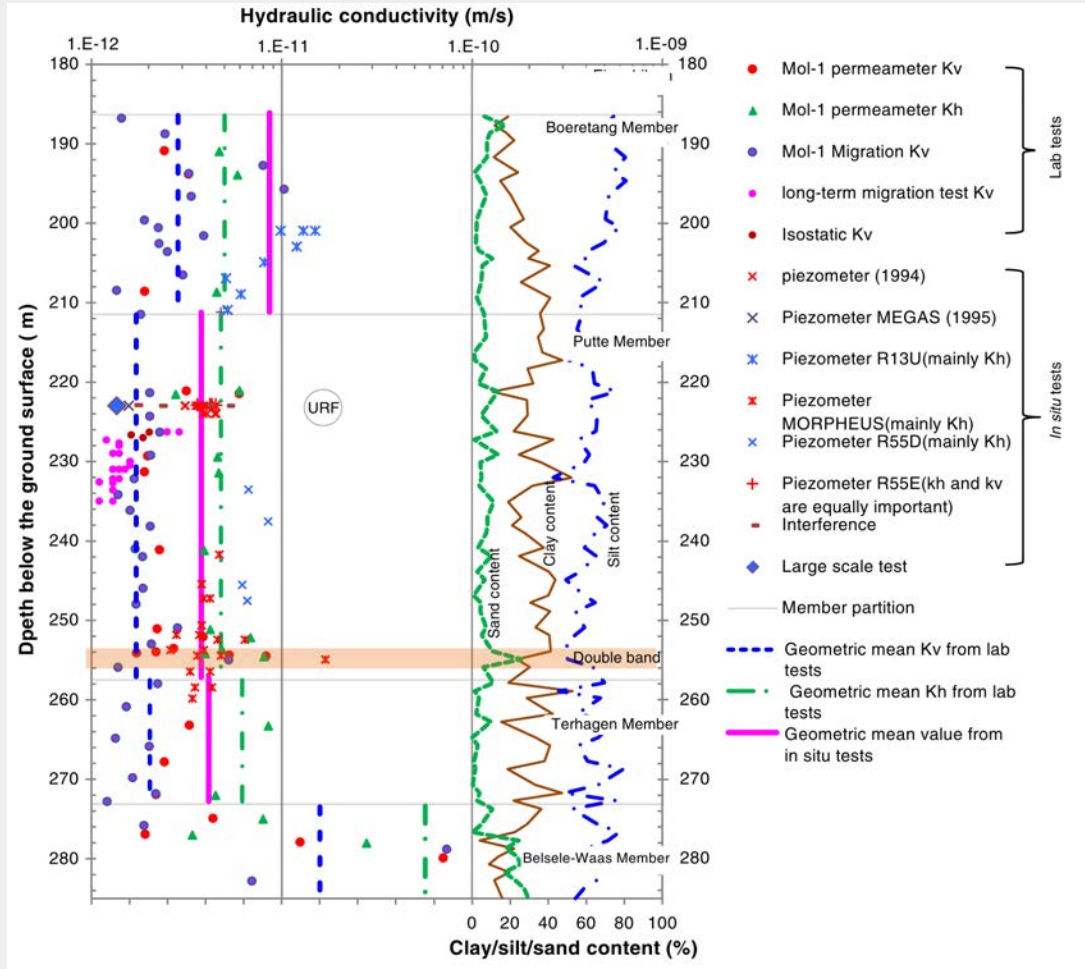
Figure 2.31.: Hydraulic conductivity profile of Boom Clay at the Mol site based on lab tests and in situ tests at the HADES URF (clay: $< 2\mu$m, silt: $\geq 2\mu$m and $< 62.5\mu$m, sand: $\geq 62.5\mu$m) (Yu et al., 2013b).

In Situ vs. laboratory measurements

From the literature it is evident that, for many intact plastic and indurated argillites, the ranges of hydraulic conductivities obtained from core samples tested in the laboratory, that is, e.g. via percolation, permeameter and isostatic/triaxial experiments, are generally in compliance with values resulting from situ measurements, that is, e.g. small scale single- or multi-piezometer tests, large-scale as well as borehole experiments (e.g. Boisson, 2005; Marivoet et al., 2009; Neuzil, 1994). This may be interpreted as evidence for the absence, or limited hydraulic significance, of fractures and other discontinuities in such formations (Mazurek et al., 2011).

Investigating the upscaling of hydraulic and transport parameters in Boom Clay, Marivoet et al. (2009) found that, given a typical grain size of a Boom Clay particle ($\approx 30\mu$m), with an REV of about 3 to 30mm the Boom Clay can be considered as homogeneous as most

experimental and modelling scales are much larger. For the in situ measurements of hydraulic conductivity, no trend was observed with respect to experiment dimensions ranging from 10cm^3 to 100m^3 in volume. Thus Marivoet et al. (2009, p25) concluded that *"upscaling does not require adaptation of the hydraulic or transport parameter values so far as variations due to macroscopic heterogeneities (e.g. layered structure of the Boom Clay) remain limited"*.

Figure 2.32 presents a summary of the mean hydraulic conductivities, within a 95% confidence interval measured at Mol in the Putte and Terhagen Members using different techniques (Yu et al., 2013b). No influence of much larger hydraulic gradients applied in the lab as opposed to those present in situ is apparent, which results in a good consistency between the lab and in situ measurements at the centimetre- and meter-scales. Moreover, the presence of pre-existing fissures in the sample does not seem to have a significant impact on the value of hydraulic conductivity obtained in the laboratory (Delage, 2010).

Spatial variability and correlation

Figure 2.33 provides an overview of laboratory measurements for the vertical and horizontal saturated hydraulic conductivity in five Belgian boreholes. For their locations see Figure 2.4. The variability in absolute values and degree of anisotropy is evident.

Wemaere et al. (2008) recently assessed the vertical and horizontal hydraulic conductivities measured via permeameter-type experiments on Boom Clay cores, in the boreholes at the Doel-2b, Zoersel, Mol-1 and Weelde-1 sites to interpret the hydraulic characteristics on the regional scale. The point statistics are summarised in Table 2.11. As already visible in Figure 2.33, the Putte and Terhagen members (considered as one unit due to their similarity) generally show a relatively small variation, $\langle \sigma_{\log K_{sat}} \rangle = [0.1; 0.3(0.7)]$, whereas the other members are more heterogeneous (e.g. Belsele-Waas member $\langle \sigma_{\log K_{sat}} \rangle = [(0.5)0.8; 1.3]$). The increase in conductivity of the Belsele-Waas member compared to the Putte+Terhagen member is dependent upon the location, e.g. from a factor of 3 at the Weelde-1 borehole to factors of 160 and 370 for $K_{sat,v}$ and $K_{sat,h}$ respectively at the Zoersel borehole.

The degree of anisotropy discussed earlier refers to the associated sample scale. However, using the harmonic means of the vertical and horizontal hydraulic conductivities over the whole Boom Clay unit (Table 2.11) may lead to a significantly higher degree of anisotropy at the formation scale, e.g. about 5 for the Mol-1 and the Doel-2b boreholes and close to 60 for the Zoersel borehole (Wemaere et al., 2008). For the Weelde-1 borehole the degree of anisotropy seems to be scale independent, that is, with the conductivities of Belsele$-$Waas member being closer to that of the Putte+Terhagen member.

Based on multiple regression employing some grain-size and other constituency parameters ($d_{10} - d_{90}$ percentages, $CaCO_3$ content, etc.), Wemaere et al. (2008) developed an empirical formulation to predict the vertical saturated hydraulic conductivity $\log K_{sat}$. However, those were site-specific relationships and no single relationship was presented. It seems that both the sand content (coarser material) and soil porosity (compaction /burial depth) are dominating the hydraulic conductivity values (Deng et al., 2011b; Yu et al., 2011), which may explain why no unique relationship was determined by Wemaere et al. (2008).
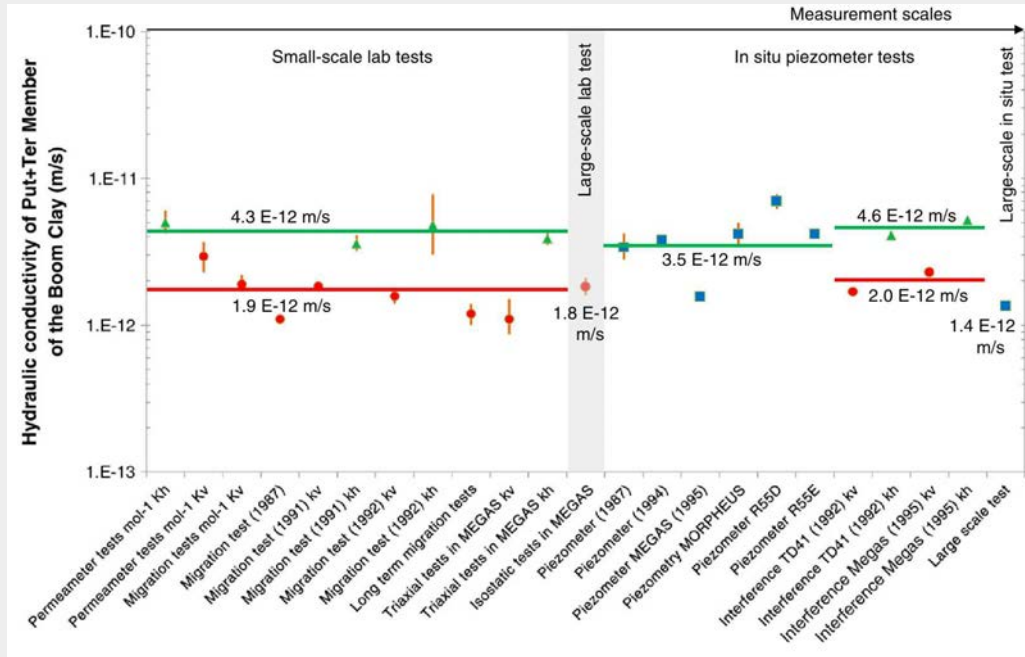
Figure 2.32.: Overview of saturated hydraulic conductivity values K_{sat}[m/s] for Putte and Terhagen Members at the Mol site. Vertical bars represent the 95% confidence interval (Yu et al., 2013b).
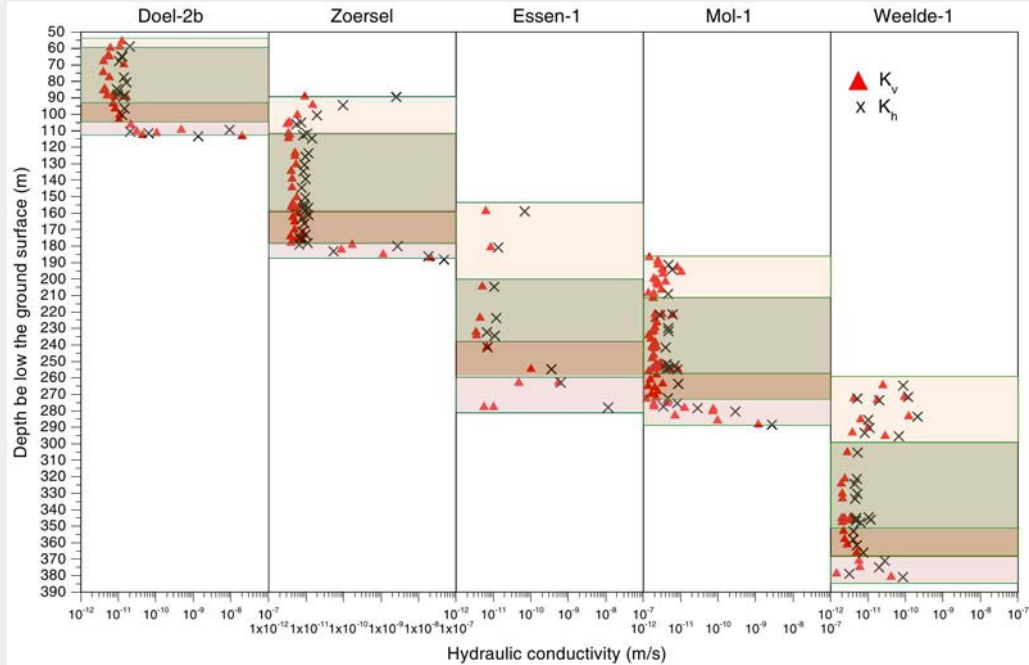
Figure 2.33.: Spatial variability and anisotropy of hydraulic conductivity in five Belgian boreholes. Sub-units for all boreholes are identical (from top to bottom): Boeretang, Putte, Terhagen, and Belsele-Waas members (Yu et al., 2013b).

Table 2.11.: Overview of the hydraulic conductivities determined in the laboratory (Wemaere et al., 2008).

Unit	Doel-2b			Zoersel			Mol-1			Weelde-1		
	n	K_v (m/s)	s	n	K_v (m/s)	s	n	K_v (m/s)	s	n	K_v (m/s)	s
Tr	–	–	–	6	5.5×10^{-12}	0.3	16	2.8×10^{-12}	0.3	9	2.2×10^{-11}	0.6
Pu + Ter	21	1.0×10^{-11}	0.7	24	4.8×10^{-12}	0.1	38	2.3×10^{-12}	0.1	15	3.8×10^{-12}	0.2
B-W	6	2.2×10^{-10}	1.1	4	7.7×10^{-10}	1.1	10	1.6×10^{-11}	0.8	4	1.1×10^{-11}	0.5
B	27	$\mathbf{1.1 \times 10^{-11}}$		34	$\mathbf{5.5 \times 10^{-12}}$		64	$\mathbf{2.8 \times 10^{-12}}$		28	$\mathbf{5.8 \times 10^{-12}}$	
	n	K_h (m/s)	s	n	K_h (m/s)	s	n	K_h (m/s)	s	n	K_h (m/s)	s
Tr	–	–	–	6	3.5×10^{-11}	1.0	3	5.0×10^{-12}	0.1	9	2.2×10^{-11}	0.6
Pu +Ter	14	1.5×10^{-11}	0.3	23	9.0×10^{-12}	0.1	12	5.0×10^{-12}	0.1	15	3.8×10^{-12}	0.2
B-W	4	3.6×10^{-10}	1.2	4	3.4×10^{-09}	1.3	5	5.7×10^{-11}	1.0	4	1.2×10^{-11}	0.8
B	18	$\mathbf{6.0 \times 10^{-11}}$		33	$\mathbf{3.2 \times 10^{-10}}$		20	$\mathbf{1.3 \times 10^{-11}}$		28	$\mathbf{1.1 \times 10^{-11}}$	

Tr: Transition zone, Pu + Ter: Putte + Terhagen, B-W: Belsele-Waas, B: Boom.
Sub-unit values are geometric means, Boom unit value is a harmonic mean according to the thicknesses of the sub-units.
n: Number of analyses, s: standard deviation of $\log K$.

Figure 2.34 shows that, for samples cored at the Essen site, the logarithm of the saturated hydraulic conductivity $\log K_{sat}$ and void radio e are linear and strongly positively correlated (Deng et al., 2011a). The plots result from constant-head percolation tests in an oedometer cell, as well as from consolidation tests using the oedometer and isotropic cell followed by back-analysis of the hydraulic conductivity using the Casagrande's method. Two relationships to predict the saturated hydraulic conductivity K_{sat} as function of the void ratio e have been proposed, that is, one using the in situ hydraulic conductivity $K_{sat,0}$ and the in situ void ratio e_0 as a scaling parameter, the second, in the absence of the in situ values using the liquid limit w_L. The hydraulic conductivity of the Essen samples as well as Mol samples could be satisfactorily predicted.

Using triaxial compression tests, Bésuelle et al. (2013) recently showed that the hydraulic conductivity K is strongly negatively correlated to the mean effective stress p' and strongly positively correlated to the void ratio e. Moreover, Cui and Tang (2013) further evaluated the results by De Craen et al. (2006) and Cui et al. (2009), showing equivalent correlations between hydraulic conductivity and void ratio.

Using a relationship proposed by Deng et al. (2011b), without specifying which one specifically, Yu et al. (2013b) used the variation in porosity of the Putte Member for the depth ranges of the five borehole profiles investigated (Figure 2.35). No clear depth trend is visible. Moreover, Yu et al. (2013b) reported that no satisfactory fit between the hydraulic conductivity could be obtained for the analysed data. Due to the lack of data the effects of factors such as mineralogy, carbonate content, etc., could not be investigated, but which they could be the factors driving unexplained regional variations (Yu et al., 2013b).

Water retention behaviour

The effects of the unsaturated state on the the water retention behaviour of Boom Clay was investigated amongst others by Bernier et al. (1997), Romero (1999), Romero et al. (1999, 2011), Romero and Vaunat (2000), Delage et al. (2007), Le et al. (2008), Romero and Jommi (2008), Lima (2011), Lima et al. (2012a,b) and Lima et al. (2013).
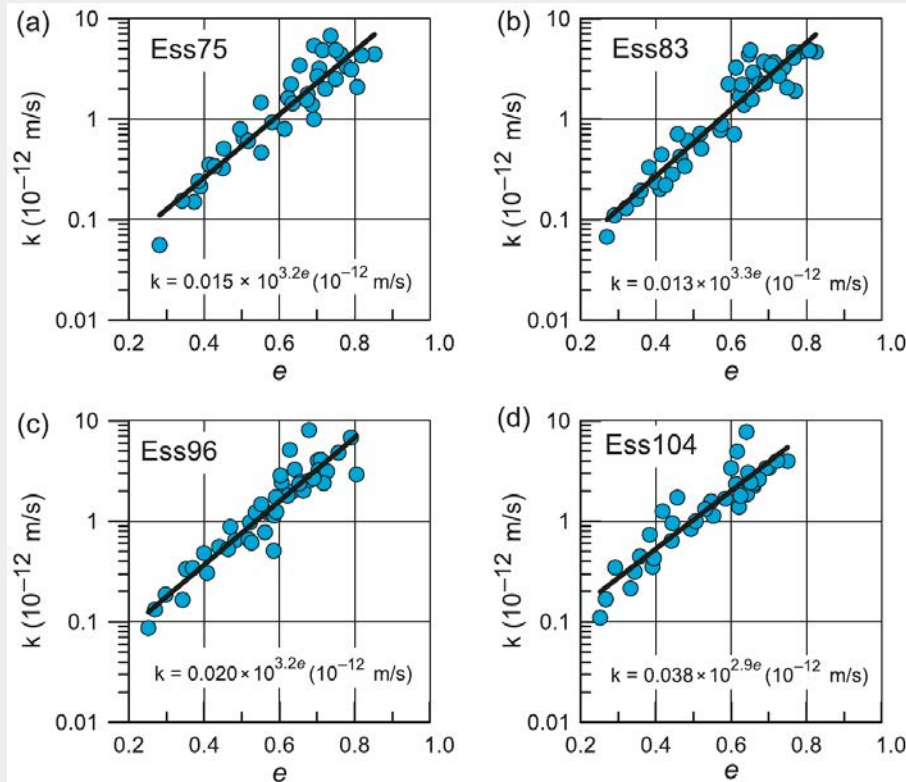
Figure 2.34.: Relationships between saturated hydraulic conductivity K_{sat} and void ratio e: (a) Ess75, (b) Ess83, (c) Ess96, and (d) Ess104 borehole (Deng et al., 2011b).

Transport and migration

Although not part of this research, numerous tracer experiments have been performed to assess the transport properties of Boom Clay in situ and in the laboratory, e.g. De Cannière et al. (1996), Aertsens et al. (2004, 2008a,b, 2013b), Mazurek et al. (2009, 2011). Recently, Aertsens et al. (2013a) presented a summary of all migration experiments performed in the HADES URF in Mol.

2.4.3.4. Thermal properties

Numerousl studies on the thermo-hydro-mechanical behaviour of natural Boom Clay have been conducted in recent years, e.g. Baldi et al. (1987, 1988, 1991a,b), Hueckel and Baldi (1990), Hueckel and Pellegrini (1992), Neerdael et al. (1992), Bernier and Neerdael (1996), De Bruyn and Labat (2002); De Bruyn and Thimus (1996), Romero (1999), Cui et al. (2000, 2009), Delage et al. (2000, 2009), Sultan et al. (2002), Romero et al. (2005), Gens et al. (2007), Le (2008), Lima et al. (2009, 2013), Hueckel et al. (2009a,b, 2011), Charlier et al. (2010b), Chalindar et al. (2010), Li et al. (2010a), Chen et al. (2011, 2012a), Lima (2011), Garitte et al. (2012) and Tsang et al. (2012). Some significant experimental efforts investigating the impact
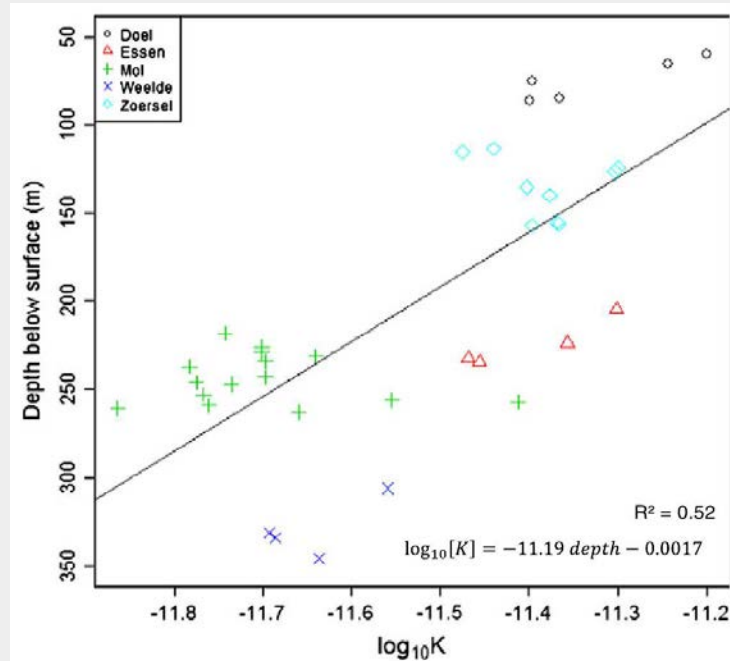
Figure 2.35.: Trend with depth for the $\log K_{sat,v}$ values (below 10-11 $\mathrm{m\,s^{-1}}$) of the Putte Member (Yu et al., 2013b).

of thermal variation on the hydro-mechanical soil properties of other argillaceous host rocks have been made, e.g. Horseman and McEwen (1996), Zhang et al. (2004, 2007a,b), Alonso et al. (2005), Wileveau (2005a,b), Gens et al. (2009), Muñoz et al. (2009) and Mohajerani et al. (2012, 2013).

State and consistency

The ambient temperature can vary significantly from site to site. At a depth of 500m an average temperature of about 20-25°C is reported in Belgium, that is, with local anomalies ranging from 15°C to 30°C (Vandenberghe and Fock, 1989). The temperature map for the Dutch subsoil at a depth of 500m presented by Rijkers et al. (1998) shows a similar trend with temperature varying between 20°C and 30°C, with significantly higher ambient temperatures ranging from 40°C to 55°C, associated with a larger spatial variation, at a depth of 1000m. The geothermal gradient up to a depth of 1000m was defined by (ONDRAF/NIRAS, 2001a) to be 3.5°C per 100m.

   The low permeability of clay ensures that the heat transport mechanism is governed by heat conduction and that advection (convective flux) is negligible (Gens et al., 2009). Hence the variation in thermal conductivity λ will govern the temperature response. Table 2.10 summarises some ranges of thermal soil property values obtained from the very limited amount of data available in the literature. Again, a difference in the vertical and horizontal thermal conductivities, λ_v and λ_h respectively, is evident. Similarly, the difference in temperature

increase measured during the ATLAS III heater test between a horizontal and an inclined observation borehole, that is, with both having the same distance to the heater, is clear evidence for an anisotropic thermal conductivity in the Boom Clay (Chen et al., 2011).

Recently, Garitte et al. (2012) characterised the thermal conductivity of three argillaceous rocks, i.e. of Callovo-Oxfordian Clay, Opalinus Clay and Boom Clay, on the basis of temperature measurements in the rock mass of four in situ heating experiments as well as results from the laboratory. The laboratory results were found to closely agree with the data obtained in the field. A set of reference thermal conductivity values for all three host rocks was proposed, all of which are anisotropic in nature. The thermal conductivity in the Boom Clay was found to be lower than in the two indurated rocks.

Volumetric response

Thermal loading may affect both the hydraulic and mechanical behaviours. The response is commonly non-linear and irreversible due to thermal yielding.

By compiling results from studies on the consolidation of five different clays, Cekerevac and Laloui (2004) showed that the preconsolidation pressure decreases with increasing temperature (Figure 2.36(a)). Figure 2.36(b) shows that, for isotropically loaded Boom Clay samples, the preconsolidation pressure decreases linearly with an increase in the applied temperature (Sultan et al., 2002). Initially the samples were isotropically loaded up to 4 MPa, then heated to 100°C and finally loaded at temperatures of 100, 70, 40 and 23°C. All four compression curves seem to converge towards a unique limit and show signs of thermal hardening with all yield points being beyond 4MPa.

The OCR was found to have a significant influence on the volumetric response of clay due to thermal loading. For different clays, contraction was reported for for low OCRs and dilation for high OCRs (e.g. Baldi et al., 1988, 1991b; Hueckel et al., 1992; Sultan et al., 2002; Towhata et al., 1993). Figure 2.37(a) shows the volumetric response of a series of Boom Clay samples, at different OCRs, to various temperature cycles ($22 \rightarrow 100$°C and $22 \rightarrow 100 \rightarrow 27$°C). Sultan et al. (2002) concluded that, (i) the plastic contraction of normally consolidated Boom Clay samples is independent of the applied mean effective stress, (ii) the thermal contraction increases with decreasing OCR values until pure contraction at $OCR = 1$, (iii) the slope of the volumetric strain during cooling is independent of the mean effective stress applied, and (iv) the temperature at which expansion transits to contraction is associated with a decreasing OCR (Figure 2.37(b)).

Thermal expansion can be described by the thermal dilation of solid and fluid phases, e.g. see the isotropic thermal dilation (expansion) coefficient α_c for clay (Boom Clay) mineral in Table 2.10, whereas the explanation of the plastic thermal contraction associated with the separation of the adsorbed water from the clay particles requires physico-chemical interactions between the molecules (e.g. Cui et al., 2009; Delage, 2013). Although α_c may vary with temperature and applied pressure, for most applications it can be assumed to be almost constant (Bolzon and Schrefler, 2005).

(a)

(b)
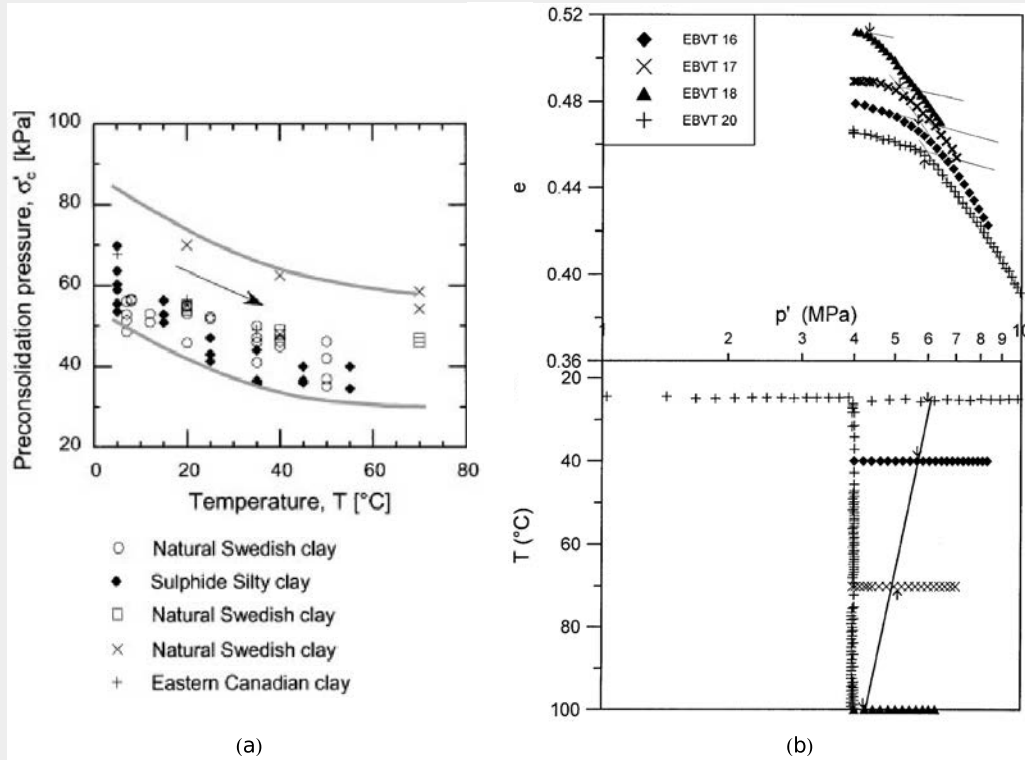
Figure 2.36.: Temperature effects on the preconsolidation pressure; (a) for five different clays (Cekerevac and Laloui, 2004), and (b) for Boom Clay (Sultan et al., 2002).

(a)

(b)
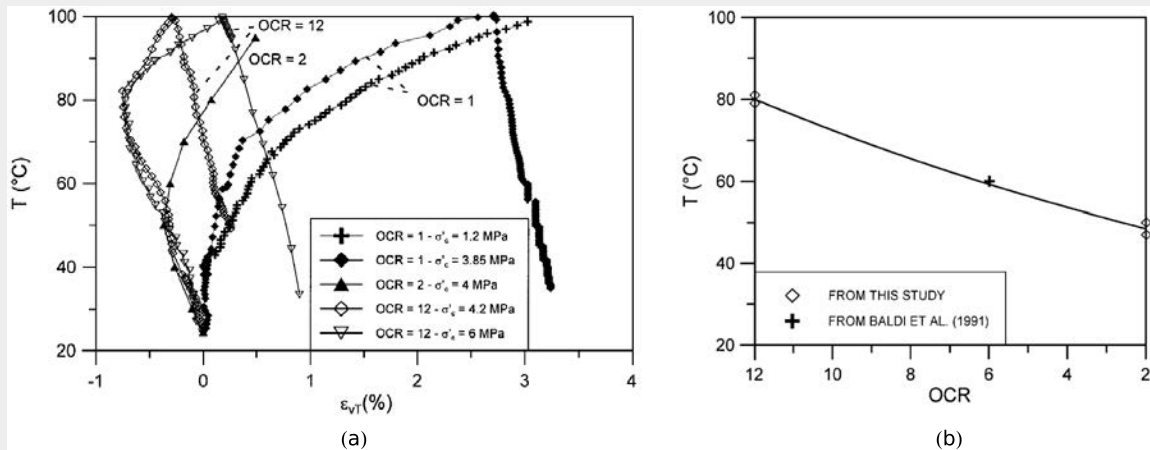
Figure 2.37.: (a) Thermal volumetric changes of Boom Clay samples at different OCRs. (b) Change of the temperature of the thermal expansion/contraction transition as a function of OCR. (Sultan et al., 2002)

The thermal expansion coefficients of clay and quartz are higher than those of calcite and feldspar, and thus a significant differential thermal expansion is to be expected between
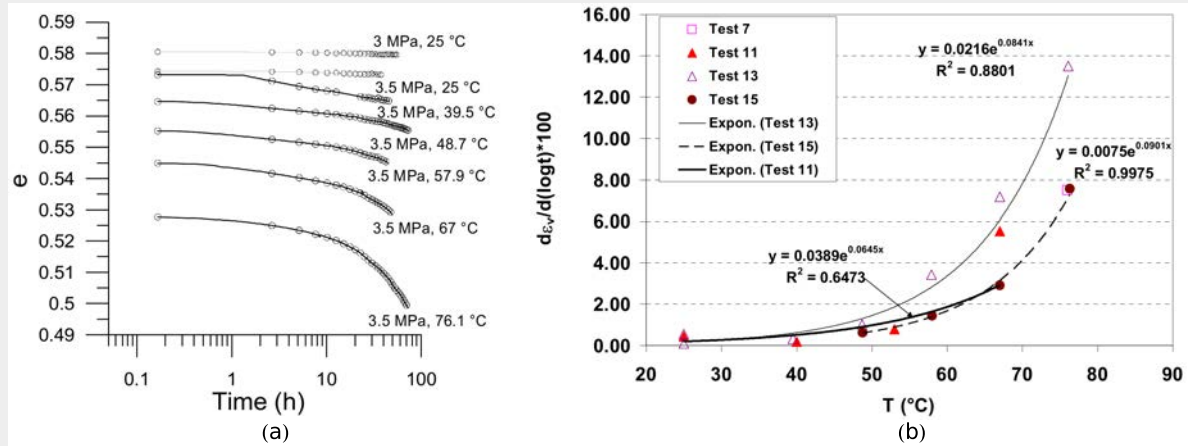
Figure 2.38.: Heating tests on Boom Clay: (a) Void ratio variation at constant temperature and constant effective pressure following two heating paths and five loading paths, and (b) Consolidation rate versus temperature of different heating tests (Cui et al., 2009).

the solid interfaces for clay-calcite and also clay-feldspar (Delage, 2013). Furthermore, the thermal expansion coefficient of water is generally about one magnitude larger than that of clay and quartz minerals (e.g. Bolzon and Schrefler, 2005; Delage, 2013; Ghabezloo and Sulem, 2009; Sultan et al., 2002). The increase in pore-water pressure due to thermal loading is often characterised by the thermal pressurisation coefficient Λ. This coefficient is strongly dependent upon the material composition, the stress state, the range of temperature change and the induced damage (Ghabezloo and Sulem, 2009). Using a heating pulse test under constant volume on natural Boom Clay, a slightly lower value was obtained on cooling than for heating (Lima et al., 2009), although both were higher than the value obtained by Vardoulakis (2002) based on results of Sultan (1997).

Le (2008) and Cui et al. (2009) investigated the time dependent behaviour of natural Boom Clay in triaxial tests at different controlled temperatures. Figure 2.38(a) shows the volumetric compression rate of a Boom Clay sample, tested under two loading paths with a constant temperature of 25°C ($2.5 \rightarrow 3.0$MPa, $3.0 \rightarrow 3.5$MPa) and a five step heating path with a constant pressure of 3.5MPa ($25 \rightarrow 40$°C, $40 \rightarrow 49$°C, $49 \rightarrow 58$°C, $58 \rightarrow 67$°C, $67 \rightarrow 76$°C). It is evident that the consolidation rate is temperature dependent, that is, it increases with higher temperature. Figure 2.38(b) presents the consolidation rate versus temperature for several tests (Test 13 corresponds to results presented in Figure 2.38(a)). Delage (2013) points out that the results by Cui et al. (2009), obtained at low stress ranges, need to be confirmed by additional experimental data at larger stress ranges.

Results of slow heating tests on slightly overconsolidated Boom Clay specimens performed by Delage et al. (2000) show that, at high temperatures from 60°C up to 90°C, the coefficient of consolidation is not significantly influenced by thermal loading. It is explained by the increase in permeability which compensates for the decrease in porosity (see later Figure 2.39). This

is of importance to assess the dissipation of pore-water pressure during the thermal phase subsequent to the emplacement of the Supercontainers, during operation and post-closure (see later Sections 2.5.3 and 2.5.4).

Shear resistance

A temperature dependency of the deviatoric response of Boom Clay, associated with a slight decrease in shear strength, was observed by Hueckel and Baldi (1990), Baldi et al. (1991a,b), Hueckel and Pellegrini (1992) and De Bruyn and Thimus (1996). De Bruyn and Labat (2002) state that the temperature levels and durations applied during the ATLAS experiment seemed to have no significant influence on the change in strength of the Boom Clay. For some other clays the friction angle at critical state reported in the literature seems to be independent of the applied temperature, e.g. Pontida clay (Hueckel and Baldi, 1990), Tody clay (Burghignoli et al., 2000), reconstituted illite (Graham et al., 2001) or kaolinitic clay (Cekerevac and Laloui, 2004). Li et al. (2007) pointed out that the limited data available, as well as their scatter, does not allow for a quantitative conclusion on the relation between shear strength and temperature for Boom Clay. Recently Hueckel et al. (2009a, 2011) presented a framework to explain the temperature dependency of soil strength based on the loading/heating path and history.

Hydraulic response

The decrease in soil porosity due to heating is associated with a variation in fluid viscosity and hydraulic conductivity. Figure 2.39(a) shows the variation in porosity and permeability obtained via a series of permeability tests on natural Boom Clay under different thermal and loading conditions (Delage et al., 2000). By decoupling the effects of temperature and porosity, a unique linear relationship between the porosity and the logarithm of the intrinsic permeability of Boom Clay was presented (Figure 2.39(b)). This interdependency with respect to the thermo-mechanical loading history points to the fact that a variation in permeability with temperature is the result of a change in fluid viscosity. Results by Chen et al. (2012a) on Boom Clay in an isostatic test also suggest that the increase of hydraulic conductivity is caused by a decrease in fluid viscosity and thus is fully reversible (Figure 2.39(c-d)).

2.5. Processes and observations of repository performance and safety

During the life-time of a repository numerous coupled physical, chemical and biological processes take place in each individual compartment of the repository system, potentially influencing the performance of other compartment barriers within the MBS. Furthermore, variations in state and boundary conditions may enhance or attenuate individual processes. To review and assess all processes in a generic way is hardly possible as the response is intrinsically system dependent. Thus this section aims to provide a selective overview of primary physical processes potentially governing the response of the OPERA repository system in the time frame between the construction of the repository and the end of the thermal (early closure) phase, i.e. with
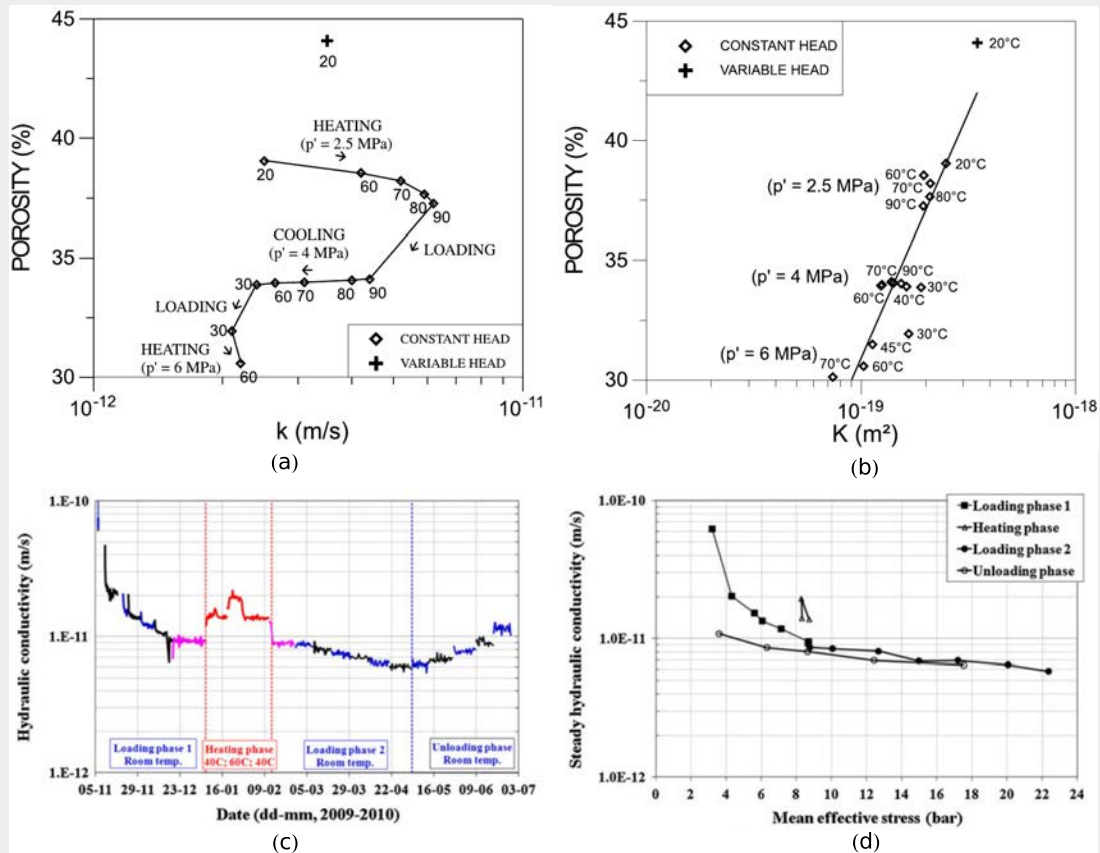
Figure 2.39.: Results of permeability tests performed on natural Boom Clay at various temperatures and stress states: (a) Variation of porosity and permeability, and (b) Variation of porosity and intrinsic permeability (Delage et al., 2000). Variation of hydraulic conductivity of Boom Clay in an isostatic test: (c) with temperature, and (d) with mean effective stress (Chen et al., 2012a).

the radionuclide containment provided by the Supercontainer.

The performance and safety functions of the MBS in the investigated repository life-time phases (Figure 1.5) are primarily governed by the near-field properties and perturbations. Figure 2.40 outlines some of the THMC perturbations and their main interacting processes over the repositorylife-time.

In recent years numerous studies on THMC coupled processes and their influence on the repository performance have been performed and published. For a waste repository situated in an argillaceous host rock a general overview may be found in the selected contributions to the international meetings on *"Clays in Natural and Engineered Barriers for Radioactive Waste Confinement"* organised by Andra (France), in cooperation with Nagra (Switzerland), Ondraf/Niras (Belgium) and SKB (Sweden), which took place in Reims (2004), Tours (2007, 2008), Lille (2008), Nantes (2011) and Montpellier (in press). Some recent state of the art papers, e.g. Hudson et al. (2005), Tsang et al. (2005); Tsang et al. (2012), Blümling et al.
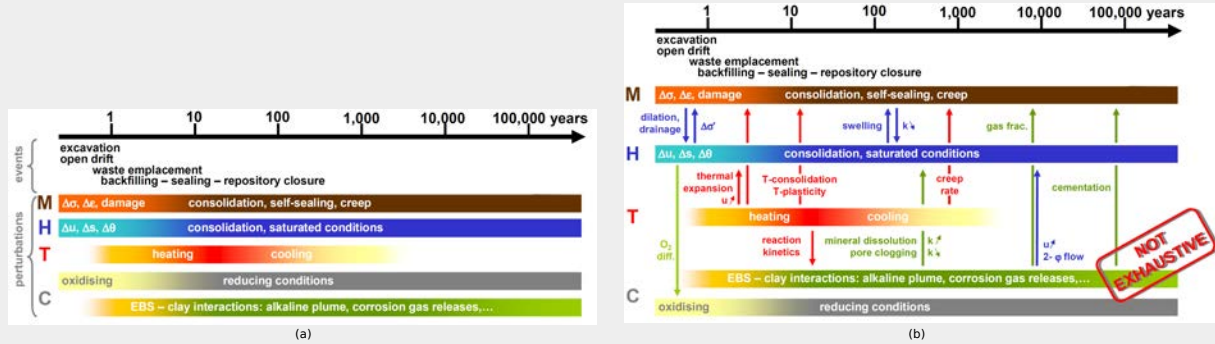
Figure 2.40.: Some of the (a) multiple THMC perturbations and (b) their main interactions in clay host rock over the lifetime of a repository (Sillen, 2010).

(2007), Delage et al. (2010), Gens (2011), Kim et al. (2011), Birkholzer et al. (2012), Cui and Tang (2013), Delage (2013), Li (2013a) and Yu et al. (2014), as well as various monographs, e.g. Stephansson et al. (2004), Kolditz et al. (2012) and Chen et al. (in press, 2015), provide a valuable resource of information. Furthermore, reports provided by the NEA Clay Club (e.g. Bock et al., 2010; Boisson, 2005; Horseman et al., 1996, 2004; NEA, 2001) and by the TIMODAZ project (e.g. Li, 2013a; Li et al., 2007, 2012b; Li et al., 2010b) provide a state of the art summary on the transient physical process governing the repository response in the near and far fields.

2.5.1. Excavation and construction phase

2.5.1.1. Construction - methods and materials

Tunnelling techniques

In the last century numerous conventional and mechanised tunnelling techniques have been applied in engineering practice (e.g. Kuesel et al., 2004; Maidl et al., 2012). Common drill and blast techniques include conventional tunnelling as well as the *New Austrian Tunnelling Method* (NATM) (Rabcewicz, 1964a,b, 1965). The latter NATM is very commonly applied, as the use of a more flexible support structure allows for the strength of the soil to be mobilised, thereby reducing the cost with respect to installing a rigid support structure.

Using Tunnelling Machines, the soil mass can be excavated using a cutter head or a cutting wheel, that is, with no support of the excavation face or support being provided either mechanically, by compressed air, slurry or earth pressure balance (Maidl et al., 2012).

Figure 2.41 schematically outlines the response of the host rock due to excavation. The total radial deformation u_c at the cavity interface is the sum of the overcut, d_{oc}, and the radial liner deformation, u_l, associated with the soil induced support cavity pressure p_c.

$$u_c = \underbrace{u_c^0 + u_c^\delta}_{d_{oc}} + u_l \tag{2.2}$$

The cutting head of the excavation shield is oversized to reduce shaft friction at the shield-soil interface during progression of the machine, which potentially could lead to the shield being trapped in the Boom Clay. In Equation 2.2, u_c^0 is the soil initial deformation during the excavation and u_c^δ is the soil deformation resulting from the closing of the residual overcut after the liner installation. The extent of the plastic zone, in which the host rock will deform in an irreversible manner, is a function of the set of soil property values $\mathbf{X}$, the initial stress condition σ^0 and the excavation boundary conditions (excavation radius r_e, unsupported excavation length l_e, excavation velocity v_e), as well as of the support structure, e.g. in the form of concrete segments placed with a lining thickness of d_l and given property values of $\mathbf{X}_l$.

The following criteria may apply for the selection of an appropriate excavation method and support structure for the construction of tunnel galleries in the context of a radioactive waste repository:

○ Limiting the convergence of the gallery during and after excavation.

○ Limiting the disturbance of the host rock during excavation.

○ Durability and safety of the support structure for the operational phase.

○ Technically and economically feasible.

For the excavation of URLs and/or repositories in stable hard rock, both drill and controlled blast techniques have been used in Sweden, Switzerland and Japan. For the sinking of a shaft and the excavation of the drift at a depth of 445m in the Callovo-Oxfordian clay rock formation at the Meuse/Haute-Marne URL in Bure, a drill-and-blast technique was used (Delay et al., 2008). For excavating the galleries at the main level of 490m depth, initially a pneumatic hammering technique and later a roadheader was used with stiff and flexible support (Armand et al., 2013). In 2013 the excavation with a *Tunnel Boring Machine* (TBM) and segment emplacement was planned to be tested (Armand et al., 2013). For excavating the galleries in the Opalinus Clay at the Mont Terri rock laboratory, dry blasting, pneumatic hammering and roadheader techniques were found to be feasible, that is, with the latter performing best.

For the excavation in plastic Boom Clay, which has a lower stiffness and strength compared to the two stiff argillites (see Section 2.4.3.2), a different technique needs to be applied. The experiences gained at the HADES URF in Mol (see Figure 2.9) during the construction of the Connection Gallery with the associated CLIPEX program (see Figures 2.11 and 2.12) and the excavation of the PRACLAY Gallery (see Figure 2.13), both at 223m depth, will be summarised hereafter. A more detailed description can be found, e.g. in Bastiaens et al. (2003), Bernier et al. (2007a,c), Charlier et al. (2010b), Van Marcke and Bastiaens (2010b) and Li (2012).

Excavation of the Connecting and PRACLAY Galleries at the HADES URF

The Connecting Gallery and the PRACLAY Gallery were excavated using a *Shield Machine* (SM) with a roadheader, see Figure 2.11(a) (Bastiaens et al., 2003; Van Marcke and Bastiaens,

d_l	...	Concrete lining thickness	u_c	...	Total soil displacement at cavity $(u_c^0 + u_c^\delta + u_l)$
d_{oc}	...	Overcut	v_e	...	Excavation velocity
l_e	...	Excavation length	$\mathbf{X}$	...	Soil property values
r_i	...	Nominal inner tunnel radius	$\mathbf{X}_l$	...	Concrete lining property values
r_e	...	Excavation radius	$\sigma_h^0 = \sigma_v^0$	...	Total in situ stress $(\sigma_0' + u_w)$
p_c	...	Cavity pressure			
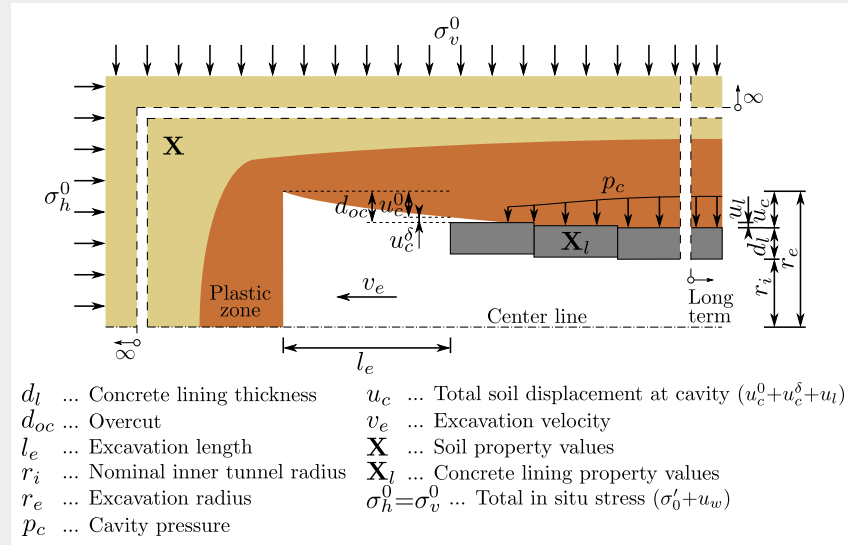
Figure 2.41.: Schematic overview of excavation process, where d_l is the concrete liner thickness, d_{oc} is the thickness of the over cut, l_e is the excavation length, p_c is the cavity pressure, r_e is the excavation radius, r_i is the nominal inner tunnel radius, u_c is the radial displacement at the cavity interface, v_e is the excavation velocity, $\mathbf{X}$ holds the soil property values, $\mathbf{X}_l$ holds the concrete liner properties, σ^0 is the total in situ stress.

2010b). The mean excavation rate was about 3 m day^{-1} for the Connecting Gallery and 2 m day^{-1} for the PRACLAY Gallery. However, based on the experience gained, Van Marcke and Bastiaens (2010b) deemed that a mean excavation rate of 10 m day^{-1} was realistic for the construction of a future repository.

The work principle of the SM consists of three phases. In the first phase the roadheader excavates the majority of the Boom Clay at the face. Subsequently, after all clay is removed in the reach of the roadheader, the shield pushes forward via hydraulic jacks shoring on the in place concrete lining ring. The cutting edges on the shield ensure a circular excavation profile of the gallery. In the third phase the jacks are retreating and the concrete lining segments are placed.

Figure 2.42 shows the shield geometry of the SM used to excavate the Connecting Gallery (Bastiaens et al., 2003). In order to reduce the shaft friction on the shield during progression, to reduce the possibility of the shield being trapped in the clay, the cutting head of the shield was oversized by 15-45mm. Due to the potentially very high frictional forces in the clay at this large depth, the use of a pipe jacking technique, that is, with the entire excavation ring of the shield being pressed into the host rock, was disregarded by EURODICE. The blades on the cutting head were designed to be adjustable from 0 to 30mm, of which the maximum 30mm was used and found to be most suitable. The 5mm conicity was designed to further reduce the friction and provide for better steering of the machine. An extra 10mm margin was designed to account for convergence of the Boom Clay over this unsupported length. The
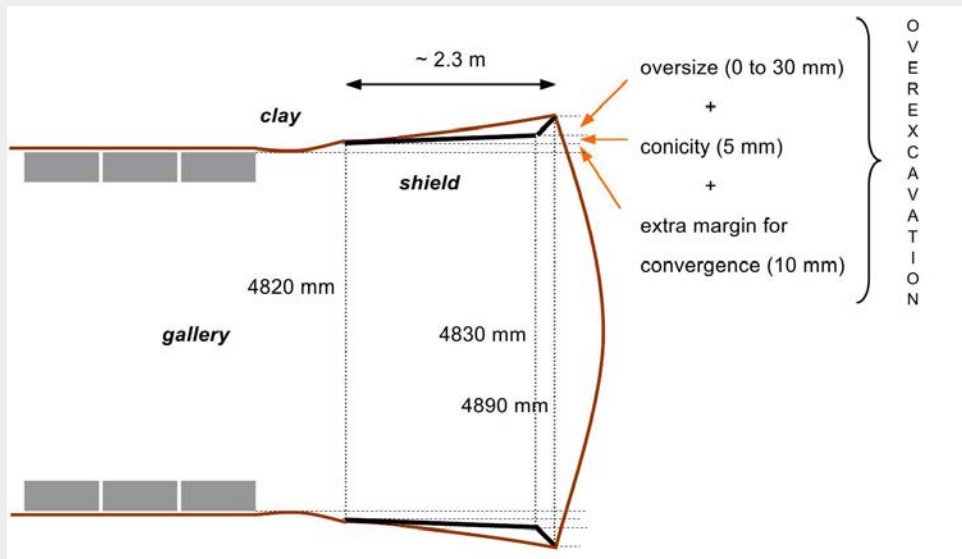
Figure 2.42.: Schematic cross section of the tunnelling shield with conical shape and adjustable cutters providing the oversize, and the total over excavation (Bastiaens et al., 2003).

jacks were designed to advance the shield for 1.2m, which allowed for the placement of one concrete support ring of 1m width.

The concrete lining segments used for the Connecting and PRACLAY Galleries at the HADES URF

A concrete support structure is required in Boom Clay to minimise the convergence of the excavated tunnel galleries and provide the necessary stability over the envisaged operational period of up to about 100 years (Figure 2.14).

At Mol, the so called *wedge-block technique* was used to install one ring of the concrete lining. For the Connecting Gallery one ring consists of 12 elements and is unbolted and independent from the adjacent ring. Utilising the wedge-block technique, two key segments are used to expand the concrete rings to sit flush on the Boom Clay. Another commonly used method is the *bolted-segments technique*, where steel segments are assembled to form one complete ring of fixed size. The resulting gap between the ring and host rock is then filled by injecting grout. Due to the large perturbation of the Boom Clay resulting from the large convergence, this method was disregarded by EURODICE (Bastiaens et al., 2003).

The concrete segments used for the lining of the Connecting Gallery had a thickness of 0.4m, were 1.0m wide and were not reinforced (Bastiaens et al., 2003). The key segments were slightly shorter with a dimension of 0.85m. The concrete used for the segments was a HSR CEM II/B-V 42.5 type, which was modified to be highly resistant to sulphates. The 95 percentile of the compressive strength was 91.3N mm^{-2}. The requirement defined by EURODICE was C65/80 class according to Eurocode 2.

Some concrete property values used at the HADES URF, to describe the mechanical, hydraulic and thermal responses of the concrete liner segments due to external and thermal loadings as part of the stability and long term safety assessments have been tabulated in Table 2.12.

2.5.1.2. HM response during the excavation and construction phase

Due to the excavation of the tunnel galleries the Boom Clay host rock will undergo a major stress release and redistribution. The contractant and/or dilatant strains resulting from this differential stresses may potentially induce micro and macro shear fractures which will influence the repository performance. In recent years, intense efforts involving experimental, theoretical and numerical studies have been undertaken to assess the EdZ/EDZ development and their impact on the performance of the repository over its lifetime (e.g. Arson and Gatmiri, 2008; Blümling et al., 2007; Charlier et al., 2008; Davies and Bernier, 2005; Horseman et al., 2004; Tsang et al., 2005; Yu et al., 2010).

EDZ/EdZ definition and development

The general definitions of the *Excavation Damaged Zone* (EDZ) and *Excavation disturbed Zone* (EdZ) were given in Section 2.3.2. However, the definition of their extent and of the processes taking place differs with the type of host rock (Davies and Bernier, 2005). For indurated and plastic clays, flow and transport properties are used as key elements in these definitions (Table 2.13).

Figure 2.43 schematically describes the variation in stresses around a supported tunnel cavity idealised in a 2D plane. From its in situ state the overconsolidated Boom Clay will undergo ideal elastic deformations until yielding occurs, with irreversible plastic deformations taking place in the closer vicinity of the tunnel. The extent of this *plastic zone*, does not

Table 2.12.: Some property value ranges governing the thermo-hydro-mechanical behaviour of the concrete lining.

Definition	Symb.	Unit	Range	Source
Density	ρ	$[\mathrm{kg\,m^{-3}}]$	2400 - 2500	[1,2]
Porosity	ϕ	$[-]$	0.15	[2]
Young's modulus	E	$[\mathrm{MPa}]$	43305	[2]
Poisson's ratio	ν	$[-]$	0.25	[2]
Intrinsic permeability	k_{sat}	$[\mathrm{m^2}]$	4.00E-018	[2]
Thermal conductivity	λ	$[\mathrm{W\,m^{-1}\,K^{-1}}]$	1.5	[1,2]
Volumetric heat capacity	$\alpha = \rho C_p$	$[\mathrm{J\,m^{-3}\,K^{-1}}]$	2.11E+06 - 2.20E+06	[1,2]
Thermal dilation coefficient	α_s	$[\mathrm{K^{-1}}]$	1.00E-05	[2]
Specific heat capacity	C_p	$[\mathrm{J\,kg^{-1}\,K^{-1}}]$	880	[1]

Sources: [1]Weetjens (2009), [2]Charlier et al. (2010b).

Table 2.13.: Definition of the EdZ and EDZ for indurated and plastic clays based on discussions given in Davies and Bernier (2005) (Tsang et al., 2005).

	Indurated clay	Plastic clay
EdZ	*"Region where only reversible processes (elastic strain, pore pressure changes, etc.) take place; not relevant to creation of preferential pathways for radionuclide migration."*	*"Zone with significant modification of state (pore pressures, stresses, etc.); no negative effects on safety."*
EDZ	*"Micro-cracked zone with damage and failure, and with weakly connected micro-cracks. A zone in which permeability increases by several orders of magnitude, owing to newly formed connected porosity - may become an issue in safety assessment. Note: EDZ is not the same as plastic or yielded zone."*	*"An evolving zone with geomechanical and geochemical modifications of state and material properties, which might have a negative effect on operational and long-term safety."*

have to coincide with the extent of the *hydraulic zone* beyond which the pore water pressure is not influenced by the cavity excavation. Furthermore, as the plastic and hydraulic zones refer to the current stress state, which influences the phase configuration, both zones do not have to coincide with the EDZ and EdZ respectively. For example, an overconsolidated plastic clay may plastify mechanically due to the excavation and thus influence the construction and pre-operational safety however, not interfering with the long-term safety of the repository, i.e. changing significantly the soil flow and transport properties.

Furthermore, the extent of the EdZ/EDZ depends on the inherent heterogeneity and anisotropy of the host rock, the tunnel excavation radius, the stiffness of the support structure and the installation procedure/time. For a tunnel in the deep-seated plastic Boom Clay, the development of the perturbated zones will be strongly influenced by the overcut d_{oc}, as the deformations of a stiff liner, u_l, are minor.

Observation at the HADES URF

In situ and laboratory investigations on the HM response of the Boom Clay during and after the excavation of the Test Drive, the Connecting Gallery and the PRACLAY Gallery at the HADES URF have been reported amongst others by Mair et al. (1992), Mertens et al. (2004), Bastiaens et al. (2007), Bernier et al. (2007a,b,c), Wileveau and Bernier (2008), Van Marcke and Bastiaens (2010b) and Yu et al. (2010).
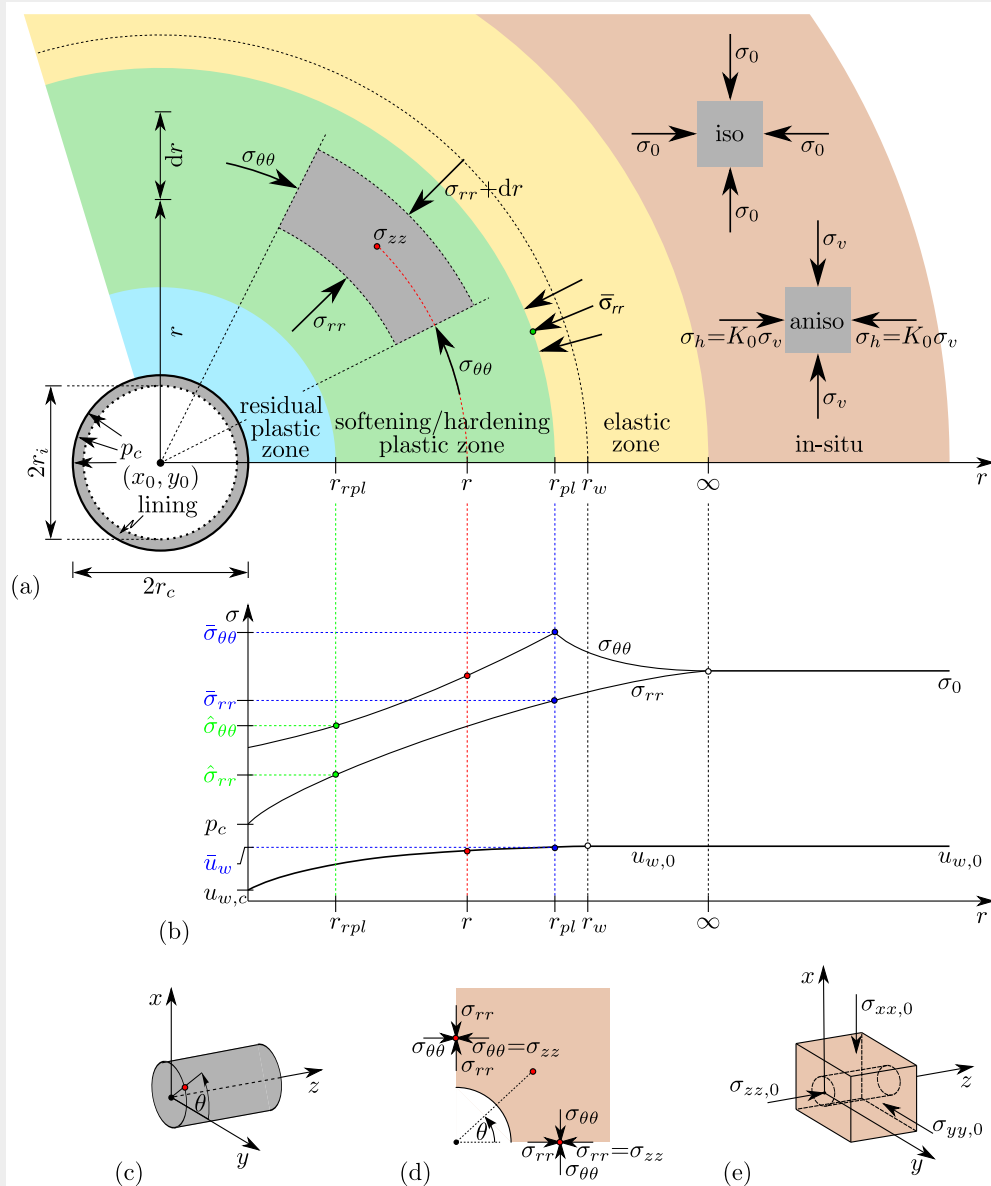
Figure 2.43.: (a) Schematic description of stresses around a cavity opening, where r_c is the excavated cavity radius, r_i is the target inner tunnel radius, p_c is the cavity pressure (i.e. acting on the liner), r is the radial polar coordinate of a point in the surrounding subsoil, r_p is the plastic (yield) radius, r_{rp} is the residual plastic radius in which the material reached the residual state, r_w is the radius beyond which the pore water pressure is not influenced by the cavity, σ_{rr} is the total radial stress, $\sigma_{\theta\theta}$ is the total tangential stress, σ_{zz} is the total axial stress, $\bar{\sigma}_{rr}$ is the total radial stress at the initial yield interface, $\sigma_{h,0}$ and $\sigma_{v,0}$ are the total horizontal and vertical in situ stresses, and K_0 is the earth pressure coefficient. (b) Associated stress in the subsoil where $\bar{\sigma}_{\theta\theta}$ is the total tangential stress at the yield interface, $\hat{\sigma}_{rr}$ and $\hat{\sigma}_{\theta\theta}$ are the total radial and tangential stress at the residual plastic interface, u_w is the pore water pressure, $u_{w,0}$ is the in situ pore water pressure, $\bar{u}_w$ is the pore water pressure at yield and $u_{w,c}$ is the pore water pressure on the cavity. (c) Tunnel coordinates with θ being the angle of y-axis rotation. (d) Total stresses around cavity. (e) Boundary conditions with σ_0 being the total far-field stress in Cartesian directions.

Figure 2.44(a) shows the mapping of some observed large shear planes and tension fissures during the manual excavation of the Mounting Chamber. These planes seem to be caused mainly by the excavation of the second shaft, as well as the Mounting Chamber itself, as they dipped towards the centre of the second shaft (Mertens et al., 2004). The planes extended up to approximately 12m from the axis of the second shaft, which had an excavation radius of about 4.5m. Due to the detachment of the larger clay blocks, the local formation of small shear planes and tension fissures was observed. Figure 2.44(b) shows a highly fractured core sample induced during drilling. Figure 2.44(c) shows the eye-shaped fractures around a borehole with an anchor installed from the mounting chamber.

Figures 2.10(a-b) and 2.11(b) showed the different fracture patterns observed during the excavation of the Connecting Gallery, in the radial direction of the tunnel liner and in front of the excavation face. With an excavation radius of 2445mm (Figure 2.42), the fracture planes originated about 6m ahead of the front and extended radially up to approximately 1m into the Boom Clay, with a distance of a few decimetres in-between each individual fracture (Bastiaens et al., 2003). The fracture pattern in Figure 2.11(b) shows that the fractures dip roughly parallel to the gallery axis.

A similar anisotropic convergence was observed during the excavation of the PRACLAY gallery (Van Marcke and Bastiaens, 2010b). The Boom Clay has a distinct horizontal bedding plane and shows both a fabric and mechanical anisotropy (Section 2.4.1 and 2.4.3.2). However, with the earth pressure at rest being $K_0 \lesssim 1.0$ (Section 2.4.2), suggesting a larger deformation in the vertical direction, (Bastiaens et al., 2003) and Van Marcke and Bastiaens (2010b) attribute the larger deformation in the horizontal direction partly to the stress reduction in the vertical direction due to the fracturing ahead of the excavation face. The radial extent of the fractured zone around the PRACLAY gallery was estimated to not exceed 75mm in the horizontal plane (Van Marcke and Bastiaens, 2010b).

The fracture pattern encountered during the excavation was confirmed by Hollow Cylinder tests on undisturbed Boom Clay samples as part of the TIMODAZ project (Charlier et al., 2010a; François et al., 2013; Labiouse et al., 2013). Figure 2.45(a) shows the eye-shaped damage zone parallel to the bedding plane. The results confirm the significance of the bedding plane inducing mechanical anisotropy. Furthermore, due to the short drainage length a faster diffusion of pore fluid parallel to the bedding plane due to the hydraulic anisotropy (Section 2.4.3.3) may have induced further anisotropic changes in the effective stress and thus contributing to the observed anisotropic displacements (Labiouse et al., 2013).

Contrary to the shear failure observed in the plastic Boom Clay, excavation-induced fractures in hard and brittle clays are of an extensive nature (e.g. Blümling et al., 2007; Tsang et al., 2005). Hollow Cylinder tests on the indurated Opalinus clay samples (Mont Terri rock laboratory) showed bedding plane splitting and buckling, with the larger deformations taking place perpendicular to the bedding plane (Figure 2.45(b); Labiouse and Vietor, 2014).
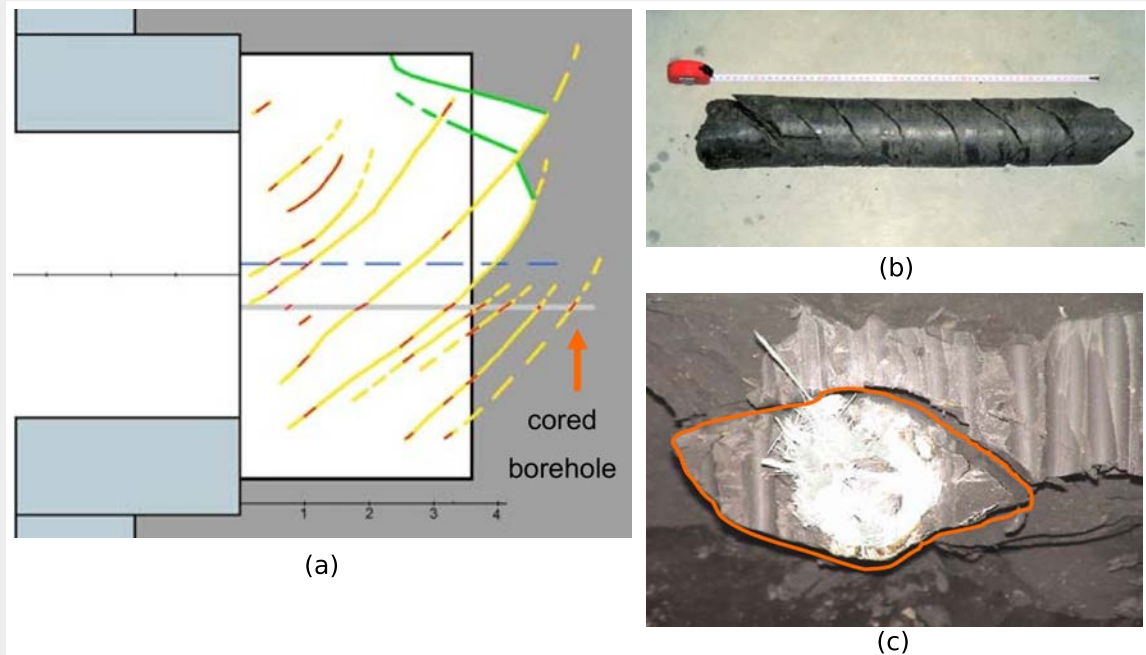
Figure 2.44.: (a) Vertical cross section through the Mounting Chamber (in red - measured shear planes, both before the excavation and during its excavation, in yellow - all the observations of shear planes, in green - tension fissures, dotted lines - extrapolations), (b) Intense fracturation of core sample due to the drilling process. (c) An anchor surrounded by resin that has partly penetrated into drilling-related fractures of the Boom Clay. (Bastiaens et al., 2003).

2.5.2. Pre-operational phase

According to the OPERA disposal concept the open phase may last for several decades (Figure 2.14), a time during which the EDZ/EdZ of the Boom Clay as well as the concrete liner may undergo significant perturbations.

Boom Clay response

Figure 2.46 shows profiles of differential pore water pressures recorded at two sections of the Connecting Gallery, about 2 years and 9 months after the construction, as part of the SELFRAC project, via multi-piezometers, as well as two profiles obtained via CLIPEX piezometers which have been installed before the construction (Bastiaens et al., 2007; Bernier et al., 2007a). The response of the different profiles show good agreement regarding the anisotropic extent of the hydraulic zone, i.e. > 40m in vertical direction and about 20m in horizontal direction (Bastiaens et al., 2007). The values in the far field being significantly lower than 100% was attributed to disturbance during the installation of the piezometers (Van Marcke and Bastiaens, 2010b).

Negative pore water pressure (suction) may evolve during the undrained dilative response

(a)   (b)
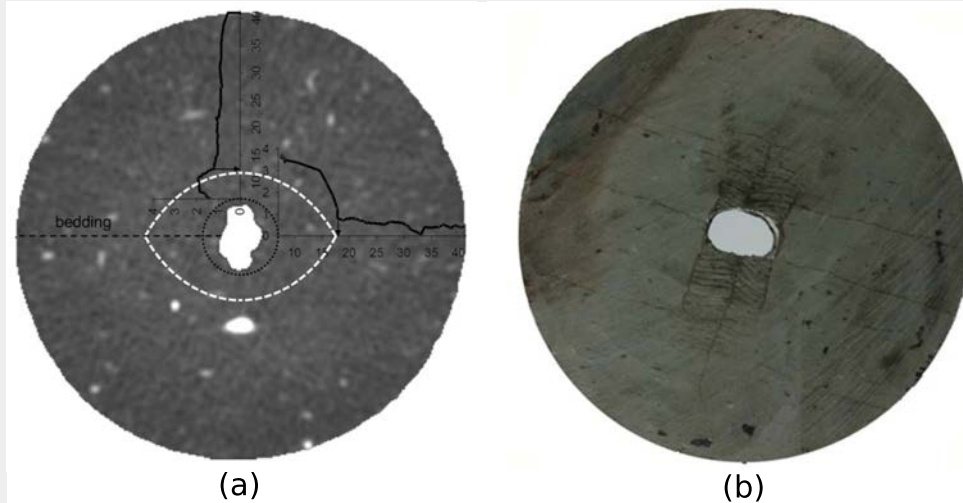
Figure 2.45.: (a) Hollow Cylinder test on Boom Clay showing eye-shaped damage zone parallel to the bedding plane (black dashed line), observed in the displacement profiles (Labiouse et al., 2013). (b) High resolution XRCT scan of the Opalinus Clay Hollow Cylinder specimen, showing bedding plane splitting and buckling (Labiouse and Vietor, 2014).
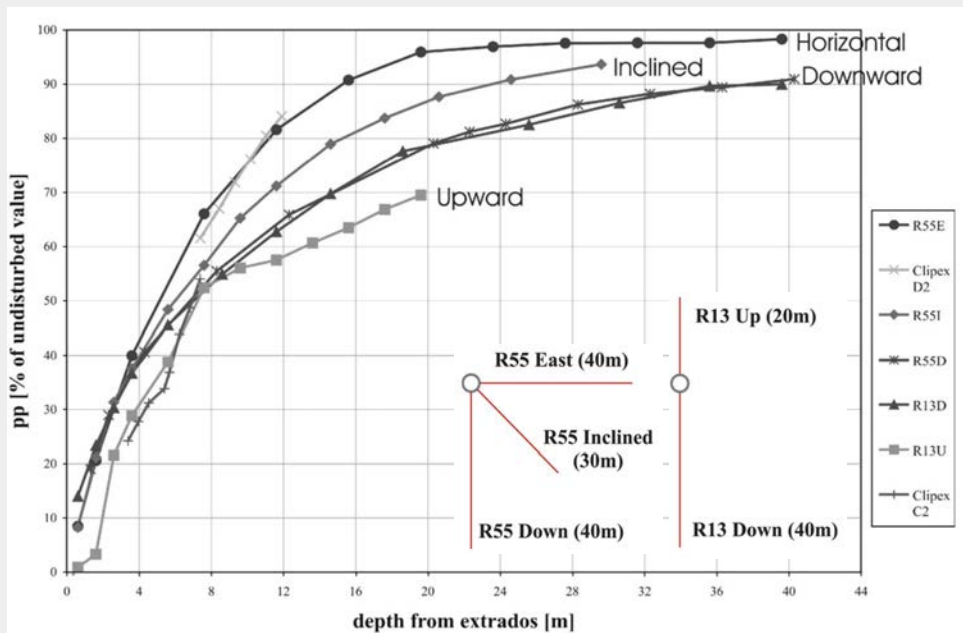
Figure 2.46.: Pore pressure measurements around the connecting gallery about 2 years and 9 months after construction, expressed as a percentage of the original undisturbed value at each measurement location from the extrados (lining exterior). The lay-out of the two piezometer sections is indicated. (Bastiaens et al., 2007)

shortly after the construction, but, as well, due to long term de-hydration of the Boom Clay in the close vicinity of the tunnel. Generally an increase in suction, and thus effective stress, is accompanied by an increase in soil strength and a decrease in hydraulic conductivity, but it may invoke further fracturing (e.g. Bernier et al., 1997; Delage et al., 2007; Gens, 2011). The dehydration of the Boom Clay may be enhanced by ventilation. Some requirements on a potential ventilation scheme of all mine zones for a repository were estimated as part of the TRUCK I project (Section 2.2.1.3).

Due to the convergence of the Boom Clay around the tunnel the cavity pressure increases. This non-linear pressure build up was monitored for the Connecting Gallery using embedded vibrating wire strain gauges (Figure 2.47). Test results by Djeran et al. (1994), Giraud and Rousset (1996) and Cui et al. (2009) suggest that creep is a significant process contributing to the transient convergence in Boom Clay.

Oxidation induced by excavation and ventilation can affect the favourable host rock characteristics and influence the engineered barrier system. The extent of the oxidised zone is generally estimated to be limited to about 1m around the HADES galleries, and probably less than 0.6m (initial estimate) around the PRACLAY gallery, that is, with the presence of gypsum being observed within the first 4.5cm in both cases (De Craen et al., 2008, 2011; Van Geet et al., 2006).

Concrete response

Degradation of the concrete based EBS components (i.e. liner, backfill, buffer) may be of a physical, chemical and/or biological nature. The prime interest in any repository design, and thus of most research, is that of ensuring the barrier performance and avoiding negative effects on other barrier components due to concrete degradation (e.g. Glasser et al., 2008;
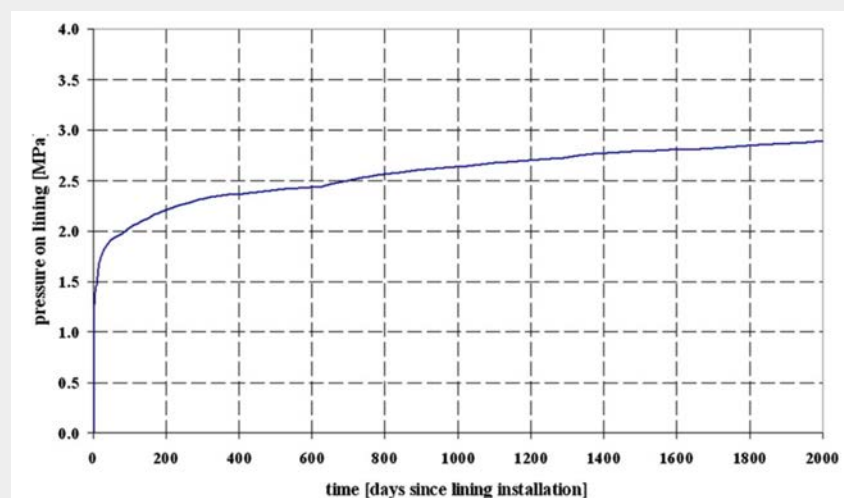
Figure 2.47.: Evolution of the average cavity pressure exerted on a lining ring of the Connecting Gallery (Van Marcke and Bastiaens, 2010b).

NEA, 2012; Read et al., 2001; Trotignon et al., 2007). However, for any technical feasibility study the concrete degradation processes of the lining segments during the open phase, which ultimately may lead to an extension of the EDZ or, in the worst case, to failure, need to be accounted for.

A typical tunnel design life ranges from 50-150 years, e.g. 100 years for the London Underground Jubilee Line Extension or 120 years for the UK's Crossrail and Channel Tunnel Rail Link projects (BTS/ICE, 2004; FHWA, 2009). The durability of the liner strongly depends on the materials used, e.g. highly sulphate resistant and not reinforced as used at the HADES URL (Section 2.5.1.1), the liner dimensions and the host environment. For example, the BTS/ICE (2004) *Tunnel lining design guide* states that "*currently there is no guide on how to design a material to meet a specified design life*" and further, "*This code goes some way to recommending various mix proportions and reinforcement cover for design lives of 50 and 100 years.*".

For example, results by De Craen et al. (2006) show that the chloride concentration, Cl^-, in the pore water is 26 mg l^{-1} at the HADES URF in Mol and up to 3100 mg l^{-1} at the Essen boreholes (Section 2.4.1). In a recent study Abbas (2014) showed that Cl^-, in higher concentrations can have a significant impact on the design life of concrete lining segments.

The incorporation of concrete liner degradation effects on the assessment of the response of the Boom Clay host rock is beyond the scope of this study; however, for a complete feasibility study the impact of concrete degradation has to be accounted for.

2.5.3. Operational phase

During exploitation, the Supercontainer will be emplaced, the backfill material installed and the disposal drift sealed. A wide range of cement and non-cement based materials can be used as potential backfill (e.g. NEA, 2012; Pusch, 2001, 2002, 2003). A large number of studies investigated the THM effects due to the re-saturation, swelling and thermal loading on non-cement based buffer materials such as bentonite, bentonite-sand mixtures and reconstituted Boom Clay (e.g. Baldi et al., 1991a,b; Bouazza et al., 1996; Delage et al., 2010; Hoffmann et al., 2007; Romero et al., 1999, 2011; Tsang et al., 2012; Villar and Lloret, 2004; Wang, 2012; Wang et al., 2012a). Besides maintaining their containment and long-term isolation requirements within the EBS (Section 2.3.2), the backfill needs to remain mechanically stable as well as chemically compatible with the Boom Clay for the long term. Within the scope of this study it is assumed that the latter function is provided by the design of the EBS. Only the response of the Boom Clay host rock due to changes in the THM gradients is further assessed.

The exploitation stage initiates the re-saturation as well as the thermal loading on the repository environment. The thermal loading from the heat-generating HLW will cause water vapour to flow outwards and thus tend to dry out the Boom Clay in the close vicinity of the gallery. With increasing distance and decreasing temperature the water vapour will condensate. These processes are very likely to induce further perturbations on each barrier. The theoretical and experimental assessment of the Boom Clay response under THM loading was the focus

of extensive research over the last two decades (e.g. Baldi et al., 1991a,b; C.-F. Tsang (Ed.), 2007; Chen et al., 2011, 2012a; Collin et al., 2002; Cui and Tang, 2013; Cui et al., 2000; De Bruyn and Labat, 2002; Delage, 2010, 2013; Delage et al., 2000; Dizier, 2011; François et al., 2009; Hong et al., 2013; Le, 2008; Li et al., 2012b; Lima et al., 2013; Monfared et al., 2012; Romero et al., 2005; Tsang et al., 2012; Zhang et al., 2007a).

Results from the ATLAS III heater test (shown in Figure 2.48(a)) show the increase in pore water pressure and average total stress with increasing heater temperature (Figure 2.48(b)). Noteworthy is the temporary drop in pore water pressure after each increase in power and vice versa in the cooling phase. Figure 2.48(c) shows the temperature variation measured at two locations in different planes, but at approximately the same distance. The temperature increase observed in the horizontally located sensor is about twice of that of the diagonally inclined sensor, which may be attributed to the anisotropic thermal conductivity (see Section 2.4.3.4).

Recent laboratory and in situ heating tests on a full scale tunnel experiment showed that, under a thermal loading of temperatures up to 85°C, the compressive stress in the concrete lining segments increased to about 25-30MPa, which is up to 35% of the compressive strength of a C80/95 concrete (Levorová and Vašíček, 2012; Vašíček and Svoboda, 2011). Hence these thermally induced compressive loads can become larger than those imposed by the Boom Clay host rock due to excavation. The thermal effects should be assessed in more detail and taken into account when designing a repository; that is, for the design of galleries still remaining open when a neighbouring gallery is in operation, but more so for any retrieval scheme for heat generating HLW from an operational gallery.

Swelling due to rehydration, consolidation and creep of the Boom Clay will result in self sealing and self healing. Which process contributes to what extent to the sealing/healing is difficult to distinguish and to quantify (Bastiaens et al., 2007). Tsang and Bernier (2005) define the processes as follows:

> *"Sealing is the reduction of fracture permeability by any hydromechanical, hydrochemical, or hydrobiochemical processes."*

> *"Healing is sealing without loss of memory of the pre-healing state. Thus for example, a healed fracture will not be a special preferred site for new fracturing just because of its history."*

Numerous studies have been undertaken to better understand and quantify the processes governing the sealing and healing of Boom Clay (e.g. Bastiaens et al., 2007; Bernier et al., 2007b; Bock et al., 2010; Marivoet et al., 2009; Monfared et al., 2012; Van Geet et al., 2005, 2008a,b, 2009; Vervoort et al., 2005; Wool, 2008), notably the SELFRAC project and the RESEAL test as part of the TIMODAZ project (Sections 2.2.3.1 and 2.2.3.2).

Figure 2.49(a) shows the the total stress estimated from two series of self-boring pressure-meter tests carried out in situ at the Connecting Gallery in the HADES URF in April 2002 and August 2004 (Bastiaens et al., 2007). The total stresses deviate from the in situ stress
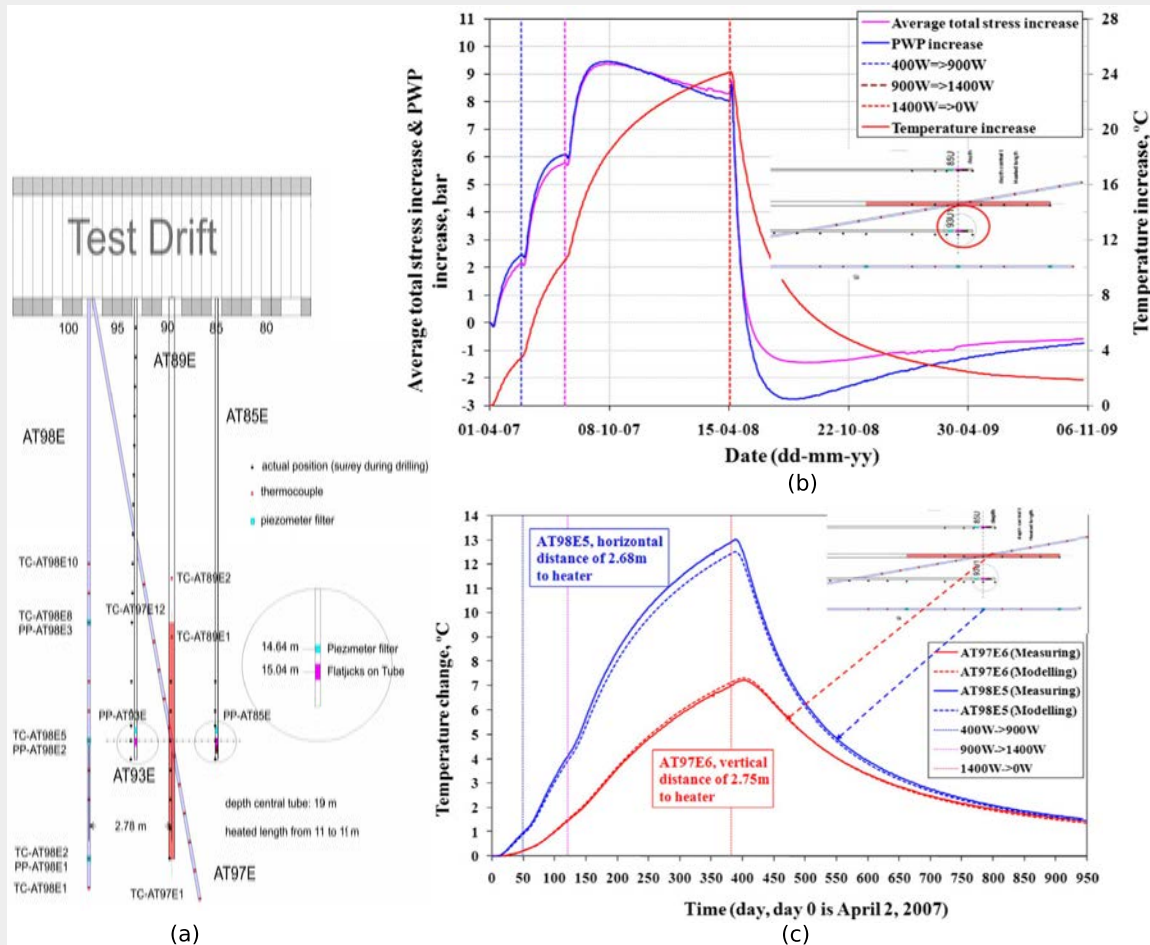
Figure 2.48.: (a) Schematic view in horizontal plane with instrumentation of the AT-LAS III in situ test. (b) Variation of average total stress, pore water pressure, and temperature in borehole AT93E, measured close to the mid-plane of the heater. (c) Measured and simulated temperature variation at locations TC-AT98E5 (same horizontal plane as the heater) and TC-AT97E6 (inclined and passing below the heater). (Chen et al., 2011).

state within a zone of about 6-8m from the liner. The increase in total stress close to the tunnel lining during the time between the two tests is clearly visible. Figure 2.49(b) shows two sets of hydraulic conductivity profiles approximated from steady state constant head measurements, obtained via piezometers installed at the HADES URF in the horizontal and vertical directions. Similar to the effective stress, an increase in hydraulic conductivity was observed within a zone of 6-8m from the tunnel liner. The hydraulic conductivity decreased within one year only slightly in the vertical profile. In the horizontal direction the results were almost identical. As laboratory results, e.g. by Volckaert et al. (1995) and Coll (2005), show a similar variation in saturated hydraulic conductivity for Boom Clay samples subjected to effective isotropic stresses in the same stress range as observed in situ (1.5-3.5MPa, Figure 2.49(a)),
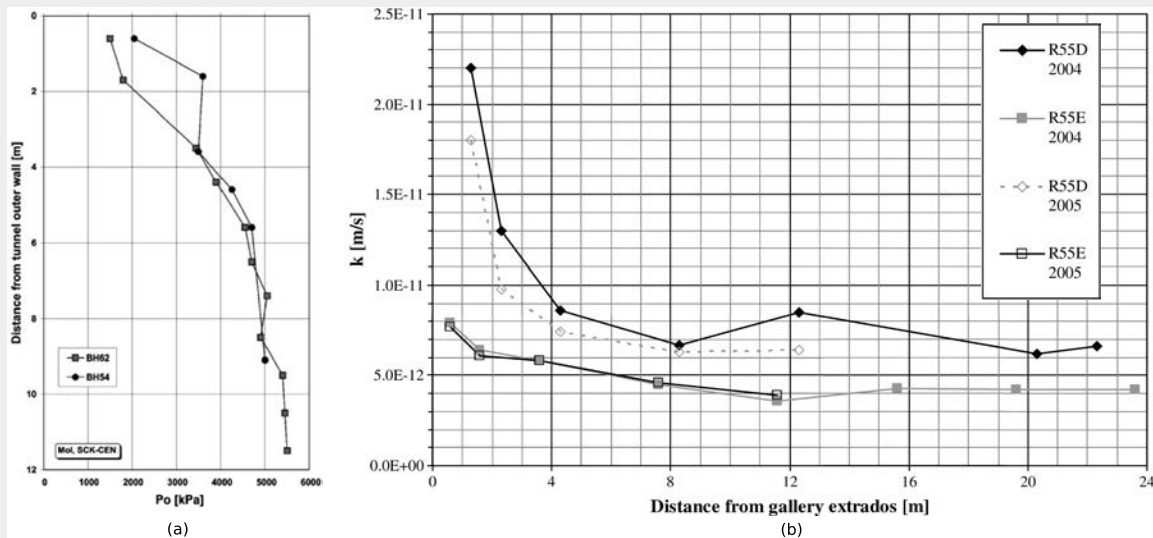
Figure 2.49.: (a) Best estimate of total stress based on self-boring pressuremeter tests performed at the HADES URF in April 2002 (BH62) and August 2004 (BH54). (b) Results of steady state, constant head measurements of the hydraulic conductivity around the Connecting Gallery performed on a horizontal (R55E) and a vertical (R55D) piezometer in 2004 and 2005. (Bastiaens et al., 2007)

Bastiaens et al. (2007) concluded that the influence of fractures around the Connecting Gallery is not significant and that any variation of hydraulic conductivity is primarily a function of the effective stress variations.

Figure 2.50 visualises the fast sealing capacity of Boom Clay (Bernier et al., 2007b). The dry and artificially fractured soil sample seen in the X-ray CT image (Figure 2.50(a)) was then saturated. Figure 2.50(b) shows the same sample after 4.5 hours with the fracture being closed. Figure 2.50(c), showing laboratory permeameter measurements on similar samples, visualises the decrease of the hydraulic conductivity due sealing with time (Vervoort et al., 2005). After the test was finished Vervoort et al. (2005) exposed the sample to the atmosphere and the original fracture reopened. This implies that, although the hydraulic conductivity of an undisturbed Boom Clay was reached, the cohesive strength was not recovered.

2.5.4. Post-closure phase

After the sealing of the repository, i.e. with all engineered containment and isolation features being installed, chemical and biological processes slowly become the driving forces on the repository performance (e.g. Cui and Tang, 2013; Delécaut, 2004; Li et al., 2012b; Lloyd and Renshaw, 2005; THERESA, 2009; Yu and Weetjens, 2009).

During the thermal phase (early closure) the energy generated from the HLW is further decreasing, which leads to a cooling of all barriers. Figures 2.51(a-b) show the evolution of the thermal output computed for the Belgium Supercontainer setup, filled with several Spent Fuel types as well as vitrified HLW, respectively (Weetjens, 2009). A cooling period, between
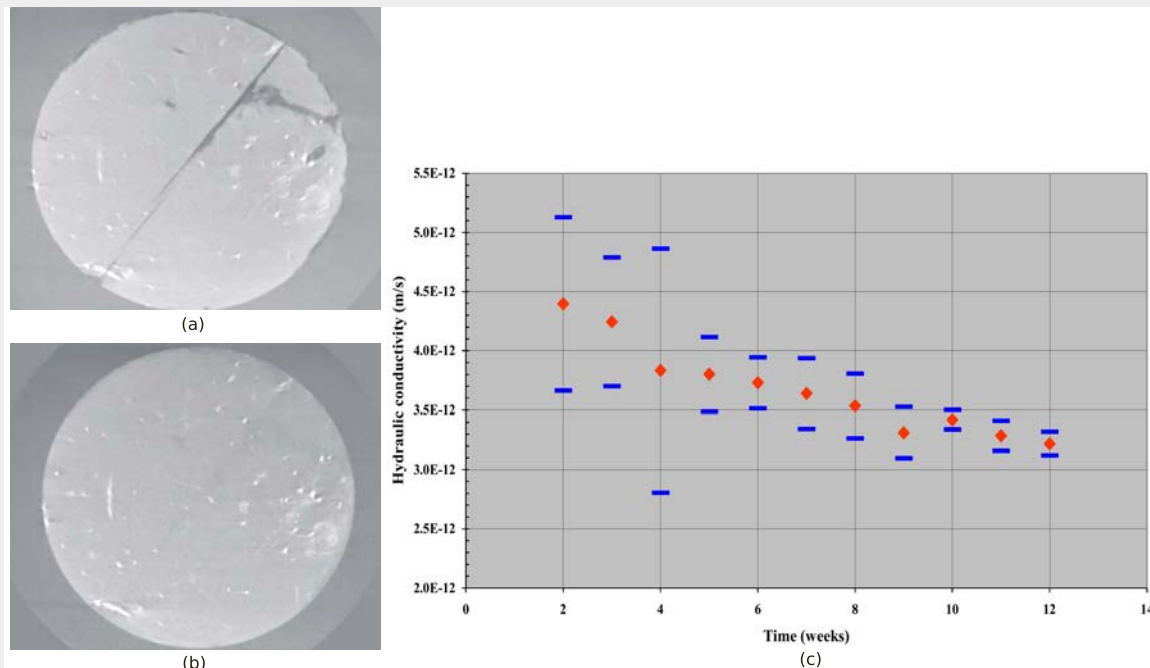
Figure 2.50.: Visualisation of the sealing process of a Boom Clay sample (‰=38 mm) by X-ray CT (a) before and (b) after saturation of the axial fracture (Bernier et al., 2007b). (c) Evolution of the hydraulic conductivity of permeameter test on a Boom Clay sample with synthetic Boom Clay water as pore water solution. The mean response and the 95% fractiles are shown (Vervoort et al., 2005).

the reactor unloading / vitrification and the backfilling of the disposal galleries, of 60 years was assumed. The initial ambient temperature was set to 16°C. Figures 2.51(c-d) show the resulting temperature variations at different locations computed via 2D axisymmetric *Finite Element Analysis* (FEA). The Boom Clay 1m behind the liner heats up to a maximum of about 60°C for the MOX-50 and 50°C for the vitrified HLW. However, due to the lower energy output of the Supercontainer filled with vitrified HLW, the soil cools down significantly faster than for the MOX-50 case. In the case of the vitrified HLW the near field EBS temperature criterion was not exceeded.

In the subsequent dissolution and geological phase (late closure), gas production and gas transport eventually becomes the driving force influencing any potential mechanical response. The transport of radionuclides from the waste pack into the near and far field becomes the key process governing the repository performance. The importance of the radionuclide transport in the excavation-damaged zone, the prediction of diffusion behaviour in nanoporous materials, or the reactive-diffusive transport characteristics are some of the remaining open research questions (Tsang et al., 2012).
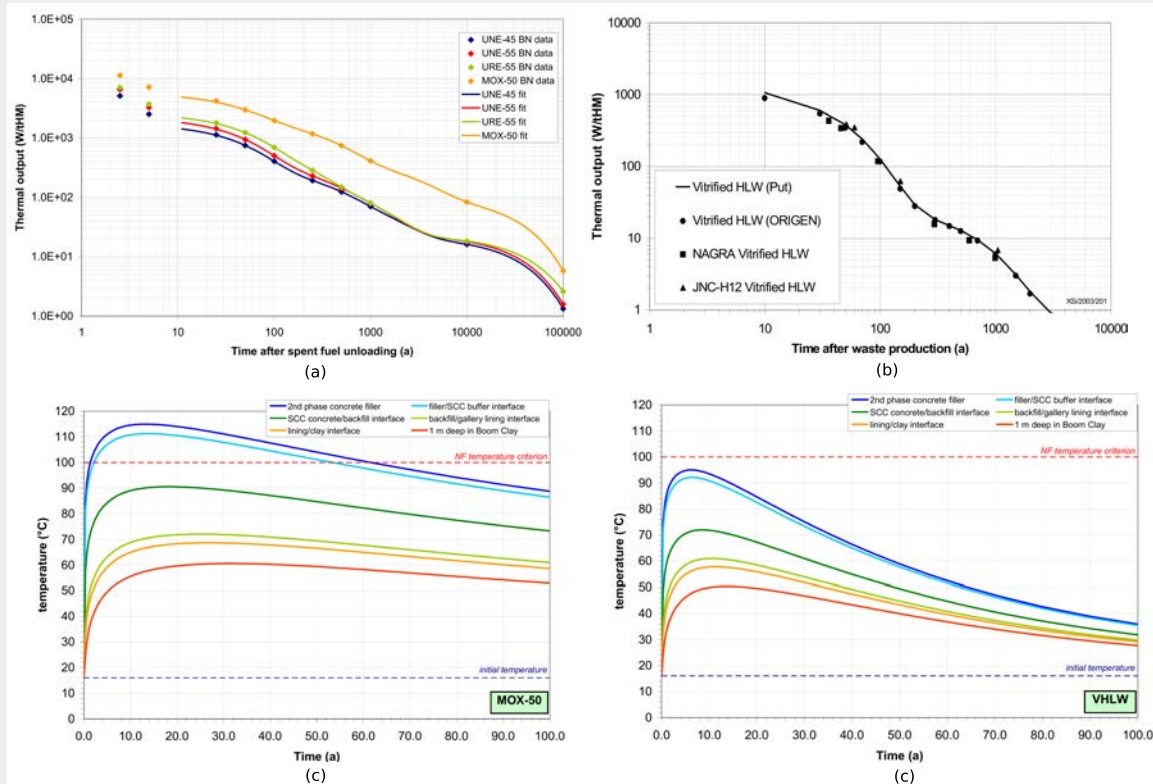
Figure 2.51.: Heat generation of Belgium Supercontainer filled with (a) several spent fuel types, and (b) vitrified HLW. Temperature evolution at different locations in the near field of a disposal gallery filled with (c) MOX-50 spent fuel, and (d) vitrified HLW. The surface cooling time is 60 years. (Weetjens, 2009)

2.5.5. Influence of the THM processes on the repository performance

Figure 2.52 shows one of the main outcomes of the *BENCHmark Tests and Guidance on Coupled Processes for Performance Assessment of Nuclear Waste Repositories* (BENCHPAR) project. The matrix ranks the different THM interactions and describes the uncertain processes which need to be addressed in a *Performance Assessment* (PA) for all repository life cycle phases. The following list of statements summarises the main findings of studies which investigated the THM effects for the Boom Clay host rock, that is, especially in terms of the EDZ development.

○ *"From a PA point of view, understanding the origin of fracturing is not of a critical importance. It is the state of the fractures and their evolution with time that is important, to assess the impact on the transport properties. The most important parameters for PA are therefore the porosity and the overall effective permeability."* (SEFLFRAC: Bastiaens et al., 2007; Bernier et al., 2007b)

○ *"Results from the TIMODAZ project indicate that the favourable properties of the clay*

1,1 Geology	1,2 Rock inhomogeneity and anisotropy, & fractures (geometry, etc.) affects rock properties/stresses	1,3 Rock porosity, rock mass permeability, and water-rock interaction affects water flow	1,4 Rock mineralogical composition and geometry of fractures affects hydrogeochemistry	1,5 Mineralogical composition, porosity, textural and structural anisotropy effects
2,1 Stress data affecting the geo-interpretation of facture systems and rock mass	2,2 Rock Mechanics	2,3 Spatial distribution of in situ stress and EDZ influences the hydrogeological regime	2,4 Stress changes near fractures zones affecting flow may change precipitation	2,5 Rocks & fracture zones subjected to higher stresses may be more thermally conductive
3,1 Hydrogeological tests and measures can affect the geo-interpretation of permeable features	3,2 Water pressure changes the effective stress	3,3 Hydro-Geology	3,4 The flow pattern affects dilution and mixing	3,5 The flow pattern will affect the temperature due to convection effects
4,1 Hydrogeochemistry interpretation affecting the interpretation of fracture min.rel.	4,2 Precipitation in fractures affects the fracture stiffnesses, strengths and creep properties	4,3 Effects of ground-water age, density, viscosity, and dissolution and precipitation	4,4 Hydro-geo-chemistry	4,5 No interaction
5,1 Thermal anisotropy and measurement affecting the geo-interpretation	5,2 Change in temperature can change the local stress, possibly leading to failure	5,3 Temperature gradients and thermal expansion in rock/fractures affect the water flow	5,4 Dissolution and precipitation enhanced by thermal gradients	5,5 Thermal Properties

Figure 2.52.: BENCHPAR interaction matrix describes the interactions between the THM processes and ranks their importance for repository PAs (Stephansson and Min, 2004; Stephansson et al., 2005).

host rock, which guarantee the effectiveness of the safety functions of the repository system, are expected to be maintained after the heating-cooling cycle. As a consequence, the results of the TIMODAZ project strengthen the SELFRAC conclusion that the (E)DZ should still not be considered as a critical issue for the long term safety of radioactive waste repositories in clay formations after the heating-cooling cycle." Yu et al. (2010, 2014)

○ *"There are no lasting effects expected of THM-related perturbations on the Boom Clay matrix structure. At the expected time of overpack failure, the porosity, density, permeability and pore diffusion coefficients are assumed to have recovered to their initial, undisturbed values."* (Weetjens et al., 2012)

○ *"Some uncertainties do remain about the long-term effects on radionuclide retention processes within the DZ when undergoing simultaneously the thermal transient and geochemical perturbations. In the case of Boom Clay, consequences of the significant*

presence of dissolved and insoluble relatively immature organic matter remain to be assessed adequately."(Yu et al., 2014)

2.6. Summary

In Section 2.2 the Dutch R&D activities on radioactive waste disposal have been reviewed. A generic repository in Boom Clay situated at 500m depth was designed as part of the TRUCK I+II studies. The mechanical response in terms of the extent of the plastic zone was found to be most sensitive to a variation in soil friction angle. The significant uncertainty in the soil property values obtained via triaxial tests performed in the TRUCK II and TRACTOR studies, that is, especially for the cohesion and soil friction angle, revealed the need for further investigations. A summary of relevant international research activities since the CORA project, especially on the Belgian Boom Clay, showed the potential of experience gained in understanding Boom Clay behaviour.

In Section 2.3 the OPERA disposal concept was summarised and the proposed repository outline discussed with respect to repository concepts of other nations. Finally this technical feasibility study was put in the context of the OPERA Safety Case.

The literature review on the in situ Boom Clay conditions, presented in Section 2.4, revealed a shortage of good quality soil test data at larger depths. Most data are available for depths until about 300m and confirm the parameter uncertainty observed in the CORA program. A spatial transformation of test results is not straight forward. As seen in comparing the intact Boom Clay from the HADES (Mol) and Essen boreholes, the difference in mineralogy and pore-water chemistry may significantly affect the hydro-mechanical material behaviour. A distinct difference in the mechanical behaviour between intact and reconstituted Boom Clay, can be observed. The shear strength of the reconstituted Boom Clay is lower than that of the intact Boom Clay due the loss of the initial bonding. Furthermore, test results suggest that the shear strength response is non-linear in triaxial compression. The structural anisotropy of the Boom Clay seems to effect significantly the geomechanical as well as the hydraulic and thermal Boom Clay behaviour.

Focusing on the excavation, open and operational phases, the coupled nature of the THM response of the Boom Clay was shown in Section 2.5. The development of a plastic zone and the increase in lining pressures is important to account for in terms of the mechanical stability of the tunnel galleries. Thermal loading can introduce significant compressive stresses in the liner. The results of different research programs suggest that the development of the EDZ is not influencing the long term repository performance and safety.

3. Interpretation of material properties and boundary conditions

3.1. Introduction

In this chapter the data on Boom Clay material properties and available boundary conditions are assessed and, as far as possible, interpreted statistically. In Section 3.2 some sources of uncertainty are addressed, their treatment in practice is outlined and their implications on this work are discussed. A description of random variables, that is variables which have statistical variation, is presented in Section 3.3. A summary of the point and spatial variability of different soil property values and state variables found in literature is presented in Section 3.4. In Section 3.5 a simple procedure is introduced to interpret the Boom Clay property values collected in the database (Appendix A), to determine the input parameters for the deterministic and reliability-based analyses in this report. The variability of concrete liner properties is summarised in Section 3.6 and Section 3.7 concludes this chapter.

3.2. Uncertainties

Deterministic analyses are the main procedure in the assessment of geotechnical performance. For a *safe* design a certain degree of uncertainty in knowledge is commonly accounted for by conservatively selecting variable values which govern the loads and resistances, that is, the so called *"conservative estimate"*. Contrary to this qualitative approach, probability theory accounts for the uncertainties in a quantitative manner, whereby the uncertainties are not reduced themselves, but, based on the current state of knowledge, addressed individually within a mathematically defined framework.

Sources of uncertainty

Uncertainties are most commonly classified into two groups, namely the *epistemic* (subjective) uncertainty associated with the current lack of knowledge, e.g. as in sampling, testing and modelling, and the *aleatory* (objective) uncertainty referring to the "true" uncertainty, e.g. the inherent spatial variability of soil property values or the variation in boundary conditions (e.g. Hacking, 1975; Helton, 1997).

Figure 3.1 shows some of the uncertainties associated with the excavation and intermediate response of a deep tunnel. The epistemic uncertainty is reducible by performing, for example, more high quality tests on undisturbed samples from depths below 500m. As physical, financial
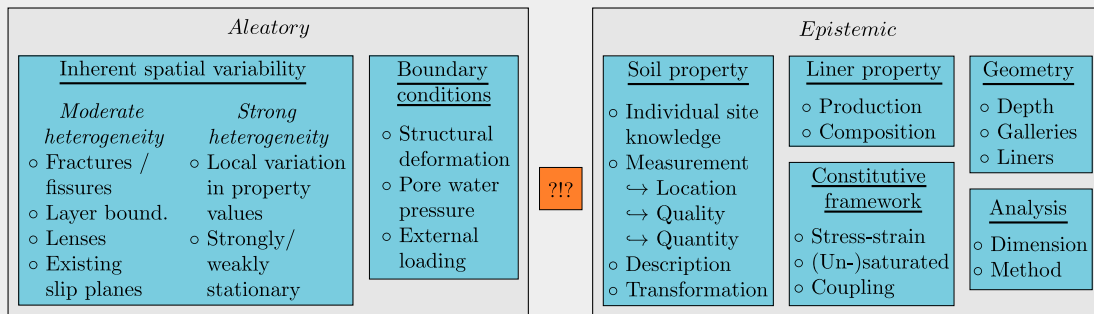
Figure 3.1.: Some sources of aleatory and epistemic uncertainty associated with the excavation and intermediate response of deep tunnels as part of a radioactive waste repository. The orange box represents the *"unknown unkowns"*.

and time constrains limit every site investigation scheme, it is generally deemed legitimate to assign the uncertainty due to the spatial variability as aleatory and as such irreducible. Furthermore, it is not possible to reduce all uncertainty nor to address them all explicitly, that is, the so called *"unknown unkowns"*. However, addressing some individual uncertainties, e.g. variation in soil property values, is an appropriate procedure in order to account for the effect of those uncertainties on the tunnel response in a quantitative manner, knowing that other uncertainties do exist, e.g. in the numerical modelling.

Parameter uncertainty

This research tries to address the uncertainty of the material property values, both of the Boom Clay and the concrete liner, with the focus on the former. A variation in soil property values obtained directly or indirectly via field or laboratory tests may result from the inherent variability, the testing (sampling, transport, procedure) or the transformation (measured quantity to soil property values), but most likely is a combination of all three (e.g. Baecher and Christian, 2003). General information on soil variability and its implications on geotechnical performance can be found, for instance, in Kulhawy and Trautmann (1996), Phoon and Kulhawy (1999a); Phoon and Kulhawy (1999b) and Uzielli et al. (2006). Studies have shown that the epistemic uncertainties can predominate (e.g. Honjo, 2011); however, a deep in-depth knowledge, e.g. of the sampling technique, transport, sampling preparation and testing procedure, is required. Practical difficulties in separating individual contributions of uncertainty are summariesed by Phoon and Kulhawy (1999a) and Uzielli et al. (2006).

3.3. Random variables

The distribution of the frequency $f_X(x)$ of individual discrete observations $(x_1, x_2, ..., x_N)$ of a random variable X may be characterised by a *Probability Density Function* (PDF), that is, a continuous function fitted to the discrete data. The lack of data mostly limits the use of a complete representation of the PDF; however, the mean μ_X, as a measure of the central

tendency, and the variance σ_X^2, as a measure of the variability, are found to be sufficient in order to describe $f_X(x)$ (e.g. Baecher and Christian, 2003; Fenton and Griffiths, 2008). A non-dimensional measure of the relative dispersion is often defined by the coefficient of variation V_X, which is the standard deviation σ_X divided by the mean μ_X.

$$\mu_X = E[X] = \int_{-\infty}^{\infty} x f_X(x) \mathrm{d}x \tag{3.1a}$$

$$\sigma_X^2 = VAR[X] = E[(X - \mu_X)^2] = \int_{-\infty}^{\infty} (x - \mu_X)^2 f_X(x) \mathrm{d}x \tag{3.1b}$$

$$V_X = \sigma_X/\mu_X \tag{3.1c}$$

Treating more than one variable as random, the key issue, and as such key difficulty, is the interdependency of the variables. This can be addressed via a covariance structure, whereby a series of cross-correlation coefficients define the strength of the relationship between variables. Since the mean and variance of the individual random variable are commonly known, a symmetric product moment cross-correlation matrix $\mathbf{R_X}$ may be set up,

$$\mathbf{R_X} = \begin{bmatrix} 1.0 & \rho_{X_1 X_2} & \cdots & \rho_{X_1 X_N} \\ \rho_{X_2 X_1} & 1.0 & \cdots & \rho_{X_2 X_N} \\ \vdots & \vdots & \ddots & \vdots \\ \rho_{X_N X_1} & \rho_{X_N X_2} & \cdots & 1.0 \end{bmatrix} \tag{3.2a}$$

$$\rho_{X_i X_j} = \frac{E[X_i, X_j] - E[X_i]E[X_j]}{\sigma_{X_i}\sigma_{X_j}} = \frac{COV_{X_i X_j}}{\sqrt{VAR_{X_i} VAR_{X_j}}} \tag{3.2b}$$

for which the product-moment (Pearson) cross-correlation coefficient $\rho_{X_i X_j}$ defines the strength of the linear relationship between two frequencies, e.g. $f_{X_i}(x_i)$ and $f_{X_j}(x_j)$, with a bivariate covariance of

$$\begin{aligned} COV_{X_i X_j} &= E\left[(X_i - E[X_i])(X_j - E[X_j])\right] \\ &= \int_{-\infty}^{\infty} \int_{-\infty}^{\infty} (x_i - \mu_{X_i})(x_j - \mu_{X_j}) f_{X_i X_j}(x_i, x_j) \mathrm{d}x_i \mathrm{d}x_j \end{aligned} \tag{3.2c}$$

The cross-correlation coefficients lower and upper bounds are $-1.0 \leq \rho_{X_i X_j} \leq 1.0$, implying perfect negative and positive linear correlation. Note that $\rho_{X_i X_j} = 0$ only implies that both random variables X_i and X_j are uncorrelated $\left(E[X_i, X_j] = E[X_i]E[X_j]\right)$, but not that the variables are independent, i.e. $f_{X_i X_j}(x_i, x_j) = f_{X_i}(x_i)f_{X_j}(x_j)$. Figure 3.2 illustrates three bivariate distributions where $\sigma_{X_i}^2 = \sigma_{X_j}^2$, but the variation in $\rho_{X_i X_j}$ may significantly alter the system response in a reliability based assessment.
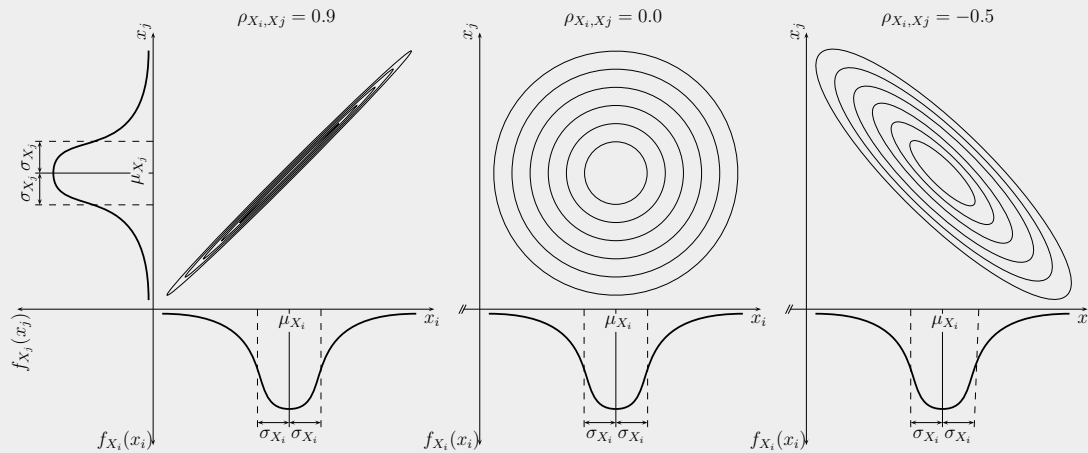
Figure 3.2.: Schematic isochrone diagrams of a bivariate joint probability density function for three different cross-correlation structures.

3.4. Variability of soil material and state variables

A summary of the point and spatial variability of soil property values and state variables found in the literature is presented in this section to provide an inside into the ranges being commonly observed. The common lack of site specific information generally restricts statistical interpretation of soil data (Christian and Baecher, 2011). However, for a reliability based assessment, into which a statistical description of soil data will feed into (Section 7), the quantitative description of this lack of data, for instance by a larger variance, is vital to represent the intrinsic effects of this lack of knowledge on the system response.

Due to lack of information, the variability of soil property values is nearly always described by a single coefficient of variation in the literature sources reviewed here; that is, defining a total uncertainty with no distinction made between epistemic and aleatory uncertainty. Furthermore, only little information on sample size, data trends, treatment of outliers, etc. are reported, which are typically required for the calculation of individual statistical parameters.

3.4.1. Point variance

Recently, Kulhawy et al. (2012) defined three ranges of coefficients of variation, V, for undrained cohesion, c_u, effective friction angle, φ', and the earth pressure at rest, K_0, for reliability calibrations (Table 3.1). They assign a low variability to good quality laboratory or field data, a medium variability to data obtained via indirect correlation and high variability to data resulting form strictly empirical correlations.

A summary of ranges of coefficients of variation reported in the literature is presented in Table 3.2. Mostly no information on the derivation of V, the mean value or even the soil type have been reported in the sources. Thus, this summary presents a general overview to indicate the absolute as well as the relative extent of the individual coefficients of variation for soil parameters, field measurements and state variables.

Table 3.1.: Ranges of the coefficient of variation, V, for reliability calibrations; undrained cohesion c_u, effective friction angle φ' and earth pressure at rest K_0 (Kulhawy et al., 2012).

Variable	Low variability	Medium variability	High variability
c_u	$0.1 \leq V_{c_u} < 0.3$	$0.3 \leq V_{c_u} < 0.5$	$0.5 \leq V_{c_u} < 0.7$
φ'	$0.05 \leq V_{\varphi'} < 0.1$	$0.1 \leq V_{\varphi'} < 0.15$	$0.15 \leq V_{\varphi'} < 0.2$
K_0	$0.3 \leq V_{K_0} < 0.5$	$0.5 \leq V_{K_0} < 0.7$	$0.7 \leq V_{K_0} < 0.9$

Table 3.2.: General summary for ranges of the coefficients of variation reported in the literature for soil parameters, field measurements and state variables.

Variable	Coeff. of variation			References
Unit weight	0.0	$\leq V_\gamma \leq$	0.2	4,8,10,15,16,18,19,20,22
Dry unit weight	0.02	$\leq V_{\gamma_d} \leq$	0.13	15,18
Porosity	0.057	$\leq V_\phi \leq$	0.355	4,6,8,9,13,16
Void ratio	0.07	$\leq V_e \leq$	0.316	3,10,12,16
Relative density	0.11	$\leq V_{D_s}^{(c)} \leq$	0.74	18
Plastic index	0.03	$\leq V_{I_p} \leq$	0.57	3,10,15,16,18
Liquidity index	0.03	$\leq V_{I_l} \leq$	0.88	3,10,15,16,18
Young's modulus	0.02	$\leq V_E \leq$	1.0	14,20,21,22
Pressuremeter/dilatometer modulus	0.15	$\leq V_{E_{PMT,D}}^{(c)} \leq$	0.65	18
Poisson's ratio	0.1	$\leq \nu^{(a,b)} \leq$	0.4	11
Bulk modulus	0.23	$\leq V_K \leq$	0.49	4,10
Effective shear strength	0.1	$\leq V_{\tau_f} \leq$	0.5	7
Effective cohesion	0.02	$\leq V_{c'} \leq$	0.7	1,2,10,19,20,22
Effective friction angle	0.02	$\leq V_{\varphi'} \leq$	0.5	4,15,16
	0.05	$\leq V_{\tan\varphi'} \leq$	0.46	10,15,22
Undrained cohesion	0.05	$\leq V_{c_u}^{(b)} \leq$	0.8	1,15,16,18,22
Saturated hydraulic conductivity	0.27	$\leq V_{K_s} \leq$	7.67	1,5,6,9,17
CPT tip resistances	0.05	$\leq V_{q_c}^{(b)} \leq$	0.4	15,16,18
CPT corrected tip resistance	0.02	$\leq V_{q_T}^{(b)} \leq$	0.17	15,18
VST undrained shear strength	0.04	$\leq V_{s_u}^{(b)} \leq$	0.44	15,18
PMT limit stress	0.1	$\leq V_{p_L}^{(b)} \leq$	0.32	15,18
Earth pressure at rest	0.15	$\leq V_{K_0}^{(b)} \leq$	0.75	15
Overconsolidation ratio	0.1	$\leq V_{OCR}^{(b)} \leq$	0.35	16

[a]Parameter range; [b]Cohesive soils (clays and clayey silts); [c]Non-cohesive soils (sand)

CPT ... *Cone Penetration Test*, VST ... *Vane Shear Test*, PMT ... *Pressuremeter Test*

Sources: [1]Lumb (1966), [2]Lumb (1970), [3]Fredlund and Dahlman (1971), [4]Schultze (1971), [5]Nielsen et al. (1973), [6]Rawls et al. (1982), [7]Whitman (1984), [8]Harr (1987), [9]Carsel and Parrish (1988), [10]Réthàti (1988), [11]Kulhawy and Mayne (1990), [12]Kulhawy (1992), [13]Russo and Bouton (1992), [14]Meyerhof (1995), [15]Phoon et al. (1995), [16]Lacasse and Nadim (1996), [17]Benson and Gribb (1997), [18]Phoon and Kulhawy (1999a), [19]Cherubini (2000), [20]Rackwitz (2000), [21]Baecher and Christian (2003), [22]Baker and Calle (2006)

The coefficients of variation of the unit weights, V_γ and V_{γ_d}, are relatively small with values > 0.1 being rare. The values of V_e and V_ϕ seem to increase for coarser grained soils. For larger mean plastic and liquidity indices the coefficients of variation, V_{I_p} and V_{I_l}, seem to decrease. The ranges of V_E reported in the literature vary significantly with the source, mostly with no soil type being reported. For the Poisson's ratio no information on V_ν were found; hence a range for clay soils has been tabulated. However, from the coefficients of variation of the bulk modulus, V_K, one might back-calculate V_ν.

The range of the coefficients of variation of the effective cohesion, $V_{c'}$, and the effective friction angle, $V_{\varphi'}$ and $V_{\tan \varphi'}$, reported in the literature is significant. Again, an interpretation of individual values/ranges reported in the literature is difficult as for instance the material, test procedure, test stress levels, etc. are not specified. However, it seems that $V_{\varphi'}$ increases for fine grained and cohesive soils, i.e. with a lower mean friction angle. In a more detailed assessment by Phoon and Kulhawy (1999a), it is evident that both triaxial compression tests and direct shear box tests result in similar coefficients of variation $V_{\varphi'}$.

A summary of ranges for the coefficient of variation for some field measurements performed in cohesive soils (clays and clayey silts) is also provided in Table 3.2. Furthermore, some ranges for the coefficient of variation of the earth pressure at rest and the overconsolidation ratio, K_0 and OCR, are provided. For the former, V_{K_0} significantly decreased with the method of evaluation, i.e. form $0.4 - 0.75$ using a *Standard Penetration Test* (SPT) to $0.2 - 0.45$ using a *Selfboring Pressuremeter Test* (SBPTM) (Phoon et al., 1995). The range of V_{OCR} was described as *"typical"* for clays by Lacasse and Nadim (1996).

If reported, the frequencies of the individual variables are mostly described to be of normal or log-normal type, for which the latter is especially required where $V_{X_i} \gtrsim 0.3$ to avoid negative values.

3.4.2. Point covariance

Point wise correlation between many soil property values may be measured directly via a series of laboratory tests, e.g. between the saturated hydraulic conductivity K_s and the void ratio e using permeability tests, or obtained indirectly, e.g. between the effective cohesion c' and the effective friction angle φ' fitting a failure envelope to shear strength data obtained via a series triaxial compression or direct shear box tests.

Much less information exists on the covariance between soil property values than for the variance of individual variables. In the literature information on directly correlated variables, mostly from geo-hydrological sources, such as between the porosity and saturated hydraulic conductivity (e.g. $\rho_{n \ln K_s} \approx 0.66$ Russo and Bouton, 1992), are in the majority. Due to the lack of data, for some indirect correlations it is only possible to obtain information on a qualitative level by assessing some general parameter ranges reported in the literature, e.g. by Kulhawy and Mayne (1990), Rackwitz (2000) or Baker and Calle (2006), and, for example, conclude that most likely $\rho_{\gamma E}$ is positive, $\rho_{\gamma \nu}$ is negative, $\rho_{\nu E}$ is negative and $\rho_{\tau_f \nu}$ is negative.

As previous studies showed, the effective shear strength parameters c' and φ' govern the

Table 3.3.: Linear cross-correlation coefficients ρ for effective shear strength paramet-
ers.

Correlation	Value	Soil	Source
$\rho_{c' \tan \varphi'}$	$-0.7^{(a)}$, $0.35^{(b)}$	Clayey silts	Lumb (1970)
$\rho_{c' \tan \varphi'}$	$-0.43^{(a)}$, $-0.72^{(b)}$	Clayey coarse sand	Lumb (1970)
$\rho_{c' \tan \varphi'}$	$-0.37^{(a)}$, $-0.03^{(b)}$	Silty coarse sand	Lumb (1970)
$\rho_{c' \varphi'}$	-0.61	Matera Blue Clays	Cherubini (1997)
$\rho_{c' \tan \varphi'}$	-0.06	Marine clay with fine silt layers	El-Ramly et al. (2006)

$^{(a)}$ Compacted samples, $^{(b)}$ Undisturbed samples

performance of the repository in terms of the extent of the plastic radius around a cavity.
Table 3.3 summarizes some linear cross-correlation coefficients obtained from the literature.
The results of Lumb (1970), obtained via triaxial compression tests for a dam construction
site in Hong Kong, show a distinct negative correlation for tests performed on compacted soil
samples. Lumb (1970) explained the lower negative up to slight positive correlation obtained
for the undisturbed samples with the low strain-rates being applied during testing. A much
larger correlation coefficient was observed for the overconsolidated Matera Blue Clays compared
to a marine clay deposit. Rackwitz (2000) and Uzielli et al. (2006) recommend, despite not
referring to any specific soil type, $\rho_{c'\varphi'} \approx -0.5$ and $-0.25 \leq \rho_{c'\varphi'} \leq -0.5$, respectively.

Figure 3.3 shows failure envelopes for Todi Clay obtained in triaxial compression tests
by Burland (1990). The response is similar to that of Boom Clay (see Figure 2.28), that
is, showing a non-linear response for intact and post-rupture failure (black dashed and solid
lines). The figure illustrates that a correlation between c' and φ' can be significantly biased, for
example, by using shear data from tests performed at different stress levels, an important detail
which is mostly not provided in the literature. The coloured dashes lines show exemplary failure
envelope fits to shear test data obtained for normal effective stresses in the range between
$1 - 2$MPa, whereas the solid lines are a fit to shear test data for a stress range between
$2 - 3$MPa. It is evident that the correlation coefficient $\rho_{c'\varphi'}$, both for intact and post-rupture
failure, will be affected when using failure envelopes obtained from tests at different stress
levels.

3.4.3. Spatial variability

The so called *scale of fluctuation* θ, or *correlation length*, commonly defines the distance over
which a random variable is strongly correlated in space. The value of θ is strongly dependent
on the soil type, the observation domain, i.e. ranging from a micro-correlation (mm) in a
soil sample to a macro-correlation (km) in a reservoir, the orientation, the testing methods,
etc.. As an indication, Phoon et al. (1995) reported scales of fluctuation in the vertical
direction $(0.1 \leq \theta_v \leq 2.2$m) and in the horizontal direction $(3.0 \leq \theta_h \leq 80.0$m) for sands
and clays based on non-normalised CPT tip resistance measurements obtained from literature.
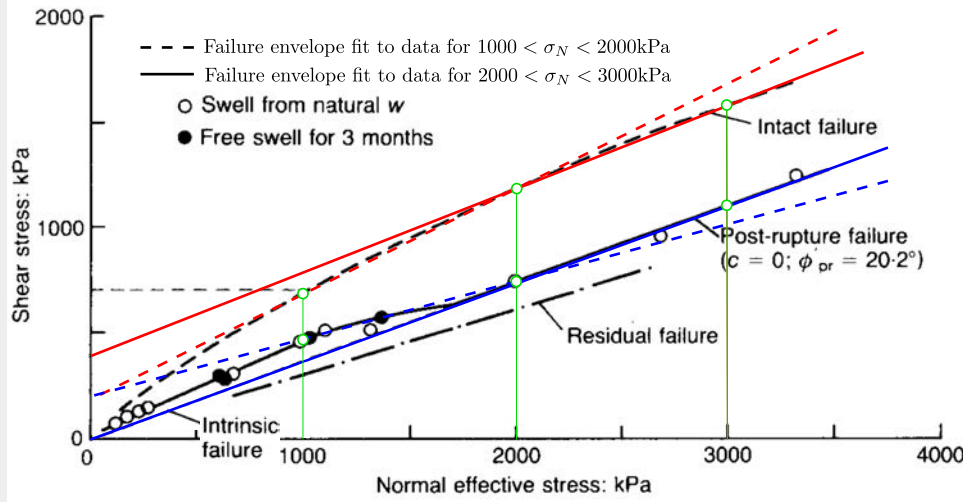
Figure 3.3.: Intact, intrinsic (reconstitutive), post-rupture and residual failure envelopes
for Todi Clay (modified from Burland, 1990), indicating potential linear approximation
for failure envelopes to test data obtained at different stress levels.

Further information on spatial variability can be found, amongst others, in Phoon and Kulhawy
(1999b), Uzielli et al. (2006), Fenton and Griffiths (2008) and Lloret-Cabot et al. (2014).

The spatial variability of soil property values may influence the interpretation of point
variance. Phoon et al. (1995) showed that the coefficient of variation, V, may decrease due
to spatial averaging.

The spatial variation of soil property values may have an impact on the geomechanical
performance of the repository; however, determining the scales of fluctuation and assessing
their influence on the system response is beyond the scope of this work.

3.5. Variation of Boom Clay property and state variables

A simple procedure is used here to assess the information provided in the small database on
Boom Clay property values and state variables presented in Appendix A. Given the nature of
this research, the focus is on the in situ states and the Boom Clay property values governing
the hydro-mechanical behaviour, tabulated in Tables A.1 and A.2, respectively.

The five step procedure, which is based on Bond and Harris (2008, p151ff) and Bond
(2011), may be summarised as follows:

(a) Using linear interpolation the best fit, $\bar{X} = f(d)$, through the samples is obtained.

(b) The residuals, $\varepsilon_i = x_i - \bar{X}(d_i)$, for each data point i are computed.

(c) Assuming a normal distribution, the sample standard deviation of the residuals, $s_\varepsilon = \left(\sum_{i=1}^{N} \sqrt{(\varepsilon_i - m_\varepsilon)^2}\right)/(N-1)$, is determined, i.e. with the sample mean of the residuals
being zero, $m_\varepsilon = 0$, and with N being the number of samples.

(d) Next, the characteristic offset of the best fit at a 95% confidence level, $\Delta_{\bar{X}_k}$, is computed. The upper/lower, i.e. *"inferior"/"superior"*, characteristic value X_k of the mean estimate of the geotechnical parameter X may be defined as $X_k = m_X \pm k_\nu s_X$, i.e. with the associated statistical coefficient being $k_\nu = t_\nu^{95}\sqrt{1/N}$ for an unknown standard deviation and with t_ν^{95} being the Student's t-value for $\nu = (N-1)$ degrees of freedom. Hence, $\Delta_{\bar{X}_k} = \pm k_\nu s_\varepsilon$.

(e) Finally the linear characteristic fit is computed by $f(\bar{X}_k(d)) = f(\bar{X}(d)) \pm \Delta_{\bar{X}_k}$.

The following assumptions apply in the above scheme: (i) the data points are independent, (ii) the residuals are normally distributed, which might not hold true for variables such as the saturated hydraulic conductivity, and (iii) the profile is weakly stationary, i.e. the mean is a function of the depth but the variance is assumed to be constant with depth.

For this evaluation, only the mean values of test data reported in the literature have been used as input. The additional information provided to each data set from the literature sources does not permit a distinction between aleatory and epistemic uncertainty. As discussed in Sections 2.2.1 and 2.4, for example, the geological evolution, the in situ stress state, the mineralogy and the pore water composition may, in parts significantly, affect the Boom Clay property values. The scarcity of data, however, does not allow these variables to be included in the current quantitative assessment.

For the in situ state variables (Table A.1) too little qualitative information is available to determine any trend and/or variance. Hence, this work will focus on the uncertainties in the soil property values, whereas the situ state variables are treated deterministically. Given the literature data the following assumptions are deemed reasonable; the vertical effective stress follows a linear (hydrostatic) profile ($\sigma'_v = \rho g d - \rho_w g d$), the average overconsolidation ratio is $\overline{OCR} \simeq 2.2$ and the initial in-situ stress state is either isotropic or anisotropic ($K_0 = 1$, $K_0 = 0.8$).

Figures 3.4(a-g) summarize the interpretation of some of the geomechanical soil data of Table A.2. The sub-figures show; (I) the data points (blue - all data, red - data below 200m depth), the best fit (solid line) and the characteristic fit (dashed line), i.e. each representing the one-sided 95% lower/upper confidence level of the mean estimate given the data available; (II) the residuals versus depth; and, (III) the *Probability Mass Function* (PMF) and *Probability Density Function* (PDF) of the residuals, i.e. with the bin width split between the blue and red data for illustration purposes.

Figures 3.4(a-b) show that the variation in dry and wet density, ρ_d and ρ, is minor; however both figures indicate a difference when neglecting samples < 200m depth. The general assumption of the unit weight being $\gamma = 20$kN m^{-3}, as applied in nearly all analyses in the literature, seems reasonable. The coefficient of variation $0.014 \lesssim V_{\gamma_d} V_\gamma \lesssim 0.024$ agrees with the lower end of the values found in the literature (Table 3.2).
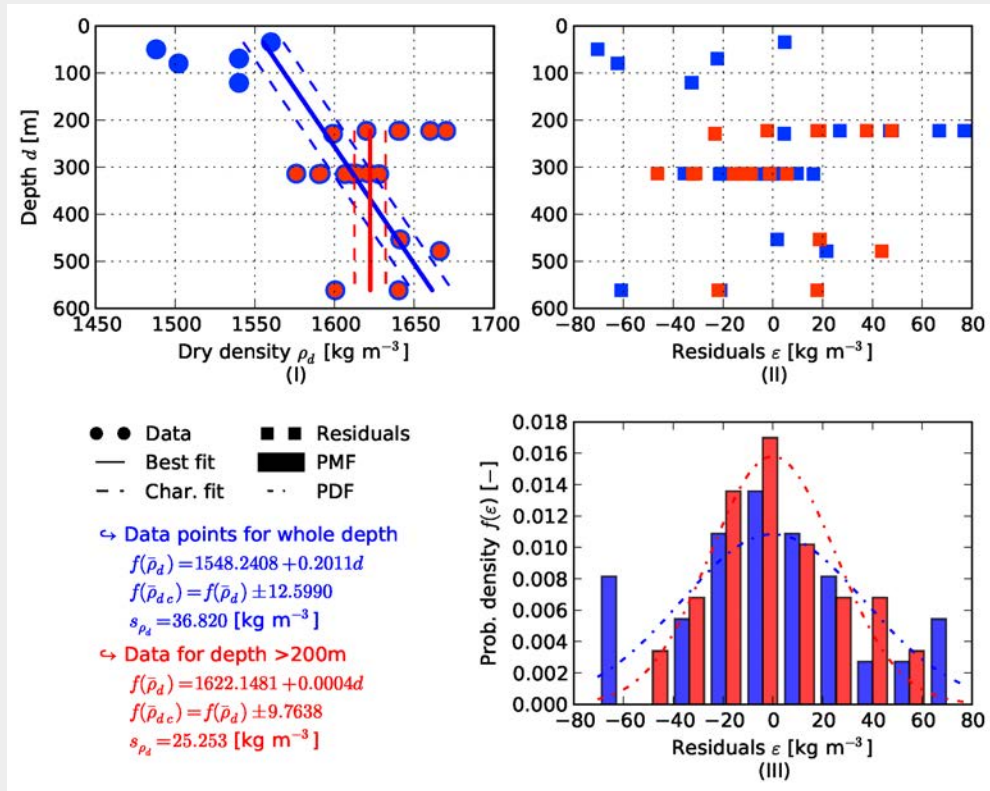
(a) Dry density ρ_d
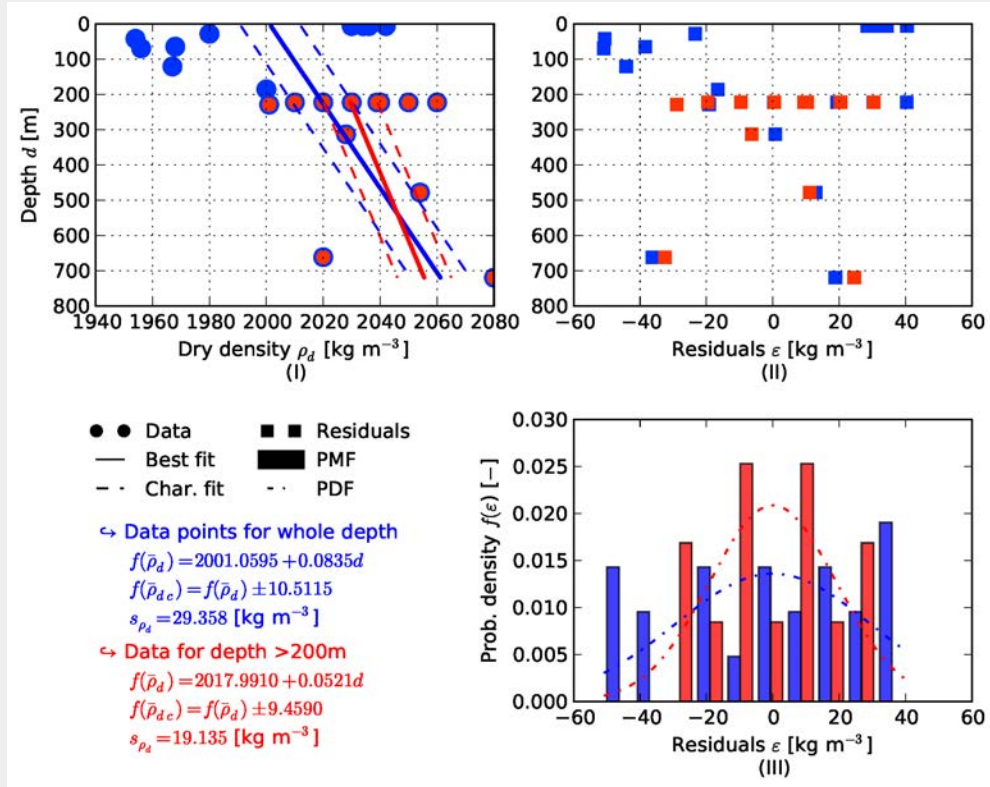
(b) Bulk density ρ
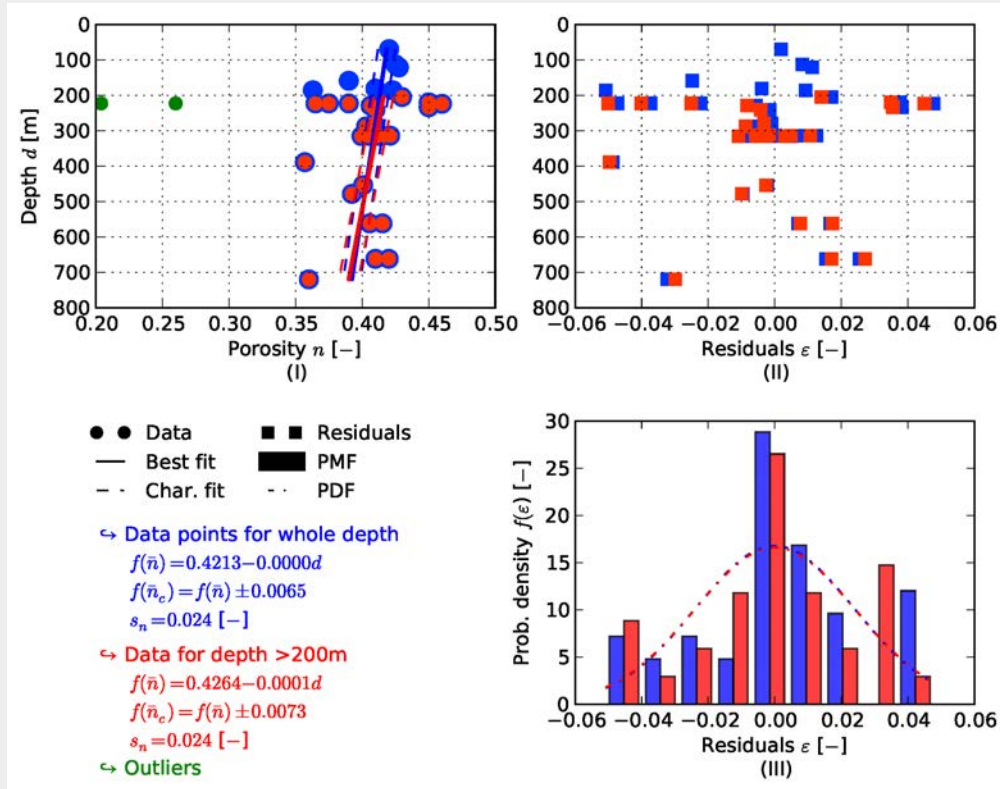
(c) Porosity n
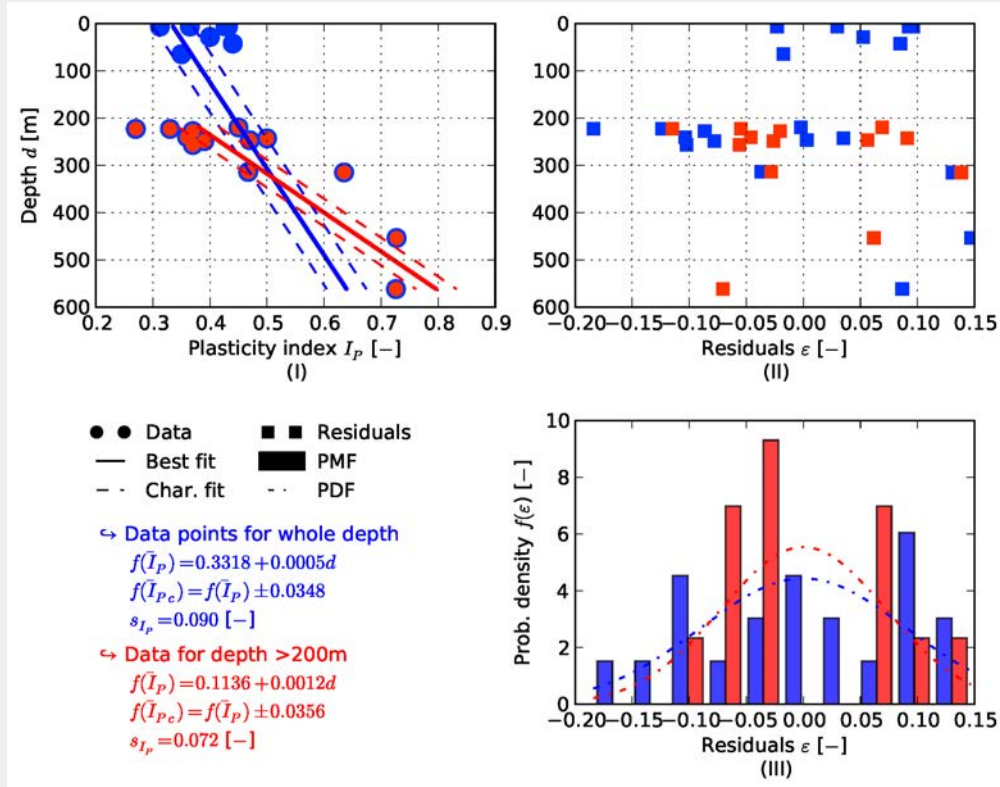
(d) Plasticity index I_P
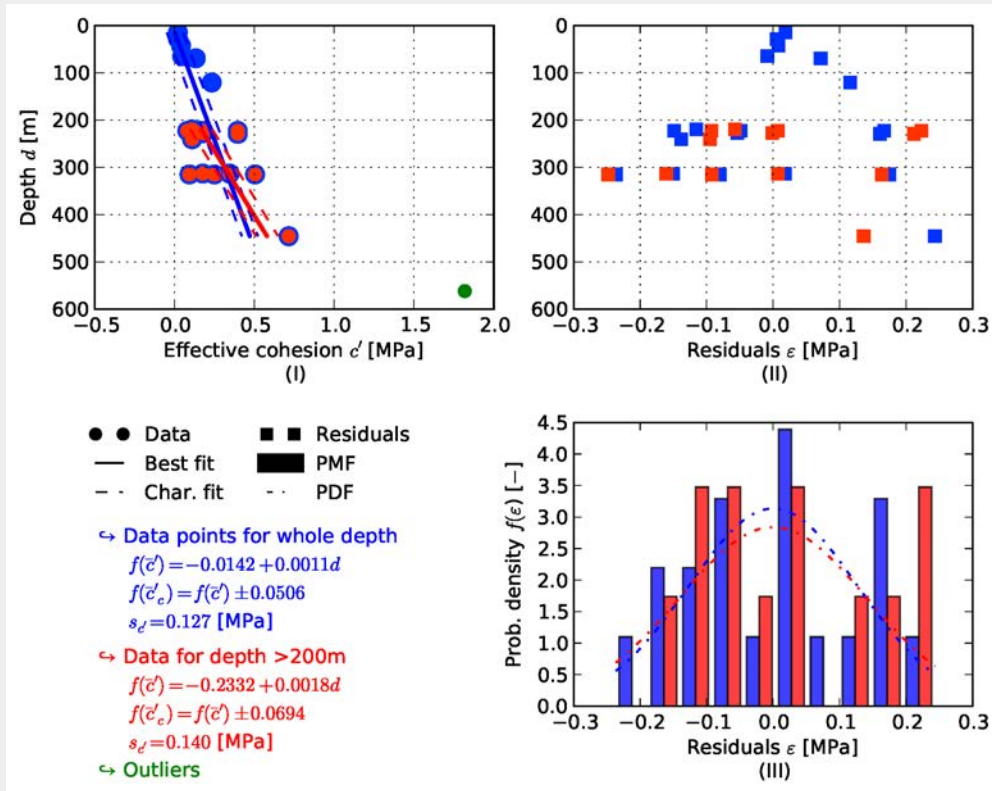
(e) Effective cohesion c' (excluding outlier)
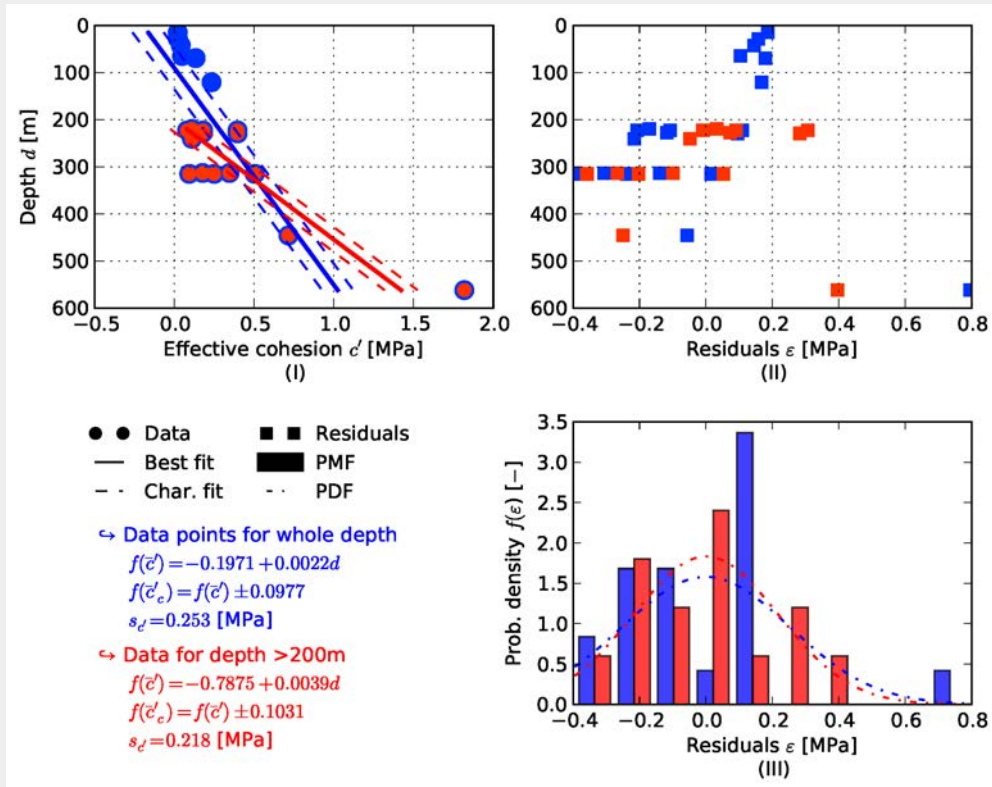
(f) Effective cohesion c' (including outlier)
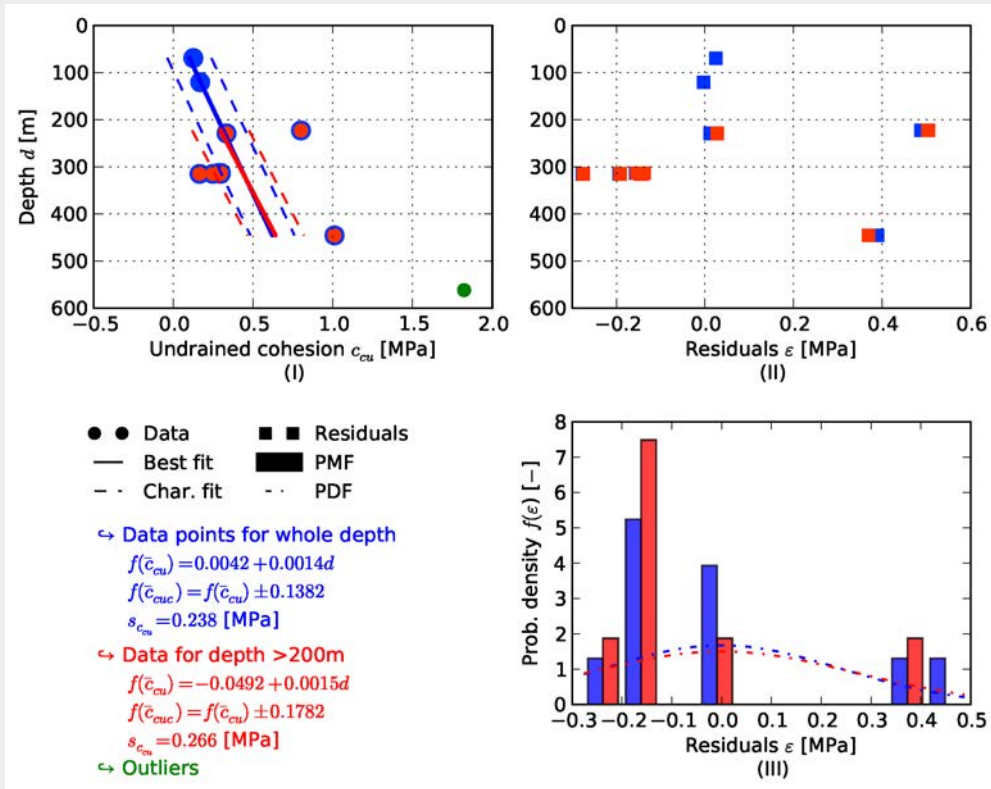
(g) Consolidated undrained cohesion c_{cu} (excluding outlier)
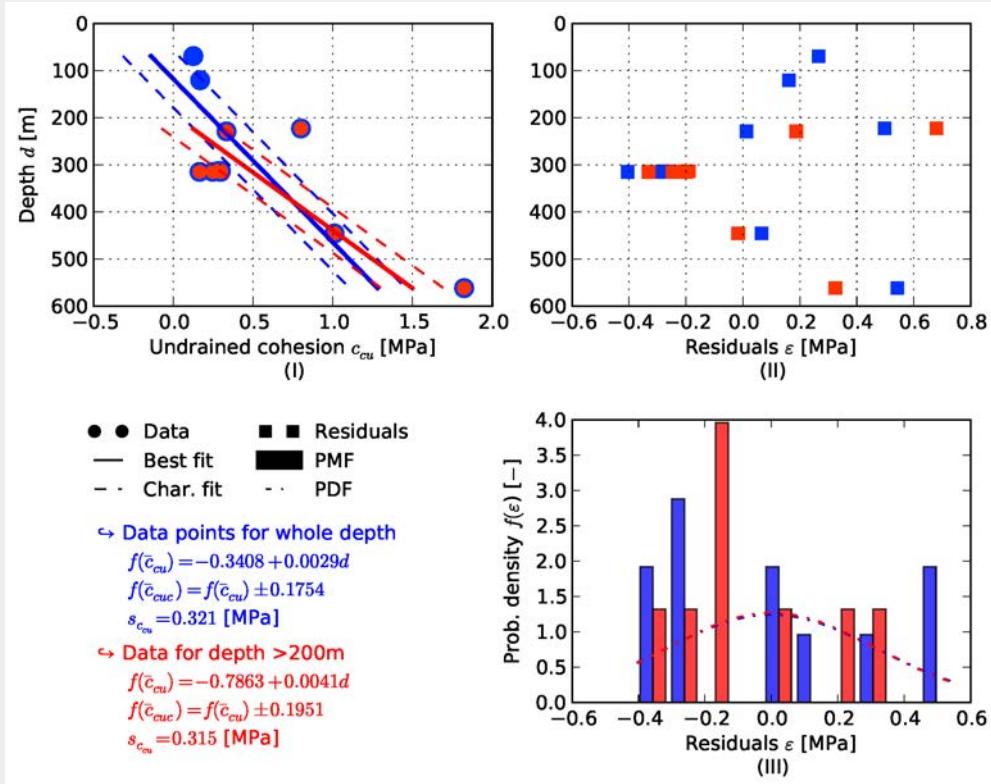
(h) Consolidated undrained cohesion c_{cu} (including outlier)
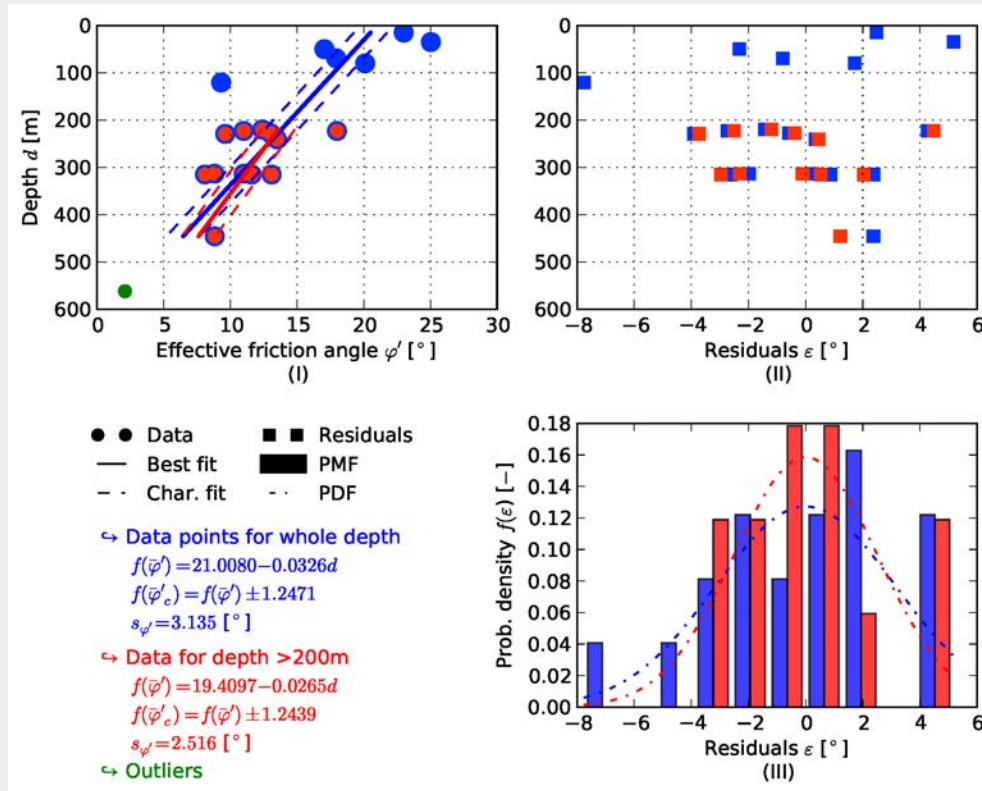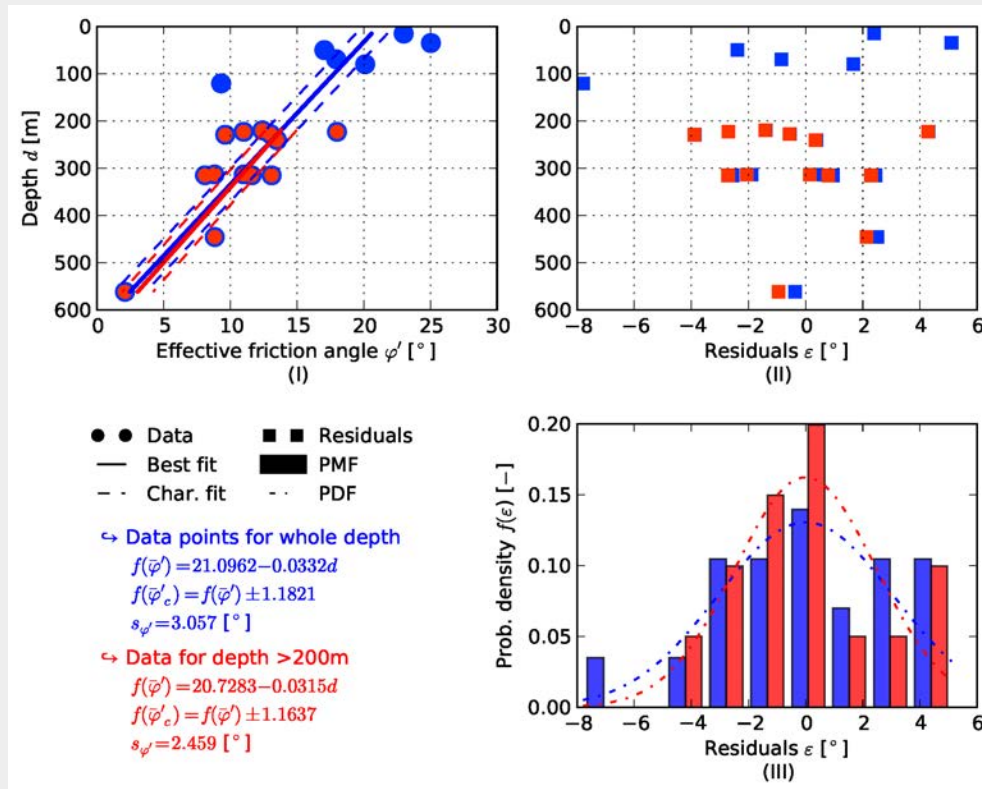
(i) Effective friction angle φ' (excluding outlier)

(j) Effective friction angle φ' (including outlier)
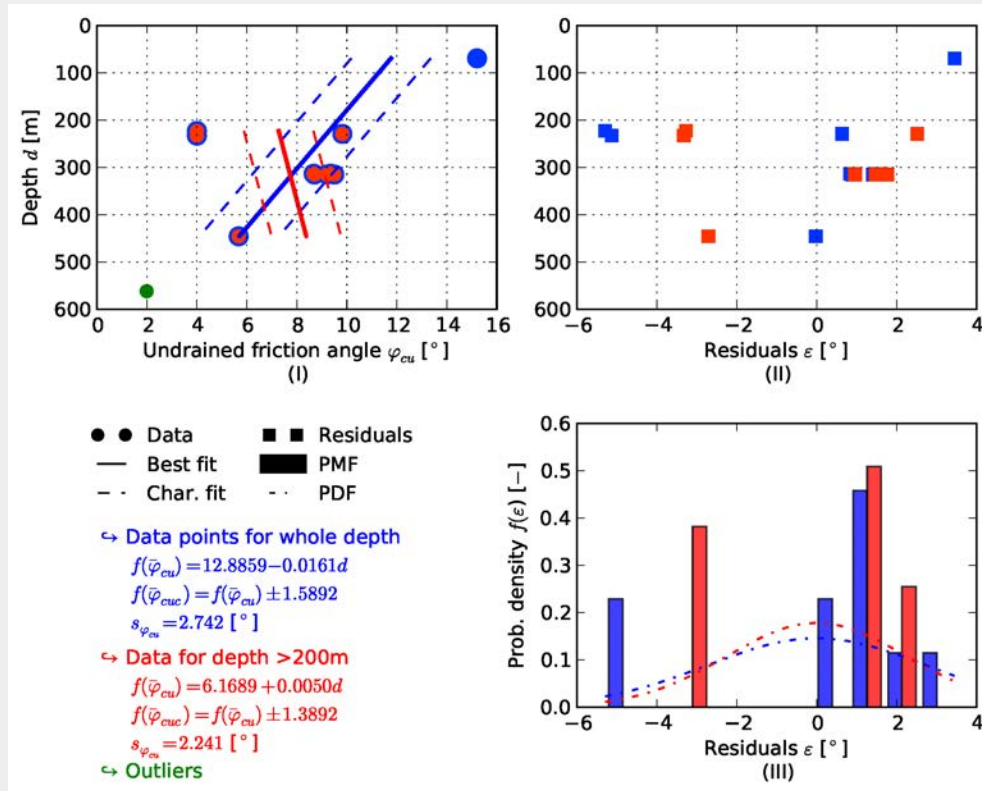
(k) Consolidated undrained friction angle φ_{cu} (excluding outlier)
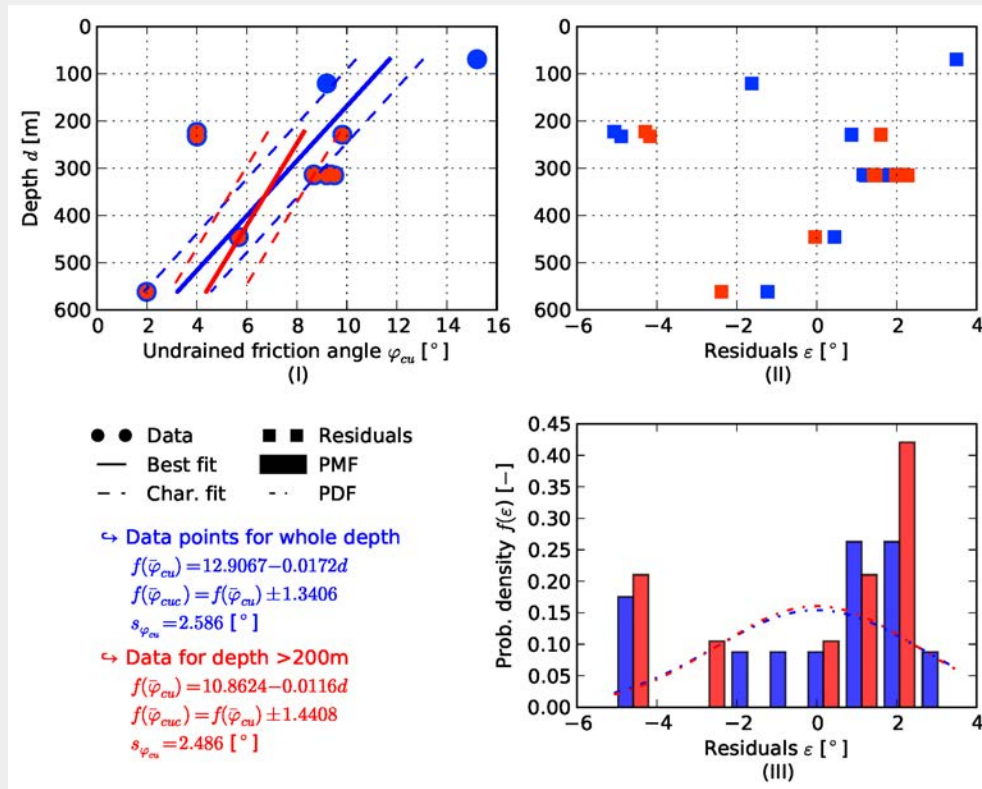
(l) Consolidated undrained friction angle φ_{cu} (including outlier)

(m) Critical State (CS) variables
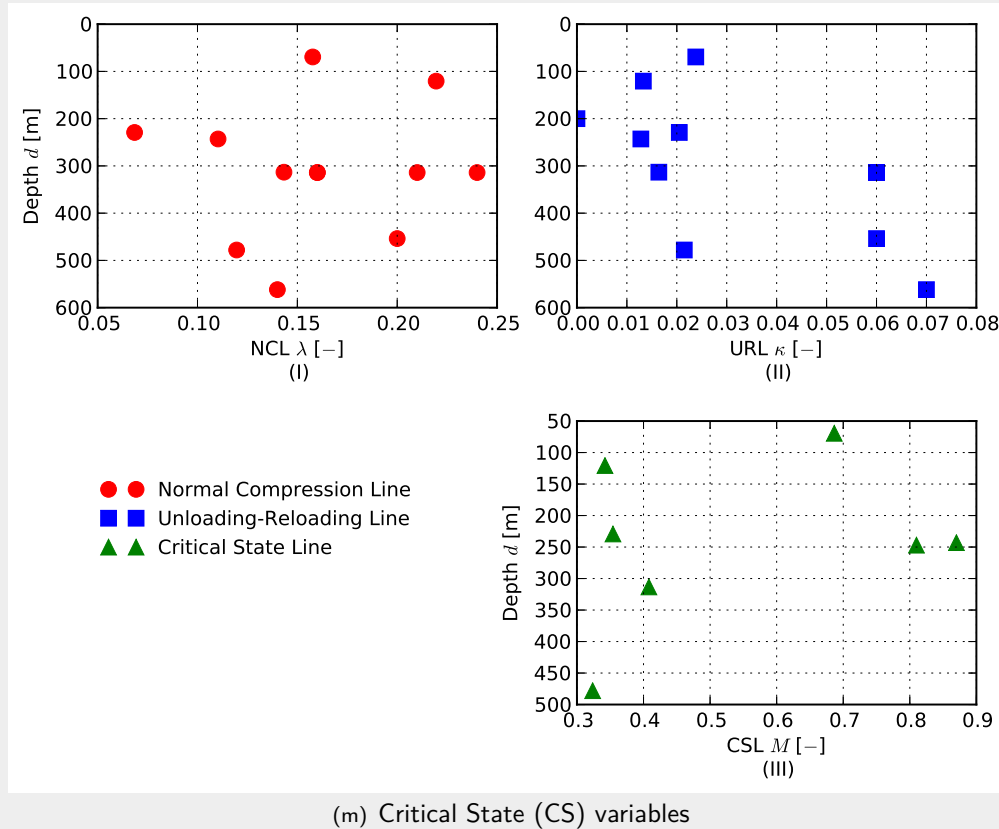
Figure 3.4.: Data interpretation (a-l): (I) Data points with best fit and characteristic
fit, (II) residuals vs. depth, and (III) probability mass and density function of the
residuals. (m) Data points of critical state variables vs. depth.

Figure 3.4(c) indicates that the soil porosity n slightly decreases with increasing depth, with the variables above 200m following the same trend. The coefficient of variation $0.057 \lesssim V_n \lesssim 0.06$ is at the lower end of the general values reported in Table 3.2 covering all soil types.

The positive depth trend of the plasticity index I_P increases when only data obtained at depth > 200m are considered (Figure 3.4(d)). The observed range for the coefficient of variation, $0.14 \lesssim V_{I_P} \lesssim 0.27$, lies within the lower to mid range of values reported in literature (Table 3.2). However, it seems that a linear fit is an inappropriate approximation, as it would lead to an unrealistically high plasticity index at depth $\gtrsim 700$m. However, more data at depth > 400m are required to identify a possible non-linearity in the data.

For the Boom Clay stiffness parameters, no estimate of the means or coefficients of variation has been made. Given the limited literature values tabulated in Table A.2, it is unreasonable to provide any specific estimates for the Young's modulus or the Poisson's ratio without further testing.

Assessing the Boom Clay shear strength property values (Figures 3.4(e-l)) some depths trend can be observed. Whereas the cohesion seems to increase with depth the friction angle decreases; that is, both for the effective and CU parameters.

As strength parameters are generally dependant on the depth, and the only available data at depths below 500m is from the Asse member (TRACTOR project), this data has been used selectively and statistical descriptions have been made both with and without this data.

Cohesion: Extrapolating the best fit, the mean cohesions at a depth of 500m are estimated to be $c' \approx \{0.54, 0.67\}$MPa and $c_{cu} \approx \{0.70, 0.70\}$MPa, by fitting all data points at all depths, or at depth > 200m respectively (blue and red lines in Figures 3.4(e) and 3.4(g)). For both cases, the very high cohesion obtained in the TRACTOR test series, sampled from the Asse member at Blija at a depth of about 561.5m, was neglected for the fit. Figures 3.4(f) and 3.4(h) show the profiles accounting for the Blija sample. Given the uncertainty of this data point, the effective and CU cohesions at 500m depth, $c' \approx \{0.90, 1.16\}$ and $c_{cu} \approx \{0.90, 1.16\}$, may significantly overestimate the true cohesion. The spatial average complying with the 95% confidence level in the characteristic mean value, as defined in the BS EN 1997-1 (2004), would reduce the input value applied in a deterministic design analysis significantly.

The coefficient of variation is smaller for the effective cohesion, $0.26 \lesssim V_{c'}{}^5 \lesssim 0.56$, than it is for the consolidated-undrained cohesion, $0.25 \lesssim V_{c_{cu}}{}^5 \lesssim 1.06$, given 19 data points for the former and 10 for the latter (not accounting for the Blija data).

Inspecting Figure 3.4(e.I-II), the effective cohesion profiles seems to be non-stationary, that is, with both the mean and variance increasing with depth. Hence the upper bound of the coefficient of variation $V_{c'} \approx 1.06$, corresponding to the near surface data points, is likely to be an overestimate, whereas the lower bound of $V_{c'} \approx 0.26$ might be an underestimate. More data are required to support this observation.

Friction angle: Linear extrapolation of the best fit results in mean friction angle estimates of $\varphi' \approx \{4.71, 6.16\}°$ and $\varphi_{cu} \approx \{4.84, 8.67\}°$; that is, by fitting all data points at all depths or at depth > 200m respectively (Figure 3.4(i) and 3.4(k)). The depth trend of the CU friction angle accounting only for data >200m is significantly altered and slightly positive. As for the cohesion, the characteristic reduction from the mean is larger for the CU friction angle.

Accounting for the Blija data at 561.5m depth, the effective friction angle profile does not significantly change and results in a values of $\varphi' \approx \{4.50, 4.99\}°$ at 500m depth (Figure 3.4(j)). However, the estimate of the CU friction angle accounting only for data >200m now follows a negative trend, leading to $\varphi_{cu} \approx \{4.30, 5.11\}°$ at 500m depth.

The coefficients of variation are estimated to be $0.15 \lesssim V_{\varphi'}{}^5 \lesssim 1.23$ and $0.22 \lesssim V_{\varphi_{cu}}{}^5 \lesssim 0.8$. Similar to the cohesion, but in a reverse sense, the upper/lower bounds of the coefficient of variation may be under/over estimated given the potential non-stationary nature of the profiles. Again, more data are required to support this observation.

---

[5]Assuming a weakly stationary profile with a depth dependent mean and a constant variance.

Most profiles suggest that a linear fit may not be appropriate for extrapolating the friction angle of the Boom Clay to greater depths, as, at depths larger 600-700m, the friction angle would be negative. However, more data at this depth are required to indicate a non-linear fit.

The data of the three critical state (CS) parameters are plotted against depth in Figure 3.4(i.I-III). No depth trend is apparent from the graphs. Due to the scarcity of data a statistical interpretation has been rejected.

Figures 3.5(a) and 3.5(b) show the cross-correlation between the soil cohesion and friction angle, in effective and CU definition respectively, transformed to normalised space ($U_i = X_i - (\mu_{X_i})/\sigma_{X_i}$). For both cases the linear correlation coefficient is negative and agrees with the ranges observed in the literature (Table 3.3). However, although the residuals have been correlated, it should be noted that these values of ρ do not solely represent a point covariance but incorporate all uncertainties, i.e. ranging from testing errors to the difference in Boom Clay composition at the different sampling locations.

3.6. Concrete liner property values

In Appendix A.1 of the CORA 17 project report (Steen and Vervoort, 1998), the liner properties used in the analysis were set to a Young's modulus of $E_l = 20,000$MPa and a Poisson's ratio of $\nu_l = 0.33$. The cement used for the lining segments installed in the connecting gallery of the HADES URF in Mol is a *Highly Sulphates Resistant* (HSR) CEM II/B-V 42.5. An average Young's modulus of 49.2 GPa was determined from four cylindrical samples in the laboratory. A compressive strength of 80Nmm^{-2} was the requested design strength, with the 95 percentile

(a)　　　　　　　　　　　　　(b)
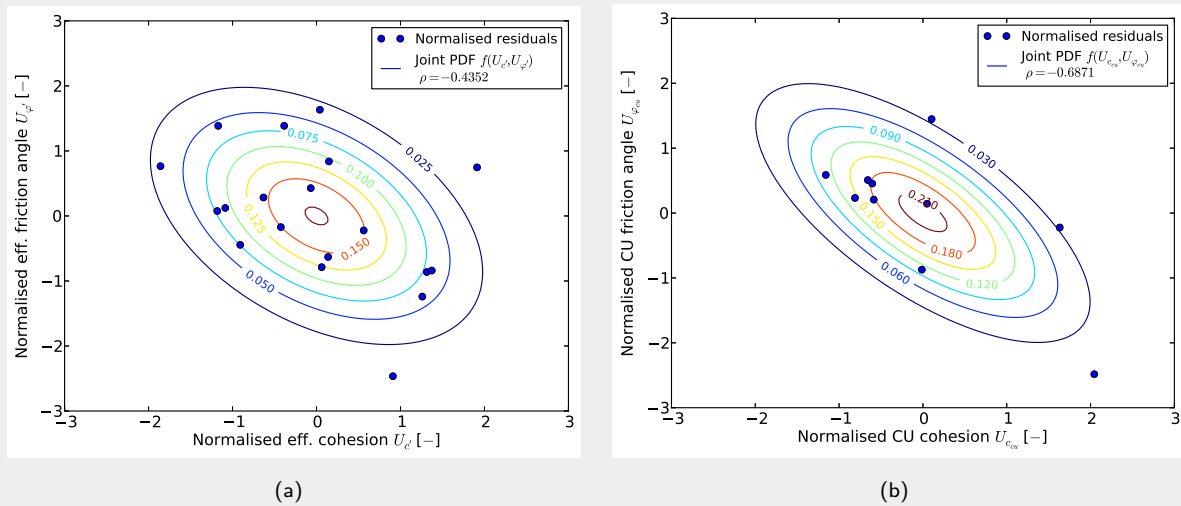
Figure 3.5.: Correlation between normalised residuals of soil cohesion and friction angle of Boom Clay, sampled at different depths, with the isochrones representing the bivariate joint probability density function.

experimentally detemined compressive strength, on cubic samples, was 91.3Nmm^{-2}, with the average being 110Nmm^{-2} (Bastiaens et al., 2003, p64).

Due to the man-made nature of the concrete liner, the uncertainty in the stiffness and strength is lower than for the Boom Clay material. Some ranges can be found in JCSS (2001b).

3.7. Conclusions

This chapter provided an introduction to the aleatory and epistemic uncertainties associated with the excavation and intermediate response of deep tunnels. It was pointed out that a distinction between individual sources contributing to the uncertainty of a random variable is cumbersome and thus they are predominantly lumped into one coefficient describing the point variance or covariance.

A review on some general ranges of the coefficients of variation on selected soil property values and state parameters was provided and discussed. The uncertainty associated with the definition of a parameter cross-correlation structure was discussed and illustrated by an example for the correlation of the soil cohesion and friction angle.

For the variation of Boom Clay property values a database has been compiled. Selected data sets have been evaluated in terms of their central tendency and variance using a simple evaluation scheme. The averaging depth was of importance for some soil property values. Due to the scarcity and variation in the data, the characteristic offset representing the 95% confidence level of the mean estimate was significant in some cases. The Boom Clay cohesion and friction angle were found to be strongly depth dependent. The covariance structure between the normalised residuals of the cohesion and friction angle was found to be negative.

Some brief information on the concrete liner property values has been provided.

4. Analytical model

4.1. Introduction

In this chapter the Boom Clay response to the excavation of a deep tunnel is investigated using an analytical formulation accounting for elasto-plastic strain-softening material behaviour. In general, analytical models do have limitations with respect to modelling, for instance, coupled and more complex soil material behaviour. Recently Graziani and Boldini (2012a,b) discuss those limitations with respect to deep tunnels in general, and specifically with respect to those tunnels located in argillaceous rock. Despite these shortcomings, two main objectives led to the development of an analytical model as part of this research project:

(a) to obtain an initial insight into the long term response of a tunnel in Boom Clay at large depth and the relative importance of soil parameter values; and

(b) to have a computationally cheap tool with which the performance of different approximate reliability based techniques can be evaluated with respect to the crude *Monte Carlo Method* (MCM), utilised later in Chapter 7.

A review of the analytical and semi-analytical formulations developed and used to assess the soil response due to tunnel excavations is given in Section 4.2. Section 4.3 provides the basic formulations to describe the stress-strain equilibrium around a cylindrical cavity. The constitutive model framework is developed in Section 4.4 and the solution algorithm subsequently outlined in Section 4.5. In Section 4.7 the model response is assessed by means of deterministic analyses for varying soil property values and boundary conditions. Section 4.8 summarizes this Chapter.

4.2. Analytical and semi-analytical investigations of tunnel performance

A selected review of some of the numerous analytical and semi-analytical methods employed in recent years to assess tunnel performance in terms of ultimate limit states and serviceability limit states is presented.

The *Convergence-Confinement Method* (CCM) is commonly employed to determine the *Ground Response Curve* (GRC), *Support Characteristic Curve* (SCC) and *Longitudinal Deformation Profile* (LDP) in tunnel design. Commonly, *Hoek-Brown* (HB) and *Mohr-Coulomb* (MC) type constitutive soil models are used within elastic-perfect plasticity, as well as elastic-brittle plasticity to determine the GRC (e.g. Brown et al., 1983; Carranza-Torres, 2004; Carranza-Torresa and Fairhurst, 1999, 2000; Detournay, 1986; Detournay and Vardoulakis, 1985; Park

and Kim, 2006). Frameworks accounting for rock masses exhibiting strain-softening behaviour have been developed, e.g. by Alonso et al. (2003), Lee and Pietruszczak (2008), Park et al. (2008) and Wang et al. (2010, 2012b). Different solutions for computing the LDP have been proposed in recent years (e.g. Panet and Guenot, 1982; Pilgerstorfer and Radončić, 2009; Vlachopoulos and Diederichs, 2009). The application of the CCM has been applied to account for time-dependent material behaviour in elastic frameworks, e.g. by Oreste (2003), Gschwandtner and Galler (2012) and Carranza-Torres et al. (2013), and including the effects of ageing by Sandrone and Labiouse (2010). Some state-of-the-art reviews on the CCM can be found in Carranza-Torresa and Fairhurst (2000), Oreste (2009), Alejano et al. (2012) and Carranza-Torres et al. (2013).

Further analytical and semi-analytical solutions have been developed for assessing the response of cylindrical cavities under drained and undrained conditions using the Cavity Expansion Method (e.g. Chen and Abousleiman, 2012, 2013; Kolymbas et al., 2012; Silvestri and Abou-Samra, 2012; Yu, 2000; Yu and Rowe, 1999), the Cavity Conversion Method (e.g. Cheng, 2012; Wang et al., 2012b) or energy based methods (e.g. Birchall, 2013).

Hydro-mechanically coupled frameworks have been developed to assess the soil behaviour around cavities excavated in ideal poro-elastic and poro-viscoelastic media (e.g. Carranza-Torres and Zhao, 2009; Dufour et al., 2009; Hoxha et al., 2004; Verruijt, 1997, 1998; Wong et al., 2008a,b), as well as in poro-plastic and poro-viscoplastic media, e.g. Giraud (1993), Giraud and Rousset (1996), Labiouse and Giraud (1998), as used for the TRUCK II study and as discussed in Barnichon and Volckaert (2003), Bobet (2010) and Bui et al. (2013). Using a poro-elastic solution, Dufour et al. (2012) recently assessed the hydromechanical post-closure behaviour of a deep gallery as part of a radioactive waste repository, taking into account a simplified life cycle.

The influence of the variation in pore water pressure around the excavated cavity on the mechanical response has been accounted, for amongst others, by Fernández (1994), Fernández and Alvarez (1994), Bobet and Nam (2007), Bobet and Nam (2007), Carranza-Torres and Zhao (2009), Fahimifar and Zareifard (2009, 2013) and Shin (2010).

4.3. Stress-strain equilibrium around a cavity

The effective stress is

$$\sigma' = \sigma - \alpha u_w \tag{4.1}$$

where u_w is the pore water pressure and $\alpha = 1 - K/K_s$ is Biot's coefficient, with K being the bulk modulus and K_s being the bulk modulus of the solid matrix (e.g. Coussy, 2004, p79). For this project, Terzaghi's effective stress is used, i.e. α is assumed to be unity, representing an incompressible fluid and solid matrix.

For the plane strain case, the effective stress tensor represented in cylindrical coordinates

simplifies to

$$\boldsymbol{\sigma}' = \begin{pmatrix} \sigma'_{rr} & \tau'_{\theta r} & \tau'_{zr} \\ \tau'_{r\theta} & \sigma'_{\theta\theta} & \tau'_{z\theta} \\ \tau'_{rz} & \tau'_{\theta z} & \sigma'_{zz} \end{pmatrix} = \begin{pmatrix} \sigma'_{rr} & \tau'_{\theta r} & 0 \\ \tau'_{r\theta} & \sigma'_{\theta\theta} & 0 \\ 0 & 0 & \sigma'_{zz} \end{pmatrix} \tag{4.2}$$

where σ'_{rr} is the effective radial stress, $\sigma'_{\theta\theta}$ is the effective tangential (hoop) stress, σ'_{zz} is the effective axial stress and $\tau'_{r\theta} = \tau'_{\theta r}$ is the effective shear stress in the plane (e.g. Kolymbas, 2008; Yu, 2000). The mean effective stress p' and the deviatoric stress q, defined via the stresses in cylindrical coordinate space, are

$$p' = \frac{1}{3}\left(\sigma'_{rr} + \sigma'_{\theta\theta} + \sigma'_{zz}\right) \tag{4.3a}$$

$$q = \sqrt{\frac{1}{2}\left[(\sigma'_{rr} - \sigma'_{\theta\theta})^2 + (\sigma'_{\theta\theta} - \sigma'_{zz})^2 + (\sigma'_{zz} - \sigma'_{rr})^2\right]} \tag{4.3b}$$

The strain tensor in cylindrical coordinates is defined as

$$\boldsymbol{\varepsilon} = \begin{pmatrix} \varepsilon_{rr} & \gamma_{\theta r} & \gamma_{zr} \\ \gamma_{r\theta} & \varepsilon_{\theta\theta} & \gamma_{z\theta} \\ \gamma_{rz} & \gamma_{\theta z} & \varepsilon_{zz} \end{pmatrix} \tag{4.4}$$

where ε_{rr} is the radial strain, $\varepsilon_{\theta\theta}$ is the tangential strain, ε_{zz} is the axial strain, and the shear strains, γ, vanish for axisymmetric deformation with zero deformation in the tangential direction, i.e. $u_\theta = 0$ (e.g. Kolymbas, 2008; Yu, 2000). Hence for a cavity in an axisymmetric plane-strain condition the radial, tangential and axial strains are

$$\varepsilon_{rr} = \frac{\partial u_r}{\partial r} \tag{4.5a}$$

$$\varepsilon_{\theta\theta} = \frac{1}{r}\frac{\partial u_\theta}{\partial \theta} + \frac{u_r}{r} = \frac{u_r}{r} \tag{4.5b}$$

$$\varepsilon_{zz} = \frac{\partial u_z}{\partial z} = 0 \tag{4.5c}$$

where r is the radial polar coordinate of the point in space under consideration, u_r is the radial displacement, z is the axial coordinate and u_z is the axial displacement (e.g. Kolymbas, 2008; Yu, 2000).

Figure 2.43(a) schematically describes the stresses around the tunnel cavity. For the in situ, i.e. far field condition, two plane strain cases may be considered. For the first case the in situ stress ratio in the plane is *isotropic*, which would be the case for a vertical cavity (shaft) with a cross-isotropic in situ horizontal stress ($\sigma_{h_x,0} = \sigma_{h_y,0}$) or for a horizontal cavity with the in situ vertical stress equating to the in situ horizontal stress ($\sigma_{v,0} = \sigma_{h,0}$). The shear stress component $\tau'_{r\theta}$ in the plane is zero (Equation 4.2). For the second case the in situ stress ratio is *anisotropic* in the computational plane, which is the case for a horizontally excavated cavity

with $\sigma_{v,0} > \sigma_{h,0}$. The latter case will introduce shear stresses in the plane. For this work an isotropic in situ stress ratio is assumed, but information on the anisotropic case is provided where appropriate.

The effective mean stress may be defined as

$$p' = \frac{1}{1+k}\left(\sigma'_{rr} + k\sigma'_{\theta\theta}\right) \tag{4.6}$$

with the scalar $k = 1$ for a cylindrical cavity and $k = 2$ for a spherical cavity (Collins and Stimpson, 1994).

In order to satisfy the plane strain condition, i.e. $\varepsilon_{zz} = 0$ (Equation 4.5c), the effective axial stress around a cavity may be written as

$$\sigma'_{zz} = \sigma'_{zz,0} + \mathrm{d}\sigma'_{zz} \tag{4.7}$$

where $\sigma'_{zz,0}$ is the in situ effective stress in the axial direction and $\mathrm{d}\sigma'_{zz}$ is the effective axial stress increment.

Given that the z-direction is set to be the tunnel axis, i.e. the out of plane direction (see Figure 2.43(c-e)), the initial (far field) condition may be defined as

$$\sigma'_{zz,0} = \frac{K_0}{2}\left(\sigma'_{xx,0} + \sigma'_{yy,0}\right) \tag{4.8}$$

where $K_0 = \nu_0/(1 - \nu_0)$ is the earth pressure coefficient at rest and ν_0 is the initial Poisson's ratio. For isotropic initial conditions, i.e. $\sigma'_{xx,0} = \sigma'_{yy,0} = \sigma'_{zz,0}$, $K_0 = 1$ and thus $\nu_0 = 0.5$.

The effective axial stress increment for a vertical cavity (shaft) may be defined as

$$\mathrm{d}\sigma'_{zz} = \nu\left(\mathrm{d}\sigma'_{rr} + \mathrm{d}\sigma'_{\theta\theta}\right) = \nu\left(\sigma'_{rr} + \sigma'_{\theta\theta}\right) - \nu\left(\sigma'_{xx,0} + \sigma'_{yy,0}\right) \tag{4.9}$$

which for a vertical cavity equates to

$$\mathrm{d}\sigma'_{zz} = \nu\left(\sigma'_{rr} + \sigma'_{\theta\theta}\right) - 2\nu\sigma'_{h,0} \tag{4.10}$$

and for a horizontal cavity equates to

$$\mathrm{d}\sigma'_{zz} = \nu\left(\sigma'_{rr} + \sigma'_{\theta\theta}\right) - \nu\left(\sigma'_{v,0} + \sigma'_{h,0}\right) \tag{4.11}$$

with ν being is the Poisson's ratio.

Substituting Equations 4.10 and 4.11 into Equation 4.7, and subsequently into Equation 4.3a, leads to the effective axial stress and the mean effective stress for a vertical shaft cavity

$$\sigma'_{zz} = \sigma'_{v,0} + \nu\left(\sigma'_{rr} + \sigma'_{\theta\theta}\right) - 2\nu\sigma'_{h,0} \tag{4.12a}$$

$$p' = \frac{1}{3}\left[(1+\nu)\left(\sigma'_{rr} + \sigma'_{\theta\theta}\right) + \sigma'_{v,0} - 2\nu\sigma'_{h,0}\right] \tag{4.12b}$$

and for a horizontal cavity

$$\sigma'_{zz} = \sigma'_{h,0} + \nu \left(\sigma'_{rr} + \sigma'_{\theta\theta} \right) - \nu \left(\sigma'_{v,0} + \sigma'_{h,0} \right) \tag{4.13a}$$

$$p' = \frac{1}{3} \left[(1 + \nu) \left(\sigma'_{rr} + \sigma'_{\theta\theta} \right) - \nu \sigma'_{v,0} + (1 - \nu) \sigma'_{h,0} \right] \tag{4.13b}$$

respectively (e.g. Abousleiman and Cui, 1998; Chen et al., 2012b; Yu and Houlsby, 1991; Yu and Rowe, 1999).

For isotropic initial stress conditions ($K_0 = 1$), Equations 4.12 and 4.13 are identical. If $K_0 < 1$, i.e. for anisotropic initial stress conditions (but isotropic material behaviour), both equations apply according to the direction in which the cavity is excavated.

For plane strain conditions the deviatoric stress (Equation 4.3b) is

$$q = \sigma'_{\theta\theta} - \sigma'_{rr} \tag{4.14}$$

(e.g. Wood, 1990).

The equilibrium of total stresses around a radial symmetric cavity in plane strain, under steady state conditions, is

$$\frac{\partial \sigma_{rr}}{\partial r} + \frac{\sigma_{rr} - \sigma_{\theta\theta}}{r} = \frac{\partial \sigma'_{rr}}{\partial r} + \frac{\sigma'_{rr} - \sigma'_{\theta\theta}}{r} + b \frac{\partial u_w}{\partial r} = 0 \tag{4.15}$$

where σ_{rr} and $\sigma_{\theta\theta}$ are the total radial and tangential stress (e.g. Carranza-Torres and Zhao, 2009; Fahimifar and Zareifard, 2013; Fernández and Alvarez, 1994; Kolymbas, 2008), see Figure 2.43. The coupling coefficient b, i.e. relating the hydraulic and mechanical responses (effect of seepage forces), is disregarded in this paper.

The boundary conditions for the problem described in Figure 2.43, and under an isotropic in situ stress ratio, are

$$\sigma_{rr}|_{r=r_c} = p_c \qquad\qquad \sigma_{rr}|_{r=\infty} = \sigma_0 = \sigma_{h,0} = \sigma_{v,0} \tag{4.16a}$$

$$u_w|_{r=r_c} = u_{w,c} = u_{w,0} \qquad\qquad u_w|_{r=\infty} = u_{w,0} \tag{4.16b}$$

where p_c and $u_{w,c}$ are the total pressure and pore water pressure at the cavity perimeter (acting on a potential liner), and σ_0 and $u_{w,0}$ are the in situ total stress and pore water pressure respectively. Equation 4.15 can be rewritten in non-dimensional form, i.e. with r being replaced by the normalised radial polar coordinate $\rho = r/r_c$ and $\frac{\partial}{\partial r} = -\frac{\rho}{r_c} \frac{\partial}{\partial \rho}$, as

$$\frac{\partial \sigma_{rr}}{\partial \rho} - \frac{\sigma_{rr} - \sigma_{\theta\theta}}{\rho} = 0 \tag{4.17}$$

4.4. Constitutive formulation

The closed-form analytical solution has been formulated with a series of simplifying assumptions:

1. a single tunnel is considered;
2. the tunnel cross section is circular;
3. plane strain conditions are considered;
4. the liner is impermeable;
5. the tunnel is excavated horizontally and deep, i.e. the cavity radius is much smaller than the depth $(r_c \ll d)$;
6. the soil exhibits *Elasto-Plastic* (EP) behaviour with linear strain softening;
7. the soil is over-consolidated;
8. the soil is homogeneous and fully water saturated;
9. the in situ stress state and material response is isotropic;
10. the liner installed is assumed to be elastic;
11. the loading on the liner is axisymmetric to the tunnel centreline; and
12. the analysis considers the steady state long term condition.

The general elasto-plastic response in incremental form is

$$\mathrm{d}\boldsymbol{\sigma}' = \mathbf{D}\,\mathrm{d}\boldsymbol{\varepsilon} \tag{4.18}$$

which, for plane strain and isotropic in situ conditions conditions (Section 4.3) can be defined solely as function of the radial and tangential stress and strain components, and thus resolves to

$$\begin{pmatrix} \mathrm{d}\sigma'_{rr} \\ \mathrm{d}\sigma'_{\theta\theta} \end{pmatrix} = \begin{bmatrix} D_{11} & D_{12} \\ D_{21} & D_{22} \end{bmatrix} \begin{pmatrix} \mathrm{d}\varepsilon_{rr} \\ \mathrm{d}\varepsilon_{\theta\theta} \end{pmatrix} \tag{4.19}$$

where $\mathbf{D}$ is the stiffness matrix, and the total radial and tangential strain rates are the sum of their respective elastic and plastic components, i.e.

$$\mathrm{d}\varepsilon_{rr} = \mathrm{d}\varepsilon^e_{rr} + \mathrm{d}\varepsilon^p_{rr} \quad \text{and} \quad \mathrm{d}\varepsilon_{\theta\theta} = \mathrm{d}\varepsilon^e_{\theta\theta} + \mathrm{d}\varepsilon^p_{\theta\theta} \tag{4.20}$$

4.4.1. Elasticity

The elastic response generally is assumed to be isotropic. However, for Boom Clay anisotropic behaviour in the elastic region has been observed (e.g. Baldi et al., 1987; Piriyakul, 2006). In this preliminary analytical study the anisotropy is not accounted for, but may be incorporated in a later model update.

Isotropic elasticity

Given Hooke's law, the elastic principle stress-strain relationship, with respect to cylindrical coordinates, in compliance form is

$$\begin{pmatrix} \mathrm{d}\varepsilon_{rr}^e \\ \mathrm{d}\varepsilon_{\theta\theta}^e \end{pmatrix} = \frac{1}{E} \begin{bmatrix} 1 & -\nu \\ -\nu & 1 \end{bmatrix} \begin{pmatrix} \mathrm{d}\sigma_{rr}'^e \\ \mathrm{d}\sigma_{\theta\theta}'^e \end{pmatrix} \tag{4.21}$$

or in stiffness form is

$$\begin{pmatrix} \mathrm{d}\sigma_{rr}'^e \\ \mathrm{d}\sigma_{\theta\theta}'^e \end{pmatrix} = \frac{E}{(1+\nu)(1-2\nu)} \begin{bmatrix} 1-\nu & \nu \\ \nu & 1-\nu \end{bmatrix} \begin{pmatrix} \mathrm{d}\varepsilon_{rr}^e \\ \mathrm{d}\varepsilon_{\theta\theta}^e \end{pmatrix} \tag{4.22}$$

where E is the Young's modulus, ν is the Poisson's ratio, $\mathrm{d}\varepsilon^e$ is the elastic strain rate and $\mathrm{d}\sigma'$ is the effective stress increment in the elastic region. Hence the radial and tangential incremental strains in plane strain are

$$\mathrm{d}\varepsilon_{rr}^e = \frac{1+\nu}{E}\left[\mathrm{d}\sigma_{rr}'^e - \nu\left(\mathrm{d}\sigma_{rr}'^e + \mathrm{d}\sigma_{\theta\theta}'^e\right)\right] \tag{4.23a}$$

$$\mathrm{d}\varepsilon_{\theta\theta}^e = \frac{1+\nu}{E}\left[\mathrm{d}\sigma_{\theta\theta}'^e - \nu\left(\mathrm{d}\sigma_{rr}'^e + \mathrm{d}\sigma_{\theta\theta}'^e\right)\right] \tag{4.23b}$$

(e.g. Bobet, 2010; Wood, 2004). The drained bulk modulus K, shear modulus G and Lame's constant λ are

$$K = \frac{E}{3(1-2\nu)} \; ; \quad G = \frac{E}{2(1+\nu)} \quad \text{and} \quad \lambda = \frac{E\nu}{(1+\nu)(1-2\nu)} \; . \tag{4.24}$$

Anisotropic elasticity

François et al. (2011, 2013) defined the elastic strain rate for Boom Clay as follows

$$\mathrm{d}\boldsymbol{\varepsilon}_{ij}^e = \mathbf{D}_{ijkl}^e \, \mathrm{d}\boldsymbol{\sigma}_{kl}^e \tag{4.25}$$

where D_{ijkl}^e accounts for cross-anisotropic or transverse isotropic elasticity. Cross-anisotropic elasticity in soil has previously been accounted for, e.g. by Barden (1963), Pickering (1970), Graham and Houlsby (1983) and Lings et al. (2000). Following Pickering (1970) and Lings et al. (2000) for a soil with a horizontal bedding plane, e.g. in the $x - y$ plane, Equation 4.25

can be extended to

$$
\begin{pmatrix}
d\varepsilon_{xx}^e \\
d\varepsilon_{yy}^e \\
d\varepsilon_{zz}^e \\
d\gamma_{yz}^e \\
d\gamma_{zx}^e \\
d\gamma_{xy}^e
\end{pmatrix}
=
\begin{bmatrix}
\frac{1}{E_{//}} & -\frac{\nu_{////}}{E_{//}} & -\frac{\nu_{\perp//}}{E_\perp} & & & \\
-\frac{\nu_{////}}{E_{//}} & \frac{1}{E_{//}} & -\frac{\nu_{\perp//}}{E_\perp} & & 0 & \\
-\frac{\nu_{//\perp}}{E_{//}} & -\frac{\nu_{//\perp}}{E_{//}} & \frac{1}{E_\perp} & & & \\
& & & \frac{1}{G_{//\perp}} & & \\
& 0 & & & \frac{1}{G_{//\perp}} & \\
& & & & & \frac{1}{G_{////}}
\end{bmatrix}
\begin{pmatrix}
d\sigma_{xx}^e \\
d\sigma_{yy}^e \\
d\sigma_{zz}^e \\
d\tau_{yz}^e \\
d\tau_{zx}^e \\
d\tau_{xy}^e
\end{pmatrix}
\tag{4.26}
$$

where $d\gamma_{ij}^e$ is the elastic shear strain rate, $d\tau_{ij}'$ is the effective shear stress increment, and $//$ and $\perp$ denote the parallel and perpendicular directions to the $x-y$ bedding plane respectively. In cross-anisotropic conditions

$$
\frac{\nu_{\perp//}}{E_\perp} = \frac{\nu_{//\perp}}{E_{//}}
\tag{4.27}
$$

4.4.2. Yield function

For this work the *Drucker-Prager* (DP; Drucker and Prager, 1952) yield function is employed (see Figure 4.1(a)):

$$
f = q - p' \tan \xi' - k'
\tag{4.28}
$$

where f is the yield function and $\tan \xi'$ and k' are material constants which are

$$
\tan \xi' = \frac{6 \sin \varphi'}{3 - \sin \varphi'} \quad \text{and} \quad k' = \frac{6c' \cos \varphi'}{3 - \sin \varphi'}
\tag{4.29}
$$

with φ' being the effective friction angle and c' being the effective cohesion. The material yields if the yield function equals zero ($f = 0$).

The hardening and softening laws employed to alter the yield function, i.e. as described in Figure 4.1(b), will be discussed in Section 4.4.4.

4.4.3. Plasticity

The plastic strain rates in the radial and tangential directions may be defined as

$$
d\varepsilon_{rr}^p = \lambda^p \frac{\partial g}{\partial \sigma_{rr}'} \quad \text{and} \quad d\varepsilon_{\theta\theta}^p = \lambda^p \frac{\partial g}{\partial \sigma_{\theta\theta}'}
\tag{4.30}
$$

with g being the plastic potential and λ^p being a scalar multiplier, or proportionality constant (e.g. Davis and Selvadurai, 2002; Yu, 2000, 2006). For this work the flow is assumed be *associated*, that is $g \equiv f$.

4.4.4. Incorporating hardening & softening

Using a one-dimensional isotropic hardening law the general second-order plastic strain tensor needs to be represented by some scalar hardening measure, e.g. defined by an accumulated plastic strain or by plastic work (e.g. Jirásek and Bažant, 2001, pp318-319; Yu, 2006, pp30-31). The cumulative deviatoric plastic strain, $\tilde{\varepsilon}^p$, (or effective plastic strain, or equivalent plastic strain), is defined by

$$\tilde{\varepsilon}^p = \int_0^{\tilde{\varepsilon}^p} \mathrm{d}\tilde{\varepsilon}^p \tag{4.31a}$$

which is approximated by the Von Mises equivalent plastic strain rate

$$\mathrm{d}\tilde{\varepsilon}^p \simeq \sqrt{\frac{2}{3}\left(\mathrm{d}\varepsilon_{\theta\theta}^p - \mathrm{d}\varepsilon_{rr}^p\right)} \tag{4.31b}$$

The yield criterion (Equation 4.28) is thus a function of $f(p', q', c', \varphi', \tilde{\varepsilon}^p)$.

Hardening/softening defined by Chen et al. (2012b)

In this work the linear strain hardening/softening formulation by Chen et al. (2012b) is implemented. Assessing the stability of vertical well bores, the formulation relates cohesion to the accumulated plastic strain $k'(\tilde{\varepsilon}^p)$ while the friction angle is assumed to remain constant. Figure 4.2 outlines the strain hardening and strain softening DP models.

Using an unconfined *Uniaxial Compression Test* (UCT) for calibration, i.e. $p' = \sigma_a'/3$ and $q = \sigma_a'$, where σ_a' is the axial effective stress, a one dimensional hardening/softening rule can be defined (Figures 4.2(a) and (c)) relating the plastic strain $\tilde{\varepsilon}^p$ to the effective yield stress
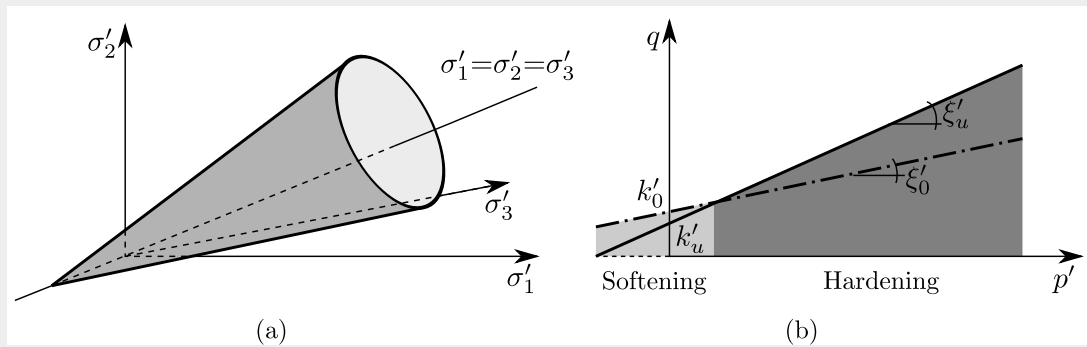
Figure 4.1.: Schematic figure showing: (a) the general Drucker-Prager (DP) yield criterion with σ_1', σ_2' and σ_3' being the effective principle stresses, and (b) the strain-softening and -hardening response for a DP yield criterion where k_0' and ξ_0' are the initial cohesive and frictional material constant and k_u' and ξ_u' are the ultimate cohesive and frictional material constant.

σ'_y, i.e.

$$\sigma'_y = a\tilde{\varepsilon}^p + \sigma'_{y,0} \tag{4.32}$$

where $\sigma'_{y,0}$ is the effective in situ yield stress and a is a scalar defined as

$$a = \frac{EE_t}{E - E_t} > 0 \tag{4.33a}$$

for strain hardening materials, and as

$$a = -\frac{EE_t}{E + E_t} < 0 \tag{4.33b}$$

for strain softening materials, with E being the Young's modulus and E_t being the tangential modulus describing the slope between in situ yield stress $\sigma'_{y,0}$ and the ultimate stress σ'_u, which is the effective failure stress σ'_f for a strain hardening and the effective residual stress σ'_r for a strain softening material.

Hence, accounting for isotropic strain hardening/softening under unconfined axial com-
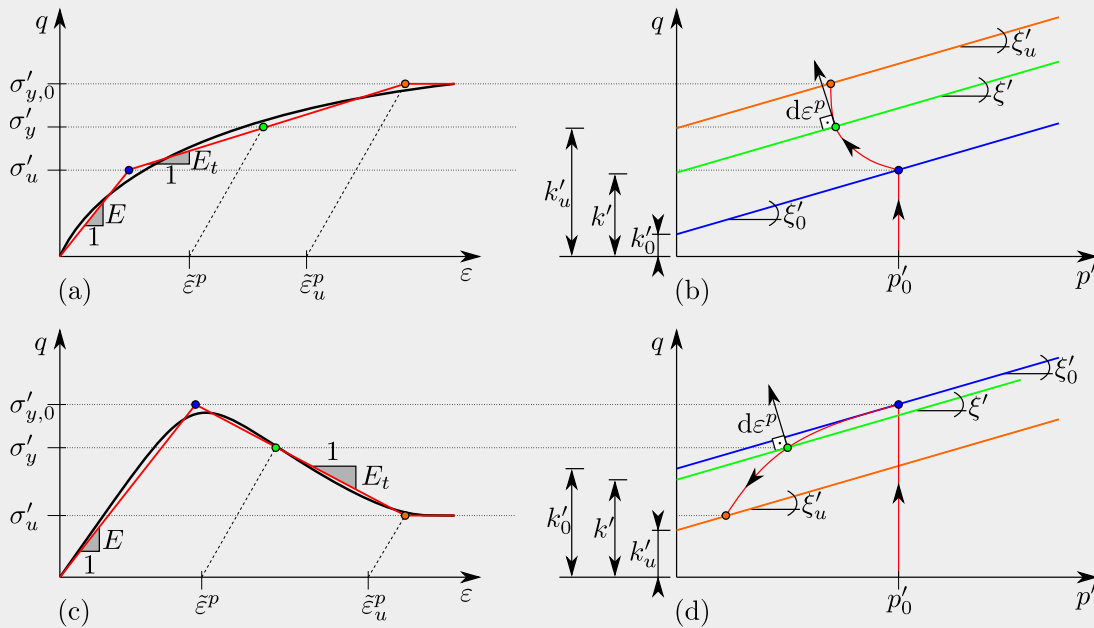
Figure 4.2.: The strain hardening/softening DP model: (a) Stress-strain curve for strain hardening material. (b) Yield and failure lines for strain hardening material with associated flow rule. (c) Stress-strain curve for strain softening material (d) Yield and failure lines for strain softening material with associated flow rule (after Chen et al., 2012b).

pression, the DP yield function defined in Equation 4.28 simplifies to

$$f = \sigma'_y \left(1 - \frac{\tan \xi'}{3}\right) - k'(\tilde{\varepsilon}^p) = (a\tilde{\varepsilon}^p + \sigma'_{y,0}) \left(1 - \frac{\tan \xi'}{3}\right) - k'(\tilde{\varepsilon}^p) = 0 \qquad (4.34)$$

Rearrangement of Equation 4.34 leads to an effective cohesion defined as a function of the cumulative plastic strains

$$k(\tilde{\varepsilon}^p) = \left(1 - \frac{\tan \xi'}{3}\right)(a\tilde{\varepsilon}^p + \sigma'_{y,0}) \qquad (4.35a)$$

which is bound by the in situ (initial) and ultimate states (Figure 4.2(b) and (d))

$$k'_0 = k'(0) = \left(1 - \frac{\tan \xi'}{3}\right)\sigma'_{y,0} \qquad (4.35b)$$

$$k'_u = k'(\varepsilon^p_u) = \left(1 - \frac{\tan \xi'}{3}\right)(a\tilde{\varepsilon}^p_u + \sigma'_{y,0}) \qquad (4.35c)$$

where the ultimate plastic strain for a hardening material ($a > 0$, Equation 4.33a) is

$$\varepsilon^p_u = \frac{\sigma'_f - \sigma'_{y,0}}{a} = \left(\sigma'_f - \sigma'_{y,0}\right)\left(\frac{1}{E_t} - \frac{1}{E}\right) \qquad (4.36a)$$

and for a softening material ($a < 0$, Equation 4.33b) it is

$$\varepsilon^p_u = \frac{\sigma'_r - \sigma'_{y,0}}{a} = \left(\sigma'_{y,0} - \sigma'_r\right)\left(\frac{1}{E} + \frac{1}{E_t}\right) \qquad (4.36b)$$

The general DP yield criterion in terms of $f(\sigma_{rr}, \sigma_{\theta\theta}, \tilde{\varepsilon}^p)$ can be defined via Equation 4.28, that is, for a vertical shaft, by inserting Equations 4.12b, 4.14, 4.31 and 4.35a

$$\begin{aligned} f(\sigma'_{rr}, \sigma'_{\theta\theta}, \tilde{\varepsilon}^p) = (\sigma'_{\theta\theta} - \sigma'_{rr}) - \frac{\tan \xi'}{3}\left[(\sigma'_{rr} + \sigma'_{\theta\theta})(1 + \nu) + \sigma'_{v,0} - 2\nu\sigma'_{h,0}\right] \\ - \left(1 - \frac{\tan \xi'}{3}\right)\left[a\frac{2}{3}\left(\varepsilon^p_{\theta\theta} - \varepsilon^p_{rr}\right) + \sigma'_{y,0}\right] = 0 \end{aligned} \qquad (4.37a)$$

and for a horizontal cavity by inserting Equations 4.13b, 4.14, 4.31 and 4.35a

$$\begin{aligned} f(\sigma'_{rr}, \sigma'_{\theta\theta}, \tilde{\varepsilon}^p) = (\sigma'_{\theta\theta} - \sigma'_{rr}) - \frac{\tan \xi'}{3}\left[(\sigma'_{rr} + \sigma'_{\theta\theta})(1 + \nu) - \nu\sigma'_{v,0} + (1 - \nu)\sigma'_{h,0}\right] \\ - \left(1 - \frac{\tan \xi'}{3}\right)\left[a\frac{2}{3}\left(\varepsilon^p_{\theta\theta} - \varepsilon^p_{rr}\right) + \sigma'_{y,0}\right] = 0 \end{aligned} \qquad (4.37b)$$

For isotropic initial conditions $(K_0 = 1)$ these equations are identical.

Assuming $K_0 = 1$ and associated flow $(g \equiv f)$, the plastic strain increments can be derived by substituting Equation 4.37 in Equation 4.30

$$\mathrm{d}\varepsilon_{rr}^p = \lambda^p \left[-1 - \frac{\tan \xi'}{3}(1 + \nu)\right] \quad \text{and} \quad \mathrm{d}\varepsilon_{\theta\theta}^p = \lambda^p \left[1 - \frac{\tan \xi'}{3}(1 + \nu)\right] \tag{4.38}$$

where the scalar λ^p, expressed in stress increments $\mathrm{d}\sigma_{rr}'$ and $\mathrm{d}\sigma_{\theta\theta}'$, can be derived from Equation 4.30:

$$\lambda^p = \frac{\left[-1 - \frac{\tan \xi'}{3}(1 + \nu)\right] \mathrm{d}\sigma_{rr}' + \left[1 - \frac{\tan \xi'}{3}(1 + \nu)\right] \mathrm{d}\sigma_{\theta\theta}'}{\frac{4}{3}a \left(1 - \frac{\tan \xi'}{3}\right)} \tag{4.39}$$

Back-substitution of Equation 4.39 in Equation 4.38 results in the plastic strain increments in the radial and tangential directions respectively,

$$\mathrm{d}\varepsilon_{rr}^p = \frac{\left[(1 + \nu)\tan \xi' + 3\right]^2 \mathrm{d}\sigma_{rr}' + \left[1/3(1 + \nu)^2 \tan^2 \xi' - 3\right] \mathrm{d}\sigma_{\theta\theta}'}{4\,a\,(3 - \tan \xi')} \tag{4.40a}$$

$$\mathrm{d}\varepsilon_{\theta\theta}^p = \frac{\left[1/3(1 + \nu)^2 \tan^2 \xi' - 3\right] \mathrm{d}\sigma_{rr}' + \left[(1 + \nu)\tan \xi' - 3\right]^2 \mathrm{d}\sigma_{\theta\theta}'}{4\,a\,(3 - \tan \xi')} \tag{4.40b}$$

By adding the elastic and plastic strain increments (Equations 4.20 and 4.23), the compliance form of the stress-strain relationship can be derived as

$$\mathrm{d}\boldsymbol{\varepsilon} = \mathbf{K}\,\mathrm{d}\boldsymbol{\sigma}' \tag{4.41a}$$

$$\mathrm{d}\varepsilon_{rr} = \left\{\frac{1 - \nu^2}{E} + \frac{\left[(1 + \nu)\tan \xi' + 3\right]^2}{4\,a\,(3 - \tan \xi')}\right\} \mathrm{d}\sigma_{rr}'$$
$$+ \left\{-\frac{\nu(1 + \nu)}{E} + \frac{\left[1/3(1 + \nu)^2 \tan^2 \xi' - 3\right]}{4\,a\,(3 - \tan \xi')}\right\} \mathrm{d}\sigma_{\theta\theta}' \tag{4.41b}$$

$$\mathrm{d}\varepsilon_{\theta\theta} = \left\{-\frac{\nu(1 + \nu)}{E} + \frac{\left[1/3(1 + \nu)^2 \tan^2 \xi' - 3\right]}{4\,a\,(3 - \tan \xi')}\right\} \mathrm{d}\sigma_{rr}'$$
$$+ \left\{\frac{1 - \nu^2}{E} + \frac{\left[(1 + \nu)\tan \xi' - 3\right]^2}{4\,a\,(3 - \tan \xi')}\right\} \mathrm{d}\sigma_{\theta\theta}' \tag{4.41c}$$

where $\mathbf{K}$ is the compliance matrix.

To solve Equation 4.19, the stiffness matrix may be derived by inversion of the compliance

matrix

$$\mathbf{D} = \begin{bmatrix} D_{11} & D_{12} \\ D_{21} & D_{22} \end{bmatrix} = \mathbf{K}^{-1} = \begin{bmatrix} K_{11} & K_{12} \\ K_{21} & K_{22} \end{bmatrix}^{-1} \tag{4.42a}$$

where

$$D_{ij} = \frac{1}{\det \mathbf{K}}(-1)^{i+j} M_{ij} = \frac{1}{\det \mathbf{K}}(-1)^{i+j} \det K_{ij} = \frac{1}{\det \mathbf{K}}(-1)^{i+j} K_{ij} \tag{4.42b}$$

with M_{ij} being the minor which for a 2×2 matrix is equal to its determinant. Thus the incremental stress-strain relationship in stiffness form is

$$\begin{pmatrix} \mathrm{d}\sigma'_{rr} \\ \mathrm{d}\sigma'_{\theta\theta} \end{pmatrix} = \begin{bmatrix} \frac{K_{22}}{\det \mathbf{K}} & \frac{-K_{21}}{\det \mathbf{K}} \\ \frac{-K_{12}}{\det \mathbf{K}} & \frac{K_{11}}{\det \mathbf{K}} \end{bmatrix} \begin{pmatrix} \mathrm{d}\varepsilon_{rr} \\ \mathrm{d}\varepsilon_{\theta\theta} \end{pmatrix} \tag{4.43}$$

where $K_{21} = K_{12}$ and thus $D_{21} = D_{12}$.

Further hardening & softening formulations

Numerous formulations for the linear/non-linear strain hardening and softening of soil and rock materials have been developed (e.g. Read and Hegemie, 1984; Wood, 2000) and are being employed to asses the influence of the soil response around an excavated cavity (e.g. François et al., 2011; Giraud et al., 2002; Salehnia et al., 2013; Yu, 2000). Three models will be introduced briefly hereafter to provide information on potential alternatives to the formulation by Chen et al. (2012b) as has been used in this report.

Hardening & softening defined by François et al. (2011)

François et al. (2011) developed an extended DP hardening/softening model for cross-anisotropic soft rock. The model has been implemented in the *Finite Element* (FE) code LAGAMINE (e.g. Charlier, 1987; Collin, 2003) by François et al. (2009) and François et al. (2013), in order to model the *Admissible Thermal Loading for Argillaceous Storage* (ATLAS) test (e.g. Chalindar et al., 2010) and some hollow cylinder tests as part of the *Thermal Impact on the Damage Zone around a Radioactive Waste Disposal in Clay Host* (TIMODAZ) project. The formulation was implemented in combination with the second gradient method for strain localisation within the FE domain (e.g. Salehnia et al., 2013).

In order to account for the anisotropic response of Boom Clay, the effective cohesion c' was defined as a directional function with respect to its bedding plane

$$c'_j = \max \left[\left(\frac{c'_{j,45°} - c'_{j,0°}}{45°} \right) \alpha_{\sigma_1} + c'_{j,0°} ; \left(\frac{c'_{j,90°} - c'_{j,45°}}{45°} \right) (\alpha_{\sigma_1} - 45°) + c'_{j,45°} \right] \tag{4.44}$$

where the subscript $j = 0$ for the initial cohesion ($c' = c'_0$), $j = r$ for the cohesion at peak

or residual state ($c' = c'_r$), and α_{σ_1} is the angle between the normal bedding plane $\vec{n}$ and the major principle stress $\vec{\sigma}_1$

$$\alpha_{\sigma_1} = \cos^{-1}\left(\frac{\vec{n} \cdot \vec{\sigma}_1}{\|\vec{n}\|\|\vec{\sigma}_1\|}\right) \tag{4.45}$$

The hardening/softening during plastic flow is introduced, via a hyperbolic variation between the initial and ultimate shear strength property values, as a function of the equivalent plastic strain

$$c' = \begin{cases} c'_0 & \tilde{\varepsilon}^p > 0 \\ c'_0 + \frac{(c'_u - c'_0)\tilde{\varepsilon}^p}{B_{c'} + \tilde{\varepsilon}^p} & \tilde{\varepsilon}^p = 0 \end{cases} \tag{4.46a}$$

$$\varphi' = \begin{cases} \varphi'_0 & \tilde{\varepsilon}^p = 0 \\ \varphi'_0 + \frac{(\varphi'_u - \varphi'_0)\tilde{\varepsilon}^p}{B_{\varphi'} + \tilde{\varepsilon}^p} & \tilde{\varepsilon}^p > 0 \end{cases} \tag{4.46b}$$

where $B_{c'}$ and $B_{\varphi'}$ were defined by François et al. (2011) simply as intrinsic *material parameters*.

Hardening & softening defined by Salehnia et al. (2013)

Using, as well, a DP yield criterion, Salehnia et al. (2013) defined the variation in effective cohesion and friction angle similar to Equation 4.46 as

$$c' = \begin{cases} c'_0 & \tilde{\varepsilon}^p > dec_{c'} \\ c'_0 + \frac{c'_u - c'_0(\tilde{\varepsilon}^p - dec_{c'})}{B_{c'} + (\tilde{\varepsilon}^p - dec_{c'})} & \tilde{\varepsilon}^p < dec_{c'} \end{cases} \tag{4.47a}$$

$$\varphi' = \begin{cases} \varphi'_0 & \tilde{\varepsilon}^p < dec_{\varphi'} \\ \varphi'_0 + \frac{\varphi'_u - \varphi'_0(\tilde{\varepsilon}^p - dec_{\varphi'})}{B_{\varphi'} + (\tilde{\varepsilon}^p - dec_{\varphi'})} & \tilde{\varepsilon}^p > dec_{\varphi'} \end{cases} \tag{4.47b}$$

where $dec_{c'}$ and $dec_{\varphi'}$ have been defined as the values of equivalent plastic strain from which hardening/softening starts, and $B_{c'}$ and $B_{\varphi'}$ are the equivalent plastic strains for which half of the difference in initial and ultimate cohesion and friction angle are reached respectively.

Hardening & softening defined by Giraud et al. (2002)

Using a MC yield envelope, Giraud et al. (2002) defined a linear strain hardening/softening law as

$$c' = \begin{cases} c'_0 + \frac{c'_r - c'_0}{\chi_u}\chi & 0 \leq \chi \leq \chi_u \\ c'_u & \chi_u \leq \chi \end{cases} \tag{4.48}$$

where χ is a hardening/softening parameter for which $\partial\chi = |\partial\varepsilon_I^p| + |\partial\varepsilon_{II}^p| + |\partial\varepsilon_{III}^p|$ is a function of the plastic strain rates in the principle stress directions. See also Giraud (1993).

4.4.5. Perfect plasticity

When the applied cavity pressure is lower than the critical cavity pressure, $p_{c,crit} < p_c$, the subsequent stress relief in the soil mass due to the excavation of the cavity will cause the soil to yield to its ultimate state and thus a residual zone develops (see Figures 2.43(a-b)). In this case Equations 4.38-4.41 no longer apply and, the strains cannot be determined solely based on the knowledge of the stresses (e.g. Davis and Selvadurai, 2002).

The residual plastic stresses are found by substituting the residual constant k_u' (Equation 4.35c), into the DP yield function f (Equation 4.37b):

$$
\begin{aligned}
f = &\left[\sigma_{\theta\theta}'^{rp}(x) - \sigma_{rr}'^{rp}(x)\right] - \frac{\tan\xi'}{3}\left\{\left[\sigma_{rr}'^{rp}(x) + \sigma_{\theta\theta}'^{rp}(x)\right](1+\nu) - \nu\sigma_{v,0}' + \right. \\
&\left. (1-\nu)\sigma_{h,0}'\right\} - k_u' = 0
\end{aligned}
\tag{4.49}
$$

for $x \le x_{rp} = r_{rp}/r_p$ and with x_{rp} being the non-dimensional residual plastic radius.

By substitution of Equations 4.18 and 4.30 into Equation 4.20, the total strain rate vector is

$$
\mathrm{d}\varepsilon = \mathrm{d}\varepsilon^e + \mathrm{d}\varepsilon^p + \mathrm{d}\varepsilon^{rp} = (\mathbf{D}^e + \mathbf{D}^p)^{-1}\,\mathrm{d}\boldsymbol{\sigma}' + \lambda^{rp}\frac{\partial g}{\partial\boldsymbol{\sigma}'}
\tag{4.50}
$$

where the elastic and plastic stiffness matrices, $\mathbf{D}^e$ and $\mathbf{D}^p$, are defined in Equations 4.22 and 4.42 respectively and λ^{rp} is the scalar multiplier for the residual plastic zone. Given that the stress remains on the yield surface, i.e. $\mathrm{d}f = \left(\frac{\partial f^{\mathsf{T}}}{\partial\boldsymbol{\sigma}'}\right)\mathrm{d}\boldsymbol{\sigma}' = 0$, the strain rate vector can be rearranged to compute the plastic multiplier

$$
\lambda^{rp} = \frac{(\mathbf{D}^e + \mathbf{D}^p)\,\mathrm{d}\varepsilon\left(\frac{\partial f}{\partial\boldsymbol{\sigma}'}\right)^{\mathsf{T}}}{\left(\frac{\partial f}{\partial\boldsymbol{\sigma}'}\right)^{\mathsf{T}}(\mathbf{D}^e + \mathbf{D}^p)\frac{\partial g}{\partial\boldsymbol{\sigma}'}}
\tag{4.51}
$$

for which, in this investigation, the associated flow ($g \equiv f$) is assumed. For more information on the derivation of λ^{rp} see for instance Davis and Selvadurai (2002, pp97-99) and Wood (2004, pp123-124).

The general elasto-plastic stress-strain relationship in the residual plastic zone, in incremental form, may then be written as

$$
\mathrm{d}\boldsymbol{\sigma}'^{rp} = \mathbf{D}^{rp}\,\mathrm{d}\varepsilon = (\mathbf{D}^e + \mathbf{D}^p)\left(\mathrm{d}\varepsilon - \lambda^{rp}\frac{\partial g}{\partial\boldsymbol{\sigma}'}\right)
\tag{4.52}
$$

where the stiffness matrix in the residual plastic zone, that is, relating the increments of

effective stress to the increments of total elasto-plastic strain, can be written as

$$\mathbf{D}^{rp} = \left[\mathbf{I} - \frac{(\mathbf{D}^e + \mathbf{D}^p) \frac{\partial g}{\partial \boldsymbol{\sigma'}} \left(\frac{\partial f}{\partial \boldsymbol{\sigma'}} \right)^{\mathsf{T}}}{\left(\frac{\partial f}{\partial \boldsymbol{\sigma'}} \right)^{\mathsf{T}} (\mathbf{D}^e + \mathbf{D}^p) \frac{\partial g}{\partial \boldsymbol{\sigma'}}} \right] (\mathbf{D}^e + \mathbf{D}^p) \tag{4.53}$$

with $\mathbf{I}$ being the identity matrix.

4.4.6. Hydraulic response

The continuity of the pore water pressure u_w may be expressed in terms of the normalised radial polar coordinate ρ as

$$\left(\frac{\partial^2}{\partial \rho^2} + \frac{1}{\rho} \frac{\partial}{\partial \rho} \right) u_w = 0 \tag{4.54}$$

Given the pressure boundary conditions defined in Equation 4.16b, the pore water pressure at any radius is

$$u_w(\rho) = u_{w,0} = u_c \tag{4.55}$$

for an impermeable lining. For a permeable lining the reduction in pore water pressure towards the liner may be approximated by employing Dupuit's assumption, with the pore water pressure profile having a logarithmic shape (e.g. Bobet, 2003; Carranza-Torres and Zhao, 2009; Fazio and Ribacchi, 1984)

$$u_w(\rho) = u_{w,c} + (u_{w,0} - u_{w,c}) \frac{\ln \rho}{\ln \rho_w} \qquad \text{for } \rho < \rho_w \tag{4.56a}$$

$$u_w(\rho) = u_{w,0} \qquad \text{for } \rho \geq \rho_w \tag{4.56b}$$

where $\rho_w = r_w / r_c$ defines the normalised radius beyond which the pore water pressure is not influenced by the cavity (see Figure 2.43(b)).

4.4.7. The concrete liner

The concrete support structure is commonly considered to be linear-elastic (e.g. Bobet, 2010; Carranza-Torres et al., 2013; Kolymbas, 2008). Following Timoshenko and Goodier (1970), for a circular homogeneous isotropic liner, the radial and tangential stresses of the liner in

cylindrical coordinates, σ_r^l and σ_θ^l, and radial displacement of the liner, u_r^l, are

$$\sigma_r^l = -\frac{p_c}{1-(r_i/r_c)^2}\left[1-\left(\frac{r_i}{r}\right)^2\right] \tag{4.57a}$$

$$\sigma_\theta^l = -\frac{p_c}{1-(r_i/r_c)^2}\left[1+\left(\frac{r_i}{r}\right)^2\right] \tag{4.57b}$$

$$u_r^l = -\frac{1+\nu_l}{E_l}\frac{p_c}{1-(r_i/r_c)^2}\left[1-2\nu_l+\left(\frac{r_i}{r}\right)^2\right]r \tag{4.57c}$$

where p_c is the compressive cavity pressure applied radially to the tunnel support structure-subsoil interface, r is the radial polar coordinate, r_i is the nominal inner tunnel radius, r_c is the cavity radius, E_l is the Young's modulus of the concrete liner and ν_l is the Poisson's ratio of concrete liner (Bobet, 2010; Brady and Brown, 2006). Given that $d_l = r_c - r_i$ is the concrete liner thickness, Equation 4.57 may be simplified for situations where $d_l \ll r_c$.

$$\sigma_\theta^l = -\frac{r_c}{d_l}p_c \tag{4.57d}$$

$$u_r^l = -\frac{1-\nu_l^2}{E_l}\frac{r_c^2}{d_l}p_c \tag{4.57e}$$

The maximum compressive support (collapse) load of the liner, p_l^{max}, is

$$p_l^{max} = \frac{\sigma_{cc}}{2}\left[1-\frac{(r_c-d_l)^2}{r_c^2}\right] \tag{4.58}$$

where σ_{cc} is the uniaxial compressive strength of concrete (Brady and Brown, 2006, p577).

4.5. Solution

The solution is found by using the following general algorithm:

(a) The stresses and strains in the elastic region are solved and the initial yield stresses determined - at this point the location of these stresses and yield location in space are unknown;

(b) The stresses and strains in the plastic region and, if present, residual plastic region, are solved - again the location of these stresses in space are unknown;

(c) The stresses, strains and deformations in the tunnel liner are calculated, as a function of cavity pressure;

(d) The equilibrium of the stresses and deformations between the tunnel liner (SRC) and the soil (GRC) are determined and the positions in space of the stresses calculated in steps (a) and (b) can be determined.

4.5.1. The elastic zone

Given Equation 4.23, the elastic radial and tangential strains in can be computed as

$$\varepsilon_{rr}^{e}(r) = \frac{1-\nu^2}{E}\sigma_{rr}^{\prime e}(r) - \frac{\nu+\nu^2}{E}\sigma_{\theta\theta}^{\prime e}(r) \tag{4.59}$$

$$\varepsilon_{\theta\theta}^{e}(r) = -\frac{\nu+\nu^2}{E}\sigma_{rr}^{\prime e}(r) + \frac{1-\nu^2}{E}\sigma_{\theta\theta}^{\prime e}(r) \tag{4.60}$$

for which the associated effective radial and tangential stresses in the elastic zone, i.e. $\sigma_{rr}^{\prime e}(r)$ and $\sigma_{\theta\theta}^{\prime e}(r)$, may differ depending on the cavity orientation and in situ stress ratio.

Assuming a fully elastic soil, with no influence of the pore water pressure $u_w(r)$, the radial displacement $u_r^e(r)$ in the subsoil will only be a function of the difference between the in situ stress in the far-field ($\sigma_{h,0}$ and $\sigma_{v,0}$) and the cavity pressure p_c. Assuming an elasto-plastic soil response, the radial stress in the elastic zone is not bound by the cavity pressure p_c but by the radial stress at the elasto-plastic interface, namely $\bar{\sigma}_{rr}$ (see Figure 2.43).

For a cylindrical cavity excavated in a subsoil subjected to an isotropic in situ stress ratio, that is, for a vertical shaft or a horizontal tunnel where $\sigma_{h,0} = \sigma_{v,0}$, the effective stresses in the elastic zone are:

$$\sigma_{rr}^{\prime e}(r) = (\sigma_{h,0}-u_{w,0}) + (\bar{\sigma}_{rr}-\sigma_{h,0})\frac{r_p^2}{r^2} = \sigma_{h,0}^{\prime} + (\bar{\sigma}_{rr}^{\prime}-\sigma_{h,0}^{\prime})\frac{r_p^2}{r^2} \tag{4.61a}$$

$$\sigma_{\theta\theta}^{\prime e}(r) = (\sigma_{h,0}-u_{w,0}) - (\bar{\sigma}_{rr}-\sigma_{h,0})\frac{r_p^2}{r^2} = \sigma_{h,0}^{\prime} - (\bar{\sigma}_{rr}^{\prime}-\sigma_{h,0}^{\prime})\frac{r_p^2}{r^2} \tag{4.61b}$$

$$\tau_{r\theta}^{\prime e}(r) = 0 \tag{4.61c}$$

$$u_w(r) = u_{w,0} \tag{4.61d}$$

(e.g. Bobet, 2010; Kolymbas, 2008; Yu, 2000). Due to the isotropic in situ stress ratio and the assumption of an ideal cylindrical cavity, no shear stresses $\tau_{r\theta}^{\prime e}$ are imposed (see Section 4.3). From Equation 4.61b it follows that

$$\bar{\sigma}_{rr}^{\prime} + \bar{\sigma}_{\theta\theta}^{\prime} = 2\sigma_{h,0}^{\prime} \tag{4.62}$$

The radial deformation in the elastic zone is computed as

$$u_r^e = -\frac{(1+\nu)}{E}(\bar{\sigma}_{rr}^{\prime}-\sigma_0^{\prime})\frac{r_p^2}{r} = \varepsilon_{\theta\theta}^e r \tag{4.63}$$

(e.g. Bobet, 2010; Kolymbas, 2008).

4.5.2. The elasto-plastic interface

The radial and tangential stresses at the interface between the elastic and plastic zones are $\bar{\sigma}_{rr}^{\prime} = \sigma_{rr}^{\prime}(r_p)$ and $\bar{\sigma}_{\theta\theta}^{\prime} = \sigma_{\theta\theta}^{\prime}(r_p)$ (see Figure 2.43(b)). Considering that the EP interface is

the initial yield surface, i.e. $\sigma'_y = \sigma'_{y,0}$ and $k' = k'(0)$ (Equations 4.32 and 4.35b), the general DP yield criterion (Equation 4.37a or 4.37b) can be rewritten.

For a horizontal cavity, the initial DP yield criterion is derived from Equation 4.37b as

$$
\begin{aligned}
f(\bar{\sigma}'_{rr}, \bar{\sigma}'_{\theta\theta}) &= (\bar{\sigma}'_{\theta\theta} - \bar{\sigma}'_{rr}) - \frac{\tan \xi'}{3} \left[(\bar{\sigma}'_{rr} + \bar{\sigma}'_{\theta\theta})(1 + \nu) - \nu \sigma'_{v,0} + (1 - \nu) \sigma'_{h,0} \right] \\
&\quad - \left(1 - \frac{\tan \xi'}{3} \right) \sigma_{y,0} = 0
\end{aligned}
\tag{4.64}
$$

from which, by substitution of Equation 4.62, the radial and tangential stresses at the elasto-plastic interface can be derived as

$$
\bar{\sigma}'_{rr} = \sigma'_{h,0} - \frac{\tan \xi'}{6} \left[3\sigma'_{h,0} + \nu(\sigma'_{h,0} - \sigma'_{v,0}) \right] - \frac{1}{2} \left(1 - \frac{\tan \xi'}{3} \right) \sigma'_{y,0}
\tag{4.65a}
$$

$$
\bar{\sigma}'_{\theta\theta} = \sigma'_{h,0} + \frac{\tan \xi'}{6} \left[3\sigma'_{h,0} + \nu(\sigma'_{h,0} - \sigma'_{v,0}) \right] + \frac{1}{2} \left(1 - \frac{\tan \xi'}{3} \right) \sigma'_{y,0}
\tag{4.65b}
$$

where $u_w(r) = \bar{u}_w = u_{w,0}$ (Equation 4.55).

From Equation 4.23, the initial strains at the EP interface for all cases in which the in situ stress is isotropic can be computed as

$$
\bar{\varepsilon}_{rr} = \frac{1 + \nu}{E} (\bar{\sigma}'_{rr} - \sigma'_{h,0})
\tag{4.66a}
$$

$$
\bar{\varepsilon}_{\theta\theta} = -\frac{1 + \nu}{E} (\bar{\sigma}'_{rr} - \sigma'_{h,0})
\tag{4.66b}
$$

4.5.3. The hardening/softening plastic zone

The radial and tangential stress and strain in the plastic zone may be defined as

$$
\sigma'^p_{rr}(r) = \bar{\sigma}'_{rr} + \Delta\sigma'^p_{rr}(r) = \bar{\sigma}'_{rr} + \left[\sigma'^p_{rr}(r) - \bar{\sigma}'_{rr} \right]
\tag{4.67a}
$$

$$
\sigma'^p_{\theta\theta}(r) = \bar{\sigma}'_{\theta\theta} + \Delta\sigma'^p_{\theta\theta}(r) = \bar{\sigma}'_{\theta\theta} + \left[\sigma'^p_{\theta\theta}(r) - \bar{\sigma}'_{\theta\theta} \right]
\tag{4.67b}
$$

$$
\varepsilon^p_{rr}(r) = \bar{\varepsilon}_{rr} + \Delta\varepsilon^p_{rr}(r) = \bar{\varepsilon}_{rr} + \left[\varepsilon^p_{rr}(r) - \bar{\varepsilon}_{rr} \right]
\tag{4.67c}
$$

$$
\varepsilon^p_{\theta\theta}(r) = \bar{\varepsilon}_{\theta\theta} + \Delta\varepsilon^p_{\theta\theta}(r) = \bar{\varepsilon}_{\theta\theta} + \left[\varepsilon^p_{\theta\theta}(r) - \bar{\varepsilon}_{\theta\theta} \right]
\tag{4.67d}
$$

where $\Delta\sigma'^p$ and $\Delta\varepsilon^p$ are the incremental stress and strain in the plastic zone with respect to the initial yield stress and strain. Using this incremental formulation, Equations 4.67a and 4.67b can be written as system of linear equations as in Equation 4.19.

$$
\sigma'^p_{rr}(r) = \bar{\sigma}'_{rr} + D_{11}\left[\varepsilon^p_{rr}(r) - \bar{\varepsilon}_{rr} \right] + D_{12}\left[\varepsilon^p_{\theta\theta}(r) - \bar{\varepsilon}_{\theta\theta} \right]
\tag{4.68a}
$$

$$
\sigma'^p_{\theta\theta}(r) = \bar{\sigma}'_{\theta\theta} + D_{21}\left[\varepsilon^p_{rr}(r) - \bar{\varepsilon}_{rr} \right] + D_{22}\left[\varepsilon^p_{\theta\theta}(r) - \bar{\varepsilon}_{\theta\theta} \right]
\tag{4.68b}
$$

Given the equilibrium around the cavity (Equation 4.15), the boundary conditions defined in Equation 4.16 (see Figure 2.43) and the incremental stresses defined in Equations 4.68, the radial displacements may be obtained via the differential equation

$$D_{11}\frac{\partial^2 u_r^p}{\partial r^2} + D_{11}\frac{\partial u_r^p}{r\partial r} - D_{22}\frac{u_r^p}{r^2} = \frac{m\left(\bar{\sigma}_{rr} - \sigma_{h,0}\right)}{r} \tag{4.69}$$

with $D_{12} = D_{21}$ and $m = 2 - \frac{1+\nu}{E}(D_{11} - 2D_{12} + D_{22})$.

The general solution for the radial displacement in the plastic zone is

$$u_r^p = c_1 r^{\alpha_1} + c_2 r^{\alpha_2} + \frac{m\left(\bar{\sigma}_{rr}' - \sigma_{h,0}'\right)r}{D_{11}(1 - \alpha_1)(1 - \alpha_2)} \tag{4.70}$$

where the coefficients $\alpha_1 = \sqrt{D_{22}/D_{11}}$ and $\alpha_2 = -\alpha_1$ (Graziani and Ribacchi, 1993). The integration constants c_1 and c_2 are obtained by applying the two boundary conditions $\Delta\sigma_{rr}' = 0$ and $\Delta\varepsilon_{\theta\theta}^p = 0$, for $r = r_p$ (Graziani and Ribacchi, 1993).

$$c_1 = -\frac{\bar{\varepsilon}_{\theta\theta}}{r_p^{\alpha_1 - 1}(\alpha_2 - \alpha_1)}\left[(1 + \alpha_2) + \frac{mE}{D_{11}(1 - \alpha_1)(1 + \nu)}\right] \tag{4.71a}$$

$$c_2 = \frac{\bar{\varepsilon}_{\theta\theta}}{r_p^{\alpha_2 - 1}(\alpha_2 - \alpha_1)}\left[(1 + \alpha_1) + \frac{mE}{D_{11}(1 - \alpha_2)(1 + \nu)}\right] \tag{4.71b}$$

Back substitution of Equations 4.71 into Equation 4.70, and subsequently into Equations 4.5a and 4.5b, leads to the plastic strains

$$\varepsilon_{rr}^p(x) = \bar{\varepsilon}_{\theta\theta}\left[\alpha_1 F_1(x) - \alpha_2 F_2(x)\right] \tag{4.72a}$$

$$\varepsilon_{\theta\theta}^p(x) = \bar{\varepsilon}_{\theta\theta}\left[F_1(x) - F_2(x)\right] \tag{4.72b}$$

with the coefficients $F(x)$ being

$$F_1(x) = \frac{1}{\alpha_2 - \alpha_1}\left[(1 + \alpha_2)x^{\alpha_1 - 1} + \frac{mE(x^{\alpha_1 - 1} - 1)}{D_{11}(1 - \alpha_1)(1 + \nu)}\right] \tag{4.73a}$$

$$F_2(x) = \frac{1}{\alpha_2 - \alpha_1}\left[(1 + \alpha_1)x^{\alpha_2 - 1} + \frac{mE(x^{\alpha_2 - 1} - 1)}{D_{11}(1 - \alpha_2)(1 + \nu)}\right] \tag{4.73b}$$

where $x = \frac{r}{r_p}$ is a non-dimensional radius.

Hence the stress in the plastic zone can be computed with respect to the plastic radius as

$$\sigma_{rr}'^p(x) = \bar{\sigma}_{rr}' + \bar{\varepsilon}_{\theta\theta}\left\{D_{11}\left[\alpha_1 F_1(x) - \alpha_2 F_2(x) + 1\right] + D_{12}\left[F_1(x) - F_2(x) - 1\right]\right\} \tag{4.74a}$$

$$\sigma_{\theta\theta}'^p(x) = \bar{\sigma}_{\theta\theta}' + \bar{\varepsilon}_{\theta\theta}\left\{D_{21}\left[\alpha_1 F_1(x) - \alpha_2 F_2(x) + 1\right] + D_{22}\left[F_1(x) - F_2(x) - 1\right]\right\} \tag{4.74b}$$

for which the plastic radius r_p is determined by solving Equation 4.74a at the cavity boundary,

i.e.

$$\sigma_{rr}^{\prime p}\left(\frac{r_c}{r_p}\right) - p_c' = 0 \tag{4.75}$$

4.5.4. Residual plastic zone

The associated critical cavity pressure $p_{c,crit}$, below which the residual state is reached, may be computed by substituting x_{rp} into Equation 4.74a, i.e.

$$p_{c,crit} = \sigma_{rr}^p\left(x_{rp}\right) = \hat{\sigma}_{rr} = \hat{\sigma}_{rr}' + \hat{u}_w \tag{4.76}$$

where $\hat{\sigma}_{rr}$ and $\hat{\sigma}_{rr}'$ are the total and effective stresses at the interface between the hardening/softening plastic zone and the residual plastic zone, i.e. the *Residual-Plastic* (RP) interface, and $\hat{u}_w$ is the pore water pressure at the RP interface.

For perfect plasticity, describing the soil response in the RP zone, the stresses are bound by the DP yield surface defined in Equation 4.49. Thus, to obtain the radial stress at any point in the RP zone, first the tangential stress is obtained as a function of the residual strength via rearrangement of Equation 4.49:

$$\sigma_{\theta\theta}^{\prime rp} = \frac{\sigma_{rr}^{\prime rp}\left[1 + \frac{\tan\xi'}{3}(1+\nu)\right] + \frac{\tan\xi'}{3}\left[(1-\nu)\sigma_{h,0}' - \nu\sigma_{v,0}'\right] + k_u'}{1 - \frac{\tan\xi'}{3}(1+\nu)} \tag{4.77}$$

and subsequently it is introduced into the equilibrium condition (Equation 4.15) to give

$$\frac{\partial\sigma_{rr}^{\prime rp}}{\partial r} + \frac{\sigma_{rr}^{\prime rp} - \left\{\sigma_{rr}^{\prime rp}(1+b) + \frac{\tan\xi'}{3}\left[(1-\nu)\sigma_{h,0}' - \nu\sigma_{v,0}'\right] + k_u'\right\}\left\{1-b\right\}^{-1}}{r}$$
$$+ \frac{\partial u_w}{\partial r} = 0 \tag{4.78}$$

where $b = \frac{\tan\xi'}{3}(1+\nu)$. For the impermeable liner, i.e. $\frac{\partial u_w}{\partial r} = 0$, the variables of the above equation can be readily separated and subsequently integrated, to give

$$\sigma_{rr}^{\prime rp} = \frac{e^{k[\ln(r)+c_3]} - l}{k} \tag{4.79}$$

where $k = \frac{1+b}{1-b} - 1$ and $l = \frac{\frac{\tan\xi'}{3}\left[(1-\nu)\sigma_{h,0}' - \nu\sigma_{v,0}'\right] + k_u'}{1-b}$. The integration constant is

$$c_3 = \frac{\ln(k\hat{\sigma}_{rr}' + l)}{k} - \ln\left(r_{rp}\right) \tag{4.80}$$

where $\hat{\sigma}_{rr}'$ is the radial stress at the RP interface (Equation 4.76).

By substituting the cavity radius r_c and the cavity pressure p_c in Equation 4.79 the residual

plastic radius r_{rp} can be computed by solving:

$$\sigma_{rr}^{rp}(r_c) = p_c = \frac{e^{k[\ln(r_c)+c_3]} - l}{k} + u_{w,c} \tag{4.81}$$

The tangential stress in the residual plastic zone can be subsequently computed via Equation 4.77.

Finally the radial deformation in the residual plastic zone, u_r^{rp}, is computed. Differentiation of Equation 4.79 with respect to the residual plastic radius r_{rp} leads to

$$\mathrm{d}\sigma_{rr}'^{rp} = r^k \underbrace{\left(-e^{k\frac{\ln(k\hat{\sigma}_{rr}'+l)}{k}} r_{rp}^{-k} \frac{1}{r_{rp}} \right)}_{a} \mathrm{d}r_{rp} \tag{4.82}$$

which defines the change in radial effective stress at a point within the residual plastic zone with respect to a change in the residual plastic radius. The variable a holds the parenthesised expression in the subsequent equations.

Substitution of Equation 4.82, along with Equations 4.5a and 4.5b, into Equation 4.19 leads to

$$\int \frac{a \cdot r^k}{D_{11}^{rp}} \cdot e^{\frac{D_{12}^{rp}}{D_{11}^{rp}}\ln(r)} \, \mathrm{d}r = \int \left(e^{\frac{D_{12}^{rp}}{D_{11}^{rp}}\ln(r)} \cdot u_r^{rp} \right)' \, \mathrm{d}r$$

$$\frac{a \cdot r \cdot e^{k\cdot\ln(r)+\frac{D_{12}^{rp}}{D_{11}^{rp}}\ln(r)}}{D_{11}^{rp}(k+1) + D_{12}^{rp}} + c_4 = e^{\frac{D_{12}^{rp}}{D_{11}^{rp}}\ln(r)} \cdot u_r^{rp} \tag{4.83}$$

from which the radial deformation in the residual plastic zone can be computed as

$$u_r^{rp} = \left[\frac{a \cdot r \cdot e^{k\cdot\ln(r)+\frac{D_{12}^{rp}}{D_{11}^{rp}}\ln(r)}}{D_{11}^{rp}(k+1) + D_{12}^{rp}} + c_4 \right] e^{-\frac{D_{12}^{rp}}{D_{11}^{rp}}\ln(r)} \tag{4.84}$$

The integration constant c_4 can be derived by inserting the boundary condition $u_r^{rp}(r_{rp}) = \hat{u}_r$, which is computed via Equation 4.70, and solved for

$$c_4 = e^{\frac{D_{12}^{rp}}{D_{11}^{rp}}\ln(r_{rp})} \cdot \hat{u}_r - \frac{a \cdot r_{rp} \cdot e^{k\cdot\ln(r_{rp})+\frac{D_{12}^{rp}}{D_{11}^{rp}}\ln(r_{rp})}}{D_{11}^{rp}(k+1) + D_{12}^{rp}} \tag{4.85}$$

4.5.5. The GRC and SCC

The *Ground Reaction Curve* (GRC) defines the radial deformation of the Boom Clay at the rock-liner cavity interface, $u_r(r_c)$, with respect to a specific cavity pressure p_c (Figure 4.3). The soil deformation $u_r(r_c)$ is computed via Equations 4.70 or 4.84.

Due to the cutting head of the excavation shield being oversized to reduce shaft friction on the shield-soil interface during progression of the machine, which potentially could lead to the shield being trapped in the Boom Clay (see Section 2.5.1.1), the total deformation u_c at the cavity interface is the sum of the overcut, d_{oc}, and the radial liner compression due to the soil induced pressure, u_l (see Equation 2.2 and Figure 2.41). The *Support Characteristic Curve* (SCC) which describes the linear-elastic radial deformation of the concrete liner is computed via Equations 4.57c or 4.57e. The liner collapse load is computed via Equation 4.58.

Figure 4.3 schematically shows that a certain liner stiffness needs to be provided to ensure the stability of the liner, that is, for an equivalent cavity pressure p_c^{eq} for which $u_r(r_c) = u_c = d_{oc} + u_l$. Given a range of GRC's resulting from the uncertainty in the soil property values, the liner with the lower stiffness fails to meet the hypothetical 95% upper-bound criterion of GRC responses. Increasing its stiffness, e.g. the liner thickness, the hypothetical criteria would be satisfied.

Figure 4.3.: Schematic Ground Reaction Curve (GRC) showing cavity pressure p_c vs. cavity deformation u_c for the mean response and between the 5-95th percentile. Support Characteristic Curves (SCC) for two linings of different stiffness are indicated. p_c^0 is the initial support pressure, p_l^{max} is the maximum (collapse) support load of the liner and p_c^{eq} is the equilibrium cavity pressure for which $u_r(r_c) = u_c$. The total soil deformation at the cavity interface u_c is a sum of the initial deformation during the excavation u_c^0, the closing of the residual overcut after liner installation u_c^δ and the radial liner compression due to the soil induced pressure u_l.

4.6. Implementation

The analytical model formulation has been implemented using the Python[6] programming language. The analytical model framework is summarised in the five steps below, that is, given the simplifying assumptions listed in Section 4.1, including the most significant components.

(1) Initialisation of the model:

(a) Read in discrete set of soil property values: c_0', c_r', φ', E, E_t, ν

(b) Set geometry, boundary conditions and liner property values: r_c, d_l, σ_0', $u_{w,0}$, E_l, ν_l, σ_{cc}

(c) Compute model variables:

$$k_0' = \frac{6c_0' \cos \varphi'}{3 - \sin \varphi'} \qquad k_u' = \frac{6c_u' \cos \varphi'}{3 - \sin \varphi'} \qquad \tan \xi' = \frac{6 \sin \varphi'}{3 - \sin \varphi'} \tag{4.29}$$

$$\sigma_{y,0}' = k_0' / \left(1 - \tan \xi' /3\right) \qquad \sigma_r' = k_r' / \left(1 - \tan \xi' /3\right) \tag{4.35b}$$

$$\varepsilon_u^p = \left(\sigma_{y,0}' - \sigma_r'\right) \left(1/E + 1/E_t\right) \quad \text{for softening material where } a < 0 \tag{4.36}$$

(2) Compute initial yield stresses and strains EP interface:

$$\bar{\sigma}_{rr}' = \sigma_{h,0}' - \tan \xi' /6 \left[3\sigma_{h,0}' + \nu(\sigma_{h,0}' - \sigma_{v,0}')\right] - 1/2 \left(1 - \tan \xi' /3\right) \sigma_{y,0}' \tag{4.65a}$$

$$\bar{\sigma}_{\theta\theta}' = \sigma_{h,0}' + \tan \xi' /6 \left[3\sigma_{h,0}' + \nu(\sigma_{h,0}' - \sigma_{v,0}')\right] + 1/2 \left(1 - \tan \xi' /3\right) \sigma_{y,0}' \tag{4.65b}$$

$$\bar{\varepsilon}_{\theta\theta} = -(1+\nu)/E \left[(\bar{\sigma}_{rr} - \bar{u}_w) - (\sigma_{h,0} - u_{w,0})\right] \tag{4.66b}$$

(3) Check if part of soil yields to residual state:

(a) Compute non-dimensional radius x_{rp} by substituting the stresses in plastic zone, $\sigma'^p(x_{rp})$ (Equation 4.74) into the equilibrium condition at the softening - residual plastic interface (Equation 4.37b).

(b) Compute critical cavity pressure by inserting Equation 4.74a in 4.76

$$p_{c,crit} = \bar{\sigma}_{rr}' + \bar{\varepsilon}_{\theta\theta} \left\{ D_{11} \left[\alpha_1 F_1(x) - \alpha_2 F_2(x) + 1\right] + D_{12} \left[F_1(x) - F_2(x) - 1\right] \right\}$$

If $p_{c,crit} > p_c$ then a residual plastic zone exists (go to 4b), else only a softening zone exists (go to 4a).

(4) Compute stresses strains and deformations in plastic zone:

(4a) Residual plastic zone does NOT exist ($p_{c,crit} \leq p_c$):

(a) Compute plastic radius by solving Equation 4.74a for r_p with $x = r_c/r_p$ and $\sigma_{rr}'^p = p_c'$.

(4b) Residual plastic zone does exist ($p_{c,crit} > p_c$):

(a) Compute residual plastic radius r_{rp} via Equation 4.81.

(b) Compute plastic radius via $r_p = r_{rp}/x_{rp}$.

If required compute stress, strain and deformation profiles in the plastic and residual plastic zone.

(5) Find equilibrium cavity pressure p_c^{eq}:

(a) Compute liner deformation u_l (Equation 4.57e).

(b) If $\delta_u = |(d_{oc} + u_l) - u_c(p_c)| < \delta_{max}$ (Figure 2.41) then set $p_c^{eq} \equiv p_c \rightarrow$ post-process data and exit module. Else updated $p_c \rightarrow$ go back to (3).

---

[6]Python: http://www.python.org/

4.7. Deterministic model response

In this section the deterministic response of Boom Clay due to the excavation of a tunnel, computed by the analytical model, is investigated by variation of the soil property values and boundary conditions.

Boom Clay property values

Table 4.1 summarises the range of soil property values $\mathbf{X} = \{c_0', c_r', \varphi, E, E_t, \nu\}$ selected based on the findings presented in Chapters 3.4 and 3.5. Each property is changed individually for all three cases, with the remaining five parameters being fixed to the values for case two.

The liner setup

The deterministic liner property values selected for this study are: Young's modulus, $E_l = 35000$MPa, Poisson's ratio, $\nu_l = 0.2$, and the uniaxial compressive strength of the concrete, $\sigma_{cc} = 80$MPa, consistent with the values given in NEN 6720 (1995). Figure 4.4(a) shows a decrease in the maximum compression strength (collapse load) of the support structure, p_c^{max}, with an increase in the cavity ratio r_c. Furthermore, the collapse load increases with an increase in liner stiffness, e.g. with an increase in the support thickness from 0.05m (e.g. shotcrete) to 0.60m (e.g. pre-fabricated lining segments). Figure 4.4(b) shows the collapse load for a uniaxial compressive strength of the concrete of $\sigma_{cc} = 45$MPa as suggested as a reference concrete for OPERA based upon the construction of the Westerscheldetunnel in the Netherlands (Verhoef et al., 2014). Figures 4.4(c) and 4.4(d) show the linear elastic increase in the liner deformation $u_l(r_c)$ for an increase in the applied cavity pressure and/or a decrease in liner thickness.

The boundary conditions

The initial and boundary conditions have been set using deterministic values. For a tunnel located at 500m depth the total in situ stresses in the horizontal and vertical directions are set to $\sigma_{h,0} = \sigma_{v,0} = 10$MPa and the in situ pore water pressure is set to $u_{w,0} = 5$MPa. For a variation in depth, e.g. to 600m and 700m, the stresses and pore water pressure are assumed

Table 4.1.: Characteristic Boom Clay property values.

Random variable	X_i	Unit	Case 1	Case 2	Case 3
Effective initial cohesion	c_0'	[MPa]	0.3	**0.5**	0.7
Effective residual cohesion	c_r'	[MPa]	0.15	**0.25**	0.35
Effective friction angle	φ'	[°]	7.5	**12.5**	17.5
Young's modulus	E	[MPa]	200	**300**	400
Tangent modulus	E_t	[MPa]	100	**150**	200
Poisson's ratio	ν	[−]	0.2	**0.3**	0.4

to remain following the hydrostatic regime. Both assumptions, i.e. the in situ stress being isotropic and following a hydrostatic regime, are deemed to be appropriate in situ conditions. This is, for the design of a generic OPERA repository, due to its specific location being unknown to date as well as based on the evaluation of available data, e.g. from the URF in Mol located at a depth of -223m where $K_0 = 0.3 - 1.0$ and $\sigma'_{v,0}$ =2.25-2.50MPa.

Figure 4.4(c) showed that for a stiff pre-fabricated liner the actual liner deformation induced by an applied external radial cavity pressure of $p_c^{max} = 10$MPa are less than 10mm. Hence, the total deformation and thus the cavity pressure in equilibrium and extent of the plastic radius will be strongly affected by the overcut of the tunnelling machine. The required overcut depends
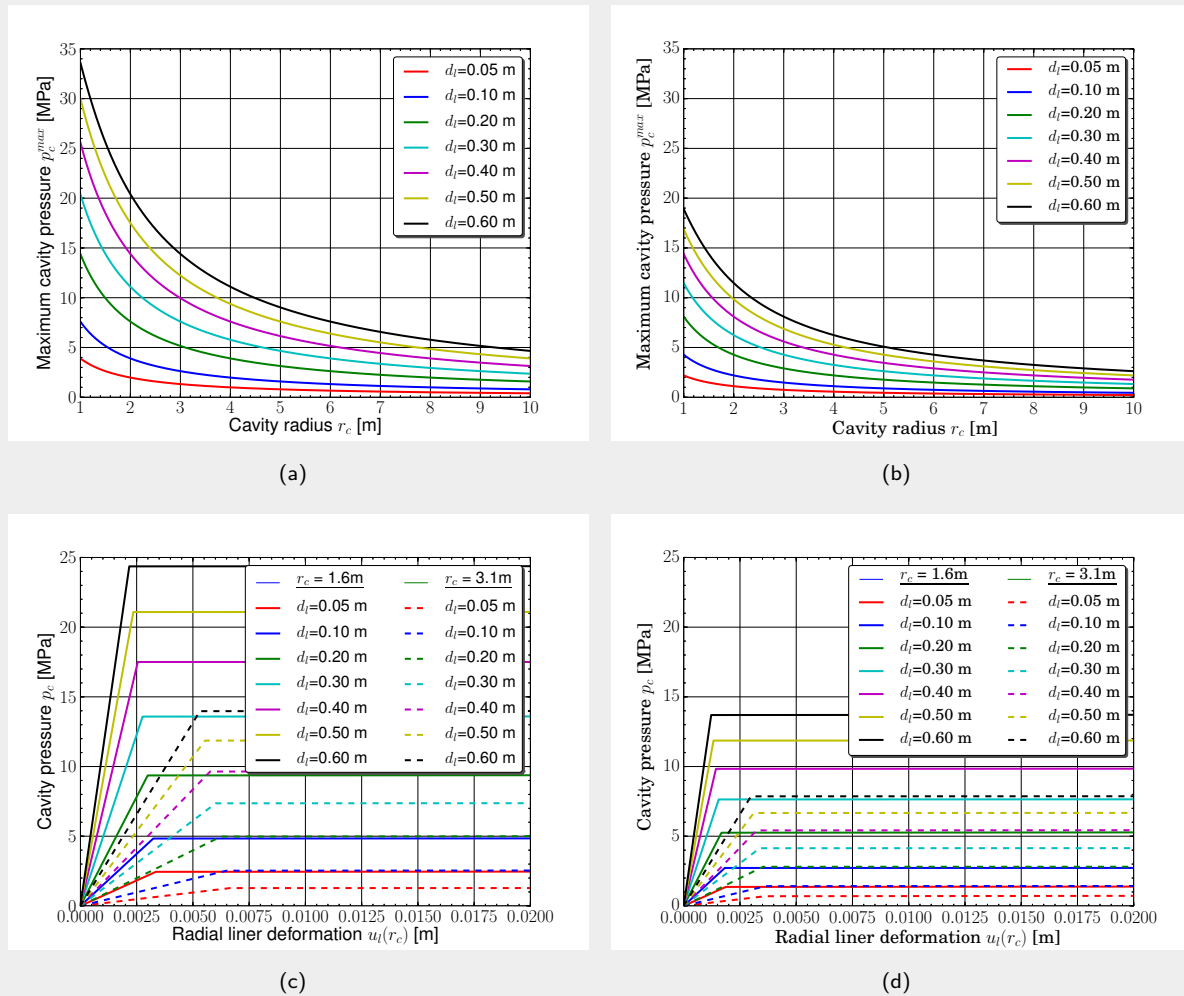
Figure 4.4.: Cavity radius r_c versus maximum compression strength of the liner p_c^{max} for different liner thickness d_l given a compressive concrete strength of (a) $\sigma_{cc} = 80$MPa and (b) $\sigma_{cc} = 45$MPa. Radial liner deformation at the cavity interface $u_l(r_c)$ versus the resulting cavity pressures p_c for different liner thickness d_l and two different cavity radii r_c given a compressive concrete strength of (c) $\sigma_{cc} = 80$MPa and (d) $\sigma_{cc} = 45$MPa.

on the excavation machine used, which is designed based on the geological and hydrological boundary conditions (e.g. Maidl et al., 2012). For instance, an overcut of 45mm was used during the excavation of the connecting gallery at the HADES URF in Mol (Bastiaens et al., 2003). In this study the influence of three different, conservatively chosen, overcuts d_{oc} of 50mm, 75mm and 100mm on the extent of the plastic radius are investigated.

The dimensions of the individual galleries given by Verhoef et al. (2011) have been tabulated in Table 2.7. Three excavation cases will be assessed here, that is, the excavation of a HLW disposal gallery ($r_c = 1.6$m), the excavation of a LILW disposal gallery or main/secondary gallery ($r_c = 2.4$m) and the excavation of the shaft ($r_c = 3.1$m).

Results

Figures 4.5 and 4.6 show the stresses around a cavity with an impermeable concrete liner, that is, for a fixed cavity pressure of $p_c = 6.5$MPa being applied and a cavity pressure in equilibrium p_c^{eq}, respectively. The latter is the response to be expected in reality when installing the same liner in a host rock with different properties. The responses are computed for the excavation of a HLW disposal cell at a depth of 500m, with a cavity radius of $r_c = 1.6$m, a concrete liner thickness of $d_l = 0.50$m and a hypothetical overcut of $d_{oc} = 75$mm. The deterministic responses have been computed for the three mean property values selected for each model parameter as defined in Table 4.1.

In both cases (Figures 4.5 and 4.6) the stresses at the EP interface, $\bar{\sigma}_{rr}$ and $\bar{\sigma}_{\theta\theta}$ (Equation 4.65), are significantly influenced by the friction angle φ' and to minor extent by the initial yield stress and thus by the initial cohesion c_0' (Equation 4.35b). The influence of the Poisson's ratio on the stresses at the EP interface vanishes due to the initial stress state being assumed to be isotropic ($\sigma_{h,0} = \sigma_{v,0}$).

Given a hypothetically fixed pressure being applied to the cavity, the non-linear increase in plastic radius r_p with a decreasing soil friction angle φ' is significant (Figure 4.5(c)). However, with the installation of the same liner for all three cases $\varphi' = \{7.5°, 12.5°, 17.5°\}$, the potentially larger deformations accompanying a weaker soil, i.e. having a lower friction angle, are compensated by a higher cavity pressures p_c^{eq}. Hence, the ultimate extent as well as the relative extent of the plastic radius decreases significantly compared to fixing the cavity pressure (Figure 4.6(c)).

Given the high confining stress associated with a tunnel located at a depth of 500m, the extent of the plastic radii are less sensitive to a variation in the initial cohesion c_0' and the residual cohesion c_r', than to a variation in the soil friction angle φ' (Figures 4.5(a)–(b) and 4.6(a)–(b)). The increase in plastic radius with decreasing cohesion becomes less significant for the higher cavity pressures in equilibrium (Figures 4.6(a)–(b)).

For a constant cavity pressure the Young's modulus only marginally influences the plastic residual radius (Figure 4.5(d)), by definition of the yield stress (Equations 4.32 and 4.33). The relative decrease in cavity pressure in equilibrium, with increasing Young's modulus, leads to

(a) Initial cohesion c'_0

(b) Residual cohesion c'_r

(c) Friction angle φ'

(d) Young's modulus E'

(e) Tangent modulus E'_t

(f) Poisson's ratio ν'
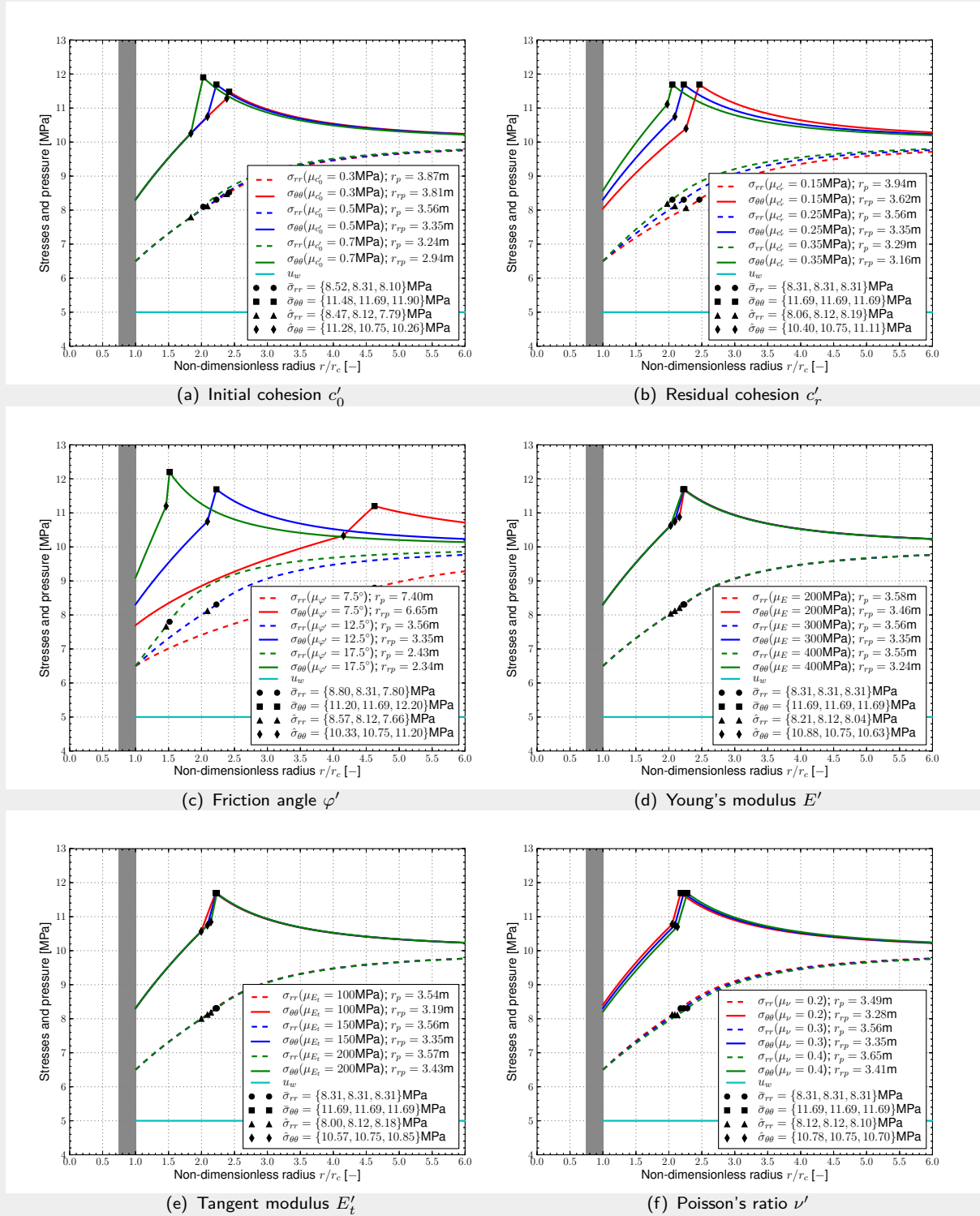
Figure 4.5.: Stress distributions around a cavity of radius $r_c = 1.6$m, at 500m depth and for a constant cavity pressure of $p_c = 6.5$MPa, for varying individual deterministic soil property values.

(a) Initial cohesion c_0'

(b) Residual cohesion c_r'

(c) Friction angle φ'

(d) Young's modulus E

(e) Tangent modulus E_t

(f) Poisson's ratio ν
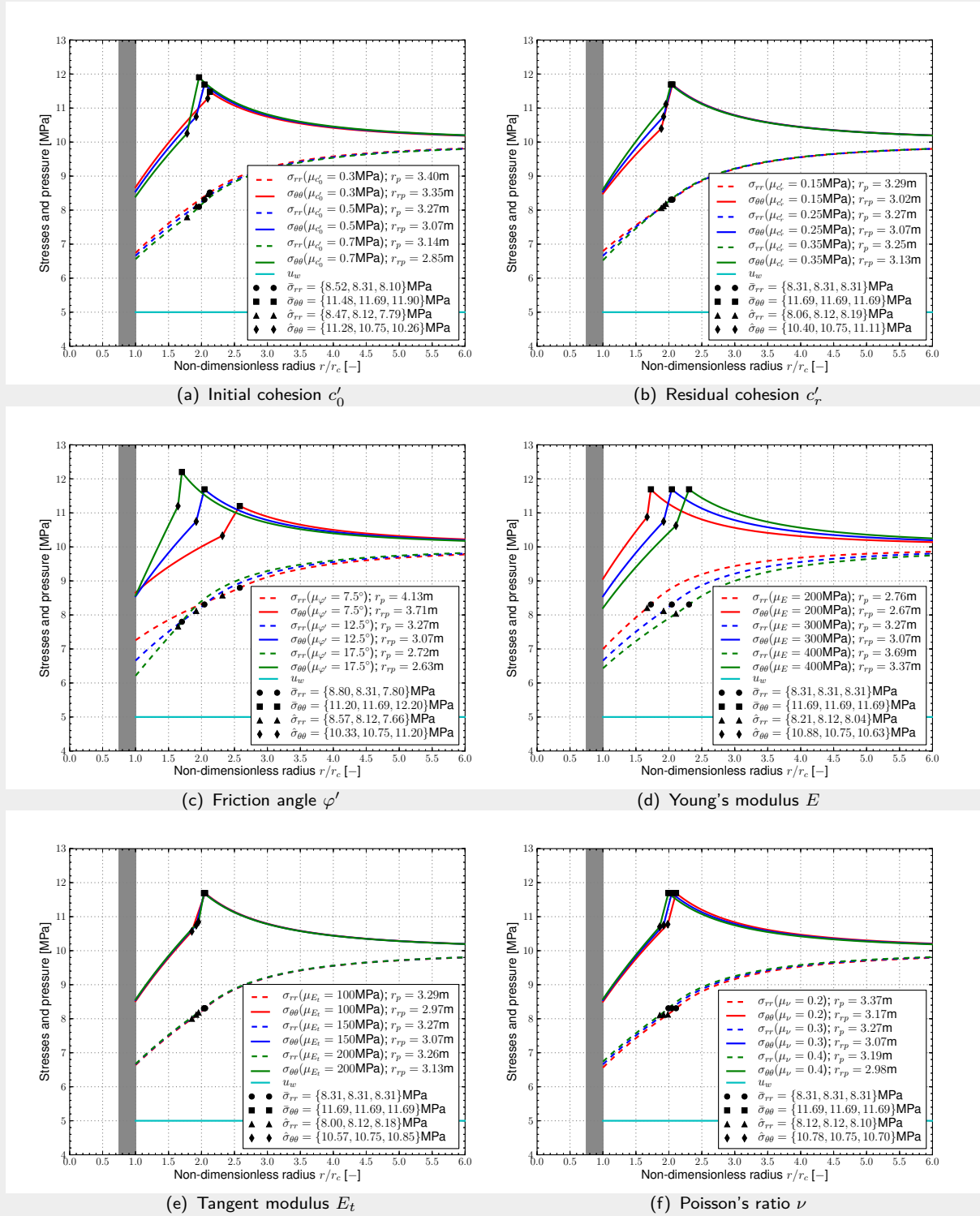
Figure 4.6.: Stress distributions resulting from the lining pressures in equilibrium p_c^{eq} around a cavity of radius $r_c = 1.6$m at 500m depth, with an impermeable concrete liner thickness of $d_l = 0.05$m and an overcut of $d_{oc} = 75$mm, for varying individual deterministic soil property values.

a more significant relative extent of the plastic zone with respect to the cavity pressure being fixed (Figure 4.6(d)). A similar but much less distinct behaviour is visible for the tangent modulus E_t (Figures 4.5(e) and 4.6(e)). A variation in Poisson's ratio influences only slightly the extent of the plastic radius (Figures 4.5(f) and 4.6(f)).

For all deterministic responses investigated, a limiting plastic radius of $r_{p,lim} = 16.67$m is satisfied for all cases investigated. Given the set boundary conditions for a HLW gallery ($d = 500$m, $r_c = 1.6$m, $d_l = 0.50$m, $d_{oc} = 75$mm), the maximum plastic radius and residual plastic radius were found for the low friction angle case ($\varphi' = 7.5°$) as $r_p = 4.13$m and $r_{rp} = 3.71$m respectively (Figure 4.6(c)). The same case resulted in the largest cavity pressure in equilibrium of $p_c^{equ} = 7.26$MPa, which is significantly lower than the collapse support load of the HLW gallery liner of $p_c^{max} = 21.09$MPa for a concrete with a compressive strength of $\sigma_{cc} = 80$MPa (Figure 4.4(a,c)). As well, for a compressive concrete strength of $\sigma_{cc} = 45$MPa (Figure 4.4(b,d)), the the collapse support load of the HLW gallery liner of $p_c^{max} = 11.86$MPa is not exceeded.

Figure 4.7 shows the Boom Clay response with respect to varying model and boundary conditions for a friction angle of $\varphi = 7.5°$, i.e. leading to an upper bound response in terms of the extent of the plastic radius and magnitude of the cavity pressure.

Figure 4.7(a) exemplary shows the stress around the cavity with no softening and a lower bound cohesion $c_0' = c_r' = 0.25$MPa, with softening $c_0' = 0.5$MPa and $c_r' = 0.25$MPa, and with no softening and upper bound cohesion $c_r' = c_0' = 0.5$MPa. Although the extent of the plastic radius is similar for the no-softening upper bound response and the softening response, the cavity pressure is significantly larger for the latter case accounting for softening.

Figure 4.7(b) shows an increase in the extent of the plastic radius and a decrease in the resulting cavity pressure due to an increasing overcut d_{oc}. The extent of the radial and tangential stresses at the EP and RP interfaces are not influenced.

With increasing depth (Figure 4.7(c)) the extent of the plastic radii slightly decrease due to the increase in confining stress, whereas the total cavity pressure significantly increases to $p_c^{equ} = 10.7$MPa for a HLW gallery located at 700m depth, which is just below the collapse load for a HLW gallery liner with a compressive concrete strength of $\sigma_{cc} = 45$MPa (Figure 4.4(d)).

Figure 4.7(d) shows the variation in the stress response for the excavation of the HLW disposal galleries ($r_c = 1.6$m, $d_l = 0.5$m) compared to the excavation of the main/secondary/LILW galleries ($r_c = 2.4$m, $d_l = 0.55$m), and the shaft ($r_c = 3.1$m, $d_l = 0.6$m). Also the non-dimensional plastic radius decreases with increasing cavity radius. The absolute extent of plastic zone increases to a maximum of 6.03m around the shaft at 500m depth. The non-linear increase in plastic radii is due to the fact that the same cavity deformation, i.e. the same overcut, was imposed for all three cases, leading to a non-linear decreasing d_{oc}/r_c ratio. The liner collapse loads, p_c^{max}, decrease when increasing the cavity radius to $r_c = 3.1$m to 11.86MPa and 7.87MPa (utilising a liner thickness of $d_l = 0.6$m and a compressive concrete strength of 80MPa and 45MPa respectively, see Figures 4.4(c-d)), which is just above the cavity pressure in equilibrium computed with this analytical model.

(a) Variation of softening response

(b) Variation of overcut d_{oc}

(c) Variation of depth d

(d) Variation of cavity radius r_c
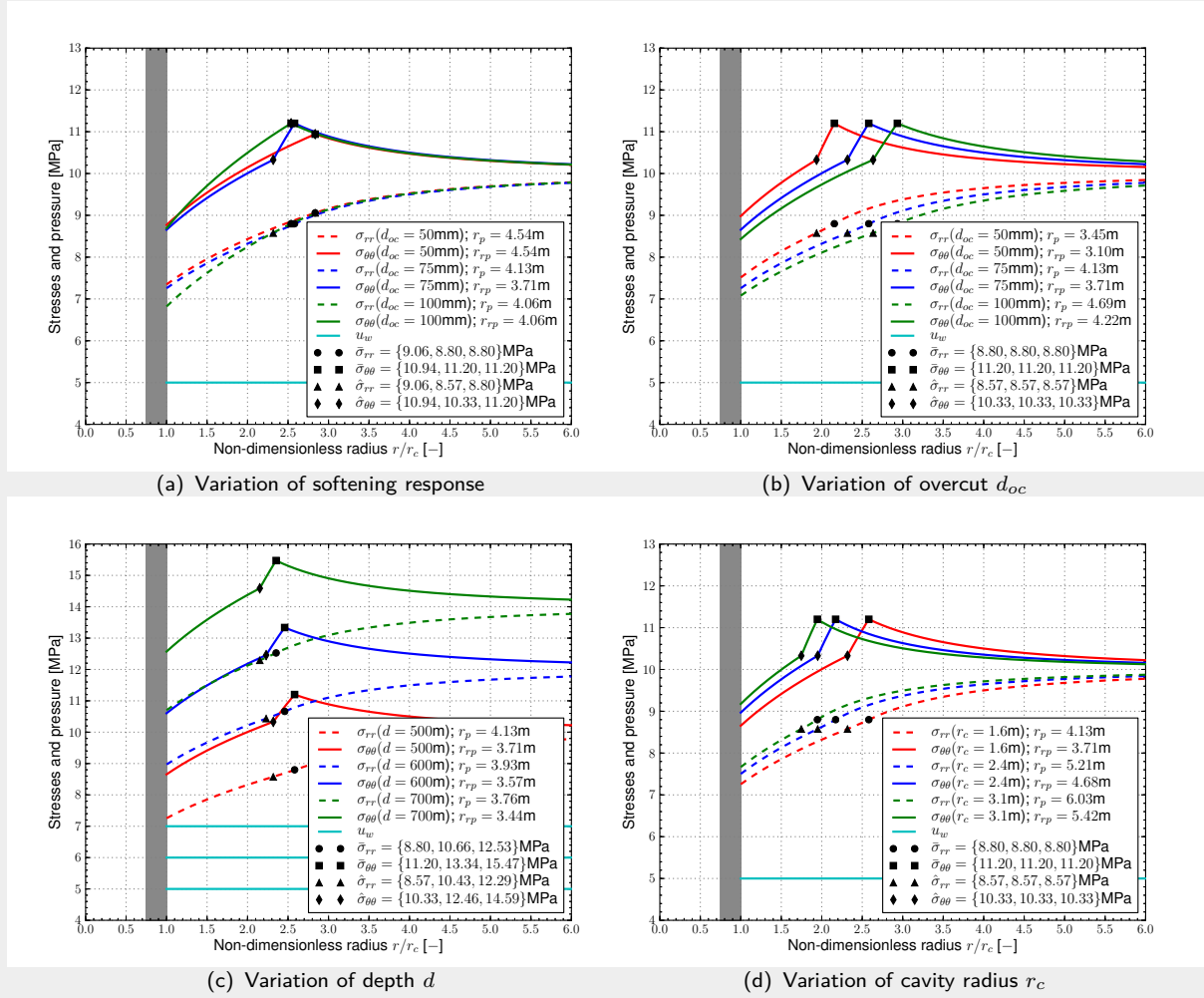
Figure 4.7.: Stresses around cavity for Boom Clay with a low friction angle of $\varphi'_{min} = \varphi' = 7.5°$, a cavity radius of $r_c = 1.6$m, a liner thickness of $d_l = 0.50$m, an overcut of $d_{oc} = 75$mm and a burying depth of 500m. The following variations are shown: (a) Boom Clay with (I) no softening and lower bound cohesion $c'_0 = c'_r = 0.25$MPa, (II) with softening $c'_0 = 0.5$MPa and $c'_r = 0.25$MPa, and (III) no softening and upper bound cohesion $c'_r = c'_0 = 0.5$MPa, (b) excavation with varying overcut d_{oc}, (c) excavation at varying depth d, and (d) excavation with varying cavity radii r_c.

For the case of a low friction angle, $\varphi' = 7.5°$, a decrease of the liner thickness for the HLW galleries from $d_l = 0.5$m to $d_l = 0.3$m and $d_l = 0.1$m increases the extent of the plastic zone slightly from 4.13m to 4.14m and 4.16m respectively. Note, the collapse load would be exceeded for the liner with a thickness of 10cm (Figure 4.4(b)). This minor variation between the plastic radii results from the low elastic liner deformation u_l with respect to the larger overcut d_{oc}.

4.8. Summary

In this chapter an analytical model for an elasto-plastic strain-softening material is presented, with the to aim to provide a simple and computationally cheap tool to assess the Boom Clay response around a tunnel, initially in a deterministic manner. The module is later implement in a probabilistic framework (see Chapter 7).

Given a set of simplifying assumptions the constitutive framework is first derived and its implementation into a computer program outlined.

The Boom Clay response, which is assessed by means of deterministic analyses for varying soil property values, showed that a variation of the friction angle φ' most affects the system response in terms of maximum plastic radius and maximum cavity pressure. Furthermore, a variation in boundary conditions result in a change in the extent of the plastic radius, primarily for changes in the overcut d_{oc} and cavity radius r_c, and cavity pressure, primarily for change in depth d of the repository.

Given the assumptions made for the presented analytical model, the limited extent of the plastic zone suggests that the spacing of the disposal galleries may be reduced. Furthermore, for all deterministic cases assessed the liner collapse load was not reached for a liner with a compressive concrete strength of $\sigma_{cc} = 80$MPa and thus a reduction in liner thickness may be possible. However, for a concrete with a lower compressive strength of 45MPa the collapse load was nearly reached when increasing the cavity radius or burying depth and therefore may not satisfy design criteria.

5. Constitutive modelling of Boom Clay

5.1. Introduction

In Section 2.4 the complex nature of the coupled THM behaviour of natural and reconstituted Boom Clay was reviewed. This Chapter aims to review the constitutive modelling of Boom Clay, to assess the performance of different models and to select one constitutive model for the later numerical modelling of the excavation of the OPERA repository galleries.

Section 5.2 summarizes some of the existing constitutive soil models used, or newly developed, to describe the THM behaviour of Boom Clay, that is, for soil element tests (stress-strain path level) as well as in numerical analyses of boundary value problems. The modelling approach utilised for selecting a constitutive soil model for this research is described in Section 5.3. In Section 5.4 four models will be tested against a set of triaxial and oedometer laboratory test data. Subsequently their individual performances will be assessed and the selection of the most suitable model justified. The formulation of the selected Hardening Soil model as well as its implementation in the PLAXIS FE software package is described in more detail in Section 5.5. A mechanical sensitivity analysis is performed under triaxial conditions in Section 5.6, that is, to see the relative change in responses due to a deterministic variations of individual model parameters. Section 5.7 concludes this Chapter.

5.2. Review of constitutive modelling of Boom Clay

Both *Mohr-Coulomb* (MC) type as well as *Cam-Clay* (CC) type soil models have been primarily used to model the mechanical behaviour of Boom Clay. Models based on critical state theory (e.g. of CC type) are accepted and widely used to model clays (e.g. Gens and Potts, 1988; Wood, 1990, 2004). In the TRUCK II project (Barnichon et al., 2000, see Section 2.2.1.4), the TRACTOR study (Wildenborg et al., 2000, see Section 2.2.1.5) and the CLIPEX project (e.g. Bastiaens et al., 2003; Bernier et al., 2007a; Li et al., 2006; Vaunat et al., 2011, see Section 2.2.3.1), both the elastic-perfectly plastic Mohr Coulomb model as well as the *Modified Cam-Clay* (MCC) model (Roscoe and Burland, 1968) have been used to model numerically the mechanical response of the Boom Clay due to the excavation of tunnel galleries in one, two and three dimensions. The *"relative simplicity"* of these models was one of the main reasons given in the reports to underlay the modellers choices.

The results obtained using the MC model, deformations and hydraulic disturbance, agree

qualitatively well with the in situ measurements but far-field variations in pore-pressure are underestimated (Li et al., 2006).

In Section 2.4.3.2 the material anisotropy leading to an anisotropic response (e.g. see Figures 2.46 and 2.49) was discussed. Based on a series of triaxial tests on natural Boom Clay, Sultan et al. (2010) proposed an elasto-plastic model accounting for isotropic and anisotropic hardening (see Figure 2.26). The model, proposed in the critical state framework and developed for triaxial stress states, captures well the change in yield surface location, size and orientation, although the formulations would have to be extended for a full mesh analysis. Yu et al. (2013a) formulated a model for Boom Clay combining a transversely isotropic elastic damage model with a modified MC criterion. As part of the TIMODAZ project, François et al. (2011) developed a *Drucker-Prager* (DP) hardening/softening model for cross-anisotropic soft rock (see Section 4.4.4, page 145), with which they were able to reproduce the eye-shaped excavation damage zone observed around an excavation in Boom Clay as well as the shear band pattern by using a numerical regularization method. Further models have been developed to account for soil structure and anisotropy in stiff and overconsolidated clays, e.g. Graham and Houlsby (1983), Whittle (1993), Liu and Carter (2002), Baudet and Stallebrass (2004), Suebsuk et al. (2010), Suebsuk et al. (2011).

The thermo-mechanical behaviour of Boom Clay was briefly discussed in Section 2.4.3.4. Hueckel and Borsetto (1990) and Hueckel and Baldi (1990) were the first to extend the MCC model to account for temperature effects on the pre-consolidation stress in Boom Clay. More advanced elasto-thermo-plastic constitutive frameworks have been developed in recent years, amongst others, by Robinet et al. (1996), Cui et al. (2000), Graham et al. (2001), Abuel-Naga et al. (2007), Laloui and François (2009) based on work by François (2008), Dizier (2011) and Hamidi et al. (2014). All of the listed non-isothermal models employ some critical state framework based on a Cam-Clay type formulation to model the mechanical response. Using the experimental results of thermo-mechanical loading tests by Baldi et al. (1991a,b), Hong et al. (2013) recently critically assessed the performance of three of these constitutive models. They showed that the thermo-mechanical response of saturated Boom Clay was reasonably well predicted by all models tested, though with each model having shown some individual drawbacks. A benchmark study for modelling the PRACLAY large scale excavation and heater in-situ experiment in two and three dimensions, as part of the TIMODAZ project (see Section 2.2.3.2), showed that the results obtained by different teams were in good agreement (Charlier et al., 2010b).

5.3. Modelling approach

For the two- and three-dimensional numerical modelling of the Boom Clay response around the repository galleries, the commercial geotechnical Finite Element code PLAXIS 2D AE and PLAXIS 3D (Plaxis, 2013b, 2014d) were utilised in this research project.

The PLAXIS software package contains a number of constitutive soil models readily available for the engineer (Plaxis, 2014c). However, the possibility exists within PLAXIS to utilize

user-defined soil models which allow for an implementation of any desired constitutive relationship for stress-strain. As discussed in Section 5.2, some advanced constitutive frameworks for modelling Boom Clay have been developed, some of which are partly/fully implemented in different research-based Finite Element programs. However, for this work it was decided to utilise existing soil models and investigate their ability to describe the features of Boom Clay relevant to modelling the excavation of a cavity at large depth. The potential implementation of a more advanced and tailored constitutive soil model framework accounting, for instance, for the anisotropy and time dependency of the material behaviour was disregarded for this study.

In the following Section 5.4, four soil models are tested against laboratory date utilising the *SoilTest facility* available in the PLAXIS software package (Plaxis, 2014d, page 148 ff), which is based on a single point algorithm. For each individual model tested, one set of parameters will be iteratively optimised to best fit the responses of three drained triaxial tests consolidated to different OCS's and one high pressure oedometer test.

5.4. Model testing

5.4.1. Material model descriptions

In this section the key features of the four models tested will be described briefly, that is, without discussing their governing equations in detail. Further information on the models can be found in Plaxis (2014c), as well as in the individual references given for each model. A detailed description of the Hardening Soil model, selected for this study, will follow in Section 5.5.

1. *The Linear Elastic-Perfectly Plastic Mohr Coulomb (LEPP-MC) model:*

   The model response is isotropic linear elastic and perfectly plastic for stress states on the Mohr Coulomb type yield surface (e.g. Wood, 2004, p 124ff). With two elastic parameters (Young's modulus E, Poisson's ratio ν), two limiting shear stress parameters (effective cohesion c', effective friction angle φ') and one parameter defining volume change due to failure (dilation angle ψ), the LEPP-MC model is the most simplistic of the four models tested.

2. *The Modified Cam-Clay (MCC) model:*

   The elasto-plastic MCC model (Roscoe and Burland, 1968), which is an extension of the original Cam-Clay model (Schofield and Wroth, 1968), is formulated in the framework of *Critical State* (CS) soil mechanics. The stress-strain relationship is defined by a *Normal Consolidation Line* (NCL) and an *Unloading-Reloading Line* (URL), both of which are assumed to be straight lines in the specific volume vs. logarithmic effective mean stress space ($v = 1 + e : \ln p'$), with their gradients being defined as λ and κ, respectively (e.g. Wood, 1990). The un-/reloading Poisson's ratio ν_{ur} is here the second variable required

to describe the elastic response. The flow on the elliptical yield locus is assumed to be associated and the isotropic hardening is a function of the volumetric plastic strains. The *Critical State Line* (CSL), i.e. the state in which a change in stress induces no volume change, is defined by the slope of the CSL, M, assuming a DP failure criterion in the π-plane, i.e. the plane normal to the hydrostatic axis in the $\sigma_1 : \sigma_2 : \sigma_3$ principal stress space.

3. *Soft Soil Creep (SS-C) model:*

   Based on the MCC model and elasto-visco-plasticity theory, Vermeer and Neher (1999) developed the SS-C model to capture phenomena such as undrained creep, overconsolidation and ageing. The model is based on a one-dimensional logarithmic creep law extended to general states of stress and strain within the framework of CS soil mechanics using a MC failure criterion. The elastic strains are computed via the un-/reloading Poisson's ratio, ν_{ur}, and the modified swelling index, κ^*. The MCC-type cap yield surface extends due to creep, that is, within 1 day (fixed model parameter) the new stress state is adapted. The modified compression index, λ^*, and the modified creep index, μ^*, specify the creep rate after 1 day (Waterman and Broere, 2004). The model is suitable to predict, for instance, the settlement of soft soils due to secondary compression under footings, or the long term deformation of soil slopes due to creep (Vermeer and Neher, 1999; Waterman and Broere, 2004).

4. *The Hardening Soil (HS) model:*

   The HS model is an elasto-plastic constitutive soil model developed by Schanz (1998) and Schanz et al. (1999). Figure 5.1 shows the model in mean stress vs. deviatoric stress, $p : q$, space. The HS model is based on a hyperbolic stress-strain relationship and consists of a shear hardening cone-type yield locus, f^s, and a compression hardening cap-type yield locus, f^c, both activated due to primary deviatoric and compressive loading, respectively.

   The material response is non-linear elastic inside the yield loci, or linear elastic under triaxial conditions (constant σ_3'). Non-linear elasto-plastic strains induced by shear hardening are primarily controlled by the secant modulus E_{50}, whereas the Oedometer modulus E_{oed} controls the elasto-plastic strains induced due to cap hardening. The MC criterion defines failure.

   The HS model is one of the advanced soil models implemented in PLAXIS which is more commonly utilised by geotechnical engineers to compute soil response under compressive loading as well as extensive-shear loading, e.g. due to soil excavation.

5.4.2. Description of selected triaxial and oedometer tests

For this investigation the results of three strain-controlled drained triaxial shear tests and one high pressure oedometer test performed by Deng et al. (2011a), on intact BC samples cored
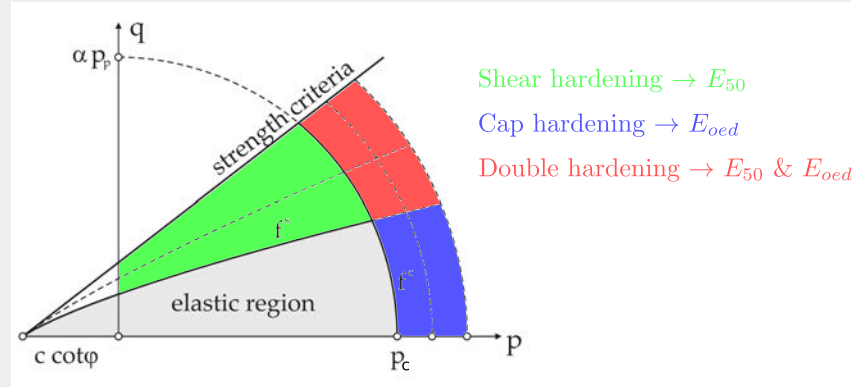
Figure 5.1.: The elasto-plastic HS model showing the shear hardening yield locus, f^s, and cap hardening yield locus, f^c, in mean stress vs. deviatoric stress, $p : q$, space where c is the cohesion, φ is the friction angle, p_c is the pre-consolidation stress, α is the HS cap parameter, E_{50} is the secant modulus and E_{oed} is the oedometer modulus (adapted from Benz, 2006).

from the Essen-1 borehole in Belgium (see Figure 2.4), are utilised to assess in detail the material response under triaxial and oedometer loading as well as to evaluate the capabilities of the four models selected to reproduce the deviatoric and volumetric behaviour observed.

Boom Clay properties, sample preparation and test setup

The soil core *Ess75* was sampled at a depth between 218.91-219.91m in the Putte member, which is the upper dark clay member of the Boom Clay (see Table 2.8). The mineralogical and physical properties of the core are tabulated in Table 5.1. With 44% the clay fraction is in the lower medium range of the spectrum of values found in the literature and the relative low smectite and high kaolinite content explain the relative low plasticity index and thus the potentially relatively low swelling potential (compare Table 5.1 to Tables 2.9 and 2.10).

Table 5.1.: Mineralogical composition of the clay fraction ($< 2\ \mu$m) and physical properties BC of core *Ess75* (Deng et al., 2011a).

Mineral	Content [%]	Variable	Symbol	Unit	Value
Chlorite	5	Specific gravity	G_s	[−]	2.65
Caolinite	35	Liquid limit	w_L	[%]	78
Illite	20	Plastic limit	w_P	[%]	33
Smectite	10	Plasticity index	I_P	[%]	45
Illite/Smectite	30	Water content	w	[%]	29.7
		Initial void ratio	e_0	[−]	0.785
		Degree of saturation	S	[%]	100
		Methylene blue value	MBV	[−]	6.47
		Carbonate content	CC	[%]	0.91

First the samples were trimmed with a wire saw (76mm in height, 38mm in diameter). No desaturation of the specimen was reported during the transport, storage and sample preparation. Subsequently the samples were installed in a triaxial apparatus and saturated with a synthetic water solution having the same chemistry as the in-situ pore water. During saturation a constant initial confining pressure corresponding to a hydrostatic in situ vertical effective stress of $\sigma'_{v,0} = 2.2$MPa was applied to prevent a potential microstructure loss due to swelling. Based on Table 2.10 the assumption of $\gamma \simeq 20$kN m^{-3} seems realistic. For all oedometer tests $\sigma'_{v,0}$ was set to 2.4MPa for convenience reasons (Deng et al., 2011a). After saturating the samples in the triaxial cell, both the confining and back pressure were increased stepwise until a back pressure of 1MPa.

Three consolidated-drained, strain-controlled triaxial tests were performed on the material of the core Ess75. The axial strain rate during shearing was kept constant, equal to $\dot{\varepsilon}_a = 1.31\times 10^{-5}$min^{-1}. In the first test (*Ess75Tr01*) the soil specimen was immediately sheared, with an *Over-Consolidation Ratio* (OCR) equal to 1, until an axial strain of $\varepsilon_a \approx 17.04\%$. In the second test (*Ess75Tr02*) the sample was isotropically unloaded to $p' = 1$MPa ($OCR = 2.2$) and then sheared up to $\varepsilon_a \approx 18.87\%$. For the third test (*Ess75Tr03*) the specimen was isotropically unloaded to $p' = 0.5$MPa ($OCR = 4.4$) and subsequently sheared until $\varepsilon_a \approx 18.48\%$. The test specifications described above are summarised in Table 5.2.

The results of the three triaxial shear tests *Ess75Tr01-03* in $p' : \varepsilon_v$, $p' : q$, $\varepsilon_a : q$ and $\varepsilon_a : \varepsilon_v$ space are shown Figure 5.2.

Summary of triaxial tests Ess75Tr01-03

Based on Figure 5.2 some general comments can be made on the behaviour of the BC material of the *Ess75* core:

○ The soil behaviour is non-linear throughout the tests.

○ The material response, in terms of mobilised shear strength, stiffness evolution and volume change, is highly dependent on the level of the confining stress and the amount of over-consolidation.

○ The soil stiffness decreases with increasing axial strain, which is significant for $\varepsilon_a \gtrsim 0.7\%$.

Table 5.2.: Triaxial test specifications (Deng et al., 2011a)

Variable	Symbol	Unit	*Ess75Tr01*	*Ess75Tr02*	*Ess75Tr03*
Isotropic consolidation stress	p'_c	[MPa]	2.2	2.2	2.2
Pressure after isotropic unloading	p'_0	[MPa]	2.2	1.0	0.5
Over-Consolidation Ratio	OCR	[$-$]	1.0	2.2	4.4
Final axial strain	ε_a	[%]	17.04	18.87	18.48

Due to the *Normally Consolidated* (NC) conditions, for which the specimen behaves in a ductile manner, as well as due to the high level of confinement applied during shearing ($\sigma'_3 = 2.2$MPa), the soil in test *Ess75Tr01* exhibits the stiffest response and the most shear strength is mobilised (Figure 5.2(b)). The specimen responds in a very plastic manner with the highest volumetric strains, ε_v, being mobilised, but the critical state seems to be not reached (Figure 5.2(d)).

The lightly *Over-Consolidated* (OC) soil sample in test *Ess75Tr02* exhibits a less stiff response and less shear strength is mobilised than for the NC sample (*Ess75Tr01*). Moreover, a peak shear stress and subsequent strain softening can be observed in Figure 5.2(b). The more brittle, i.e. less plastic, response can be further justified by the smaller amount of volumetric strains generated compared to the test *Ess75Tr01* (Figure 5.2(d)). Again, neither the contraction of the specimen nor the deviator stress reached a residual state which, again, may be due to the relatively high level of confinement.

The moderately OC material tested in *Ess75Tr03* shows the least stiff response and the lowest values of mobilised shear strength. Again, a distinct peak and subsequent strain soften-
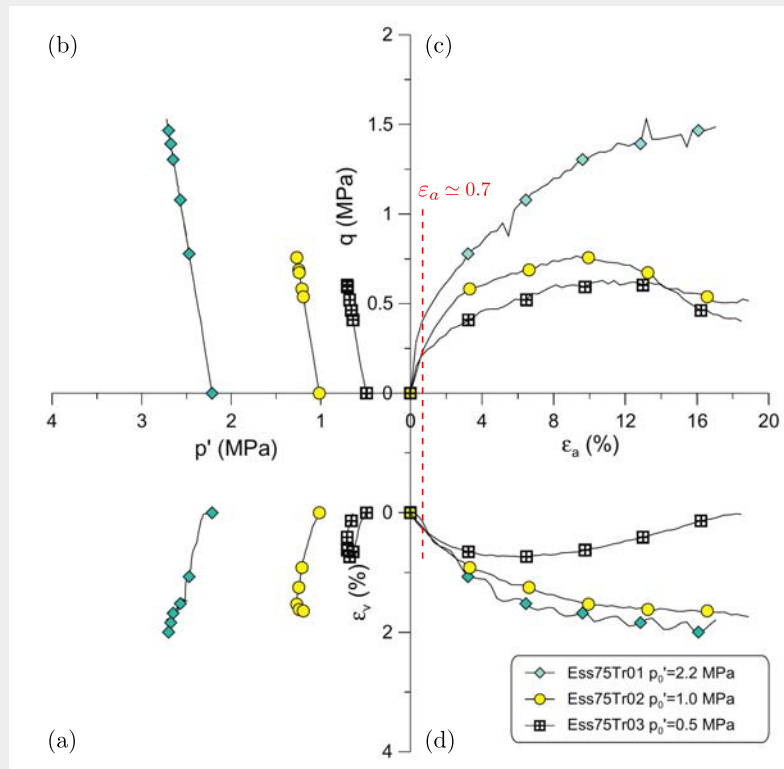
Figure 5.2.: Results of three triaxial shear tests (*Ess75Tr01-03*) in (a) effective mean vs. volumetric stain, $p' : \varepsilon_v$, space, (b) effective mean stress vs. deviatoric stress, $p' : q$, space, (c) axial strain vs. deviatoric stress, $\varepsilon_a : q$, space, and (d) axial strain vs. volumetric strain, $\varepsilon_a : \varepsilon_v$, space, with p'_0 being the consolidation pressure after isotropic unloading (Deng et al., 2011a).

ing can be observed (Figure 5.2(b)). Moreover, due to the large OCR of 4.4 the soil response is dilatant, that is, with a dilatancy angle of $\psi = 1.966° \simeq 2°$ (Deng et al., 2011a). Generally, the same dilatant response would also be expected for test *Ess75Tr02*; however, it seems to have been prevented by the relatively large value of $\sigma'_3 = 1.0$MPa being applied. Hence, it seems that a high level of confinement may cause suppression of the dilatancy of the BC material from the *Ess75* core, for lower values of OCR.

Deng et al. (2011a) determined an effective cohesion of $c' = 0.11$MPa, an effective friction angle of $\varphi' = 12.4°$ and initial Young's moduli, E_0, of 103.8MPa, 50.0MPa and 30.8MPa for tests *Ess75Tr01*, *Ess75Tr02* and *Ess75Tr03*, respectively. The friction angle was back-calculated from a linear fit to the non-curved CSL in the higher stress range (>2MPa) in $p' : q$ space (dashed line in Figure 2.28(b)).

5.4.3. Performance of the material models

Figure 5.3 shows the numerical simulation of the four soil models as well as the test data of the three triaxial tests *Ess75Tr01-03* in $\varepsilon_a : q$ and $\varepsilon_a : \varepsilon_v$ space. The simulated and observed response of the high pressure oedometer test *Ess75Oedo1* is shown in Figure 5.4, in terms of $\sigma'_v : e$ and time:displacement graphs.

Again, one set of parameters for each individual material model was calibrated to best fit all test data. For models which make use of the MC failure criterion, i.e. the LEPP-MC, SS-C and HS model, the effective shear strength parameters determined by Deng et al. (2011a) were fixed ($c' = 0.11$MPa, $\varphi' = 12.4°$). The angle of dilatancy was set to $\psi = 2°$ for test *Ess75Tr03* on the moderately OC sample, and set to zero for the tests *Ess75Tr01* and *Ess75Tr02*. For the SS-C model the time-steps and elapsed times have been set to the test set-up by Deng et al. (2011a).

The performance of each material model is now discussed.

The Linear Elastic-Perfectly Plastic Mohr Coulomb (LEPP-MC) model:

The MC failure criterion predicts the value of deviatoric stress at the end of the test *Ess75Tr01* with very high accuracy (Figure 5.3(a)). It also predicts fairly well the peak deviatoric stress, q_p, in the tests *Ess75Tr02* and *Ess75Tr03* (Figures 5.3(c,e)). The model accounts for the stress dependency of the peak shear strength of the material such that it decreases for a decreasing confinement ($\sigma'_3 = 2.2$MPa $\rightarrow q_p = 1.48$MPa, $\sigma'_3 = 1.0$MPa $\rightarrow q_p = 0.82$MPa and $\sigma'_3 = 0.5$MPa $\rightarrow q_p = 0.55$MPa). However, the LEPP-MC model cannot capture the non-linear dependency of the stiffness and mobilised shear strength of the BC material with respect to the level of confinement and with respect to the value of the OCR.

Furthermore, whereas the volumetric strains at the end of NC test *Ess75Tr01* are predicted with good accuracy (Figure 5.3(b)), this does not hold true for the other two tests on the OC samples (Figures 5.3(d,f)).

The best fit to the triaxial tests results was obtained for a Young's modulus of $E' = 40$MPa and a Poisson's ration of $\nu = 0.25$.
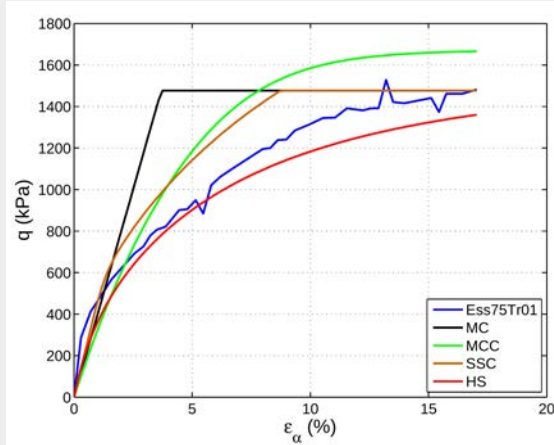
(a) *Ess75Tr01*
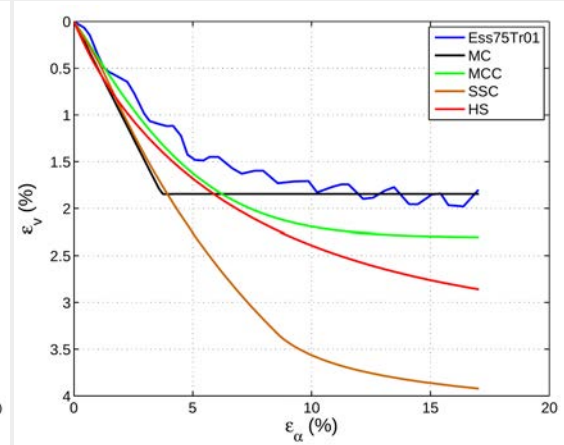
(b) *Ess75Tr01*
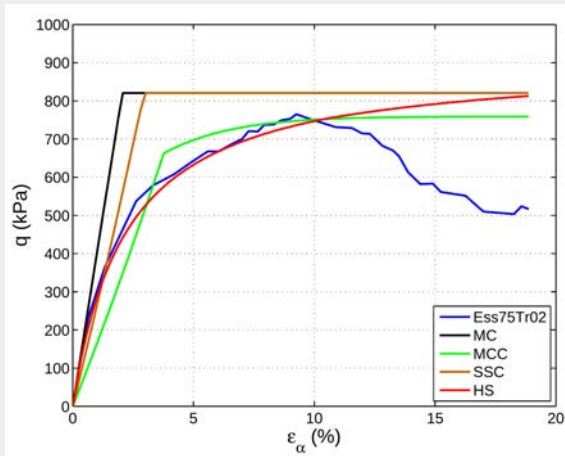
(c) *Ess75Tr02*
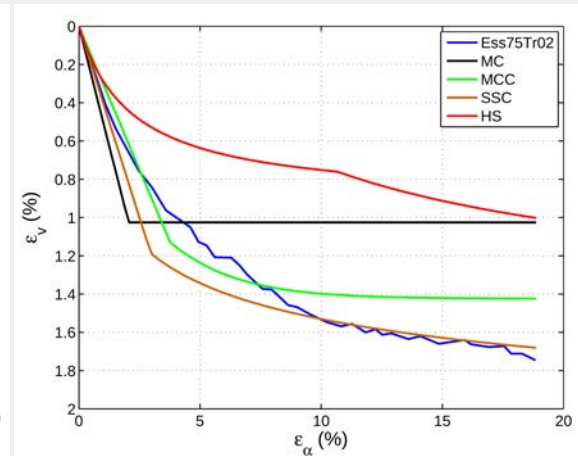
(d) *Ess75Tr02*
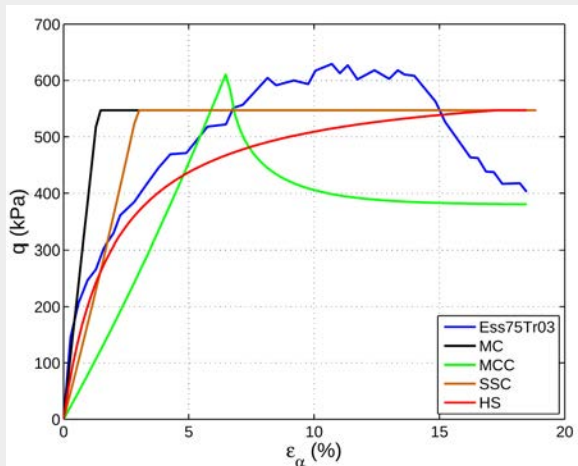
(e) *Ess75Tr03*
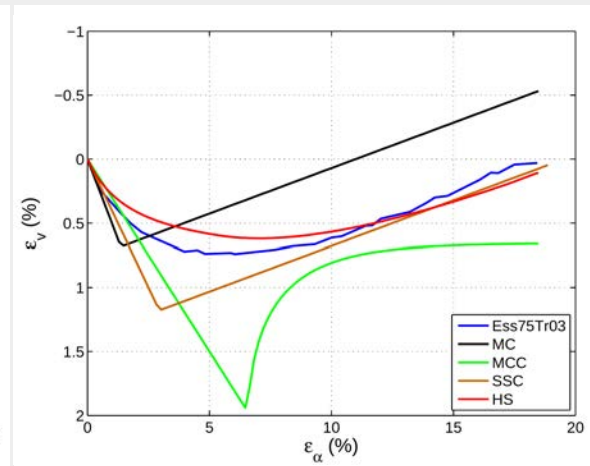
(f) *Ess75Tr03*

Figure 5.3.: Numerical simulation of triaxial tests *Ess75Tr01-03* with four soil models; (a,c,e) axial strains, ε_a, versus deviatoric stress, q, and (b,d,f) axial strains, φ_a, versus volumetric strain ε_v. The laboratory test data (blue line) have been digitised from Figures 5.2(c-d), Deng et al. (2011a).
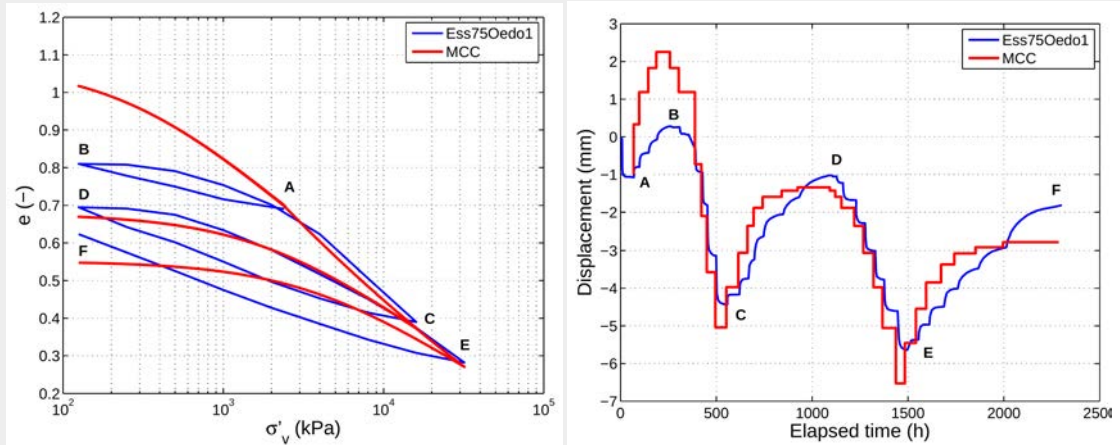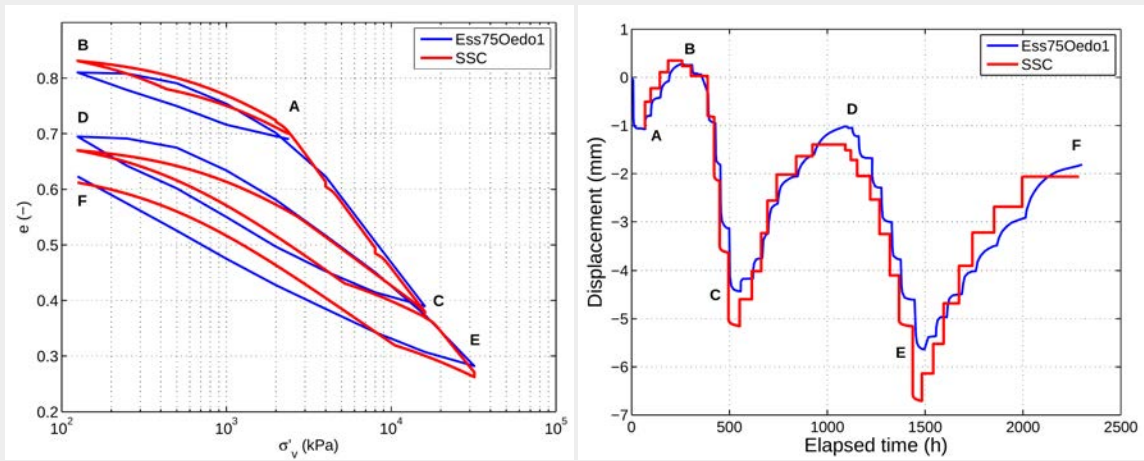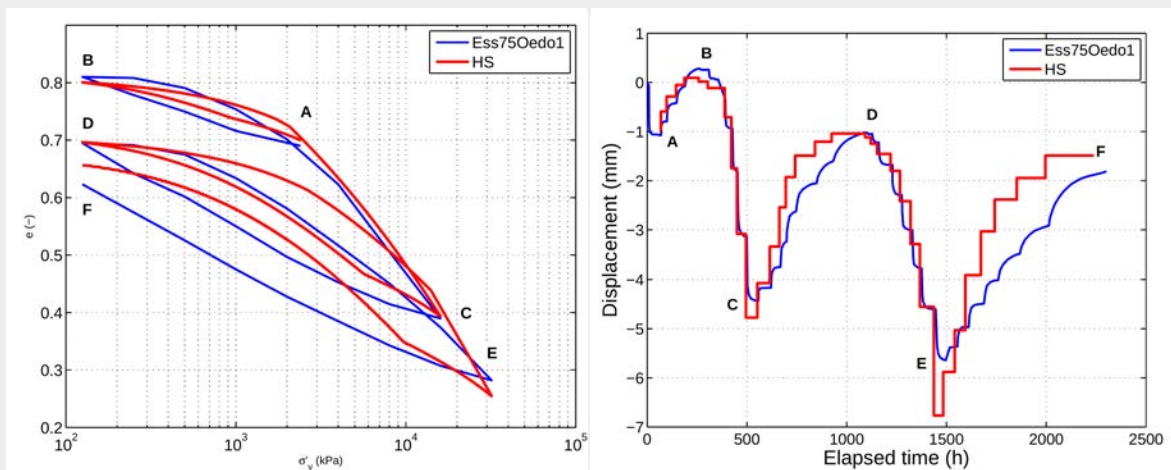
Figure 5.4.: Numerical simulation of the high pressure oedometer test *Ess75Oedo1* with three soil models; (a,c,e) vertical effective stress, σ'_v, versus void ratio, e, and (b,d,f) time versus displacement. The laboratory test data (blue line) have been digitised from Deng et al. (2011a).

The Modified Cam-Clay (MCC) model:

The MCC model is capable of capturing the non-linear response of the soil in the *Ess75Tr01* test with the BC sample being NC (Figure 5.3(a)). Even though the stiffness and mobilised shear strength of the material is initially underestimated and later overestimated by MCC, the shape of the $\varepsilon_a : q$ curve is similar to that of the real test. Furthermore, a slight overestimation of the volumetric strains can be observed in the $\varepsilon_a : \varepsilon_v$ plot (Figure 5.3(b)).

For the *Ess75Tr02* test ($OCR = 2.2$), the evolution of the mobilised shear strength and stiffness of the soil are not reproduced well before yield, neither in $\varepsilon_a : q$ space nor $\varepsilon_a : \varepsilon_v$ space (Figures 5.3(c-d)). On the other hand, strain hardening develops after yield and the peak strength of the sample is predicted accurately. Moreover, the evolution of volumetric strain is fairly well captured, as in the case of the *Ess75Tr01* test.

In the case of the *Ess75Tr03* test ($OCR = 4.4$) the material non-linearity is not well captured before yield (Figure 5.3(e-f)). The inclination of the compression curve ($\delta q / \delta \varepsilon_a \approx$ 9.25MPa) has decreased with respect to test *Ess75Tr02* ($\delta q / \delta \varepsilon_a \approx 17.43$MPa) (Figure 5.3(c)), which indicates the dependency of the stiffness on the level of confinement ($\sigma_3' = 1.0$MPa for test *Ess75Tr02* and $\sigma_3' = 0.5$MPa for test *Ess75Tr03*). The value of the peak strength is very similar to that of the real test, although it is reached at a smaller strain ε_a. Strain softening occurs after yield, an aspect of the BC which is accounted for, although poorly, only by the MCC model. The response in $\varepsilon_a : \varepsilon_v$ space is not well reproduced (Figure 5.3(f)).

The response of the MCC model for the *Ess75Oedo1* test, in terms of $\sigma_v' : e$ and time vs. displacement graphs is shown in Figures 5.4(a-b). The inclination of the virgin compression lines is very similar to that of the real data (Figure 5.4(a)). The same holds true for the void ratio and the displacement (Figures 5.4(a-b)) at points C, D and E. Nevertheless, the model predicts very strong swelling during the first unloading path (A-B). The significant hysteresis of the BC material during the unloading-reloading loops, as shown in Figure 2.22(b), is not captured.

The best fit for the MCC model was obtained for a compression index of $\lambda = 0.12$, a swelling index of $\kappa = 0.10$, a CSL inclination of $M = 0.606$ and an unloading-reloading Poisson's ratio of $\nu_{ur} = 0.35$.

The Soft Soil Creep (SS-C) model:

The SS-C model predicts initially a slightly softer, and later a much stiffer, response of the NC Boom Clay in test *Ess75Tr01* (Figure 5.3(a)). The non-linear material response is reproduced however, failure of the material is reached at a lower shear strain level. Severe divergence from the results obtained by Deng et al. (2011a) is observed in the $\varepsilon_a : \varepsilon_v$ space (Figure 5.3(b)). Note, an OCR of approximately 1.1 ($p_c' = 2.4$) was used in the SS-C model set-up in order to prevent excessive creep volumetric strains.

For the *Ess75Tr02* test ($OCR = 2.2$) and the *Ess75Tr03* test ($OCR = 4.4$), the response of the model is similar to that of a LEPP-MC model, especially in terms of the $\varepsilon_a : q$ space (Figures 5.3(c-e)). The stiffness in the elastic domain is confining stress-dependent,

as it decreases for a decreasing confinement ($\delta q/\delta\varepsilon_a \approx 27.7$MPa for test *Ess75Tr02* and $\delta q/\delta\varepsilon_a \approx 18.6$MPa for test *Ess75Tr03*). The post-peak volumetric response is well captured both for $OCR = 2.2$ and 4.4 (Figures 5.3(d,f)), even though for the latter the $\varepsilon_a : \varepsilon_v$ curve is bi-linear.

The computed responses for the *Ess75Oedo1* test are very similar to the test results presented by Deng et al. (2011a) (Figure 5.4(c-d)). In addition, the hysteresis is predicted fairly well, especially for the second unloading-reloading loop (path C-D, Figure 5.4(c)). The change in inclination of the unloading and reloading branches is also predicted. The time effect, which can be identified by the curvature in the elapsed time vs. displacement graph for the reloading paths B-C and D-E in Figure 5.4(d), is predicted by the model; however, this is not the case for the unloading paths due to purely elastic strains being generated.

The best fit to the test data for the SS-C model was achieved with a modified compression index of $\lambda^* = 0.12$, a modified swelling index of $\kappa^* = 0.07$, a modified creep index of $\mu^* = 0.00172$ and an unloading-reloading Poisson's ratio of $\nu_{ur} = 0.3$.

The Hardening Soil (HS) model:

The HS model seems to reproduce well the deviatoric response for all tests (Figures 5.3(a,c,e)). The process of strain hardening of the BC samples is very well reproduced before reaching the peak for all triaxial tests, although the predicted stiffness is somewhat lower than that of the soil specimens for the *Ess75Tr01* and *Ess75Tr03* tests. The performance of the HS model is good for OC conditions, especially in the lower ranges of axial strain, a fact that was not observed for the other models evaluated. However, the strain softening response of the material is not predicted.

The volumetric behaviour of the BC is fairly well captured for the simulation of the *Ess75Tr01* test (Figure 5.3(b)) and very well reproduced for the *Ess75Tr03* test (Figure 5.3(f)). Nevertheless, the modelled response is very different from the material behaviour observed for the *Ess75Tr02* test where the OCR is 2.2 (Figure 5.3(d)).

The BC response in oedometer stress conditions is well reproduced by the HS model. The inclination of the virgin compression line and the values of the void ratio at the end of the un-/reloading paths predicted by the model are similar to those of the tested soil samples (Figure 5.4(e)). Furthermore, the hysteresis exhibited by the specimen is captured qualitatively well. The change in slope of the unloading and reloading branches is fairly well simulated. The estimated displacements are similar to these of the tested soil sample, that is, except for point E (Figure 5.4(f)).

The best fit of the test data for the HS model was achieved with a reference secant modulus of $E_{50}^{ref} = 8.53$MPa, a reference unloading-reloading modulus of $E_{ur}^{ref} = 20.94$MPa, a reference oedometer modulus of $E_{oed}^{ref} = 11.0$MPa, a rate of stress dependency of stiffness parameter of $m = 0.7$ and an un-/reloading Poisson's ratio of $\nu_{ur} = 0.30$.

5.4.4. Model comparison and selection

Table 5.3 summarizes the model parameter for the four models assessed. It can be seen that, both for the LEPP-MC and MCC models, most parameters are within the ranges observed in previous studies, i.e. with the drained Young's modulus and the URL slope showing lower values than reported in the literature (Table 2.10 and A.2).

   Although being the most simplistic model, the LEPP-MC model predicts the failure of the BC fairly well. However, the strain hardening process observed in the results of the triaxial tests is not reproduced. Moreover, the model does not hold any memory of the pre-consolidation of the material. Calibration of the model for oedometer tests was not possible.

   The MCC model seems to perform well in drained triaxial compression for NC conditions. It also holds memory of the pre-consolidation of the soil. Moreover, it is the only model that accounts for strain softening (qualitatively) for the moderately OC case where $OCR = 4.4$.

Table 5.3.: Summary of BC model parameters from Deng et al. (2011a) and best fit parameter values for the *Ess75* test data.

Model	Variable	Symbol	Value	Unit
Deng et al. (2011)	Initial Young's modulus	E_0	$103.8^{(a)}$ $50.0^{(b)}$ $30.8^{(c)}$	[MPa]
	Effective friction angle	φ'	12.4	[°]
	Effective cohesion	c'	0.11	[MPa]
	Dilatancy angle	ψ	$0^{(a,b)}$ / $2^{(c)}$	[°]
LEPP-MC	Young's modulus	E'	40.0	[MPa]
	Poisson's ratio	ν	0.25	[−]
MCC	Slope of NCL line	λ	0.12	[−]
	Slope of URL line	κ	0.10	[−]
	Slope of CSL	M	0.606	[−]
	Un-/reloading Poisson's ratio	ν_{ur}	0.35	[−]
SS-C	Modified compression index	λ^*	0.12	[−]
	Modified swelling index	κ^*	0.07	[−]
	Modified creep index	μ^*	0.00172	[−]
	Un-/reloading Poisson's ratio	ν_{ur}	0.30	[−]
HS	Reference secant modulus	E_{50}^{ref}	$8.53^{(d)}$	[MPa]
	Reference un-/reloading modulus	E_{ur}^{ref}	$20.94^{(d)}$	[MPa]
	Reference oedometer modulus	E_{oed}^{ref}	$11.0^{(d)}$	[MPa]
	Rate of stress dependency of stiffness	m	0.7	[−]
	Un-/reloading Poisson's ratio	ν_{ur}	0.30	[−]

[a] Test *Ess75Tr01*; [b] Test *Ess75Tr02*; [c] Test *Ess75Tr03*; [d] Reference stress $p^{ref} = 0.1$MPa.

However, the model does not capture well the BC response for $OCR = 2.2$ and $OCR = 4.4$ in the deviatoric $\varepsilon_a : q$ space. The model prediction for the simulation of the oedometer test might be considered as adequate, that is, with respect to the evolution of the void ratio with respect to the vertical effective stress on the reloading paths.

The SS-C model has not performed well in reproducing the deviatoric response of the triaxial tests, i.e. in $\varepsilon_a : q$ space. Furthermore, the volumetric strains, ε_v, are strongly over predicted for the NC case with $OCR \approx 1.1$. On the other hand, the volumetric response of the BC is well simulated for OCR equal to 2.2 and 4.4. Moreover, the SS-C model resulted in the best fit, among the tested models, for reproducing the soil response under one-dimensional loading conditions. The SS-C is the only model that accounts for the viscous (time-dependent) response of the BC.

The HS model is considered to reproduce best the non-linearity of the BC response under triaxial shear loading conditions, that is, with respect to computing the mobilisation of shear strength and the change in stiffness. These aspects of the soil response are well predicted for both NC and OC conditions. The performance of the model is also deemed to be very good for the simulation of the oedometer test. However, the volumetric response of the soil is not well predicted for the *Ess75Tr02* test with the BC being lightly overconsolidated ($OCR = 2.2$). The HS model also does not account for strain softening.

Even though the SS-C model captured very well the response of the BC in oedometer loading, in addition to it being the only model that accounts for material time-dependency, its performance in shearing, which is expected to be a dominant process in the tunnelling process, is considered to be not sufficient to outperform the HS model.

Hence, it is concluded that the overall performance of the HS model is better than that of the other three tested models, as it captures sufficiently most aspects of the BC response under drained triaxial compression and oedometer loading conditions.

5.5. The Hardening Soil (HS) model

The basics of the HS model have been outlined in Section 5.4.1. In this section the constitutive formulations are summarized to provide a basis for the interpretation and discussion of the results of the mechanical sensitivity analysis (Section 5.6), as well as of the later full mesh FE analyses (Chapters 6 and 7). For additional information see Schanz et al. (1999), Benz (2006) and Plaxis (2014c).

5.5.1. Yield function for shear hardening

The HS model shear hardening yield function f^s (Figure 5.1) is based on the hyperbolic stress-strain relationship for drained triaxial loading originally developed by Kondner and Zelasko (1963), and later adapted by Duncan and Chang (1970) in the context of elasticity. The formulation was extended to an elasto-plastic framework for which Schanz et al. (1999) defined

the yield function

$$f^s = \frac{2}{E_i} \frac{q}{1 - q/q_a} - \frac{2q}{E_{ur}} - \gamma^p \tag{5.1}$$

where E_i is the initial secant modulus (Figure 5.5(a)), E_{ur} is the elastic unloading-reloading modulus, $q = \sigma_1 - \sigma_3$ is the deviatoric stress, q_a is the asymptotic shear strength and γ^p holds the accumulated plastic deviatoric strains (strain-hardening parameter), i.e.

$$\gamma^p = 2\varepsilon_a^p - \varepsilon_v^p \approx 2\varepsilon_a^p \tag{5.2}$$

for which Schanz et al. (1999) assume that, for hard soils, the plastic volumetric strains, ε_v^p, are very low compared to the plastic axial strains, ε_a^p, and thus negligible.

The initial secant modulus is

$$E_i = \frac{2E_{50}}{2 - R_f} = \frac{2E_{50}}{2 - q_f/q_\alpha} \tag{5.3}$$

with E_{50} being the secant modulus and R_f being the failure ratio relating the asymptotic shear strength q_a to the ultimate deviatoric stress q_f (Figure 5.5(a)):

$$q_f = (c \cot \varphi - \sigma_3') \frac{2 \sin \varphi}{1 - \sin \varphi} \tag{5.4}$$

where c is the cohesion, φ is the friction angle and σ_3' is the cell pressure in triaxial stress conditions or the smallest principal stress in general stress conditions.

The secant modulus due to primary deviatoric loading and the unloading-reloading modulus are defined as

$$E_{50} = E_{50}^{ref} \left(\frac{c \cos \varphi - \sigma_3' \sin \varphi}{c \cos \varphi + p^{ref} \sin \varphi} \right)^m \tag{5.5}$$

$$E_{ur} = E_{ur}^{ref} \left(\frac{c \cos \varphi - \sigma_3' \sin \varphi}{c \cos \varphi + p^{ref} \sin \varphi} \right)^m \tag{5.6}$$

where E_{50}^{ref} is the reference secant modulus, E_{ur}^{ref} is the reference unloading-reloading modulus, p^{ref} is a reference stress, usually taken equal to 100kPa (Plaxis, 2014c) and m defines the rate of stress dependency. Note that σ_3' is negative for compression and that p^{ref} is an absolute pressure. As illustrated in Figure 5.5(a), E_{50}^{ref} passes through the intersect of the axial strain ε_a and deviatoric stress q at $q_f/2$, that is, performing a drained triaxial test under a constant confining stress σ_3.

The constant m defining the level of stress dependency of stiffness of a material usually ranges from 0.5 for sands to 1 for soft soils Brinkgreve (2011). It is determined from two triaxial tests carried out on the same material at different confining stress levels, $\sigma_3'^{(1)}$ and $\sigma_3'^{(2)}$
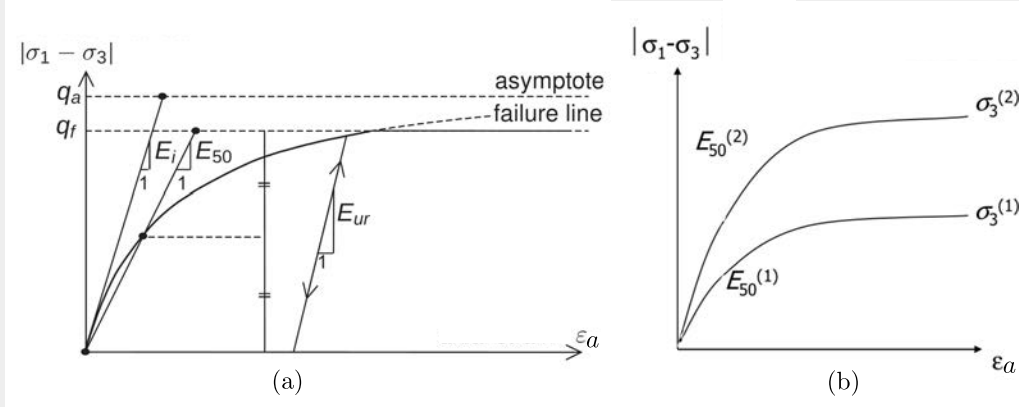
Figure 5.5.: (a) Hyperbolic stress-strain relationship for a standard drained triaxial test in shear strain ε_a vs. deviatoric stress q space, where E_i is the initial secant modulus, E_{50} is the secant modulus, E_{ur} is the unloading-reloading modulus, q_a is the asymptotic value of the shear strength and q_f is the ultimate deviatoric stress (Plaxis, 2014c). (b) Results from two triaxial compression tests at different confining stress σ_3 (Brinkgreve, 2011).

(Figure 5.5(b)). Once the secant moduli corresponding to each confining pressure, i.e. $E_{50}^{(1)}$ and $E_{50}^{(2)}$ respectively, are estimated, m is calculated (Brinkgreve, 2011).

$$\frac{E_{50}^{(1)}}{E_{50}^{(2)}} = \left(\frac{\sigma_3'^{(1)}}{\sigma_3'^{(2)}} \right)^m \quad \Rightarrow \quad m = \frac{\ln \left(E_{50}^{(1)}/E_{50}^{(2)} \right)}{\ln \left(\sigma_3'^{(1)}/\sigma_3'^{(2)} \right)} \tag{5.7}$$

The elastic strains upon primary loading or unloading-reloading are

$$\varepsilon_1^e = \varepsilon_a^e = \frac{q}{E_{ur}} \tag{5.8a}$$

$$\varepsilon_2^e = \varepsilon_3^e = -\nu_{ur} \frac{q}{E_{ur}} \tag{5.8b}$$

where ν_{ur} is the unloading/reloading Poisson's ratio. From Equations 5.1 and 5.2, the plastic axial strain generated whilst on the shear yield locus is

$$\varepsilon_a^p \approx 1/2 \bar{f} = \frac{1}{E_i} \frac{q}{1 - q/q_a} - \frac{q}{E_{ur}} \tag{5.9}$$

From Equations 5.8a and 5.9 it follows that

$$\varepsilon_a = \varepsilon_a^e + \varepsilon_a^p \approx \frac{1}{E_i} \frac{q}{1 - q/q_a} \tag{5.10}$$

Transforming Equation 5.1 into principal stress space, two functions define the shear yield

locus

$$f_{12}^s = \frac{2q_a}{E_i} \frac{(\sigma_1 - \sigma_2)}{q_a - (\sigma_1 - \sigma_2)} - \frac{2(\sigma_1 - \sigma_2)}{E_{ur}} - \gamma^p \tag{5.11a}$$

$$f_{13}^s = \frac{2q_a}{E_i} \frac{(\sigma_1 - \sigma_3)}{q_a - (\sigma_1 - \sigma_3)} - \frac{2(\sigma_1 - \sigma_3)}{E_{ur}} - \gamma^p \tag{5.11b}$$

with γ^p (Equation 5.2) being the relevant parameter for the frictional hardening (Schanz et al., 1999).

The flow rule relating the plastic volumetric strain rate $\dot{\varepsilon}_v^p$ to the plastic shear strain rate $\dot{\gamma}^p$ is

$$\dot{\varepsilon}_v^p = \sin \psi_m \dot{\gamma}^p \tag{5.12}$$

where ψ_m is the mobilised dilatancy angle. A similar stress-dilatancy theory to that proposed by Rowe (1962) was adapted by Schanz and Vermeer (1996), i.e.

$$\begin{aligned}
&\text{for } \sin \varphi_m < 3/4 \sin \varphi && \rightarrow \psi_m = 0° \\
&\text{for } \sin \varphi_m \geq 3/4 \sin \varphi \text{ and } \psi > 0° && \rightarrow \sin \psi_m = \max \left(\frac{\sin \varphi_m - \sin \varphi_{cv}}{1 - \sin \varphi_m \sin \varphi_{cv}}, 0° \right) \\
&\text{for } \sin \varphi_m \geq 3/4 \sin \varphi \text{ and } \psi \leq 0° && \rightarrow \psi_m = \psi \\
&\text{for } \varphi = 0° && \rightarrow \psi_m = 0°
\end{aligned} \tag{5.13}$$

where φ_{cv} and φ_m are the critical state (or constant volume) and mobilised friction angles, respectively:

$$\sin \varphi_m = \frac{\sigma_1' - \sigma_3'}{\sigma_1' + \sigma_3' - 2c \cot \varphi} \tag{5.14a}$$

$$\sin \varphi_{cv} = \frac{\sin \varphi_f - \sin \psi_f}{1 - \sin \varphi_f \sin \psi_f} \tag{5.14b}$$

where φ_f and ψ_f are the friction and dilatancy angles at failure, respectively. For failure conditions, i.e. $\varphi_m = \varphi_f$, from Equations 5.13 and 5.14b it follows that

$$\sin \psi_f = \frac{\sin \varphi_f - \sin \varphi_{cv}}{1 - \sin \varphi_f \sin \varphi_{cv}} \tag{5.15}$$

No plastic volumetric strains during shear hardening are generated for $\psi = 0°$, according to Equations 5.12 and 5.13. From Equations 5.13-5.14 it follows that, for small stress ratios, $\varphi_m < \varphi_{cv}$, the material contracts ($\psi < 0°$), whereas it dilates for higher stress ratios, $\varphi_m > \varphi_{cv}$, ($\psi > 0°$).

Using a non-associated flow rule Schanz et al. (1999) defined the plastic potential functions as

$$g^s_{12} = \frac{\sigma'_1 - \sigma'_2}{2} - \frac{\sigma'_1 + \sigma'_2}{2} \sin \psi_m \tag{5.16a}$$

$$g^s_{13} = \frac{\sigma'_1 - \sigma'_3}{2} - \frac{\sigma'_1 + \sigma'_3}{2} \sin \psi_m \tag{5.16b}$$

where ψ_m is the mobilised dilatancy angle (Equations 5.13).

5.5.2. Cap yield surface

The HS model cap yield function f^c (Figure 5.1) is defined as

$$f^c = \frac{\tilde{q}^2}{\alpha^2} + p'^2 - p_c'^2 \tag{5.17}$$

where p'_c is the isotropic pre-consolidation pressure and $\tilde{q}$ is a deviatoric stress measure of the HS model, defined as

$$\tilde{q} = \sigma'_1 + (\delta - 1) \sigma'_2 - \delta \sigma'_3 \tag{5.18}$$

where $\delta = (3 + \sin \varphi)/(3 - \sin \varphi)$. For triaxial compression, i.e. $\sigma'_1 > \sigma'_2 = \sigma'_3$, Equation 5.18 simplifies to $\tilde{q} = q = \sigma'_1 - \sigma'_3$. For triaxial extension, i.e. $\sigma'_1 = \sigma'_2 > \sigma'_3$, the deviatoric stress measure is $\tilde{q} = \delta (\sigma'_1 - \sigma'_3)$.

The general isotropic and deviatoric pre-consolidation pressures are

$$p'_c = \frac{1}{3} \left(1 + 2K^{NC}_0\right) \sigma'_{v,c} \quad \text{and} \quad q_c = \left(1 - K^{NC}_0\right) \sigma'_{v,c} \tag{5.19}$$

where $\sigma'_{v,c}$ is the effective vertical pre-consolidation pressure and the coefficient of earth pressure at rest under normally consolidated conditions. In the case of $K^{NC}_0 \neq 1$, an *"equivalent"* pre-consolidation pressures $p_c'^{eq}$ replaces p'_c:

$$p_c'^{eq} = \sqrt{(p')^2 + \frac{q^2}{\alpha^2}} \tag{5.20}$$

where p' and q are the mean and deviatoric stresses defining a stress state on the cap yield surface.

The HS model parameter α defines the intersect of the cap with the deviatoric axis (see Figure 5.1) and as such controls the ratio of the plastic volumetric strain rate $\dot{\varepsilon}^p_v$ and the plastic deviatoric strain rate $\dot{\gamma}^p_s$ at any given stress state at yield. The parameter α is determined as a function of the coefficient of earth pressure at rest in NC conditions, for which the default value in PLAXIS is set to $K^{NC}_0 = 1 - \sin \varphi$ as proposed by Jaky (1944).

The plastic potential on the cap is defined by an associated flow rule, i.e. $g^c \equiv f^c$. Please note, the original definition of the HS model cap strains (see Schanz et al., 1999) diverges

slightly from the formulation implementation within PLAXIS. Following Plaxis (2014c), and Brinkgreve (2014) the plastic volumetric strain rate due to cap hardening is computed as

$$\dot{\varepsilon}_v^{pc} = \frac{K_s/K_c - 1}{K_s^{ref}} \left[\left(\frac{p_c + c \cot \varphi}{p^{ref} + c \cot \varphi} \right)^{-m} \right] \dot{p} \tag{5.21a}$$

where K_c is the elasto-plastic bulk modulus in isotropic primary compression, K_s is the bulk modulus in isotropic swelling and K_s^{ref} is the reference bulk modulus in unloading-reloading:

$$K_s^{ref} = \frac{E_{ur}^{ref}}{3(1 - 2\nu_{ur})} \tag{5.21b}$$

The ratio of the isotropic swelling modulus to the compression modulus, K_s/K_c, is an internal HS model cap parameter which may be approximated as

$$K_s/K_c \approx \frac{E_{ur}^{ref}}{E_{oed}^{ref}} \frac{K_0^{NC}}{(1 + 2K_0^{NC})(1 - 2\nu_{ur})} \tag{5.22}$$

where E_{oed}^{ref} is the reference oedometer modulus (Brinkgreve, 2014). The oedometer modulus is defined by

$$E_{oed} = E_{oed}^{ref} \left(\frac{c \cos \varphi - \frac{\sigma_3'}{K_0^{NC}} \sin \varphi}{c \cos \varphi + p^{ref} \sin \varphi} \right)^m \tag{5.23}$$

where the reference oedometer modulus E_{oed}^{ref} is determined as the tangent of the oedometer response in $\varepsilon_a : \sigma_v'$ space at a reference pressure p^{ref} (Figure 5.6(a)).

The yield contour of the HS model in principal stress space is shown in Figure 5.6(b).

5.5.3. On the HS model implementation in PLAXIS FE program

Initial stress conditions:

In a full mesh FE analysis, the initial horizontal effective stresses $\sigma_{h0}' = K_0 \sigma_{v0}'$ will be computed for a default earth pressure at rest

$$K_0 = \frac{K_0^{NC}(|\sigma_{v0}'| + POP) - \frac{\nu_{ur}}{1 - \nu_{ur}} POP}{|\sigma_{v0}'|} \qquad \text{or} \tag{5.24a}$$

$$K_0 = OCR\, K_0^{NC} - \frac{\nu_{ur}}{1 - \nu_{ur}}(OCR - 1) \tag{5.24b}$$

where $POP = |\sigma_c' - \sigma_{v0}'|$ (Figure 5.7) is the pre-overburden pressure and $OCR = \sigma_c'/\sigma_{v0}'$ is the over-consolidation ratio (Plaxis, 2014c).

(a)   (b)
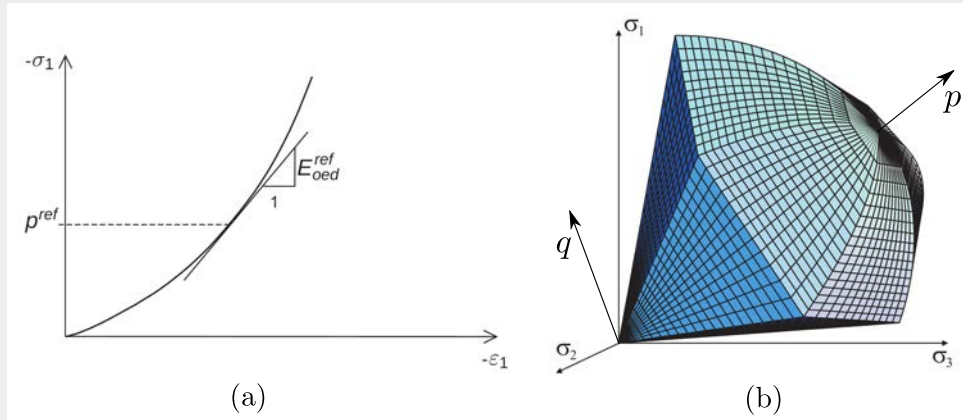
Figure 5.6.: (a) Oedometer response in axial strain ε_1 vs. vertical effective stress σ_1' space for determination of the reference oedometer modulus E_{oed}^{ref} and reference stress p^{ref} (Plaxis, 2014c). (b) Yield surfaces of HS model for cohesionless soil in principal stress space, $\sigma_1{:}\sigma_2{:}\sigma_3$, in its ultimate MC failure criterion position with the mean stress vs. deviatoric stress, $p:q$, plane being highlighted (Benz, 2006).

Initial position of the shear hardening locus:

In the PLAXIS *SoilTest facility* the initial cap yield locus can be set at any position between the hydrostatic axis and the failure surface. In the full mesh analysis the cap yield surface is initialised along the K_0^{NC}-line (Figure 5.7).
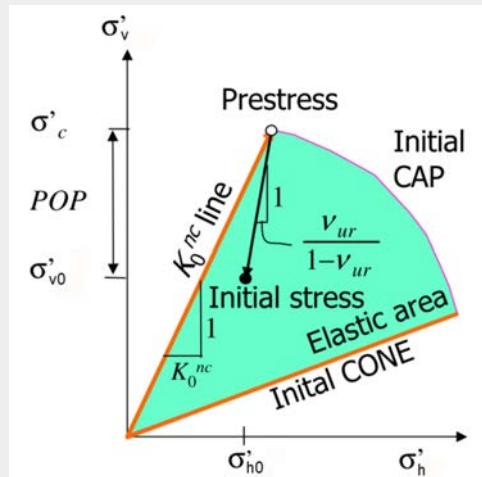
Figure 5.7.: Determination of the initial horizontal effective stresses, σ_{h0}', for a full mesh FE analysis for the HS model, where σ_{v0}' is the initial vertical effective stress, σ_c' is the vertical pre-consolidation stress, K_0^{NC} is the coefficient of earth pressures at rest in NC conditions, ν_{ur} is the unloading-reloading Poisson's ratio and POP is the pre-overburden pressure (after Brinkgreve, 2011).

Input parameters of the HS model:

The input parameters for the HS model, as implemented in PLAXIS 2D AE and PLAXIS 3D (Plaxis, 2013b, 2014d), are listed in Table 5.4. The parameters corresponding to the laboratory tests on core *Ess75* are indicated.

The compression and swelling indices, C_c and C_s respectively, are an alternative to computing the reference parameters E_{oed}^{ref} and E_{ur}^{ref}, where

$$C_c = \frac{2.3\,(1+e_0)\,p^{ref}}{E_{oed}^{ref}} \tag{5.25a}$$

$$C_s \simeq \frac{2.3\,(1+e_0)\,(1+\nu)\,(1-2\nu)\,p^{ref}}{(1-\nu)\,E_{ur}^{ref}} \tag{5.25b}$$

depending, in this PLAXIS formulation, on the the initial void ratio e_0. These formulation are primarily used for soft soils where the rate of stress dependency of the soil stiffness is set to $m = 1$ and $E_{50}^{ref} = 1.25 E_{oed}^{ref}$ (Plaxis, 2014c). Note that, for soils having a large cohesion, the above formulations become less accurate (Brinkgreve, 2014).

The failure ratio and the reference stress are set to the default values, i.e. $R_f = 0.9$ and $p^{ref} = 0.1$MPa (Plaxis, 2014c). The default earth pressure at rest for NC conditions is computed to be $K_0^{NC} = 1 - \sin\varphi'$ (Jaky, 1944). A tensile strength and depth dependency of the cohesion was not accounted for in this work.

Comments on the PLAXIS internal HS model algorithm

Due to PLAXIS being a proprietary software package (Plaxis, 2014a), it is not possible to obtain an insight into the internal HS model algorithm. However, in order to assess the response of Boom Clay as part of a mechanical sensitivity analysis (later Section 5.6) or a reliability based design calculation (later Chapter 7), it is important to address the physical basis for any potential parameter correlation.

Three *"internal"* parameters may be used to better explain the model response, for which the specific values can be retrieved from the PLAXIS *SoilTest facility* output file.

○ α: Defines the position of the cap (Figure 5.1, Equation 5.1) and as such $\dot{\varepsilon}_v^{pc}/\dot{\gamma}^{pc}$. Plaxis (2014c, p 73) defines that $\alpha \leftrightarrow K_0^{NC}$.

○ K_s/K_c: The ratio of the isotropic swelling to compression moduli controls the magnitude of the plastic volumetric cap strains ε_v^{pc} (Equation 5.21a), with $K_s = f(E_{ur}, \nu_{ur})$ and $K_c \leftrightarrow E_{oed}^{ref}$ (Plaxis, 2014c, p 73). An approximation of K_s/K_c is provided in Equation 5.22 (Brinkgreve, 2014).

○ G_{50}^{ref}: The reference shear modulus in primary loading controls the deviatoric strains mainly due to shear hardening.

A derivation of these internal parameters for double hardening situations in closed form does not exist. A numerical algorithm iteratively simulates the user input, that is, E_{ur}^{ref} in a

Table 5.4.: Input parameters for the HS model as implemented in PLAXIS, with reference values to the laboratory tests on core *Ess75*.

Variable	Symbol	Value	Unit
(Effective) friction angle	φ	12.4[a]	[°]
(Effective) cohesion	c	0.11[a]	[MPa]
Dilatancy angle	ψ	0[a,b] 2.0[a,c]	[°]
Reference secant modulus	E_{50}^{ref}	8.53[d]	[MPa]
Reference un-/reloading modulus	E_{ur}^{ref}	11.0[d]	[MPa]
Reference oedometer modulus	E_{oed}^{ref}	20.94[d]	[MPa]
Rate of stress dependency of stiffness	m	0.7[d]	[−]
Un-/reloading Poisson's ratio	ν_{ur}	0.3[d]	[−]
Compression index	C_c	−	[−]
Swelling index	C_s	−	[−]
Initial void ratio	e_0	−	[−]
Reference stress for stiffness	p^{ref}	0.1[e]	[MPa]
K_0-value for normal consolidation	K_0^{NC}	0.7853[f]	[−]
Failure ratio	R_f	0.9[e]	[−]
Tensile strength	σ_{ten}^{hs}	−	[MPa]
Increase in cohesion per unit depth	c_{inc}^{hs}	−	[MPa m^{-1}]

[a] Deng et al. (2011a); [b] Test *Ess75Tr01-02*; [c] Test *Ess75Tr03*; [d] Best fit (Table 5.3); [e] Plaxis (2014c); [f] $K_0^{NC} = 1 - \sin \varphi'$ (Jaky, 1944)

triaxial element test, as well as E_{oed}^{ref} and K_0^{NC} in an oedometer element test (Benz, 2006; Brinkgreve, 2014). Furthermore, the elasto-plastic shear modulus G_{50}^{ref} can not be directly computed from E_{50}^{ref}, as this stiffness is not used in the concept of elasticity (Schanz et al., 1999).

5.6. Mechanical sensitivity analysis

In this section the effect of varying individual HS model parameters on the stress-strain response for the triaxial tests *Ess75Tr01-03* is investigated. The simulations are performed utilising the PLAXIS *SoilTest facility*. The shear hardening locus was initialised on the hydrostatic axis, i.e. leading to the immediate generation of elasto-plastic strains.

The HS model parameters listed in Table 5.4 will be referred to as the best fit data set. Individual parameters will be varied one at a time, that is, with the other parameters remaining fixed to the best fit, as defined in Table 5.5. Note, that the ranges of some parameters tested may exceed the lower and upper bounds of the BC specific parameter.

Figures 5.8(a-p) show the HS model predictions of the Boom Clay response for the variation

Table 5.5.: Cases investigated for the mechanical sensitivity analysis involving the variation of individual Boom Clay property values.

Variable	Symbol	Unit	Variables				
Reference secant modulus	E_{50}^{ref}	[MPa]	5.0	6.0	7.0	8.53	10.0
Reference un-/reloading modulus	E_{ur}^{ref}	[MPa]	17.06	20.94	25.0	30.0	35.0
Reference oedometer modulus	E_{oed}^{ref}	[MPa]	7.0	9.0	11.0	13.0	15.0
Rate of stress dep. of stiffness	m	[−]	0.4	0.55	0.7	0.8	0.9
Un-/reloading Poisson's ratio	ν_{ur}	[−]	0.202	0.23	0.25	0.30	0.4
Dilatancy angle	ψ	[°]	0.0 [a]	1.0	2.0 [b]	3.0	4.0
Effective friction angle	φ'	[°]	7.5	10.0	12.4	15.0	17.5
Effective cohesion	c'	[MPa]	0.05	0.11	0.15	0.25	0.5

HS parameter: best fit, lower bound and upper bound values.

For calibration applied in: [a] test *Ess75Tr01*, and [b] test *Ess75Tr02-03*.

of all parameters. Figures 5.9(a-f) summarize the effect of varying each parameter on the internal parameters G_{50}^{ref}, α and K_s/K_c, whose values are not effected by the test performed.

E_{50}^{ref}: An increase of the reference secant modulus, E_{50}^{ref}, leads to a stiffer material response (Figure 5.8(a)), as both E_{50} and E_i increase (Equations 5.5 and 5.3). The minor decrease in both α and K_s/K_c (Figure 5.9(a)) indicates that the location of the cap, and thus $\dot{\varepsilon}_v^{pc}$ (Equation 5.21a), is almost unaffected. Furthermore, with increasing E_{50}^{ref} the cap yield locus is reached earlier for the lightly OC sample and the peak volumetric strain is reached at a lower axial strain level for the moderately OC dilative sample. The elasto-plastic shear modulus G_{50}^{ref} increases with increasing E_{50}^{ref} (Figure 5.9(a)), leading to an increase in mobilised shear resistance (Figure 5.8(b)).

E_{ur}^{ref}: The volumetric response of the Boom Clay becomes stiffer in the elastic domain with an increase in the reference un-/reloading modulus E_{ur}^{ref} (Figure 5.8(c)). The significant increase in both α and K_s/K_c for larger values of E_{ur}^{ref} (Figure 5.9(b) and Equation 5.22) leads to a steeper cap and thus to a larger plastic volumetric cap strain rate $\dot{\varepsilon}_v^{pc}$ (Equations 5.21a). For the OC samples the volumetric strains reduce significantly with an increase in E_{ur}^{ref}, that is, with the elastic strains primarily governing the volumetric response due to the steeper cap. A minor decrease in the elasto-plastic shear modulus G_{50}^{ref} is observed for larger values of E_{ur}^{ref} (Figure 5.9(b)). The deviatoric response is not influenced by a variation of E_{ur}^{ref} (Figure 5.8(d)).

E_{oed}^{ref}: An increase in the reference oedometer modulus E_{oed}^{ref} induces lower volumetric strains ε_v as the soil becomes stiffer (Figure 5.8(e)), a fact which is also reflected in the decrease in G_{50}^{ref}, α and K_s/K_c (Figure 5.9(c) and Equation 5.22), leading to a shallower cap. The reduction in ε_v is significant for the NC case, as the stress state is located on the

cap from the beginning. For the lightly and moderately OC case the effect reduces significantly. The deviatoric response is insignificantly affected by a variation in E_{oed}^{ref} (Figure 5.8(f)).

m: A reduction in the rate of stress dependency of the stiffness, m, results in larger volumetric strains ε_v (Figure 5.8(g)), which is associated with a reduction in E_{oed} as $m \leq 1$ (Equations 5.23). Note that, in the cases tested here, the stress states were always higher than the reference stress p^{ref}. Similarly, the reduction in E_{ur} induces larger elastic volumetric strains (Equation 5.6). The cap parameter α, as well as the swelling to compression ratio K_s/K_c, slightly decrease with increasing m. The deviatoric response becomes stiffer with increasing m (Figure 5.8(g)), that is, with the difference becoming less significant for an increasing OCR. The elasto-plastic shear modulus G_{50}^{ref} is only slightly affected and seems to have a minimum for an intermediate value of m (Figure 5.9(d)).

ν_{ur}: A reduction in the un-/reloading Poisson's ratio, ν_{ur}, is associated with a significant reduction in α and K_s/K_c (Figure 5.9(e) and Equation 5.22), which results in the cap becoming more shallow and thus less plastic volumetric strains are generated (Figure 5.8(i)). In contrast to the elastic volumetric strains increase. The elasto-plastic shear modulus G_{50}^{ref} reaches a maximum when the Poisson's ratio is approaching its lower bound (Figure 5.9(e)). Values of $\nu_{ur} < 0.2$ lead to somewhat unrealistic results in the volumetric vs. axial strain space. The deviatoric response is only slightly affected by a variation in ν_{ur} (Figure 5.8(j)).

ψ: An increase in the angle of dilatancy, ψ, leads to larger expansive volumetric strains being generated (Figure 5.8(k)), that is, even more so for the OC samples. The deviatoric response is not effected by a variation in ψ (Figure 5.8(l)). A variation in ψ does not affect any of the internal parameters G_{50}^{ref}, α and K_s/K_c.

c': An increase in the effective cohesion, c', leads to significantly larger volumetric strains, ε_v, that is, especially for lightly and moderately OC samples (Figure 5.8(m)). The stiffer soil response associated with an increase in c', especially E_i and E_{50}, (Equations 5.3 and 5.5), influences significantly the deviatoric response (Figure 5.8(n)). A variation in c' does not affect any of the internal parameters G_{50}^{ref}, α and K_s/K_c.

φ': For the lightly and moderately OC samples, an increase in φ' leads to larger volumetric compressive strains (Figure 5.8(o)) associated with the significant increase in α, potentially associated with the reduction in K_0^{NC}, which compensates the minor decrease in K_s/K_c (Figure 5.9(f)). The variation in soil friction angle has the most significant effect on the deviatoric response amongst all parameters varied (Figure 5.8(p)), that is, with the effect decreasing for samples with a larger OCR.

(a) Reference secant modulus E_{50}^{ref}

(b) Reference secant modulus E_{50}^{ref}

(c) Reference un-/reloading modulus E_{ur}^{ref}

(d) Reference un-/reloading modulus E_{ur}^{ref}

(e) Reference oedometer modulus E_{oed}^{ref}

(f) Reference oedometer modulus E_{oed}^{ref}

(g) Rate of stress dep. of stiffness m

(h) Rate of stress dep. of stiffness m

(i) Un-/reloading Poisson's ratio ν_{ur}

(j) Un-/reloading Poisson's ratio ν_{ur}

(k) Dilation angle ψ

(l) Dilation angle ψ
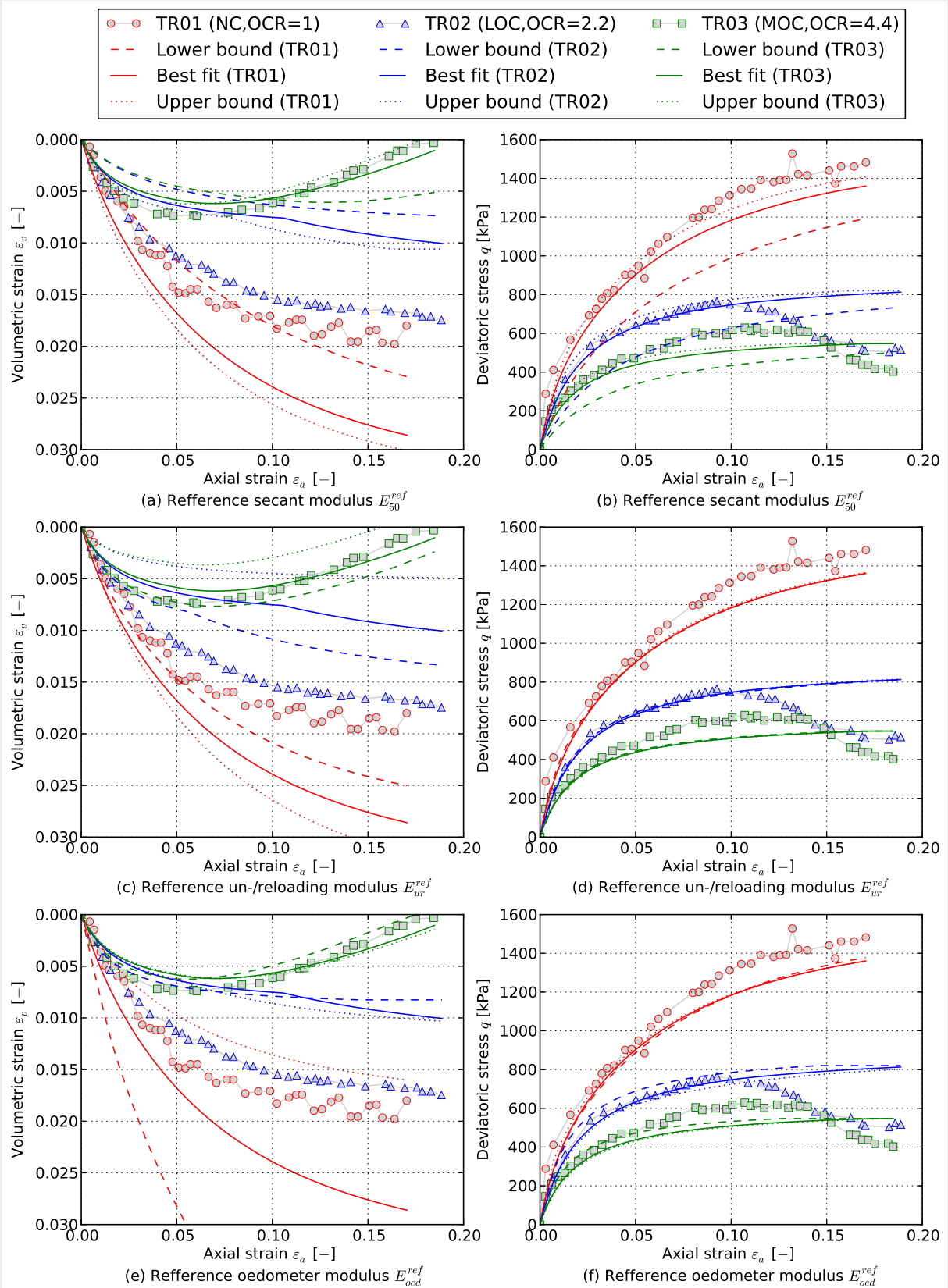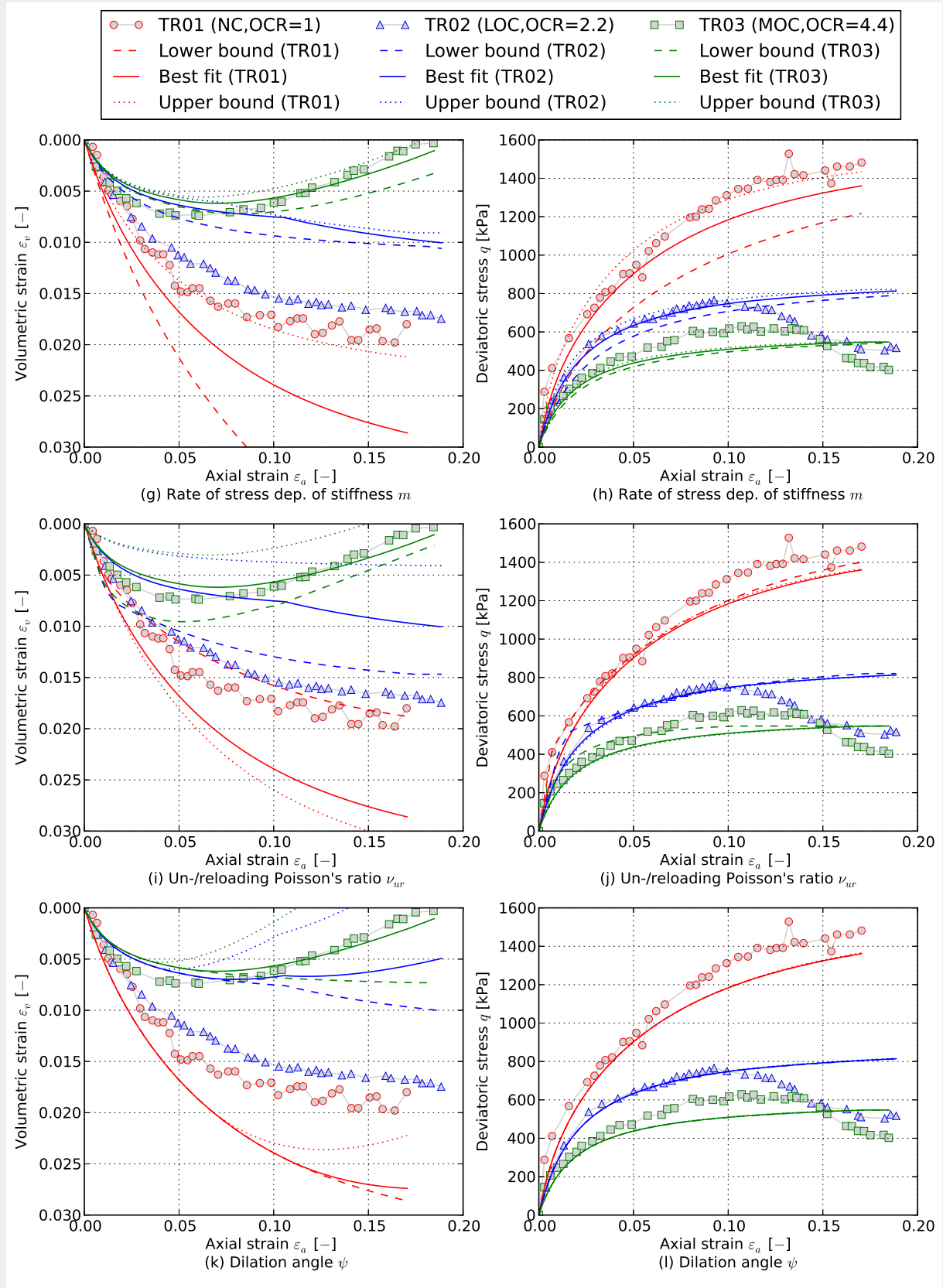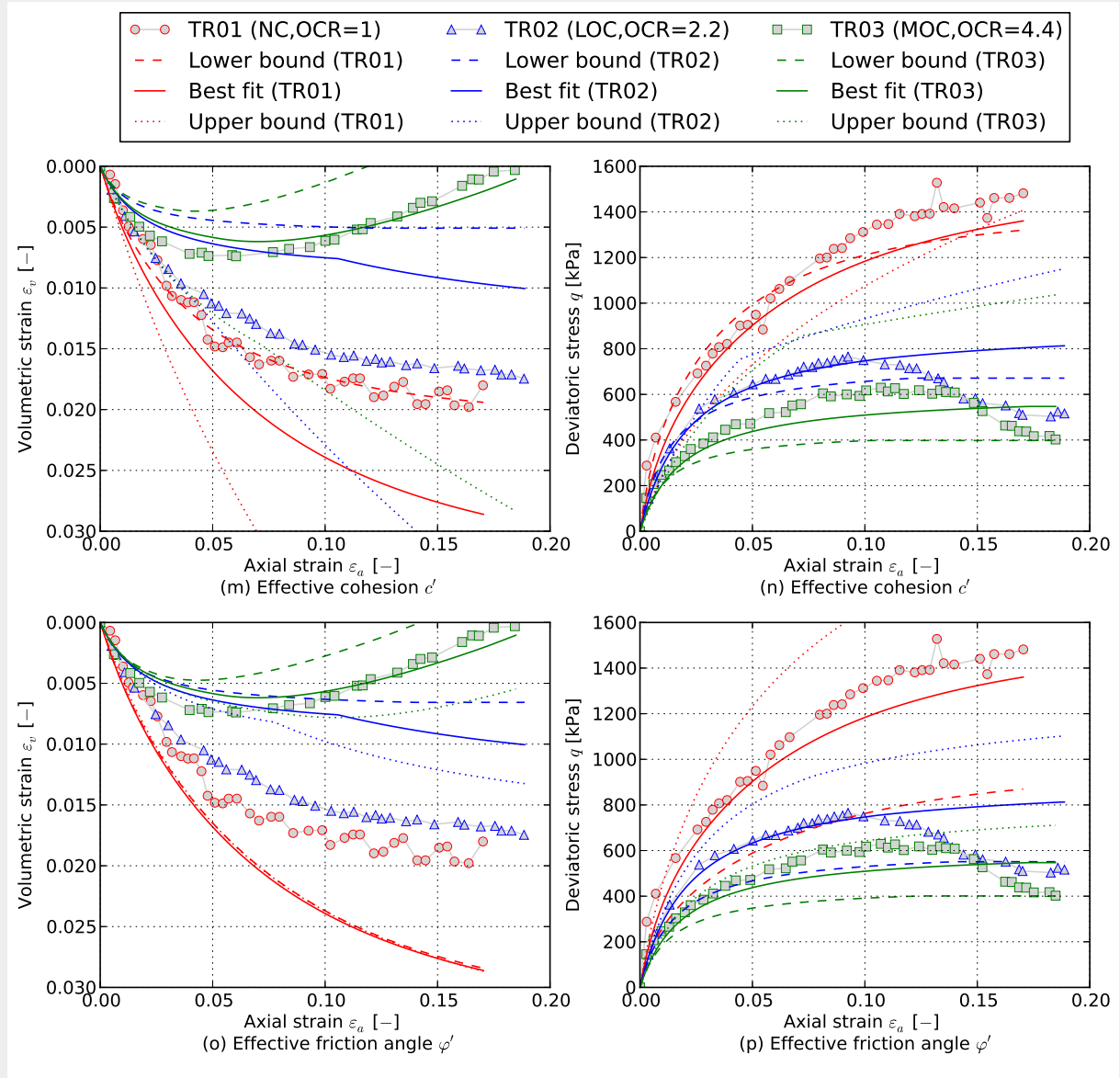
Figure 5.8.: Response of numerical simulation of Boom Clay subjected to drained triaxial compressive loading (*Ess75Tr01-03* Deng et al., 2011a), for a deterministic variation of individual HS material parameters (Table 5.5), in both $\varepsilon_a : \varepsilon_v$ and $\varepsilon_a : q$ spaces.
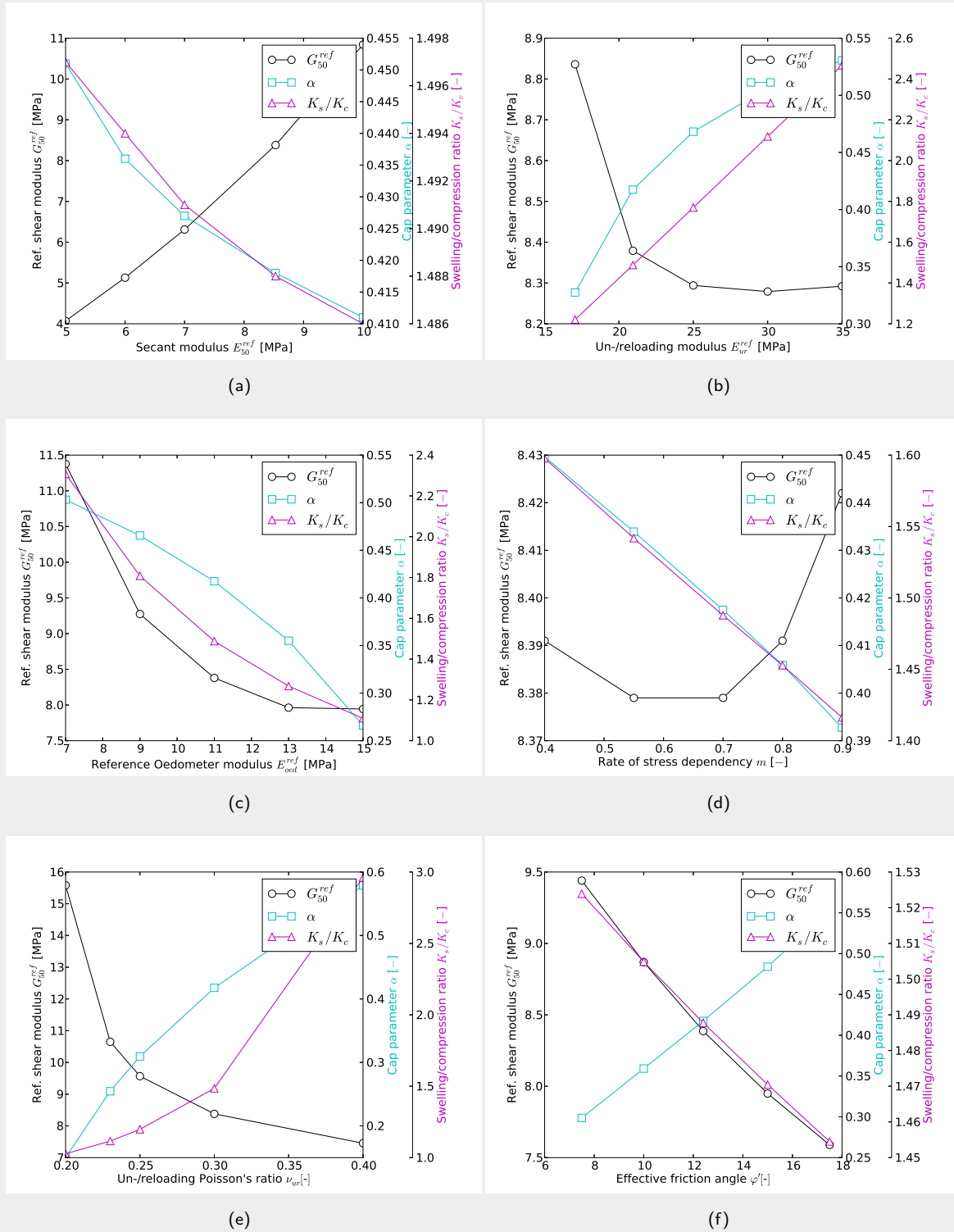
Figure 5.9.: Variation of the reference shear modulus in primary loading, G_{50}^{ref}, the cap parameter, α, and the swelling/compression ratio, K_s/K_c, due to variations of six HS model parameters (Table 5.5). A variation of friction angle φ' or dilatancy angle ψ does not influence the internal parameters and is not shown.

5.7. Summary

In this chapter the constitutive modelling of Boom Clay for the numerical analysis of a deep tunnel excavation was investigated.

Following a review on the constitutive modelling of Boom Clay, four soil models have been validated against a set of test data containing three drained triaxial tests consolidated to different overconsolidation ratios and one high pressure oedometer test. Fitting one set of parameters for each model to the complete data set, the *Hardening Soil* (HS) model was found to perform best given the nature of the excavation problem to be analysed.

Subsequently, the formulation of the HS model was summarized and the implementation in the PLAXIS FE software package discussed.

Finally a mechanical sensitivity analysis of the stress-strain response of a Boom Clay sample consolidated to different OCR's and under triaxial compressive loading was performed by varying the HS model parameters individually between lower and upper bounds. The results show that the material response is strongly dependent on the OCR. Variations in the elastic/elastoplastic stiffness parameters, as well as in the effective cohesion, significantly effect the volumetric response of the Boom Clay sample. The deviatoric response was primarily effected by a variation in the effective friction angle and, to lesser extent, by a variation in the effective cohesion.

6. Numerical modelling

6.1. Introduction

In this Chapter the excavation of a tunnel in a deep Boom Clay formation is numerically assessed in two and three dimensions, utilising the PLAXIS FE software package.

In Section 6.2 the short- and long-term response of the Boom Clay is assessed, for two-dimensional plane strain conditions using the HS model. A mechanical sensitivity analysis is performed by varying individual model parameters and boundary conditions, to assess their impact on the extent of the plastic zone and the liner forces. The three-dimensional transient excavation process of a single tunnel is modelled numerically in Section 6.3 to investigate the impact of the excavation process. The main findings of this chapter are presented in Section 6.4.

6.2. Two-dimensional modelling

In this section the deterministic response of the Boom Clay due to the excavation of a tunnel is investigated, by varying of the HS model parameter, state variables and boundary conditions.

6.2.1. Model set-up

The two-dimensional plane strain analyses have been performed with PLAXIS 2D AE (Plaxis, 2014d). Figure 6.1 shows the base set-up of the numerical model for a deterministic analysis at 500m depth. The bottom boundary is fixed. The left-side and right-side boundaries are fixed in the horizontal direction and free in the vertical direction. The initial vertical effective stress in the domain is set to be hydrostatic, i.e. $\sigma'_{zz} = (\gamma - \gamma_w)d$. Utilising Equation 5.24b, the initial horizontal effective stresses are then computed ($\sigma'_{xx} = K_0\sigma'_{zz}$). This so-called *K0 procedure* which, other than in the gravitational loading procedure, accounts for the OCR, is applied to the initial domain (Figure 6.1(a)). Subsequently, the upper part of the mesh is then removed from the initial domain to result in the 80×160m model domain with a total vertical stress of $\sigma'_z = 4.2$MPa applied along the top boundary (Figure 6.1(b)). The domain is discretised using 15-node triangular elements and refined in the close vicinity of the tunnel (Figure 6.1(c)). In the basic HLW gallery setup ($r_c = 1.6$m, $d_{oc} = 75$mm, $d = 500$m; see set A and B in Section 6.2.3) the domain is discretised by 8554 elements with 68946 nodes.

As for the analytical analyses, the tunnel cross-section is circular and the installed tunnel liner is assumed to behave linear elastically. The liner property values are summarized in Table
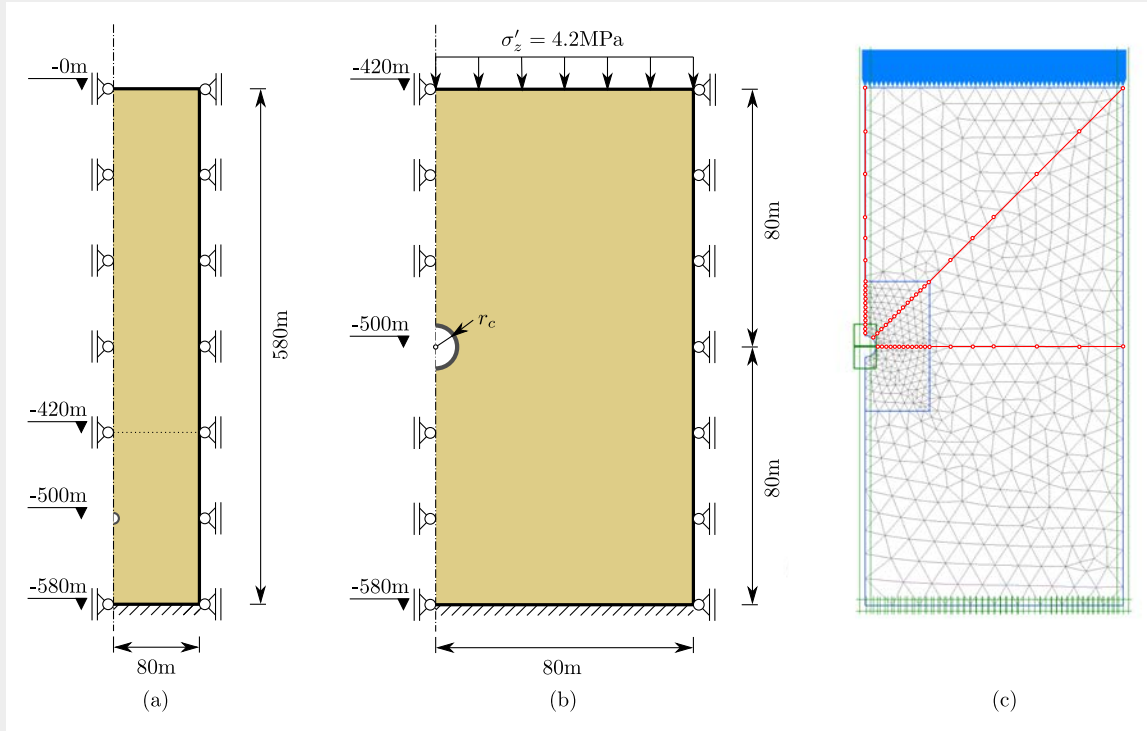
Figure 6.1.: Base set-up for a deterministic two-dimensional plane strain analysis at 500m depth: (a) Initial domain for *K0 procedure*; (b) Model domain and boundary conditions; (c) Discretisation using 15-node triangular elements and three profile axes (horizontal, vertical, diagonal).

6.1. The individual dimensions of the OPERA repository galleries have been tabulated in Table 2.7. The deterministic concrete stiffness property values have been set equal to the values employed in the analytical analyses (Section 4.7). The axial and bending stiffnesses for the liner are calculated per tunnel meter, and the interface between the liner and host rock is assumed to be rigid.

The tunnel response for three overexcavation radii, $d_{oc} = \{0.05, 0.075, 0.1\}$m, will be assessed. The convergence of the Boom Clay host rock is simulated by imposing a contraction of the cavity. This method relies on the contraction of the finite element mesh boundary at the tunnel liner interface, which is computed as the relative reduction in cross sectional area between the excavated tunnel, $A_e = \pi r_e{}^2$, and the nominal tunnel design, $A_c = \pi r_c{}^2$. The advantage of this procedure is that the tunnel and surrounding soil are in stress equilibrium; however, as lower the stiffness of the concrete as more stress re-distributed and thus the computed radial deformation may be slightly lower than the prescribed overcut (Möller, 2006).

Table 6.1.: Circular concrete liner property values.

Variable	Symbol	Unit	HLW	LILW	Shaft
Cavity radius	r_c	[m]	1.6	2.4	3.1
Liner thickness	d_l	[m]	0.5	0.55	0.6
Young's modulus	E_l	[MPa]	35 000	35 000	35 000
Poisson's ratio	ν_l	[−]	0.2	0.2	0.2
Axial stiffness*	EA^{**}	[MN m^{-1}]	17 500	19 250	21 000
Bending stiffness*	EI^{***}	[MN m^2 m^{-1}]	364.58	485.26	630.00

* Properties determined from liner geometry and Young's modulus.
** Cross section area per tunnel lining meter: $A = d$ [m^2 m^{-1}]
*** Moment of intertia per tunnel lining meter: $I = 1/12 d^3$ [m^4 m^{-1}]

For an excavation radius of $r_e = r_c + d_{oc}$ the associated radial convergence is computed as

$$c_r = \frac{\Delta V_e}{V_e} = \frac{\pi (r_c)^2 - \pi (r_c + d_{oc})^2}{\pi (r_c + d_{oc})^2} \tag{6.1}$$

6.2.2. Parameter selection

As discussed in Section 3.5, given the limited extent of experimental data available, it is very difficult to specify a set of characteristic Boom Clay property values and state variables. Table 6.2 summarizes the parameters that have been varied individually in this mechanical sensitivity analysis, that is, with the remaining parameters being fixed to *mean* values.

The effective cohesion and friction angle coincide with the values selected for the analytical analyses (Section 4.7) and cover a wide range of values potentially to be expected below 500m depth (Figure 3.4). The mean values of the secant modulus, E_{50}, were set equal to the Young's modulus E. The un/reloading modulus, E_{ur}, was set to be three times the secant modulus, based upon Plaxis (2014c), which suggests a ratio of $E_{ur}^{ref} = 3 E_{50}^{ref}$ for *"many practical cases"*; however this is noted to be slightly higher than the ratio observed for the triaxial tests (Table 5.5) and may decrease with an increasing overconsolidation ratio. The oedometer modulus, E_{oed}, was set equal to the secant modulus. The reference values have been approximated for a minor principal effective stress of $\sigma_3' \simeq -5$MPa, considering an isotropic stress state at 500m depth, see Equations 5.5 and 5.6, rounded to the nearest 10kPa. The reference stiffnesses are the input to the HS model and represent a normalised measure of stiffness. Hence, it is these parameters will be considered as random variables. This leads, when assessing tunnels at different depths, to a different stiffness as $E(\sigma_3')$ (see Equations 5.5, 5.6 and 5.23).

A Boom Clay dilation angle of $\psi = 0°$ is set as a mean value when other parameters varied. The mean boundary conditions are defined by an earth pressure at rest of $K_0 = 1$ (isotropic initial stress state) and by an overconsolidation ratio of $OCR = 2.2$. The remainder of the soil property values are treated as deterministic.

Table 6.2.: Boom Clay soil property values and state variables for a mechanical sensitivity analysis to assess a deep tunnel excavation. Mean parameters set (when other parameters vary) are printed in bold.

Random variable	X_i	Unit	Lower μ_{X_i}	Mid μ_{X_i}	Upper μ_{X_i}
Effective cohesion	c'	[MPa]	0.3	**0.5**	0.7
Effective friction angle	φ'	[°]	7.5	**12.5**	17.5
Secant modulus*	E_{50}^{ref}/E_{50}	[MPa]	80/200	**120/300**	160/400
Unloading/reloading modulus*	E_{ur}^{ref}/E_{ur}	[MPa]	240/600	**360/900**	480/1200
Oedometer modulus **	E_{oed}^{ref}/E_{oed}	[MPa]	80/200	**120/300**	160/400
Unloading/reloading Poisson's ratio	ν_{ur}	[−]	0.25	**0.3**	0.35
HS model exponent	m	[−]	0.7	**0.8**	0.9
Dilation angle	ψ	[°]	**0.0**	2.0	4.0
Earth pressure at rest	K_0	[−]	0.8	0.9	**1.0**
Over-consolidation ratio	OCR	[−]	2.0	**2.2**	2.4
Unit weight	γ	[kPa]		**20**	
Void ratio	e	[−]		**0.7**	
Reference stress	p^{ref}	[MPa]		**0.1**	
Failure ratio	R_f	[−]		**0.9**	
Earth pressure at rest NC-state	K_0^{NC}	[−]		$1 - \sin \varphi'$	

* E^{ref} is approximated for E at 500m depth with $\sigma_3' \simeq -5$MPa and $p^{ref} = 0.1$MPa.
** $E_{oed}^{ref} = E_{50}^{ref}$

6.2.3. Analyses set-up

For the two-dimensional model set-up (Figure 6.1), a set of undrained and drained steady state analyses are performed. The undrained analyses simulate the immediate response of the low permeability Boom Clay, due to the excavation of the tunnel gallery after liner emplacement. The drained analyses simulate the Boom Clay response in the longer term pre-operational and early post-closure phases assuming the liner is impermeable. Three sets of analyses have been performed for both undrained and drained conditions.

Set A assesses the response of the Boom Clay to variations in the seven main HS model parameters, $\mathbf{X} = \{c', \varphi', E_{50}^{ref}, E_{50}^{oed}, E_{ur}^{ref}, \nu_{ur}, m\}$, for a HLW gallery setup ($r_c = 1.6$m, $d_{oc} = 75$mm, $d = 500$m) with $\psi = 0°$, $K_0 = 1$ and $OCR = 2.2$. For this mechanical sensitivity analysis, each HS model parameter is varied individually between its lower and upper bound values, with the remainder of the variables being fixed to their mean values (Table 6.2, in bold).

The effect of an increasing dilation angle, ψ, a decrease in the earth pressure at rest, K_0, leading to an anisotropic initial stress field, as well as a variation in the overconsolidation ratio, OCR, on the Boom Clay response is assessed in Set B.

Set C1 assesses the response of the Boom Clay for an increase in the overcut to $d_{oc} = 100$mm, for a HLW gallery at 500m depth. In set C2 the Boom Clay response of a LILW cavity,

with a radius of $r_c = 2.4$m at 500m depth with an overcut of $d_{oc} = 75$mm, is investigated. For set C3 the excavation depth is increased to $d = 700$m, with $r_c = 2.4$m and $d_{oc} = 75$mm. For the sets C1 to C3, three critical parameter combinations have been applied; i.e. for a lower bound cohesion, a lower bound friction angle and an upper bound reference secant modulus.

6.2.4. Excavation phase

Table 6.3 summarises the response of the Boom Clay, in terms of the extent of the *Hardening Zone* (HZ) and *Plastic Zone* (PZ), as well as the liner forces, for all undrained analyses performed for sets A-C.

Set A:

Figure 6.2 shows the effective radial and tangential stress distributions in the horizontal profile (left-hand side) and the total radial and tangential stress and pore water pressure distributions in the vertical profile (right-hand side), for the variation of the individual HS model parameters and boundary conditions assessed in set A under undrained conditions.

Assuming a fully saturated and undrained response of the Boom Clay during and immediately after the excavation, there is no change in volume. Hence, the deformation due to the contraction of the tunnel induces negative excess pore water pressure changes, which decrease the pore water pressure, u_w, in the vicinity of the tunnel for stress states located on the yield surface.

An increase in the strength parameters, i.e. cohesion and friction angle, c' and φ', reduces the plastic and hardening radii (Figures 6.2(a-d). The extent of the hardening is significantly larger than the extent of the perfectly plastic zone, the latter defining a stress state located on the failure envelope. Given $K_0 = 1$, the response is isotropic and $r^h \approx r^v$ (see Figures 6.2(a-b) and Figures 6.5(a,c,e) for the variation in cohesion c'). The reduction in the soil friction angle results in a larger pore water pressure on the liner, potentially due to the lower volumetric strains generated (compare with Figure 5.8(o)), which in turn increases the cavity pressure and thus the normal, shear and bending forces in the liner.

As for the Young's modulus, E, in the linear elastic perfectly plastic analytical model, in this HS model an increase in the reference secant modulus, E_{50}^{ref}, results in an increase in the hardening and plastic zone and a decrease in the cavity pressure (see Figures 4.6(d) and 6.2(e-f)). Figure 6.3(a) shows the stress path in $p' : q$ space for a point located on the horizontal profile behind the concrete liner ($x = 1.65$m, $y = -500$m) subjected to an undrained extension for three different reference tangent moduli. With decreasing E_{50}^{ref}, the hardening yield locus, which is initiated on the K_0^{NC}-line (see Section 5.5.3), is reached at a higher deviatoric stress and thus, given the prescribed displacement by the overcut, less stresses have to be redistributed, resulting in a smaller hardening and plastic zone. Figure 6.3(b) shows the corresponding shear strains, γ_s, plotted against the deviatoric stress, q, which corresponds

Table 6.3.: Undrained analyses - responses due to variation of model parameters, state variables and boundary conditions.

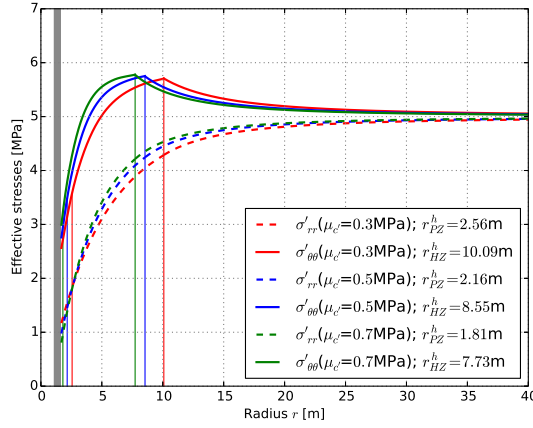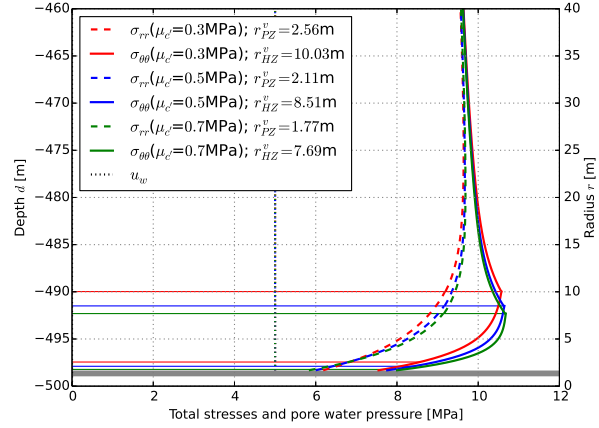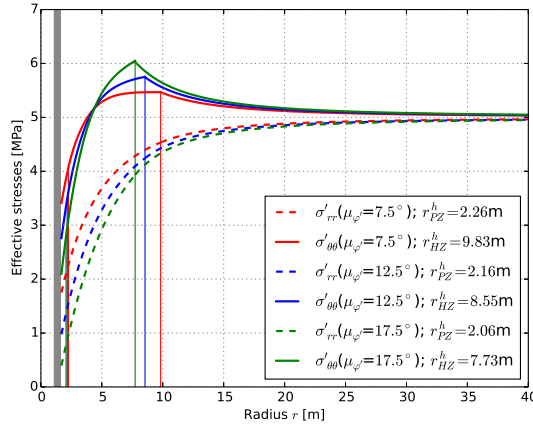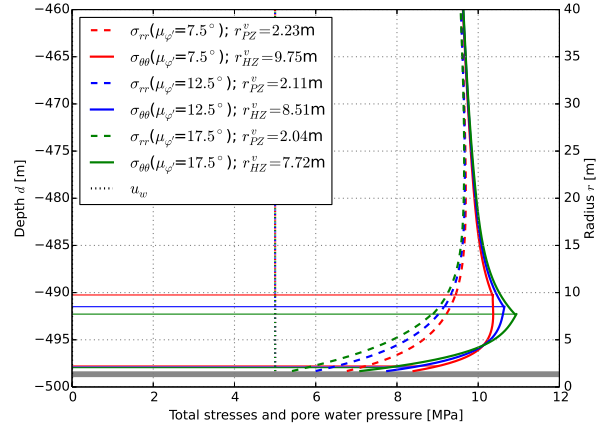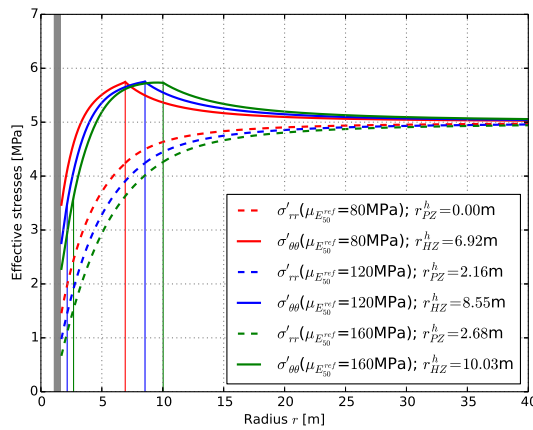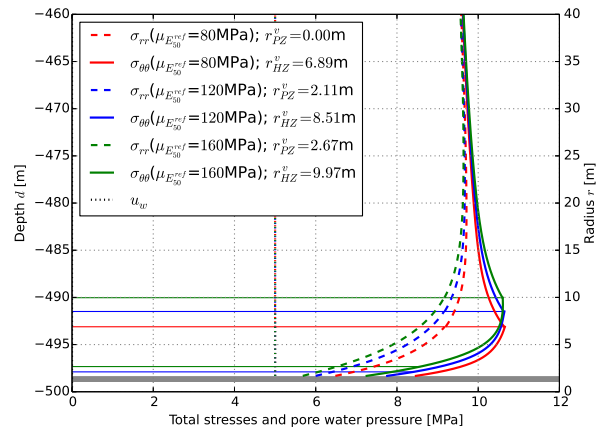| Set	Var. X	Unit	Val.	r_{PZ}^h [m]	r_{PZ}^v [m]	r_{HZ}^h [m]	r_{HZ}^v [m]	$p_{c,max}$ [MPa]	u_w [MPa]	$N_{l,max}$ $\left[\frac{kN}{m}\right]$	$|Q_{l,max}|$ $\left[\frac{kN}{m}\right]$	$M_{l,max}$ $\left[\frac{kN\,m}{m}\right]$
(A)	c'	[MPa]	0.30	2.415	2.420	11.864	11.739	4.915	1.698	-8429	8.43	-65.4
			0.50	1.938	1.892	10.110	10.026	4.798	1.668	-8269	8.27	-59.4
			0.70	1.697	1.695	9.076	9.039	4.628	1.676	-8027	8.03	-54.2
	φ'	[°]	7.50	2.180	2.175	11.508	11.365	6.065	2.433	-10337	10.34	-83.4
			12.50	1.938	1.892	10.110	10.026	4.798	1.668	-8269	8.27	-59.4
			17.50	1.734	1.748	9.209	9.172	3.616	0.980	-6341	6.34	-36.9
	E_{50}^{ref}	[MPa]	80.00	0*	0*	8.192	8.151	5.463	2.193	-9397	9.40	-70.2
			120.00	1.938	1.892	10.110	10.026	4.798	1.668	-8269	8.27	-59.4
			160.00	2.562	2.558	11.726	11.615	4.288	1.320	-7403	7.40	-52.0
	E_{oed}^{ref}	[MPa]	80.00	2.415	2.420	10.340	10.264	4.561	1.471	-7867	7.87	-54.4
			120.00	1.938	1.892	10.110	10.026	4.798	1.668	-8269	8.27	-59.4
			160.00	1.805	1.775	10.063	9.973	4.883	1.758	-8414	8.41	-61.4
	E_{ur}^{ref}	[MPa]	240.00	1.938	1.892	10.110	10.026	4.798	1.668	-8269	8.27	-59.4
			360.00	1.938	1.892	10.110	10.026	4.798	1.668	-8269	8.27	-59.4
			480.00	1.938	1.892	10.110	10.026	4.798	1.668	-8269	8.27	-59.4
	ν_{ur}	[−]	0.25	1.982	1.956	10.268	10.228	4.730	1.556	-8153	8.15	-58.4
			0.30	1.938	1.892	10.110	10.026	4.798	1.668	-8269	8.27	-59.4
			0.35	1.929	1.892	9.884	9.845	4.869	1.809	-8386	8.38	-60.4
	m	[−]	0.70	1.847	1.866	9.492	9.438	4.924	1.762	-8485	8.48	-61.2
			0.80	1.938	1.892	10.110	10.026	4.798	1.668	-8269	8.27	-59.4
			0.90	2.034	1.989	10.748	10.651	4.675	1.582	-8055	8.05	-57.8
(B)	ψ	[°]	0.00	1.938	1.892	10.110	10.026	4.798	1.668	-8269	8.27	-59.4
			2.00	1.929	1.892	10.089	10.026	4.719	0.832	-8162	8.16	-58.
			4.00	1.847	1.866	10.063	9.974	4.485	-0.847	-7820	7.82	-53.6
	K_0	[−]	0.80	1.814	1.828	14.945	6.049	4.996	2.205	-8353	8.34	-140.4
			0.90	1.882	1.989	12.168	7.819	4.874	1.913	-8248	8.24	-113.4
			1.00	1.938	1.892	10.056	10.026	4.798	1.668	-8269	8.27	-59.4
	OCR	[−]	2.00	1.938	1.892	10.226	10.155	4.811	1.680	-8290	8288	-59.6
			2.20	1.938	1.892	10.110	10.026	4.798	1.668	-8269	8.27	-59.4
			2.40	1.938	1.892	9.974	9.878	4.787	1.658	-8250	8249	-59.3
(C1)	c'	[MPa]	0.30	2.819	2.794	13.851	13.608	4.539	1.365	-7976	7.97	-63.5
	φ'	[°]	7.50	2.534	2.511	13.407	13.158	5.744	2.146	-9997	9.99	-80.4
	E_{50}^{ref}	[MPa]	160.00	2.978	2.963	13.648	13.468	3.857	0.935	-6854	6.85	-49.5
(C2)	c'	[MPa]	0.30	2.928	2.933	14.532	14.173	5.462	2.178	-13664	13.71	-73.6
	φ'	[°]	7.50	2.682	2.638	14.049	13.736	6.542	2.872	-16330	16.37	-86.4
	E_{50}^{ref}	[MPa]	160.00	3.122	3.092	14.336	14.046	4.910	1.867	-12329	12.36	-55.2
(C3)	c'	[MPa]	0.30	2.356	2.364	11.301	11.073	7.395	2.836	-12678	19.16	-349.3
	φ'	[°]	7.50	2.159	2.139	10.830	10.667	9.182	3.902	-15631	10.25	-378.8
	E_{50}^{ref}	[MPa]	160.00	2.519	2.477	11.103	10.963	6.779	2.466	-11682	17.23	-335.4

Set A and B: Variation of model parameters and stress state variables for HLW gallery with $r_c = 1.6$m, $d_{oc} = 75$mm and $d = 500$m.

Set C: Variation of boundary conditions for three critical variables for: (C1) HLW gallery with $r_c = 1.6$m, $d_{oc} = 100$mm and $d = 500$m, (C2) LILW gallery with $r_c = 2.4$m, $d_{oc} = 75$mm and $d = 500$m, and (C3) HLW gallery with $r_c = 1.6$m, $d_{oc} = 75$mm and $d = 700$m.

* Failure surface not reached.

(a) Cohesion c'

(b) Cohesion c'

(c) Friction angle φ'

(d) Friction angle φ'

(e) Reference secant modulus E_{50}^{ref}

(f) Reference secant modulus E_{50}^{ref}

(g) Reference oedometer modulus E_{oed}^{ref}

(h) Reference oedometer modulus E_{oed}^{ref}

(i) Reference un-/reloading modulus E_{ur}^{ref}

(j) Reference un-/reloading modulus E_{ur}^{ref}

(k) Un-/reloading Poisson's ratio ν_{ur}

(l) Un-/reloading Poisson's ratio ν_{ur}

(m) Rate of stress dep. of stiffness m (n) Rate of stress dep. of stiffness m
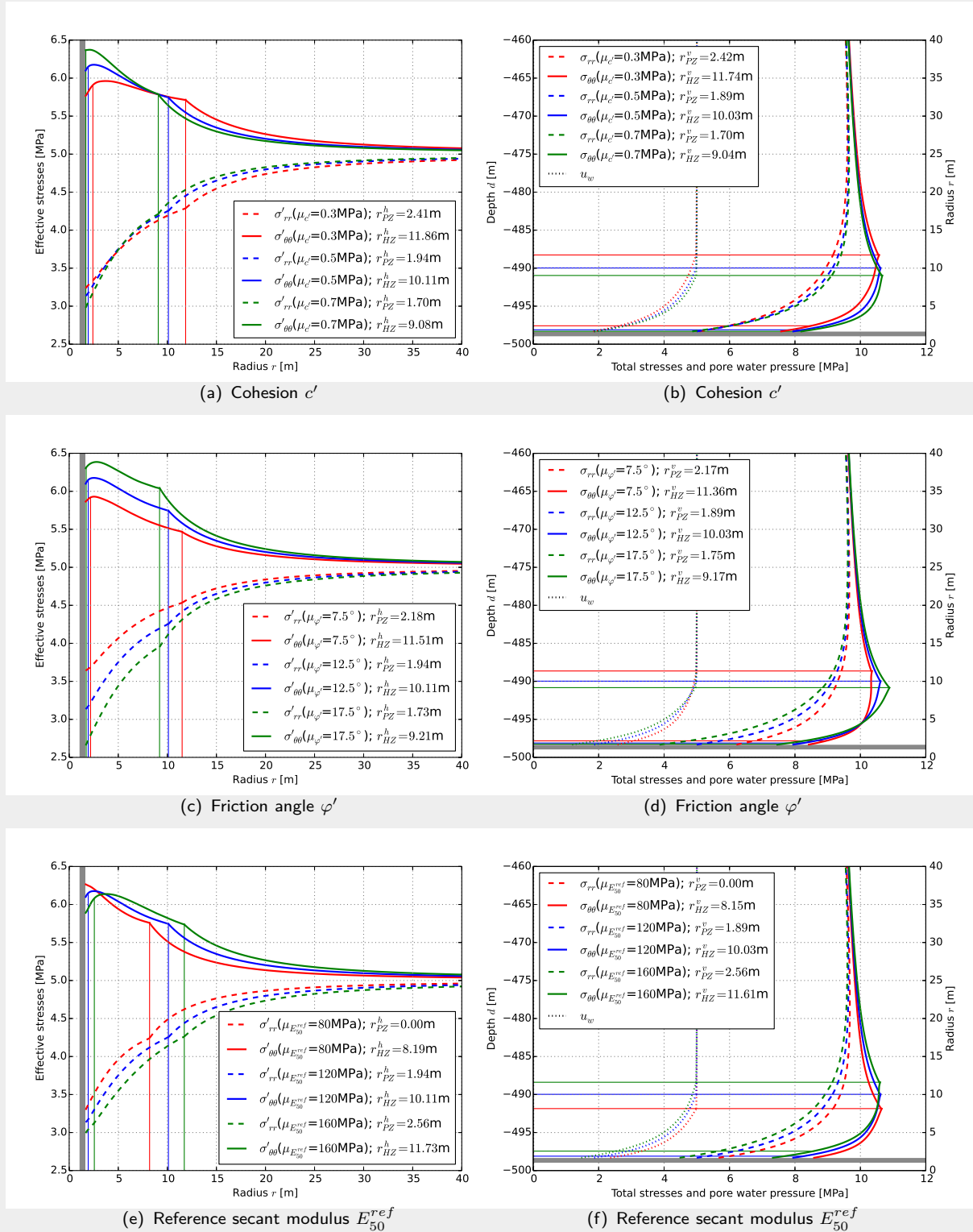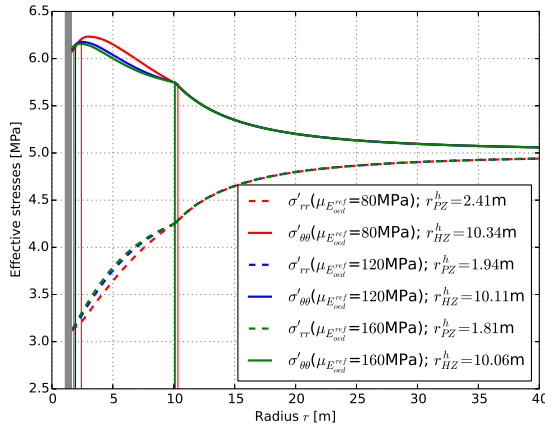
Figure 6.2.: Set A - undrained response: HLW gallery with $r_c = 1.6$m, $d_{oc} = 75$mm and $d = 500$m: (a,c,e,g,i,k,m) effective radial and tangential stress distributions in the horizontal profile, (b,d,f,h,j,l,n) total radial and tangential stress and pore water pressure distributions in the vertical profile.

with the findings discussed on Figure 5.9(a). Increasing the reference secant modulus to $E_{50}^{ref} = 160$MPa, the plastic radius reached a relative maximum of $r_{PZ}^{h} = 2.56$m with respect to all other variations tested for set A, whereas for the lower bound, $E_{50}^{ref} = 80$MPa, the failure locus is not reached (see Table 6.3).

An increase in the reference oedometer modulus, E_{oed}^{ref}, results in a decrease in the radial extent of the hardening and plastic zones (Figures 6.2(g-h) and Table 6.3). The impact of a

(a)   (b)
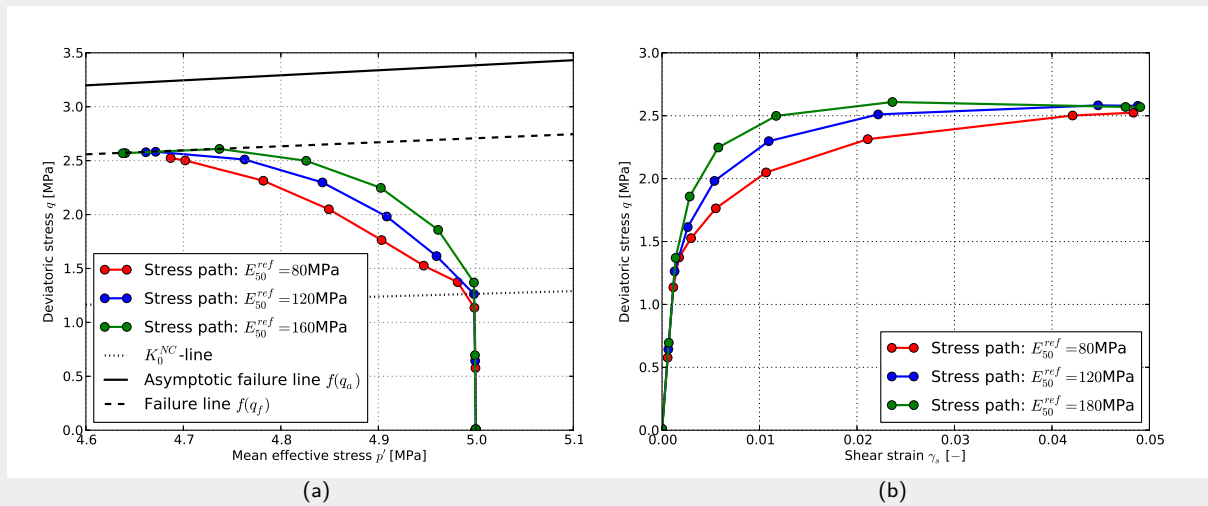
Figure 6.3.: Boom Clay response to variation of reference secant modulus E_{50}^{ref}: (a) Mean effective stress p' versus deviatoric stress q, and (b) shear strain γ_s versus deviatoric stress q.

(a) Angle of dilatancy ψ

(b) Angle of dilatancy ψ

(c) Earth pressure at rest K_0

(d) Earth pressure at rest K_0

(e) Overconsolidation ratio OCR

(f) Overconsolidation ratio OCR
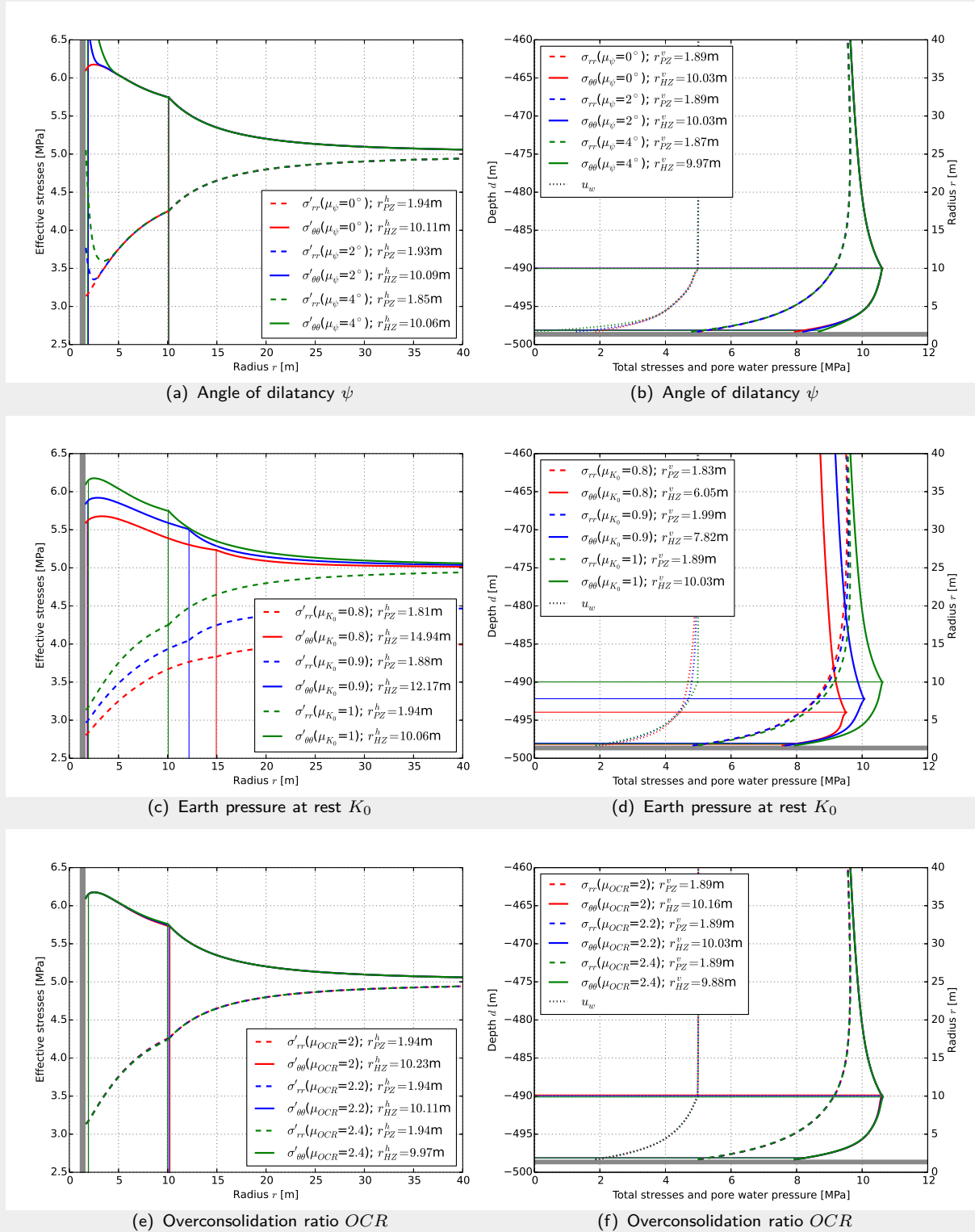
Figure 6.4.: Set B - undrained response: HLW gallery with $r_c = 1.6$m, $d_{oc} = 75$mm and $d = 500$m: (a,c,e) effective radial and tangential stress distributions in horizontal direction, (b,d,f) total radial and tangential stress and pore water pressure distributions in vertical direction.

variation in E_{oed}^{ref} is more significant on the location of the plastic zone than on the hardening zone. Although the cap yield surface is not touched, this response may be explained by the adjustment of the internal model parameters (see Figure 5.9(c)), especially the potential reduction of the elasto-plastic shear modulus, G_{50}^{ref}, with increasing E_{oed}^{ref}.

A variation of the reference unloading/reloading modulus, E_{ur}^{ref}, or the unloading/reloading Poisson's ratio, ν_{ur}, does not affect the undrained Boom Clay response (Figures 6.2(i-l) and Table 6.3). Similarly, an increase in the HS model exponent, m, defining the stress dependency of the stiffness only slightly increases the extent of the hardening and plastic zones (Figures 6.2(m-n) and Table 6.3).

Set B:

Figure 6.4 shows the effective radial and tangential stress distributions in the horizontal profile, and the total radial and tangential stress and pore water pressure distributions in the vertical profile, for an excavation of a HLW gallery at 500m depth for set B.

Figures 6.4(a-b) show that an increase in the Boom Clay dilation angle, ψ_d, insignificantly reduces the extent of the hardening and fully plastic zone. The literature study showed that the dilation angle might be significant (Table 2.10 and A.2). Hence, the reduction in pore water pressure, associated with a more dilative material, down to negative values (Table 6.3) should be further investigated and potentially limited by a tension cut-off criteria.

Table A.1 showed that the in situ stress is most likely anisotropic, i.e. with the earth pressure at rest being $K_0 < 1$. Figures 6.4(c-d) show the Boom Clay stress response around a HLW gallery with different K_0 values. With increasing degree of in situ stress anisotropy, the extent of the hardening in the horizontal direction becomes significantly larger than in the vertical direction (see Table 6.3 and Figures 6.5(b,d,f)). The extent of the plastic zone is less affected by the variation in K_0. The hardening zone extending in diagonal direction from the tunnel in Figure 6.5(a) for a low earth pressure at rest of $K_0 = 0.8$ is due to the shear hardening surface being touched earlier due to the shear stresses induced by the in situ stress anisotropy.

Figures 6.4(e-f) show that the overconsolidation ratio, OCR, does not significantly influence the Boom Clay response.

Set C:

Figure 6.6 shows the effective radial and tangential stress distributions in the horizontal profile, and the total radial and tangential stress and pore water pressure distributions in the vertical profile, for set C. For this set three HS model parameters whose variations resulted in the largest extents in the plastic and hardening zones, have been selected, that is the lower cohesion $c' = 0.3$MPa, the lower friction angle $\varphi' = 7.5°$ and the upper secant reference modulus $E_{50}^{ref} = 160$MPa.

(a) Cohesion $c' = 300$MPa

(b) Earth pressure at rest $K_0 = 0.8$

(c) Cohesion $c' = 500$MPa

(d) Earth pressure at rest $K_0 = 0.9$

(e) Cohesion $c' = 700$MPa

(f) Earth pressure at rest $K_0 = 1.0$
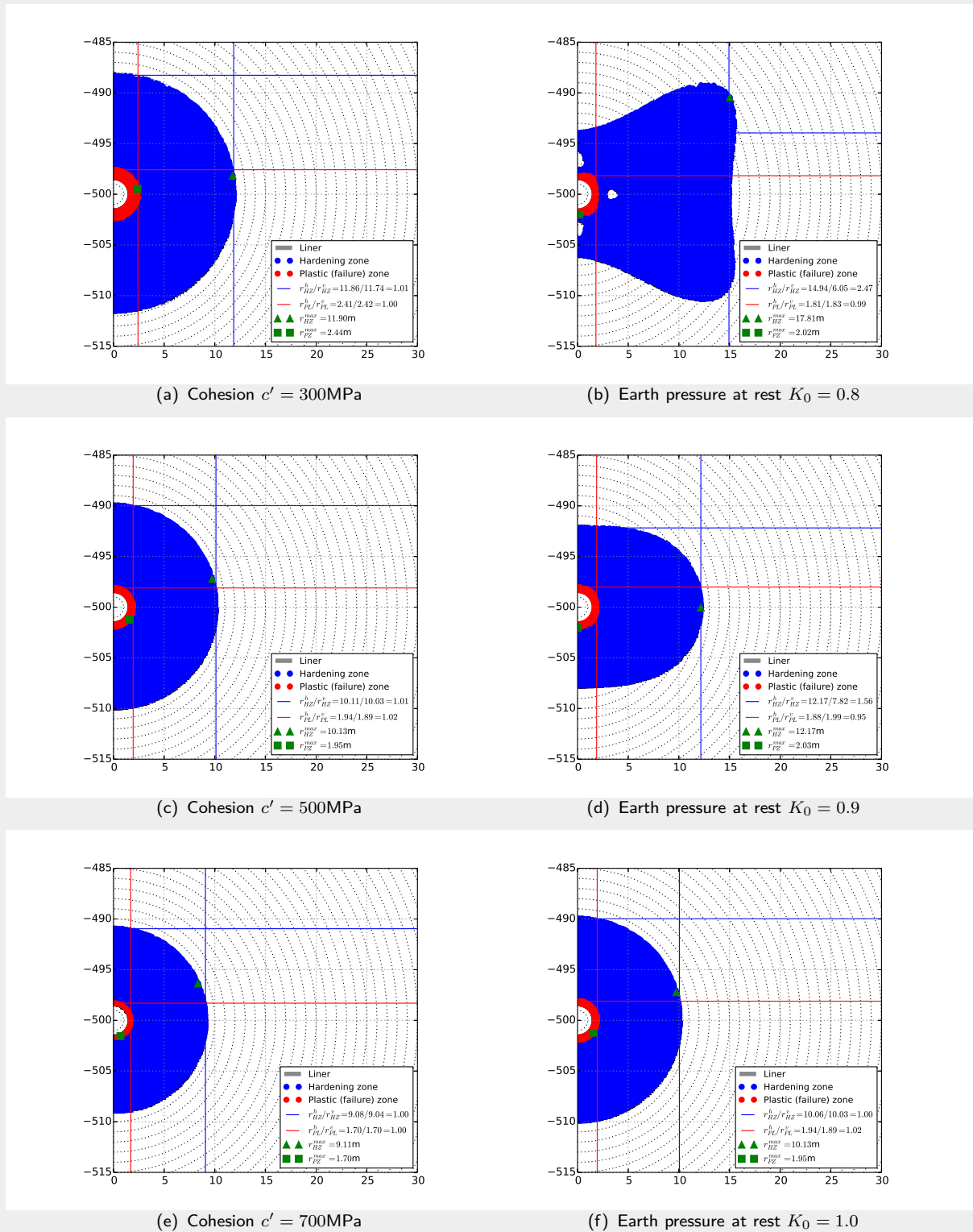
Figure 6.5.: Undrained response: Gaussian integration points showing the extent of the *Plastic Zone* (PZ) and *Hardening Zone* (HZ): (a,c,e) for a variation of the cohesion, c', in an isotropic setting ($K_0 = 1$), and (b,d,f) for a variation of the earth pressure at rest, K_0.

Figures 6.6(a-d) show that an increase of the overcut to $d_{oc} = 100$mm or of the cavity radius to $r_c = 2.4$m increases the extent of the hardening and plastic zones with respect to set A (see Table 6.3). The lower friction angle, $\varphi' = 7.5°$, results in the maximum cavity pressure of $p_c = 6.54$ and thus maximum liner forces.

Figures 6.6(e-f) shows, similar to the the analytical response (Figure 4.7(c)), that an increase in depth influences only marginally the extent of the hardening and plastic zones, but significantly increases the cavity pressure and thus the forces and moments in the liner. Note that the HS model parameters have been kept equal to the values for a tunnel at 500m depth. Given that $|\sigma_3'|$ will increase with depth, so does the stress dependent stiffness moduli E_{50}, E_{oed} and E_{ur} (see Equations 5.5, 5.6 and 5.23).

6.2.5. Pre-operational and early post-closure phase

In the pre-operational and early post-closure phase analyses, the Boom Clay is assumed to be fully water saturated and to respond in a drained fashion. The tunnel liner is assumed to be impermeable to ensure the accessibility and safety of galleries; however, due to degradation of the concrete the liner may become semi-permeable. Hence the pore water pressure in the surrounding host rock is assumed to approach the initial (hydrostatic) conditions during the consolidation phase.

The responses of all drained deterministic analyses have been summarised in Table 6.4.

Set A:

Figure 6.7 shows the effective radial and tangential stress distributions in the horizontal profile (left-hand side), and the total radial and tangential stress and pore water pressure distributions in the vertical profile (right-hand side), for the variation of the individual HS model parameters and boundary conditions assessed in set A under drained conditions.

Compared to the undrained response, the extent of the hardening decreases whereas the plastic zone increases for all cases of varying the seven main HS model parameters. The response is again isotropic, with the largest values reached for the case of a lower bound cohesion, c', a lower bound friction angle, φ', an upper bound reference secant modulus, E_{50}^{ref}, and a lower bound reference oedometer modulus, E_{oed}^{ref} (Table 6.4). Compared to the Boom Clay response computed with the analytical model (Figure 4.6), the response using the HS model suggests that a variation in cohesion and stiffness becomes more important than a variation in the friction angle, that is, with respect to the extent of the plastic zone. However, with respect to the cavity pressure, and thus the liner forces, which are larger for all cases analysed in set A compared to the undrained response, a low friction angle results in the largest cavity pressure, which is in agreement with the observation of the analytical model.

(a) Set C1: Overcut $d_{oc} = 10$mm

(b) Set C1: Overcut $d_{oc} = 10$mm

(c) Set C2: Cavity radius $r_c = 2.4$m

(d) Set C2: Cavity radius $r_c = 2.4$m
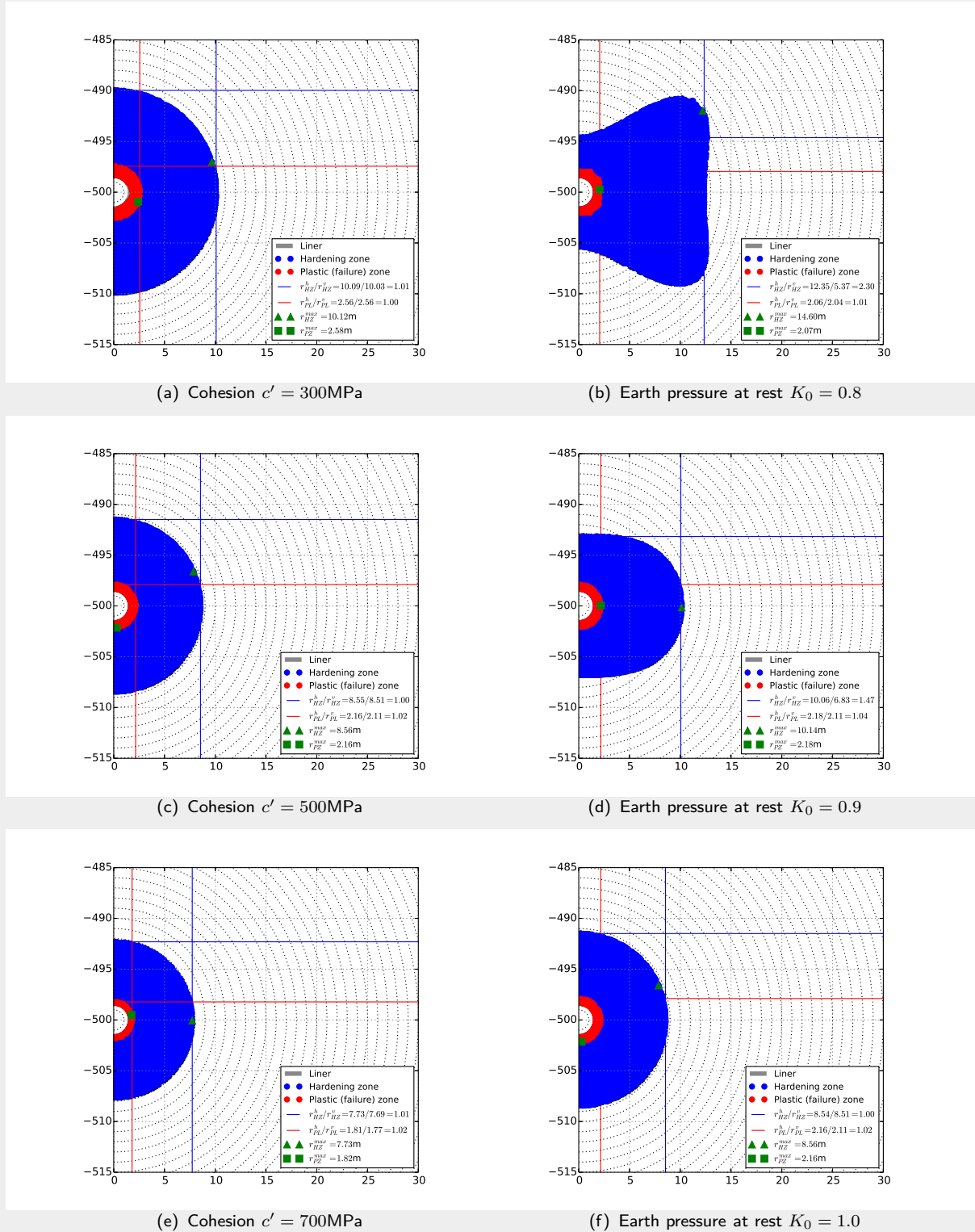
(e) Set C3: Excavation depth $d = 700$m

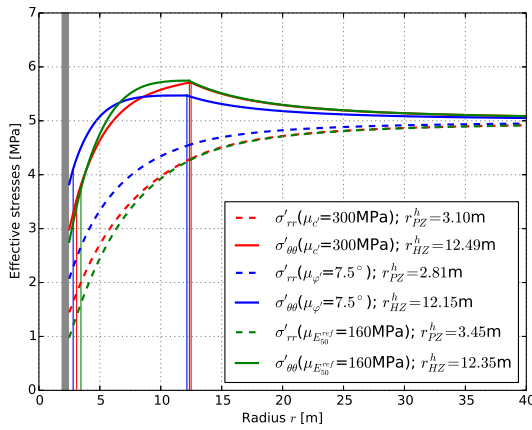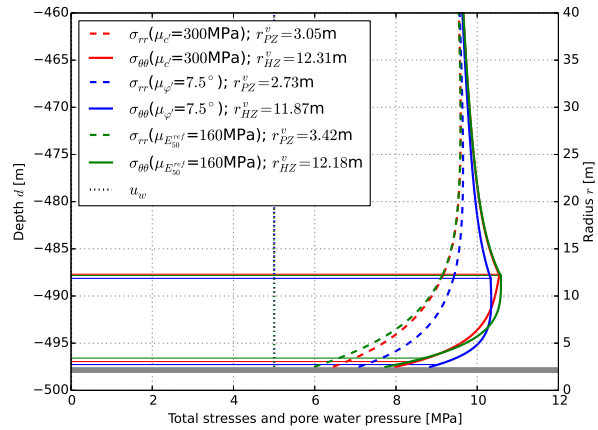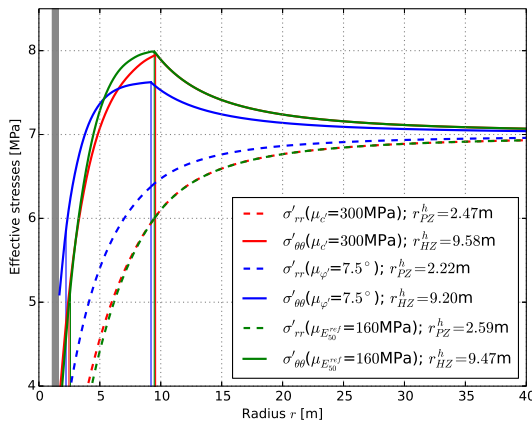(f) Set C3: Excavation depth $d = 700$m
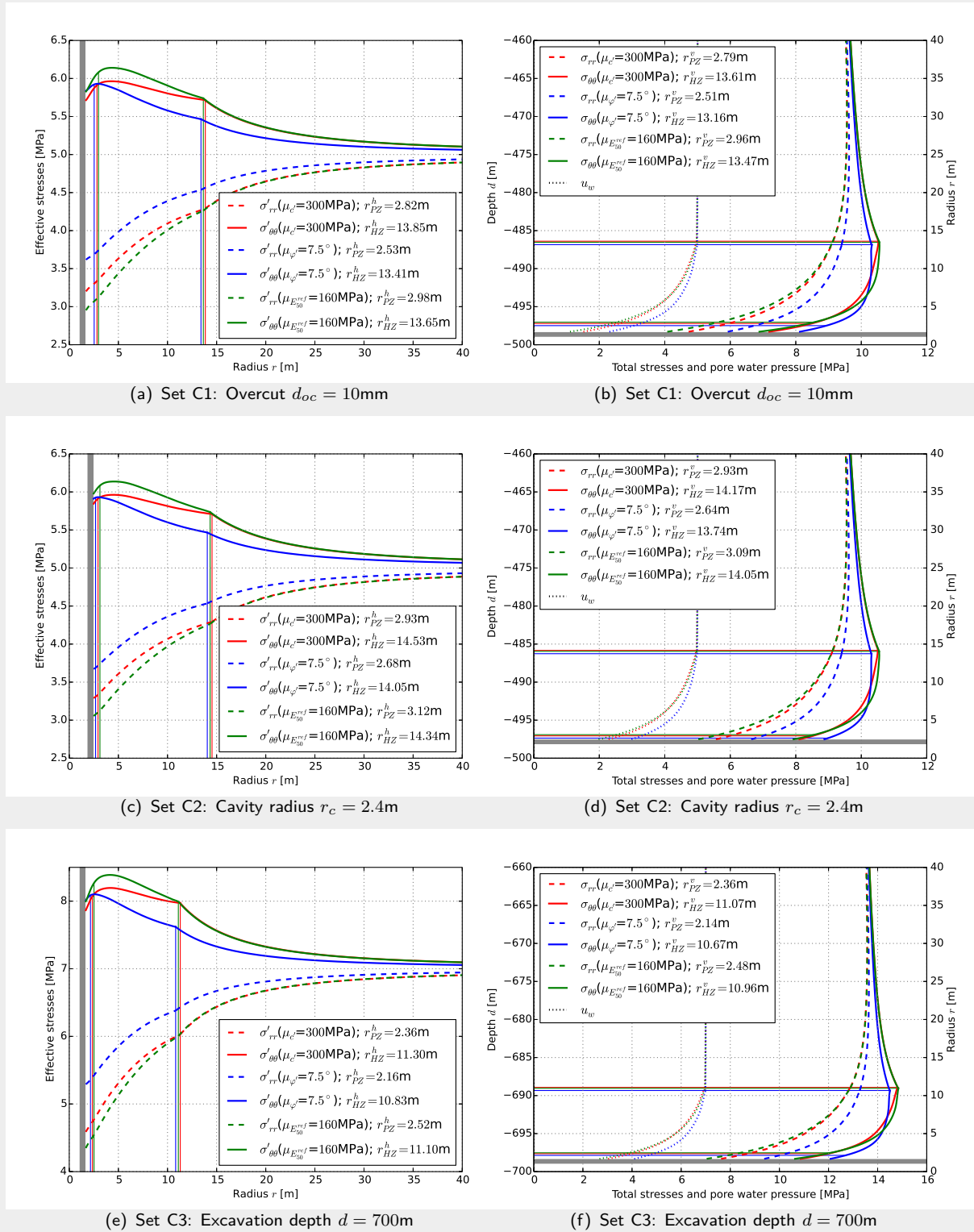
Figure 6.6.: Set C - undrained response: (C1) HLW gallery with $r_c = 1.6$m, $d_{oc} = 100$mm and $d = 500$m, (C2) LILW gallery with $r_c = 2.4$m, $d_{oc} = 75$mm and $d = 500$m, and (C3) HLW gallery with $r_c = 1.6$m, $d_{oc} = 75$mm and $d = 700$m: (a,c,e) effective radial and tangential stress distributions in horizontal direction, (b,d,f) total radial and tangential stress and pore water pressure distributions in vertical direction.

Table 6.4.: Drained analyses - responses due to variation of model parameters, state variables and boundary conditions.

Set	Var. X	Unit	Val.	r_{PZ}^h [m]	r_{PZ}^v [m]	r_{HZ}^h [m]	r_{HZ}^v [m]	$p_{c,max}$ [MPa]	u_w [MPa]	$N_{l,max}$ $\left[\frac{kN}{m}\right]$	$|Q_{l,max}|$ $\left[\frac{kN}{m}\right]$	$M_{l,max}$ $\left[\frac{kN\,m}{m}\right]$
(A)	c'	[MPa]	0.30	2.562	2.558	10.089	10.026	6.097	5.000	-10361	10.36	-81.8
			0.50	2.157	2.107	8.545	8.506	5.879	5.000	-10027	10.03	-76.0
			0.70	1.805	1.775	7.732	7.693	5.703	5.000	-9735	9.73	-71.4
	φ'	[°]	7.50	2.260	2.225	9.826	9.749	6.666	5.000	-11316	11.31	-92.0
			12.50	2.157	2.107	8.545	8.506	5.879	5.000	-10027	10.03	-76.0
			17.50	2.062	2.044	7.732	7.721	5.308	5.000	-9045	9.04	-63.5
	E_{50}^{ref}	[MPa]	80.00	0*	0*	6.921	6.887	6.342	5.000	-10820	10.82	-84.3
			120.00	2.157	2.107	8.545	8.506	5.879	5.000	-10027	10.03	-76.0
			160.00	2.681	2.668	10.034	9.968	5.584	5.000	-9531	9.53	-71.3
	E_{oed}^{ref}	[MPa]	80.00	2.619	2.600	8.815	8.754	5.759	5.000	-9817	9.82	-73.6
			120.00	2.157	2.107	8.545	8.506	5.879	5.000	-10027	10.03	-76.0
			160.00	1.995	1.989	8.501	8.442	5.951	5.000	-10115	10.11	-77.1
	E_{ur}^{ref}	[MPa]	240.00	2.157	2.107	8.545	8.506	5.879	5.000	-10027	10.03	-76.0
			360.00	2.157	2.107	8.545	8.506	5.879	5.000	-10027	10.03	-76.0
			480.00	2.157	2.107	8.545	8.506	5.879	5.000	-10027	10.03	-76.0
	ν_{ur}	[−]	0.25	2.180	2.175	8.465	8.410	5.884	5.000	-10035	10.03	-76.0
			0.30	2.157	2.107	8.545	8.506	5.879	5.000	-10027	10.03	-76.0
			0.35	2.102	2.089	8.671	8.596	5.882	5.000	-10010	10.01	-76.0
	m	[−]	0.70	2.062	2.044	8.065	7.998	5.973	5.000	-10164	10.16	-77.4
			0.80	2.157	2.107	8.545	8.506	5.879	5.000	-10027	10.03	-76.0
			0.90	2.206	2.175	9.064	9.004	5.809	5.000	-9892	9.89	-74.7
(B)	ψ	[°]	0.00	2.157	2.107	8.545	8.506	5.879	5.000	-10027	10.03	-76.0
			2.00	2.157	2.107	8.514	8.449	5.891	5.000	-10034	10.03	-76.2
			4.00	2.157	2.107	8.383	8.329	5.911	5.000	-10072	10.07	-76.7
	K_0	[−]	0.80	2.062	2.044	12.353	5.373	5.931	5.000	-9861	9.86	-134.7
			0.90	2.180	2.107	10.056	6.833	5.896	5.000	-9886	9.88	-115.1
			1.00	2.157	2.107	8.542	8.506	5.879	5.000	-10027	10.03	-76.0
	OCR	[−]	2.00	2.145	2.107	8.663	8.596	5.890	5.000	-10038	10.04	-76.2
			2.20	2.157	2.107	8.545	8.506	5.879	5.000	-10027	10.03	-76.0
			2.40	2.157	2.107	8.465	8.410	5.886	5.000	-10015	10.01	-75.9
(C1)	c'	[MPa]	0.30	3.029	3.002	11.709	11.560	5.906	5.000	-10215	10.21	-80.0
	φ'	[°]	7.50	2.567	2.558	11.428	11.314	6.424	5.000	-11134	11.13	-89.3
	E_{50}^{ref}	[MPa]	160.00	3.152	3.104	11.604	11.496	5.373	5.000	-9322	9.32	-68.8
(C2)	c'	[MPa]	0.30	3.097	3.052	12.491	12.305	6.391	5.000	-15952	16.00	-81.3
	φ'	[°]	7.50	2.812	2.733	12.147	11.868	7.009	5.000	-17471	17.52	-90.3
	E_{50}^{ref}	[MPa]	160.00	3.452	3.418	12.353	12.178	5.911	5.000	-14776	14.82	-67.7
(C3)	c'	[MPa]	0.30	2.466	2.386	9.578	9.464	8.913	7.000	-15111	8.13	-369.8
	φ'	[°]	7.50	2.224	2.196	9.201	9.089	9.940	7.000	-16819	5.83	-389.0
	E_{50}^{ref}	[MPa]	160.00	2.587	2.477	9.468	9.356	8.403	7.000	-14297	7.71	-359.7

Set A and B: Variation of model parameter and stress state variables for HLW gallery with $r_c = 1.6$m, $d_{oc} = 75$mm and $d = 500$m.

Set C: Variation of boundary conditions for three critical variables for: (C1) HLW gallery with $r_c = 1.6$m, $d_{oc} = 100$mm and $d = 500$m, (C2) LILW gallery with $r_c = 2.4$m, $d_{oc} = 75$mm and $d = 500$m, and (C3) HLW gallery with $r_c = 1.6$m, $d_{oc} = 75$mm and $d = 700$m.

* Failure surface not reached.

(a) Cohesion c'

(b) Cohesion c'

(c) Friction angle φ'

(d) Friction angle φ'

(e) Reference secant modulus E_{50}^{ref}

(f) Reference secant modulus E_{50}^{ref}

(g) Reference oedometer modulus E_{oed}^{ref}

(h) Reference oedometer modulus E_{oed}^{ref}

(i) Reference un-/reloading modulus E_{ur}^{ref}

(j) Reference un-/reloading modulus E_{ur}^{ref}

(k) Un-/reloading Poisson's ratio ν_{ur}

(l) Un-/reloading Poisson's ratio ν_{ur}

(m) Rate of stress dep. of stiffness m (n) Rate of stress dep. of stiffness m

Figure 6.7.: Set A - drained response: HLW gallery with $r_c = 1.6$m, $d_{oc} = 75$mm and $d = 500$m: (a,c,e,g,i,k,m) effective radial and tangential stress distributions in horizontal direction, (b,d,f,h,j,l,n) total radial and tangential stress and pore water pressure distributions in vertical direction.

Set B:

The effect of variation of the dilation angle, ψ, and overconsolidation ratio, OCR, on the extent of the hardening/plastic zone and on the cavity pressure, are negligible (Figures 6.8(a,b,e,f)). As for the undrained cases, the effect of having an anisotropic in situ stress field on the anisotropy of the extent of the plastic zone is very small (compare Figures 6.4(c-d) and 6.8(c-d)). Compared to the undrained cases, for the drained cases the degree of anisotropy of the hardening zone slightly decreases due the reduction in the extent of the hardening zone (compare Figures 6.5(b,d,f) and 6.9(b,d,f)).

Set C:

The drained responses for set C are shown in Figure 6.10. As for the undrained cases of set C, an increase in the overcut or cavity radius primarily extends the plastic and hardening zones, whereas an increase the gallery depth primarily affects the cavity pressure. A maximum extent of the plastic zone of $r_{PZ}^h = 3.45$m was obtained for the upper bound reference secant modulus of $E_{50}^{ref} = 160$MPa. For the lower bound friction of $\varphi' = 7.5°$ a maximum cavity pressure of $p_c = 9.94$ was obtained.

(a) Angle of dilatancy ψ

(b) Angle of dilatancy ψ

(c) Earth pressure at rest K_0

(d) Earth pressure at rest K_0

(e) Overconsolidation ratio OCR

(f) Overconsolidation ratio OCR
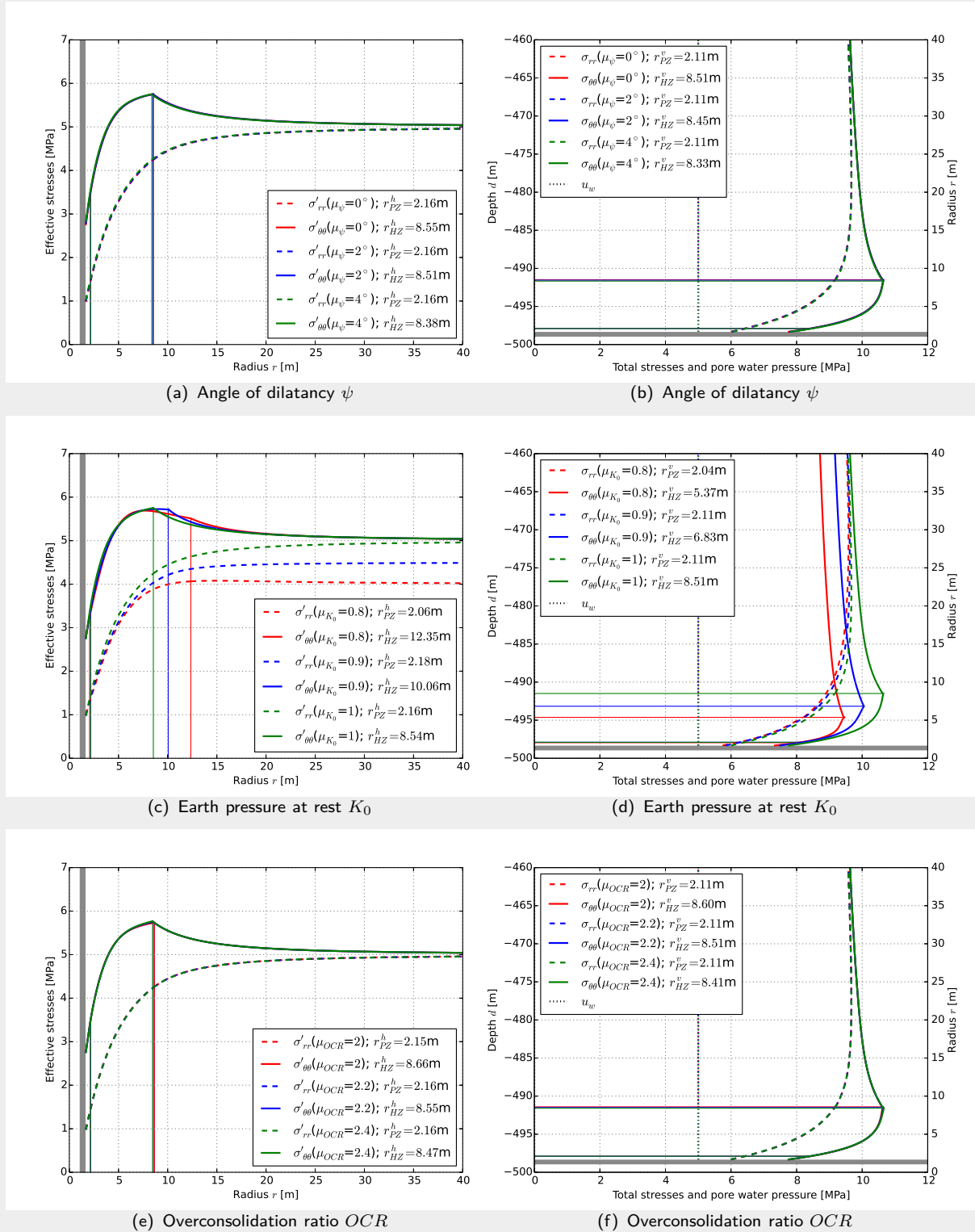
Figure 6.8.: Set B - drained response: HLW gallery with $r_c = 1.6$m, $d_{oc} = 75$mm and $d = 500$m: (a,c,e) effective radial and tangential stress distributions in horizontal direction, (b,d,f) total radial and tangential stress and pore water pressure distributions in vertical direction.

(a) Cohesion $c' = 300\text{MPa}$

(b) Earth pressure at rest $K_0 = 0.8$

(c) Cohesion $c' = 500\text{MPa}$

(d) Earth pressure at rest $K_0 = 0.9$

(e) Cohesion $c' = 700\text{MPa}$

(f) Earth pressure at rest $K_0 = 1.0$

Figure 6.9.: Drained response: Gaussian integration points showing the extent of the *Plastic Zone* (PZ) and *Hardening Zone* (HZ): (a,c,e) for a variation of the cohesion, c', in an isotropic setting ($K_0 = 1$), and (b,d,f) for a variation of the earth pressure at rest, K_0.
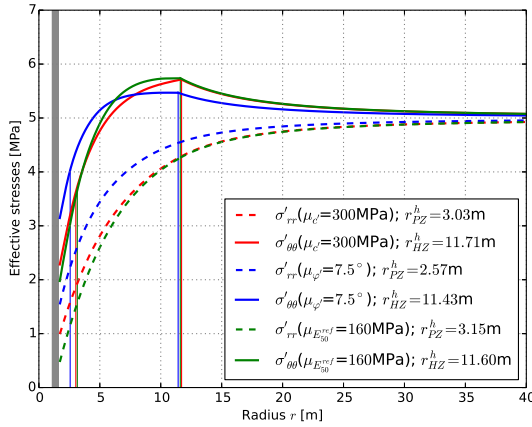
(a) Set C1: Overcut $d_{oc} = 10$mm
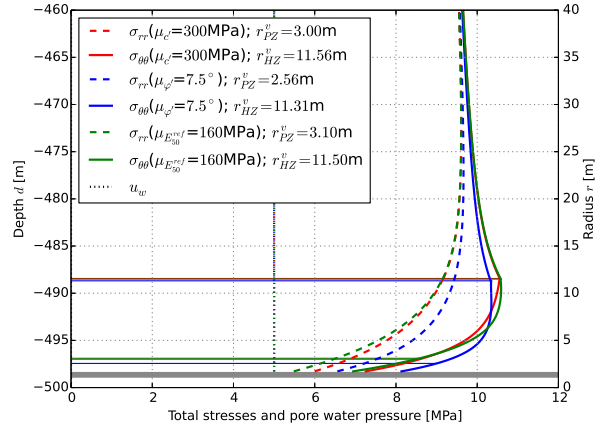
(b) Set C1: Overcut $d_{oc} = 10$mm

(c) Set C2: Cavity radius $r_c = 2.4$m

(d) Set C2: Cavity radius $r_c = 2.4$m

(e) Set C3: Excavation depth $d = 700$m
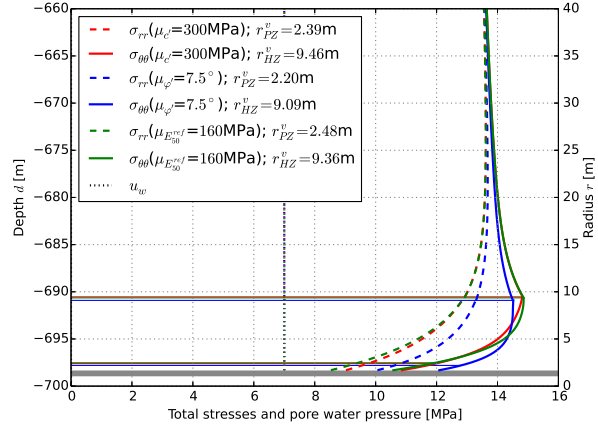
(f) Set C3: Excavation depth $d = 700$m

Figure 6.10.: Set C - drained response: (C1) HLW gallery with $r_c = 1.6$m, $d_{oc} = 100$mm and $d = 500$m, (C2) LILW gallery with $r_c = 2.4$m, $d_{oc} = 75$mm and $d = 500$m, and (C3) HLW gallery with $r_c = 1.6$m, $d_{oc} = 75$mm and $d = 700$m: (a,c,e) effective radial and tangential stress distributions in horizontal direction, (b,d,f) total radial and tangential stress and pore water pressure distributions in vertical direction.

6.3. Three-dimensional modelling

In this Section the staged excavation of a single tunnel gallery is modelled in a three dimensional undrained FE analysis. For this example the excavation of a HLW gallery ($r_c = 1.6$m, $d_{oc} = 75$mm) at a depth of $z = 500$m is simulated utilising the HS model. For the HS parameter values and in situ conditions the mean estimates (bold values in Table 6.2) have been assumed.

Figure 6.11(a) shows a schematic drawing of the excavation process using a *Shield Machine* (SM). This technique was selected for the excavation of the PRACLAY and Connection Gallery at the HADES URF in Mol (see Section 2.5.1.1) however, other techniques are as well applicable. The length of the shield was chosen be $l_s = 2$m, which is similar to the machine used in Mol. The excavation length, l_e, was set to be equal to the length of one concrete liner segment, $l_s = 1$m. In practice this length is likely to be slightly longer in order for the hydraulic jacks to be retrieved after each excavation step.

Figure 6.11(b) shows the model domain. The 60m long gallery is excavated in y-direction in two main phases. The first phase, 30m are excavated instantly without modelling the advancement of the machine. A contraction boundary is applied instantly, similar to the two-dimensional simulations. The remaining 30m are excavated in 30 steps of 1m. The deformation of the Boom Clay will be recorded on the nodal points on three longitudinal profiles, one vertical profile and one horizontal profile.

The analysis is simplified by using a steady state undrained analysis. The conicity of the open shield (i.e. the overcut) allows the machine to move without getting trapped in the clay however, the stress relief in the soil induces elastic, and potentially plastic, deformation. In reality the Boom Clay has only a limited time to deform, that is, until the liner is installed after 3m of excavation (shield + unsupported excavation length). The assumption of the liner being in direct contact with the Boom Clay after installation is valid as commonly the installation of key segments ensures a flush fit. The deformation of the Boom Clay over the first 3m (shield + unsupported excavation length) is here assumed to increase linearly from a zero at the fixed boundary at the cutting edge to $d_{oc} = 75$mm at the last liner liner installed (Figure 6.11(a)).

Figure 6.11(c) shows the initial vertical effective domain which is discretised by $262\,734$ 10-node tetrahedral elements with $381\,890$ nodes.

Figure 6.12 shows the three longitudinal deformation profiles in advance of excavation front, which is located at $y_{excav} = 45$m. The Figure shows that due to the staged excavation the Boom Clay deforms about 8-10m ahead of the excavation front. The longitudinal deformation u_y, computed at the tunnel center profile P1, is significantly larger than the deformations u_z and u_x along the profiles P2 and P3.

Figure 6.13 shows the cone shaped longitudinal deformation, u_y, in at the excavation front, which extends as well outside of the excavation radius. Figure 6.14 shows the vertical deformation, u_z, in a three-dimensional plot. The Figure shows that the deformation increases when accounting for the staged excavation.
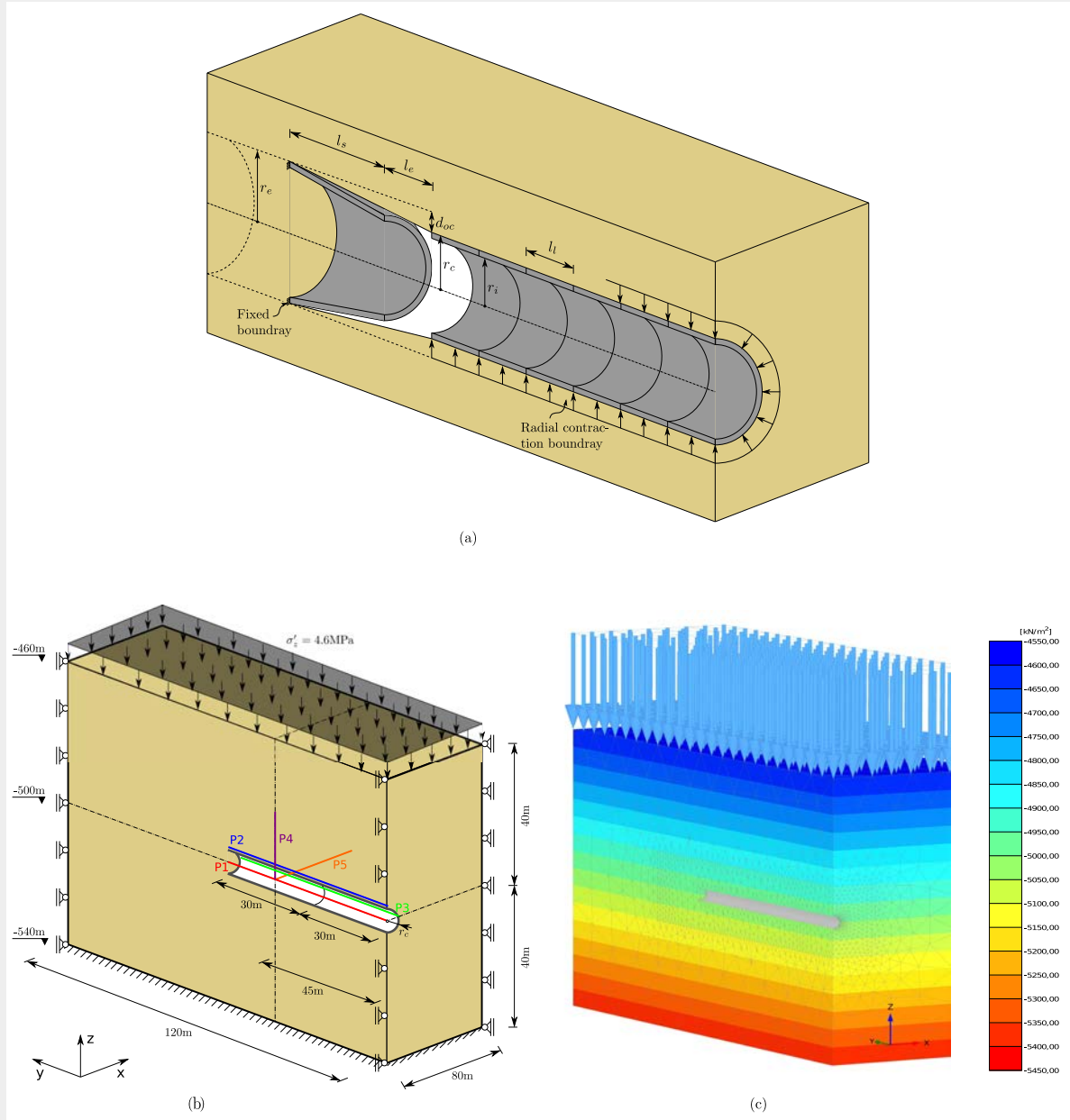
Figure 6.11.: Three-dimensional excavation of a single tunnel gallery: (a) schematic description of the excavation, (b) model domain, and (c) initial effective vertical stress and discretisation. The three longitudinal profiles are $P1 = \{0, 30...60, -500\}$m, $P2 = \{0, 30...60, -498\}$m and $P3 = \{2, 30...60, -500\}$m, the vertical profile is $P4 = \{0, 45, -480... -498\}$m and the horizontal profile is $P5 = \{2...20, 45, -500\}$m.
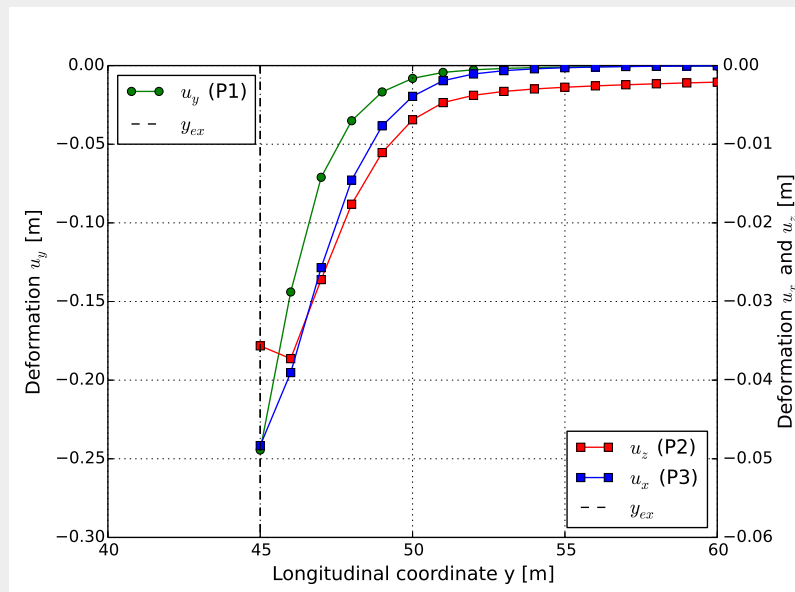
Figure 6.12.: Displacement profiles in front of excavation front located at $y_{excav} = 45$m for the longitudinal profiles P1, P2 and P3 (see Figure 6.11(b)).
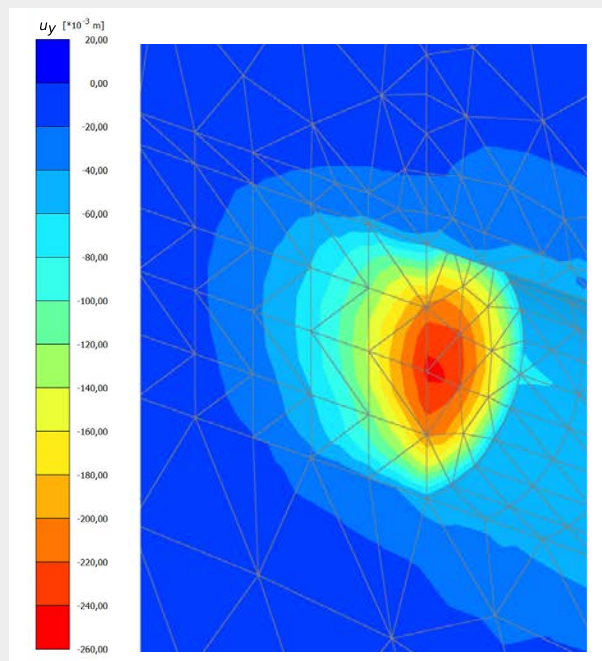
Figure 6.13.: Longitudinal deformation, u_y, at the excavation front.
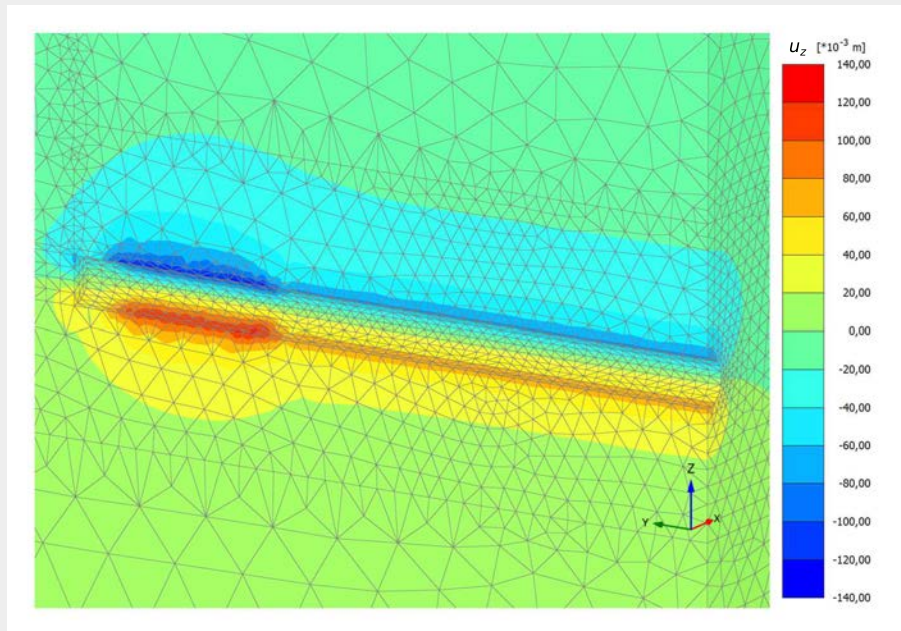
Figure 6.14.: Vertical deformation, u_z, at the cavity wall.

Figure 6.15 shows the displacement u_z and u_x along the vertical and horizontal profiles P4 and P5 (located at $y = 45$m) as the excavation front progresses from $y_{ex} = 30$m to $y_{ex} = 60$m. The Figures show that due to the staged excavation the deformation exceed the deformation induced by the overcut ($d_{oc} = 75$mm).

6.4. Summary

In this Chapter the response the Boom Clay due to the excavation of a single horizontal tunnel gallery was investigated utilising the HS model in two- and three dimensional analyses. A mechanical sensitivity analysis was performed by varying individually the HS model parameters, the in situ stress states and the boundary conditions in a two-dimensional set-up simulating both the excavation in an undrained analysis as well as the pre-operational and early post-closure phase in a drained analysis. For the critical parameters some three-dimensional analyses were subsequently to assess the the difference to the two-dimensional approximation.

Assuming a fully drained response after consolidation, the extent of hardening and plastic zone as well as the cavity pressure increased compared to the undrained response. Compared to the analytical investigation (Section 4.7) where a reduction in the soil friction angle resulted in the largest plastic zone, in both the drained and undrained numerical investigation, utilising the HS model, the cohesion, the reference secant modulus and the reference oedometer modulus become more important. The relatively low extent of the plastic zone (< 3m) suggests, in agreement with the analytical results, that a gallery spacing of 50m, as proposed in the reference design (Verhoef et al., 2011), is sufficient for the tunnel stability and may be reduced
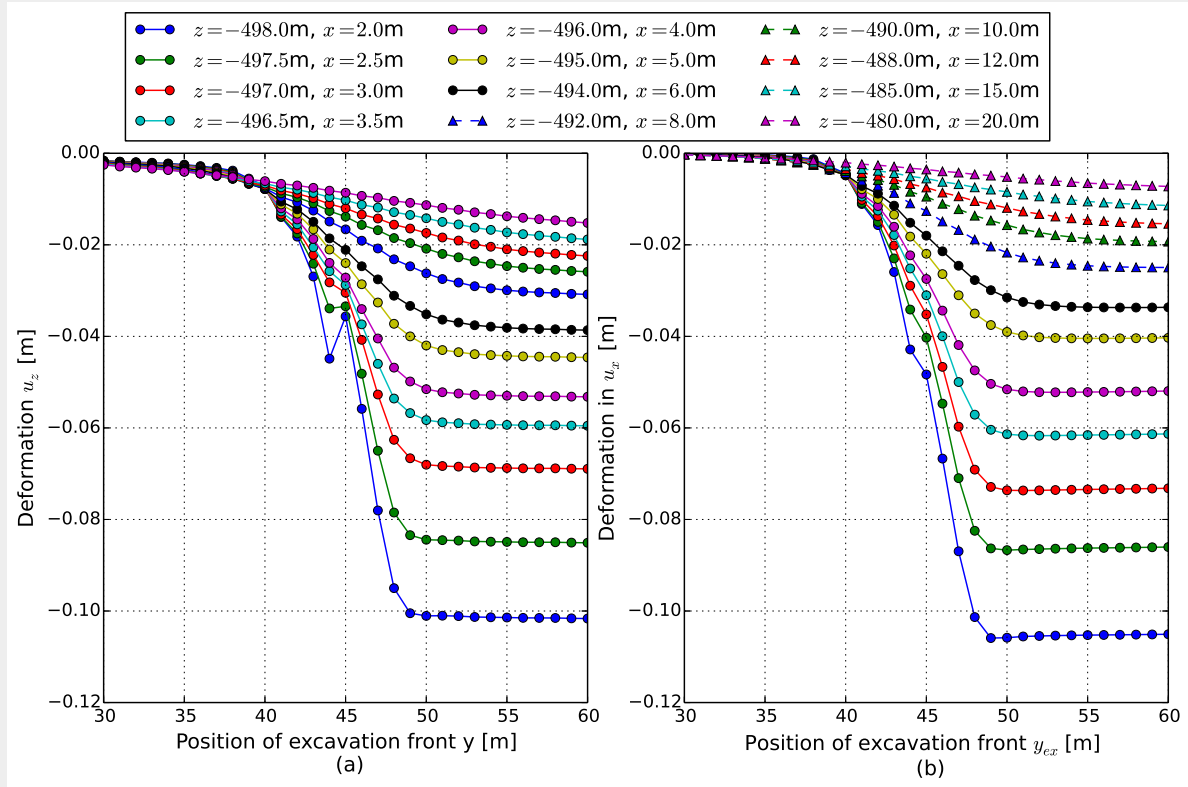
Figure 6.15.: Displacement u_z and u_x along the vertical and horizontal profiles, P4 and P5, with progression of the excavation front.

as part of a design optimisation process.

The preliminary three-dimensional Finite Element analysis showed that deformation of the Boom Clay around the tunnel gallery may increase significantly when accounting for the staged excavation process.

7. Probabilistic assessment

7.1. Introduction

There are numerous sources of uncertainty which need to be accounted for in engineering design. By using *Reliability Based Design* (RBD) methods, rather than design approaches based on deterministic analysis, these uncertainties can be accounted for in a rational manner. With an increasing problem complexity, the use of RBD methods allows for a more systematic and verifiable decision making process, which better ensures the safety and serviceability of each system component over their life cycle.

In Section 7.2 an introduction to RBD methods is given. Subsequently the model framework is outlined, the methods utilised are mathematically described and the limit state functions are defined. Finally a strategy to assess the sensitivity of the response to each random variable, within a probabilistic framework, has been described.

In Section 7.3 the performance of a tunnel excavated in Boom Clay at the proposed repository depth has been assessed, by implementing the analytical model developed in Chapter 4 within a probabilistic framework. In Section 7.4 the same problem is assessed by utilising the two-dimensional Finite Element model (Chapter 6).

7.2. Reliability Based Design (RBD)

7.2.1. Introduction

The performance, G, of a geomechanical system, is commonly assessed deterministically, by comparing the system response(s) to a given limit state(s). Given the system resistance, R, and the load on the system, L, a system safety margin may be defined as $Z = R - L$. Hence if we define the performance in terms of system safety, i.e. $G \equiv Z$, the performance is satisfactory if $G > 0$ and unsatisfactory if $G \leq 0$.

In a deterministic analysis, the system performance is a function of a set of discrete variables, $\mathbf{x}$, defining the physical system (material property values, boundary conditions, etc.). Hence, in order to ensure that $G > 0$, uncertainties are often accounted for qualitatively by selecting the variables as *"cautious estimates"* based on site specific knowledge, regulations, common practice and engineers' individual experience. However, by employing a design framework based on probability theory, the uncertainties associated with individual variables can be accounted for explicitly within a mathematically defined framework.

The system performance, $G(\mathbf{X})$, now becomes a function of the random variables $\mathbf{X} = \{X_1, X_2, ..., X_N\}$, which are defined by their point and spatial statistics (see Section 3.4).

This way, the effect of individual uncertainties on the probability of design failure, as well as the associated risks, can be quantified, and thus it allows for a more systematic and verifiable decision making process.

The *probability of failure* P_f is defined as the probability of the system performance being unsatisfactory. In generalised form

$$P_f = P[G(\mathbf{X}) \leq 0] = \int_{\mathcal{D}_f} f_\mathbf{X}(\mathbf{x})\mathrm{d}\mathbf{x} = F_{G(\mathbf{X})}(0) \tag{7.1}$$

where $\mathcal{D}_f$ denotes the failure domain for which $G(\mathbf{X}) \leq 0$, $f_\mathbf{X}(\mathbf{x})$ is the joint *Probability Density Function* (PDF) of the random variables $\mathbf{X}$ and $F_{G(\mathbf{X})}$ is the *Cumulative Distribution Function* (CDF) of the performance function (Figure 7.1). The *reliability*, defined as the probability of failure not occurring, is $R_f = 1 - P_f$.

To solve Equation 7.1, different approximate or simulation based methods are commonly utilised, as generally the full joint PDF of $\mathbf{X}$ not is known and neither is direct integration possible.

RBD methods may be classified into four levels (ISO 2394, 1998; JCSS, 2001a; Lemaire, 2009):

Level 0 - *Deterministic analyses* employing empirical safety factors which have been derived based on experience and individual expertise.
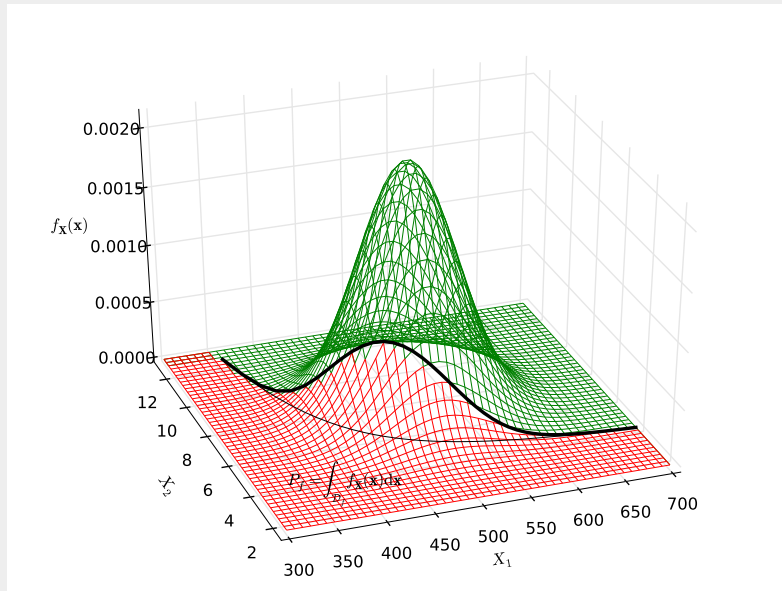
Figure 7.1.: Illustrative joint probability density function, with normally distributed random variables $\mathbf{X} = \{X_1, X_2\} \sim \mathcal{N}$ indicating the failure domain $\mathcal{D}_f$ for which the failure probability is computed.

Level 1 - *Semi-probabilistic methods* for which the failure probability is not computed directly. For any ultimate limit state or serviceability design situation, the uncertainties are accounted for by employing sets of partial factors on actions and/or resistance, which have been calibrated for target reliability levels with respect to specific reliability and/or consequence classes (e.g. Eurocodes BS EN 1990, 2002; BS EN 1997-1, 2004).

Level 3 - *Approximate probabilistic methods* employing mathematical frameworks in which the probability of failure is computed as a point estimate for the most critical load-resistance combination on an approximate limit state surface. Approximate methods include the *First Order Second Moment* (FOSM), the *Point Estimate Method* (PEM) and the *First/Second Order Reliability Method* (FORM/SORM).

Level 4 - *Fully probabilistic methods* are simulation-based frameworks from which the random variables sample directly from the multivariate joint PDF, $f_{\mathbf{X}}(\mathbf{x})$. Methods include the *Monte Carlo Method* (MCM) as well as adaptive techniques incorporating, for instance, directional or importance sampling schemes.

Further information on reliability based design methods can be found in Ang and Tang (1975, 1984), Baecher and Christian (2003), Ditlevsen and Madsen (2007), Fenton and Griffiths (2008), Phoon (2008), Lemaire (2009) and Hicks and Jommi (2014).

7.2.2. RBD model framework

Figure 7.2 outlines the RBD model framework employed in this work. The principle can be applied to any engineering problem but is explained here for the excavation of a tunnel.

In the pre-processing phase, the covariance structure of the random variables, $\mathbf{X}$, is set up based on their point statistics (mean, variance and cross-correlation). The limit states are also defined, e.g. set to a maximum allowable extent of the plastic zone. Finally the mechanical model (analytical or numerical) is set up.

A RBD module has been developed based on the *Open source initiative to Treat Uncertainties, Risks'N Statistics* (OpenTURNS[7]) scientific library (OpenTURNS, 2014a). In this research, two principal design methods have been employed; that is, the MCM and the approximate FORM/SORM. In the assessment, the RBD module sends a single set of deterministic model parameters $\mathbf{x} = \{x_1, x_2, ..., x_N\}$, sampled from $\mathbf{X}$, to the mechanical model, and receives back a response measure, e.g. plastic radius. This communication continues for a set number of realisations (MCM) or until a convergence criterion is satisfied (FORM/SORM).

In the RBD post-processing, the probabilities of failure and the sensitivity indices are computed. Given multiple limit states the reliability of the system is evaluated for the critical performance function.

The later general post processing, which is beyond the scope of this work, refers to the reduction in variance of the random variables potentially leading to a higher system reliability.

---

[7]OpenTURNS: http://www.openturns.org/
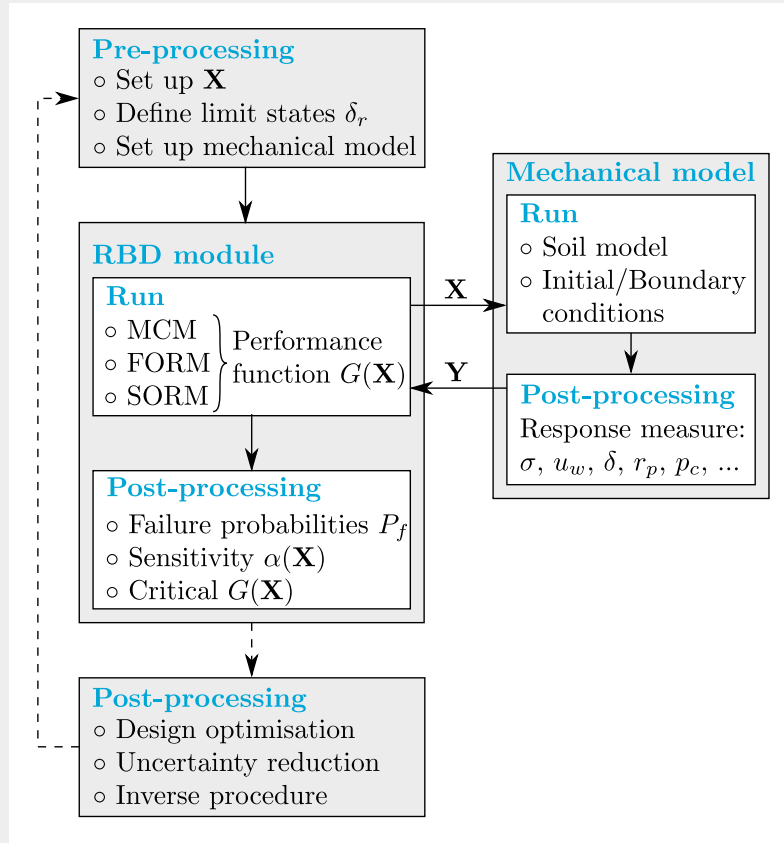
Figure 7.2.: Flow chart showing the employed RBD model framework.

This process may include an optimisation of the repository design, a reduction of uncertainties (for instance by performing more high quality laboratory and in situ tests on samples at larger depth for sensitive variables), or the implementation of a sequential/inverse analysis scheme incorporating new observations or field measurements.

7.2.3. RBD methods

Monte Carlo Method (MCM)

Utilising MCM, the probability of failure is computed numerically by simulating a sequence of N_r independent realisations, for which each $\mathbf{x}$ is sampled from the joint PDF $f_{\mathbf{X}}(\mathbf{x})$ of all variables in the random vector $\mathbf{X}$:

$$P_f = \int_{x_1 \in \mathcal{D}_f} \cdots \int_{x_N \in \mathcal{D}_f} f_{\mathbf{X}}(\mathbf{x}) \, d\mathbf{x} \approx \frac{1}{N_r} \sum_{i=1}^{N_r} I_i^{\mathcal{D}_f} = \frac{N_f}{N_r} \tag{7.2}$$

where $\mathcal{D}_f$ denotes the failure domain, I is the indicator function where $I_i^{\mathcal{D}_f} = 1$ for $G(\mathbf{x}_i) \leq 0$ and $I_i^{\mathcal{D}_f} = 0$ for $G(\mathbf{x}_i) > 0$, and N_f is the number of Monte Carlo realisations which failed the design criteria (Figures 7.1 and 7.3(a)).

MCM is generally is capable of computing the failure probability for complex and highly non-linear systems. However, to do so, the number of realisations N_r may be significant. Given the central limit theorem (e.g. Ang and Tang, 1975), the failure probability is normally distributed, $P_f \sim \mathcal{N}$. Hence, for a typical target failure probability of 0.001 and a maximum error of $\varepsilon = 0.0001$, at a confidence level of 90% the required number realisations would be

$$N_r \geq P_f R_f \left(\frac{u_{0.1/2}}{\varepsilon}\right)^2 = 0.001\ 0.999 \left(\frac{1.645}{0.0001}\right)^2 = 270\,332 \tag{7.3}$$

where $u_{0.1/2} = 1.645$ is the discrete value for a Gaussian distribution at $P[U > u_{0.1/2}] = 0.1/2$, corresponding to a two-sided significance of 10% (e.g. Fenton and Griffiths, 2008; Honjo, 2008).

First/Second Order Reliability Method (FORM/SORM)

FORM and SORM are commonly used approximate RBD methods, and have been successfully used for various geotechnical applications, such as for analysing slopes (e.g. Griffiths et al., 2007, 2009, 2010; Low and Tang, 2007), shallow and deep foundations (e.g. Bauer and Puła, 2000; Chan and Low, 2012; Puła, 2007) and tunnels (e.g. Li and Low, 2010; Lü et al., 2011a,b, 2013).

The *First Order Reliability Method* (Hasofer and Lind, 1974) is based on the approximation of the failure probability, $\hat{P}_f$, by the the so-called *reliability index* β, which is an invariant geometrical measure in standard normal (Gaussian) space (Figure 7.3(b)). This requires a transformation of the random variables from their physical space, e.g. $X_1 \sim \mathcal{N}(\mu_{X_1}, \sigma_{X_1})$ and
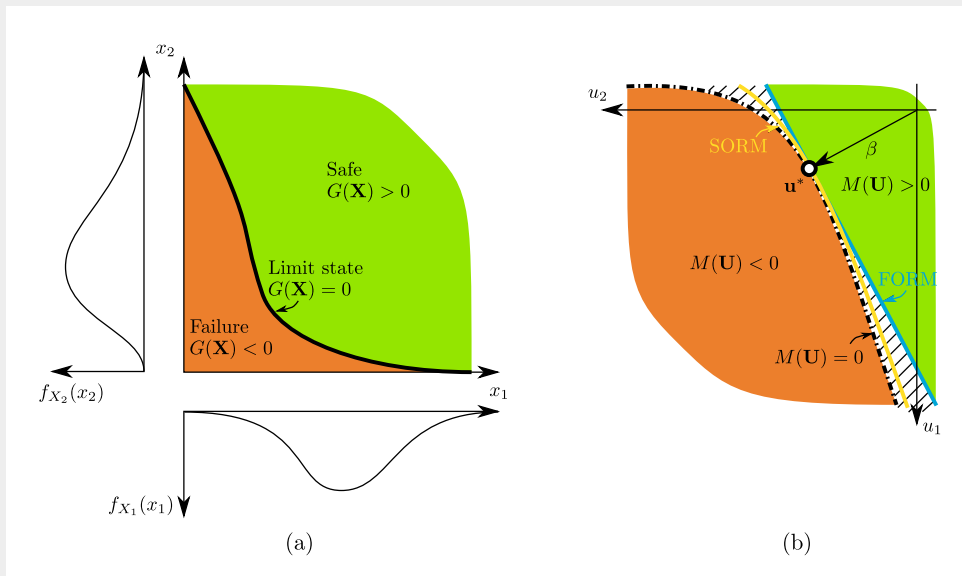
Figure 7.3.: Performance function: (a) in bi-variate physical space $\mathbf{X} = \{X_1, X_2\}$ with $X_1 \sim \mathcal{N}$ and $X_2 \sim \ln\mathcal{N}$, and (b) in standard normal space where $\mathbf{U} \sim \mathcal{N}(\mathbf{0}, \mathbf{1}, \mathbf{I})$ and $\mathbf{u}^*$ is the design point.

$X_2 \sim \ln \mathcal{N}(\mu_{X_2}, \sigma_{X_2})$, into standard normal space $\mathbf{U} \sim \mathcal{N}(\mathbf{0}, \mathbf{1}, \mathbf{I})$ (Figure 7.3(a $\rightarrow$ b)).

The FORM reliability index is a scalar describing the vector length between the expected response, $\mu_{M(\mathbf{U})}$, and the critical design point, $\mathbf{u}^*$, as a multiple of the standard deviation $\sigma_{M(\mathbf{U})}$:

$$\beta = -\Phi^{-1}(\hat{P}_f) = \Phi^{-1}(\hat{R}_f) = \sqrt{\{\mathbf{u}^*\}^{\mathrm{T}}\{\mathbf{u}^*\}} \tag{7.4}$$

where $\hat{P}_f$ is the approximate failure probability, $\hat{R}_f$ is the approximate reliability, $\Phi^{-1}(\cdot)$ is the inverse CDF of the performance function in Gaussian space, $M(\mathbf{U})$, and $\mathbf{u}^*$ is the design point at which the limit state surface is approximated as a linear function (Figure 7.3(b)).

Correlated normalised random variables, $\hat{\mathbf{U}}$, can be transformed via Cholesky decomposition, $\mathbf{u} = \mathbf{L}_{\hat{\mathbf{U}}}^{-1}\hat{\mathbf{u}}$ (e.g. Lemaire, 2009), and thus Equation 7.4 may be rewritten as

$$\beta = \sqrt{\hat{\mathbf{u}}^{\mathrm{T}} \left(\mathbf{L}_{\hat{\mathbf{U}}} \mathbf{L}_{\hat{\mathbf{U}}}^{\mathrm{T}} \right) \hat{\mathbf{u}}} = \sqrt{\hat{\mathbf{u}}^{\mathrm{T}} \mathbf{R}_{\hat{\mathbf{U}}}^{-1} \hat{\mathbf{u}}} \tag{7.5}$$

where $\mathbf{L}_{\hat{\mathbf{U}}}$ is the lower triangular matrix and $\hat{\mathbf{U}} \sim \mathcal{N}(\mathbf{0}, \mathbf{1}, \mathbf{R}_{\hat{\mathbf{U}}})$ holds the normalised correlated multivariate random variables, with $\mathbf{R}_{\hat{\mathbf{U}}}$ being the symmetric and positive defined product-moment cross-correlation matrix (see Equation 3.2). Hence, for $\mathbf{X} \sim \mathcal{N}$ then:

$$\beta = \sqrt{\left[\frac{\mathbf{x} - \mu_{\mathbf{X}}}{\sigma_{\mathbf{X}}} \right]^{\mathrm{T}} \mathbf{R}_{\hat{\mathbf{U}}}^{-1} \left[\frac{\mathbf{x} - \mu_{\mathbf{X}}}{\sigma_{\mathbf{X}}} \right]} \tag{7.6}$$

For the computation of the design point, different optimisation algorithms exist to find $\mathbf{u}^* = \mathrm{argmin}\{|\mathbf{u}| \, |M(\mathbf{u}) = 0\}$ (e.g. Lemaire, 2009; Lopez and Beck, 2012). In the Open-TURNS library different nearest point algorithms have been implemented, which is a *Constrained optimization by linear approximation* (Cobyla) algorithm, the Abdo-Rackwitz-Fiessler algorithm (Abdo and Rackwitz, 1991; Rackwitz and Fiessel, 1978) and a *Sequential Quadratic Programming* (SQP) algorithm (OpenTURNS, 2014b).

The *Second Order Reliability Method* (SORM) extends FORM by using a quadratic limit state surface to approximate the limit state surface at the design point. The reliability index can be computed using the Tvedt (1989), Hohenbichler et al. (1987) or Breitung (1984) approximation (OpenTURNS, 2014b). A potential increase in approximation accuracy, utilising SORM over FORM, depends on the non-linearity of the *true* limit state function and the quality of the design point. However, for both the FORM and SORM, the approximation error can not be quantified (Lemaire, 2009). Hence, as described in Section 4.1, one reason for the development of an analytical model as part of this research was to provide a computationally cheap tool to compare the predictive performance of the approximate methods (FORM/SORM) with the computationally more expensive, fully probabilistic methods (MCM).

7.2.4. Limit states and performance functions

A design criterion for assessing tunnel stability may be defined in terms of a limiting plastic radius $r_{p,lim}$ (e.g. ITA, 1988). In the initial design specifications of the OPERA repository (Verhoef et al., 2011), the LILW and HLW disposal cells are spaced $b_c = 50$m apart (Table 2.7). Assuming the stability criterion is to be defined that one third of the soil between the galleries is required to remain in the elastic zone (e.g. TRUCK studies Barnichon et al., 2000; Steen and Vervoort, 1998), the limiting plastic radius is $r_{p,lim} = 1/3 b_c = 16.67$m. A second limit state is defined by the maximum compressive support (collapse) load of the concrete liner, p_l^{max}, (Equation 4.58 and Figure 4.4(a)). The two performance functions are therefore defined here as $G_1(\mathbf{X}) = r_p - r_{p,lim}$ and $G_2(\mathbf{X}) = p_c - p_l^{max}$.

7.2.5. Importance and sensitivity assessment

In Sections 4.7, 5.6 and 6.2, so called *mechanical sensitivity* analyses have been performed to assess the response of the mechanical system to deterministic variations of individual material property values. However, the significance of each random variable is not only a function of the geomechanical system, but also of the variance and covariance structure of the random variables. For instance, the mechanical significance of a certain random variable X_1 may be small; however if X_1 has a relatively high probabilistic dispersion compared to another mechanically more important variable, X_2, e.g. $\sigma_{X_1}^2 >> \sigma_{X_2}^2$, failure may be more sensitive to X_1. Nevertheless, a mechanical sensitivity assessment is a useful tool to potentially define the system response to changes in variables, and may be used as preliminary reasoning for treating a specific variable as random or deterministic within a stochastic analysis.

Utilising a RBD framework, *sensitivity* may be defined as the importance of each random variable with respect to the probability of failure or the sensitivity of the point statistics (mean, variance) to the performance function parameters (e.g. Ditlevsen and Madsen, 2007; Lemaire, 2009). An advantage of using FORM is that the both sensitivity factors are already a by-product of the algorithm itself, by computing the probability of failure as a point estimate in Gaussian space (see Figure 7.4).

The derivative of the reliability index β provides a straightforward interpretation of the sensitivity (importance) to the standardised random variables, $\mathbf{U}$. This type of sensitivity is most commonly used due to both its simplicity and significance, and is employed in this framework.

Looking at Figure 7.4, it follows from the geometrical interpretation that

$$\mathbf{u}^* = \boldsymbol{\alpha}\beta \tag{7.7}$$

with $\boldsymbol{\alpha} = \{\alpha_1, \alpha_2, ..., \alpha_n\}^{\mathrm{T}}$ being a vector holding the importance factors

$$\alpha_i = \left.\frac{\partial\beta}{\partial u_i}\right|_{\mathbf{u}^*} \tag{7.8}$$
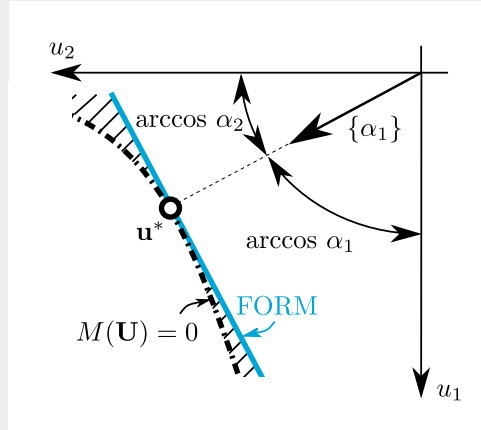
Figure 7.4.: FORM importance factors at the design point.

where $\sum_{i=1}^{n} \alpha_i^2 = 1$.

7.3. Tunnel performance using analytical framework

7.3.1. Experimental set-up

Table 7.1 shows the point statistics for the random soil property values $\mathbf{X} = \{c_0', c_r', \varphi, E, E_t, \nu\}$ selected for this case study. The experimental set-up consists of nine cases in which different combinations of the mean and coefficient of variation are applied to each of the six random variables:

$$
X_i^k = \begin{bmatrix} \langle \mu_1, V_1 \rangle^1 & \langle \mu_2, V_1 \rangle^2 & \langle \mu_3, V_1 \rangle^3 \\ \langle \mu_1, V_2 \rangle^4 & \langle \mu_2, V_2 \rangle^5 & \langle \mu_3, V_2 \rangle^6 \\ \langle \mu_1, V_3 \rangle^7 & \langle \mu_2, V_3 \rangle^8 & \langle \mu_3, V_3 \rangle^9 \end{bmatrix}
\tag{7.9}
$$

where X_i is the random variable and k is the case. The other five variables remain random rather than being fixed to deterministic values in order to simulate data scatter, i.e. $X_j = \langle \mu_2, V_2 \rangle^5$ for all $j \neq i$ in $\mathbf{X}$. Hence a total of $6 \times 8 + 1 = 49$ cases are analysed as part of this part of the study, using the analytical model to describe the soil response.

For each parameter three mean values have been selected at the lower, intermediate and upper end of the potential range, observed at depths below 500m (Table 7.1). These mean values correspond to the values tested in the deterministic study (Table 4.1, Section 4.7). The deviations of the mean for all stiffness related parameters deviate by $|\Delta\mu_{1,3}/\mu_2| = 1/3$ and all shear strength related mean estimates deviate by $|\Delta\mu_{1,3}/\mu_2| = 2/5$. The deviation of the coefficients of variation has been selected to be $\Delta V_{1,3}/V_2 = 3/5$ for all variables. Figure 7.5 shows the continuous target frequencies of all six individual random variables with respect to the nine cases assessed. Due to the lack of information a normal distribution was selected
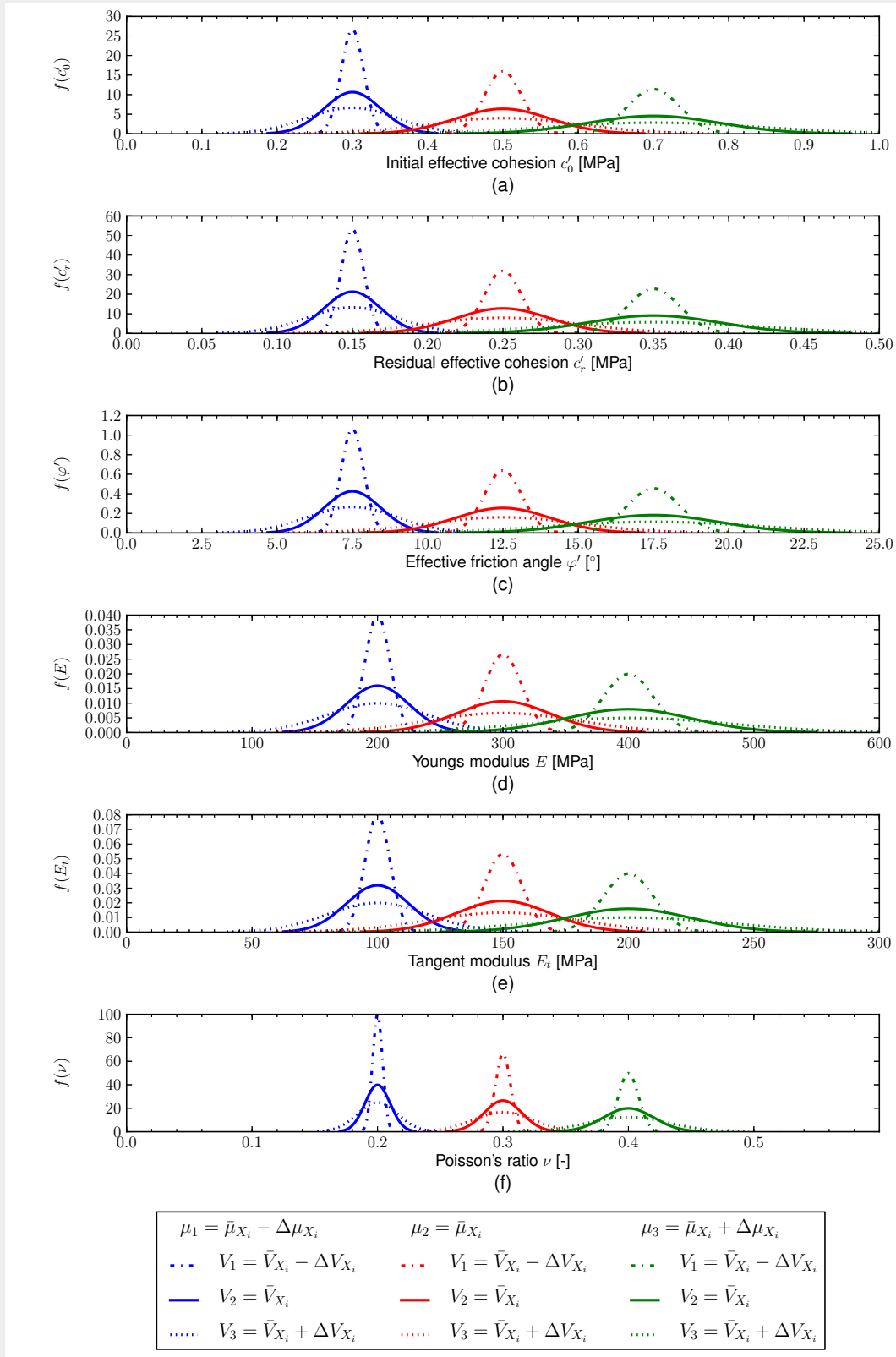
Figure 7.5.: Frequencies of all nine cases for each of the six soil parameters according to Table 7.1.

Table 7.1.: Characteristic set of point statistics for random properties values.

Random variable	X_i	Unit	μ_1	μ_2	μ_3	V_1	V_2	V_3	$X_i \sim$
Effective initial cohesion	c_0'	[MPa]	0.3	**0.5**	0.7	0.05	**0.125**	0.2	$\mathcal{N}(\mu, \sigma^2)$
Effective residual cohesion	c_r'	[MPa]	0.15	**0.25**	0.35	0.05	**0.125**	0.2	$\mathcal{N}(\mu, \sigma^2)$
Effective friction angle	φ'	[°]	7.5	**12.5**	17.5	0.05	**0.125**	0.2	$\mathcal{N}(\mu, \sigma^2)$
Young's modulus	E	[MPa]	200	**300**	400	0.05	**0.125**	0.2	$\mathcal{N}(\mu, \sigma^2)$
Tangent modulus	E_t	[MPa]	100	**150**	200	0.05	**0.125**	0.2	$\mathcal{N}(\mu, \sigma^2)$
Poisson's ratio	ν	[−]	0.2	**0.3**	0.4	0.05	**0.125**	0.2	$\mathcal{N}(\mu, \sigma^2)$

for this investigation, although the use of a bounded distribution is may become necessary for variables such as the Poisson's ratio.

Employing the Monte Carlo Method (MCM), a total of $N_r = 25\,000$ realisations per case investigated will be simulated using the analytical model. For each of the 49 cases, one uncorrelated and one correlated scenario will be investigated to serve as an illustration of the potential effect of parameter correlation on the system response. Hence, a total of 98 cases are to be investigated for a HLW disposal gallery ($r_c = 1.6$m, $d_{oc} = 75$mm, $d = 500$m) corresponding to the deterministic cases investigated in Section 4.7 (Figure 4.5). This leads to approximately 2.5 million analyses. Additional calculations will be performed by changing the boundary conditions, i.e. cavity radius, overcut and depth (corresponding to Figure 4.7(b-d)). For the most critical case, an analysis with $N_r = 300\,000$ realisations will be performed satisfying Equation 7.3.

Given that there is significantly less data available for describing the correlation between individual soil parameters, reasonable estimates have been made for the correlated scenario where appropriate. The cross-correlation matrix is defined for the correlated scenarios as

$$\mathbf{R_U} = \begin{bmatrix} 1.0 & 0.75 & -0.5 & 0.5 & 0.25 & 0.5 \\ \rho_{c_r',c_0'} & 1.0 & -0.5 & 0.5 & 0.25 & 0.5 \\ \rho_{\varphi',c_0'} & \rho_{\varphi',c_r'} & 1.0 & 0.25 & 0.25 & -0.5 \\ \rho_{E,c_0'} & \rho_{E,c_r'} & \rho_{E,\varphi'} & 1.0 & 0.5 & -0.25 \\ \rho_{E_t,c_0'} & \rho_{E_t,c_r'} & \rho_{E_t,\varphi'} & \rho_{E_t,E} & 1.0 & -0.25 \\ \rho_{\nu,c_0'} & \rho_{\nu,c_r'} & \rho_{\nu,\varphi'} & \rho_{\nu,E} & \rho_{\nu,E_t} & 1.0 \end{bmatrix} \tag{7.10}$$

7.3.2. Monte Carlo simulation

In this section the tunnel performance obtained via Monte Carlo simulation will be assessed. For all analyses performed on the 98 cases, the plastic radius did not exceed the limiting plastic radius of $r_{p,lim} = 16.67$m and the cavity pressure p_c did not exceed the maximum compressive support (collapse) load of the concrete liner p_l^{max}. Hence, in order to assess the impact on any parameter variation on the performance, the limit states have been set to $r_{p,lim} = r_c + 3.0$m for $G_1(\mathbf{X}) = r_p - r_{p,lim}$, corresponding to a limiting plastic zone exceeding 3m into the Boom

Clay (which may be a reasonable choice for limiting the extent of the EDZ, i.e. a serviceability rather than stability criteria), and $p_l^{max} = 8$MPa for $G_2(\mathbf{X}) = p_c - p_l^{max}$, corresponding to maximum cavity pressure for a hypotetically thin concrete liner of about 0.17m for a HLW gallery of $r_c = 1.6$m (Figure 4.4(a)).

Cavity stability at 500m depth

Figures 7.6 and 7.7 show radar plots illustrating the variation of the failure probability $P_f(G_1(\mathbf{X}) \leq 0)$ for each random variable.

As for the deterministic response, the soil friction angle φ' significantly influences the response. An increase in the coefficient of variation (Figure 7.6(a→c)), as well as a decrease in the mean estimate (Figure 7.7(c→a)), increases the failure probability. Figures 7.8 and 7.9 show the frequencies of the plastic radii r_p for nine uncorrelated cases and the cumulative frequencies for the three mean cases ($\mu_{\varphi'}$) and a large coefficient of variation, respectively. It is evident that the variance of the response increases with increasing uncertainty in the friction angle. For the example assessed here, the response based on the correlated random variables results in lower failure probabilities, which is, in part, attributed to the strong hypothetical negative correlation $\rho_{\varphi',c_0'}$ applied (Equation 7.10). Thus, employing uncorrelated soil property values will lead to a more conservative estimate. Hence, similar to a reduction in parameter variance, the quantitative determination of the covariance structure may lead to a design optimization.

Furthermore, Figure 7.9 shows that, for the critical case of $\mu_{\varphi'} = 7.5°$ and $V_\varphi = 0.2$, an increase in the number of realisations to $N_r = 300\,000$ significantly affects the computed failure probabilities at the tails. However, as the probability $P[r_p > 7.0\text{m}]$ is approximately 10^{-5} for the uncorrelated case, a potential design criteria of $r_{p,lim} = 16.67$m would be adequately satisfied.

As for the friction angle, for both c_0' and c_r', an increase in the mean cohesion or a decrease in its coefficient of variation results in a lower failure probability (Figures 7.6-7.7). The cumulative distributions for different c_0' cases, shown in Figure 7.10, highlights that the parameter covariance structure may be of more influence on the performance than the variance of the initial cohesion itself.

As observed in the deterministic assessment (Figure 4.5(d)), the Boom Clay response to an increase in the Young's modulus, E', leads to larger plastic deformation due to the deformation boundary condition on the tunnel cavity. Thus the probability of failure increases with an increasing Young's modulus as shown in Figure 7.11. Again, accounting for a potential cross-correlation reduces the failure probability.
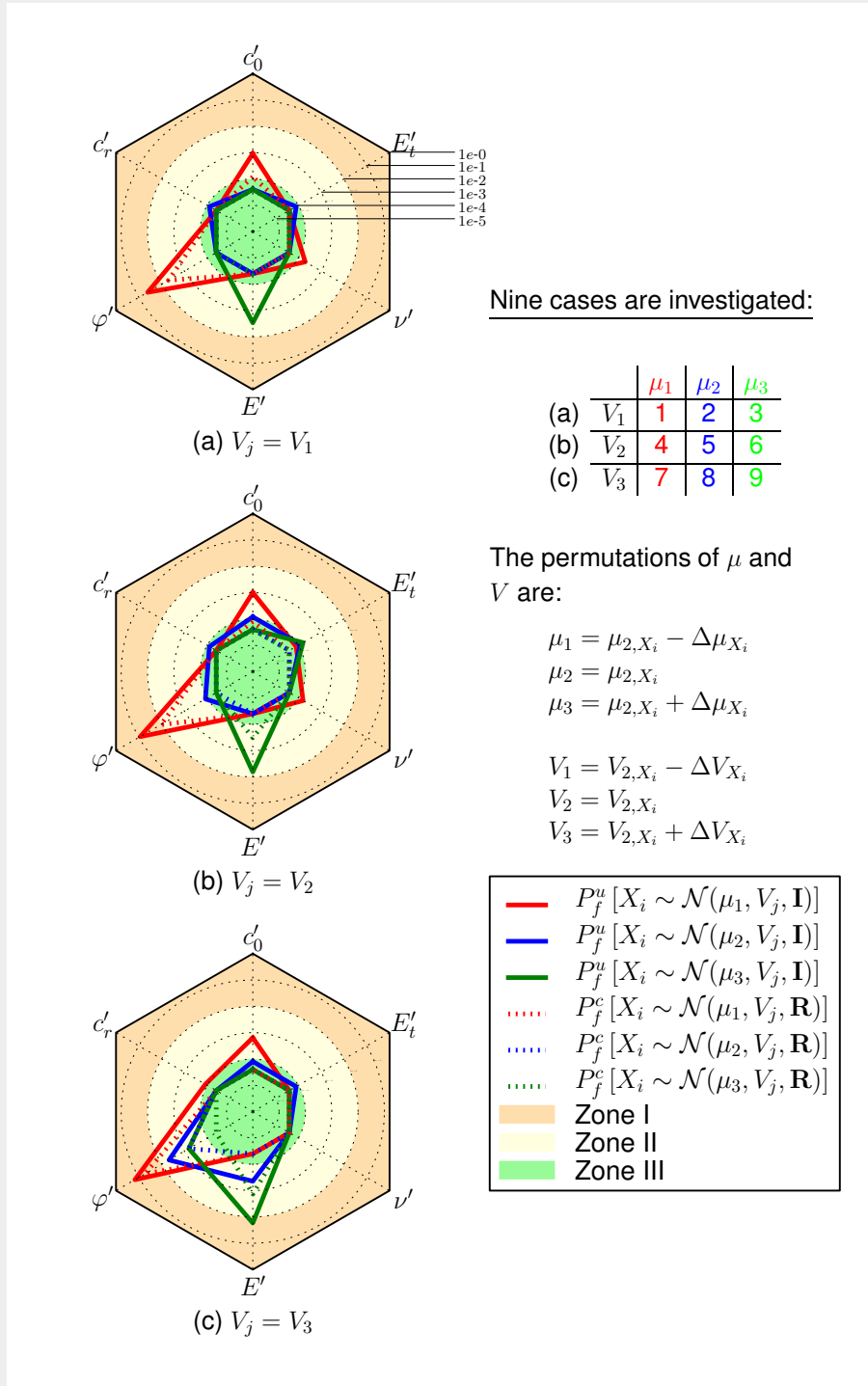
Figure 7.6.: Radar plot of $P_f(G_1(\mathbf{X}) \leq 0)$ of nine cases investigated for each of the six random variables (Equation 7.9), i.e. both for uncorrelated and correlated set of random variables, for a HLW gallery ($r_c = 1.6$m, $d_{oc} = 75$mm, $d = 500$m). Sub-plots (a) to (c) indicate an increase in target coefficient of variation V_j. The three mean μ_{1-3} values remain constant for all sub-plots. The radial axes are in $\log$-scale.
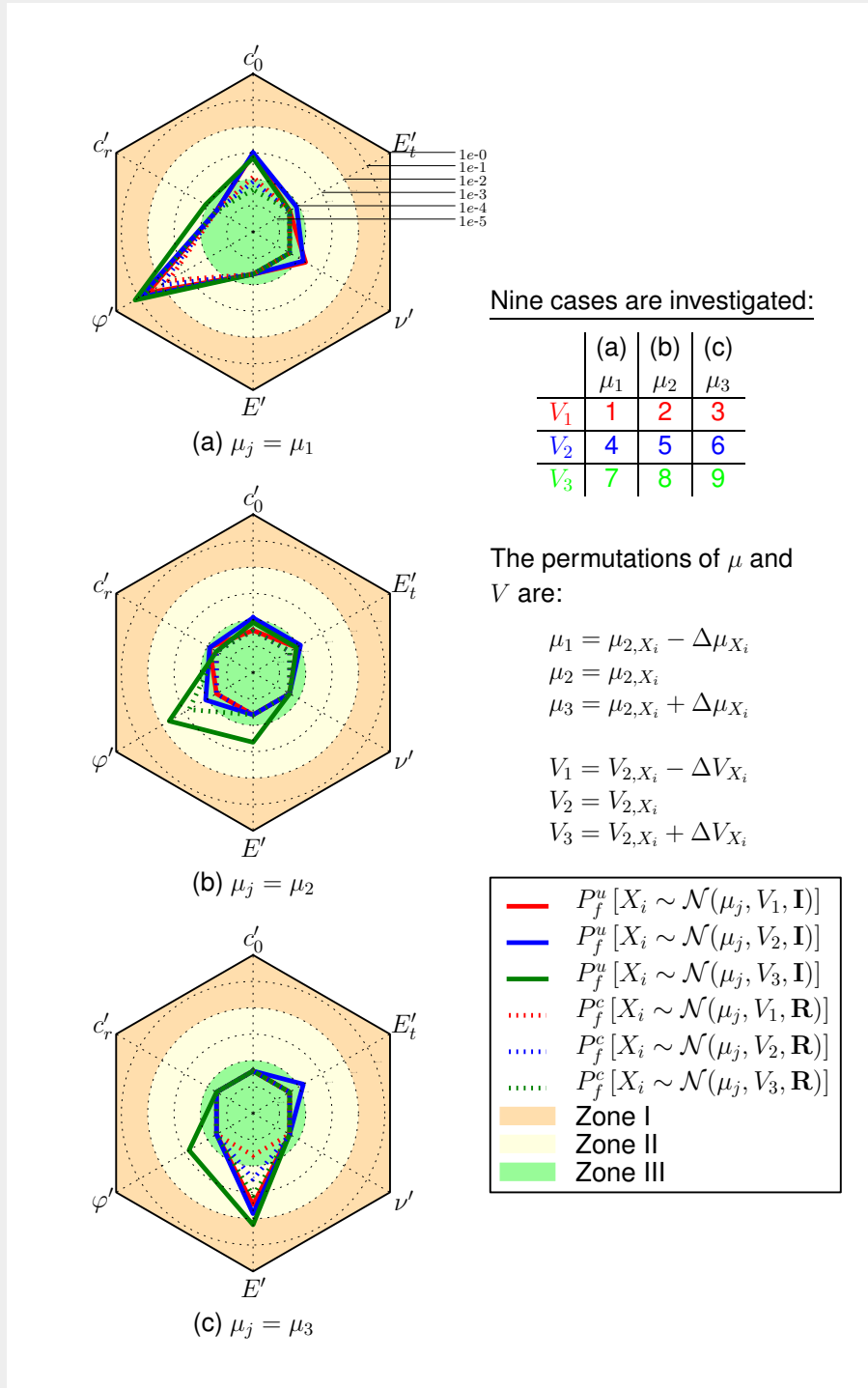
Figure 7.7.: Radar plot of $P_f(G_1(\mathbf{X}) \leq 0)$ for variation of nine cases investigated for each of the six random variables (Equation 7.9), i.e. both for uncorrelated and correlated set of random variables, for a HLW gallery ($r_c = 1.6$m, $d_{oc} = 75$mm, $d = 500$m). Sub-plots (a) to (c) indicate an increase in target μ_j. The three coefficients of variation V_{1-3} remain constant for all sub-plots. The radial axes are in $\log$-scale.
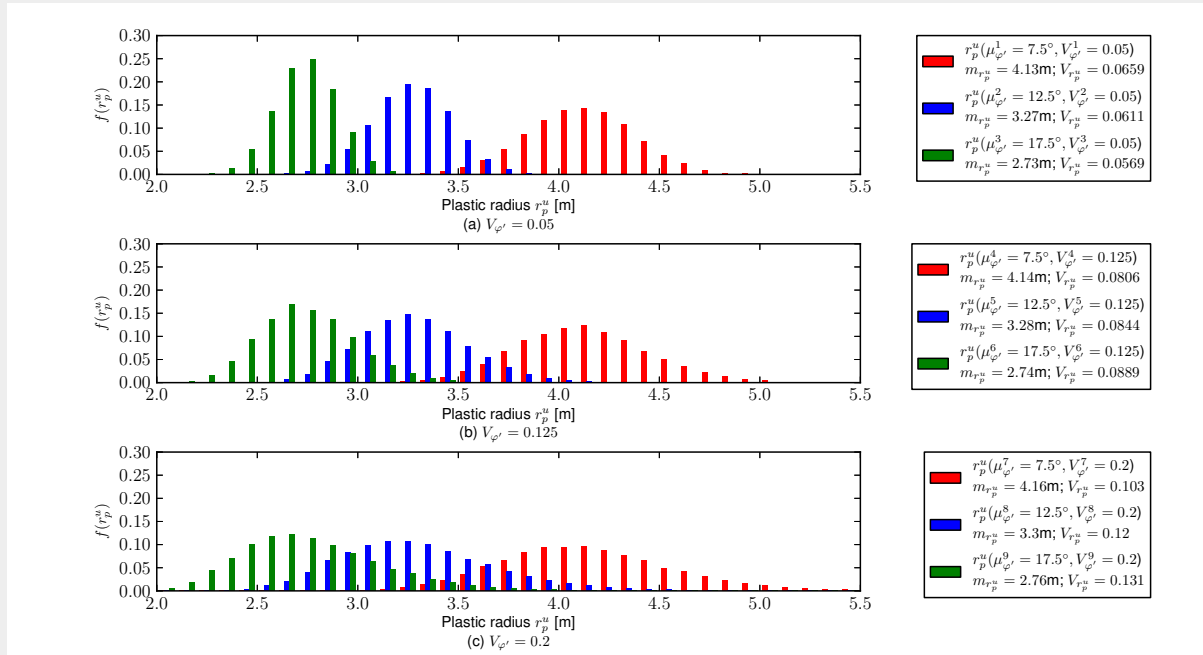
Figure 7.8.: Frequencies of plastic radii r_p for nine cases of the variation in soil friction angle φ' for the uncorrelated case for a HLW gallery ($r_c = 1.6$m, $d_{oc} = 75$mm, $d = 500$m).
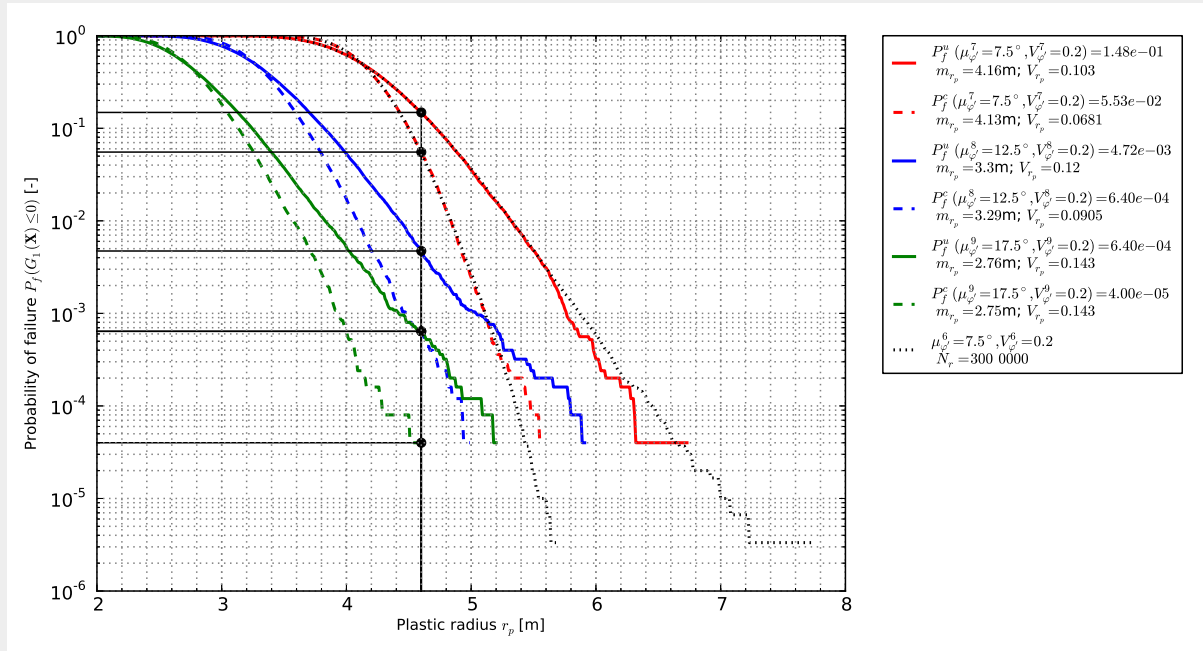
Figure 7.9.: Logarithmic cumulative frequencies of plastic radii r_p for three mean friction angles $\mu_{\varphi'}$ and a large coefficient of variation $V_{\varphi'}$ for a HLW gallery ($r_c = 1.6$m, $d_{oc} = 75$mm, $d = 500$m).
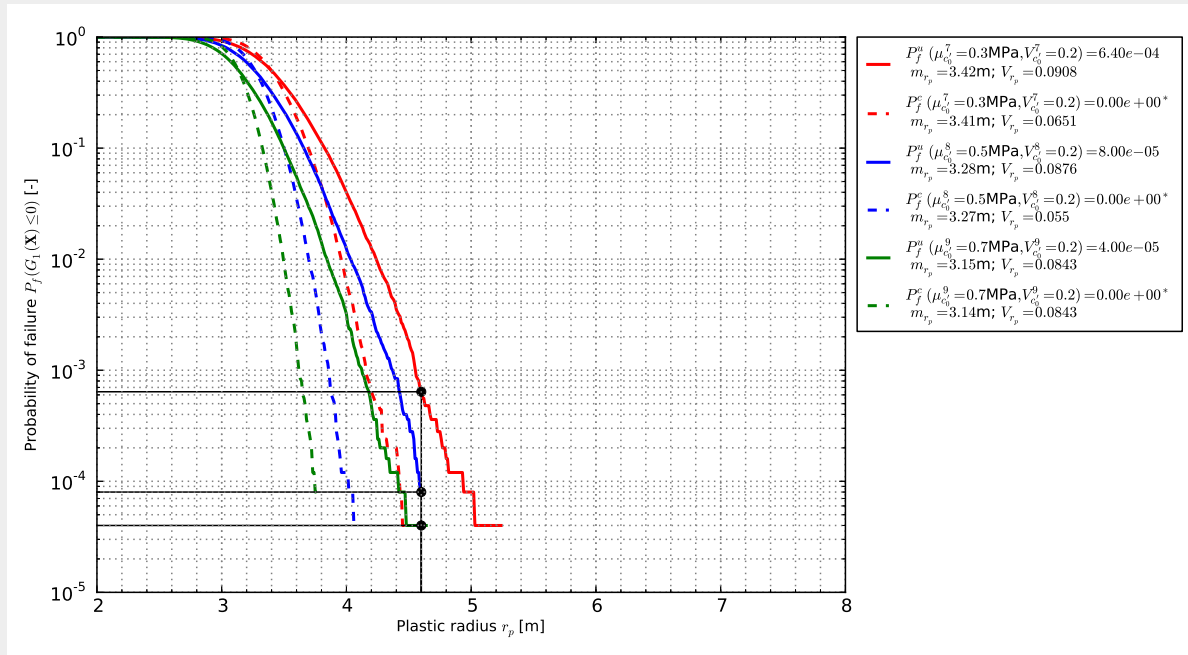
Figure 7.10.: Logarithmic cumulative frequencies of plastic radii r_p for three mean initial cohesions $\mu_{c'}$ and a large coefficient of variation $V_{c'}$ for a HLW gallery ($r_c = 1.6$m, $d_{oc} = 75$mm, $d = 500$m).
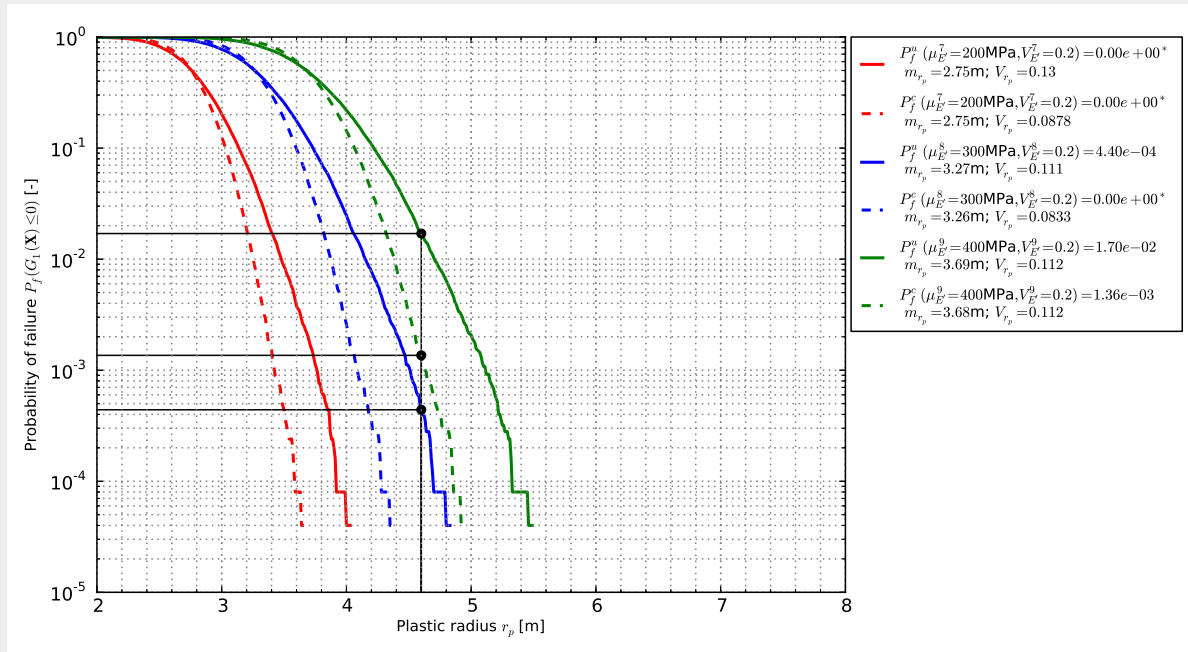
Figure 7.11.: Logarithmic cumulative frequencies of plastic radii r_p for three mean Young's moduli $\mu_{E'}$ and a large coefficient of variation $V_{E'}$ for a HLW gallery ($r_c = 1.6$m, $d_{oc} = 75$mm, $d = 500$m).
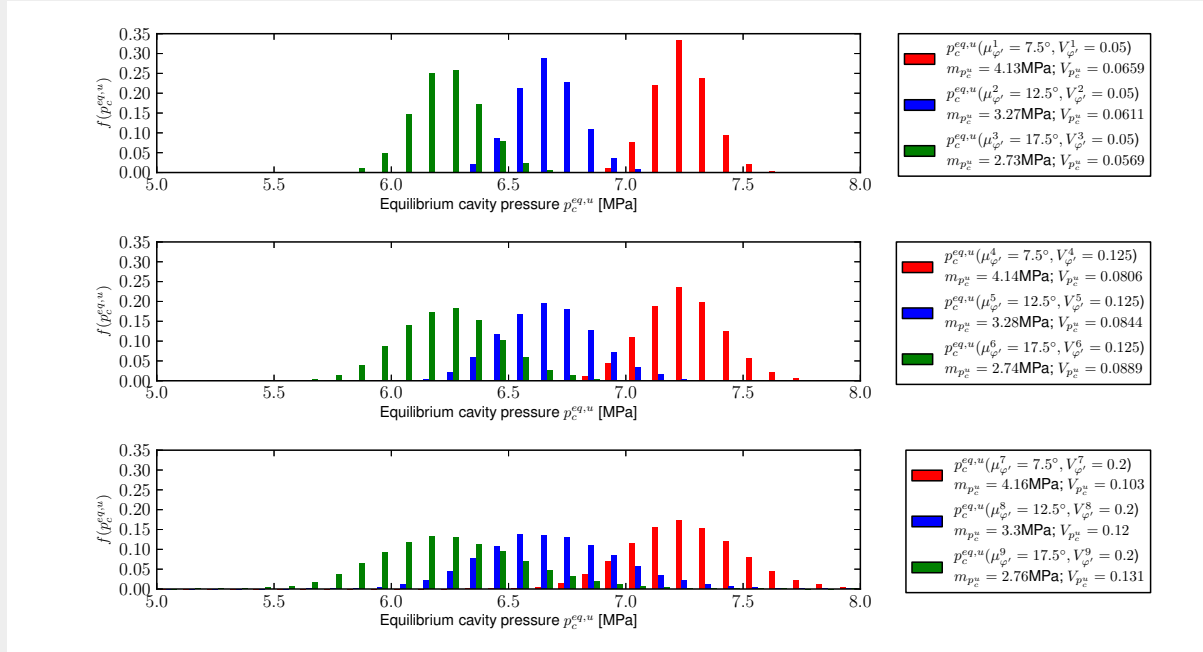
Figure 7.12.: Frequencies of the cavity pressure in equilibrium p_c^{eq} for nine cases of the variation in soil friction angle φ' for the uncorrelated case for a HLW gallery ($r_c = 1.6$m, $d_{oc} = 75$mm, $d = 500$m).

The effect of both the tangent modulus, E_t', and the Poisson's ratio, ν', are only slightly affected by any variation in the mean or coefficient of variation. This corresponds with the the deterministic observations (Figures 4.5(e) and 4.5(f)).

Figure 7.12 shows frequencies of the cavity pressure in equilibrium, p_c^{eq}, exemplary for nine cases of the variation in soil friction angle φ'. The variance of the response increases with increasing mean and coefficient of variation, $\mu_{\varphi'}$ and $V_{\varphi'}$. Figure 7.13 shows the increase in cavity pressure with decreasing mean Young's modulus $\mu_{E'}$. In contrast to the plastic radius, accounting for the parameter correlation would now underestimate a potential failure probability.

Influence of cavity size

With increasing cavity size the absolute plastic radii increase; however, the relative plastic radii decrease (see Figure 4.7(d)). As exemplary shown for the variation in mean friction angle $\mu_{\varphi'}$ in Figure 7.14, the variance of the responses increases with increasing cavity radius r_c. Furthermore, the difference between the mean responses, Δm_{r_p}, increases with increasing r_c.

Influence of the overcut

Figure 7.15 shows the response frequency of the plastic radii r_p for three cases of a varying mean friction angle and with a constant coefficient of variation for three different excavation
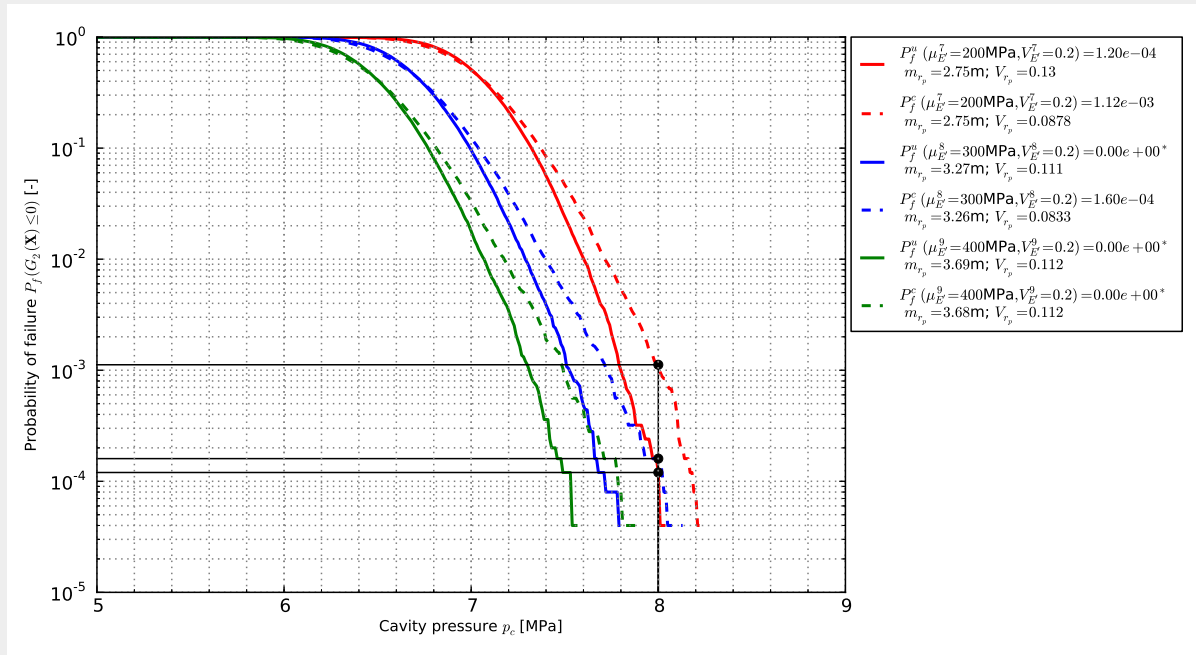
Figure 7.13.: Logarithmic cumulative frequencies of the cavity pressure in equilibrium p_c^{eq} for three mean Young's moduli $\mu_{E'}$ and a large coefficient of variation $V_{E'}$ for a HLW gallery ($r_c = 1.6$m, $d_{oc} = 75$mm, $d = 500$m).
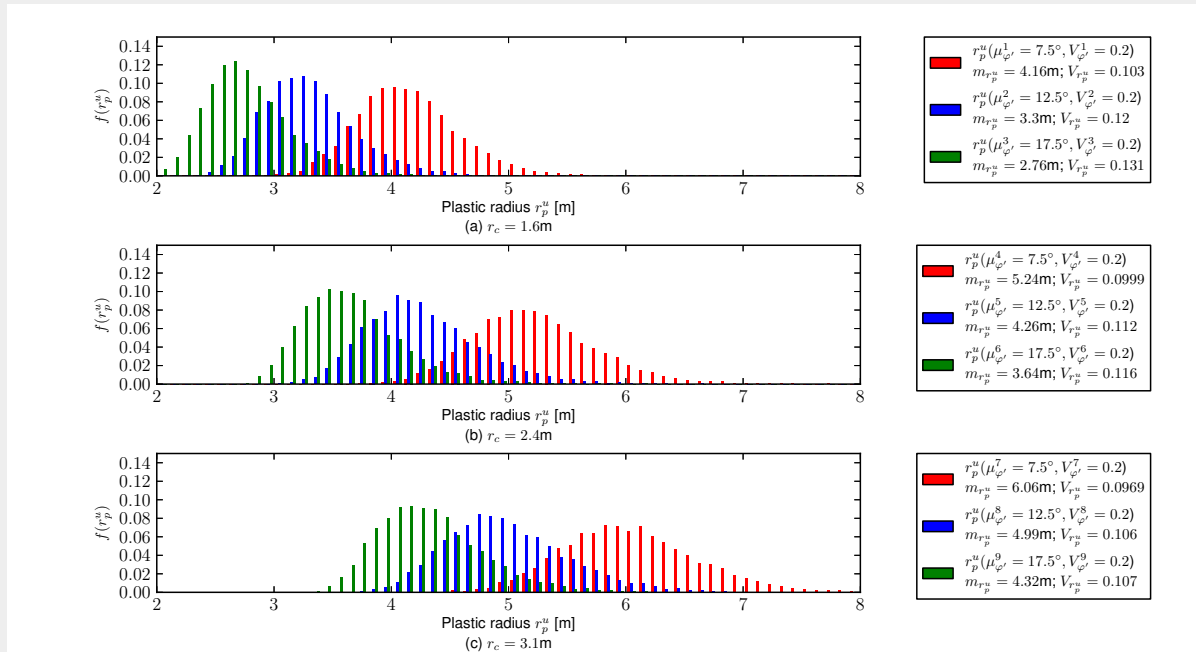
Figure 7.14.: Frequencies of plastic radii r_p for three mean friction angles $\mu_{\varphi'}$ and three excavation radii r_c of 1.6m (HLW gallery), 2.4m (LILW gallery) and 3.1 (shaft), at 500m depth and with an overcut of $d_{oc} = 75$mm.
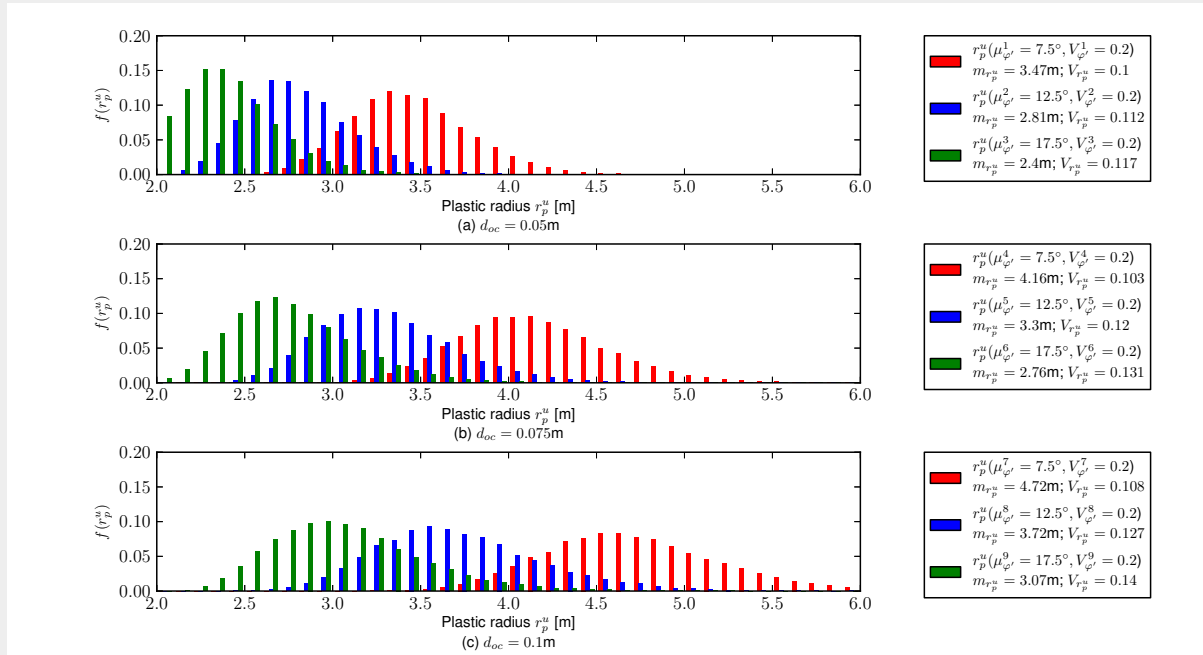
Figure 7.15.: Frequencies of plastic radii r_p for three mean friction angles $\mu_{\varphi'}$ and three different overcuts d_{oc} for a HLW gallery ($r_c = 1.6$m) at 500m depth.
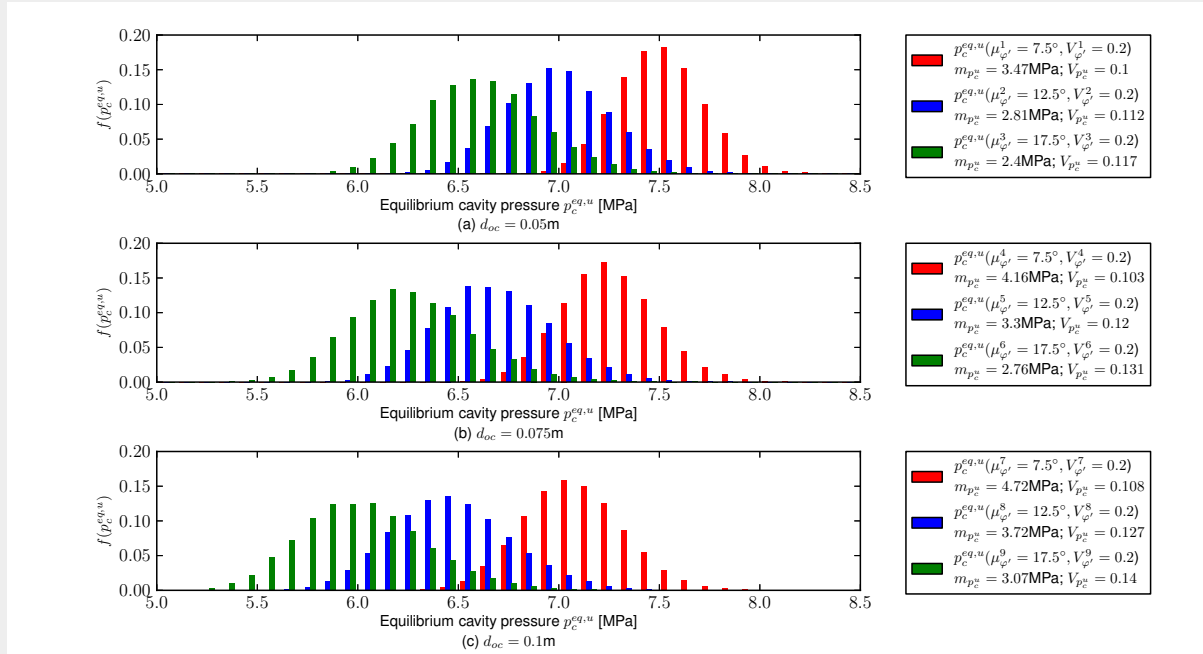
Figure 7.16.: Frequencies of equilibrium cavity pressure p_c^{eq} for three mean friction angles $\mu\varphi'$ and three different overcuts d_{oc} for a HLW gallery ($r_c = 1.6$m) at 500m depth.

overcuts, for a tunnel located at a depth of 500m. A limitation of soil deformation at the cavity interface accompanying the reduction in overcut reduces the extent of the plastic radius for a cavity pressure in equilibrium (Figure 4.7(b)). Both the difference in the mean responses, Δm_{r_p}, as well as the coefficient of variation, V_{r_p}, increase with increasing overcut.

The cavity pressure in equilibrium p_c^{eq} decreases with increasing overcut, as more stress is redistributed in the soil mass due to the larger deformation (Figure 7.16). This decrease is accompanied by a decreasing difference in the mean responses, $\Delta m_{p_c^{eq}}$, and a slight increase in the coefficient of variation, $V_{p_c^{eq}}$.

Influence of the repository depth

Figure 7.17 shows the response frequency of the plastic radius for a HLW gallery located at depths of 500m, 600m and 700m. Whereas the mean response, m_{r_p}, as well as the difference in the mean response, Δm_{r_p}, decrease slightly with depth, the variance of the responses is unaffected by depth. More significant is the effect of a variation in depth on the absolute value of the cavity pressure p_c^{eq} (Figure 7.18). However, the difference in the mean response, $\Delta m_{p_c^{eq}}$, as well as the in coefficient of variation, $\Delta V_{p_c^{eq}}$, are relatively unaffected by a change in depth. Figure 7.19 plots the the plastic radius against the cavity pressure for the critical combination of a low mean friction angle of $\mu_\varphi = 7.5°$ and a large coefficient of variation of $V_\varphi = 0.2$ for all three depths.
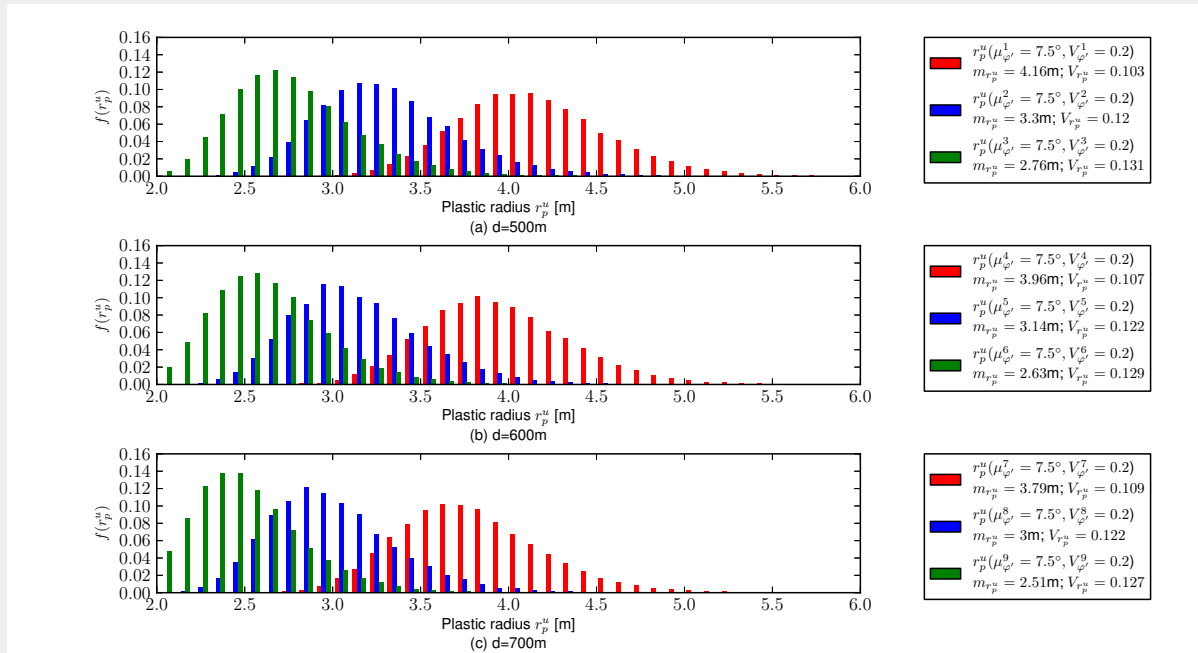
Figure 7.17.: Frequencies of plastic radii r_p for a HLW gallery ($r_c = 1.6$m, $d_{oc} = 75$mm) with three mean friction angles $\mu_{\varphi'}$ located at three different repository depths.
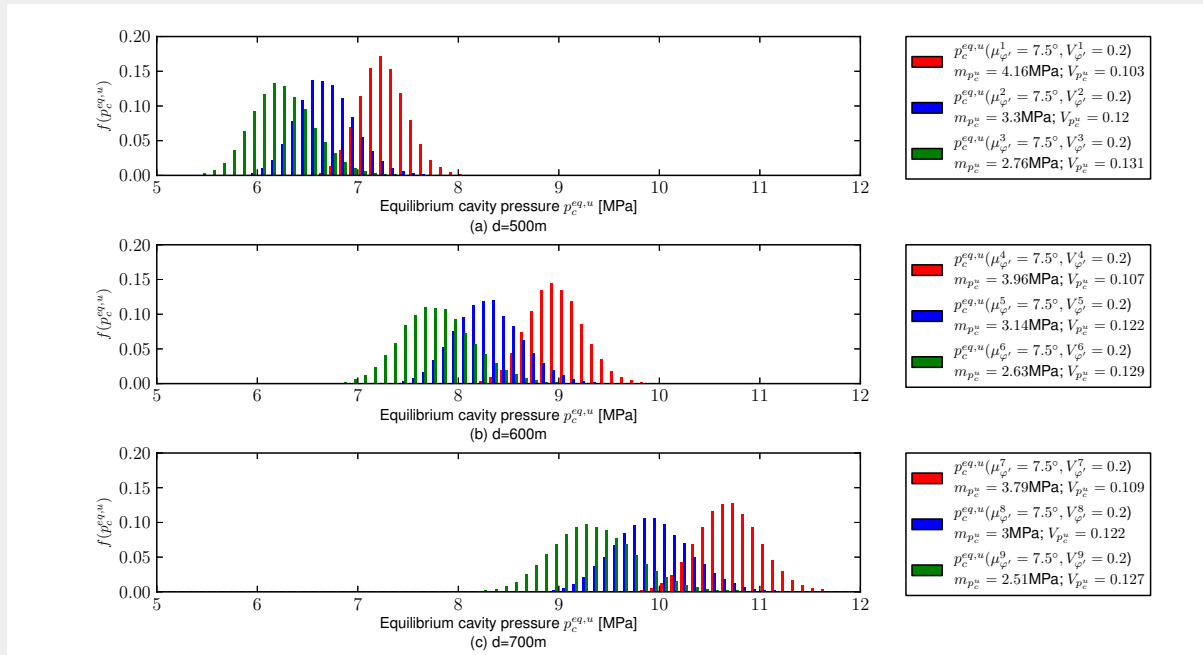
Figure 7.18.: Frequencies of equilibrium cavity pressure p_c^{eq} for a HLW gallery ($r_c = 1.6$m, $d_{oc} = 75$mm) with three mean friction angles $\mu_{\varphi'}$ located at three different repository depths.
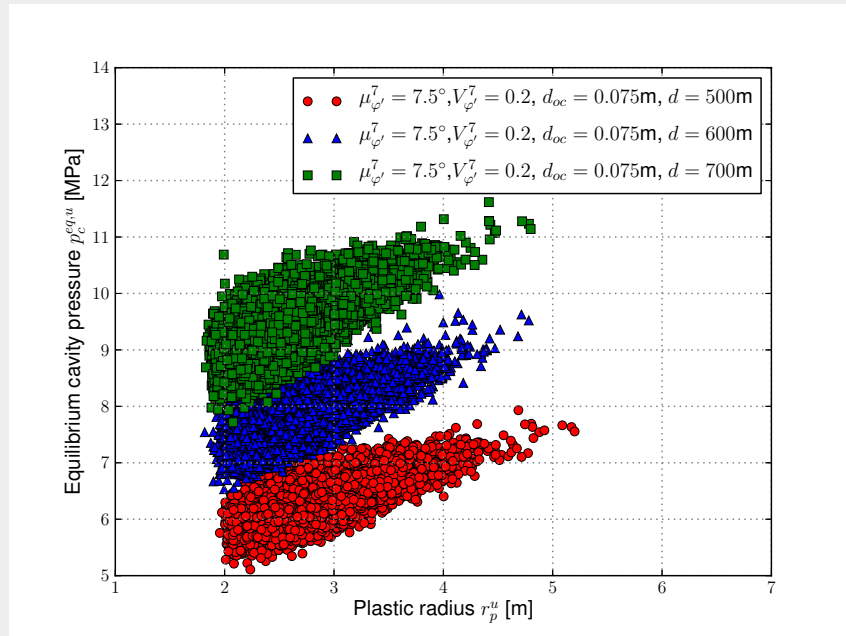
Figure 7.19.: Plastic radius r_p versus equilibrium cavity pressure p_c^{eq} for a HLW gallery ($r_c = 1.6$m, $d_{oc} = 75$mm) located at three different repository depths in a Boom Clay with a low mean friction angle of $\mu_{\varphi'} = 7.5°$.

7.3.3. Performance of FORM/SORM

In this section, the performance of the FORM and SORM approximate RBD methods is assessed with respect to the MC simulations. From Figures 4.6, 7.6, 7.7 and 7.9 it is evident that, for a HLW gallery in the basic setup ($r_c = 1.6$m, $d_{oc} = 75$mm, $d = 500$m), the plastic radius computed via the analytical model is most sensitive to a variation in mean and/or coefficient of variation of the soil friction angle, φ', and resulted in the highest failure probabilities for the uncorrelated case. Hence the assessment in this Section focuses on this nine uncorrelated φ'-cases (Table 7.1 and Equation 7.9).

Figure 7.20 shows that the absolute and relative errors of the FORM approximation of the failure probability, with respect to the MC simulations, is good. Given that the number of realisations, i.e. the number of iterative calls to the limit state function, is significantly lower than the number of MC realisations, FORM performs computationally very efficiently. The SORM approximation slightly decreases the approximation error for most cases.

Note that the number of $25\,000$ MC realisations used in this study was selected for a general comparison of the system response with respect to varying parameters under different settings. This number needs to be increased for a more thorough comparison between the FORM/SORM approximation and the MC simulations.
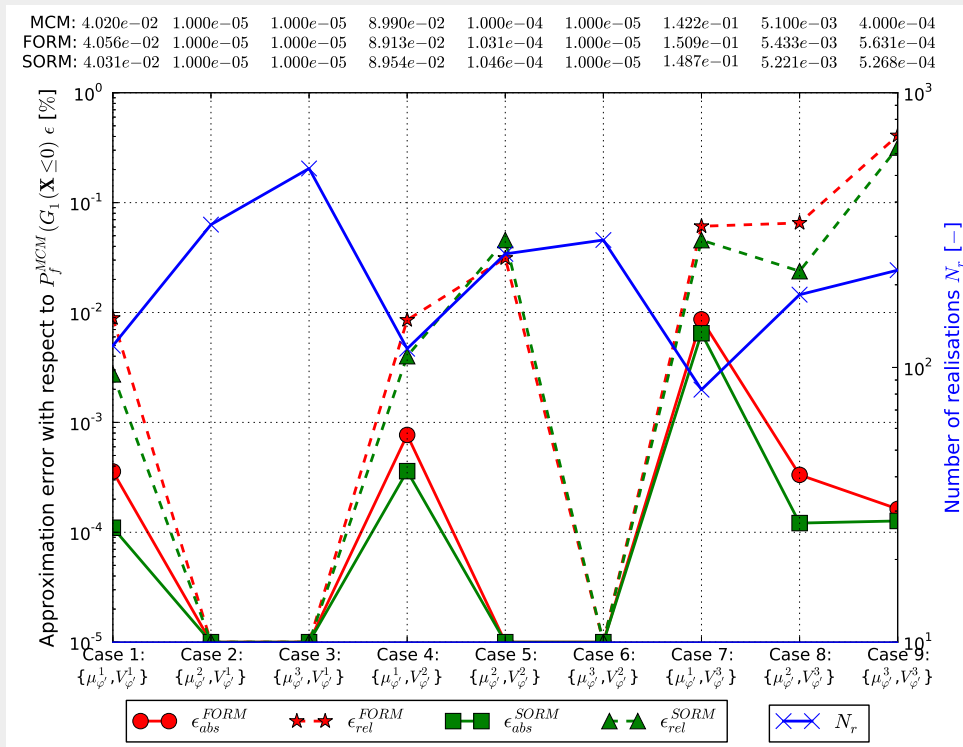
Figure 7.20.: FORM/SORM approximation for the nine φ'-cases. Left-hand axis showing the absolute approximation error, ϵ_{abs}, and relative approximation error, ϵ_{rel}, of the failure probability computed with respect to the MC simulation. Right-hand axis showing the number of iterations. Top axis showing the absolute failure probability.

7.3.4. Sensitivity analysis

The analytical model was mechanically most sensitive to a variation in soil friction angle (Figure 4.6). Figure 7.21 now shows the importance factors; that is, the sensitivity of each parameter with respect to the probability of failure, for the nine φ'-cases assessed in Section 7.3.1.

In contrast to the mechanical sensitivity, this sensitivity measure also accounts for the uncertainty in each parameter X_i, and is thus affected both by a variation in the mean estimate, μ_{X_i}, and in the coefficient of variation, COV_{X_i}. For Cases 1-3, the uncertainty in the friction angle is lower than that of the other 5 parameters. The importance of the Young's modulus is dominant for Cases 1-2, but the friction angle becomes more important for Case 3 with the largest mean estimate. The initial cohesion is more important than the friction angle only for Case 1. With increasing coefficient of variation of the soil friction angle, Cases 4-6 and 7-9, the friction angle becomes more important. For all 9 cases the importance of the Poisson's ration, ν, is small and the importance of the residual cohesion c'_r and tangent stiffness, E_t, are insignificant.

7.4. Tunnel performance using 2D numerical framework

In this Section the FORM module of the reliability-based toolbox will be tested using the computationally significantly more expansive 2D Finite Element program. The setup of the mechanical model is identical to the pre-operational assessment of a HLW gallery ($r_c = 1.6$m,
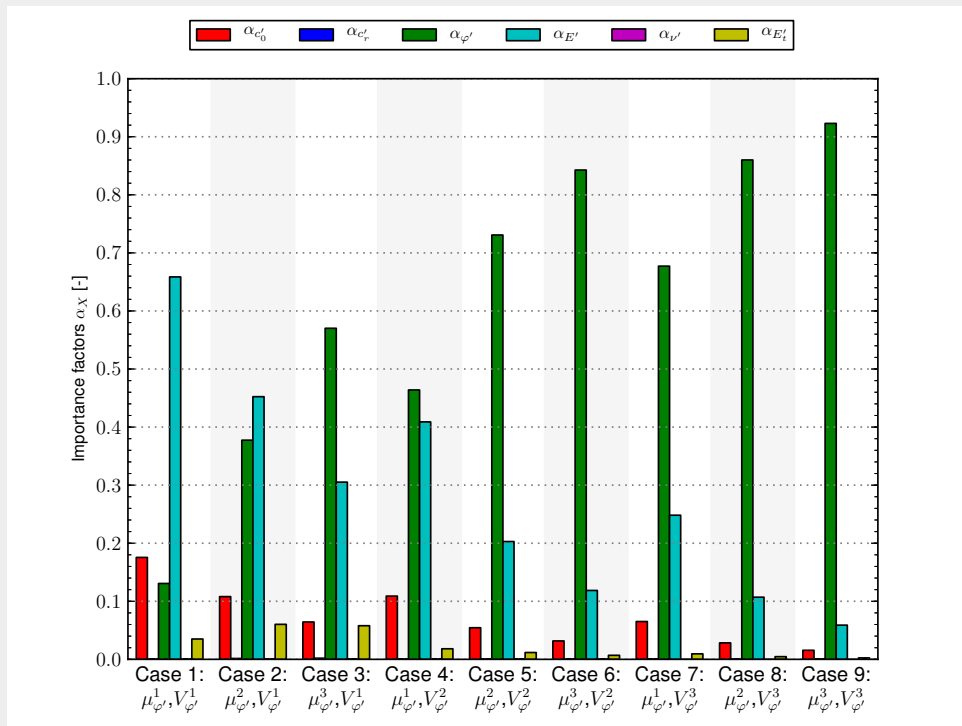
Figure 7.21.: Importance factors α_{X_i} for the nine φ'-cases.

$d_{oc} = 75$mm) at 500m depth in drained conditions (see Section 6.2.1), as this resulted in a slightly more unfavorable response (see Sections 6.2.4 and 6.2.5).

The mechanical sensitivity analyses presented in Section 6.2 show that the current design of a single HLW gallery is most likely geomechanically stable, i.e. the extent of the plastic radius as well as the cavity pressure induced by the excavation of the gallery are limited. Hence, the performance of the HLW gallery will be assessed for a critical set random variables in this report to demonstrate the functionality of the framework.

From Tables 6.4 it becomes apparent that both the extent of the plastic and hardening zone, as well as the magnitude of the cavity pressure, become larger with an increase in the secant reference modulus. Therefore, in this assessment the mean reference secant modulus is set to $\mu_{E_{50}^{ref}} = 160$MPa. The coefficients of variation, $V_{E_{50}^{ref}}$, is varied between 0.05, 0.125 and 0.2. The remaining HS model parameters are set to be random variable defined by a individual mean value (effective cohesion $\mu_{c'} = 0.5$MPa, effective friction angle, $\mu_{\varphi'} = 12.5°$, Oedometer reference modulus, $\mu_{E_{oed}^{ref}} = 120$MPa, un-/reloading reference modulus, $\mu_{E_{ur}^{ref}} = 360$MPa, un-/reloading Poisson's ratio, $\mu_{\nu_{ur}} = 0.3$ and HS model exponent, $\mu_{m} = 0.8$) and a coefficient of variation (equal for all parameters $V_{X_i} = 0.125$). All random variables are assumed to follow a normal distributed. A potential cross-correlation is not accounted for.

A hypothetical limit state cavity pressure is set to $p_l^{max} = 7$MPa and thus $G_3(\mathbf{X}) = p_c - p_l^{max}$. The computed probabilities of failure, i.e. $P_f = P[G_3(\mathbf{X}) \leq 0]$, are $1.38E - 06$, $4.98E - 06$ and $3.14E - 4$, for the case of a low, medium and high coefficient of variation, respectively. For a design optimisation, this relatively low failure probability may suggest to reduce the liner thickness for this specific cases (see Figure 4.4).

Figure 7.22 shows the importance factors α_{X_i} for the three cases investigated. The Figure shows that the probability of failure is most sensitive to an uncertainty in the effective friction angle, φ', and the reference secant modulus, E_{50}^{ref}. With increasing uncertainty in the reference secant modulus, that is, with an increase in the coefficient of variation (Case $1\rightarrow3$), the performance becomes more sensitive to this variance.

7.5. Conclusions

In this Chapter a reliability-based framework has been developed to asses the geomechanical performance of an individual tunnel gallery of the OPERA repository reference design using the simulation based *Monte Carlo Method* (MCM), as well as the approximate *First-* and *Second Order Reliability Methods* (FORM/SORM).

This preliminary probabilistic investigation is based on sets of point statistics of the soil property values which have been derived from a literature study. Due to the scarcity of data, representative sets of point statistics (mean, variance, covariance) have been selected to compute the probability of failure as well as the sensitivity of the performance with respect to the degree of uncertainty in the Boom Clay parameters. Both the analytical and numerical assessment mechanical models have been implemented within the framework.
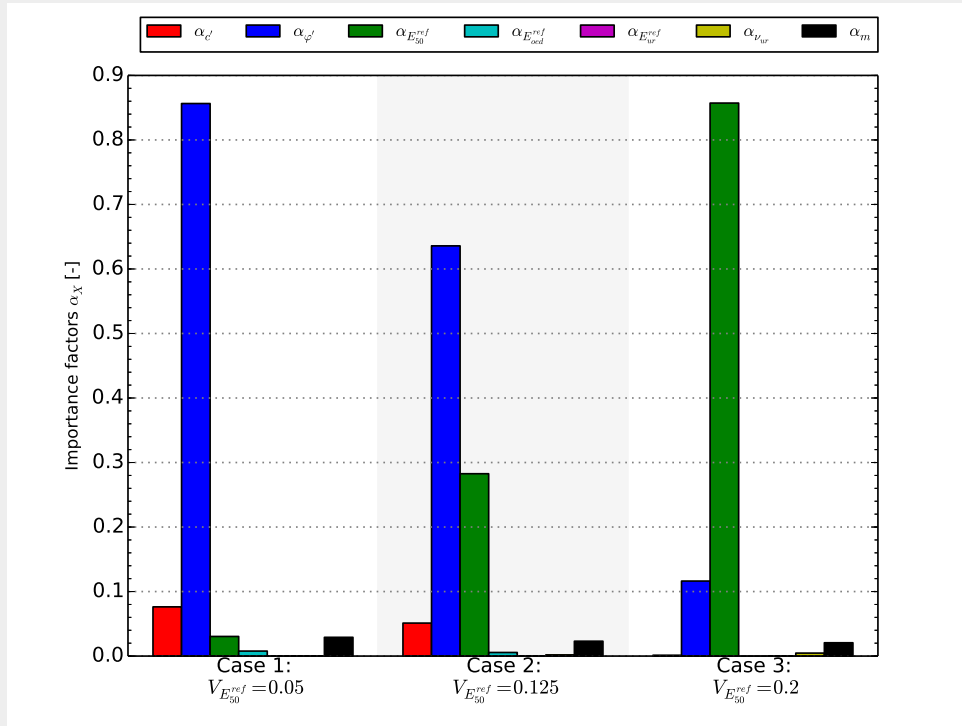
Figure 7.22.: Importance factors α_{X_i} for the three coefficients of variation $V_{E_{ur}^{ref}}$.

From the analyses performed in can be concluded that, by reducing of the spacing of the HLW and LILW disposal cells to $b_c = 25$m, i.e. $r_{p,lim} = 8.33$m, the failure probabilities may remain within acceptable bounds. However, the mean estimate and variance of individual random variables, as well the cross-correlation between random variable, can significantly influence the performance function. For the cases investigated, FORM and SORM approximated well the failure probability and thus the computation time can be significantly reduced when using the Finite Element mechanical model.

8. Thermal response

8.1. Introduction

An initial thermal assessment is presented in this section for the OPERA design. As an initial scoping exercise, a range of cases has been carried out in order to assess the initial variability in the thermal response of the Boom Clay due to the thermal load from the waste.

The source term based upon the waste is first assessed in Section 8.2. An assessment of the material parameters for the Boom Clay is presented in Section 8.3, split into three scenarios to allow for the parameter ranges. Section 8.4 presents the numerical modelling theory, setup and results. A summary is given in Section 8.5.

8.2. Assessment of source term

The thermal load applied to the Boom Clay from the radioactive waste is derived from the heat output of the waste. There are two main types of heat emitting waste, with the main properties listed below (Verhoef et al., 2011):

- HLW
  - ↪ Stored in CSD-V canisters.
  - ↪ Approximate number of canisters is 625.
  - ↪ A single canister per supercontainer.

- SNF
  - ↪ Stored in ECN canisters.
  - ↪ Approximate number of canisters is 150.
  - ↪ Two canisters per supercontainer.

For both types of waste, it is possible that the contents are derived from a generation II nuclear reactor using UOX fuel, however, the majority of the spent fuel is derived from the research reactors at Delft and Petten (Haart, 2014). This fuel will have a lower heat output as it is typically in the reactors for a significantly shorter period of time, although details of the thermal output have not been found. The CSD-V canisters contain approximately 380kg of COGEMA glass (Meeussen and Rosca-Bocancea, 2014), which, based upon the re-processing process and SAFIR 2 project (ONDRAF/NIRAS, 2001a), Sillen and Marivoet (2007) equate

to an equivalent of 1.33tHM per canister. The ECN canisters are stated to contain a maximum of 0.383tHM (Meeussen and Rosca-Bocancea, 2014), but will have two canisters per supercontainer, yielding therefore a maximum total of 0.766tHM per supercontainer.

Following the approach of Sillen and Marivoet (2007), the heat fluxes can be derived using a sum of exponential functions

$$Q_{tHM} = A_i e^{-\lambda_i t} \tag{8.1}$$

where Q_{tHM} is the heat flux per tonne of heavy metal, A_i and λ_i are fitting parameters and t is the time elapsed since the production of the waste form. The values of the first and mainly contributing four parameters for A_i and λ_i are presented in Table 8.1, for both HLW and UOX (based upon UOX with a burnup of 45GWd/tHM) (Sillen and Marivoet, 2007).

The supercontainer will be of 2.5m length (Verhoef et al., 2011) and, assuming a worst case scenario, that the supercontainers are placed into the disposal drift without any intermediate gap, the heat flux per meter length of the disposal drift can be calculated as:

$$Q_m = \frac{Q_{tHM} M_{tHM}}{l_{sc}} \tag{8.2}$$

where Q_m is the heat flux per metre of the disposal gallery, M_{tHM} is the mass of heavy metal per supercontainer and l_{sc} is the length of the supercontainer. The combination of Equations 8.2 and 8.1 yields Figure 8.1. It can be seen that the HLW initially gives a higher output, but after approximately 30 years the spent fuel (UOX) provides a higher output. In the proposed disposal system the storage time will be at least 100 years (Verhoef et al., 2011), as indicated by the thick black line in Figure 8.1; therefore, in all calculations the spent fuel heat output will be used to ensure conservatism.

8.3. Material parameters

8.3.1. Boom Clay

The material properties are based upon the ranges presented in Table 2.10. In the following modelling three scenarios have been adopted: a worst case scenario (Scenario High), a mid-range scenario (Scenario Mid), which can be considered the most likely, and a best case scenario (Scenario Low), based upon the Boom Clay property values. This will give an indication of the sensitivity of the thermal behaviour to the variation of the Boom Clay. The material parameters that form these scenarios are found in Table 8.2. The thermal conductivity has been considered to be isotropic in this work for simplicity, although it is noted that this may affect the results. The extreme values of the ranges have been utilised, so are likely to encompass the real behaviour including anisotropic behaviour. In this case the specific heat

Table 8.1.: Coefficients for Equation 8.1 (Sillen and Marivoet, 2007).

Waste	A_1 [W tHM^{-1}]	A_2 [W tHM^{-1}]	A_3 [W tHM^{-1}]	A_4 [W tHM^{-1}]	λ_1 [a^{-1}]	λ_2 [a^{-1}]	λ_3 [a^{-1}]	λ_1 [a^{-1}]
UOX	1362	152.8	207.5	30.00	0.02343	0.007486	0.001581	6.753×10^{-5}
HLW	5021	1205	27.04	0.7576	0.3894	0.02458	1.63×10^{-3}	6.55×10^{-5}

capacity and thermal conductivity are the bulk values, encompassing both the fluid and solid components as the available information was limited.

8.3.2. Concrete and canister

The thermal conductivity of concrete is typically 2.5W/mK and this is likely to be higher than the conductivity of the Boom Clay (as will the canister conductivity). Additionally, the volumes of the concrete and canister material will be minor compared to that of the Boom Clay and with specific heat capacities of the same magnitude mean that they will only have a very limited effect on the temperature distribution. This indicates that the Boom Clay will control the heat flow, and therefore the heat flux will be assumed to be directly applied onto the Boom Clay interface.
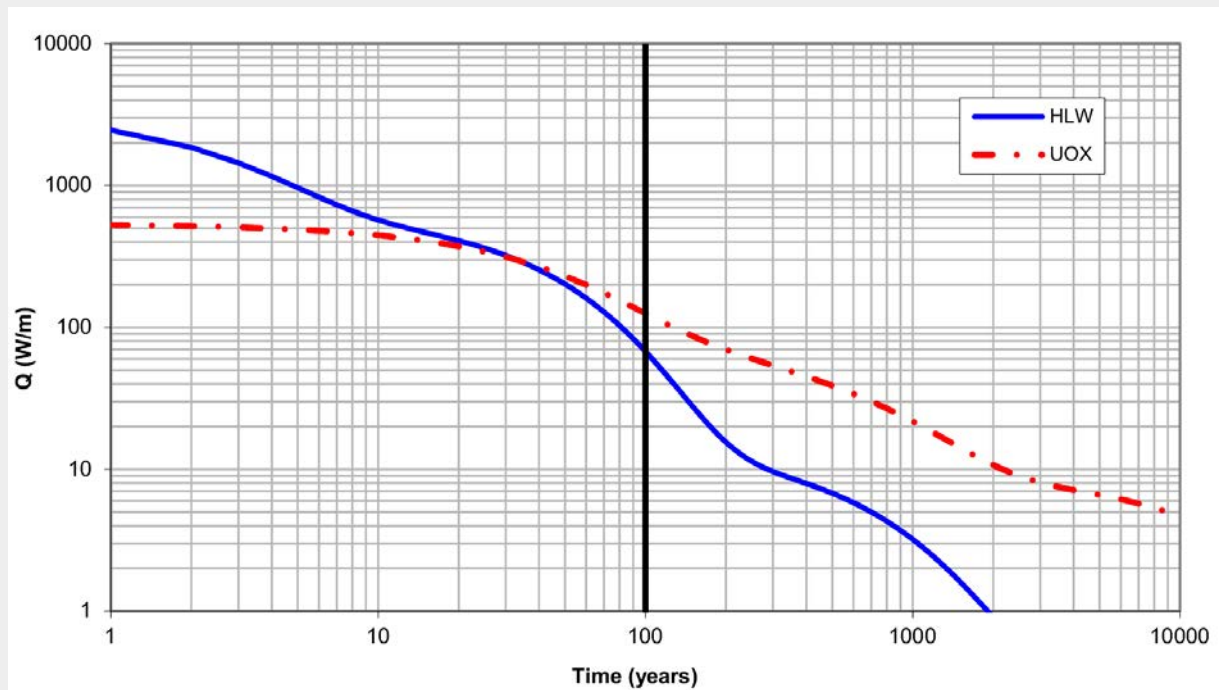
Figure 8.1.: Heat flux per metre for both UOX and HLW.

Table 8.2.: Parameters for the two scenarios for the thermal analyses, based upon Tables 2.10, A.2 and A.3.

Definition	Symb.	Unit	Scenario High*	Scenario Mid*	Scenario Low*
Bulk density (sat.)	ρ	[kg m^{-3}]	1900	2000	2100
Thermal conductivity	λ	[W m^{-1} K^{-1}]	1.06	1.4	1.7
Specific heat capacity	C_p	[J kg^{-1} K^{-1}]	1333	1400	1470

* For sources to ranges of the individual parameters please see Tables A.2 and A.3.

8.4. Numerical 2D modelling

For all modelling in this chapter a 2D cross-sectional model will be utilised. The length of the tunnel is 45m (Verhoef et al., 2011) and therefore is long in comparison to the diameter. In addition, adjacent tunnels are considered parallel, as the proposed convergence of the tunnels is small compared to the tunnel spacing of 50m (Verhoef et al., 2011). The numerical modelling strategy is to consider two cases:

○ Case 1 - A single disposal tunnel - here the effect of a single tunnel will be explored.

○ Case 2 - Multiple tunnels - where the thermal effects are allowed to interact.

The thermal load is equal is both cases. The thermal modelling has been undertaken using Plaxis Beta 2015 which includes thermal behaviour (Plaxis, 2014b).

8.4.1. Heat Flow

The governing equation for heat flow, in a saturated medium, has been derived based upon the conservation of energy

$$\frac{\partial \Omega}{\partial t} = - \triangledown \cdot \mathbf{Q} + Q_T \tag{8.3}$$

where Ω is the heat content, $\mathbf{Q}$ is the heat flux and Q_T is a heat source or sink term. The heat content is defined as the spatial average of the heat contents of the liquid and solid phases and can be expressed as

$$\Omega = T\Big[\left(1-n\right)C_{ps}\rho_s + nC_{pw}\rho_w\Big] \tag{8.4}$$

where C_p is the specific heat capacity of the water or solid defined by the subscripts. The heat flux in this work is defined by Fourier's law and considers only conduction, as, due to the

low permeability of the Boom Clay, convective flow will be minimal. Therefore the flux can be defined as

$$\mathbf{Q} = -\lambda \bigtriangledown T \tag{8.5}$$

8.4.2. Domain

The model domain and boundary conditions for Case 1 and Case 2 are shown in Figures 8.2(a,c). The mesh discretisation for each case is shown in Figures 8.2(b,d). The domain is 100m thick, following Verhoef et al. (2011), and in Case 1 the horizontal extent has been selected to be 100m so that the boundary will not unduly affect the results. For Case 2 the horizontal extent is determined by the proposed tunnel spacing of 50m. It is recognised that in Case 2, a plane of symmetry exists vertically at the horizontal mid point, however as simulation run times are small, it was thought that this domain offers better visualisation.

The initial conditions are set at $T = 295$K, which corresponds to the mid-value found experimentally at 500m depth in Belgium by Vandenberghe and Fock (1989). A time-dependent boundary condition has been set on the tunnel boundaries in a step-wise fashion. The derived function for spent fuel per meter of tunnel was divided by the circumference to give a flux boundary condition in $\mathrm{W\,m^{-2}}$ and is shown in Figure 8.3, with the applied boundary condition shown by the black line.

8.4.3. Assessment of cases

The temperature results from all three scenarios of Case 1 and Case 2 are found in Figure 8.4. On the left are the results from Case 1 and on the right Case 2. At the peak temperature of Scenario Mid, for both cases, a contour plot is shown in Figure 8.5. The dips that can be observed in the temperature evolution are due to the step-wise boundary condition.

A wide range of possible thermal effects have been identified in the SAFIR 2 project (ONDRAF/NIRAS, 2001b). In general, three limits have been suggested: 1) the clay should not exceed $100°$C, reduced to about $85°$C, in order to achieve the $100°$C limit, 2) a maximum average increase of $6°$C over an overlaying aquifer, and 3) a maximum increase of $0.5°$C for the biosphere. Given that the effects on the wider environment are difficult to assess due to the wide range of possible locations and scenarios, the results have been assessed mainly in terms of peak temperature at the Boom Clay/supercontainer interface. Moreover, due to the limited amounts of heat emitting waste, assessing the heat behaviour using a 2D model would yield substantially over-conservative results.
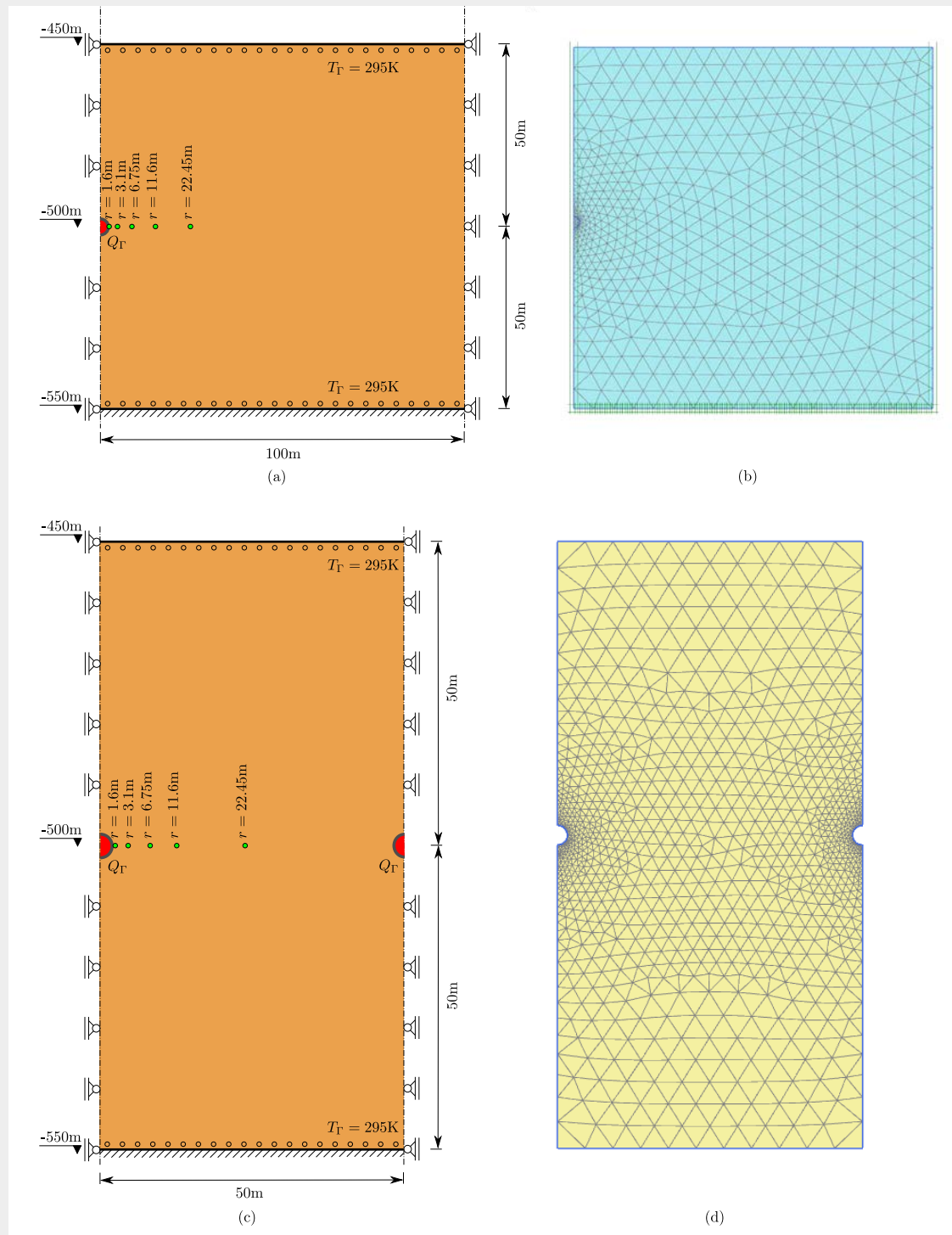
Figure 8.2.: Model domain with boundary conditions for two-dimensional thermal analysis, (a) Case 1 and (b) Case 2, with the associated FE mesh discretsations shown in (b,d).
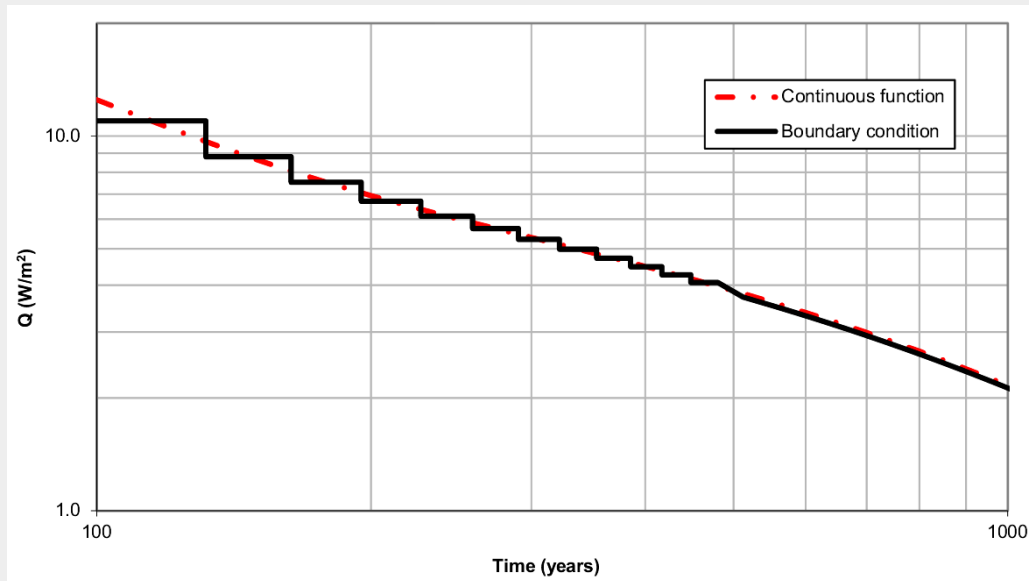
Figure 8.3.: Heat flux per square metre and the step-wise boundary condition.

Case 1 - A single disposal tunnel

In Case 1 the range of peak temperatures is from 343.4K ($70.3°$C) for Scenario High, 332.7K ($59.6°$C) for Scenario Mid and 326.5K ($53.4°$C) for Scenario Low. It is noted that this range is rather limited, given the fairly large range of material property values and represents an increase from the initial temperature of between 31.5K and 48.4K (31.5 and $48.4°$C) . The peak temperature occurs in all scenarios for Case 1 at the end of the first step in the thermal flux boundary condition at approximately 30 years. That the peak occurs when the boundary condition reduces, means that the precise time of the peak cannot be determined, but it is in this time frame. The peak temperatures at points further away from the tunnel lining are delayed, with the peak temperature increasing by 10.7K at 22.45m from the tunnel centre, occurring at around 100 years.

Case 2 - Multiple tunnels

For Case 2, the temperature after about 30 years, which is at the end of the first step in the thermal flux boundary condition, are similar in all scenarios to that in Case 1, with the maximum for Scenario High of 344.7K ($71.6°$C), 334.3K ($61.2°$C) for Scenario Mid and 328.1K ($55.0°$C) for Scenario Low. After this point the temperature decline is substantially less than for Case 1. In all three scenarios the temperature is virtually unchanged at the end of the second step in the boundary condition at approximately 60 years. Therefore the peak temperature is maintained for longer when considering adjacent tunnels. As can be seen in Figure 8.5, the temperatures in the horizontal direction from the tunnel centreline are substantially higher in this case than the temperatures in the vertical direction, due to the thermal interaction, with the difference being the greatest at the mid-point between the tunnels. The peak at the cen-

(a) Case 1 - Scenario High

(b) Case 2 - Scenario High

(c) Case 1 - Scenario Mid

(d) Case 2 - Scenario Mid

(e) Case 1 - Scenario Low

(f) Case 2 - Scenario Low
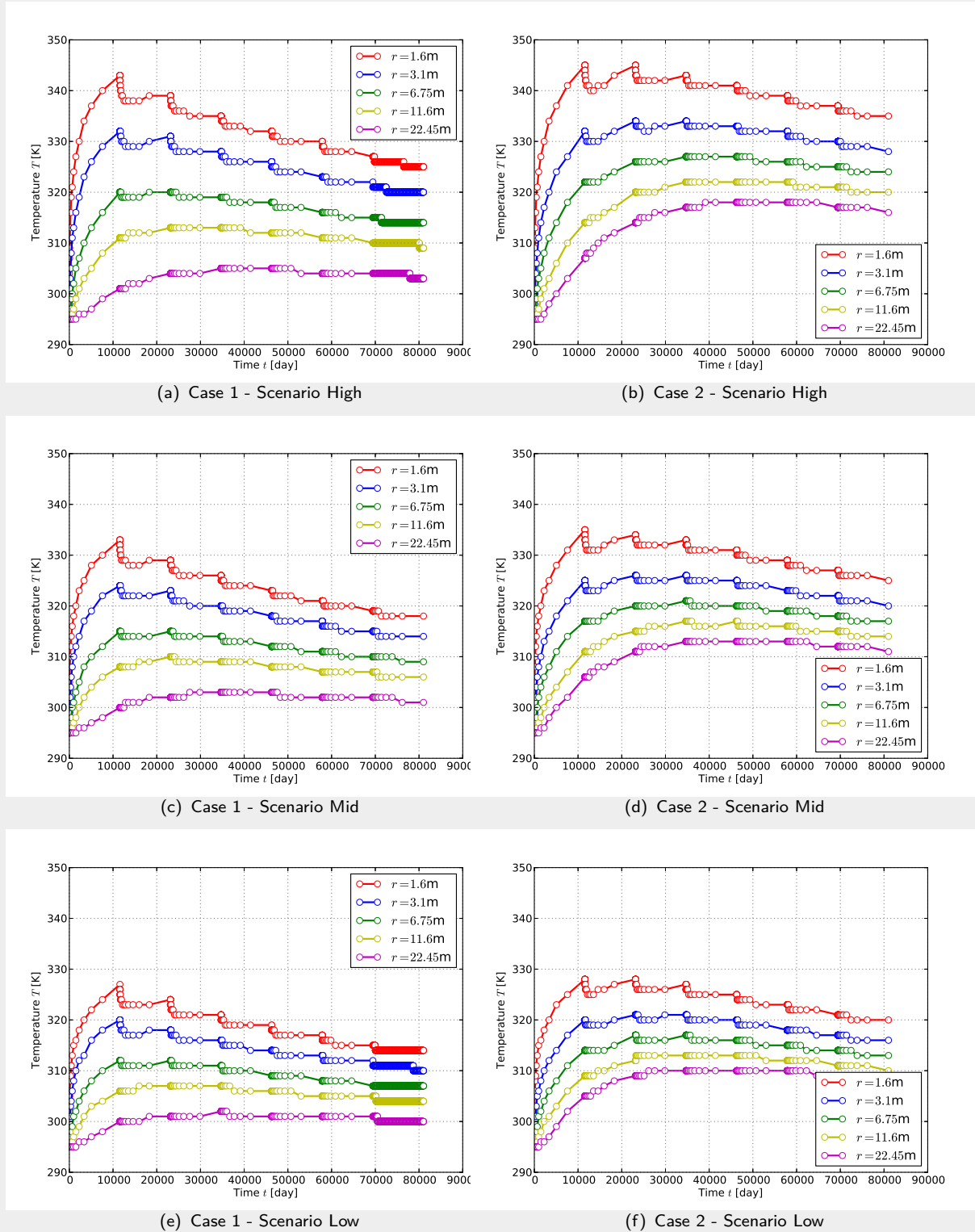
Figure 8.4.: Results of Case 1 and Case 2 in time at points 1.6m, 3.1m, 6.75m, 11.6m and 22.45m along a horizontal line from the centre of the tunnel. Figures (a) and (b) represent Scenario High, (c) and (d) Scenario Mid and (e) and (f) Scenario Low.

(a) Case 1 - Scenario High

(b) Case 2 - Scenario High

(c) Case 1 - Scenario Mid

(d) Case 2 - Scenario Mid

(e) Case 1 - Scenario Low

(f) Case 2 - Scenario Low
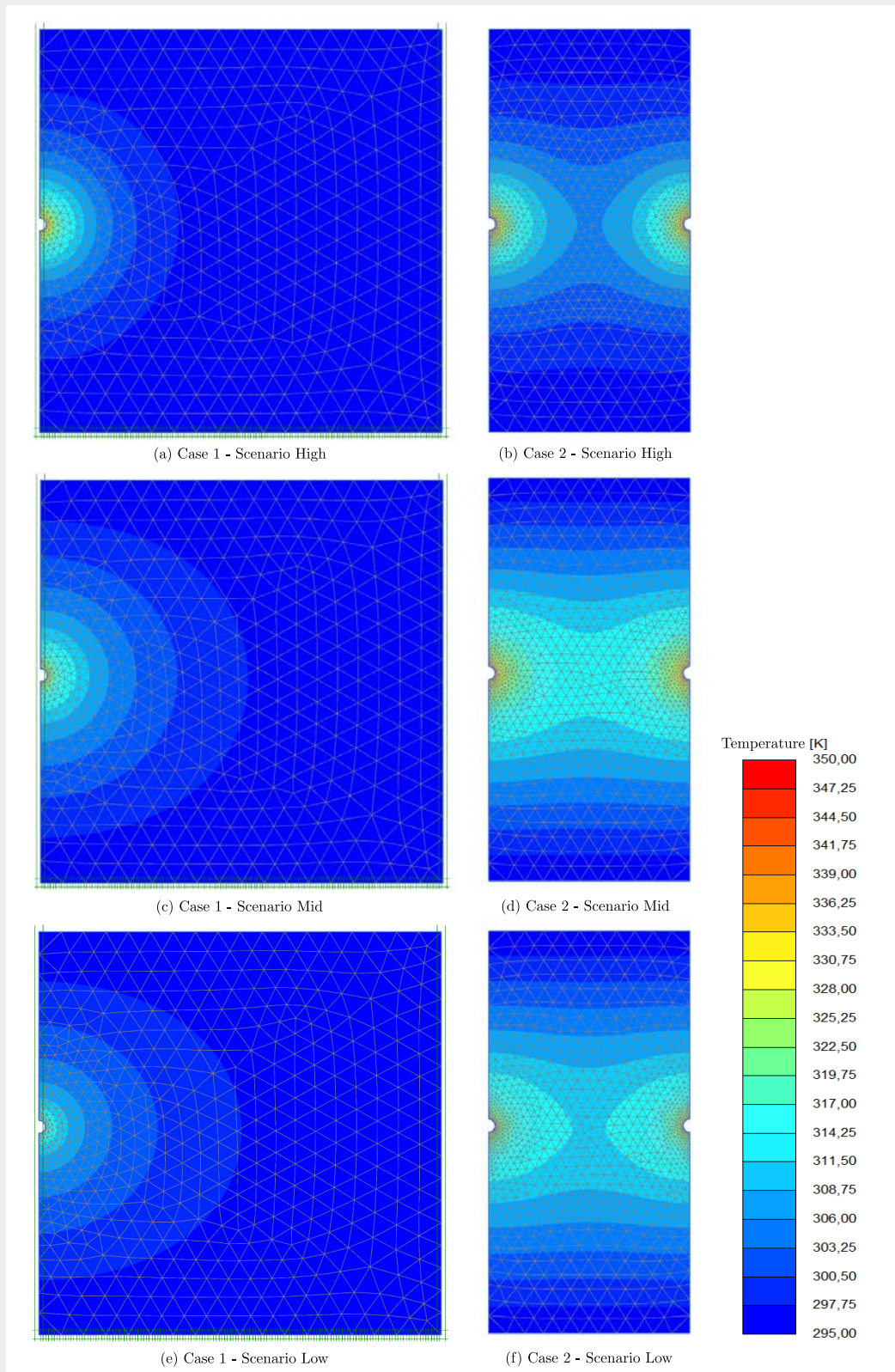
Figure 8.5.: Contour plot of the temperature distribution from Scenario Mid at the peak temperature for (a,c,e) Case 1 and (b,d,f) Case 2.

tral point occurs at approximately 130 years and represents a temperature increase of 23.1K ($23.1°$C).

In neither case considered here, or in any of the scenarios, is the limit of $85°$C suggested by ONDRAF/NIRAS (2001b) exceeded. Therefore it can be concluded that, in terms of thermal behaviour, there is scope to reduce tunnel spacing or increase the amount of waste per length of disposal tunnel.

8.5. Summary

In this chapter, an initial thermal assessment of a repository in Boom Clay at 500m depth has been presented. Only limited material information is known and therefore the full reported range has been included for assessment. It is shown that the maximum increase in temperature, as expected, will be at the Boom Clay-tunnel lining interface. This maximum temperature is likely to be between 345K and 328K; that is, between $72°$C and $55°$C. The spent fuel from a generation II reactor is shown to have the highest thermal output per metre of disposal tunnel within the current disposal concept, although it is recognised that the majority of the spent fuel in the Netherlands will have a lower thermal output as it originated from research reactors. The low predicted temperatures are in part due to the long period of interim storage and also due to the proposed disposal method. In no case or scenario simulated does the temperature exceed the proposed limit of about $85°$C, which, given the conservatism in the material parameter selection and thermal output selection, means that there is scope, in terms of thermal behaviour, to reduce the tunnel spacing or increase the waste density.

9. Discussion and conclusions

9.1. Summary

The feasibility of the current OPERA repository reference design has been assessed for individual tunnel galleries at realistic disposal depths, with respect to the Boom Clay geomechanical behaviour, during the excavation, and during the pre-operational and early post-closure phases. An analytical elasto-plastic strain-softening model has been developed for the preliminary assessment of the main features of the host rock response, but also to provide a computationally cheap tool to test the *Reliability Based Design* (RBD) framework. A more advanced constitutive soil model, the *Hardening Soil* (HS) model, was selected to model the Boom Clay response numerically in two and three dimensions by utilising the PLAXIS *Finite Element* (FE) software package. These geomechanical models have been modularised and implemented in the RBD model framework developed in this work, based on the *Open source initiative to Treat Uncertainties, Risks'N Statistics* (OpenTURNS) scientific library. Using the simulation based *Monte Carlo Method* (MCM), as well as the approximate *First-* and *Second Order Reliability Methods* (FORM/SORM), the probability of failure as well as the sensitivity of the performance with respect to the degree of uncertainty in the Boom Clay parameters can be computed.

Chapter 1

The context for the report is detailed in Chapter 1, with the background of the OPERA research programme, including preceding research programmes, outlined. The objectives, methodology and scope of the work presented in this report are given.

Chapter 2

Chapter 2 provides a selective literature review, aiming to provide background information for the assessment of a Dutch radioactive waste repository in Boom Clay. The topics reviewed are: R&D into deep geological radioactive waste disposal facilities (Section 2.2) including the two major research programmes previously undertaken in the Netherlands (OPLA and CORA), an overview of the Dutch OPERA reference design in Boom Clay (Section 2.3), the in situ conditions and soil property values of the Boom Clay formation (Section 2.4), and an overview of primary physical processes potentially governing the response of the OPERA repository system in the time frame between the construction of the repository and the end of the thermal (early closure) phase (Section 2.5).

Chapter 3

The available data on Boom Clay material properties and in situ conditions are assessed and, as far as possible, interpreted statistically in Chapter 3. In Section 3.2 some sources of uncertainties are addressed, their treatment in practice is outlined and their implications for this work are discussed. A description of random variables, that is variables which have statistical variation, is presented in Section 3.3. A summary on the point and spatial variability of different soil property values and state variables found in literature is presented in Section 3.4. In Section 3.5, a simple procedure is introduced to interpret the Boom Clay property values collected in the database (Appendix A), to determine the input parameters for the deterministic and reliability based analyses in this report. The variability of concrete liner properties is briefly summarised in Section 3.6.

Chapter 4

In Chapter 4, an analytical formulation accounting for elasto-plastic strain-softening Boom Clay behaviour has been developed, to assess the host rock response due to the excavation of a deep tunnel. A review of the analytical and semi-analytical formulations developed and used to assess the soil response due, to the tunnel excavations, is given in Section 4.2. Section 4.3 presents the formulations for describing the stress-strain equilibrium around a cylindrical cavity. The constitutive model framework is developed in Section 4.4 and the solution algorithm has been subsequent outlined in Section 4.5. In Section 4.7 the model response is assessed, by means of deterministic analyses for varying soil property values and boundary conditions.

Chapter 5

The performance of different advanced constitutive models has been assessed in Chapter 5, to select the most suitable model for the numerical modelling of the excavation of the OPERA repository galleries. Section 5.2 summarizes some of the existing constitutive soil models that have been used, or developed, to describe the THM behaviour of Boom Clay. The approach utilised for selecting a constitutive soil model for this research is described in Section 5.3 and four models have been tested against triaxial and oedometer laboratory test data (Section 5.4). Subsequently their performances have been assessed and the *Hardening Soil* (HS) model selected. The formulation of the selected HS model, as well as its implementation in the PLAXIS FE software package, is therefore described in more detail in Section 5.5. A mechanical sensitivity analysis is presented for triaxial conditions in Section 5.6, to see the relative change in responses due to the deterministic variation of individual model parameters.

Chapter 6

In Chapter 6 the excavation of a tunnel in a deep Boom Clay formation has been numerically assessed in two and three dimensions, utilising the PLAXIS FE software package. In Section 6.2, the short- and long-term responses of the Boom Clay have been assessed in two-dimensional plane strain conditions using the HS model. A mechanical sensitivity analysis is performed by

varying individual model parameters and boundary conditions, to assess their impact on the extent of the plastic zone and on the liner forces. The three-dimensional transient excavation process of a single tunnel is modelled numerically in Section 6.3 to investigate the impacts of the excavation process.

Chapter 7

In Chapter 7 the analytical and numerical assessment mechanical models are implemented within a Reliability Based Design framework, to account for the uncertainties in the material properties in a systematic, quantitative and verifiable manner. RBD methods are introduced in Section 7.2, and subsequently the model framework employed here is described and the limit state functions are defined. Finally a strategy to assess the sensitivity of the response to each random variable, within a probabilistic framework, has been described. In Section 7.3 the performance of a tunnel excavated in Boom Clay at the repository depth has been assessed, by implementing the analytical model developed in Chapter 4 within a probabilistic framework. In Section 7.4 the same problem is assessed by utilising the two-dimensional Finite Element model (Chapter 6).

Chapter 8

An initial thermal assessment of the OPERA reference design is presented in Chapter 8. The source term based upon the waste has been assessed in Section 8.2, followed by an assessment of the material parameters for the Boom Clay split into three scenarios to allow for the parameter ranges (Section 8.3). Section 8.4 presents the numerical modelling theory, setup and results.

Chapter 9

Chapter 9 presents the summary, discussion and conclusion on this report.

Appendix A

Appendix A provides a database of Boom Clay property values and state variables collected from literature.

9.2. Discussion

This section aims to discuss some of the main outcomes of the review, development and assessment part of this report (see Figure 1.6), and to put them into a general context in terms of design, safety and cost.

Data and uncertainty

For the current development phase of the OPERA repository, the two main sources contributing to the uncertainty are: firstly, the scarcity of good quality data on intact Boom Clay samples

retrieved from depth ≥ 500m tested under various stress-strain conditions; and secondly, the variability of the geological setting, as well as the geochemical and geomechanical host rock properties between potential disposal sites. More testing will obviously result in a better understanding of the parameter variance, as well as the covariance; however, to distinguish between epistemic uncertainty (e.g. testing error) and aleatory uncertainty (e.g. local variability) is difficult (Section 3.2) and so, based on the current knowledge, a lumping of both uncertainties is a reasonable approach. However, the data collected in the database (Appendix A), which have been evaluated in Section 3, comprise test data from different locations. In Section 2.4 the effect of a different regional location on the composition and thus mechanical behaviour of the Boom Clay was discussed (e.g. see discussion on Figures 2.19 and 2.28(a)). Hence, not only the mean estimate of a Boom Clay property value, but most likely as well the variance and covariance, will be affected by the location and depth of the Boom Clay host rock.

The relevance of an analytical model

The development of the analytical elasto-plastic strain-softening model allows a computationally cheap tool, a) to investigate various changes in material parameters, and b) to test the RBD framework. The response of this axisymmetric model, in terms of both the extent of the plastic zone and the cavity pressure, compares well to the results obtained with the two-dimensional FE model (compare Figure 4.6 and 6.7). While not all of the features of Boom Clay behaviour can be reproduced, the majority can, and this means that this model can be further used. With further development, the analytical model can readily be extended to account for an anisotropic in situ stress state, cross-anisotropic elasticity, or a strain-softening dependent soil friction angle, in order to extend its applicability. This similarity in the response, means that the model can be used for testing the ability of different RBD methods for approximating the performance, failure probability and parameter sensitivity. It also enables practical reliability calculations to be undertaken utilising more complex (and time consuming) constitutive models.

Constitutive modelling of Boom Clay

The results in Chapter 5 show that the conventional and advanced constitutive soil models are capable of reproducing many of the main features of the Boom Clay behaviour. The models were calibrated against three drained triaxial compression tests consolidated to different over-consolidation ratios and one high pressure oedometer test. The HS model was found to perform best and used for the numerical modelling of the excavation induced Boom Clay response. However, no model was seen to be able to reproduce all features observed in a qualitative and quantitative manner. In particular, the HS model is unable to reproduce strain-softening behaviour or creep.

The stress ranges under which the triaxial tests were performed were much lower than the in situ stresses at realistic disposal depths ≥ 500m (see Figure 5.2), which will affect the determination of stiffness and strength parameters (e.g. see Figures 2.21, 2.28(b) and 2.29)

and thus potentially the cross-correlations between the parameters (see discussion to Figure 3.3).

While this may affect the specific quantitative results, the qualitative behaviour is likely to be well reproduced, unless key features of the stress state have not been well predicted, e.g. the OCR.

Although the understanding and modelling of Boom Clay features such as stiffness anisotropy, creep or THM coupling, which are not included here, are a key part of any repository assessment and development process, the calibration of existing models to test data obtained on site specific intact Boom Clay samples under the desired boundary conditions (e.g. stress level, compressive and extensive stress path, OCR, etc.), in combination with an incorporation of the parameter uncertainty, can be seen to be able to reproduce the main features of geomechanical behaviour. Therefore, it is reasonable to use these models to assess the feasibility of the geomechanical design of the repository system.

Numerical modelling

In this report the three-dimensional modelling of the cavity excavation is preliminary. The two-dimensional Finite Element analysis provided a good insight into the drained and undrained response of the Boom Clay however, the three-dimensional analysis showed that the response may be significantly affected by the staged excavation process. Utilising the HS model, the 2D mechanical sensitivity analyses showed that the Boom Clay response, that is, in terms of the extent of the plastic zone and magnitude of the radial cavity pressure, my be altered significantly with varying model parameter. Before advancing in the 3D modelling, the uncertainty in the soil property values should to be reduced, the effect of the hydro-mechanical coupling needs to be assessed in 2D analyses and the possible excavation techniques and associated construction sequence should to be specified.

The reliability of defining uncertainty:

Using OpenTURNS libraries, a RBD module has been developed to assess the performance of the tunnel galleries, by utilising the simulation based MCM as well as the approximate FORM/SORM. For all Monte Carlo simulations, the maximum extent of the plastic zone and the maximum cavity pressure computed satisfied the specified ultimate limit state criteria for the given OPERA tunnel reference design, i.e. $r_{PZ} < 16.67$m and $p_c < p_c^{max}$ (see Section 7.3). Hence, the performance was evaluated with respect to a *hypothetical* set of limit states ($r_p^{lim} = r_c + 3$m, $p_c^{max} = 8$MPa), which may be better suited to restricting the excavated disturbed/damaged zone. The results show that, besides the determination of the mean estimate of the soil parameter, the variance and covariance of the random variables may significantly affect the performance and parameter sensitivity. Especially the role of the parameter cross-correlation should not be underestimated; in particular, by better assessing cross-correlations of material parameters reliability may be increased as uncertainty is constrained.

In a standard deterministic analysis the uncertainty in the result is not quantifiable. Often,

this is accounted for by simply choosing conservative input parameters. On the other hand, utilising a RBD framework the uncertainty in the response is quantifiable and thus provides a much higher quality of information. However, this quantitative approach relies upon the quality of the quantification/estimate of the uncertainty of the random variables. For example, an underestimated variance may result in a falsely optimistic estimation of the system reliability. In general, however, fewer data results in a larger uncertainty of the random variables, whereas increasing data results in a reduction of the input (and therefore output) uncertainty and thereby to an increasing in confidence in the result.

Thermal response

The thermal response has been assessed based upon a number of assumptions, with a conclusion that the thermal behaviour will not unduly affect the performance of the repository. The major assumption, based upon current plans, is the length of surface storage time. Any reduction in the storage time will require a reassessment of the thermal performance. The limits that the assessment uses for the assessment of thermal performance, based upon temperatures, are less obvious than for those of, e.g. stability. In this work, only a single limit that may affect geomechanical performance of the repository has been selected ($85°$C to ensure temperatures are below $100°$C); other limits are more site specific and have, therefore, not been assessed. However, this chosen limit is largely arbitrary and there is scope to increase or decrease it.

In this work a 2D approach has been undertaken and it is noted that, as only a single row of disposal galleries are planned to be constructed, due to the 3D behaviour the temperatures are likely to be lower than those simulated. As no temperatures exceeded limits, however, it was not considered necessarily to undertake 3D simulations. Of more significance is the choice of material parameters. The material parameters chosen were based upon very little data, and therefore cannot be deemed reliable. A range of parameters were chosen and selected in combinations, in such a way that produced a worst, a best and an average response base upon the available data.

To further reduce the thermal effects the policies relating to waste segregation could be modified. By mixing heat producing and non-heat producing waste, significantly lower temperatures would be realised. However, it is clear that this must be considered as part of a comprehensive safety assessment.

9.3. Conclusions

The feasibility of the current OPERA repository reference design has been assessed for individual tunnel galleries at realistic disposal depths, with respect to the geomechanical Boom Clay behaviour, during the excavation, pre-operational and early post-closure phases. In all aspects investigated, i.e. the tunnel stability and initial thermal response, the reference design seemed feasible, with scope to reduce the tunnel lining thickness or reduce the gallery spacing.

A selective review of aspects related to geological disposal and past research on this topic

has been made, revealing a shortage of high quality data from repository depths. The majority of data have been collected at depths less than 300m. From the available data, spatial and property value uncertainties are observed. Moreover, by comparing data from intact samples from Mol and Essen, differences in pore-water chemistry and mineralogy are observed that may lead to significant differences in geomechanical behaviour. A database of obtained material parameters has been compiled with links to the original data sources. These data have been statistically described where feasible.

An analytical model describing a tunnel construction in Boom Clay has been produced. The geomechanical behaviour of the main features of the Boom Clay has been included using a strain-softening elasto-plastic constitutive model. An elastic model of the tunnel lining, limited at the yield strength, has been linked to this model to give the overall response. This model gives a computationally cheap way of assessing the tunnel behaviour, as well as the sensitivity of various Boom Clay behaviours via parametric studies and the developed reliability model. It has been shown, via comparison to finite element models, that the analytical model gives a good approximation of expected behaviour. The HS model implemented in PLAXIS has been shown to simulate most features of the Boom Clay geomechanical behaviour recorded in oedometer and triaxial tests. However, strain softening and creep behaviour are not accounted for. The HS model was shown to be sensitive to the over-consolidation ratio.

The excavation of a single horizontal tunnel gallery was investigated utilising the HS model in two- and three dimensional FE analyses. The geomechanical response in terms of the extent of hardening and plastic zone as well as the cavity pressure was slightly more unfavorable in drained than in undrained conditions. Compared to the analytical investigation (Section 4.7) where a reduction in the soil friction angle resulted in the largest plastic zone, in both the drained and undrained numerical investigation, utilising the HS model, the cohesion, the reference secant modulus and the reference oedometer modulus become more important. The relatively low extent of the plastic zone suggests, in agreement with the analytical results, that a gallery spacing of 50m, as proposed in the reference design (Verhoef et al., 2011), is sufficient for the tunnel stability and may be reduced as part of a design optimisation process. The preliminary three-dimensional Finite Element analysis showed that deformation of the Boom Clay around the tunnel gallery may increase significantly when accounting for the staged excavation process.

A Reliability Based Design framework has been set up so that model responses can be incorporated in a probabilistic way. In this way, the reliability of the response can be assessed and quantified along with the sensitivity to parameter uncertainties. The framework has been tested via the analytical model and used for the numerical model to assess the reliability. The repository, based upon the data input, has been shown to be feasible for stability, with a plastic radius lower than required for stability in all cases. A sensitivity analysis has been undertaken, revealing that the tunnel performance may be more sensitive to the shear strength parameters or to the stiffness parameters, depending on the variance and covariance of the model parameters.

Prior to major firm conclusions on the feasibility of a specific repository design, significantly

more geomechanical data would be required. Moreover, the impact of creep and material anisotropy should be assessed, as should the geomechanical performance of tunnel/gallery crossings, and the behaviour and impact on safety of the excavated disturbed/damaged zones should be understood.

9.4. Recommendations

Further to this study, to better assess the feasibility of a radioactive waste repository in the Netherlands, the following recommendations are made:

- ○ Data collection
    - ↪ More material data at the repository depth should be collected.
    - ↪ Data on a variety of stress paths are needed to better test material models.
    - ↪ Data regarding anisotropy and creep behaviour should be collected.
    - ↪ Data regarding the cross-correlation of material parameters would be useful.
    - ↪ More data on the thermal behaviour of Boom Clay is required.
    - ↪ More data on the thermo-hydro-mechanical behaviour of Boom Clay is required.
- ○ Modelling
    - ↪ Develop the analytical model to include stress anisotropy.
    - ↪ Develop numerical material models that include anisotropy and creep, in addition to the features found in the Hardening Soil model.
    - ↪ Consider utilising models those include small strain behaviour e.g. (Benz, 2006; Plaxis, 2013a).
    - ↪ Analyse the impact of tunnel crossings and plugs.
    - ↪ Account for uncertainties other that in the soil property values - e.g. in situ conditions (vertical stress, pore water pressure, K_0, OCR), boundary conditions (concrete liner tolerance, thermal loading, construction sequence), local heterogeneity of the THMC soil property values and concrete property values (stiffness, strength, degradation).
    - ↪ Analyse other (coupled) processes, e.g. thermo-hydro-mechanical and chemical processes in the near-field.
- ○ Reliability framework
    - ↪ Incorporation and testing of other reliability techniques, e.g. directional or importance sampling schemes.

↪ Extend the model to assess the system reliability, e.g. the stability of multiple tunnels and gallery crossings, transient coupling of uncertainties for different processes at different stages in the repository life time (see Figure 1.5) and multiple failure modes.

○ Feasibility

↪ Assess the design in terms of constructability, safety functions and retrievability, e.g. dead-end and curved galleries are more difficult and costly to construct.

↪ Include the construction process - e.g. construction sequence of primary, secondary and dead-end disposal galleries, construction methods, excavation velocity and sequence, constructibility of curved part of the primary gallery and tunnel crossings, construction safety and ventilation.

↪ Incorporate non-geomechanical processes in the reliability framework e.g. limited tunnel distance in case of leakage during construction, uncertainty in the Super-container and concrete material for the case of retrieval, and uncertainty in waste quantities to modify the repository layout.

↪ Include the whole risk profile - combining failure probabilities, vulnerabilities and consequence, in order to compute technical, financial and societal risks.

References

Abbas, S. (2014). Structural and Durability Performance of Precast Segmental Tunnel Linings. PhD thesis. London, Canada: The University of Western Ontario.

Abdo, T. and R. Rackwitz (1991). A New Beta-Point Algorithm for Large Time-Invariant and Time-Variant Reliability Problems. In: *Reliability and Optimization of Structural Systems '90*. Ed. by A. Der Kiureghian and P. Thoft-Christensen. Vol. 61. Lecture Notes in Engineering Volume. Berlin Heidelberg: Springer-Verlag, pp. 285–309.

Abousleiman, Y. and L. Cui (1998). Poroelastic solutions in transversely isotropic media for wellbore and cylinder. In: *International Journal of Solids and Structures* 35 (34–35), 4905–4929.

Abuel-Naga, H., D. Bergado, A. Bouazza and G. Ramana (2007). Volume change behaviour of saturated clays under drained heating conditions: experimental results and constitutive modeling. In: *Canadian Geotechnical Journal* 44 (8), 942–956.

Adrichem van Boogaert, A. H. and W. F. P. Kouwe (1993–1997). *Stratigraphic nomenclature of The Netherlands; revision and update by RGD and NOPEGA*. Haarlem, the Netherlands: Rijks Geologische Dienst.

Aertsens, M., I. Wemaere and L. Wouters (2004). Spatial variability of transport parameters in the Boom Clay. In: *Applied Clay Science* 26 (1–4), 37–45.

Aertsens, M., A. Dierckx, M. Put, H. Moors, K. Janssen, L. Van Ravestyn, M. Van Gompel and P. De Canniére (2005). *Determination of the hydraulic conductivity, the product ηR of the porosity η and the retardation factor R, and the apparent diffusion coefficient Dp on Boom Clay cores from the Mol-1 drilling, Report R-3503*. Mol, Belgium: SCK·CEN.

Aertsens, M., P. De Cannière, K. Lemmens, N. Maes and H. Moors (2008a). Overview and consistency of migration experiments in clay. In: *Physics and Chemistry of the Earth, Parts A/B/C, MIGRATION 2007, 11th International Conference on the Chemistry and Migration Behaviour of Actinides and Fission Products in the Geosphere* 33 (14–16), 1019–1025.

Aertsens, M., M. Van Gompel, P. De Cannière, N. Maes and A. Dierckx (2008b). Vertical distribution of H^{14}CO$_3^-$ transport parameters in Boom Clay in the Mol-1 borehole. In: *Physics and Chemistry of the Earth, Parts A/B/C, Clays in Natural & Engineered Barriers for Radioactive Waste Confinement* 33 (Supplement 1), S61–S66.

Aertsens, M., N. Maes, L. van Ravestyn and S. Brassinnes (2013a). Overview of radionuclide migration experiments in the HADES Underground Research Facility at Mol (Belgium). In: *Clay Minerals* 48 (2), 153–166.

Aertsens, M., N. Maes, S. Labat, M. Van Gompel and T. Maes (2013b). Vertical Distribution of HTO and ^{125}I$^-$ Transport Parameters in Boom Clay in the Essen-1 Borehole. In: *Physics and Chemistry of the Earth, Parts A/B/C, Clays in Natural & Engineered Barriers for Radioactive Waste Confinement* 65, 90–97.

Al-Mukhtar, M., N. Belanteur, D. Tessier and S. K. Vanapalli (1996). The fabric of a clay soil under controlled mechanical and hydraulic stress states. In: *Applied Clay Science* 11 (2–4), 99–115.

Alejano, L. R., A. Rodríguez-Dono and M. Veiga (2012). Plastic radii and longitudinal deformation profiles of tunnels excavated in strain-softening rock masses. In: *Tunnelling and Underground Space Technology* 30, 169–182.

Alonso, E., L. R. Alejano, F. Varas, G. Fdez-Manín and C. Carranza-Torres (2003). Ground response curves for rock masses exhibiting strain-softening behaviour. In: *International Journal for Numerical and Analytical Methods in Geomechanics* 27 (13), 1153–1185.

Alonso, E. E., J. Alcoverro, F. Coste, L. Malinsky, V. Merrien-Soukatchoff, I. Kadiri, T. Nowak, H. Shao, T. S. Nguyen, A. P. S. Selvadurai, G. Armand, S. R. Sobolik, M. Itamura, C. M. Stone, S. W. Webb, A. Rejeb, M. Tijani, Z. Maouche, A. Kobayashi, H. Kurikami, A. Ito, Y. Sugita, M. Chijimatsu, L. Börgesson, J. Hernelind, J. Rutqvist, C.-F. Tsang and P. Jussila (2005). The FEBEX benchmark test: case definition and comparison of modelling approaches. In: *International Journal of Rock Mechanics & Mining Sciences* 42 (5–6), 611–638.

ANDRA (Dec. 2005a). *Dossier 2005 Argile − Synhtesis, Evaluation of the feasibility of a geological repository in an argillaceous formation, Meuse/Haute-Marne site*. Agence nationale pour la gestion des déchets radioactifs. URL: http://www.andra.fr/international/download/andra-international-en/document/editions/266va.pdf.

— (Dec. 2005b). *Dossier 2005 Argile − Tome, Architecture and management of a geological repository*. Agence nationale pour la gestion des déchets radioactifs. URL: http://www.andra.fr/international/download/andra-international-en/document/editions/268va.pdf.

— (Dec. 2005c). *Dossier 2005 Argile − Tome, Phenomenological evolution of a geological repository*. Agence nationale pour la gestion des déchets radioactifs. URL: http://www.andra.fr/international/download/andra-international-en/document/editions/269va.pdf.

— (Dec. 2005d). *Dossier 2005 Argile − Tome, Safety evaluation of a geological repository*. Agence nationale pour la gestion des déchets radioactifs. URL: http://www.andra.fr/international/download/andra-international-en/document/editions/270va.pdf.

Ang, A. H.-S. and W. H. Tang (1975). *Probability Concepts in Engineering Design*. Vol. 1: Basic Principles. New York, US: Wiley.

— (1984). *Probability Concepts in Engineering Design*. Vol. 2: Decision, Risk and Reliability. New York, US: Wiley.

Armand, G., F. Leveau, C. Nussbaum, R. de La Vaissiere, A. Noiret, D. Jaeggi, P. Landrein and C. Righini (2013). Geometry and Properties of the Excavation-Induced Fractures at the Meuse/Haute-Marne URL Drifts. In: *Rock Mechanics and Rock Engineering* 47 (1), 21–41.

Arson, C. and B. Gatmiri (2008). On damage modelling in unsaturated clay rocks. In: *Physics and Chemistry of the Earth, Parts A/B/C, Clays in Natural & Engineered Barriers for Radioactive Waste Confinement* 33 (Supplement 1), S407–S415.

Atkinson, J. (2007). Peak strength of overconsolidated clays. In: *Géotechnique* 7 (2), 127–135.

Baecher, G. B. and J. T. Christian (2003). *Reliability and Statistics in Geotechnical Engineering*. John Wiley & Sons, Ltd.

Baekelandt, L., D. Brosemer, P. De Preter, P. Raimbault, E. Biurrun, A. Lommerzheim, H. Codée, R. van Kleef, B. Hageman, J. Alonso, A. Rodriguez Beceiro, J. Santiago, P. De Gelder, I. Servaes, J.P. Samain, H. Vreys, P. Stallaert, P. De Grauwe, P. Bogorinski, U. Oppermann, H. Selling, M. C. Ruiz López, A. Jimenez and F. Rodriguez Arévalo (1996). *Building the Safety Case for a hypothetical underground repository in clay*. EC Contract ETNU-CT93-0102, Final report.

Baker, J. and E. Calle (2006). *JCSS Probabilistic Model Code, Section 3.7: Soil Properties*. Zürich, Switzerland: Joint Committee on Structural Safety.

Baldi, G., M. Borsetto and T. Hueckel (1987). *Calibration of mathematical models for simulation of thermal, seepage and mechanical behaviour of Boom clay, Report EUR-10924*. Luxembourg: Commission of the European Comunity.

Baldi, G., T. Hueckel and R. Pellegrini (1988). Thermal volume changes of the mineralwater system in low-porosity clay soils. In: *Canadian Geotechnical Journal* 25 (4), 807–825. URL: http://duke.edu/~hueckel/papers/baldihueckel88.pdf.

Baldi, G., T. Hueckel, A. Peano and R. Pellegrini (1991a). *Developments in modelling of thermo-hydro-geomechanical behaviour of Boom clay and clay-based buffer materials (Volume 1), Final report, Report EUR-13365/1*. Luxenbourg: Commission of the European Comunity. URL: http://bookshop.europa.eu/en/developments-in-modelling-of-thermo-hydro-geomechanical-behaviour-of-boom-clay-and-clay-based-buffer-materials-pbCDNA13365/downloads/CD-NA-13-365-EN-C/CDNA13365ENC_001.pdf;pgid=y8dIS7GUWMdSR0EAlMEUUsWb00003e2dDIWR;sid=_xqLHdau-ROLGoecj-YVurSL-MmNznRtg0o=?FileName=CDNA13365ENC_001.pdf&SKU=CDNA13365ENC_PDF&CatalogueNumber=CD-NA-13-365-EN-C.

— (1991b). *Developments in modelling of thermo-hydro-geomechanical behaviour of Boom clay and clay-based buffer materials (Volume 2), Final report, Report EUR-13365/2*. Luxenbourg: Commission of the European Comunity. URL: http://bookshop.europa.eu/en/developments-in-modelling-of-thermo-hydro-geomechanical-behaviour-of-boom-clay-and-clay-based-buffer-materials-pbCDNB13365/downloads/CD-NB-13-365-EN-C/CDNB13365ENC_001.pdf?FileName=CDNB13365ENC_001.pdf&SKU=CDNB13365ENC_PDF&CatalogueNumber=CD-NB-13-365-EN-C.

Barden, L. (1963). Stresses and Displacements in a Cross-Anisotropic Soil. In: *Géotechnique* 13 (3), 198–210.

Barnichon, J.-D. and G. Volckaert (2003). Observations and predictions of hydromechanical coupling effects in the Boom clay, Mol Underground Research Laboratory, Belgium. In: *Hydrogeology Journal* 11 (1), 193–202.

Barnichon, J. D., B. Neerdael, J. Grupa and A. Vervoort (Jan. 2000). *CORA Project TRUCK-II*. Mol, Belgium: Waste & Disposal Department SCK·CEN. URL: http://www.covra.nl/cms-file/get/iFileId/2477.

Bastiaens, W., F. Bernier, M. Buyens, M. Demarche, X. L. Li, J.-M. Linotte and J. Verstricht (Dec. 2003). *The extension of the HADES underground research facility at Mol, Belgium - The Connecting Gallery*. EIG EURODICE.

Bastiaens, W., F. Bernier and X. L. Li (May 2006). An overview of long-term HM measurements around HADES URF. In: *EUROCK 2006, Multiphysics coupling and long term behaviour in rock mechanics*. Liège, Belgium: Balkema, pp. 15–26.

— (2007). SELFRAC: Experiments and conclusions on fracturing, self-healing and self-sealing processes in clays. In: *Physics and Chemistry of the Earth, Parts A/B/C, Clay in natural and engineered barriers for radioactive waste confinement - Part 2* 32 (8–14), 600–615.

Baudet, B. and S. Stallebrass (2004). A constitutive model for structured clays. In: *Géotechnique* 54 (4), 269–278.

Bauer, J. and W. Puła (2000). Reliability with respect to settlement limit-states of shallow foundations on linearly-deformable subsoil. In: *Computers and Geotechnics* 26 (3–4), 281–308.

Beaufays, R., W. Blommaert, J. Bronders, P. De Canniére, P. del Marmol, P. Henrion, M. Monsecour, J. Patyn and M. Put (1994). *Characterization of the Boom clay and its multilayered hydrogeological environment, Final report, Report EUR 14961 EN*. Luxenbourg: Commission of the European Comunity. URL: http://bookshop.europa.eu/en/characterization-of-the-boom-clay-and-its-multilayered-hydrogeological-environment-pbCDNA14961/downloads/CD-NA-14-961-EN-C/CDNA14961ENC_001.pdf?FileName=CDNA14961ENC_001.pdf&SKU=CDNA14961ENC_PDF&CatalogueNumber=CD-NA-14-961-EN-C.

Belanteur, N., S. Tacherifet and M. Pakzad (1997). Etude des comportements mécanique, thermo-mécanique et hydro-mécanique des argiles gonflantes et non gonflantes fortement compactées. In: *Revue française de géotechnique* 78, 31–50.

Benson, C. H. and M. M. Gribb (1997). Measuring Unsaturated Hydraulic Conductivity in the Laboratory and Field. In: *Unsaturated Soil Engineering Practice (GSP 68), ASCE*, pp. 113–168.

Benz, T. (2006). Small-Strain Stiffness of Soils and its Numerical Consequences. PhD thesis. Stuttgart, Germany: Mitteilung 55, Institut für Geotechnik, Universität Stuttgart, Universität Stuttgart.

Bernier, F. and B. Neerdael (1996). Overview of in-situ thermomechanical experiments in clay: Concept, results and interpretation. In: *Engineering Geology* 41 (1–4), 51–64.

Bernier, F., G. Volckaert, E. Alonso and M. Villar (1997). Suction-controlled experiments on Boom clay. In: *Engineering Geology* 47 (4), 325–338.

Bernier, F., X. L. Li, J. Verstricht, J. D. Barnichon, W. Bastiaens, J. M. Palut, J. K. Ben Slimane, M. Ghoreychi, J. Gaombalet, F. Huertas, J. M. Galera, K. Merrien, F. J. Elorza and C. Davies (Dec. 2007a). *CLay Instrumentation Programme for the EXtension of an underground research laboratory, CLIPEX - Final Report*. EURODICE.

Bernier, F., X. L. Li, W. Bastiaens, L. Ortiz, M. Van Geet, L. Wouters, B.Frieg, P. Blümling, J. Desrues, G. Viaggiani, C. Coll, S. Chanchole, V. De Greef, R. Hamza, L. Malinsky A. Vervoort, Y. Vanbrabant, B. Debecker, J. Verstraelen, A. Govaerts, M. Wevers, V. Labiouse, S. Escoffier, J. F. Mathier, L. Gastaldo and C. Bühler (Dec. 2007b). *Fractures and self-healing within the excavated damaged zone in clays. SELFRAC - Final report*. European Commission nuclear science and technology. URL: `ftp://ftp.cordis.europa.eu/pub/fp5-euratom/docs/selfrac_projrep_en.pdf`.

Bernier, F., X.-L. Li and W. Bastiaens (2007c). Twenty-five years geotechnical observation and testing in the Tertiary Boom Clay formation. In: *Géotechnique* 57 (2), 229–237.

Bésuelle, P., G. Viggiani, J. Desrues, C. Coll and P. Charrier (2013). A Laboratory Experimental Study of the Hydromechanical Behavior of Boom Clay. In: *Rock Mechanics and Rock Engineering* 47 (1), 143–155.

Birchall, J. T. (2013). Energy-based models for the design of cavities located in creeping media. PhD thesis. Durham, UK: Durham University.

Birkholzer, J., J. Houseworth and C.-F. Tsang (2012). Geologic Disposal of High-Level Radioactive Waste: Status, Key Issues, and Trends. In: *Annual Review of Environment and Resources* 37, 79–106.

Blümling, P., F. Bernier, P. Lebon and C. D. Martin (2007). The excavation damaged zone in clay formations time-dependent behaviour and influence on performance assessment. In: *Physics and Chemistry of the Earth, Parts A/B/C, Clay in natural and engineered barriers for radioactive waste confinement - Part 2* 32 (8–14), 588–599.

Bobet, A. (2003). Effect of pore water pressure on tunnel support during static and seismic loading. In: *Tunnelling and Underground Space Technology* 18 (4), 377–393.

— (2010). Characteristic Curves for Deep Circular Tunnels in Poroplastic Rock. In: *Rock Mechanics and Rock Engineering* 43 (2), 185–200.

Bobet, A. and S. W. Nam (2007). Stresses around Pressure Tunnels with Semi-permeable Liners. In: *Rock Mechanics and Geotechnical Engineering* 40 (3), 287–315.

Bock, H., B. Dehandschutter, C. D. Martin, M. Mazurek, A. de Haller, F. Skoczylas and C. Davy (2010). *Self-sealing of Fractures in Argillaceous Formations in the Context of Geological Disposal of Radioactive Waste - Review and Synthesis, No. 6148*. OECD Nuclear Energy Agency (NEA). URL: `http://www.oecd-nea.org/rwm/reports/2010/nea6184-self-sealing.pdf`.

Boisson, J.-Y. (2005). *Clay Club Catalogue of Characteristics of Argillaceous Rocks*. OECD Nuclear Energy Agency (NEA), No. 4436. URL: `http://www.oecd-nea.org/rwm/reports/2005/nea4436-argillaceous-catalogue.pdf`.

Bolzon, G. and B. A. Schrefler (2005). Thermal effects in partially saturated soils: a constitutive model. In: *International Journal for Numerical and Analytical Methods in Geomechanics* 29 (9), 861–877.

Bond, A. (2011). A procedure for determining the characteristic value of a geotechnical parameter. In: *Proceedings of the Third International Symposium on Geotechnical Safety and Risk (ISGSR)*. Ed. by N. Vogt, B. Schuppener, D. Straub and G. Bräu. Munich, Germany, pp. 419–426.

Bond, A. and A. Harris (2008). *Decoding Eurocode 7*. London - New York: Taylor & Francis Group.

Bossart, P. (2012). *Characteristics of the Opalinus Clay at Mont Terri*. Mont Terri Project. URL: http://www.mont-terri.ch/internet/mont-terri/de/home/geology/key_characteristics.parsys.49924.DownloadFile.tmp/characteristicsofopa.pdf.

Bossart, P. and M. Thury (2007). Research in the Mont Terri Rock laboratory: Quo vadis? In: *Physics and Chemistry of the Earth, Parts A/B/C, Clay in natural and engineered barriers for radioactive waste confinement - Part 1* 32 (1–7), 19–31.

Bouazza, A., W. F. Van Impe and W. Haegeman (1996). Some mechanical properties of reconstituted Boom clay. In: *Geotechnical & Geological Engineering* 14 (4), 341–352.

Brady, B. H. G. and E. T. Brown (2006). *Rock Mechanics for underground mining*. 3rd ed. Dordrecht, NL: Springer.

Breitung, K. (1984). Asymptotic approximations for multivariate integrals. In: *Journal of Engineering Mechanics Division, ASCE* 110 (3), 357–366.

Bremmer, C. N., H. J. Simmelink, A. H. Heidema, A. Hoogendoorn and H. J. M. Pagnier (June 1996). *Kartering slecht-doorlatende laagpakketten van Tertiaire Formaties - CAR I rapport*. Heerlen, the Netherlands: Rijks Geologische Dienst. URL: http://www.covra.nl/cms-file/get/iFileId/2508.

Brinkgreve, R. B. J. (2011). *Behaviour of Soils and Rocks*. Lecture notes (CIE 4361), Delft University of Technology, Delft, The Netherlands.

— (2014). *Personal communication*. Delft University of Technology, Delft, The Netherlands.

Broek, W. M. G. T. van den, M. J. V. Menken, H. C. Heilbron J. P. A. Roest, D. G. M. van Oers and H. H. Meijer (1993). *Final report retrievability of radioactive waste, Final report OPLA project MIJBO-1A / 54595*. Delft University of Technology.

Brown, E. T., J. W. Bray, B. Ladanyi and H. Evert (1983). Ground Response Curves for Rock Tunnels. In: *Journal of Geotechnical Engineering* 109 (1), 15–39.

Bruggeman, C. and M. De Craen (June 2011). *Boom Clay natural organic matter - Status Report 2011, External Report ER-206*. Mol, Belgium: SCK·CEN. URL: http://publications.sckcen.be/dspace/bitstream/10038/7888/1/er_206.pdf.

BS EN 1990 (2002). *Eurocode 0: Basis of structural design*. Comité Européen de Normalisation (CEN), Brussels, Belgium, British Standards Institution (BSI), London, UK.

BS EN 1997-1 (2004). *Eurocode 7: Geotechnical design − Part 1: General rules*. Comité Européen de Normalisation (CEN), Brussels, Belgium, British Standards Institution (BSI), London, UK.

BTS/ICE (2004). *Tunnel lining design guide*. Thomas Telford Limited: The British Tunnelling Society and The Institution of Civil Engineers.

Bui, T. A., F. Deleruyelle, H. Wong, N. Dufour and C. Leo (2013). Analytical approach to the creep and hydromechanical couplings around underground cavities. In: *Proceedings of the fith Biot conference on Poromechanics*. Vienna, Austria, pp. 1289–1298.

Burghignoli, A., A. Desideri and S. Miliziano (2000). A laboratory study on the thermomechanical behaviour of clayey soils. In: *Canadian Geotechnical Journal* 37 (4), 764–780.

Burland, B., S. Rampello, V. N. Georgiannou and G. Calabresi (1996). A laboratory study of the strength of four stiff clays. In: *Géotechnique* 46 (3), 491–514.

Burland, J. B. (1989). Ninth Laurits Bjerrum Memorial Lecture: "Small is beautiful" − the stiffness of soils at small strains. In: *Canadian Geotechnical Journal* 26 (4), 499–510.

Burland, J. B. (1990). On the compressibility and shear strength of natural clays. In: *Géotechnique* 40 (3), 329–378.

C.-F. Tsang (Ed.) (2007). Special Issue: The Decovalex-THMC Project (Safety assessment of nuclear waste repositories), 21 articles. In: *Environmental Geology* 57 (6), 1217–1390.

Carranza-Torres, C. (2004). Elasto-plastic solution of tunnel problems using the generalized form of the Hoek-Brown failure criterion. In: *International Journal of Rock Mechanics and Mining Sciences − Proceedings of the ISRM SINOROCK 2004 Symposium* 41 (Supplement 1), 629–639.

Carranza-Torres, C. and J. Zhao (2009). Analytical and numerical study of the effect of water pressure on the mechanical response of cylindrical lined tunnels in elastic and elasto-plastic porous media. In: *International Journal of Rock Mechanics and Mining Sciences* 46 (3), 531–547.

Carranza-Torres, C., B. Rysdahl and M. Kasim (2013). On the elastic analysis of a circular lined tunnel considering the delayed installation of the support. In: *International Journal of Rock Mechanics and Mining Sciences* 61, 57–85.

Carranza-Torresa, C. and C. Fairhurst (1999). The elasto-plastic response of underground excavations in rock masses that satisfy the Hoek-Brown failure criterion. In: *International Journal of Rock Mechanics and Mining Sciences* 36 (6), 777–809.

— (2000). Application of the Convergence-Confinement method of tunnel design to rock masses that satisfy the Hoek-Brown failure criterion. In: *Tunnelling and Underground Space Technology* 15 (2), 187–213.

Carsel, R. F. and R. S. Parrish (1988). Developing Joint Probability Distributions of Soil Water Retention Characteristics. In: *Water Resources Research* 24 (5), 755–769.

Cekerevac, C. and L. Laloui (2004). Experimental study of thermal effects on the mechanical behaviour of a clay. In: *International Journal for Numerical and Analytical Methods in Geomechanics* 28 (3), 209–228.

Chalindar, S., R. Charlier, F. Collin, A. Dizier, B. François, J. Fokkens, B. Garitte, A. Gens, C. Guangjing, J. Hart, L. Laloui and X. Sillen (2010). *Deliverable D13 - Annex 4, In situ heating test ATLAS in Mol*. Thermal Impact on the Damaged Zone Around a Radioactive Waste Disposal in Clay Host Rocks (TIMODAZ). URL: http://www.timodaz.eu/deliverables.aspx?dwnld=D13Annex4Atlasvf.doc&itemid=74104daf-0aa4-45e5-bf8e-29093e13c303&id=WP5.2.

Chan, C. L. and B. K. Low (2012). Practical second-order reliability analysis applied to foundation engineering. In: *nternational Journal for Numerical and Analytical Methods in Geomechanics* 36 (11), 1387–1409.

Chandler, R. J. (2000). The Third Glossop Lecture − Clay sediments in depositional basins: The geotechnical cycle. In: *Quarterly Journal of Engineering Geology and Hydrogeology* 33, 7–39.

— (2010). Stiff sedimentary clays: geological origins and engineering properties. In: *Géotechnique* 60 (12), 891–902.

Charlier, R. (1987). Approche unifiée de quelques problèmes non linéaires de mécanique des milieux continus par la méthode des éléments finis. PhD thesis. Liège, France: Université de Liège.

Charlier, R., R. Chambon, X.-L. Li, A. Dizier, Y. Sieffert, F. Collin and S. Levasseur (2008). TIMODAZ − Modelling the Excavated Damage Zone around an underground gallery - Coupling mechanical, thermal and hydraulical aspects. In: 7th *European Commission Conference on the Management and Disposal of Radioactive Waste (Euradwaste '08), Community Policy and Research & Training Activities*. Luxembourg, pp. 441–445. URL: ec.europa.eu/research/energy/pdf/euradwaste_08.pdf.

Charlier, R., R. Chambon, F. Collin, A. A. Dizier, B. François, B. Garitte, A. Gens, C. Guangjing, L. Laloui, F. Marinelli and Y. Sieffert (2010a). *Deliverable D13 - Annex 1, Hollow cylinder test in Boom Clay*. Thermal Impact on the Damaged Zone Around a Radioactive Waste Disposal in Clay

Host Rocks (TIMODAZ). URL: http://www.timodaz.eu/deliverables.aspx?dwnld=D13An nex1HollowCylindersBCvf.doc&itemid=74104daf-0aa4-45e5-bf8e-29093e13c303&id=W P5.2.

Charlier, R., F. Collin, A. Dizier, S. Fauriel, A. Gens, C. Guangjing, L. Laloui, T. Meynet, F. Pascon, J.-P. Radu, P. Van Marcke and J. Vaunat (2010b). *Deliverable D13 - Annex 6, Large scale excavation and heater in-situ experiment: the PRACLAY experiment modelling.* Thermal Impact on the Damaged Zone Around a Radioactive Waste Disposal in Clay Host Rocks (TIMODAZ). URL: http:// www.timodaz.eu/deliverables.aspx?dwnld=D13Annex6Praclayvf.pdf&itemid=74104daf -0aa4-45e5-bf8e-29093e13c303&id=WP5.2.

Chen, G. J., X. Sillen, J. Verstricht and X. L. Li (2011). ATLAS III in situ heating test in Boom clay: Field data, observation and interpretation. In: *Computers and Geotechnics* 38 (5), 683–696.

Chen, G. J., T. Maes, F. Vandervoort, X. Sillen, P. Van Marcke, M. Honty, M. Dierick and P. Vanderniepen (2012a). Thermal Impact on Damaged Boom Clay and Opalinus Clay: Permeameter and Isostatic Tests with μCT Scanning. In: *Rock Mechanics and Rock Engineering* 47 (1), 87–99.

Chen, S. L. and Y. N. Abousleiman (2012). Exact undrained elasto-plastic solution for cylindrical cavity expansion in modified Cam Clay soil. In: *Géotechnique* 62 (5), 447–456.

— (2013). Exact drained solution for cylindrical cavity expansion in modified Cam Clay soil. In: *Géotechnique* 63 (6), 510–517.

Chen, S. L., Y. N. Abousleiman and K. K. Muraleetharan (2012b). Closed-Form Elastoplastic Solution for the Wellbore Problem in Strain Hardening/Softening Rock Formations. In: *International Journal of Geomechanics* 12 (4), 494–507.

Chen, W., X. L. Li and H. D. Yu (in press, 2015). *Hydro-mechanical Coupled Creep Behaviour of Boom Clay: Numerical Investigations and 30 Years In Situ Measurements.* CRC Press.

Cheng, Y. M. (2012). Modified Kastner Formula for Cylindrical Cavity Contraction in MohrÂηCoulomb Medium for Circular Tunnel in Isotropic Medium. In: *Journal of Mechanics* 28 (1), 163–169.

Cherubini, C. (1997). Data and considerations on the variability of geotechnical properties of soil. In: *Proceedings of the International Conference on Safety and Reliability (ESREL) 97*. Lisbon, Portugal, pp. 1583–1591.

— (2000). Reliability evaluation of shallow foundation bearing capacity on $c' - \varphi'$ soils. In: *Canadian Geotechnical Journal* 37 (1), 264–269.

Christian, J. T. and G. B. Baecher (2011). Unresolved Problems in Geotechnical Risk and Reliability. In: Proceedings of GeoRisk 2011: Geotechnical Risk Assessment and Management, *Geotechnical Special Publications (GSP) 224, ASCE*. Ed. by C. H. Juang, K.-K. Phoon, A. J. Puppala, R. A. Green and G. A. Fenton. Atlanta, Georgia, US, pp. 50–63.

Clayton, C. R. I. (2011). Stiffness at small strain: research and practice. In: *Géotechnique* 61 (1), 5–37.

Clayton, C. R. I. and G. Heymann (2001). Stiffness of geomaterials at very small strains. In: *Géotechnique* 51 (3), 245–255.

Coll, C. (2005). Endommagement des Roches Argileuses et Perméabilité Induite au Voisinage D'ouvrage Souterrains. PhD thesis. Grenoble, France: Université Joseph Fourier Grenoble 1. URL: http:// tel.archives-ouvertes.fr/docs/00/04/84/31/PDF/tel-00010193.pdf.

Collin, F. (2003). Couplages thermo-hydro-mécaniques dans les sols et les roches tendres partiellement saturés. PhD thesis. Liège, France: Université de Liège.

Collin, F., X. L. Li, J. P. Radu and R. Charlier (2002). Thermo-hydro-mechanical coupling in clay barriers. In: *Engineering Geology* 64 (2–3), 179–193.

Collins, I. F. and J. R. Stimpson (1994). Similarity solutions for drained a undrained cavity expansions in soils. In: *Géotechnique* 44 (1), 21–34.

Coop, M. R., J. H. Atkinson and R. N. Taylor (1995). Strength, yielding, and stiffness in structured and unstructured soils. In: *11th European Conference on Soil Mechanics and Foundation Engineering*. 8, pp. 55–62.

CORA (Feb. 2001a). *Retrievable disposal of radioactive waste in The Netherlands - Summary*. The Hague, the Netherlands: Commission of Radioactive Waste Disposal. URL: http://www.covra.nl/cms-file/get/iFileId/2482.

— (Feb. 2001b). *Terugneembare berging, een begaanbaar pad? Onderzoek naar de mogelijkheden van terugneembare berging van radioactief afval in Nederland - Eindrapport*. The Hague, the Netherlands: Commission of Radioactive Waste Disposal. URL: http://www.covra.nl/cms-file/get/iFileId/2458.

Cotecchia, F. and R. J. Chandler (1997). The infuence of structure on the pre-failure behaviour of a natural clay. In: *Géotechnique* 47 (3), 523–544.

— (2000). A general framework for the mechanical behaviour of clays. In: *Géotechnique* 50 (4), 431–447.

Coussy, O. (2004). *Poromechanics*. John Wiley & Sons Ltd.

Craeye, B. (2010). Early-Age Thermo-Mechanical Behaviour of Concrete Supercontainers for Radwaste Disposal. PhD thesis. Gent, Belgium: Universiteit Gent.

Cui, Y.-J. and A. M. Tang (2013). On the chemo-thermo-hydro-mechanical behaviour of geological and engineered barriers. In: *Journal of Rock Mechanics and Geotechnical Engineering* 5 (3), 169–178.

Cui, Y. J., N. Sultan and P. Delage (2000). A thermomechanical model for clays. In: *Canadian Geotechnical Journal* 37 (3), 607–620.

Cui, Y.-J., T. T. Le, A-M. Tang, P. Delage and X.-L. Li (2009). Investigating the time-dependent behaviour of Boom clay under thermo-mechanical loading. In: *Géotechnique* 59 (4), 319–329.

Davies, C. and F. Bernier (2005). Impact of the excavation disturbed or damaged zone (EDZ) on the performance of radioactive waste geological repositories, Proceedings o a European Commission Cluster Conference and Workshop. In: *European Commission nuclear science and technology*. Luxembourg. URL: http://bookshop.europa.eu/en/impact-of-the-excavation-disturbed-or-damaged-zone-edz-on-the-performance-of-radioactive-waste-geological-repositories-pbKINA21028/.

Davis, R. O. and A. P. S. Selvadurai (2002). *Plasiticy and Geomechanics*. Cambridge University Press.

De Bruyn, D. and S. Labat (2002). The second phase of ATLAS: the continuation of a running THM test in the HADES underground research facility at Mol. In: *Engineering Geology* 64 (2–3), 309–316.

De Bruyn, D. and J.-F. Thimus (1996). The influence of temperature on mechanical characteristics of Boom clay: the results of an initial laboratory programme. In: *Engineering Geology* 41 (1–4), 117–126.

De Cannière, P., H. Moors, P. Lolivier, P. De Preter and M. Put (1996). *Laboratory and in situ migration experiments in the Boom clay, Final report, Report EUR 16927 EN*. Luxenbourg: Commission of the European Comunity. URL: http://bookshop.europa.eu/en/laboratory-and-in-situ-migration-experiments-in-the-boom-clay-pbCGNA16927/downloads/CG-NA-16-927-EN-C/CGNA16927ENC_001.pdf?FileName=CGNA16927ENC_001.pdf&SKU=CGNA16927ENC_PDF&CatalogueNumber=CG-NA-16-927-EN-C.

De Craen, M. (2005). *Geochemical characterisation of specific Boom Clay intervals, R-4080*. Mol, Belgium: SCK·CEN.

De Craen, M., D. Delleuze, G. Volckaert, A. Sneyers and M. Put (2000). *The Boom Clay as natural analogue, Final report to NIRAS/ONDRAF for the period 1997-1999, R-3444*. Mol, Belgium: SCK·CEN.

De Craen, M., L. Wang, M. Van Geet and H. Moors (2004). *Geochemistry of Boom Clay pore water at the Mol site, BLG-990*. Mol, Belgium: SCK·CEN. URL: http://www.sckcen.be/nl/content/download/16123/217784/file/Geochemistry\%20of\%20Boom\%20Clay\%20pore\%20-\%20Status\%202004.pdf.

De Craen, M., I. Wemaere, S. Labat and M. Van Geet (Nov. 2006). *Geochemical analyses of Boom Clay pore water and underlying aquifers in the Essen-1 borehole, External Report ER-19*. Mol, Belgium: SCK·CEN. URL: http://publications.sckcen.be/dspace/bitstream/10038/430/1/er_19.pdf.

De Craen, M., M. Van Geet, M. Honty, E. Weetjens and X. Sillen (2008). Extent of oxidation in Boom Clay as a result of excavation and ventilation of the HADES URF: Experimental and modelling assessments. In: *Physics and Chemistry of the Earth, Parts A/B/C, Clays in Natural & Engineered Barriers for Radioactive Waste Confinement* 33 (Supplement 1), S350–S362.

De Craen, M., M. Honty, M. Van Geet, E. Weetjens, X. Sillen and L. Wang (Nov. 2011). *Overview of the oxidation around galleries in Boom Clay (Mol, Belgium) − Status 2008, External Report ER-189*. Mol, Belgium: SCK·CEN. URL: http://publications.sckcen.be/dspace/bitstream/10038/7560/1/er_189.pdf.

Decleer, J., W. Viaene and N. Vandenberghe (1983). Relationships between chemical, physical and mineralogical characteristics of the Rupelian Boom Clay. In: *Clay Minerals* 18 (1), 1–10.

Dedecker, F. and D. Billaux (2010). *Deliverable D13 − Annex 3, Hollow cylinder tests on Opalinus Clay*. Thermal Impact on the Damaged Zone Around a Radioactive Waste Disposal in Clay Host Rocks (TIMODAZ). URL: http://www.timodaz.eu/deliverables.aspx?dwnld=D13Annex3HollowCylindersOPAvf.doc&itemid=74104daf-0aa4-45e5-bf8e-29093e13c303&id=WP5.2.

Dehandschutter, B., S. Vandycke, M. Sintubin, N. Vandenberghe, P. Gaviglio, J.-P. Sizun and L. Wouters (2004). Microfabric of fractured Boom Clay at depth: a case study of brittle-ductile transitional clay behaviour. In: *Applied Clay Science* 26 (1–4), 389–401.

Dehandschutter, B., S. Vandycke, M. Sintubin, N. Vandenberghe and L. Wouters (2005). Brittle fractures and ductile shear bands in argillaceous sediments: inferences from Oligocene Boom Clay (Belgium). In: *Journal of Structural Geology* 27 (5), 1095–1112.

Delage, P. (2010). *Deliverable 5: THM Characterisation and Input for Simulation*. Thermal Impact on the Damaged Zone Around a Radioactive Waste Disposal in Clay Host Rocks (TIMODAZ).

— (2013). On the thermal impact on the excavation damaged zone around deep radioactive waste disposal. In: *Journal of Rock Mechanics and Geotechnical Engineering* 5 (3), 179–190.

Delage, P., N. Sultan and Y. J. Cui (2000). On the thermal consolidation of Boom clay. In: *Canadian Geotechnical Journal* 37 (2), 343–354.

Delage, P., T.-T. Le, E.-M Tang, Y. J. Cui and X. L. Li (2007). Suction effects in deep Boom Clay block samples: Geotechnique symposium on stiff sedimentary clays - genesis and engineering behaviour. In: *Géotechnique* 57 (1), 239–244.

Delage, P., N. Sultan, Y.-J. Cui and X. L. Li (2009). Permeability changes in Boom clay with temperature. In: *International Conference and Workshop "Impact of Thermo-Hydro-Mechanical-Chemical (THMC) processes on the safety of underground radioactive waste repositories*. European Union, Luxembourg. URL: http://arxiv.org/pdf/1112.6396v1.

Delage, P., Y. J. Cui and A. M. Tang (2010). Clays in radioactive waste disposal. In: *Journal of Rock Mechanics and Geotechnical Engineering* 2 (2), 111–123.

Delay, J., P. L. Forbes and J. Roman (2008). The Meuse/Haute-Marne Underground Research Laboratory: Seven Years of Scientific Investigations. In: *Selected papers from the third international meeting on Clays in Natural & Engineered Barriers for Radioactive Waste Confinement*. Science and Technology Series 334. Lille, France: Andra, Chatenay-Malabry. URL: www.nantes2010.com/doc/pdf/lille/01_Delay.pdf.

Delécaut, G. (2004). The geochemical behaviour of uranium in the Boom clay. PhD thesis. Louvain, Belgium: Université catholique de Louvain. URL: http://dial.academielouvain.be/handle/boreal:5344?site_name=UCL.

Della Vecchia, G., C. Jommi, A. Lima and E. Romero (2010). Some remarks on the hydro-mechanical constitutive modelling of natural and compacted Boom clay. In: *Proceedings of the Fifth International Conference on Unsaturated Soils (UNSAT)*. Ed. by E. Alonso and A. Gens. 803–809. Barcelona, Spain.

Deng, Y. F., A. M. Tang, Y. J. Cui, X. P. Nguyen, X. L. Li and L. Wouters (2011a). Laboratory Hydro-mechanical Characterisation of Boom Clay at Essen and Mol. In: *Physics and Chemistry of the Earth, Parts A/B/C, Clays in Natural & Engineered Barriers for Radioactive Waste Confinement* 36 (17–18), 1878–1890.

Deng, Y.-F., A.-M. Tang, Y.-J. Cui and X.-L. Li (2011b). Study on the hydraulic conductivity of Boom clay. In: *Canadian Geotechnical Journal* 48 (10), 1461–1470.

Deng, Y. F., Y. J. Cui, A. M. Tang, X. L. Li and X. Sillen (2012). An experimental study on the secondary deformation of Boom clay. In: *Applied Clay Science* 59–60, 19–25.

Desbois, G., J. L. Urai and P. A. Kukla (2009). Morphology of the pore space in claystones – evidence from BIB/FIB ion beam sectioning and cryo-SEM observations. In: *eEarth* 4, 15–22. URL: www.electronic-earth.net/4/15/2009/ee-4-15-2009.pdf.

Desbois, G., J. L. Urai and M. De Craen (May 2010). *In-situ and direct characterization of porosity in Boom Clay (Mol site, Belgium) by using novel combination of ion beam cross-sectioning, SEM and cryogenic methods - Motivation first results and perspective, External Report ER-124*. Mol, Belgium: SCK·CEN. URL: http://publications.sckcen.be/dspace/bitstream/10038/7081/1/er_124.pdf.

Detournay, E. (1986). Elastoplastic Model of a Deep Tunnel for a Rock with Variable Dilatancy. In: *Rock Mechanics and Geotechnical Engineering* 108 (19), 99–108.

Detournay, E. and I. Vardoulakis (1985). Determination of the Ground Reaction Curve using the Hodograph Method. In: *International Journal of Rock Mechanics and Mining Sciences & Geomechanics Abstracts* 22 (3), 173–176.

Ditlevsen, O. and H. O. Madsen (2007). *Structural Reliability Methods*. 2nd ed. Chichester, UK: John Wiley & Sons Ltd.

Dizier, A. (2011). Caractérisation des effets de température dans la zone endommagée autour de tunnels de stockage de déchets nucléaires dans des roches argileuses (Thermal effect characterisation in the excavated damaged zone around tunnels for nuclear waste disposal in agilaceous rocks). PhD thesis. Liége, Belgium: Université de Liége. URL: http://orbi.ulg.ac.be/bitstream/2268/98834/1/These\%20ADIZIER.pdf.

Djeran, I., B. Bazargan, A. Giraud and G. Rousset (1994). *Etude expérimental du comportement Thermo-Hydro-Mecanique de l'argile de Boom. Rapport final, Report No. 94-002*. Mol, Belgium: SCK·CEN.

Djéran-Maigre, I., D. Tessier, D. Grunberger, B. Velde and G. Vasseur (1998). Evolution of microstructures and of macroscopic properties of some clays during experimental compaction. In: *Marine and Petroleum Geology* 15 (2), 109–128.

Drucker, D. C. and W. Prager (1952). Soil mechanics and plastic analysis for limit design. In: *Quarterly of Applied Mathematics* 10 (2), 157–165.

Dufour, N., C. J. Leo and F. Deleruyelle (2009). Hydromechanical responses of a decommissioned backfilled tunnel drilled into a poro-viscoelastic medium. In: *Soils and Foundations* 49 (4), 495–507.

Dufour, N., H. Wong, F. Deleruyelle and C. J. Leo (2012). Hydromechanical Postclosure Behavior of a Deep Tunnel Taking into Account a Simplified Life Cycle. In: *International Journal of Geomechanics* 12 (5), 549–559.

Duncan, J. M. and C.-Y. Chang (1970). Nonlinear analysis of stress and strain in soil. In: *Journal of the Soil Mechanics and Foundation Division (ASCE)* 96, 1629–1653.

Dutch Government (Apr. 1993). *Cabinet position on underground disposal (Kabinetsstandpunt over de vraag of de diepe ondergrond mag en kan worden gebruikt voor het opbergen van afval)*. NEPP-action 62.

El-Ramly, H., N. R. Morgenstern and D.M. Curden (2006). Lodalen slide: A probabilistic assessment. In: *Canadian Geotechnical Journal* 43 (9), 956–968.

Fahimifar, A. and M. R. Zareifard (2009). A theoretical solution for analysis of tunnels below groundwater considering the hydraulic-mechanical coupling. In: *Tunnelling and Underground Space Technology* 24 (6), 634–646.
— (2013). A new closed-form solution for analysis of unlined pressure tunnels under seepage forces. In: *International Journal for Numerical and Analytical Methods in Geomechanics* 37 (11), 1591–1613.

Fazio, A. Lembo and R. Ribacchi (1984). Influence of seepage on tunnel stability. In: *Design and Performance of Underground Excavations*. Ed. by E. T. Brown and J. A. Hudson. British Geotechnical Society, UK, pp. 173–181.

Fenton, G. A. and D. V. Griffiths (2008). *Risk assessment in geotechnical engineering*. New York: John Wiley & Sons, Inc.

Fernández, G. (1994). Behavior of pressure tunnels and guidelines for liner design. In: *Journal of Geotechnical Engineering* 120 (10), 1768–1791.

Fernández, G. and T. Alvarez (1994). Seepage-induced effective stresses and water pressures around pressure tunnels. In: *Journal of Geotechnical Engineering* 120 (1), 108–128.

FHWA (Dec. 2009). *Technical Manual for Design and Construction of Road Tunnels – Civil Elements, Publication No. FHWA-NHI-10-034*. Washington, US: U.S. Department of Transportation Federal Highway Administration.

FORGE (2010). *Review of Boom Clay and Opalinus Clay parameters, Report D4.6 - VER 1.0*. Euratom 7th Framework Programme Project: FORGE. URL: www.bgs.ac.uk/forge/docs/reports/D4.6.pdf.

François, B. (2008). Thermo-Plasticity of Fine-Grained Soils at Variou Saturation States: Application to Nuclear Waste Disposal. PhD thesis. École Polytechnique Fédérale de Lausanne.

François, B., L. Laloui and C. Laurent (2009). Thermo-hydro-mechanical simulation of ATLAS in situ large scale test in Boom Clay. In: *Computers and Geotechnics* 36 (4), 626–640.

François, B., F. Collin, A. Dizier and R. Charlier (Apr. 2011). An extended Drucker-Prager hardening model for cross-anisotropy of soft rocks. In: *Proceedings of the 2nd international Symposium on Computational Geomechanics (COMGEO II)*. Ed. by S. Pietruszczak and G. N. Pande. Cavtat-Dubrovnik, Croatia, pp. 142–152.

François, B., V. Labiouse A. Dizier, F. Marinelli, R. Charlier and F. Collin (2013). Hollow Cylinder Tests on Boom Clay: Modelling of Strain Localization in the Anisotropic Excavation Damaged Zone. In: *Rock Mechanics and Rock Engineering* 47 (1), 71–86. DOI: 10.1007/s00603-012-0348-5.

Fredlund, D. G. and A. E. Dahlman (1971). Geotechnical Properties of Glacial Sediments. In: *Proceedings of the 1st International Conference on Applications of Statistics and Probability in Soil and Structural Engineering*. Hong Kong, pp. 204–228.

Garitte, B., A. Gens, J. Vaunat and G. Armand (2012). Thermal Conductivity of Argillaceous Rocks: Determination Methodology Using In Situ Heating Tests. In: *Rock Mechanics and Rock Engineering* 47 (1), 111–129.

Gasparre, A., S. Nishimura, N. A. Minh, R. J. Jardine and M. R. Coop (2007). The stiffness of natural London Clay. In: *Geotechénique* 57 (1), 33–47.

Gedeon, M., I. Wemaere and S. Labat (2011). Characterization of groundwater flow in the environment of the Boom Clay formation. In: *Physics and Chemistry of the Earth, Parts A/B/C, Clays in Natural & Engineered Barriers for Radioactive Waste Confinement* 36 (17–18), 1486–1495.

Gens, A. (2011). On the hydromechanical behaviour of argillaceous hard soils−weak rocks (Keynote Lecture). In: *Geotechnics of Hard Soils − Weak Rocks, Proceedings of the 15th European Conference on Soil Mechanics and Geotechnical Engineering*. Ed. by A. Anagnostopoulos, M. Pachakis and Ch. Tsatsanifos. Vol. 4, pp. 71–118.

— (Feb. 2012). Geomechanics of argillaceous rocks for nuclear waste disposal. In: *Presentation at the International Post - TIMODAZ Workshop*. Mont Terri rock laboratory, Saint-Ursanne, Switzerland. URL: http://www.argenco.ulg.ac.be/timodaz/pdf/session\%201/S1-L1-Gens.pdf.

Gens, A. and D. M. Potts (1988). Critical state models in computational geomechanics. In: *Engineering Computations* 5 (3), 178–197.

Gens, A., J. Vaunat, B. Garitte and Y. Wileveau (2007). In situ behaviour of a stiff layered clay subject to thermal loading: observations and interpretation. In: *Géotechnique* 57 (2), 207–228.

Gens, A., M. Sánchez, L. Do, N. Guimaraes, E. E. Alonso, A. Lloret, S. Olivella, M. V. Villar and F. Huertas (2009). A full-scale in situ heating test for high-level nuclear waste disposal: observations, analysis and interpretation. In: *Géotechnique* 59 (4), 377–399.

Georgiannou, V. N. and J. B. Burland (2001). A laboratory study of post-rupture strength. In: *Géotechnique* 51 (8), 665–675.

Ghabezloo, S. and J. Sulem (2009). Stress dependent thermal pressurization of a fluid-saturated rock. In: *Rock Mechanics and Rock Engineering* 42 (1), 1–24.

Giraud, A. (1993). Couplages thermo-hydro-mécaniques dans les milieux poreux peu perméables. PhD thesis. Paris, France: Ecole nationale des ponts et chaussées.

Giraud, A. and G. Rousset (1996). Time-dependent behaviour of deep clays. In: *Engineering Geology* 41 (1–4), 181–195.

Giraud, A., F. Homand and V. Labiouse (2002). Explicit solutions for the instantaneous undrained contraction of hollow cylinders and spheres in porous elastoplastic medium. In: *International Journal for Numerical and Analytical Methods in Geomechanics* 26 (3), 231–258.

Glasser, F. P., J. Marchand and E. Samson (2008). Durability of concrete − Degradation phenomena involving detrimental chemical reactions. In: *Cement and Concrete Research* 38 (2), 226–246.

Graham, J. and G.T. Houlsby (1983). Anisotropic elasticity of a natural clay. In: *Géotechnique* 33 (2), 165–180.

Graham, J., N. Tanaka, T. Crilly and M. Alfaro (2001). Modified Cam-Clay modelling of temperature effects in clays. In: *Canadian Geotechnical Journal* 38 (3), 608–621.

Graziani, A. and D. Boldini (2012a). Influence of Hydro-Mechanical Coupling on Tunnel Response in Clays. In: *Journal of Geotechnical and Geoenvironmental Engineering* 138 (3), 415–418.

— (2012b). Remarks on axisymmetric modelling of deep tunnels in argillaceous formations. I: Plastic clays. In: *Tunnelling and Underground Space Technology* 28, 70–79.

Graziani, A. and R. Ribacchi (1993). Critical conditions for a tunnel in a strain softening rock. In: *Proceedings of the International Symposium on Assessment and Prevention of Failure Phenomena in Rock Engineering*. Istanbul, Turkey, pp. 199–204.

Griffiths, D. V., G. A. Fenton and M. D. Denavit (2007). Traditional and advanced probabilistic slope stability analysis. In: *Probabilistic Applications in Geotechnical Engineering (GSP 170), ASCE*, pp. 1–10.

Griffiths, D. V., J. Huang and G. A. Fenton (2009). Influence of Spatial Variability on Slope Reliability Using 2-D Random Fields. In: *Journal of Geotechnical and Geoenvironmental Engineering* 135 (10), 1367–1378.

— (2010). Comparison of Slope Reliability Methods of Analysis. In: *Proceedings of the GeoFlorida: Advance in Analysis, Modeling and Design*. West Palm Beach, FL, US, pp. 1952–1961.

Gschwandtner, G. G. and R. Galler (2012). Input to the application of the convergence confinement method with time-dependent material behaviour of the support. In: *Tunnelling and Underground Space Technology* 27 (1), 13–22.

Haart, J. (Dec. 2014). *Report on the determination of the inventory, OPERA-PU-NRG1112A*. Centrale Organisatie Voor Radioactief Afval (COVRA N.V.)

Hacking, I. (1975). *The Emergence of Probability Theory*. Cambridge, UK: Cambridge University Press.

Hamidi, A., S. Tourchi and C. Khazaei (2014). Thermomechanical Constitutive Model for Saturated Clays Based on Critical State Theory. In: *International Journal of Geomechanics, (doi: http://dx.doi.org/10.1061/(ASCE)GM.1943-5622.0000402)*.

Harr, M. E. (1987). *Reliability-based design in civil engineering*. New York: McGraw-Hill.

Hasofer, A. M. and N. C. Lind (1974). Exact and invariant second-moment code format. In: *Journal of Engineering Mechanics Division, ASCE* 100 (1), 111–121.

Heijdra, J. J., J. Bekkering, J. V. D. Gaag, P. H. V. D. Kleyn and J.Prij (1995). *Retrievability of radioactive waste from a deep underground disposal facility, Report 16197 EN*. Luxembourg: European Commission nuclear science and technology. URL: http://bookshop.europa.eu/en/retrieva bility-of-radioactive-waste-from-a-deep-underground-disposal-facility-pbCGNA 16197/downloads/CG-NA-16-197-EN-C/CGNA16197ENC_001.pdf;pgid=y8dIS7GUWMdSR0EA lMEUUsWb0000wKk84hOm;sid=hX1U-OJt4RRUjbNJtprKX4BIyB5KikCu-S0=?FileName=CGNA1 6197ENC_001.pdf&SKU=CGNA16197ENC_PDF&CatalogueNumber=CG-NA-16-197-EN -C.

Helton, J. C. (1997). Uncertainty and sensitivity analysis in the presence of stochastic and subjective uncertainty. In: *Journal of Statistical Computation and Simulation* 57 (1–4), 3–76.

Hemes, S., G. Desbois, J. L. Urai, M. de Craen and M. Honty (Feb. 2011). *Comparative study on porosity in fine- and coarse-grained Boom Clay samples (Mol-Dessel reference site, Belgium) − Pore characterization down to the nm-scale, using BIB-SEM methods: methodology and first results, External Report ER-208*. Mol, Belgium: SCK·CEN. URL: http://publications.sckc en.be/dspace/bitstream/10038/7480/1/er_157.pd.

— (Mar. 2012). *Variability of the morphology of the pore space in Boom Clay from BIB-SEM, FIB and MIP investigations on representative samples − 2nd project report (December 2011), External report ER-208*. Mol, Belgium: SCK·CEN. URL: http://publications.sckcen.be/d space/bitstream/10038/7752/1/er_208.pdf.

Hemes, S., G. Desbois, J. L. Urai, M. De Craen and M. Honty (2013). Homogeneity vs. Heterogeneity of Porosity in Boom Clay. In: *Clay characterisation from nanoscopic to microscopic resolution, "Clay Club" Workshop Proceedings, NEA/RWM/CLAYCLUB(2013)1, OECD Nuclear Energy Agency, Radioactive Waste Management*. Paris, France, pp. 105–108. URL: www.ged.rwth-aac hen.de/files/publications/publication_1697.pdf.

Henrion, P. N., M. Monsecour, A. Fonteyne, N. Hermans P. Manfroy, B. Neerdael and D. de Bruyn (1984). *Characterisation of the Boom Clay, Semi-annual report 18, Contract WAS-334-83-7-B(RS), R&D Programme on Radioactive Disposal into Geological Formation.* SCK·CEN.

Hicher, P. Y., H. Wahyudi and D. Tessier (2000). Microstructural analysis of inherent and induced anisotropy in clay. In: *Mechanics of Cohesive-frictional Materials* 5 (5), 341–371.

Hicks, M. A. and C. Jommi (2014). Doctoral School 2014: Stochastic Analysis and Inverse Modelling. In: Grenoble, France. URL: http://alertgeomaterials.eu/data/school/2014/2014_ALERT_schoolbook.pdf.

Hight, D. W., A. Gasparre, S. Nishimura, N. A. Minh, R. J. Jardine and M. R. Coop (2007). Characteristics of the London Clay from the Terminal 5 site at Heathrow Airport. In: *Géotechnique* 57 (1), 2–18.

Hoffmann, C., E. E. Alonso and E. Romero (2007). Hydro-mechanical behaviour of bentonite pellet mixtures. In: *Physics and Chemistry of the Earth* 32 (8–14), 832–849.

Hohenbichler, M., S. Gollwitzer, W. Kruse and R. Rackwitz (1987). New light on first- and second-order reliability methods. In: *Structural Safety* 4 (4), 267–284.

Hong, P. Y., J. M. Pereira, A. M. Tang and Y. J. Cui (2013). On some advanced thermo-mechanical models for saturated clays. In: *International Journal for Numerical and Analytical Methods in Geomechanics* 37 (17), 2952–2971.

Honjo, Y. (2008). Monte Carlo simulation in reliability analysis. In: *Reliability-Based Design in Geotechnical Engineering: Computations and Applications.* Ed. by K.-K. Phoon. London - New York: Taylor & Francis Group, pp. 169–191.

— (2011). Keynote Lecture: Challenges in geotechnical Reliability Based Design. In: *Proceedings of the Third International Symposium on Geotechnical Safety and Risk (ISGSR).* Ed. by N. Vogt, B. Schuppener, D. Straub and G. Bräu. Munich, Germany, pp. 11–27.

Honty, M. (June 2010). *CEC of the Boom Clay − a review, ER-134.* Mol, Belgium: SCK·CEN. URL: http://publications.sckcen.be/dspace/bitstream/10038/7217/1/er_134.pdf.

Honty, M. and M. De Craen (Apr. 2009). *Mineralogy of the Boom Clay in the Essen-1 borehole, External Report 194.* Mol, Belgium: SCK·CEN. URL: http://publications.sckcen.be/dspace/bitstream/10038/1063/1/er_87.pdf.

— (Feb. 2012). *Boom Clay mineralogy − qualitative and quantitative aspects: Status 2011, External Report 187.* Mol, Belgium: SCK·CEN. URL: http://publications.sckcen.be/dspace/bitstream/10038/7939/1/er_194.pdf.

Horseman, S. T. and T. J. McEwen (1996). Thermal constraints on disposal of heat-emitting waste in argillaceous rocks. In: *Engineering Geology* 41 (1–4), 5–16.

Horseman, S. T., M. G. Winter and D. C. Entwistle (1987). *Geotechnical Characterization of Boom Clay in Relation to the Disposal of Radioactive Waste.* Commission of the European Communities.

— (1993). Triaxial experiments on Boom Clay. In: *The engineering geology of weak rock.* Ed. by J. C. Cripps, J. M. Coulthard, M. G. Culshaw S. R. Hencher and C. F. Moon. Rotterdam, pp. 36–43.

Horseman, S. T., J. J. W. Higgo, J. Alexander and J. F. Harrington (1996). *Water, Gas and Solute Movement through Argillaceous Media - A "Clay Club" Report.* CC-96/1. Paris, France: OECD Nuclear Energy Agency, Radioactive Waste Management. URL: http://www.oecd-nea.org/rwm/reports/1996/water.pdf.

Horseman, S. T., R. J. Cuss and H. J. Reeves (2004). Clay Club Initiative: Self-healing of Fractures in Clay-rich Host Rocks. In: *Stability and Buffering Capacity of the Geosphere for Long-term Isolation of Radioactive Waste, Application to Argillaceous Media "Clay Club" Workshop Proceedings, NEA No. 5303.* NEA/OECD, pp. 117–134. URL: http://www.oecd-nea.org/rwm/reports/2005/nea5303-stability-buffering.pdf.

Hoxha, D., A. Giraud, A. Blaisonneau, F. Homand and C. Chavant (2004). Poroplastic modelling of the excavation and ventilation of a deep cavity. In: *International Journal for Numerical and Analytical Methods in Geomechanics* 28 (4), 339–364.

Hudson, J. A., O. Stephansson and J. Andersson (2005). Guidance on numerical modelling of thermo-hydro-mechanical coupled processes for performance assessment of radioactive. In: *International Journal of Rock Mechanics and Mining Sciences, Research results from the Decovalex III & Benchpar projects* 42 ((5–6)), 850–870.

Hueckel, T. and G. Baldi (1990). Thermoplasticity of Saturated Clays: Experimental Constitutive Study. In: *Journal of Geotechnical Engineering* 116 (12), 1778–1796.

Hueckel, T. and M. Borsetto (1990). Thermoplasticity of saturated soils and shales: Constitutive equations. In: *Journal of Geotechnical Engineering* 116 (12), 1765–1777.

Hueckel, T. and R. Pellegrini (1992). Effective stress and water pressure in saturated clays during heating-cooling cycles. In: *Canadian Geotechnical Journal* 29 (6), 1095–1102. URL: http://duke.edu/~hueckel/papers/cooling_cycles_failure.pdf.

Hueckel, T., E. Tutumluer and R. A. Pellegrini (1992). Note on non-linear elasticity of isotropic overconsolidated clays. In: *International Journal for Numerical and Analytical Methods in Geomechanics* 16, 603–618.

Hueckel, T., B. François and L. Laloui (2009a). Explaining thermal failure in saturated clay. In: *Géotechnique* 59 (3), 197–212. URL: http://www.researchgate.net/publication/37464701_Explaining_thermal_failure_in_saturated_clays/file/79e4150d07e4ce7ae8.pdf.

Hueckel, T., L. Laloui and B. François (2009b). Implications of thermal sensitivity of the static internal friction angle. In: *Proceedings of the 1st international Symposium on Computational Geomechanics (COMGEO I)*. Ed. by S. Pietruszczak, G. N. Pande, C. Tamagnini and R. Wan. Juan-Les-Pins, France, pp. 104–115. URL: http://duke.edu/~hueckel/papers2/Thermal%20Friction%20Inequ.pdf.

Hueckel, T., B. François and L. Laloui (2011). Temperature-dependent internal friction of clay in a cylindrical heat source problem. In: *Géotechnique* 61 (10), 831–844.

ICK (Apr. 1979). *Mogelijkheden van opslag van radioactieve afvalstoffen in zoutvoorkomens in Nederland*. Ministerie van Volksgezondheid en Milieuhygiëne, ICK rapport 53.

ISO 2394 (1998). General principles on reliability for structures. In:

ITA (1988). Guidelines for the design of tunnels, International Tunnelling and Underground Space Association (ITA) working group on general approaches to the design of tunnels. In: *Tunnelling and Underground Space Technology* 3 (3), 237–249.

Jaky, J. (1944). The coefficient of earth pressure at-rest (in Hungarian). In: *Journal of Society of Hungarian Architects and Engineers* 7, 355–358.

JCSS (2001a). *Probabilistic Model Codes*. Joint Committee on Structural Safety.

—— (2001b). *Probabilistic Model Codes, Part 3.1: Resistance Models - Concrete properties*. Joint Committee on Structural Safety.

Jirásek, M. and P. Bažant (2001). *Inelastic Analysis of Structures*. Wiley.

Kgd. of the Netherlands (Sept. 2011). *Joint convention on the safety of spent fuel management and on the safety of radioactive waste management, National Report of the Kingdom of the Netherlands, Fourth review conference (May 2012)*. The Hague, the Netherlands: Ministry of Economic Affairs, Agriculture and Innovation Ministry of Foreign Affairs. URL: http://www.government.nl/files/documents-and-publications/reports/2011/10/12/joint-convention-on-the-safety-of-spent-fuel-management-and-on-the-safety-of-radioactive-waste-management/joint-convention-on-the-safety-of-spent-fuel-management-and-on-the-safety-of-radioactive-waste-management.pdf.

Kim, J.-S., S.-K. Kwon, M. Sanchez and G.-C. Cho (2011). Geological Storage of High Level Nuclear Waste. In: *KSCE Journal of Civil Engineering* 15 (4), 721–737.

Kolditz, O., U.-J. Görke, H. Shao and W. Wang (2012). *Thermo-Hydro-Mechanical-Chemical Processes in Porous Media*. Ed. by T. J. Barth, M. Griebel, D. E. Keyes, R. M. Nieminen, D. Roose and T. Schlick. Vol. 86. Lecture Notes in Computational Science and Engineering. Heidelberg Dordrecht London New York: Springer.

Kolymbas, D. (2008). *Tunnelling and Tunnel Mechanics − A Rational Approach to Tunnelling*. Springer.

Kolymbas, D., P. Wagner and A. Blioumi (2012). Cavity expansion in cross-anisotropic rock. In: *International Journal for Numerical and Analytical Methods in Geomechanics* 36 (2), 128–139.

Kondner, R. L. and J. S. Zelasko (1963). A hyperbolic stress-strain formulation for sands. In: *2nd Pan. Am. Conf. Soil Mech. Found. Eng. (ICOSFE)*. Vol. 1. Brazil, pp. 289–394.

Kuesel, T. R., E. H. King and H. Elwyn J. O. Bickel (2004). *Tunnel Engineering Handbook*. 2nd ed. Dordrecht, the Nehterlands: Kluwer Academic Publishers Group.

Kulhawy, F. H. (1992). On evaluation of static soil properties. In: *Stability and performance of slope and embankments II, Geotechnical Special Publication (GSP 31), ASCE*. Ed. by R. B. Seed and R. W. Boulanger. New York, pp. 95–115.

Kulhawy, F. H. and P. W. Mayne (1990). *Manual on Estimating Soil Properties for Foundation Design*. Electric Power Research Institute, Palo Alto, California, US: Final Report EL-6800, Research Project 1493-6,

Kulhawy, F. H. and C. H. Trautmann (1996). Estimation of in-Situ test uncertainty. In: *Uncertainty in the Geologic Environment: from Theory to Practice, Proceeding of Uncertainty '96, Geotechnical Special Publication No. 58*. Ed. by C. D. Shackelford, P. P. Nelson and M. J. S. Roth. Madison, Wisconsin, US, pp. 269–286.

Kulhawy, F. H., K. K. Phoon and Y. Wang (2012). Reliability-Based Design of Foundations - A Modern View. In: Keynote Lectures from GeoCongress 2012: Geotechnical Engineering State of the Art and Practice, *Geotechnical Special Publication (GSP) 226, ASCE*. Ed. by K. Rollins and D. Zekkos. Oakland, California, U.S.

Kursten, B. and F. Druyts (2008). Methodology to make a robust estimation of the carbon steel overpack lifetime with respect to the Belgian Supercontainer design. In: *Journal of Nuclear Materials* 379 (1–3), 91–96.

Labat, S., J. Marivoet, I. Wemaere and Tom Maes (June 2008). *Essen-1 borehole of the hydro/05neb campaign: technical aspects and hydrogeological investigations, External Report ER-68*. Mol, Belgium: SCK·CEN. URL: http://publications.sckcen.be/dspace/bitstream/10038/827/1/er_68.pdf.

Labiouse, V. and A. Giraud (1998). Analytical solutions for the undrained response of a poro-elasto-plastic medium around a cylindrical opening. In: *Proceedings of the First Biot Conference on Poromechanics*. Ed. by J.-F. Thimus, Y. Abousleiman, A. H.-D. Cheng, O. Coussy and E. Detournay. Louvain la Neuve, Belgium, pp. 439–444.

Labiouse, V. and T. Vietor (2014). Laboratory and in situ simulation tests of the Excavation Damaged Zone around galleries in Opalinus Clay. In: *Rock Mechanics and Rock Engineering* 47 (1), 57–70.

Labiouse, V., C. Sauthier and S. You (2013). Hollow Cylinder Simulation Experiments of Galleries in Boom Clay Formation. In: *Rock Mechanics and Rock Engineering* 47 (1), 43–55.

Lacasse, S. and F. Nadim (1996). Reliability and Probabilistic methods. In: *Uncertainty in the Geologic Environment: from Theory to Practice, Proceeding of Uncertainty '96, Geotechnical Special Publication No. 58*. Ed. by C. D. Shackelford, P. P. Nelson and M. J. S. Roth. Madison, Wisconsin, US, pp. 49–75.

Laenen, B. (1997). The geochemical signature of relative sea-level cycles recognised in the Boom Clay. PhD thesis. Leuven, Belgium: Katholieke Universiteit Leuven.

Laloui, L. (1993). Modélisation du comportement thermo-hydro-mécanique des milieux poreux an-élastique. PhD thesis. Paris, France: Ecole Centrale de Paris.

Laloui, L. and B. François (2009). ACMEG-T: soil thermoplasticity model. In: *Journal of Engineering Mechanics* 135 (9), 932–944.

Lambe, T. W. and R. V. Whitman (1969). *Soil Mechanics*. New York, US: John Wiley & Sons.

Le, T. T. (2008). Comportement thermo-hydro-mécanique de l'argile de Boom. PhD thesis. Paris, France: École Nationale des Ponts et Chaussées. URL: http://pastel.archives-ouvertes.fr/docs/00/50/08/29/PDF/These_LE_Trung_Tinh.pdf.

Le, T. T., A. M. Tang, E. Romero, P. Delage, A. Gens, X. L. Li, Y. J. Cui and A. Lima (2008). Water retention properties of Boom clay. In: *Proceedings of the 1st European Conference (E-UNSAT)*. Ed. by D. G. Toll, C. E . Augarde, D. Gallipoli and S. J . Wheeler. 229–234. Durham, UK.

Lee, Y.-K. and S. Pietruszczak (2008). A new numerical procedure for elasto-plastic analysis of a circular opening excavated in a strain-softening rock mass. In: *Tunnelling and Underground Space Technology* 23 (5), 588–599.

Lemaire, M. (2009). *Structural Reliability*. London - Hoboken: ISTE Ltd. and John Wiley & Sons, Inc.

Leroueil, S. and P. R. Vaughan (1990). The general and congruent effects of structure in natural soils and weak rocks. In: *Géotechnique* 40 (3), 467–488.

Levorová, M. and R. Vašíček (2012). The response of tunnel lining on thermal loading. In: *Rudarsko-Geolosko-Naftni Zbornik* 24 (4), 67–71.

Li, H.-Z. and B. K. Low (2010). Reliability analysis of circular tunnel under hydrostatic stress field. In: *Computers and Geotechnics* 37 (1–2), 50–58.

Li, Q., C.W.W. Ng and G.B. Liu (2012a). Determination of small-strain stiffness of Shanghai clay on prismatic soil specimen. In: *Canadian Geotechnical Journal* 49, 986–993.

Li, X. (2013a). TIMODAZ: A successful international cooperation project to investigate the thermal impact on the EDZ around a radioactive waste disposal in clay host rocks. In: *Journal of Rock Mechanics and Geotechnical Engineering* 5 (3), 231–242.

Li, X., F. Bernier, T. Vietor and P. Lebon (Oct. 2007). *Deliverable 2: State of the art THMC. Thermal Impact on the Damaged Zone Around a Radioactive Waste Disposal in Clay Host Rocks (TIMODAZ)*. URL: http://www.timodaz.eu/deliverables.aspx?dwnld=TIMODAZD2formatECfinal.doc&itemid=bc9c5d91-17e1-4cec-929c-2c8a49ff777f&id=WP2.

Li, X., L. Jing and P. Blaser (Eds.) (2012b). *Impact of thermo-hydro-mechanical chemical (THMC) processes on the safety of underground radioactive waste repositories*. Luxembourg, 29 September - 1 October 2009: Proceedings of the European Commission TIMODAZ-THERESA International Conference, European Commission. URL: http://bookshop.europa.eu/en/impact-of-thermo-hydro-mechanical-chemical-thmc-processes-on-the-safety-of-underground-radioactive-waste-repositories-pbKINA25527/downloads/KI-NA-25527-EN-C/KINA25527ENC_002.pdf?FileName=KINA25527ENC_002.pdf&SKU=KINA25527ENC_PDF&CatalogueNumber=KI-NA-25527-EN-C.

Li, X. L. (2006). *General project scope and objectives*. Thermal Impact on the Damaged Zone Around a Radioactive Waste Disposal in Clay Host Rocks (TIMODAZ). URL: http://www.timodaz.eu/deliverables.aspx?dwnld=generalprojectscopeandobjectiveofTIMODAZ.doc&itemid=d1692162-a073-4652-b7f3-547330c5ddf3&id=WP1.

— (Feb. 2012). PRACLAY experiment in URL HADES, Praclay heater and Seal tests. In: *Presentation at the International Post - TIMODAZ Workshop*. Mont Terri rock laboratory, Saint-Ursanne,

Switzerland. URL: http://www.argenco.ulg.ac.be/timodaz/pdf/session\%203/S3-L4-Li.pdf.

Li, X. L. (2013b). *Personal communication (13-02-2013)*. SCK·CEN, EIG EURODICE.

Li, X. L. and F. Bernier (2005). *Hydraulic and initial boundary conditions - optimisation of the plug length*. Mol: European Underground Research Infrastructure for Disposal of Nuclear Waste in Clay Environment (EURIDICE).

Li, X. L., W. Bastiaens and F. Bernier (May 2006). The hydromechanical behaviour of the Boom clay observed during excavation of the connecting gallery at Mol site. In: *EUROCK 2006, Multiphysics coupling and long term behaviour in rock mechanics*. Liège, Belgium: Balkema, pp. 467–472.

Li, X. L., W. Bastiaens, P. Van Marcke, J. Verstricht, G. J. Chen, E. Weetjens and X. Sillen (2010a). Design and development of large-scale in-situ PRACLAY heater test and horizontal high-level radioactive waste disposal gallery seal test in Belgian HADES. In: *International Journal of Rock Mechanics and Mining Sciences* 2 (2), 103–110.

Li, X. L., C. Arson, W. Bastiaens, F. Bernier, P. Blaser, P. Bèsuelle, R. Charlier, R. Chambon, F. Collin, Czímerová A, P. Delage, F. Dedecker, A. Dizier, M. De Craen, S. Fauriel, B. François, H. Fisch, T. Fierz, J. Fokkens, B. Garitte, A. Gens, B. Gatmiri, P. Gérard, C. Guangjing, L. Gastaldo, M. Honty, Reyes-Montes, J. M. Haycox, J. Hart, J. R. Andrews, V. Labiouse, L. Laloui, M. Levorova, P. Lebon, Y. Li, P. Illing, S. Levasseur, M. Monfared, F. Marinelli, T. Meynet, J. Madejová, M. Osacký, J. Pacovsky, J.-P. Radu, M. Rizzi, Y. Sieffert, X. Sillen, C. Sauthier, S. Salager, C. Schroeder, J. Sulem, G. Viggiani, P. Van Marcke, J. Vaunat, T. Vietor, J. Verstricht, R. Vasicek, L. Vigne, L. Wang, E. Weetjens, W. S. Pettitt, S. You and C. Zhang (2010b). *Final activity report*. Thermal Impact on the Damaged Zone Around a Radioactive Waste Disposal in Clay Host Rocks (TIMODAZ). URL: http://www.timodaz.eu/deliverables.aspx?dwnld=FinalActivityReportvfassubmittedtoEC.doc&itemid=d1692162-a073-4652-b7f3-547330c5ddf3&id=WP1.

Lille (2008). Proceedings of the third international meeting on "Clays in Natural & Engineered Barriers for Radioactive Waste Confinement" - Supplement 1. In: *Physics and Chemistry of the Earth, Parts A/B/C*. Ed. by J.-F. Aranyossy, M. Cathelineau, N. Clauer, M. Delage, R. Dohrman, C. Fairhurst, A. M. Fernández, J.-L. Michelot, T. Popp, J. Stucki and F. Villieras. Vol. 33. 17-20 September 2007, Lille, France, S1–S544.

Lima, A. (2011). Thermo-hydro-mechanical behaviour of two deep Belgian clay formations: Boom and Ypresian Clays. PhD thesis. Barcelona, Spain: Universitat Politècnica de Catalunya (UPC).

Lima, A., E. Romero, A. Gens, J. Muñoz and X. L. Li (2009). Heating Pulse Tests under Constant Volume on Natural Boom clay. In: *International Symposium on Unsaturated Soil Mechanics and Deep Geological Nuclear Waste Disposal (UNSAT-WASTE 2009)*. Shanghai, China, pp. 136–141. URL: http://upcommons.upc.edu/e-prints/bitstream/2117/9922/1/PosterLuxembourg_LRVGL_THMC_P60Lima\%20et\%20al.pdf.

Lima, A., E. Romero, Y. Pina, A. Gens and X. Li (2012a). Water Retention Properties of Two Deep Belgian Clay Formations. In: *Unsaturated Soils: Research and Applications*. Ed. by C. Mancuso, C. Jommi and F. D'Onza. Vol. 1, pp. 179–184.

Lima, A., E. Romero and Y. Pina (2012b). Water retention properties of two deep Tertiary clay formations within the context of radioactive waste disposal. In: *Simpósio Brasileiro de Solos Nao Saturados. "VII Brazilian Symposium on Unsaturated Soil"*. Ed. by G. F. N. Gitirana, M. M. A. Mascarenha and J. Camapum de Carvalho. Pirenópolis-GO, Brazil, pp. 315–321. URL: http://upcommons.upc.edu/e-prints/bitstream/2117/15431/1/WRPBF_Limaetal_VIISimposioBrasil_paper_def.pdf.

Lima, A., E. Romero, A. Gens, X. L. Li and J. Vaunat (2013). Multiphysical Testing of Soils and Shales. In: ed. by L. Laloui and A. Ferrari. Springer Series in Geomechanics and Geoengineering. Berlin: Springer-Verlag. Chap. Thermo-Hydraulic Behaviour of Boom Clay Using a Heating Cell: An Experimental Study, pp. 163–168.

Lings, M. L., D. S. Pennington and D. F. T. Nash (2000). Anisotropic stiffness parameters and their measurement in a stiff natural clay. In: *Géotechnique* 50, 109–125.

Liu, M. D. and J. P. Carter (2002). A structured Cam Clay model. In: *Canadian Geotechnical Journal* 39 (6), 1313–1332.

Lloret-Cabot, M., G. A. Fenton and M. A. Hicks (2014). On the estimation of scale of fluctuation in geostatistics. In: *Georisk: Assessment and Management of Risk for Engineered Systems and Geohazards* 8 (2), 129–140.

Lloyd, J. R. and J. C. Renshaw (2005). Bioremediation of radioactive waste: radionuclide-microbe interactions in laboratory and field-scale studies. In: *Current Opinion in Biotechnology* 16 (3), 254–260.

Lopez, R. H. and A. T. Beck (2012). Reliability-Based Design Optimization Strategies Based on FORM: A Review. In: *Journal of the Brazilian Society of Mechanical Sciences and Engineering* 34 (4), 506–514. URL: www.scielo.br/pdf/jbsmse/v34n4/a12v34n4.pdf.

Low, B. K. and W. H. Tang (2007). Efficient spreadsheet algorithm for first-order reliability method. In: *Journal of Geotechnical and Geoenvironmental Engineering* 133 (12), 1378–1387.

Lü, Q., C. L. Chan and B. K. Low (2011a). Probabilistic analysis of underground rock excavations using response surface method and SORM. In: *Computers and Geotechnics* 38 (8), 1008–1021.

— (2011b). Reliability analysis of ground-support interaction in circular tunnels using the response surface method. In: *International Journal of Rock Mechanics and Mining Sciences* 48 (8), 1329–1343.

— (2013). System Reliability Assessment for a Rock Tunnel with Multiple Failure Modes. In: *Rock Mechanics and Rock Engineering* 46 (4), 821–833.

Lumb, P. (1966). The variability of natural soils. In: *Canadian Geotechnical Journal* 3, 74–97.

— (1970). Safety factors and probability distribution of soil strength. In: *Canadian Geotechnical Journal* 7 (3), 225–242.

Maes, N., L. Wang, G. Delécaut, T. Beauwens, M. Van Geet, M. Put, E. Weetjens, J. Marivoet, J. van der Lee, P. Warwick, A. Hall, G. Walker, A. Maes, C. Bruggeman, D. Bennett, T. Hicks, J. Higgo and D. Galson (2004). *Migration case study: transport of radionuclides in a reducing clay sediment (TRANCOM-II), Final report*. Luxembourg: European Commission nuclear science and technology. URL: http://bookshop.europa.eu/en/migration-case-study-pbKINA21022/downloads/KI-NA-21-022-EN-S/KINA21022ENS_002.pdf?FileName=KINA21022ENS_002.pdf&SKU=KINA21022ENS_PDF&CatalogueNumber=KI-NA-21-022-EN-S.

Maidl, B., M. Herrenknecht, U. Maidl and G. Wehrmeyer (2012). *Mechanised Shield Tunnelling*. 2nd ed. Berlin: Ernst & Sohn.

Mair, R. J., R. N. Taylor and B. G. Clarke (1992). *Repository tunnel construction in deep clay formations, Final report, EUR-13964 EN*. Luxembourg: European Commission nuclear science and technology. URL: http://bookshop.europa.eu/en/repository-tunnel-construction-in-deep-clay-formations-pbCDNA13964/downloads/CD-NA-13-964-EN-C/CDNA13964ENC_001.pdf;pgid=y8dIS7GUWMdSR0EAlMEUUsWb0000tAxTrwkt;sid=K7HOIR9LQJ7OI07OPtxQhn1uZtLQUxiYLWI=?FileName=CDNA13964ENC_001.pdf&SKU=CDNA13964ENC_PDF&CatalogueNumber=CD-NA-13-964-EN-C.

Marivoet, J., D. Jacques, M. Van Geet, W. Bastiaens and I. Wemaere (Sept. 2009). *Considerations on Upscaling of Hydraulic and Transport Parameters for a Plastic Clay Formation, External Report ER-102*. Mol, Belgium: SCK·CEN. URL: http://publications.sckcen.be/dspace/bitstream/10038/1236/1/er_102.pdf.

Mazurek, M., P. Alt-Epping, A. Bath, T. Gimmi and H. N. Waber (2009). *Natural Tracer Profiles Across Argillaceous Formations: The CLAYTRAC Project*. Paris, France: OECD Nuclear Energy Agency (OECD/NEA).

Mazurek, M., P. Alt-Epping, A. Bath, T. Gimmi, H. Niklaus Waber, S. Buschaert, P. De Cannière, M. De Craen, A. Gautschi, S. Savoye, A. Vinsot, I. Wemaere and L. Wouters (2011). Natural tracer profiles across argillaceous formations. In: *Applied Geochemistry* 26 (7), 1035–1064.

Meeussen, J.C.L. and E. Rosca-Bocancea (Oct. 2014). *Determination of the inventory, PartB: Matrix composition, OPERA-PU-NRG112B*. Centrale Organisatie Voor Radioactief Afval (COVRA N.V.)

Mendoza, R. C. (Mar. 2004). Determination of Lateral Stresses in Boom Clay using Lateral Stress Oedometer. MA thesis. Enschede, the Netherlands: International Institute for Geo-Information Science and Earth Observation. URL: www.itc.nl/library/papers_2004/msc/ereg/cordero_mendoza.pdf.

Mertens, J., W. Bastiaens and B. Dehandschutter (2004). Characterisation of induced discontinuities in the Boom Clay around the underground excavations (URF, Mol, Belgium). In: *Applied Clay Science* 26 (1–4), 413–428. URL: www.euridice.be/downloads/mertens\%20et\%20al.pdf.

Meyerhof, G. G. (1995). Development of geotechnical limit state design. In: *Canadian Geotechnical Journal* 32 (1), 128–136.

Mohajerani, M., P. Delage, J. Sulem, M. Monfared, A. M. Tang and B. Gatmiri (2012). A laboratory investigation of thermally induced pore pressures in the Callovo-Oxfordian claystone. In: *International Journal of Rock Mechanics and Mining Sciences* 52, 112–121.
— (2013). The thermal volume changes of the Callovo-Oxfordian claystone. In: *International Journal of Rock Mechanics and Mining Sciences* 47 (1), 131–142.

Möller, S. (2006). Tunnel induced settlements and structural forces in linings. PhD thesis. Stuttgart, Germany: Mitteilung 54, Institut für Geotechnik, Universität Stuttgart, Universität Stuttgart.

Monfared, M., J. Sulem, P. Delage and M. Mohajerani (2012). On the THM behaviour of a sheared Boom clay sample: Application to the behaviour and sealing properties of the EDZ. In: *Engineering Geology* 124, 47–58.

Montpellier (in press). Proceedings of the fifth international meeting on "Clays in Natural & Engineered Barriers for Radioactive Waste Confinement". In: *Physics and Chemistry of the Earth, Parts A/B/C*. 22-25 October 2012, Montpellier, France.

Muñoz, J. J., E. E. Alonso and A. Lloret (2009). Thermo-hydraulic characterisation of soft rock by means of heating pulse tests. In: *Géotechnique* 59 (4), 293–306.

Nantes (2011). Proceedings of the fourth international meeting on "Clays in Natural & Engineered Barriers for Radioactive Waste Confinement". In: *Physics and Chemistry of the Earth, Parts A/B/C*. Ed. by J.-F. Aranyossy, A.-M. Fernandez, R. Dorhmann, P. Delage, C. Faihurst, J.-L. Michelot, T. Popp, M. Cathelineau, M. van Geet, B. Gatmiri, M. Gascoyne, J. Bruno and F. Villieras. Vol. 36. 17–18. 29 March - 1 April 2010, Nantes, France, pp. 1437–2002.

NDA (Dec. 2010a). *Geological Disposal, Generic disposal facility designs, NDA/RWMD/048*. Nuclear Decomposition Authority. URL: http://www.nda.gov.uk/documents/upload/Geological-Disposal-Generic-disposal-facility-designs-December-2010.pdf.
— (Dec. 2010b). *Geological Disposal, Generic Post-closure Safety Assessment, NDA/RWMD/030*. Nuclear Decomposition Authority. URL: http://www.nda.gov.uk/documents/upload/Geological-Disposal-Generic-disposal-facility-designs-December-2010.pdf.

NEA (2001). *IGSC Working Group on Measurement and Physical Understanding of Groundwater Flow through Argillaceous Media (CLAY CLUB), Self-healing topical session procedings*. OECD Nuclear Energy Agency, Radioactive Waste Management. URL: http://www.oecd-nea.org/rwm/docs/2001/rwm-clayclub2001-5.pdf.
— (2007). *Radioactive Waste Management and Decommissioning in The Netherlands*. OECD Nuclear Energy Agency. URL: http://www.oecd-nea.org/html/rwm/profiles/Netherlands_report_web.pdf.

NEA (2008). *Radioactive Waste Management Programmes in OECD/NEA Member Countries - Netherlands*. OECD Nuclear Energy Agency. URL: http://www.oecd-nea.org/html/rwm/profiles/Netherlands_profile_web.pdf.

— (May 2012). *Cementitious Materials in Safety Cases for Geological Repositories for Radioactive Waste: Role, Evolution and Interactions; A Workshop organised by the OECD/NEA Integration Group for the Safety Case and hosted by ONDRAF/NIRAS*. OECD Nuclear Energy Agency, Radioactive Waste Management Committee. URL: www.oecd-nea.org/rwm/docs/2012/rwm-r2012-3.pdf.

Neerdael, B., R. Beaufays, M. Buyens, D. De Bruyn and M. Voet (1992). *Geomechanical behaviour of Boom clay under ambient and elevated temperature conditions, Final report, Report EUR 14154 EN*. Commission of the European Comunity. URL: http://bookshop.europa.eu/en/geomechanical-behaviour-of-boom-clay-under-ambient-and-elevated-temperature-conditions-pbCDNA14154/downloads/CD-NA-14-154-EN-C/CDNA14154ENC_001.pdf;pgid=y8dIS7GUWMdSR0EAlMEUUsWb0000_aFvxhIl;sid=NfG1KQJxWT21DVMd1OorjmBUlzLJeaCySaE=?FileName=CDNA14154ENC_001.pdf&SKU=CDNA14154ENC_PDF&CatalogueNumber=CD-NA-14-154-EN-C.

NEN 6720 (1995). *Betonvoorschriften TGB 1990. Constructieve eisen en rekenmethoden*. Nederlands Normalisatie Instituut, Delft, The Netherlands.

Neuzil, C. E. (1994). How permeable are clays and shales? In: *Water Resources Research* 30 (2), 145–150.

Nielsen, D. R., J. W. Biggar and K. T. Erh (1973). Spatial variability of field-measured soil-water properties. In: *Hilgardia* 42, 215–259.

Nishimura, S., N. A. Minh and R. J. Jardine (2007). Shear strength anisotropy of natural London Clay. In: *Géotechnique* 57 (1), 49–62.

ONDRAF/NIRAS (Dec. 2001a). *SAFIR 2 - Safety Assessment and Feasibility Interim Report 2*. Brussels, Belgium: Belgian agency for radioactive waste and enriched fissile materials, NIROND 2001-06 E. URL: www.neras.be/engels/PDF/Part01-Text01-Chap1-10.pdf.

— (Dec. 2001b). *Technical overview of the SAFIR 2 report - Safety Assessment and Feasibility Interim Report 2*. Brussels, Belgium: Belgian agency for radioactive waste and enriched fissile materials, NIROND 2001-05 E. URL: http://www.neras.be/engels/PDF/.

OpenTURNS (2014a). *Reference Guide, 1.4, openturns-doc-2014.09*. Airbus - EDF - PhiMeca, France: OpenTURNS. URL: http://doc.openturns.org/openturns-latest/pdf/OpenTURNS_ReferenceGuide.pdf.

— (2014b). *User Manual for the Textual User Interface, 1.4, openturns-doc-2014.09*. Airbus - EDF - PhiMeca, France: OpenTURNS. URL: http://doc.openturns.org/openturns-latest/pdf/OpenTURNS_UserManual_TUI.pdf.

Oreste, P. (2009). The Convergence-Confinement Method: Roles and Limits in Modern Geomechanical Tunnel Design. In: *American Journal of Applied Sciences* 6 (4), 757–771.

Oreste, P. P. (2003). A Procedure for Determining the Reaction Curve of Shotcrete Lining Considering Transient Conditions. In: *Rock Mechanics and Rock Engineering* 36 (3), 209–236.

Oritz, L. (1997). *Etudes de performance à long terme: Analyse des données hydrauliques dans la zone perturbée autour du laboratoire souterrain HADES, Report R-3162*. SCK·CEN.

Ortiz, L., M. Put, D. de Bruyn, K. Moerkens and F. Bernier (1996). *Geological disposal of conditioned high-level radioactive waste. Task 4.4: large scale measurement of the hydraulic conductivity of the Boom Clay, Final Report 1994-1995, Restricted Report R-3095*. Mol, Belgium: SCK·CEN.

Ortiz, L., G. Volckaert, P. de Cannière, M. Put, M. A. Sen, S. T. Horseman, J. F. Harrington, M. Impey and S. Einchcomb (1997). *MEGAS — Modelling and experiments on gas migration in repository host rocks, Final report - Phase 2, Report EUR 17453 EN*. Luxenbourg: Commission of the European Comunity. URL: http://bookshop.europa.eu/en/megas-pbCGNA17453/download

s/CG-NA-17-453-EN-C/CGNA17453ENC_001.pdf?FileName=CGNA17453ENC_001.pdf&SKU=C
GNA17453ENC_PDF&CatalogueNumber=CG-NA-17-453-EN-C.

Panet, M. and A. Guenot (1982). Analysis of convergence behind the face of a tunnel. In: *Proceedings International Symposium Tunnelling82*. London, UK, pp. 197–204.

Park, K.-H. and Y.J. Kim (2006). Analytical solution for a circular opening in an elastic-brittle-plastic rock. In: *International Journal of Rock Mechanics and Mining Sciences* 43 (4), 616–622.

Park, K.-H., B. Tontavanich and J.-G. Lee (2008). A simple procedure for ground response curve of circular tunnel in elastic-strain softening rock masses. In: *Tunnelling and Underground Space Technology* 23, 151–159.

Phoon, K.-K. (2008). *Reliability-Based Design in Geotechnical Engineering: Computations and Applications*. London - New York: Taylor & Francis Group.

Phoon, K. K. and F. H. Kulhawy (1999a). Characterization of geotechnical variability. In: *Canadian Geotechnical Journal* 36, 612–624.

Phoon, K.-K., F. H. Kulhawy and M. D. Grigoriu (1995). *Reliability-Based Design of Foundations for Transmission and Line Structures*. Electric Power Research Institute, Palo Alto, California, US: Final Report EPRI TR-105000, Research Project 1493-04,

Phoon, K.K. and F.H. Kulhawy (1999b). Evaluation of geotechnical property variabaility. In: *Canadian Geotechnical Journal* 36, 625–639.

Picard, J.-M. (1994). Écrouissage thermique des argiles saturées: application au stockage des déchets radioactifs. PhD thesis. Paris, France: École Nationale des Ponts et Chaussées. URL: http://pastel.archives-ouvertes.fr/docs/00/57/40/24/PDF/1994TH_PICARD_JM_NS18466.pdf.

Picard, J. M., B. Bazargan and G. Rousset (1994). *Essai thermo-hydro-mechanique dans une argile profonde: Essai CACTUS, EUR 15482*. Luxembourg: European Commission nuclear science and technology. URL: http://bookshop.europa.eu/fr/essai-thermo-hydro-m-canique-dans-une-argile-profonde-pbCDNA15482/downloads/CD-NA-15-482-FR-C/CDNA15482FRC_001.pdf;pgid=y8dIS7GUWMdSR0EAlMEUUsWb0000-g7nWOzi;sid=kug7a5IZq5w7OcLXtn2lzPA8MCtHO5XKlDs=?FileName=CDNA15482FRC_001.pdf&SKU=CDNA15482FRC_PDF&CatalogueNumber=CD-NA-15-482-FR-C.

Pickering, D. J. (1970). Anisotropic Elastic Parameters for Soil. In: *Géotechnique* 20 (3), 271–276.

Pilgerstorfer, T. and N. Radončić (2009). Prediction of spatial displacement development. In: *Geomechanics and Tunnelling* 2 (3), 250–259.

Piriyakul, K. (2006). Anisotropic Stress-Strain Behaviour of Belgian Boom Clay in the Small Strain Region. PhD thesis. Gent, Belgium: Universiteit Gent. URL: www.geotechnics.ugent.be/docs/phdkeera.pdf.

Piriyakul, K. and W. Haegeman (2007). Void ratio function for elastic shear moduli for Boom Clay. In: *Géotechnique* 57 (2), 245–248.

— (2009). Stiffness anisotropy of Boom Clay. In: *Proceedings of the 17th International conference on Soil Mechanics and Geotechnical Engineering: The academia and practice of geotechnical engineering*. Ed. by M. Hamza, M. Shahien and Y. El-Mossallam. Amsterdam, The Netherlands: IOS Press, pp. 167–171.

Plaxis (2013a). *PLAXIS 3D 2013 - Material models manual*. Delft, The Netherlands: Plaxis bv.

— (2013b). *PLAXIS 3D 2013 - Reference Manual*. Delft, The Netherlands: Plaxis bv.

— (2014a). *PLAXIS 2D - General information*. Delft, The Netherlands: Plaxis bv.

— (2014b). *PLAXIS 2D 2015.00 Beta complementary manual*. Delft, The Netherlands: Plaxis bv.

— (2014c). *PLAXIS 2D Anniversary Edition - Material models manual*. PLAXIS bv, Delft, The Netherlands: Plaxis bv.

— (2014d). *PLAXIS 2D Anniversary Edition - Reference Manual*. Delft, The Netherlands: Plaxis bv.

Puła, W. (2007). Reliability of Laterally Loaded Rigid Piles. In: *Probabilistic Methods in Geotechnical Engineering*. Ed. by D. V. Griffith and G. A. Fenton. Wien - New York: Springer, pp. 169–183.

Pusch, R. (Dec. 2001). *The Buffer and Backfill Handbook, Part 2: Materials and techniques, Technical Report TR-02-12*. Stockholm, Sweden: Svensk Kärnbränslehantering AB (SKB). URL: http://www.skb.se/upload/publications/pdf/TR-02-12.pdf.

— (Apr. 2002). *The Buffer and Backfill Handbook, Part 1: Definitions, basic relationships, and laboratory methods, Technical Report TR-02-20*. Stockholm, Sweden: Svensk Kärnbränslehantering AB (SKB). URL: www.skb.se/upload/publications/pdf/TR-02-20.pdf.

— (Jan. 2003). *The Buffer and Backfill Handbook, Part 3: Models for calculation of processes and behaviour, Technical Report TR-03-07*. Stockholm, Sweden: Svensk Kärnbränslehantering AB (SKB). URL: www.skb.se/upload/publications/pdf/TR-03-07.pdf.

Rabcewicz, L. (1964a). The New Austrian Tunnelling Method. Part 1. In: *Water Power* November, 453–457.

— (1964b). The New Austrian Tunnelling Method. Part 2. In: *Water Power* December, 511–515.

— (1965). The New Austrian Tunnelling Method. Part 3. In: *Water Power* January, 19–24.

Rackwitz, R. (2000). Reviewing probabilistic soils modelling. In: *Computers and Geotechnics* 26 (3–4), 199–223.

Rackwitz, R. and B. Fiessel (1978). Structural reliability under combined random load sequences. In: *Computers and Stuctures* 5, 489–494.

Rawls, W. J., D. L. Brakensiek and K. E. Saxton (1982). Estimation of Soil Water Properties. In: *Transactions of the ASAE* 25 (5), 1316–1320.

Read, D., F. P. Glasser, C. Ayora, M. T. Guardiola and A. Sneyers (2001). Mineralogical and microstructural changes accompanying the interaction of Boom Clay with ordinary Portland cement. In: *Advances in Cement Research* 13 (4), 175–183.

Read, H. E. and G. A. Hegemie (1984). Strain softening of rock, soil and concrete − a review article. In: *Mechanics of Materials Volume, Issue 4, December , Pages* 3 (4), 271–294.

Reims (2004). Proceedings of the first international meeting on "Clays in Natural & Engineered Barriers for Radioactive Waste Confinement". In: *Physics and Chemistry of the Earth, Parts A/B/C*. Ed. by J.-F. Aranyossy, A. Decarreau, H. J. Herbert and P. Landais. Vol. 29. 1. 9-12 December 2002, Reims, France, pp. 1–136.

Rétháti, L. (1988). *Probabilistic solutions in geotechnics*. Vol. 46. Developments in Geotechnical Engineering. Elsevier.

RGD (1984). *Inventarisatie van slecht-doorlatende laagpakketten in de ondergrond van het Nederlandse vasteland, Rapport Nr. OP 6009*. Rijks Geologische Dienst.

Rider, M. (2002). *The geological interpretation of well logs*. Ed. by 2. Rider-French Consulting Ltd.

Rijkers, R. H. B., D. I. Huisman, G. de Lang, J. P. Weijers and W. Witmans-Parker (1998). *Inventarisatie geomechanische, geochemische en geohydrologische eigenschappen van Tertiaire kleipakketten CAR Fase II - Eindrapport*. Nederlands Instituut vor Toegepaste Geowetenschappen (TNO). URL: http://www.covra.nl/cms-file/get/iFileId/2475.

Robinet, J.-C., A. Rahbaoui, F. Plas and P. Lebon (1996). A constitutive thermomechanical model for saturated clays. In: *Engineering Geology* 41 (1–4), 145–169.

Romero, E. (1999). Characterisation and Thermo-Hydro-Mechanical behaviour of unsaturated boom clay: An experimental study. PhD thesis. Barcelona, Spain: Universitat Politècnica de Catalunya (UPC).

Romero, E. and C. Jommi (2008). An insight into the role of hydraulic history on the volume changes of anisotropic clayey soils. In: *Water Resources Research* 44 (5), W12412.

Romero, E. and J. Vaunat (2000). Retention curves of deformable clays. In: *Experimental Evidence and Theoretical Approaches in Unsaturated Soils*. Ed. by A. Tarantino and C. Mancuso. Rotterdam: Balkema, pp. 91–106.

Romero, E., A. Gens and A. Lloret (1999). Water permeability, water retention and microstructure of unsaturated compacted Boom clay. In: *Engineering Geology* 54 (1–2), 117–127.

Romero, E., M.V. Villar and A. Lloret (2005). Thermo-hydro-mechanical behaviour of two heavily overconsolidated clays. In: *Engineering Geology, Issues in Nuclear Waste Isolation Research* 81 (3), 255–268.

Romero, E., G. Della Vecchia and C. Jommi (2011). An insight into the water retention properties of compacted clayey soils. In: *Géotechnique* 61 (4), 313–328.

Roscoe, K. H. and J. B. Burland (1968). *On the generalised stress-strain behaviour of 'wet' clay*. Engineering Plasticity, Cambridge University Press, pp. 535–609.

Rowe, P. W. (1962). The stress-dilatancy relation for static equilibrium of an assembly of particles in contact. In: *In Proc. of the Royal Society of London*. Vol. 269. A, Mathematical andPhysical Sciences, pp. 500–527.

Russo, D. and M. Bouton (1992). Statistical Analysis of Spatial Variability in Unsaturated Flow Parameters. In: *Water Resources Research* 28 (7), 1911–1925.

Salehnia, F., R. Charlier and S. Levasseur (2013). Modeling of strain localization around the radioactive waste disposal galleries. In: *Coupled Phenomena in Environmental Geotechnics*.

Sandrone, F. and V. Labiouse (2010). Analysis of the evolution of road tunnels equilibrium conditions with a convergence-confinement approach. In: *Rock Mechanics and Rock Engineering* 43 (2), 201–218.

Schanz, T. (1998). Zur Modellierung des mechanischen Verhaltens von Reibungsmaterialien. PhD thesis. Stuttgart, Germany: Mitteilung 45, Institut für Geotechnik, Universität Stuttgart, Universität Stuttgart.

Schanz, T. and P. A. Vermeer (1996). Angles of friction and dilatancy of sand. In: *Géotechnique* 46 (1), 145–151.

Schanz, T., P. A. Vermeer and P. G. Bonnier (1999). The Hardening Soil model − formulation and verification. In: *Proceedings Plaxis Symposium "Beyond 2000 in Computational Geotechnics"*. Amsterdam: Balkema, pp. 281–296.

Schittekat, J., J. Henriet and N. Vandenberghe (1983). Geology and geotechnique of the Scheldt Surge Barrier, characteristics of and overconsolidated clay. In: *8th International Harbour Congress*. Antwerp, Belgium, pp. 121–136.

Schofield, A. N. and C. P. Wroth (1968). *Critical state soil mechanics*. London, UK: McGraw Hill.

Schultze, E. (1971). Frequency Distributions and Correlation of Soil Properties. In: *Proceedings of the 1st International Conference on Applications of Statistics and Probability in Soil and Structural Engineering*. Hong Kong, pp. 371–387.

Shin, J. H. (2010). Analytical and combined numerical methods evaluating pore water pressure on tunnels. In: *Geotechénique* 60 (2), 141–145.

Sillen, X. (2010). *Introduction to tomorrow's group exercise (presenation)*. Barcelona, Spain, 13-15 January: Second TIMODAZ Training Course: Impact of THMC Processes on Performance Assessment. URL: http://www.timodaz.eu/course.aspx?dwnld=Exerciseintroduction.pdf.

Sillen, X. and J. Marivoet (May 2007). *Thermal impact of a HLW repository in clay, Deep disposal of vitrified high-level waste and spent fuel, External report SCK·CEN-ER-38*. SCK·CEN.

Silvestri, V. and G. Abou-Samra (2012). Analytical solution for undrained plane strain expansion of a cylindrical cavity in modified cam clay. In: *Geomechanics and Engineering* 4 (1), 19–37.

Simpson, B. (2010). Engineering in stiff sedimentary clays. In: *Géotechnique* 60 (12), 903–911.

Simpson, B., G. Calabresi, H. Sommer and M. Wallays (1979). Design parameters for stiff clays. In: *Design Parameters in Geotechnical Engineering, Proceedings of the VII European Conference on Soil Mechanics and Foundation Engineerin (ECSMF)*. Vol. 5. Brighton, UK, pp. 91–126.

Skempton, A. W. (1969). The consolidation of clays by gravitational compaction. In: *Quarterly Journal of the Geological Society* 125, 373–411.

— (1984). The Colloidal "Activity" of Clays, Reprinted from Proc. 3rd Int. Conf. Soil Mech., Zurich, 1953, 1, 57–61. In: *Selected papers on soil mechanics*. Ed. by F.R.S. A. W. Skempton. London, UK: Thomas Telford Limited, pp. 60–64.

Spagnoli, G., M. Feinendegen and D. Rubinos (2012). Modification of clay adhesion to improve tunnelling excavation. In: *Proceedings of the ICE − Ground Improvement* 166 (1), 21–31.

Steen, B. van de and A. Vervoort (Aug. 1998). *Mine Design in Clay, CORA Project TRUCK-I*. Leuven, Belgium: Karholieke Universiteit Leuven. URL: http://www.covra.nl/cms-file/get/iFileId/2476.

Stephansson, O. and K.-B. Min (2004). Thermo-Hydro-Mechanical (THM) Coupled Processes for Performance and Safety Assessments of Nuclear Waste Repository: Lessons Learnt from EC BENCHPAR Project. In: 6th *European Commission Conference on the Management and Disposal of Radioactive Waste (Euradwaste '04), Community Policy and Research & Training Activities*. Luxembourg. URL: ftp://ftp.cordis.europa.eu/pub/fp6-euratom/docs/euradwaste04pro_posj-stephansson_en.pdf.

Stephansson, O., J. A. Hudson and L. Jing (2004). *Coupled Thermo-Hydro-Mechanical-Chemical Processes in Geo-Systems - Fundamentals, Modelling, Experiments and Applications*. Vol. 2. Geoengineering book series. Amsterdam, the Netherlands: Elsevier.

Stephansson, O., J. A. Hudson and J. Anderson (2005). *Guidance document on THM coupled processes in performance assessment (Benchpar), Final report*. European Commission nuclear science and technology. URL: http://cordis.europa.eu/documents/documentlibrary/82706711EN6.pdf.

Suebsuk, J., S. Horpibulsuk and M. D. Liu (2010). Modified Structured Cam Clay: A generalised critical state model for destructured, naturally structured and artificially structured clays. In: *Computers and Geotechnics* 37 (7–8), 956–968.

— (2011). A critical state model for overconsolidated structured clays. In: *Computers and Geotechnics* 38 (5), 648–658.

Sultan, N. (1997). Etude du comportement thermo-mécanique de l'argile de Boom: expériences et modélisation. PhD thesis. Paris, France: École Nationale des Ponts et Chaussées.

Sultan, N., P Delagea and Y.J Cui (2002). Temperature effects on the volume change behaviour of Boom clay. In: *Engineering Geology* 64 (2–3), 135–145.

Sultan, N., Y.-J. Cui and P. Delage (2010). Yielding and plastic behaviour of Boom Clay. In: *Géotechnique* 60 (9), 657–666.

THERESA (2009). *Coupled Thermal-Hydrological-Mechanical-Chemical Processes for Application in Repository Safety Assessment, Project description & Status*. European Commission. URL: ftp://ftp.cordis.europa.eu/pub/fp6-euratom/docs/theresa-project-presentation-flyer-v2_en.pdf.

Timoshenko, S. P. and J. N. Goodier (1970). *Theory of elasticity*. 3rd ed. New York: McGraw-Hill Book Company.

Tinh, L. E. Trung (2008). Component thermo-hydro-méchanique de l'agrile de Boom. PhD thesis. Paris, France: École Nationale des Ponts et Chaussées.

Tours (2007). Proceedings of the second international meeting on "Clays in Natural & Engineered Barriers for Radioactive Waste Confinement" - Part 1. In: *Physics and Chemistry of the Earth, Parts A/B/C*. Ed. by J.-F. Aranyossy. Vol. 32. 1–7. 14-18 March 2005, Tours, France, pp. 1–538.

— (2008). Proceedings of the second international meeting on "Clays in Natural & Engineered Barriers for Radioactive Waste Confinement" - Part 2. In: *Physics and Chemistry of the Earth, Parts A/B/C*. Ed. by J.-F. Aranyossy. Vol. 32. 8–14. 14-18 March 2005, Tours, France, pp. 539–966.

Towhata, I., P. Kuntiwattanakul, I. Seko and K. Ohishi (1993). Volume change of clays induced by heating as observed in consolidation tests. In: *Soils and Foundations* 33 (4), 170–183.

Trotignon, L., V. Devallois, H. Peycelon, C. Tiffreau and X. Bourbon (2007). Predicting the long term durability of concrete engineered barriers in a geological repository for radioactive waste. In: *Physics and Chemistry of the Earth, Parts A/B/C, Clay in natural and engineered barriers for radioactive waste confinement - Part 1* 32 (1–7), 259–274.

Tsang, C.-F. and F. Bernier (2005). Definitions of excavation disturbed zone and excavation damaged zone. In: *Impact of the excavation disturbed or damaged zone (EDZ) on the performance of radioactive waste geological repositories, Proceedings o a European Commission Cluster Conference and Workshop*. Ed. by C. Davies and F. Bernier. Luxembourg. URL: http://bookshop.europa.eu/en/impact-of-the-excavation-disturbed-or-damaged-zone-edz-on-the-performance-of-radioactive-waste-geological-repositories-pbKINA21028/.

Tsang, C.-F., F. Bernier and C. Davies (2005). Geohydromechanical processes in the Excavation Damaged Zone in crystalline rock, rock salt, and indurated and plastic clays - in the context of radioactive waste disposal. In: *International Journal of Rock Mechanics and Mining Sciences* 42 (1), 109–125.

Tsang, C.F., J. D. Barnichon, J. Birkholzer, X. L. Li, H. H. Liu and X. Sillen (2012). Coupled thermo-hydro-mechanical processes in the near field of a high-level radioactive waste repository in clay formations. In: *International Journal of Rock Mechanics and Mining Sciences* 49, 31–44.

Tvedt, L. (1989). Second Order Reliability by an Exact Integral. In: Lecture Notes in Engineering Volume 48. Ed. by P. Thoft-Christensen, 377–384.

Uzielli, M., S. Lacasse, F. Nadim and K. K. Phoon (2006). Soil variability analysis for geotechnical practice. In: *Proceedings of the 2nd International Workshop on Characterisation and Engineering Properties of Natural Soils*. Vol. 3. Singapore: Taylor & Francis, pp. 1653–1752.

Van Geet, M. (2004). *Characterisation of Boom Clay organic matter: mobile and immobile fraction, Report R-3884*. Mol, Belgium: SCK·CEN.

Van Geet, M., N. Maes, M. Aertsens, G. Volckaert, C. Imbert and P. Billaud (June 2005). *A large scale in situ demonstration test for repository sealing in an argillaceous host rock − phase II (RESEAL II PROJECT), Final report on laboratory tests (WP1), External Report ER-1*. Mol, Belgium: SCK·CEN. URL: http://publications.sckcen.be/dspace/bitstream/10038/238/1/er_1.pdf.

Van Geet, M., M. De Craen, E. Weetjens and X. Sillen (Feb. 2006). *Extent of oxidising conditions in the host formation, External Report ER-5*. Mol, Belgium: SCK·CEN. URL: http://publications.sckcen.be/dspace/bitstream/10038/232/1/er_05.pdf.

Van Geet, M., W. Bastiaens, G. Volckaert, E. Weetjens, X. Sillen, A. Gens, M. V. Villar, Ch. Imbert, M. Filippi, and F. Plas (2008a). Installation and evaluation of a large-scale in situ shaft seal experiment in Boom Clay. In: *Selected papers from the third international meeting on Clays in Natural & Engineered Barriers for Radioactive Waste Confinement*. Science and Technology Series 334. Lille, France: Andra, Chatenay-Malabry, pp. 95–109. URL: http://www.nantes2010.com/doc/abstracts/data/pdf/073_074_O_03A_3.pdf.

Van Geet, M., W. Bastiaens and L. Ortiz (2008b). Self-sealing capacity of argillaceous rocks: Review of laboratory results obtained from the SELFRAC project. In: *Physics and Chemistry of the Earth, Parts A/B/C, Clays in Natural & Engineered Barriers for Radioactive Waste Confinement* 33 (Supplement 1), S396–S406.

Van Geet, M., W. Bastiaens, G. Volckaert, E. Weetjens, X. Sillen, N. Maes, Ch. Imbert, P. Billaud, G. Touzé, M. Filippi, F. Plas, M. V. Villar, M. García-Gutiérrez, M. Mingarro, A. Gens and B. Vallejan (2009). *RESEAL II A large-scale in situ demonstration test for repository sealing in an argillaceous host rock − Phase II, Final report, EUR 24161 EN*. Luxembourg: European Commission nuclear science and technology. URL: http://cordis.europa.eu/documents/documentlibrary/110282821EN6.pdf.

van Impe, W. F. (1993). Boom Clay for storage of nuclear waste (discussion session 2b). In: *Geotechnical engineering of hard soils-soft rocks*. Ed. by A. E. Al Athen. Rotterdam, the Netherlands: A. A. Balkema, pp. 1885–1895.

Van Keer, I. and M. De Craen (2001). *Sedimentology and Diagenetic Evolution of the Boom Clay: State of the Art, Report R-3483*. SCK·CEN.

Van Marcke, P. and W. Bastiaens (2010a). Construction of the Praclay experimental gallery at the Hades URF. In: *Fourth international meeting on Clays in Natural & Engineered Barriers for Radioactive Waste Confinement*. Nantes, France, pp. 53–54. URL: http://www.nantes2010.com/doc/abstracts/data/pdf/053_054_O_02A_3.pdf.
— (2010b). Excavation induced fractures in a plastic clay formation: Observations at the HADES URF. In: *Journal of Structural Geology* 32 (11), 1677–1684.

Vandenberghe, N. (1978). *Verhandelingen / Koninklijke academie voor wetenschappen, letteren en schone kunsten van Belgie. Klasse der wetenschappen (Jrg. 40, no. 147)*. Sedimentology of the Boom Clay (Rupelian) in Belgium.
— (2003). Rupel Group. In: *Symposium on the Paleogene, preparing for modern life and climate*. Ed. by S. Geets, M. Maréchal, P. Laga, M. De Ceuckelaire and S. Gouwy. Leuven, Belgium.

Vandenberghe, N. and W. Fock (1989). Temperature data in the subsurface of Belgium. In: *Tectonophysics* 164 (2–4), 237–250.

Vandenberghe, N., P. Laga, E. Steurbaut, J. Hardenbol and P. R. Vail (1998). Tertiary sequence stratigraphy at the southern border of the North Sea basin in Belgium. In: *Mesozoic and Cenozoic Sequence Stratigraphy of European Basins, SEPM (Society for Sedimentary Geology) Special Publication No* 60, 119–154. URL: http://sp.sepmonline.org/content/sepspecpub/sepspmes/1/SEC10.body.pdf.

Vandenberghe, N., S. Van Simaeys, E. Steurbaut, J.W.M. Jagt and P. J. Felder (2004). Stratigraphic architecture of the Upper Cretaceous and Cenozoic along the southern border of the North Sea Basin in Belgium. In: *Netherlands Journal of Geosciences / Geologie en Mijnbouw* 83 (3), 155–171.

Vandenberghe, N., M. D. C. de Craen and J. Grupa (Mar. 2014). *Geological and geohydrological characterization of the Boom Clay and its overburden, OPERA-PU-TNO411*. Centrale Organisatie Voor Radioactief Afval (COVRA N.V.) URL: http://www.covra.nl/cms-file/get/iFileId/2785.

Vardoulakis, I. (2002). Dynamic thermo-poro-mechanical analysis of catastrophic landslides. In: *Géotechnique* 52 (3), 157–171.

Vaunat, J., A. Gens, R. de Vasconcelos and X. L. Li (Apr. 2011). Analysis of the excavation of a deep drift in a tertiary clay. In: *Proceedings of the 2nd international Symposium on Computational Geomechanics (COMGEO II)*. Ed. by S. Pietruszczak and G. N. Pande. Cavtat-Dubrovnik, Croatia, pp. 587–598.

Vašíček, Radek and J. Svoboda (2011). Long-term lining performance − Civil engineering problem of potential retrieval of buried spent nuclear fuel. In: *Nuclear Engineering and Design* 241 (4), 1233–1237.

Verhoef, E. (July 2011). *Meerjarenplan, OPERA-PG-COV002*. Centrale Organisatie Voor Radioactief Afval (COVRA N.V.) URL: http://www.covra.nl/cms-file/get/iFileId/2533.

Verhoef, E. and T. Schröder (June 2011). *Research Plan, OPERA-PG-COV004*. Centrale Organisatie Voor Radioactief Afval (COVRA N.V.) URL: http://www.covra.nl/cms-file/get/iFileId/2444.

Verhoef, E., E. Neeft, J. Grupa and A. Poley (June 2011). *Outline of a disposal concept in clay, OPERA-PG-COV008*. Centrale Organisatie Voor Radioactief Afval (COVRA N.V.) URL: http://www.covra.nl/cms-file/get/iFileId/2417.

Verhoef, E. V., A. M. G. de Bruin, R. B. Wiegers, E. A. C. Neeft and G. Deissmann (Apr. 2014). *Cementitious materials in OPERA disposal concept in Boom Clay, OPERA-PG-COV020*. Centrale Organisatie Voor Radioactief Afval (COVRA N.V.) URL: http://www.covra.nl/cms-file/get/iFileId/2786.

Vermeer, P. and H. Neher (1999). A soft soil model that accounts for creep. In: *Proceedings Plaxis Symposium "Beyond 2000 in Computational Geotechnics"*. Amsterdam: Balkema, pp. 249–261.

Verruijt, A. (1997). A complex variable solution for a deforming circular tunnel in an elastic half-plane. In: *International Journal for Numerical and Analytical Methods in Geomechanics* 21 (2), 77–89.

— (1998). Deformations of an elastic half plane with a circular cavity. In: *International Journal of Solids and Structures* 35 (21), 2795–2804.

Vervoort, A., W. Bastiaens, F. Bernier, S. Chanchole, C. Coll, B. Debecker, V. De Greef, J.Desrues, S. Escoffier, L. Gastaldo, A. Govaerts, R. Hamza, V. Labiouse, X. Ling Li, L. Malinsky, J.-F. Mathier, L. Ortiz, Y. Vanbrabant, M. Van Geet, J. Verstraelen, G. Viaggiani and M. Wevers (Nov. 2005). *Fractures and self-healing within the excavated damaged zone in clays. Laboratory tests (results and interpretation) − Deliverable 2*. European Commission nuclear science and technology.

Villar, M. V. and A. Lloret (2004). Influence of temperature on the hydro-mechanical behaviour of a compacted bentonite. In: *Applied Clay Science* 26 (1–4), 337–350.

Vlachopoulos, N. and M. S. Diederichs (2009). Improved Longitudinal Displacement Profiles for Convergence Confinement Analysis of Deep Tunnels. In: *Rock Mechanics and Rock Engineering* 42 (2), 131–146.

Volckaert, G., L. Ortiz, P. De Canniére, M. Put, S. T. Horseman, J. F. Harrington, V. Fioravante and M. Impey (1995). *MEGAS − Modelling and experiments on gas migration in repository host rocks, Final report - Phase 1, Report EUR 17453 EN*. Luxembourg: Commission of the European Comunity. URL: http://bookshop.europa.eu/en/megas-pbCGNA16235/downloads/CG-NA-16-235-EN-C/CGNA16235ENC_001.pdf?FileName=CGNA16235ENC_001.pdf&SKU=CGNA16235ENC_PDF&CatalogueNumber=CG-NA-16-235-EN-C.

Volckaert, G., F. Bernier, X. Sillen, M. Van Geet, J.-C. Mayor, I. Göbel, P. Blümling, B. Frieg and K. Su (2004). Similarities and Differences in the Behaviour of Plastic and Indurated Clays. In: *6th European Commission Conference on the Management and Disposal of Radioactive Waste (Euradwaste '04), Community Policy and Research & Training Activities*. Luxembourg. URL: ftp://ftp.cordis.europa.eu/pub/fp6-euratom/docs/euradwaste04pro_6-7-volckaert_en.pdf.

VROM (Sept. 1984). *Radioactive waste policy in The Netherlands, An outline of the Government's position*. Ministry of Housing, Physical Planning and the Environment.

VROM (Nov. 2002). *Radioactive waste management; Policy perspective 2002 - 2010 (Beleidsstandpunt onderzoek radioactief afval), Letter of Assistant Secretary to Lower House 28674*. Ministry of Housing, Physical Planning and the Environment.

Wang, Q. (2012). Hydro-mechanical behaviour of bentonite-based materials used for high-level radioactive waste disposal. PhD thesis. Paris, France: École Nationale des Ponts et Chaussées.

Wang, Q., A. M. Tang, Y.-J. Cui, P. Delage and B. Gatmiri (2012a). Experimental study on the swelling behaviour of bentonite/claystone mixture. In: *Engineering Geology* 124, 59–66.

Wang, S., X. Yin, H. Tang and X. Ge (2010). A new approach for analyzing circular tunnel in strain-softening rock masses. In: *International Journal of Rock Mechanics and Mining Sciences* 47, 170–178.

Wang, S., S. Yin and Z. Wu (2012b). Strain-softening analysis of a spherical cavity. In: *International Journal for Numerical and Analytical Methods in Geomechanics* 36 (2), 182–202.

Waterman, D. and W. Broere (2004). *Practical application of the Soft Soil Creep model*. Delft, The Netherlands: Plaxis bv. URL: http://kb.plaxis.nl/publications/practical-application-soft-soil-creep-model.

Watson, S., T. Hicks, G. Towler, D. Reedha, A. Paulley, T. Baldwin and A. Bond (May 2009). *Post-closure Performance Assessment: Consideration of a Co-located Geological Disposal Facility in the Safety Case, Under contract to the NDA*. Oakham, United Kingdom: Galson Sciences Ltd. for Radioactive Waste Management Directorate and Nuclear Decommissioning Authority. URL: http://www.nda.gov.uk/documents/biblio/upload/Post-closure-Performance-Assessment-Consideration-of-a-Co-located-Geological-Disposal-Facility-in-the-Safety-Case.pdf.

Weerts, H. J. T., P. Cleveringa, J. H. J. Ebbing abd F. D. Lang and W. E. Westerhoff (2000). *De lithografische indeling van Nederland. Formaties uit het Tertiair en kwartair, TNO-NITG rapport 00-95-A*. Utrecht, the Netherlands: Nederlands Instituut vor Toegepaste Geowetenschappen (TNO).

Weetjens, E. (Feb. 2009). *Update of the near field temperature evolution calculations for disposal of UNE-55, MOX-50 and vitrified HLW in a supercontainer- based geological repository*. Mol, Belgium: SCK·CEN-ER-86. URL: http://publications.sckcen.be/dspace/bitstream/10038/1039/1/er_86.pdf.

Weetjens, E., J. Marivoet and J. Govaerts (Sept. 2012). *Preparatory Safety Assessment, Conceptual model description of the reference case, External report ER-215*. Mol, Belgium: SCK·CEN. URL: http://publications.sckcen.be/dspace/bitstream/10038/7905/1/er_215.pdf.

Wemaere, I., J. Marivoet and S. Labat (2008). Hydraulic conductivity variability of the Boom Clay in north-east Belgium based on four core drilled boreholes. In: *Physics and Chemistry of the Earth, Parts A/B/C, Clays in Natural & Engineered Barriers for Radioactive Waste Confinement* 33 (Supplement 1), S24–S36.

Whitman, R. V. (1984). Evaluating the Calculated Risk in Geotechnical Engineering. In: *Journal of Geotechnical Engineering* 110 (2), 143–188.

Whittle, A. J. (1993). Evaluation of a constitutive model for overconsolidated clays. In: *Géotechnique* 43 (2), 289–313.

Wildenborg, A.F.B., B. Orlic, G. de Lange, C. S. de Leeuw, F. van Weert, E. J. M. Veling, S. de Cock, J. F. Thimus, C. Lehnen-de Rooij and E. J. den Haan (Oct. 2000). *Transport of RAdionuclides disposed of in Clay of Tertiary ORigin (TRACTOR) - Final report*. Utrecht, the Netherlands: Netherlands Institute of Applied Geoscience TNO - National Geological Suruey. URL: http://www.covra.nl/cms-file/get/iFileId/2478.

Wileveau, Y. (2005a). *THM behaviour of host rock (HE-D experiment): Progress Report, Part 1, Technical Report TR 2005-03*. Mont Terri Project. URL: http://www.mont-terri.ch/interne

t/mont-terri/de/home/experiments/documentation/gratisberichte.parsys.50286.do
wnloadList.75006.DownloadFile.tmp/tr200503part1.pdf.

Wileveau, Y. (2005b). *THM behaviour of host rock (HE-D experiment): Progress Report, Part 2, Technical Report TR 2005-03*. Mont Terri Project. URL: http://www.mont-terri.ch/interne
t/mont-terri/en/home/experiments/documentation/gratisberichte.parsys.50286.do
wnloadList.75095.DownloadFile.tmp/tr200503part2.pdf.

Wileveau, Y. and F. Bernier (2008). Similarities in the hydromechanical response of Callovo-Oxfordian clay and Boom Clay during gallery excavation. In: *Physics and Chemistry of the Earth, Parts A/B/C, Clays in Natural & Engineered Barriers for Radioactive Waste Confinement* 33 (Supplement 1), S343–S349.

Wong, H., M. Morvan, F. Deleruyelle and C. J. Leo (2008a). Analytical study of mine closure behaviour in a poro-viscoelastic medium. In: *International Journal for Numerical and Analytical Methods in Geomechanics* 32 (14), 1737–1761.

— (2008b). Analytical study of mine closure behaviour in a poroelastic medium. In: *Computers and Geotechnics* 35 (5), 645–654.

Wood, D. M. (1990). *Soil Behaviout and Critical State Soil Mechanics*. New York, US: Cambridge University Press.

— (2004). *Geotechnical Modelling*. Vol. 1. Applied Geotechnics. New York, US: CRC Press.

Wood, M. Rouainia D. M. (2000). A kinematic hardening constitutive model for natural clays with loss of structure. In: *Géotechnique* 50 (2), 153–164.

Wool, R. P. (2008). Self-healing materials: a review. In: *Soft Matter* 4 (3), 400–418. URL: http://bg.bilkent.edu.tr/jc/papers/b711716g.pdf.

Wouters, L. and N. Vandenberghe (1994). *Geologie van de Kempen: Een synthese*. Brussels, Belgium: NIRAS (Nationale Instelling voor Radioactief Afval en Verrijkte Splijtstoffen).

Wouters, L., M. Herron, V. Abeels, M. Hagood and J. Strobel (1999). Innovative applications of dual range Fourier transform infrared spectroscopy to analysis of Boom Clay mineralogy. In: *Aardkundige mededelingen* 9, 159–168.

Yilmaz, I. (2009). Swell potential and shear strength estimation of clays. In: *Allpied Clay Sciences* 46 (4), 376–384.

Yu, H.-D., W.-Z. Chen, S.-P. Jia, J.-J. Cao and X.-L. Li (2012). Experimental study on the hydro-mechanical behavior of Boom clay. In: *International Journal of Rock Mechanics and Mining Sciences* 53, 159–165.

Yu, H. D., W. Z. Chen, X. L. Li and X. Sillen (2013a). A Transversely Isotropic Damage Model for Boom Clay. In: *Rock Mechanics and Rock Engineering* , 1–13. DOI: 10.1007/s00603-012-0346-7.

Yu, H. S. (2000). *Cavity Expansion Methods in Geomechanics*. Dordrecht, the Netherlands: Kluwer Academic Publishers.

— (2006). *Plasticity and Geotechnics*. Vol. 13. Advances in Mechanics and Mathematics. Berlin: Springer.

Yu, H. S. and G. T. Houlsby (1991). Finite cavity expansion in dilatant soils. In: *Géotechnique* 41 (2), 173–183.

Yu, H. S. and R. K. Rowe (1999). Plasticity solutions for soil behaviour around contracting cavities and tunnels. In: *International Journal for Numerical and Analytical Methods in Geomechanics* 23 (12), 1245–1279.

Yu, L. and E. Weetjens (Oct. 2009). *Summary of Gas Generation and Migration. Current State-of-the-Art, EExternal Report ER-106*. Mol, Belgium: SCK·CEN. URL: http://publications.sc
kcen.be/dspace/bitstream/10038/1209/1/er_106.pdf.

Yu, L., E. Weetjens, T. Vietor and J. Hart (2010). *Integration of TIMODAZ results within the Safety Case and recommendations for repository design (D14), Final report of WP6*. Thermal Impact on the Damaged Zone Around a Radioactive Waste Disposal in Clay Host Rocks (TIMODAZ). URL: http://www.timodaz.eu/deliverables.aspx?dwnld=D14vf.pdf&itemid=a7b4ce8a-4697-4516-bc0b-31b45fe4e598&id=WP6.

Yu, L., M. Gedeon, I. Wemaere, J. Marivoet and M. De Craen (May 2011). *Boom Clay Hydraulic Conductivity. A synthesis of 30 years of research, External Report ER-122*. Mol, Belgium: SCK·CEN. URL: http://publications.sckcen.be/dspace/bitstream/10038/7504/1/er_122.pdf.

Yu, L., B. Rogiers, M. Gedeon, J. Marivoet, M. De Craen and D. Mallants (2013b). A critical review of laboratory and in-situ hydraulic conductivity measurements for the Boom Clay in Belgium. In: *Applied Clay Science* 75–76, 1–12.

Yu, L., E. Weetjens, X. Sillen, T. Vietor, X. L. Li, P. Delage, V. Labiouse and R. Charlier (2014). Consequences of the Thermal Transient on the Evolution of the Damaged Zone Around a Repository for Heat-Emitting High-Level Radioactive Waste in a Clay Formation: a Performance Assessment Perspective. In: *Rock Mechanics and Rock Engineering* 47 (1), 3–19. DOI: 10.1007/s00603-013-0409-4.

Zeelmaekers, E. (2011). Computerized qualitative and quantitative clay mineralogy: introduction and application to known geological cases. PhD thesis. Leuven, Belgium: Katholieke Universiteit Leuven. Groep Wetenschap en Technologie: Heverlee.

Zeelmaekers, E., M. Honty, A. Derkowski, M. De Craen, N. Vandenberghe and M. Van Geet (2010). A new and improved methodology for qualitative and quantitative mineralogical analysis of Boom Clay. In: *Fourth international meeting on Clays in Natural & Engineered Barriers for Radioactive Waste Confinement*. Nantes, France, pp. 73–74. URL: http://www.nantes2010.com/doc/abstracts/data/pdf/073_074_O_03A_3.pdf.

Zhang, C. and T. Rothfuchs (2004). Experimental study of the hydro-mechanical behaviour of the Callovo-Oxfordian argillite. In: *Clays in Natural and Engineered Barriers for Radioactive Waste Confinement, Applied Clay Science* 26 (1–4), 325–336.

Zhang, C.-L., T. Rothfuchs, H. Moog, J. Dittrich and J. Müller (Mar. 2004). *Thermo-Hydro-Mechanical and Geochemical Behaviour of the Callovo-Oxfordian Argillite and the Opalinus Clay (GRS - 202)*. Braunschweig, Germany: Gesellschaft für Anlagenund Reaktorsicherheit (GRS) mbH. URL: http://www.grs.de/sites/default/files/fue/grs_202_thm_geochemclay.pdf.

Zhang, C.-L., T. Rothfuchs, K. Su and N. Hoteit (2007a). Experimental study of the thermo-hydro-mechanical behaviour of indurated clays. In: *Physics and Chemistry of the Earth, Parts A/B/C, Clay in natural and engineered barriers for radioactive waste confinement - Part 2* 32 (8–14), 957–965.

Zhang, C.-L., T. Rothfuchs, N. Jockwer, K. Wieczorek, J. Dittrich, J. Müller, L. Hartwig and M. Komischke (Feb. 2007b). *Thermal Effects on the Opalinus Clay (GRS - 224), A Joint Heating Experiment of ANDRA and GRS at the Mont Terri URL (HE-D Project)*. Braunschweig, Germany: Gesellschaft für Anlagenund Reaktorsicherheit (GRS) mbH. URL: http://www.grs.de/sites/default/files/fue/grs_224_thermeff_clay.pdf.

A. Database on Boom Clay property values and state variables

This Appendix presents an small database of Boom Clay property values and state variables collected in the literature as part of the OPERA-PG-TUD311 work package.

The tables presented contain the in situ state variables of the Boom Clay host rock (Table A.1), Boom Clay property values governing the hydro-mechanical behaviour (Table A.2) and Boom Clay property values governing the thermal behaviour (Table A.3).

The property and state values are tabulated in terms of range, mean and standard deviation, with additional information being provided as available in the references, i.e. depth, location, test and notes. Please note that this tables provide a summary of a large number of data from the literature however, the information provided into the dataset may not be exhaustive.

Table A.1.: In situ state variables of Boom Clay.

Definition	Symb.	Unit	Range ⟨min;max⟩		μ	σ	Depth	Test[1]	Location	Note	Source
Coefficient of earth pressure at rest	K_0	[−]	0.30	0.90	0.90 0.90 0.80		223.00 223.00 223.00		Mol (B) Mol (B) Mol (B) Mol (B)	Ref. to Horseman et al. (1993) Reference HADES in situ investigations from pressuremeter, dilatometer, self-boring pressuremeter (SBP), hydrofracturing tests, borehole breakouts analysis and back analysis of the stresses in the liner by Bernier et al. (2007a).	ONDRAF/NIRAS (2001a) Coll (2005) Delage et al. (2007) Bernier et al. (2007c)
			0.50	0.80					Mol (B)	Ref. to lab. investigations by Henrion et al. (1984) and Horseman et al. (1987).	Bernier et al. (2007c)
					0.90 1.00 0.84		223.00 223.00 223.00		Mol (B) Mol (B) Mol (B)	Based on SAFIR II Jaky (1944) => (OCR=2.3, φ'=20°)	Mertens et al. (2004) Lima (2011) Baldi et al. (1991b)
Coef. earth pres. at rest	K_0^{NC}	[−]			0.57 0.58 0.74		223.00 223.00 247.00		Mol (B) Mol (B) Mol (B)	Estimated Jaky (1944) formula Based in Plasticity Index PI.	Baldi et al. (1991b). Baldi et al. (1991b) Horseman et al. (1987)
Coef. earth pres. at rest	K_0^{OC}	[−]			1.53 1.14		247.00 247.00		Mol (B) Mol (B)	Based on elastic theory. Based on Alpan (1967).	Horseman et al. (1987) Horseman et al. (1987)
Overconsolidation ratio	OCR	[−]	2.05	2.64	2.40 2.17 2.10 2.30 1.18 1.16 2.05		247.00 223.00 223.00 223.00 223.00 223.00 247.00 223.00		Mol (B) Mol (B) Mol (B) Mol (B) Mol (B) Mol (B) Mol (B) Mol (B)	HADES Unclear Unclear	Horseman et al. (1987) Coll (2005) Li et al. (2007) Delage et al. (2007) Lima (2011) Chandler (2000) Chandler (2000) Baldi et al. (1991b)
Yield stress ratio	YSR	[−]	2.30	2.40	2.00 1.70		230.00 223.00 247.00	OED OED	Mol (B) Mol (B) Mol (B)	Referencing Coop et al. (1995).	Cotecchia and Chandler (2000) Chandler (2000) Chandler (2000)
Total vertical stress	σ_v	[MPa]			4.60 4.50 4.50 4.50		223.00 223.00 223.00 223.00		Mol (B) Mol (B) Mol (B) Mol (B)	Estimate Estimate Estimate	Mertens et al. (2004) Bastiaens et al. (2006) Bernier et al. (2007c) Lima (2011)
Effective vertical stress	σ_v'	[MPa]			2.40 2.50 2.30 2.25 2.25		223.00 247.00 223.00 223.00 223.00		Mol (B) Mol (B) Mol (B) Mol (B) Mol (B)	Estimate Estimate Estimate	Mertens et al. (2004) Horseman et al. (1987) Bastiaens et al. (2006) Bernier et al. (2007c) Lima (2011)
Pore water pressure	u_w	[MPa]			2.20 2.20 2.25		223.00 223.00 223.00		Mol (B) Mol (B) Mol (B)	Estimate Estimate	Mertens et al. (2004) Bastiaens et al. (2006) Bernier et al. (2007c)

↪ Table continues on next page.

Table A.1.: (continued)

Definition	Symb.	Unit	Range ⟨min;max⟩		μ	σ	Depth	Test[1]	Location	Note	Source
					2.25		223.00		Mol (B)	Estimate	Lima (2011)
					2.31		223.00		Mol (B)	ATLAS II (ring83)	De Bruyn and Labat (2002)
					2.27		223.00		Mol (B)	ATLAS II (ring 93)	De Bruyn and Labat (2002)
Preconsolidation pressure	σ_c	[MPa]			1.39		69.42	HCD	Doel 2b (B)		Barnichon et al. (2000)
					2.41		120.57	HCD	Zoersel (B)		Barnichon et al. (2000)
					4.58		229.23	HCD	Mol (B)		Barnichon et al. (2000)
					6.27		313.30	HCD	Weelde (B)	Series 1	Barnichon et al. (2000)
					9.65		545.75	HCD	Blija (NL)		Barnichon et al. (2000)
			5.00	6.00					Mol (B)	Isotropic preconsolidation stress	Li et al. (2007)
					4.85		223.00	OED	Mol (B)	ONA1 sample, casagrande method	Yu et al. (2012)
					5.07		223.00	OED	Mol (B)	ONA2 sample, Casagrande method	Yu et al. (2012)
					5.01		223.00	OED	Mol (B)	ONA3 sample, Casagrande method	Yu et al. (2012)
					5.01		223.00	OED	Mol (B)	Average, Casagrande method	Yu et al. (2012)
					5.20		223.00	OED	Mol (B)	Vertical effective pre-consolidation stress	Lima (2011)
					6.08		223.00		Mol (B)	Initial isotropic max. pre-compression	Baldi et al. (1991b)
Ambient temperature	T	[°]	16.50	16.60			223.00		Mol (B)	ATLAS II	De Bruyn and Labat (2002)
					16.00						Li et al. (2007)

[1] Test type: HCD … Hydrostatic, Consolidated and Drained; OED … Oedometer test

Table A.2.: Boom clay property values governing the hydro-mechanical behaviour.

Definition	Symb.	Unit	Range ⟨min;max⟩		μ	σ	Depth		Test[1]	N[2]	Location	Note	Source
Dry density	ρ_d	[kg m⁻³]	1610	1780									Gens (2012); Gens et al. (2007)
					1540		69.23	69.68			Doel 2b (B)	TRUCK II	Barnichon et al. (2000)
					1540		120.47	121.22			Zoersel (B)	TRUCK II	Barnichon et al. (2000)
					1599		224.52	229.28			Mol (B)	TRUCK II	Barnichon et al. (2000)
					1621		313.22	313.55			Weelde (B)	TRUCK II	Barnichon et al. (2000)
					1666		454.50	478.50			Blija (NL)	TRUCK II	Barnichon et al. (2000)
			1661	1702				223.00			Mol (B)	ATLAS II	De Bruyn and Labat (2002)
					1610		313.22	313.55	Lab		Weelde (B)	TRUCK II - set 2	Wildenborg et al. (2000)
					1607		314.22	315.10	Lab		Weelde (B)	TRACTOR	Wildenborg et al. (2000)
					1590		314.22	315.10	Lab		Weelde (B)	TRACTOR	Wildenborg et al. (2000)
					1612		314.22	315.10	Lab		Weelde (B)	TRACTOR	Wildenborg et al. (2000)
					1600		561.50	561.85	Lab		Blija (NL)	TRACTOR, Asse member	Wildenborg et al. (2000)
					1576		313.55	314.05	Lab		Weelde (B)	TRACTOR	Wildenborg et al. (2000)
					1628		314.22	315.10	Lab		Weelde (B)	TRACTOR	Wildenborg et al. (2000)
					1614		313.55	314.05	Lab		Weelde (B)	TRACTOR	Wildenborg et al. (2000)
					1591		313.55	314.05	Lab		Weelde (B)	TRACTOR	Wildenborg et al. (2000)
					1641		453.50	453.80	Lab		Blija (NL)	TRACTOR	Wildenborg et al. (2000)
					1640		561.50	561.85	Lab		Blija (NL)	TRACTOR, Asse member	Wildenborg et al. (2000)
					1641			223.00	Lab		Mol (B)	ONA1 sample	Yu et al. (2012)
					1670			223.00	Lab		Mol (B)	ONA2 sample	Yu et al. (2012)
					1660			223.00	Lab		Mol (B)	ONA3 sample	Yu et al. (2012)
					1620			223.00	Lab		Mol (B)	CU1 sample	Yu et al. (2012)
					1620			223.00	Lab		Mol (B)	CU2 sample	Yu et al. (2012)
					1640			223.00	Lab		Mol (B)	CU3 sample	Yu et al. (2012)
					1900			243.00			Mol (B)		Baldi et al. (1987, 1991a,b)
					1560		22.00	35.00	Lab	327	Antwerp (B)	BK1 layer	Schittekat et al. (1983)
					1488		35.00	50.00	Lab	162	Antwerp (B)	BK2 layer	Schittekat et al. (1983)
					1502		50.00	80.00	Lab	48	Antwerp (B)	BK3 layer	Schittekat et al. (1983)
			1650	1710				223.00			Mol (B)		Lima (2011)
Bulk density (sat.)	ρ	[kg m⁻³]	1900	2100				200.00				Ref. to NEA (1995) report	Barnichon et al. (2000)
					2000			186.00			Mol (B)	From Boisson (2005)	Bock et al. (2010)
					1956		69.23	69.68			Doel 2b (B)	TRUCK II	Barnichon et al. (2000)
					1967		120.47	121.22			Zoersel (B)	TRUCK II	Barnichon et al. (2000)
					2001		224.52	229.28			Mol (B)	TRUCK II	Barnichon et al. (2000)
					2028		313.22	313.55			Weelde (B)	TRUCK II	Barnichon et al. (2000)
					2054		454.50	478.50			Blija (NL)	TRUCK II	Barnichon et al. (2000)
			1900	2100									Mertens et al. (2004)
			2018	2059				223.00			Mol (B)	ATLAS II	De Bruyn and Labat (2002)
					1950			220.00	FDC	0[3]	S05-01, Offshore		Rijkers et al. (1998)
					2020			662.00	FDC	0[3]	Q07-04, Offshore		Rijkers et al. (1998)
					2080			720.00	FDC	0[3]	M11-01, Offshore		Rijkers et al. (1998)
					2030		5.00	8.00		[4]			Piriyakul and Haegeman (2007)
					2036		5.00	8.00		[4]			Piriyakul and Haegeman (2007)
					2042		5.00	8.00		[4]			Piriyakul and Haegeman (2007)
					2034		5.00	8.00		[4]			Piriyakul and Haegeman (2007)
					2040			223.00	Lab		Mol (B)	ONA1 sample	Yu et al. (2012)

↪ Table continues on next page.

Table A.2.: (continued)

Definition	Symb.	Unit	Range ⟨min;max⟩		μ	σ	Depth		Test[1]	N[2]	Location	Note	Source
					2050			223.00	Lab		Mol (B)	ONA2 sample	Yu et al. (2012)
					2060			223.00	Lab		Mol (B)	ONA3 sample	Yu et al. (2012)
					2010			223.00	Lab		Mol (B)	CU1 sample	Yu et al. (2012)
					2020			223.00	Lab		Mol (B)	CU2 sample	Yu et al. (2012)
					2030			223.00	Lab		Mol (B)	CU3 sample	Yu et al. (2012)
					1980	22.00		35.00	Lab	327	Antwerp (B)	BK1 layer	Schittekat et al. (1983)
					1954	35.00		50.00	Lab	162	Antwerp (B)	BK2 layer	Schittekat et al. (1983)
					1968	50.00		80.00	Lab	48	Antwerp (B)	BK3 layer	Schittekat et al. (1983)
			1990	2050				223.00			Mol (B)		Lima (2011)
Solid (grain) density	ρ_s	[kg m^{-3}]			2650			186.00			Mol (B)	From Boisson (2005)	Bock et al. (2010)
					2658	69.23		69.68			Doel 2b (B)	TRUCK II	Barnichon et al. (2000)
					2692	120.47		121.22			Zoersel (B)	TRUCK II	Barnichon et al. (2000)
					2694	224.52		229.28			Mol (B)	TRUCK II	Barnichon et al. (2000)
					2722	313.22		313.55			Weelde (B)	TRUCK II	Barnichon et al. (2000)
					2741	454.50		478.50			Blija (NL)	TRUCK II	Barnichon et al. (2000)
					2722	313.22		313.55	Lab		Weelde (B)	TRUCK II - set 2	Wildenborg et al. (2000)
					2712	314.22		315.10	Lab		Weelde (B)	TRACTOR	Wildenborg et al. (2000)
					2712	314.22		315.10	Lab		Weelde (B)	TRACTOR	Wildenborg et al. (2000)
					2712	314.22		315.10	Lab		Weelde (B)	TRACTOR	Wildenborg et al. (2000)
					2760	561.50		561.85	Lab		Blija (NL)	TRACTOR, Asse member	Wildenborg et al. (2000)
					2722	313.55		314.05	Lab		Weelde (B)	TRACTOR	Wildenborg et al. (2000)
					2712	314.22		315.10	Lab		Weelde (B)	TRACTOR	Wildenborg et al. (2000)
					2722	313.55		314.05	Lab		Weelde (B)	TRACTOR	Wildenborg et al. (2000)
					2722	313.55		314.05	Lab		Weelde (B)	TRACTOR	Wildenborg et al. (2000)
					2738	453.50		453.80	Lab		Blija (NL)	TRACTOR	Wildenborg et al. (2000)
					2760	561.50		561.85	Lab		Blija (NL)	TRACTOR, Asse member	Wildenborg et al. (2000)
					2740			159.00	Field		Essen (B)	Essen-1, Transition Zone	Aertsens et al. (2013b)
					2700			181.00	Field		Essen (B)	Essen-1, Transition Zone	Aertsens et al. (2013b)
					2720			205.00	Field		Essen (B)	Essen-1, Putte Member	Aertsens et al. (2013b)
					2660			224.00	Field		Essen (B)	Essen-1, Putte Member	Aertsens et al. (2013b)
					2720			232.00	Field		Essen (B)	Essen-1, Putte Member	Aertsens et al. (2013b)
					2700			234.00	Field		Essen (B)	Essen-1, Putte Member	Aertsens et al. (2013b)
					2750			241.00	Field		Essen (B)	Essen-1, Terhagen Member	Aertsens et al. (2013b)
					2670							Referenced in Tinh (2008) and François et al. (2009)	Belanteur et al. (1997)
					2705	22.00		35.00	Lab	327	Antwerp (B)	BK1 layer	Schittekat et al. (1983)
					2703	35.00		50.00	Lab	162	Antwerp (B)	BK2 layer	Schittekat et al. (1983)
					2703	50.00		80.00	Lab	48	Antwerp (B)	BK3 layer	Schittekat et al. (1983)
					2670			223.00			Mol (B)		Lima (2011)
Specific gravity	G_s	[−]			2.6500	218.91		219.91			Essen (B)	Ess75, Putte member	Deng et al. (2011a)
					2.6400	226.65		227.65			Essen (B)	Ess83, Putte member	Deng et al. (2011a)
					2.6800	239.62		240.62			Essen (B)	Ess96, Terhagen member	Deng et al. (2011a)
					2.6800	247.90		248.91			Essen (B)	Ess104, Terhagen member	Deng et al. (2011a)
					2.6700	255.92		256.93			Essen (B)	Ess112, Terhagen member	Deng et al. (2011a)
					2.7100	5.00		8.00			[4]		Piriyakul and Haegeman (2007)
					2.6900	5.00		8.00			[4]		Piriyakul and Haegeman (2007)

↪ Table continues on next page.

Table A.2.: (continued)

Definition	Symb.	Unit	Range ⟨min	;max⟩	μ	σ	Depth		Test[1]	N^2	Location	Note	Source
					2.7000		5.00	8.00			[4]		Piriyakul and Haegeman (2007)
					2.7100		5.00	8.00			[4]		Piriyakul and Haegeman (2007)
					2.6700						Mol (B)		Lima (2011)
					2.6700							Reconstituted Boom Clay	Al-Mukhtar et al. (1996)
Porosity	n	[−]	0.3500	0.4000									Gens (2012)
			0.3000	*									Gens et al. (2007)
			0.3600	0.4000				200.00				Ref. to NEA (1995) report	Barnichon et al. (2000)
					0.3630			186.00			Mol (B)	From Boisson (2005)	Bock et al. (2010)
					0.4203		69.23	69.68			Doel 2b (B)	TRUCK II	Barnichon et al. (2000)
					0.4276		120.47	121.22			Zoersel (B)	TRUCK II	Barnichon et al. (2000)
					0.4064		224.52	229.28			Mol (B)	TRUCK II	Barnichon et al. (2000)
					0.4047		313.22	313.55			Weelde (B)	TRUCK II	Barnichon et al. (2000)
					0.3923		454.50	478.50			Blija (NL)	TRUCK II	Barnichon et al. (2000)
					0.3900			223.00			Mol (B)		Bernier et al. (2007c)
					0.3900			223.00			Mol (B)		Bastiaens et al. (2006)
			0.3900	0.4000				223.00			Mol (B)		Mertens et al. (2004)
			0.3630	0.3780				223.00			Mol (B)	ATLAS II	De Bruyn and Labat (2002)
					0.4500			220.00	FDC	0 [3]	S05-01, Offshore		Rijkers et al. (1998)
					0.4100			662.00	FDC	0 [3]	Q07-04, Offshore		Rijkers et al. (1998)
					0.3600			720.00	FDC	0 [3]	M11-01, Offshore		Rijkers et al. (1998)
					0.4500			220.00	CNL	0 [3]	S05-01, Offshore		Rijkers et al. (1998)
					0.4200			662.00	CNL	0 [3]	Q07-04, Offshore		Rijkers et al. (1998)
					0.4088		313.22	313.55	Lab		Weelde (B)	TRUCK II - set 2	Wildenborg et al. (2000)
					0.4073		314.22	315.10	Lab		Weelde (B)	TRACTOR	Wildenborg et al. (2000)
					0.4135		314.22	315.10	Lab		Weelde (B)	TRACTOR	Wildenborg et al. (2000)
					0.4056		314.22	315.10	Lab		Weelde (B)	TRACTOR	Wildenborg et al. (2000)
					0.4153		561.50	561.85	Lab		Blija (NL)	TRACTOR, Asse member	Wildenborg et al. (2000)
					0.4211		313.55	314.05	Lab		Weelde (B)	TRACTOR	Wildenborg et al. (2000)
					0.3995		314.22	315.10	Lab		Weelde (B)	TRACTOR	Wildenborg et al. (2000)
					0.4070		313.55	314.05	Lab		Weelde (B)	TRACTOR	Wildenborg et al. (2000)
					0.4153		313.55	314.05	Lab		Weelde (B)	TRACTOR	Wildenborg et al. (2000)
					0.4008		453.50	453.80	Lab		Blija (NL)	TRACTOR	Wildenborg et al. (2000)
					0.4057		561.50	561.85	Lab		Blija (NL)	TRACTOR, Asse member	Wildenborg et al. (2000)
					0.3900								Li et al. (2007)
					0.4250		54.00	113.00			Doel 2b (B)	[5]	Yu et al. (2013b)
					0.4230		90.00	186.00			Zoersel (B)	[5]	Yu et al. (2013b)
					0.4090		152.00	280.00			Essen-1 (B)	[5]	Yu et al. (2013b)
					0.4030		185.00	288.00			Mol-1 (B)	[5]	Yu et al. (2013b)
					0.3570		259.00	389.00			Weelde-1 (B)	[5]	Yu et al. (2013b)
					0.2040			223.00	SEM		Mol (B)	[7]	Desbois et al. (2009)
					0.2600			223.00	SEM		Mol (B)	[7]	Desbois et al. (2009)
					0.3900			159.00	Field		Essen (B)	Essen-1, Transition Zone	Aertsens et al. (2013b)
					0.4100			181.00	Field		Essen (B)	Essen-1, Transition Zone	Aertsens et al. (2013b)
					0.4300			205.00	Field		Essen (B)	Essen-1, Putte Member	Aertsens et al. (2013b)
					0.4600			224.00	Field		Essen (B)	Essen-1, Putte Member	Aertsens et al. (2013b)
					0.4500			232.00	Field		Essen (B)	Essen-1, Putte Member	Aertsens et al. (2013b)

Table A.2.: (continued)

Definition	Symb.	Unit	Range ⟨min;max⟩		μ	σ	Depth		Test[1]	N[2]	Location	Note	Source
					0.4500			234.00	Field		Essen (B)	Essen-1, Putte Member	Aertsens et al. (2013b)
					0.4100			241.00	Field		Essen (B)	Essen-1, Terhagen Member	Aertsens et al. (2013b)
					0.4000	0.0100					Essen (B)	Essen-1, Transition Zone + terhagen	Aertsens et al. (2013b)
					0.4500	0.0100					Essen (B)	Essen-1, Putte Member	Aertsens et al. (2013b)
					0.4300	0.0300					Essen (B)	Essen-1, All	Aertsens et al. (2013b)
					0.3650			223.00	Lab		Mol (B)	Sampled at connecting gallery.	Bésuelle et al. (2013)
					0.3750			243.00			Mol (B)		Baldi et al. (1987, 1991a,b)
			0.358	0.3820				223.00			Mol (B)		Lima (2011)
Void ratio	e	[−]			0.7850		218.91	219.91			Essen (B)	Ess75, Putte member	Deng et al. (2011a)
					0.7300		226.65	227.65			Essen (B)	Ess83, Putte member	Deng et al. (2011a)
					0.7150		239.62	240.62			Essen (B)	Ess96, Terhagen member	Deng et al. (2011a)
					0.7000		247.90	248.91			Essen (B)	Ess104, Terhagen member	Deng et al. (2011a)
					0.7550		255.92	256.93			Essen (B)	Ess112, Terhagen member	Deng et al. (2011a)
					0.6690			223.00	Lab		Mol (B)	ONA1 sample	Yu et al. (2012)
					0.6700			223.00	Lab		Mol (B)	ONA2 sample	Yu et al. (2012)
					0.6650			223.00	Lab		Mol (B)	ONA3 sample	Yu et al. (2012)
					0.6970			223.00	Lab		Mol (B)	CU1 sample	Yu et al. (2012)
					0.6990			223.00	Lab		Mol (B)	CU2 sample	Yu et al. (2012)
					0.6770			223.00	Lab		Mol (B)	CU3 sample	Yu et al. (2012)
			0.5600	0.618				223.00			Mol (B)		Lima (2011)
Gravimetric water content	w	[−]	0.200	0.300									Gens (2012)
			0.095	*									Gens et al. (2007)
			0.190	0.240				200.00				Ref. to NEA (1995) report	Barnichon et al. (2000)
			0.215	0.215				186.00			Mol (B)	From Boisson (2005)	Bock et al. (2010)
					0.270		69.23	69.68			Doel 2b (B)	TRUCK II	Barnichon et al. (2000)
					0.277		120.47	121.22			Zoersel (B)	TRUCK II	Barnichon et al. (2000)
					0.254		224.52	229.28			Mol (B)	TRUCK II	Barnichon et al. (2000)
					0.251		313.22	313.55			Weelde (B)	TRUCK II	Barnichon et al. (2000)
					0.235		454.50	478.50			Blija (NL)	TRUCK II	Barnichon et al. (2000)
					0.297		218.91	219.91			Essen (B)	Ess75, Putte member	Deng et al. (2011a)
					0.272		226.65	227.65			Essen (B)	Ess83, Putte member	Deng et al. (2011a)
					0.265		239.62	240.62			Essen (B)	Ess96, Terhagen member	Deng et al. (2011a)
					0.277		247.90	248.91			Essen (B)	Ess104, Terhagen member	Deng et al. (2011a)
					0.273		255.92	256.93			Essen (B)	Ess112, Terhagen member	Deng et al. (2011a)
			0.300	0.400				223.00			Mol (B)		Bastiaens et al. (2006)
			0.190	0.240				223.00			Mol (B)		Mertens et al. (2004)
			0.205	0.221				223.00			Mol (B)	ATLAS II	De Bruyn and Labat (2002)
					0.240			220.00	CNL	0[3]		S05-01, Offshore	Rijkers et al. (1998)
					0.220			662.00	CNL	0[3]		Q07-04, Offshore	Rijkers et al. (1998)
					0.249		313.22	313.55	Lab		Weelde (B)	TRUCK II - set 2	Wildenborg et al. (2000)
					0.253		314.22	315.10	Lab		Weelde (B)	TRACTOR	Wildenborg et al. (2000)
					0.261		314.22	315.10	Lab		Weelde (B)	TRACTOR	Wildenborg et al. (2000)
					0.254		314.22	315.10	Lab		Weelde (B)	TRACTOR	Wildenborg et al. (2000)
					0.258		561.50	561.85	Lab		Blija (NL)	TRACTOR, Asse member	Wildenborg et al. (2000)
					0.254		313.55	314.05	Lab		Weelde (B)	TRACTOR	Wildenborg et al. (2000)

Table A.2.: (continued)

Definition	Symb.	Unit	Range ⟨min;max⟩		μ	σ	Depth		Test[1]	N[2]	Location	Note	Source
					0.252		314.22	315.10	Lab		Weelde (B)	TRACTOR	Wildenborg et al. (2000)
					0.239		313.55	314.05	Lab		Weelde (B)	TRACTOR	Wildenborg et al. (2000)
					0.243		313.55	314.05	Lab		Weelde (B)	TRACTOR	Wildenborg et al. (2000)
					0.230		453.50	453.80	Lab		Blija (NL)	TRACTOR	Wildenborg et al. (2000)
					0.230		561.50	561.85	Lab		Blija (NL)	TRACTOR, Asse member	Wildenborg et al. (2000)
			0.220	0.270									Li et al. (2007)
					0.294		5.00	8.00				[4]	Piriyakul and Haegeman (2007)
					0.240		5.00	8.00				[4]	Piriyakul and Haegeman (2007)
					0.283		5.00	8.00				[4]	Piriyakul and Haegeman (2007)
					0.233		5.00	8.00				[4]	Piriyakul and Haegeman (2007)
					0.243			223.00	Lab		Mol (B)	ONA1 sample	Yu et al. (2012)
					0.238			223.00	Lab		Mol (B)	ONA2 sample	Yu et al. (2012)
					0.238			223.00	Lab		Mol (B)	ONA3 sample	Yu et al. (2012)
					0.240			223.00	Lab		Mol (B)	CU1 sample	Yu et al. (2012)
					0.242			223.00	Lab		Mol (B)	CU2 sample	Yu et al. (2012)
					0.238			223.00	Lab		Mol (B)	CU3 sample	Yu et al. (2012)
			0.200	0.25				223.00	Lab		Mol (B)	Sampled at connecting gallery.	Bésuelle et al. (2013)
Degree of water saturation	S	[−]			1.0093		69.23	69.68			Doel 2b (B)	TRUCK II	Barnichon et al. (2000)
					0.9856		120.47	121.22			Zoersel (B)	TRUCK II	Barnichon et al. (2000)
					0.9912		224.52	229.28			Mol (B)	TRUCK II	Barnichon et al. (2000)
					0.9801		313.22	313.55			Weelde (B)	TRUCK II	Barnichon et al. (2000)
					0.9909		454.50	478.50			Blija (NL)	TRUCK II	Barnichon et al. (2000)
					1.0000		218.91	219.91			Essen (B)	Ess75, Putte member	Deng et al. (2011a)
					0.9800		226.65	227.65			Essen (B)	Ess83, Putte member	Deng et al. (2011a)
					0.9900		239.62	240.62			Essen (B)	Ess96, Terhagen member	Deng et al. (2011a)
					1.0000		247.90	248.91			Essen (B)	Ess104, Terhagen member	Deng et al. (2011a)
					0.9700		255.92	256.93			Essen (B)	Ess112, Terhagen member	Deng et al. (2011a)
			0.9400	1.0000				223.00			Mol (B)	ATLAS II	De Bruyn and Labat (2002)
					0.9830		313.22	313.55	Lab		Weelde (B)	TRUCK II - set 2	Wildenborg et al. (2000)
					1.0010		314.22	315.10	Lab		Weelde (B)	TRACTOR	Wildenborg et al. (2000)
					1.0070		314.22	315.10	Lab		Weelde (B)	TRACTOR	Wildenborg et al. (2000)
					1.0100		314.22	315.10	Lab		Weelde (B)	TRACTOR	Wildenborg et al. (2000)
					0.9940		561.50	561.85	Lab		Blija (NL)	TRACTOR, Asse member	Wildenborg et al. (2000)
					0.9500		313.55	314.05	Lab		Weelde (B)	TRACTOR	Wildenborg et al. (2000)
					1.0270		314.22	315.10	Lab		Weelde (B)	TRACTOR	Wildenborg et al. (2000)
					0.9480		313.55	314.05	Lab		Weelde (B)	TRACTOR	Wildenborg et al. (2000)
					0.9310		313.55	314.05	Lab		Weelde (B)	TRACTOR	Wildenborg et al. (2000)
					0.9400		453.50	453.80	Lab		Blija (NL)	TRACTOR	Wildenborg et al. (2000)
					0.9290		561.50	561.85	Lab		Blija (NL)	TRACTOR, Asse member	Wildenborg et al. (2000)
					0.9640				Lab		Mol (B)	ONA1 sample	Yu et al. (2012)
					0.9740				Lab		Mol (B)	ONA2 sample	Yu et al. (2012)
					0.9810				Lab		Mol (B)	ONA3 sample	Yu et al. (2012)
					0.9500				Lab		Mol (B)	CU1 sample	Yu et al. (2012)
					0.9520				Lab		Mol (B)	CU2 sample	Yu et al. (2012)
					0.9670				Lab		Mol (B)	CU3 sample	Yu et al. (2012)
			0.9100	1				223.00			Mol (B)		Lima (2011)

Table A.2.: (continued)

Definition	Symb.	Unit	Range ⟨min;max⟩		μ	σ	Depth		Test[1]	N[2]	Location	Note	Source
Liquid limit	w_L	[−]	0.5500	0.8000				223.00			Mol (B)	Char. range HADES.	Gens et al. (2007); Li et al. (2007)
					0.7800		218.91	219.91			Essen (B)	Ess75, Putte member	Deng et al. (2011a)
					0.7000		226.65	227.65			Essen (B)	Ess83, Putte member	Deng et al. (2011a)
					0.6900		239.62	240.62			Essen (B)	Ess96, Terhagen member	Deng et al. (2011a)
					0.6800		247.90	248.91			Essen (B)	Ess104, Terhagen member	Deng et al. (2011a)
					0.6200		255.92	256.93			Essen (B)	Ess112, Terhagen member	Deng et al. (2011a)
					0.6400		22.00	80.00			Antwerp (B)	Reconstituted, shallow	Bouazza et al. (1996)
					0.7520		313.55	314.05			Weelde (B)	TRACTOR	Wildenborg et al. (2000)
					0.9320		314.22	315.10			Weelde (B)	TRACTOR	Wildenborg et al. (2000)
					1.0390		453.50	453.80			Blija (NL)	TRACTOR	Wildenborg et al. (2000)
					1.0510		561.50	561.85			Blija (NL)	TRACTOR, Asse member	Wildenborg et al. (2000)
					0.6538		5.00	8.00		4			Piriyakul and Haegeman (2007)
					0.6595		5.00	8.00		4			Piriyakul and Haegeman (2007)
					0.5751		5.00	8.00		4			Piriyakul and Haegeman (2007)
					0.5412		5.00	8.00		4			Piriyakul and Haegeman (2007)
					0.5600						Mol (B)		Lima (2011)
			0.3090	0.6300	0.5100	0.0830					Mol (B)		Bésuelle et al. (2013)
					0.6000			223.00	Lab		Mol (B)	Sampled at connecting gallery.	Baldi et al. (1987, 1991a,b)
					0.6660			243.00					
			0.5900	0.7600								Referenced in Tinh (2008) and François et al. (2009)	Belanteur et al. (1997)
			0.6000	0.7000							Mol (B)		Baldi et al. (1988)
					0.6600						Mol (B)		Horseman et al. (1987)
					0.6950								Sultan (1997)
					0.7000							Reconstituted Boom Clay	Al-Mukhtar et al. (1996)
					0.6600		22.00	35.00	Lab	327	Antwerp (B)	BK1 layer	Schittekat et al. (1983)
					0.7300		35.00	50.00	Lab	162	Antwerp (B)	BK2 layer	Schittekat et al. (1983)
					0.6000		50.00	80.00	Lab	48	Antwerp (B)	BK3 layer	Schittekat et al. (1983)
Plastic limit	w_P	[−]			0.3300		218.91	219.91			Essen (B)	Ess75, Putte member	Deng et al. (2011a)
					0.3300		226.65	227.65			Essen (B)	Ess83, Putte member	Deng et al. (2011a)
					0.3300		239.62	240.62			Essen (B)	Ess96, Terhagen member	Deng et al. (2011a)
					0.2900		247.90	248.91			Essen (B)	Ess104, Terhagen member	Deng et al. (2011a)
					0.2500		255.92	256.93			Essen (B)	Ess112, Terhagen member	Deng et al. (2011a)
					0.2700						Antwerp (B)	Reconstituted, shallow	Bouazza et al. (1996)
					0.2850		313.55	314.05			Weelde (B)	TRACTOR	Wildenborg et al. (2000)
					0.2980		314.22	315.10			Weelde (B)	TRACTOR	Wildenborg et al. (2000)
					0.3120		453.50	453.80			Blija (NL)	TRACTOR	Wildenborg et al. (2000)
					0.3250		561.50	561.85			Blija (NL)	TRACTOR, Asse member	Wildenborg et al. (2000)
			0.2300	0.2900									Li et al. (2007)
					0.2223		5.00	8.00		4			Piriyakul and Haegeman (2007)
					0.2321		5.00	8.00		4			Piriyakul and Haegeman (2007)
					0.2102		5.00	8.00		4			Piriyakul and Haegeman (2007)
					0.2289		5.00	8.00		4			Piriyakul and Haegeman (2007)
					0.2900			223.00			Mol (B)		Lima (2011)
					0.2600			223.00	Lab		Mol (B)	Sampled at connecting gallery.	Bésuelle et al. (2013)

↪ Table continues on next page.

Table A.2.: (continued)

Definition	Symb.	Unit	Range ⟨min	max⟩	μ	σ	Depth	Test[1]	N^{2}	Location	Note	Source
			0.2200	0.2600							Referenced in Tinh (2008) and François et al. (2009)	Belanteur et al. (1997)
			0.1300	0.1900						Mol (B)		Baldi et al. (1988)
					0.2500					Mol (B)		Horseman et al. (1987)
					0.2500							Sultan (1997)
					0.2500						Reconstituted Boom Clay	Al-Mukhtar et al. (1996)
Plasticity index	I_P	[−]	0.3200	0.5100			223.00			Mol (B)	Characteristic range HADES	Volckaert et al. (2004); Gens et al. (2007); Li et al. (2007)
					0.4500		218.91 219.91			Essen (B)	Ess75, Putte member	Deng et al. (2011a)
					0.3700		226.65 227.65			Essen (B)	Ess83, Putte member	Deng et al. (2011a)
					0.3600		239.62 240.62			Essen (B)	Ess96, Terhagen member	Deng et al. (2011a)
					0.3900		247.90 248.91			Essen (B)	Ess104, Terhagen member	Deng et al. (2011a)
					0.3700		255.92 256.93			Essen (B)	Ess112, Terhagen member	Deng et al. (2011a)
					0.4670		313.55 314.05			Weelde (B)	TRACTOR	Wildenborg et al. (2000)
					0.6350		314.22 315.10			Weelde (B)	TRACTOR	Wildenborg et al. (2000)
					0.7270		453.50 453.80			Blija (NL)	TRACTOR	Wildenborg et al. (2000)
					0.7260		561.50 561.85			Blija (NL)	TRACTOR, Asse member	Wildenborg et al. (2000)
					0.4315		5.00 8.00			[4]		Piriyakul and Haegeman (2007)
					0.4274		5.00 8.00			[4]		Piriyakul and Haegeman (2007)
					0.3649		5.00 8.00			[4]		Piriyakul and Haegeman (2007)
					0.3123		5.00 8.00			[4]		Piriyakul and Haegeman (2007)
					0.3300		223.00	Lab		Mol (B)	Sampled at connecting gallery.	Bésuelle et al. (2013)
			0.3700	0.5000							Referenced in Tinh (2008) and François et al. (2009)	Belanteur et al. (1997)
			0.4500	0.5500						Mol (B)		Baldi et al. (1988)
					0.4700					Mol (B)		Horseman et al. (1987)
					0.4450							Sultan (1997)
					0.4500						Reconstituted Boom Clay	Al-Mukhtar et al. (1996)
					0.4000		22.00 35.00	Lab	327	Antwerp (B)	BK1 layer	Schittekat et al. (1983)
					0.4400		35.00 50.00	Lab	162	Antwerp (B)	BK2 layer	Schittekat et al. (1983)
					0.3500		50.00 80.00	Lab	48	Antwerp (B)	BK3 layer	Schittekat et al. (1983)
					0.2700		223.00			Mol (B)		Lima (2011)
Effective Young's modulus	E	[MPa]	200.00	400.00								Gens (2012); Gens et al. (2007)
			200.00	400.00			200.00					Barnichon et al. (2000)
					300.0		223.00			Mol (B)	Ref. to NEA (1995) report Estimated from analysis and interpretation of the in situ measurements made during excavation of the test drift	Bernier et al. (2007c)
					300.0		223.00			Mol (B)	Characteristic range HADES.	Volckaert et al. (2004) Mertens et al. (2004) Li et al. (2007)
			200.00	400.00	300.0							
					500.00		223.00	HPC		Mol (B)	Sampled at connecting gallery - Response measured upon unloading and reloading.	Bésuelle et al. (2013)
					150.00		223.00	HPC		Mol (B)	Sampled at connecting gallery - Initial slope.	Bésuelle et al. (2013)

↪ Table continues on next page.

Table A.2.: (continued)

Definition	Symb.	Unit	Range ⟨min;max⟩		μ	σ	Depth		Test[1]	N^2	Location	Note	Source
					330.00							Ref. to Laloui (1993)	François et al. (2009)
					680.000		18.00	22.00	SWV		Antwerp (B)	BK0 layer	Schittekat et al. (1983)
					735.000		22.00	35.00	SWV		Antwerp (B)	BK1 layer	Schittekat et al. (1983)
Dynamic Young's modulus	E_{dyn}	[MPa]	1832.65	3056.42			220		DT	0 [3]		[6]	Rijkers et al. (1998)
			1752.51	2790.97			350		DT	0 [3]		[6]	Rijkers et al. (1998)
			1634.10	2417.32			565		DT	0 [3]		[6]	Rijkers et al. (1998)
			1976.80	3546.73			585		DT	0 [3]		[6]	Rijkers et al. (1998)
			1980.34	3546.77			605		DT	0 [3]		[6]	Rijkers et al. (1998)
			1805.60	2955.95			645		DT	0 [3]		[6]	Rijkers et al. (1998)
			1976.96	3546.90			660		DT	0 [3]		[6]	Rijkers et al. (1998)
			2039.90	3781.17			660		DT	0 [3]		[6]	Rijkers et al. (1998)
			1753.24	2791.70			685		DT	0 [3]		[6]	Rijkers et al. (1998)
			1977.03	3546.96			690		DT	0 [3]		[6]	Rijkers et al. (1998)
			1998.03	3417.61			700		DT	0 [3]		[6]	Rijkers et al. (1998)
			1935.09	3686.84			700		DT	0 [3]		[6]	Rijkers et al. (1998)
			1980.56	3543.49			705		DT	0 [3]		[6]	Rijkers et al. (1998)
			1917.63	3333.71			705		DT	0 [3]		[6]	Rijkers et al. (1998)
			2186.86	4344.21			710		DT	0 [3]		[6]	Rijkers et al. (1998)
			1938.63	3417.66			720		DT	0 [3]		[6]	Rijkers et al. (1998)
			1980.62	3547.06			735		DT	0 [3]		[6]	Rijkers et al. (1998)
			1861.80	3138.02			760		DT	0 [3]		[6]	Rijkers et al. (1998)
			1970.20	3505.17			765		DT	0 [3]		[6]	Rijkers et al. (1998)
			2249.94	4610.08			775		DT	0 [3]		[6]	Rijkers et al. (1998)
			1991.20	3638.06			775		DT	0 [3]		[6]	Rijkers et al. (1998)
			2043.71	3781.47			800		DT	0 [3]		[6]	Rijkers et al. (1998)
			2082.25	3942.39			840		DT	0 [3]		[6]	Rijkers et al. (1998)
			1917.94	3334.02			850		DT	0 [3]		[6]	Rijkers et al. (1998)
			2043.84	3785.10			860		DT	0 [3]		[6]	Rijkers et al. (1998)
			1914.53	3330.62			890		DT	0 [3]		[6]	Rijkers et al. (1998)
			2001.95	3645.30			890		DT	0 [3]		[6]	Rijkers et al. (1998)
			1974.00	3547.42			900		DT	0 [3]		[6]	Rijkers et al. (1998)
			2043.94	3788.69			905		DT	0 [3]		[6]	Rijkers et al. (1998)
			1988.13	3589.54			970		DT	0 [3]		[6]	Rijkers et al. (1998)
			2114.14	4047.71			1030		DT	0 [3]		[6]	Rijkers et al. (1998)
			2037.39	3785.65			1110		DT	0 [3]		[6]	Rijkers et al. (1998)
			1915.04	3331.12			1120		DT	0 [3]		[6]	Rijkers et al. (1998)
			2184.42	4345.26			1190		DT	0 [3]		[6]	Rijkers et al. (1998)
			2268.62	4681.20			1320		DT	0 [3]		[6]	Rijkers et al. (1998)
			2184.83	4345.66			1375		DT	0 [3]		[6]	Rijkers et al. (1998)
			2219.90	4471.65			1425		DT	0 [3]		[6]	Rijkers et al. (1998)
Effective Poisson's ratio	ν	[−]	0.400	0.450			200.00					Ref. to NEA (1995) report	Barnichon et al. (2000)
					0.430		186.00				Mol (B)	From Boisson (2005)	Bock et al. (2010)
					0.125						Mol (B)	Characteristic range HADES.	Volckaert et al. (2004); Bernier et al. (2007c)

Table A.2.: (continued)

Definition	Symb.	Unit	Range ⟨min;max⟩	μ	σ	Depth		Test[1]	N[2]	Location	Note	Source
				0.400								Mertens et al. (2004)
				0.200								Lima (2011); Romero (1999)
				0.134							Ref. to Laloui (1993)	François et al. (2009)
				0.480		18.00	22.00	SWV		Antwerp (B)	BK0 layer	Schittekat et al. (1983)
				0.468		22.00	35.00	SWV		Antwerp (B)	BK1 layer	Schittekat et al. (1983)
Compression index	C_c	[−]		0.2100			223.00	OED		Mol (B)	ONA1 sample	Yu et al. (2012)
				0.1800			223.00	OED		Mol (B)	ONA2 sample	Yu et al. (2012)
				0.1810			223.00	OED		Mol (B)	ONA3 sample	Yu et al. (2012)
				0.1900			223.00	OED		Mol (B)	Average	Yu et al. (2012)
				0.3780		218.91	219.91	OED		Essen (B)	Ess75, Putte member	Deng et al. (2011a)
				0.3450		226.65	227.65	OED		Essen (B)	Ess83, Putte member	Deng et al. (2011a)
				0.3750		239.62	240.62	OED		Essen (B)	Ess96, Terhagen member	Deng et al. (2011a)
				0.3270		247.90	248.91	OED		Essen (B)	Ess104, Terhagen member	Deng et al. (2011a)
				0.3020		255.92	256.93	OED		Essen (B)	Ess112, Terhagen member	Deng et al. (2011a)
				0.4050			223.00	OED		Mol (B)		Deng et al. (2011a)
Swelling index	C_s	[−]		0.0220			223.00	OED		Mol (B)	ONA1 sample	Yu et al. (2012)
				0.0260			223.00	OED		Mol (B)	ONA2 sample	Yu et al. (2012)
				0.0280			223.00	OED		Mol (B)	ONA3 sample	Yu et al. (2012)
				0.0250			223.00	OED		Mol (B)	Average	Yu et al. (2012)
				0.1050		218.91	219.91	OED		Essen (B)	Ess75, Putte member, a-b	Deng et al. (2011a)
				0.1100		226.65	227.65	OED		Essen (B)	Ess83, Putte member, a-b	Deng et al. (2011a)
				0.0780		239.62	240.62	OED		Essen (B)	Ess96, Terhagen member, a-b	Deng et al. (2011a)
				0.0660		247.90	248.91	OED		Essen (B)	Ess104, Terhagen member, a-b	Deng et al. (2011a)
				0.0410		255.92	256.93	OED		Essen (B)	Ess112, Terhagen member, a-b	Deng et al. (2011a)
				0.0990			223.00	OED		Mol (B)		Deng et al. (2011a)
				0.1580		218.91	219.91	OED		Essen (B)	Ess75, Putte member, e-f	Deng et al. (2011a)
				0.1390		226.65	227.65	OED		Essen (B)	Ess83, Putte member, e-f	Deng et al. (2011a)
				0.1360		239.62	240.62	OED		Essen (B)	Ess96, Terhagen member, e-f	Deng et al. (2011a)
				0.1200		247.90	248.91	OED		Essen (B)	Ess104, Terhagen member, e-f	Deng et al. (2011a)
				0.0820		255.92	256.93	OED		Essen (B)	Ess112, Terhagen member, e-f	Deng et al. (2011a)
				0.1570			223.00	OED		Mol (B)		Deng et al. (2011a)
Effective cohesion	c'	[MPa]		1.0000			200.00				from NEA (1995) report	Barnichon et al. (2000)
				0.1330			69.42	CU	(1;3)	Doel 2b (B)	TRUCK II	Barnichon et al. (2000)
				0.2330			120.57	CU	(1;3)	Zoersel (B)	TRUCK II	Barnichon et al. (2000)
				0.3960			229.23	CU	(1;3)	Mol (B)	TRUCK II	Barnichon et al. (2000)
				0.1770			313.30	CU	(1;3)	Weelde (B)	TRUCK II - Series 1	Barnichon et al. (2000)
				0.3450			313.30	CU	(1;3)	Weelde (B)	TRUCK II - Series 2	Barnichon et al. (2000)
				0.7150			445.75	CU	(1;3)	Blija (NL)	TRUCK II	Barnichon et al. (2000)
				0.1100		218.91	219.91	CD	(1;3)	Essen (B)	Ess75, Putte member	Deng et al. (2011a)
				0.1800		226.65	227.65	CD	(1;3)	Essen (B)	Ess83, Putte member	Deng et al. (2011a)
				0.1100		239.62	240.62	CD	(1;3)	Essen (B)	Ess96, Terhagen member	Deng et al. (2011a)
				0.1800			223.00	CD		Mol (B)	Compression + extension	Coll (2005)
				0.3960			223.00			Mol (B)	General characteristic value	Mertens et al. (2004)
				0.0210		5.00	25.00	CD	(1;3)	Rumst (B)	near Antwerp (B)	Spagnoli et al. (2012)
				0.0100				CU		Antwerp (B)	Reconstituted, shallow, post-peak	Bouazza et al. (1996)

↪ Table continues on next page.

Table A.2.: (continued)

Definition	Symb.	Unit	Range ⟨min	;max⟩	μ	σ	Depth		Test[1]	N[2]	Location	Note	Source
					0.5040		314.22	315.10	CU	(1;3)	Weelde (B)	TRACTOR	Wildenborg et al. (2000)
					0.0930		314.22	315.10	CU	(1;3)	Weelde (B)	TRACTOR	Wildenborg et al. (2000)
					0.2490		314.22	315.10	CU	(1;3)	Weelde (B)	TRACTOR	Wildenborg et al. (2000)
					1.8180		561.50	561.85	CU	(1;3)	Blija (NL)	TRACTOR, Asse member	Wildenborg et al. (2000)
					0.3000			223.00			Mol (B)	Characteristic range HADES. Range from numerous tests. Averaged over a range of mean effective stress of 2.5-4 Mpa.	Volckaert et al. (2004); Bernier et al. (2007c); Li et al. (2007)
					0.0800			223.00	HPC		Mol (B)	Sampled at connecting gallery.	Bésuelle et al. (2013)
					0.1340							Ref. to Laloui (1993)	François et al. (2009)
			0.0130	*	0.0220		22.00	35.00	CU	327	Antwerp (B)	BK1 layer	Schittekat et al. (1983)
			0.0210	*	0.0400		35.00	50.00	CU	162	Antwerp (B)	BK2 layer	Schittekat et al. (1983)
			0.0430	*	0.0480		50.00	80.00	CU	48	Antwerp (B)	BK3 layer	Schittekat et al. (1983)
			0.1750	0.300								Average near surface. Ref. to Schittekat et al. (1983) and Al-Mukhtar et al. (1996).	Dehandschutter et al. (2005)
Consolidated undrained cohesion	c_{cu}	[MPa]			0.1250			69.42	CU	(1;3)	Doel 2b (B)	TRUCK II	Barnichon et al. (2000)
					0.1680			120.57	CU	(1;3)	Zoersel (B)	TRUCK II	Barnichon et al. (2000)
					0.3330			229.23	CU	(1;3)	Mol (B)	TRUCK II	Barnichon et al. (2000)
					0.2810			313.30	CU	(1;3)	Weelde (B)	TRUCK II - Series 1	Barnichon et al. (2000)
					0.2980			313.30	CU	(1;3)	Weelde (B)	TRUCK II - Series 2	Barnichon et al. (2000)
					1.0100			445.75	CU	(1;3)	Blija (NL)	TRUCK II	Barnichon et al. (2000)
			0.5000	1.0000				223.00			Mol (B)		ONDRAF/NIRAS (2001b); Bastiaens et al. (2006)
					0.2960		314.22	315.10	CU	(1;3)	Weelde (B)	TRACTOR	Wildenborg et al. (2000)
					0.2470		314.22	315.10	CU	(1;3)	Weelde (B)	TRACTOR	Wildenborg et al. (2000)
					0.1640		314.22	315.10	CU	(1;3)	Weelde (B)	TRACTOR	Wildenborg et al. (2000)
					1.8230		561.50	561.85	CU	(1;3)	Blija (NL)	TRACTOR, Asse member	Wildenborg et al. (2000)
			0.5000	1.3000								Range from numerous tests.	Li et al. (2007)
					0.80			223.00	CU	(1;6)	Mol (B)	ATLAS samples	De Bruyn and Labat (2002)
Effective friction angle	φ'	[°]	18.00	22.00				200.00				Ref. to NEA (1995) report	Barnichon et al. (2000)
					17.94			69.42	CU	(1;3)	Doel 2b (B)	TRUCK II	Barnichon et al. (2000)
					9.31			120.57	CU	(1;3)	Zoersel (B)	TRUCK II	Barnichon et al. (2000)
					9.62			229.23	CU	(1;3)	Mol (B)	TRUCK II	Barnichon et al. (2000)
					11.01			313.30	CU	(1;3)	Weelde (B)	TRUCK II - Series 1	Barnichon et al. (2000)
					8.81			313.30	CU	(1;3)	Weelde (B)	TRUCK II - Series 2	Barnichon et al. (2000)
					8.83			445.75	CU	(1;3)	Blija (NL)	TRUCK II	Barnichon et al. (2000)
					12.40		218.91	219.91	CD	(1;3)	Essen (B)	Ess75, Putte member	Deng et al. (2011a)
					13.00		226.65	227.65	CD	(1;3)	Essen (B)	Ess83, Putte member	Deng et al. (2011a)
					13.50		239.62	240.62	CD	(1;3)	Essen (B)	Ess96, Terhagen member	Deng et al. (2011a)
					18.00			223.00	CD		Mol (B)	Compression + extension	Coll (2005)
					11.00			223.00			Mol (B)	General characteristic value near Antwerp (B)	Mertens et al. (2004)
					23.00		5.00	25.00	CD	(1;3)	Rumst (B)		Spagnoli et al. (2012)
					18.50				CU		Antwerp (B)	Reconstituted, shallow, post-peak	Bouazza et al. (1996)
					8.10		314.22	315.10	CU	(1;3)	Weelde (B)	TRACTOR	Wildenborg et al. (2000)

↪ Table continues on next page.

Table A.2.: (continued)

Definition	Symb.	Unit	Range ⟨min;max⟩		μ	σ	Depth		Test[1]	N[2]	Location	Note	Source
					13.10		314.22	315.10	CU	(1;3)	Weelde (B)	TRACTOR	Wildenborg et al. (2000)
					11.60		314.22	315.10	CU	(1;3)	Weelde (B)	TRACTOR	Wildenborg et al. (2000)
					2.10		561.50	561.85	CU	(1;3)	Blija (NL)	TRACTOR, Asse member	Wildenborg et al. (2000)
			18.00	25.00				223.00			Mol (B)	Characteristic range HADES. Range from numerous tests. Averaged over a range of mean effective stress of 2.5-4 Mpa.	Volckaert et al. (2004); Bernier et al. (2007c); Li et al. (2007)
					18.00			223.00	HPC		Mol (B)	Sampled at connecting gallery.	Bésuelle et al. (2013)
					19.50							Ref. to Laloui (1993)	François et al. (2009)
			17.00	*	25.04		22.00	35.00	CU	327	Antwerp (B)	BK1 layer	Schittekat et al. (1983)
			12.92	*	17.05		35.00	50.00	CU	162	Antwerp (B)	BK2 layer	Schittekat et al. (1983)
			15.32	*	20.11		50.00	80.00	CU	48	Antwerp (B)	BK3 layer	Schittekat et al. (1983)
					18.00							Average near surface. Ref. to Schittekat et al. (1983) and Al-Mukhtar et al. (1996).	Dehandschutter et al. (2005)
Consolidated undrained friction angle	φ_u	[°]			4.00			200.00				Ref. to NEA (1995) report	Barnichon et al. (2000)
					15.21			69.42	CU	(1;3)	Doel 2b (B)	TRUCK II	Barnichon et al. (2000)
					9.20			120.57	CU	(1;3)	Zoersel (B)	TRUCK II	Barnichon et al. (2000)
					9.82			229.23	CU	(1;3)	Mol (B)	TRUCK II	Barnichon et al. (2000)
					9.35			313.30	CU	(1;3)	Weelde (B)	TRUCK II - Series 1	Barnichon et al. (2000)
					8.67			313.30	CU	(1;3)	Weelde (B)	TRUCK II - Series 2	Barnichon et al. (2000)
					5.67			445.75	CU	(1;3)	Blija (NL)	TRUCK II	Barnichon et al. (2000)
					4.00			223.00			Mol (B)		ONDRAF/NIRAS (2001b); Bastiaens et al. (2006)
					9.20		314.22	315.10	CU	(1;3)	Weelde (B)	TRACTOR	Wildenborg et al. (2000)
					8.70		314.22	315.10	CU	(1;3)	Weelde (B)	TRACTOR	Wildenborg et al. (2000)
					9.50		314.22	315.10	CU	(1;3)	Weelde (B)	TRACTOR	Wildenborg et al. (2000)
					2.00		561.50	561.85	CU	(1;3)	Blija (NL)	TRACTOR, Asse member	Wildenborg et al. (2000)
			2.00	4.00								Range from numerous tests.	Li et al. (2007)
					4.0			223.00	CU	(1;6)	Mol (B)	ATLAS samples	De Bruyn and Labat (2002)
Dilation angle	ψ	[°]	0.0	10.0				223.00			Mol (B)	Averaged over a range of mean effective stress of 2.5-4 Mpa.. For the numerical analysis $\psi_d = 0°$ was adopted.	Bernier et al. (2007c)
			0.0	10.0				223.00			Mol (B)	Characteristic range HADES.	Volckaert et al. (2004); Bernier et al. (2007c)
			4.0	11.0				223.00	HPC		Mol (B)	Sampled at connecting gallery.	Bésuelle et al. (2013)
					23.0							Ref. to Laloui (1993)	François et al. (2009)
Unconfined Compression Strength (UCS)	q_u	[MPa]	2.00	2.80									Gens (2012)
					2.00								Gens et al. (2007)
					2.00			186.00			Mol (B)	From Boisson (2005)	Bock et al. (2010)
					2.00						Mol (B)		Bernier et al. (2007c)
			2.20	2.80									Mertens et al. (2004)
					2.50			223.00	HPC		Mol (B)	Sampled at connecting gallery.	Bésuelle et al. (2013)
NCL slope	λ	[−]	0.1100	0.1600				200.00				Ref. to NEA (1995) report	Barnichon et al. (2000)

Table A.2.: (continued)

Definition	Symb.	Unit	Range ⟨min;max⟩		μ	σ	Depth		Test[1]	N[2]	Location	Note	Source
					0.1577			69.42	HCD	(1;1)	Doel 2b (B)	TRUCK II	Barnichon et al. (2000)
					0.2195			120.57	HCD	(1;1)	Zoersel (B)	TRUCK II	Barnichon et al. (2000)
					0.0685			229.23	HCD	(1;1)	Mol (B)	TRUCK II	Barnichon et al. (2000)
					0.1433			313.30	HCD	(1;1)	Weelde (B)	TRUCK II - Series 1	Barnichon et al. (2000)
					0.1196			478.00	HCD	(1;1)	Blija (NL)	TRUCK II	Barnichon et al. (2000)
			0.1290	0.1300					CU		Antwerp (B)	Reconstituted, shallow	Bouazza et al. (1996)
					0.2400		313.55	314.05	OED		Weelde (B)	TRACTOR, $p'_c = 6.4$MPa	Wildenborg et al. (2000)
					0.1600		313.55	314.05	OED		Weelde (B)	TRACTOR, $p'_c = 6.5$MPa	Wildenborg et al. (2000)
					0.2100		313.55	314.05	OED		Weelde (B)	TRACTOR, $p'_c = 8.0$MPa	Wildenborg et al. (2000)
					0.1600		313.55	314.05	OED		Weelde (B)	TRACTOR, $p'_c = 6.4$MPa	Wildenborg et al. (2000)
					0.2000		453.50	453.80	OED		Blija (NL)	TRACTOR, $p'_c = 7.4$MPa	Wildenborg et al. (2000)
					0.1400		561.50	561.85	OED		Blija (NL)	TRACTOR, Asse member, $p'_c = 7.5$MPa	Wildenborg et al. (2000)
			0.1300	0.1780								Range from numerous tests.	Li et al. (2007)
					0.1103			243.00			Mol (B)		Baldi et al. (1991b)
URL slope	κ	$[-]$	0.02000	0.05000				200.00				Ref. to NEA (1995) report	Barnichon et al. (2000)
					0.0238			69.42	HCD	(1;1)	Doel 2b (B)	TRUCK II	Barnichon et al. (2000)
					0.0133			120.57	HCD	(1;1)	Zoersel (B)	TRUCK II	Barnichon et al. (2000)
					0.0205			229.23	HCD	(1;1)	Mol (B)	TRUCK II	Barnichon et al. (2000)
					0.0164			313.30	HCD	(1;1)	Weelde (B)	TRUCK II - Series 1	Barnichon et al. (2000)
					0.0215			478.00	HCD	(1;1)	Blija (NL)	TRUCK II	Barnichon et al. (2000)
					0.0390				CU		Antwerp (B)	Reconstituted, shallow	Bouazza et al. (1996)
					0.0600		313.55	314.05	OED		Weelde (B)	TRACTOR, $p'_c = 6.4$MPa	Wildenborg et al. (2000)
					0.0600		313.55	314.05	OED		Weelde (B)	TRACTOR, $p'_c = 6.5$MPa	Wildenborg et al. (2000)
					0.0600		313.55	314.05	OED		Weelde (B)	TRACTOR, $p'_c = 8.0$MPa	Wildenborg et al. (2000)
					0.0600		313.55	314.05	OED		Weelde (B)	TRACTOR, $p'_c = 6.4$MPa	Wildenborg et al. (2000)
					0.0600		453.50	453.80	OED		Blija (NL)	TRACTOR, $p'_c = 7.4$MPa	Wildenborg et al. (2000)
					0.0700		561.50	561.85	OED		Blija (NL)	TRACTOR, Asse member, $p'_c = 7.5$MPa	Wildenborg et al. (2000)
			0.01300	0.0460								Range from numerous tests.	Li et al. (2007)
					0.0128			243.00			Mol (B)		Baldi et al. (1991b)
CSL slope	M	$[-]$			0.6865			69.42	HCD	(1;1)	Doel 2b (B)	TRUCK II	Barnichon et al. (2000)
					0.3421			120.57	HCD	(1;1)	Zoersel (B)	TRUCK II	Barnichon et al. (2000)
					0.3541			229.23	HCD	(1;1)	Mol (B)	TRUCK II	Barnichon et al. (2000)
					0.4081			313.30	HCD	(1;1)	Weelde (B)	TRUCK II-Series 1	Barnichon et al. (2000)
					0.3236			478.00	HCD	(1;1)	Blija (NL)	TRUCK II	Barnichon et al. (2000)
					0.7100				CU		Antwerp (B)	Reconstituted, shallow	Bouazza et al. (1996)
					0.8700			243.00			Mol (B)		Baldi et al. (1991b)
					0.8100			247.00	CU		Mol (B)		Horseman et al. (1987)
Saturated hydraulic conductivity	K_{sat}	$[\text{m s}^{-1}]$	2.00E-12	5.00E-12									Gens (2012); Gens et al. (2007)
					7.00E-12			186.00			Mol (B)	From Boisson (2005)	Bock et al. (2010)
			2.00E-12	4.00E-12							Mol (B)		Bernier et al. (2007c)
					1.00E-12						Mol (B)	Approximately	Bastiaens et al. (2006)
			2.00E-12	6.30E-12							Mol (B)	HADES (Oritz, 1997)	Bastiaens et al. (2006)

↪ Table continues on next page.

Table A.2.: (continued)

Definition	Symb.	Unit	Range ⟨min;max⟩		μ	σ	Depth		Test[1]	N[2]	Location	Note	Source
			1.60E-12	4.50E-12					MPM[8]		Mol (B)	Test Drift (Oritz, 1997)	Bastiaens et al. (2006)
					1.40E-12						Mol (B)		Bastiaens et al. (2006)
			4.00E-12	6.00E-12							Mol (B)	Around the connecting gallery	Bastiaens et al. (2006)
					6.10E-12	2.00E-13	159.00		Field		Essen (B)	Essen-1, Transition Zone	Aertsens et al. (2013b)
					8.20E-12	4.00E-13	181.00		Field		Essen (B)	Essen-1, Transition Zone	Aertsens et al. (2013b)
					5.20E-12	2.00E-13	205.00		Field		Essen (B)	Essen-1, Putte Member	Aertsens et al. (2013b)
					4.40E-12	1.00E-13	224.00		Field		Essen (B)	Essen-1, Putte Member	Aertsens et al. (2013b)
					3.50E-12	1.00E-13	232.00		Field		Essen (B)	Essen-1, Putte Member	Aertsens et al. (2013b)
					3.60E-12	2.00E-13	234.00		Field		Essen (B)	Essen-1, Putte Member	Aertsens et al. (2013b)
					6.80E-12	3.00E-13	241.00		Field		Essen (B)	Essen-1, Terhagen Member	Aertsens et al. (2013b)
					2.50E-12	1.80E-12				38	Mol (B)	Mol-1	Aertsens et al. (2013b)
					9.30E-12	4.50E-12				8	Doel (B)	Doel 2b	Aertsens et al. (2013b)
					5.40E-12	1.70E-12				7	Essen (B)	Essen-1	Aertsens et al. (2013b)
					2.94E-12		223.00		HPC		Mol (B)	Sampled at connecting gallery.	Bésuelle et al. (2013)
Vertical saturated hydraulic conductivity	$K_{sat,v}$	[m s^{-1}]			1.00E-12						Mol (B)	Approximately	Bastiaens et al. (2006)
					1.90E-12						Mol (B)	Average URL	Bastiaens et al. (2006)
			1.70E-12	2.30E-12					[9]		Mol (B)		Bastiaens et al. (2006)
			1.30E-12	3.40E-12					Lab		Mol (B)		Rijkers et al. (1998)
					2.10E-12				In situ		Mol (B)		Rijkers et al. (1998)
			1.00E-08	4.00E-08							Westerschelde (NL)		Rijkers et al. (1998)
			4.00E-12	6.00E-12									Li et al. (2007)
					6.20E-12		158.94	159.12	Lab		Essen (B)	W0 to W3, core 14	Labat et al. (2008)
					8.40E-12		180.9	181.08	Lab		Essen (B)	W0 to W3, core 36	Labat et al. (2008)
					5.00E-12		204.7	204.88	Lab		Essen (B)	Boom (Putte), core 60	Labat et al. (2008)
					4.40E-12		223.69	223.87	Lab		Essen (B)	Boom (Putte), core 79	Labat et al. (2008)
					3.40E-12		232.2	232.4	Lab		Essen (B)	Boom (Putte), core 88	Labat et al. (2008)
					3.50E-12		234.41	234.59	Lab		Essen (B)	Boom (Putte), core 90	Labat et al. (2008)
					6.70E-12		241.33	241.53	Lab		Essen (B)	Boom (Terhagen), core 97	Labat et al. (2008)
					1.00E-10		254.71	254.89	Lab		Essen (B)	Boom (Terhagen), core 110	Labat et al. (2008)
					5.43E-10		262.85	263.03	Lab		Essen (B)	Boom (Belsele-Waas), core 118	Labat et al. (2008)
					1.00E-11		277.86	278.04	Lab		Essen (B)	Boom (Belsele-Waas), core 133	Labat et al. (2008)
					4.74E-11		263.05	263.15	Lab		Essen (B)	Boom (Belsele-Waas), core 119	Labat et al. (2008)
					5.55E-12		277.76	277.86	Lab		Essen (B)	Boom (Belsele-Waas), core 133	Labat et al. (2008)
Horizontal saturated hydraulic conductivity	$K_{sat,h}$	[m s^{-1}]			4.60E-12						Mol (B)	Average URL	Bastiaens et al. (2006)
			4.10E-12	5.20E-12					[9]		Mol (B)		Bastiaens et al. (2006)
			3.50E-12	7.90E-12					Lab		Mol (B)		Rijkers et al. (1998)
					4.50E-12				In situ		Mol (B)		Rijkers et al. (1998)
			2.00E-12	4.00E-12									Li et al. (2007)
					6.81E-11		158.94	159.12	Lab		Essen (B)	W0 to W3, core 14	Labat et al. (2008)
					1.33E-11		180.9	181.08	Lab		Essen (B)	W0 to W3, core 36	Labat et al. (2008)
					1.04E-11		204.7	204.88	Lab		Essen (B)	Boom (Putte), core 60	Labat et al. (2008)
					1.18E-11		223.69	223.87	Lab		Essen (B)	Boom (Putte), core 79	Labat et al. (2008)
					6.65E-12		232.2	232.4	Lab		Essen (B)	Boom (Putte), core 88	Labat et al. (2008)
					1.08E-11		234.41	234.59	Lab		Essen (B)	Boom (Putte), core 90	Labat et al. (2008)
					6.92E-12		241.33	241.53	Lab		Essen (B)	Boom (Terhagen), core 97	Labat et al. (2008)

Table A.2.: (continued)

Definition	Symb.	Unit	Range ⟨min;max⟩		μ	σ	Depth		Test[1]	N^2	Location	Note	Source
					3.51E-10		254.71	254.89	Lab		Essen (B)	Boom (Terhagen), core 110	Labat et al. (2008)
					6.22E-10		262.85	263.03	Lab		Essen (B)	Boom (Belsele-Waas), core 118	Labat et al. (2008)
					1.15E-08		277.86	278.04	Lab		Essen (B)	Boom (Belsele-Waas), core 133	Labat et al. (2008)
Hydraulic	K_h/K_v	[−]	2.00	3.00			186.00				Mol (B)	From Boisson (2005)	Bock et al. (2010)
conductivity					2.00						Mol (B)	Approximation	Bastiaens et al. (2006)
anisotropy					10.98		158.94	159.12	Lab		Essen (B)	W0 to W3, core 14	Labat et al. (2008)
					1.58		180.9	181.08	Lab		Essen (B)	W0 to W3, core 36	Labat et al. (2008)
					2.08		204.7	204.88	Lab		Essen (B)	Boom (Putte), core 60	Labat et al. (2008)
					2.68		223.69	223.87	Lab		Essen (B)	Boom (Putte), core 79	Labat et al. (2008)
					1.96		232.2	232.4	Lab		Essen (B)	Boom (Putte), core 88	Labat et al. (2008)
					3.09		234.41	234.59	Lab		Essen (B)	Boom (Putte), core 90	Labat et al. (2008)
					1.04		241.33	241.53	Lab		Essen (B)	Boom (Terhagen), core 97	Labat et al. (2008)
					3.51		254.71	254.89	Lab		Essen (B)	Boom (Terhagen), core 110	Labat et al. (2008)
					1.15		262.85	263.03	Lab		Essen (B)	Boom (Belsele-Waas), core 118	Labat et al. (2008)
					1150.00		277.86	278.04	Lab		Essen (B)	Boom (Belsele-Waas), core 133	Labat et al. (2008)

*   Upper/lower limit not defined

[1]   Test type: CD ... Consolidated and Drained triaxial test; CNL ... Geophysical Neutron Log; CU ... Consolidated and Undrained triaxial test; DT ... sonic log; FDC ... geophysical density log; HCD ... Hydrostatic, Consolidated and Drained triaxial test; HPC ... High Pressure Cell; Lab ... Laboratory; MPM ... Macropermeameter; OED ... Oedometer; SEM ... Scanning Electron Microscopy ; SWV ... Seismic Wave Veleocity

[2]   Tests: (Number of tests;Number of samples).

[3]   Oosterschelde-Ameland (NL).

[4]   Sint-Katelijne-Waver.

[5]   Mean porosity was calculated for each of the five boreholes using only data within the interquartile range (between 25th and 75th percentile; from now on referred to as 50% trimmed mean).

[6]   Indirect, related to velocity of compressional waves, data points digitised.

[7]   Measured porosity, in (a)freeze dried samples, Boom clay/Mol site/HADES borehole 2003-9/connecting gallery/Ring13U/5.82 m to 5.975 m above the Hades URF (intrados).

[8]   Single point steady state measurements.

[9]   Two multi point interference tests around the Test Drift.

Table A.3.: Boom Clay property values govern the thermal behaviour.

Definition	Symb.	Unit	Range ⟨min;max⟩		Depth	Location	Note	Source
Thermal conductivity	λ	[W m^{-1} K^{-1}]		1.690				Boisson (2005)
				1.350		Mol (B)	ATLAS	Li et al. (2007)
				1.700			SAFIR2	Li et al. (2007)
				1.440		Mol (B)	Lab	Li et al. (2007)
				1.350			Used in analysis	Chen et al. (2011)
				1.450		Mol (B)	Used in isotropic analysis	Weetjens (2009)
				1.350	223.00	Mol (B)	Proposed reference equivalent thermal conductivity	Garitte et al. (2012)
				1.350	223.00	Mol (B)	ATLAS (standard deviation 0.05)	Garitte et al. (2012)
				1.440	223.00	Mol (B)	Lab	Garitte et al. (2012)
				1.690				Horseman and McEwen (1996)
Vertical thermal conductivity	λ_v	[W m^{-1} K^{-1}]		1.310			Used in analysis	Chen et al. (2011)
				1.250	223.00	Mol (B)	From ATLAS III with reference to report to be published	Weetjens (2009)
				1.060	223.00	Mol (B)	Proposed reference vertical thermal conductivity	Garitte et al. (2012)
				1.060	223.00	Mol (B)	ATLAS[1]	Garitte et al. (2012)
				1.180	223.00	Mol (B)	Lab	Garitte et al. (2012)
Horizontal thermal conductivity	λ_h	[W m^{-1} K^{-1}]		1.650			Used in analysis	Chen et al. (2011)
				1.700	223.00	Mol (B)	from ATLAS III with reference to report to be published	Weetjens (2009)
				1.550	223.00	Mol (B)	Proposed reference horizontal thermal conductivity	Garitte et al. (2012)
				1.550	223.00	Mol (B)	ATLAS[1]	Garitte et al. (2012)
				1.600	223.00	Mol (B)	Lab	Garitte et al. (2012)
Degree of anisotropy	λ_h/λ_v	[−]		1.260				Chen et al. (2011)
				1.360				Weetjens (2009)
				1.462	223.00	Mol (B)		Garitte et al. (2012)
				1.462	223.00	Mol (B)		Garitte et al. (2012)
				1.356	223.00	Mol (B)		Garitte et al. (2012)
Thermal diffusivity	α	[m^2 s^{-1}]		5.90E-07				Boisson (2005)
				5.96E-07				Horseman and McEwen (1996)
Vol. heat capacity	C	[J m^{-3} K^{-1}]		2.84E-006				Li et al. (2007)
				2.83E-006				Horseman and McEwen (1996)
Thermal dilation coefficient	α_s	[m^3 m^{-3} K^{-1}]	1.00E-05	5.00E-05				Li et al. (2007)
				1.00E-05				Picard (1994)
				1.00E-05			Approximation	Bolzon and Schrefler (2005)
				3.00E-05				Vardoulakis (2002)
				1.30E-05			Value taken from François et al. (2009)	Laloui (1993)
				1.00E-05	223.00	Mol (B)		Baldi et al. (1987, 1991a,b)
Coef. to determine β_p	α_p	[m^3 m^{-3} K^{-1}]		1.00E-04				Picard (1994)
				1.00E-04			Approximation	Bolzon and Schrefler (2005)
Undr. therm. pressurization	Λ	[MPa K^{-1}]		0.060				Vardoulakis (2002)
			0.108	0.189	223.00	Mol (B)		Lima et al. (2009)

[1] Corrected average values (average of the parallel sen- sors and perpendicular sensors considering a power loss of 5%)